

Hot-Mix Asphalt Performance-Related Specification Based on Viscoelastoplastic Continuum Damage (VEPCD) Models

PUBLICATION NO. FHWA-HRT-21-093

JANUARY 2022



U.S. Department of Transportation
Federal Highway Administration

Research, Development, and Technology
Turner-Fairbank Highway Research Center
6300 Georgetown Pike
McLean, VA 22101-2296

FOREWORD

This report addresses the need for more effective long-term quality strategies for pavement construction. Performance-related specifications (PRS) are one such strategy, since the methodology considers long-term pavement performance as part of the construction acceptance and payment arrangement between the highway agency and contractor. This arrangement prioritizes quality, encourages innovation, and protects the funding agency from accepting and paying for substandard materials and construction.

The explicit goal of asphalt concrete–performance modeling is to provide better design and analysis of asphalt pavement structures to resist and better predict pavement failure. The efforts documented in this report have led to performance models like the simplified viscoelastic continuum damage model, shift rutting model, and healing model. This report also documents a mixture level data analysis program, FlexMAT™ version 1.1 and a pavement performance analysis program, FlexPAVE™ version 1.1, that utilizes the material-level performance models and predicts the evolution of the two main forms of pavement distress (i.e., cracking and permanent deformation) using the outputs from FlexMAT.^(1,2)

The research team has verified the FlexPAVE™ program and performance models using a total of 60 asphalt mixtures from 47 different pavement structures in Canada, China, South Korea, and the United States. Efficient test protocols have been proposed to obtain inputs for the suggested models using the asphalt mixture performance tester. The pavement performance predicted by the characterized performance models and FlexPAVE™ program matches field performance with reasonable accuracy and forms the foundation of PRSs applicable to asphalt pavement. This document is intended to introduce the developed models and software programs to asphalt pavement research community and state highway agencies.

Cheryl Allen Richter, P.E., Ph.D.
Director, Office of Infrastructure
Research and Development

Notice

This document is disseminated under the sponsorship of the U.S. Department of Transportation (USDOT) in the interest of information exchange. The U.S. Government assumes no liability for the use of the information contained in this document.

The U.S. Government does not endorse products or manufacturers. Trademarks or manufacturers' names appear in this report only because they are considered essential to the objective of the document.

Quality Assurance Statement

The Federal Highway Administration (FHWA) provides high-quality information to serve Government, industry, and the public in a manner that promotes public understanding. Standards and policies are used to ensure and maximize the quality, objectivity, utility, and integrity of its information. FHWA periodically reviews quality issues and adjusts its programs and processes to ensure continuous quality improvement.

TECHNICAL REPORT DOCUMENTATION PAGE

1. Report No. FHWA-HRT-21-093	2. Government Accession No.	3. Recipient's Catalog No.	
4. Title and Subtitle Hot-Mix Asphalt Performance Related Specification Based on Viscoelastoplastic Continuum Damage (VEPCD) Models		5. Report Date January 2022	
		6. Performing Organization Code	
7. Author(s) Y. Richard Kim (ORCID: 0000-0003-3295-977X), M.N. Guddati, Yeong-Tae Choi, Dahae Kim, Amirhossein Norouzi, Yizhuang David Wang, Behrooz Keshavarzi, Morteza Ashouri, Amir Ghanbari, Andrew D. Wargo, B. Shane Underwood		8. Performing Organization Report No.	
9. Performing Organization Name and Address North Carolina State University Department of Civil, Construction, and Environmental Engineering Campus Box 7908 Raleigh, NC 27695		10. Work Unit No.	
		11. Contract or Grant No. DTFH61-08-H-00005	
12. Sponsoring Agency Name and Address Office of Research and Technology Services Federal Highway Administration 6300 Georgetown Pike McLean, VA 22101		13. Type of Report and Period Covered Final Report; February 2008– December 2020	
		14. Sponsoring Agency Code HRDI-20	
15. Supplementary Notes Kathrine Petros (HRDI-20; ORCID: 0000-0002-1253-0813) served as the Contracting Officer's Representative.			
16. Abstract This report develops and verifies material and structural models for asphalt mixture performance-related specifications (AM-PRS). The models the research team developed and verified in this study include the simplified viscoelastic continuum damage (S-VECD) model for fatigue cracking, the shift model as a permanent deformation model, the healing model based on the viscoelastic continuum damage (VECD) theory, and a structural model called the FlexPAVE™ program. ^(94,119) The FlexPAVE program simulates pavement response and performance under moving loads and climatic changes in the field. In this study, the research team tested and modeled a total of 60 asphalt mixtures from 47 different pavement structures to calibrate and validate the performance models and software. The FlexMAT program processed the laboratory data to determine material properties of these mixes, which the research team then input to the FlexPAVE program with section-specific structure, traffic, and climatic conditions to predict the performance of the 47 asphalt pavements studied. The research team found that the FlexPAVE program can predict field performance with reasonable accuracy. Although not included in the FlexMAT program, efforts from this study resulted in the development of a healing model based on the VECD theory and the impact resonance test method that provides an efficient and inexpensive means of determining the dynamic modulus of asphalt concrete.			
17. Key Words Performance-related specification, fatigue, rutting, healing, viscoelastic, continuum damage, transfer function, FlexMAT, FlexPAVE, impact resonance		18. Distribution Statement No restrictions. This document is available to the public through the National Technical Information Service, Springfield, VA 22161. http://www.ntis.gov	
19. Security Classif. (of this report) Unclassified	20. Security Classif. (of this page) Unclassified	21. No. of Pages 418	22. Price N/A

Form DOT F 1700.7 (8-72)

Reproduction of completed page authorized.

Recommended citation: Federal Highway Administration, Hot-Mix Asphalt Performance Related Specification Based on Viscoelastoplastic Continuum Damage (VEPCD) Models (Washington, DC: 2021)
<https://doi.org/10.21949/1521679>

SI* (MODERN METRIC) CONVERSION FACTORS

APPROXIMATE CONVERSIONS TO SI UNITS

Symbol	When You Know	Multiply By	To Find	Symbol
LENGTH				
in	inches	25.4	millimeters	mm
ft	feet	0.305	meters	m
yd	yards	0.914	meters	m
mi	miles	1.61	kilometers	km
AREA				
in ²	square inches	645.2	square millimeters	mm ²
ft ²	square feet	0.093	square meters	m ²
yd ²	square yard	0.836	square meters	m ²
ac	acres	0.405	hectares	ha
mi ²	square miles	2.59	square kilometers	km ²
VOLUME				
fl oz	fluid ounces	29.57	milliliters	mL
gal	gallons	3.785	liters	L
ft ³	cubic feet	0.028	cubic meters	m ³
yd ³	cubic yards	0.765	cubic meters	m ³
NOTE: volumes greater than 1,000 L shall be shown in m ³				
MASS				
oz	ounces	28.35	grams	g
lb	pounds	0.454	kilograms	kg
T	short tons (2,000 lb)	0.907	megagrams (or "metric ton")	Mg (or "t")
TEMPERATURE (exact degrees)				
°F	Fahrenheit	5 (F-32)/9 or (F-32)/1.8	Celsius	°C
ILLUMINATION				
fc	foot-candles	10.76	lux	lx
fl	foot-Lamberts	3.426	candela/m ²	cd/m ²
FORCE and PRESSURE or STRESS				
lbf	poundforce	4.45	newtons	N
lbf/in ²	poundforce per square inch	6.89	kilopascals	kPa
APPROXIMATE CONVERSIONS FROM SI UNITS				
Symbol	When You Know	Multiply By	To Find	Symbol
LENGTH				
mm	millimeters	0.039	inches	in
m	meters	3.28	feet	ft
m	meters	1.09	yards	yd
km	kilometers	0.621	miles	mi
AREA				
mm ²	square millimeters	0.0016	square inches	in ²
m ²	square meters	10.764	square feet	ft ²
m ²	square meters	1.195	square yards	yd ²
ha	hectares	2.47	acres	ac
km ²	square kilometers	0.386	square miles	mi ²
VOLUME				
mL	milliliters	0.034	fluid ounces	fl oz
L	liters	0.264	gallons	gal
m ³	cubic meters	35.314	cubic feet	ft ³
m ³	cubic meters	1.307	cubic yards	yd ³
MASS				
g	grams	0.035	ounces	oz
kg	kilograms	2.202	pounds	lb
Mg (or "t")	megagrams (or "metric ton")	1.103	short tons (2,000 lb)	T
TEMPERATURE (exact degrees)				
°C	Celsius	1.8C+32	Fahrenheit	°F
ILLUMINATION				
lx	lux	0.0929	foot-candles	fc
cd/m ²	candela/m ²	0.2919	foot-Lamberts	fl
FORCE and PRESSURE or STRESS				
N	newtons	2.225	poundforce	lbf
kPa	kilopascals	0.145	poundforce per square inch	lbf/in ²

*SI is the symbol for International System of Units. Appropriate rounding should be made to comply with Section 4 of ASTM E380.
(Revised March 2003)

TABLE OF CONTENTS

EXECUTIVE SUMMARY	1
Material Models	1
S-VECD Model for Fatigue Cracking Performance.....	1
Shift Model for Rutting Performance	4
Healing Model	5
The FlexMAT™ Program for Mixture Level Data Analysis.....	6
The FlexPAVE Program	6
Field Validation.....	8
Practical Significance.....	9
Material Characterization.....	9
Performance Prediction.....	10
CHAPTER 1. INTRODUCTION	13
Problem Statement.....	13
Objectives.....	15
CHAPTER 2. HISTORICAL EFFORT TO IMPLEMENT PRS.....	17
WesTrack Project Performance-Related Specifications	18
Procedures.....	19
Performance Models	20
NCHRP 9-22 Project Quality Related Specification Software	22
Performance Models (Closed-Form Solutions)	23
Pay Adjustment Factor.....	24
SHRP2 Renewal Project R07	26
CHAPTER 3. MATERIALS USED IN THE PROJECT.....	29
Overview	29
FHWA ALF	29
NCAT Test Track	32
MIT Project.....	35
KEC Test Road	38
NYSDOT Project.....	39
Binzhou, China Perpetual Pavement Project	42
LaDOTD SHRP2 R07 Project	44
New England RAP Mixtures	45
Sample Fabrication.....	45
Field Simulation and Test Air Void Determination.....	45
Sample Fabrication Procedure	47
CHAPTER 4. PERFORMANCE MODELS AND CALIBRATION METHODS	51
Linear Viscoelastic Model	51
Introduction.....	51
Impact Resonance Test	54
Fatigue Performance Model.....	57
Introduction.....	57
S-VECD Model.....	58

Fatigue Failure Criteria	61
Statistical Analysis of Test Results	79
Use of D^R Criterion in Pavement Performance Predictions	86
Permanent Deformation Model	91
Introduction	91
Testing Program—Triaxial Repeated Load Permanent Deformation Test	92
Incremental Model	93
Permanent Deformation Model (Shift Model)	95
Characteristics of Shift Factors	102
Composite Loading Block Test with State Variable	106
Suggested TSS Testing Protocol	110
TSS Test Protocol Verification	114
Simplified TSS Test Method	120
Testing Plan	120
Specimen Preparation	120
Effects of Test Parameters on the Shift Model	121
Verification of Shift Model Calibrated by SSR	133
Use of Actuator Displacement	136
Comparison Among SSR, TSS, and Flow Number Tests	138
Summary	140
Healing Model	140
Introduction	140
Testing Program	141
Characteristics of Healing	143
Characteristic Protocol	152
Damage Evolution Prediction	153
Model and Protocol Verification	161
Summary of Test Methods and Models for PRS Methodology	171
CHAPTER 5. FLEXPAVE PROGRAM	173
Introduction	173
Simplifying Idea	174
Time-Scale Separation	175
Segments	177
Life Stage	178
Layered Viscoelastic Moving Load Analysis	178
Elastic Layer	179
Viscoelastic Layer	180
FlexPAVE Program Engines	181
Solvers	182
Traffic Analysis	182
Thermal Analysis	184
Damage Calculation	185
Rutting Calculation	187
Extrapolation	188
Percent Damage Definition	189
FlexPAVE Program Features	191

General Information.....	191
Materials and Structure.....	192
Fatigue and Rutting.....	192
Climate.....	193
Traffic.....	194
Output and Analysis Options.....	197
CHAPTER 6. PERFORMANCE EVALUATION OF ASPHALT MIXTURES	201
FHWA ALF	201
NCAT Test Track	206
MIT-WMA Project.....	220
MIT-RAP Project.....	228
NYSDOT Perpetual Pavement Project.....	232
KEC Test Road	236
Binzhou Perpetual Pavement Project	242
LaDOTD Pavements.....	246
SUMMARY of the Chapter	248
CHAPTER 7. FIELD VERIFICATION.....	249
Background	249
Fatigue Cracking Predictions	249
Fatigue Damage Calculation.....	249
FHWA ALF	252
NCAT Test Track	254
MIT-RAP	259
MIT-WMA.....	261
KEC.....	263
Binzhou.....	268
Permanent Deformation Predictions.....	271
FHWA ALF	272
NCAT.....	276
MIT	278
KEC.....	280
Binzhou.....	285
Conclusions.....	287
CHAPTER 8. CONCLUSIONS AND FUTURE WORK	289
Conclusions.....	289
Current Research Efforts.....	290
Future Work.....	291
APPENDIX A. USER MANUAL FOR FLEXPAVE VERSION 1.1	293
Introduction.....	293
Software Release	293
Getting Started.....	293
Installation.....	293
Wrapper.....	301
GUI Overview.....	304
Standard Menu and Toolbar.....	305

Navigational Panel	306
Data Panel	306
Error Panel	307
Inputs	307
General Information.....	308
Basic Information.....	308
Analysis Options.....	309
Design Structure.....	310
Layer Properties	310
Climate Data	317
Traffic Data.....	322
Outputs.....	328
Time History Plots	330
Spatial Distribution Contours	331
Saving Results.....	331
Examples.....	333
Response Analysis	333
Performance Analysis	342
APPENDIX B. IR DYNAMIC MODULUS TEST	351
Background	351
IR Test Method for Thin Disk Specimens	353
Case 1	353
Case 2.....	358
Experimental Investigation	358
Materials and Specimen Fabrication.....	358
Testing Plan	359
Optimal Test Conditions	360
Test Temperature	361
Case 1 Versus Case 2.....	362
Ball Size and Drop Height	366
Specimen Thickness.....	366
Comparison With Dynamic Modulus Testing.....	368
APPENDIX C. EXCEL FLEXMAT VERSION 1.1 MANUAL	375
Overview	375
Dynamic Modulus and Cyclic Fatigue Template.....	375
Instructions.....	375
Input Data.....	375
Dynamic Modulus Data	377
Fatigue Data Validity	379
Output Fatigue	381
Input to FlexPAVE	382
SSR Template	382
Instructions.....	383
Input Data.....	383
Permanent Strain Model Coeff	384
Input to FlexPAVE	386

REFERENCES..... 389

LIST OF FIGURES

Figure 1. Graphs. Four material functions used in the S-VECD model.	4
Figure 2. Illustration. Linking permanent strains developed under composite loading history to those developed in the reference test. ⁽¹³⁾	5
Figure 3. Screenshot. S_{xx} (transverse stress) distribution (contour plot) at peak stress time.	7
Figure 4. Screenshot. Stress history plot at center of wheel path.	7
Figure 5. Screenshot. Damage factor distribution after 20-yr simulation.....	8
Figure 6. Screenshot. Rut depth development.	8
Figure 7. Illustration. Continuum of highway specifications. ⁽²²⁾	17
Figure 8. Illustration. WesTrack performance prediction model hierarchy. ⁽¹⁷⁾	19
Figure 9. Graph. Example of cumulative frequency distribution for NCHRP 9-22 rutting module.	25
Figure 10. Graph. Example of penalty/bonus factor predetermined by agency and contractors. ⁽²³⁾ (Note: The horizontal line from (X1, Y1) extends beyond the graph boundary, indicating that the maximum bonus factor is capped at Y1.).....	26
Figure 11. Illustration. Acceptance characteristics tiers for asphalt pavement. ⁽²²⁾	27
Figure 12. Illustration. FHWA ALF experiment overview. ⁽²⁶⁾	30
Figure 13. Illustration. NCAT Test Track layout. ⁽²⁷⁾	32
Figure 14. Illustration. NCAT Test Track pavement sections with different thicknesses (in) and mixture combinations.	33
Figure 15. Illustrations. MIT pavement sections.	36
Figure 16. Illustration. Layout of KEC test sections.	38
Figure 17. Illustration. Binzhou pavement structure layout for each section. ⁽³⁰⁾	42
Figure 18. Graph. Relationship between as-constructed and in-service air void contents.	46
Figure 19. Illustration. Example of calculating air void-content reduction (NCAT-FW section).	47
Figure 20. Illustration. Loose mix sampling schematic.	48
Figure 21. Graph. Example of measured dynamic modulus values at different frequencies and temperatures.	52
Figure 22. Graph. Dynamic modulus master curve.	53
Figure 23. Graph. Example of a t-T shift factor curve.	53
Figure 24. Illustration. Schematic view of stress, pseudostrain, and pseudostiffness definitions. ⁽⁵⁰⁾	59
Figure 25. Graph. Pseudohysteresis loops for controlled CX cyclic tests. ⁽¹¹⁾	64
Figure 26. Schematics. Representation of pseudostiffness and total dissipated pseudostrain energy in the S-VECD model. ⁽¹¹⁾	66
Figure 27. Graphs. Illustration for the G^R failure criteria. ⁽¹¹⁾	68
Figure 28. Graphs. Relationship between the cumulative W^R_C and number of cycles to failure under different test modes and temperatures. ⁽¹¹⁾	70
Figure 29. Graph. Relationship between the cumulative $(1 - C)$ and number of cycles under different test modes and temperatures. ⁽¹¹⁾	71
Figure 30. Graph. Relationship between $Sum(1 - C)$ to failure and N_f . ⁽¹¹⁾	71
Figure 31. Graphs. Failure identification using the D^R criterion in arithmetic and log-log scale. ⁽¹¹⁾	72
Figure 32. Graphs. Implementation of new failure criterion using different mixtures. ⁽¹¹⁾	74

Figure 33. Graphs. Implementation of new failure criterion using ALF mixtures. ⁽¹¹⁾	76
Figure 34. Graphs. Implementation of new failure criterion using MIT mixtures with different RAP contents. ⁽¹¹⁾	77
Figure 35. Graph. Damage characterization curves of NCAT surface mixtures. ⁽¹¹⁾	79
Figure 36. Illustration. Schematic of pavement structures for representative sections at the KEC test road.	86
Figure 37. Graph. G^R failure criterion for the asphalt mixtures used in the KEC test road. ⁽⁶⁸⁾	87
Figure 38. Graphs. Damage contours predicted using the two different failure criteria. ⁽⁶⁸⁾	89
Figure 39. Graphs. Predicted percent damage area for the KEC test sections using the two failure criteria.	90
Figure 40. Graphs. Fitting results of incremental model for FHWA mixture. ⁽¹³⁾	94
Figure 41. Graphs. Verification of load time shifting for FHWA mixture. ⁽¹³⁾	100
Figure 42. Graphs. Verification of stress shifting for the FHWA mixture and the NY9.5B mixtures. ⁽¹³⁾	102
Figure 43. Graphs. Load-time shift factors and deviatoric stress shift factors of the FHWA and NY9.5B mixtures. ⁽¹³⁾	104
Figure 44. Illustration. Linking the composite loading test to the TRLPD test. ⁽¹³⁾	108
Figure 45. Graphs. Predictions by the shift model calibrated using the composite test. ⁽¹⁾	110
Figure 46. Graph. Example of a cumulative density function of permanent strain according to pavement temperatures at Angelica, NY. ⁽¹⁾	113
Figure 47. Illustrations. Schematic diagram of proposed testing protocol. ⁽¹⁾	114
Figure 48. Graphs. Random loading history at 47°C. ⁽¹⁾	116
Figure 49. Graph. Calibration process with protocol testing for the NY9.5B mixture. ⁽¹⁾	117
Figure 50. Graphs. Predictions of the model calibrated by protocol testing. ⁽¹⁾	118
Figure 51. Graphs. Effect of number of temperatures on shift factors. ⁽⁹⁷⁾	123
Figure 52. Graph. Averaged reduced load time shift factor from PRS database. ⁽⁹⁷⁾	124
Figure 53. Graphs. Comparison of calibration processes for TSS and SSR protocols. ⁽⁹⁷⁾	129
Figure 54. Graphs. Effect of rest periods on permanent strains with reversed loading blocks. ⁽⁹⁷⁾	131
Figure 55. Graphs. Random loading history predictions with various rest periods for RS9.5B. ⁽⁹⁷⁾	135
Figure 56. Graph. Effect of rest period in the rut depth prediction from the SSR test. ⁽⁹⁷⁾	136
Figure 57. Graph. Comparison of RS9.5B mixture permanent strains based on actuator displacement and loose-core LVDTs. ⁽⁹⁷⁾	137
Figure 58. Graph. Rut depth prediction of RS9.5B using FlexPAVE based on loose-core LVDTs, actuator displacement, and corrected strains. ⁽⁹⁷⁾	138
Figure 59. Graphs. Typical group-rest healing test with 30-s rest period.....	143
Figure 60. Graphs. Results of group-rest healing test at 30°C with 30-s rest period.	145
Figure 61. Graphs. Parameters for calculating pseudostiffness and percent healing.....	147
Figure 62. Graphs. Percent healing according to pseudostiffness and rest period.	149
Figure 63. Graphs. Relationship between percent healing and reduced rest period.	150
Figure 64. Graph. Fitting parameters for percent healing master curves with pseudostiffness.	151
Figure 65. Graphs. Healing master curves fitted using three selective tests.....	153
Figure 66. Graph. Damage characteristic curves for all the tests at 30°C.....	154

Figure 67. Graphs. Damage characteristic curves for continuous fatigue test and pulse-rest healing tests at 30°C.....	156
Figure 68. Graph. Damage characteristic curves for continuous fatigue test and pulse-rest healing tests in the $\log(1 - C) - \log(S)$ space after shifting at 30°C.	157
Figure 69. Graph. $1/h(C, RP_R)$ as a function of pseudostiffness and reduced rest period.	158
Figure 70. Graph. Damage characteristic curves for continuous fatigue test and pulse-rest tests using the new scheme.....	159
Figure 71. Graphs. Comparison of damage characteristic curves from actual pulse-rest healing tests and shifting procedure at 30°C.....	161
Figure 72. Graphs. Comparison of healing properties between SBS and RS9.5B mixtures at different temperatures and rest periods.	163
Figure 73. Graphs. Healing master curves of SBS mixture.....	164
Figure 74. Graph. Damage characteristic curve for continuous fatigue test.....	165
Figure 75. Graphs. Comparison of damage characteristic curves for actual pulse-rest healing tests and predictions.	167
Figure 76. Graphs. Strain history of pulse-rest test.	168
Figure 77. Graph. Comparison between measured and predicted strain amplitudes.....	169
Figure 78. Illustration. Flowchart of proposed protocol for healing model.....	170
Figure 79. Illustration. Pavement performance analysis framework in the FlexPAVE program.	176
Figure 80. Illustration. Coordinate definition in the FlexPAVE program.	179
Figure 81. Illustration. Reference area for percent damage definition. ⁽¹⁰⁹⁾	190
Figure 82. Illustration. Pavement performance analysis and design life.	192
Figure 83. Screenshot. Example of temperature input (EICM case).	194
Figure 84. Screenshot. Determining contact area shape for wheels in the FlexPAVE program.	195
Figure 85. Screenshot. S_{xx} distribution at peak stress time.	197
Figure 86. Screenshot. Stress history plot at center of wheel path.	198
Figure 87. Screenshot. Damage factor distribution after 20-yr simulation.....	199
Figure 88. Screenshot. Percent damage evolution.	199
Figure 89. Screenshot. Rut depth development.	200
Figure 90. Graphs. Linear viscoelastic characteristic curves for FHWA ALF mixtures. ⁽¹¹¹⁾	202
Figure 91. Graph. Damage characteristic curves for FHWA ALF mixtures. ⁽¹¹¹⁾	203
Figure 92. Graph. Failure criterion curves for FHWA ALF mixtures. ⁽¹¹¹⁾	203
Figure 93. Graphs. Permanent deformation results from TSS tests of FHWA ALF mixtures. ⁽⁹⁹⁾	206
Figure 94. Graphs. Linear viscoelastic characteristic curves for NCAT surface mixtures. ⁽¹¹¹⁾	207
Figure 95. Graphs. Linear viscoelastic characteristic curves for NCAT intermediate mixtures. ⁽¹¹¹⁾	208
Figure 96. Graphs. Linear viscoelastic characteristic curves for NCAT base mixtures. ⁽¹¹¹⁾	209
Figure 97. Graphs. Damage characteristic curves for NCAT mixtures. ⁽¹¹¹⁾	211
Figure 98. Graphs. G^R versus N_f curves for NCAT mixtures. ⁽¹¹¹⁾	212
Figure 99. Graphs. TSS test results for NCAT surface mixtures.....	215
Figure 100. Graphs. TSS test results for NCAT intermediate mixtures.	217
Figure 101. Graphs. TSS test results for NCAT base mixtures.	219

Figure 102. Graphs. Linear viscoelastic characteristic curves for MIT-WMA surface-layer mixtures. ⁽¹¹²⁾	221
Figure 103. Graphs. Linear viscoelastic characteristic curves for MIT-WMA bottom-layer mixtures. ⁽¹¹²⁾	222
Figure 104. Graphs. Damage characteristic curves for MIT-WMA mixtures. ⁽¹¹²⁾	223
Figure 105. Graphs. G^R versus N_f curves for MIT-WMA mixtures. ⁽¹¹²⁾	224
Figure 106. Graphs. Permanent strain levels of MIT-WMA surface-layer mixtures.	226
Figure 107. Graphs. TSS test results for MIT-WMA mixtures with 35-percent RAP.	227
Figure 108. Graphs. Linear viscoelastic characteristic curves for MIT-RAP mixtures. ⁽¹¹²⁾	228
Figure 109. Graph. Damage characteristic curves for MIT-RAP mixtures. ⁽¹¹²⁾	229
Figure 110. Graph. G^R versus N_f curves for MIT-RAP mixtures. ⁽¹¹²⁾	229
Figure 111. Graphs. TSS test results for MIT-RAP mixtures.....	231
Figure 112. Graph. Comparison of permanent strain levels for MIT-RAP mixtures at the high temperature.....	232
Figure 113. Graphs. Linear viscoelastic characteristic curves for NYSDOT mixtures.....	233
Figure 114. Graph. Damage characteristic curves for NYSDOT mixtures.	234
Figure 115. Graph. Failure criterion curves for NYSDOT mixtures.....	234
Figure 116. Graphs. TSS test results for NYSDOT mixtures.....	236
Figure 117. Graphs. Linear viscoelastic characteristic for KEC mixtures. ⁽¹¹⁴⁾	237
Figure 118. Graph. Damage characteristic curves for KEC mixtures. ⁽¹¹⁴⁾	238
Figure 119. Graph. Failure criterion curves for KEC mixtures. ⁽¹¹⁴⁾	239
Figure 120. Graphs. TSS test results for the KEC mixtures. ⁽¹¹⁴⁾	241
Figure 121. Graphs. Linear viscoelastic characteristic curves for Binzhou mixtures. ⁽³⁰⁾	243
Figure 122. Graph. Damage characteristic curves for Binzhou mixtures. ⁽³⁰⁾	244
Figure 123. Graph. Failure criterion curves for Binzhou mixtures. ⁽³⁰⁾	244
Figure 124. Graphs. TSS test results for the Binzhou mixtures.....	246
Figure 125. Graphs. Linear viscoelastic characteristic curves for LaDOTD mixtures.....	247
Figure 126. Graph. Damage characteristic curves for LaDOTD mixtures.	247
Figure 127. Graphs. TSS test results for the LaDOTD mixtures.....	248
Figure 128. Contours. Damage factors of 20-yr simulations of FHWA ALF sections. ⁽⁶⁸⁾	251
Figure 129. Graphs. Cracking evolution in FHWA ALF sections. ⁽⁶⁸⁾	253
Figure 130. Graphs. Measured cracking area versus predicted damage area. ⁽⁶⁸⁾	254
Figure 131. Contours. Four-year FlexPAVE simulation results for NCAT mixtures. ⁽⁶⁸⁾	258
Figure 132. Graphs. Cracking evolution in NCAT Test Track sections.....	259
Figure 133. Graph. Measured cracking area versus predicted damage area for NCAT Test Track sections. ⁽⁶⁸⁾	259
Figure 134. Contours. Twenty-year FlexPAVE simulation results for MIT-RAP mixtures.	261
Figure 135. Contours. Twenty-year FlexPAVE simulation results for MIT-WMA mixtures....	263
Figure 136. Contours. Six-year FlexPAVE simulation results for KEC test road sections.....	267
Figure 137. Graphs. Damage and cracking evolution in KEC test sections. ⁽⁶⁸⁾	268
Figure 138. Contours. Fifteen-year FlexPAVE simulation results for the Binzhou test road sections. ⁽⁶⁸⁾	271
Figure 139. Graph. FlexPAVE prediction of percent damage area increase for the Binzhou pavements. ⁽⁶⁸⁾	271
Figure 140. Graphs. Rut depth comparisons of FHWA test sections using the original unbound material model.....	274

Figure 141. Graphs. Rut depth comparisons of FHWA test sections using the MEPDG unbound material model.....	276
Figure 142. Graph. Original unbound material model measured versus predicted rut depths for NCAT Test Track sections after 2 yr of traffic.	277
Figure 143. Graph. MEPDG unbound material model measured versus predicted rut depths for NCAT Test Track sections after 2 yr of traffic.	277
Figure 144. Graphs. Original unbound material model measured versus predicted rut depths for MIT sections.....	279
Figure 145. Graphs. MEPDG unbound material measured versus predicted rut depths for MIT sections.....	280
Figure 146. Graphs. Effects of different parameters on rutting performance for KEC sections using the original unbound material model.	283
Figure 147. Graphs. Effects of different parameters on rutting performance for KEC sections using the MEPDG unbound material model.	285
Figure 148. Graph. Original unbound material model measured versus predicted rut depths of Binzhou sections.	286
Figure 149. Graph. MEPDG unbound material model measured versus predicted rut depths of Binzhou sections.....	287
Figure 150. Screenshot. Window to start FlexPAVE setup.....	294
Figure 151. Screenshot. FlexPAVE license agreement.	295
Figure 152. Screenshot. Selecting the destination location.	296
Figure 153. Screenshot. Start installation.	297
Figure 154. Screenshot. MCR installer.....	298
Figure 155. Screenshot. MCR license agreement.	299
Figure 156. Screenshot. Finalize the FlexPAVE setup.....	300
Figure 157. Screenshot. Overview of FlexPAVE wrapper.....	301
Figure 158. Screenshot. Get Password window.....	302
Figure 159. Screenshot. Run FlexPAVE window.	303
Figure 160. Screenshot. Overview of FlexPAVE GUI.....	304
Figure 161. Screenshot. Standard menu and toolbar.	305
Figure 162. Screenshot. Batch Mode Analysis window.	306
Figure 163. Screenshot. General Information tab.....	308
Figure 164. Screenshot. Design Structure tab.....	310
Figure 165. Screenshot. Dynamic modulus input screen.....	311
Figure 166. Screenshot. Viscoelastic material parameters obtained from test data.....	312
Figure 167. Screenshot. Format of Excel file to input rutting property data.	316
Figure 168. Screenshot. Adding material properties to program database.....	317
Figure 169. Screenshot. EICM database module.....	318
Figure 170. Screenshot. EICM temperature data for pavement response analysis.....	319
Figure 171. Screenshot. Isothermal temperature input.	319
Figure 172. Screenshot. Manually input temperature data for pavement response analysis.	320
Figure 173. Screenshot. Temperature data from EICM database for pavement performance analysis.	321
Figure 174. Screenshot. Temperature data for pavement performance analysis.	322
Figure 175. Screenshot. Adding vehicle data to program database.....	323
Figure 176. Screenshot. Design Vehicle Information tab.....	323

Figure 177. Screenshot. Traffic Data tab.....	324
Figure 178. Screenshot. Axle Configuration dialogue box.....	325
Figure 179. Screenshot. Special truck configuration.....	326
Figure 180. Screenshot. Output and analysis options.....	327
Figure 181. Illustration. Coordinate system.....	328
Figure 182. Screenshot. Output tab.....	329
Figure 183. Screenshot. Loading the output for pavement performance analysis.....	329
Figure 184. Screenshot. Example of stress time history plot.....	330
Figure 185. Screenshot. Example of spatial distribution contour plot.....	331
Figure 186. Screenshot. Export wizard.....	332
Figure 187. Screenshot. Editing plot lines.....	332
Figure 188. Screenshot. Export results as a table.....	333
Figure 189. Screenshot. General Information tab for pavement response analysis.....	335
Figure 190. Screenshot. Material properties of first asphalt layer.....	336
Figure 191. Screenshot. Material properties of second asphalt layer.....	336
Figure 192. Screenshot. Material properties of aggregate base layer.....	337
Figure 193. Screenshot. Material properties of subgrade layer.....	338
Figure 194. Screenshot. Isothermal input for climate data.....	339
Figure 195. Screenshot. General inputs for traffic load.....	340
Figure 196. Screenshot. Evaluation points.....	341
Figure 197. Screenshot. S_{xx} distribution at peak stress time.....	342
Figure 198. Screenshot. Stress history plot at center of wheel path.....	342
Figure 199. Screenshot. General information for performance analysis.....	344
Figure 200. Screenshot. Material properties of first asphalt concrete layer for performance analysis.....	344
Figure 201. Screenshot. Material properties of second asphalt concrete layer for performance analysis.....	345
Figure 202. Screenshot. EICM input.....	345
Figure 203. Screenshot. Traffic input for performance analysis.....	346
Figure 204. Screenshot. Wheel properties.....	347
Figure 205. Screenshot. Output and analysis options.....	348
Figure 206. Screenshot. Transverse stress distribution (response results).....	349
Figure 207. Screenshot. Damage factor distribution after 20-yr simulation.....	349
Figure 208. Screenshot. Percent damage distribution as a function of time.....	350
Figure 209. Screenshot. Rut depth development.....	350
Figure 210. Graphs. Example of signals for one of the specimens.....	352
Figure 211. Illustration. Half-power bandwidth method.....	352
Figure 212. Illustrations. Pickup and impact points in different cases for IR test setup. ⁽¹²¹⁾	354
Figure 213. Illustrations. Test setup in IR tests. ⁽¹²¹⁾	355
Figure 214. Photos. Test device in different setups in IR tests. ⁽¹²¹⁾	356
Figure 215. Graphs. CVs of resonant frequency and phase angle for case 1-1. ⁽¹²¹⁾	362
Figure 216. Graph. Comparison of dynamic modulus values between IR test and conventional test. ⁽¹²¹⁾	363
Figure 217. Graphs. CVs in case 1 and case 2.....	364
Figure 218. Graphs. CVs with different ball sizes. ⁽¹²¹⁾	365
Figure 219. Graphs. CVs with balls dropped at different heights. ⁽¹²¹⁾	366

Figure 220. Graphs. Comparison of $ E^* _{T 342}$ and $ E^* _{IR}$ test results obtained from specimens at different thicknesses. ⁽¹²¹⁾	368
Figure 221. Graphs. Comparison of material properties measured from IR tests and T 342-11 tests for NY9.5, NY19, and NY25 mixtures.	371
Figure 222. Screenshot. Input Data tab.....	377
Figure 223. Screenshot. Dynamic Modulus Data tab.	377
Figure 224. Screenshot. Prony Series table.	378
Figure 225. Screenshot. Alpha calculation.	379
Figure 226. Screenshot. Fatigue Data Validity tab.	380
Figure 227. Screenshot. Output Fatigue tab.....	381
Figure 228. Screenshot. Input to FlexPAVE tab.....	382
Figure 229. Screenshot. Instructions tab.....	383
Figure 230. Screenshot. Input Data tab.....	384
Figure 231. Screenshot. Permanent Strain Model Coeff tab.	385
Figure 232. Screenshot. Inputs to FlexPAVE tab.	386
Figure 233. Screenshot. Rutting Strain Index parameter tab.	387

LIST OF TABLES

Table 1. FHWA ALF hot mix asphalt materials information.....	31
Table 2. NCAT Test Track asphalt mixture information.....	34
Table 3. MIT WMA asphalt mixture information (NMAS 16 mm).....	37
Table 4. MIT RAP asphalt mixture information (NMAS 16 mm).	37
Table 5. KEC test road mixture information.	39
Table 6. Gradations of the KEC test road mixtures.....	39
Table 7. NYSDOT mixture information.	41
Table 8. HMA material description.	43
Table 9. LaDOTD mixture information.....	44
Table 10. New England RAP mixture information.	45
Table 11. Summary of D^R values for study mixtures.	78
Table 12. Test data for two representative asphalt mixtures.	79
Table 13. Statistical analysis of test data using linear regression method.....	82
Table 14. Statistical analysis of test data assuming normal D^R value distribution.	85
Table 15. Mixture information and test conditions for TRLPD tests.	92
Table 16. Testing plan for verifying the proposed testing protocol.....	115
Table 17. Summary of TSS test protocol.....	119
Table 18. Summary of various tests performed in this study on RS9.5B mixture.	121
Table 19. Comparison of testing temperature selection methods.....	125
Table 20. Pulse time at different temperatures.	126
Table 21. Coefficients for shift model.....	132
Table 22. Comparison of permanent deformation testing methods.....	139
Table 23. Fitting parameters for percent healing master curves.....	152
Table 24. Characteristic test conditions for SBS mixture (group-rest test).....	162
Table 25. Verification test conditions for SBS mixture.....	165
Table 26. Example showing the amount of time saved using proposed protocol.....	169
Table 27. D^R values for FHWA ALF mixtures.....	203
Table 28. D^R values for NCAT Test Track mixtures.....	213
Table 29. D^R values for MIT-WMA mixtures.....	224
Table 30. D^R values for MIT-RAP mixtures.....	230
Table 31. D^R values for NYSDOT mixtures.....	234
Table 32. D^R values for KEC mixtures.....	239
Table 33. D^R values for Binzhou mixtures.	244
Table 34. D^R values of LADOTD mixtures.....	247
Table 35. Summary of fatigue predictions.....	288
Table 36. Summary of rutting predictions.....	288
Table 37. Format of text file to input dynamic modulus experimental data.....	311
Table 38. Format of Excel file to input dynamic modulus data.....	313
Table 39. Format of Excel file to input S-VECD fatigue property data.....	314
Table 40. Format of EICM text file (e.g., WY nodal temp).	318
Table 41. Format of text file to input temperature manually.....	320
Table 42. Format of the text file to input coordinates of evaluation points.....	328
Table 43. Prony coefficients for first asphalt concrete layer (left) and second asphalt concrete layer (right).	334

Table 44. Shift factor parameters for first (top) and second (bottom) asphalt concrete layer. ...	334
Table 45. Fatigue performance model parameters for first (top) and second (bottom) asphalt concrete layer.	343
Table 46. Rutting performance model parameters for first (top) and second (bottom) asphalt concrete layer.	343
Table 47. IR test set-up summary for thin disk specimens.	353
Table 48. Summary of IR test conditions.	360
Table 49. Measured and assumed Poisson's ratios for case 1 and case 2.	362
Table 50. Resonant frequency (Hz) of IR test results for a 16-mm-diameter ball dropped from a 20-cm height.	372
Table 51. Damping ratio of IR test results for a 16-mm-diameter ball dropped from a 20-cm height.	372

LIST OF ABBREVIATIONS

3D FEM	three-dimensional finite-element method
AADTT	average annual daily truck traffic
ABC	aggregate base course
ALF	Accelerated Load Facility
AMPT	asphalt mixture performance tester
AM-PRS	asphalt mixture-performance-related specifications
AQC	acceptance quality characteristics
AVL	low air void content
COS	control on-specimen strain
CR-TB	crumb rubber-terminal blend
CS	controlled stress
CV	coefficient of variation
CX	controlled crosshead
DD	degree-days
DMR	dynamic modulus ratio
DPSE	dissipated pseudostrain energy
DSR	dynamic shear rheometer
EICM	Enhanced Integrated Climatic Model
ESAL	equivalent single-axle load
FEM	finite-element method
FFE	Fourier finite element
FFT	fast Fourier transform
FHWA	Federal Highway Administration
GUI	graphical user interface
HMA	hot-mix asphalt
IR	impact resonance
ISV	internal state variable
KEC	Korea Expressway Corporation
LaDOTD	Louisiana Department of Transportation and Development
LCC	life cycle cost
LEA	layered elastic analysis
LOE	line of equality
LSPM	large stone porous mixture
LVDT	linear variable differential transformer
LVEA	layered viscoelastic analysis
LVEMA	layered viscoelastic moving-load analysis
MCR	MATLAB Compiler Runtime
MEPDG	<i>Mechanistic-Empirical Pavement Design Guide</i>
MIT	Manitoba Infrastructure and Transportation
MSR	minimum strain rate
NCAT	National Center for Asphalt Technology
NCHRP	National Cooperative Highway Research Program
NMAS	nominal maximum aggregate size
NYSDOT	New York State Department of Transportation

OGFC	open-graded friction course
PCC	portland concrete cement
PG	performance grade
PLD	predicted life difference
PRS	performance-related specifications
QA	quality assurance
QRSS	Quality-Related Specification Software
RAP	reclaimed asphalt pavement
RSI	Rutting Strain Index
RTFO	rolling thin film oven
RVE	representative volume entity
SBS	styrene butadiene styrene
SHRP	Strategic Highway Research Program
SMA	stone matrix asphalt
SSR	Stress Sweep Rutting (test method)
S-VECD	simplified viscoelastic continuum damage
TRLPD	triaxial repeated load permanent deformation
TRS	thermorheologically simple
TSS	triaxial stress sweep
t-SS	time-stress superposition
t-T	time-temperature
t-TS	time-temperature superposition
VECD	viscoelastic continuum damage
WMA	warm-mix asphalt

EXECUTIVE SUMMARY

This report details findings from a Federal Highway Administration (FHWA)-funded study to develop performance prediction models for asphalt mixtures and asphalt pavements as the basis for performance-related specifications (PRS). An introduction outlining the research objectives and scope of the project is provided in chapter 1. Chapter 2 reviews historical asphalt pavement PRS projects, and chapter 3 describes asphalt materials and pavements used in this study. Chapter 4 of this report presents performance prediction models, a key component of PRS, that evaluate the quality of constructed asphalt pavements, and chapter 5 describes the pavement performance analysis program, FlexPAVE™ version 1.1, that utilizes these performance prediction models and predicts the evolution of the two main forms of pavement distress (i.e., cracking and permanent deformation).⁽¹²⁾ Chapter 6 presents the performance evaluation results of various asphalt mixtures tested in this study, while chapter 7 describes the field verification of the developed performance prediction models and the FlexPAVE program. Finally, conclusions from this study and future research recommendations are given in chapter 8. Appendices A, B, and C present the user manual for FlexPAVE version 1.1, development of the impact resonance dynamic modulus test, and Excel-based FlexMAT™ version 1.1 manual.

Performance prediction models this project included were a fatigue cracking model, a healing model, and a permanent deformation model. The project also developed efficient test protocols as characterization methods of these models. The study implemented the performance prediction models in a structural model—the FlexPAVE program—which uses three-dimensional layered viscoelastic analysis to compute responses and long-term performance of asphalt pavements under moving loads and changing climatic conditions.

This Executive Summary section provides a brief overview of the performance prediction models, the FlexPAVE program, field validation, and calibration efforts used in this study. It also discusses the practical significance of the outcomes of this research.

MATERIAL MODELS

Three models were developed in this research project to predict the fatigue cracking, rutting, and healing performance of asphalt mixtures. Chapter 4 details model development, test protocols, and analysis results.

S-VECD Model for Fatigue Cracking Performance

The simplified viscoelastic continuum damage (S-VECD) model is a simplified version of the full viscoelastic continuum damage (VECD) model.⁽¹⁻⁷⁾ The simplification reduces the analysis time and effort and alleviates the need to perform the millions of calculations required for applying the full VECD model to a loading history with tens of thousands of cycles.

The S-VECD model is based on three mechanistic principles. The first is the use of pseudostrain. Pseudostrain removes the viscoelastic effects (i.e., the effects of loading rate and temperature) on asphalt mixture behavior from the stress–strain data and allows accurate modeling of other mechanisms, such as fatigue damage and healing. The second principle is the continuum damage theory, which provides a mechanistic foundation to model the growth of microcracks and

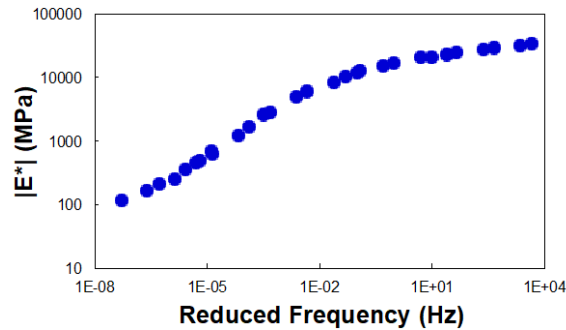
eventual macrocracks. The third principle is the time–temperature superposition (t–TS) principle with growing damage. This principle allows t–TS factors obtained from linear viscoelastic tests, such as dynamic modulus testing, to represent the effects of time and temperature on the behavior of asphalt mixtures with growing damage. The implications of this principle are significant because it allows tests performed at a single combination of loading rate and temperature to evaluate asphalt mixture performance under various combinations of loading rates and temperatures.

This study implemented cyclic fatigue testing to characterize asphalt mixtures using these principles. The major advantage of this test is its use of relatively uniform stresses and strains in the middle portion of the test specimen, which allows for accurate application of the three mechanistic principles without being affected by specimen geometry, boundary conditions, and so on. Another advantage of cyclic fatigue testing is that it can use the asphalt mixture performance tester (AMPT). The AMPT cyclic fatigue test method was developed as a part of this research project and was balloted and approved by the American Association of State Highway and Transportation Officials (AASHTO) as TP 107, *Standard Method of Test for Determining the Damage Characteristic Curve of Asphalt Concrete from Direct Tension Cyclic Fatigue Tests*.⁽³⁷⁾

Chapter 4 describes the calculations behind the S-VECD model, but the practical implications of the model are explained in this section. Two important engineering properties result from applying the three principles to stress–strain data obtained from the cyclic fatigue test. The first is the relationship (known as the damage characteristic curve) between pseudostiffness (C) and the damage parameter (S). C represents the integrity of the test specimen, and S represents the amount of fatigue damage in the specimen. A reduction in the C value implies an increased level of fatigue damage. The second engineering property is the relationship between fatigue life in terms of number of cycles to failure (N_f) and the average reduction in pseudostiffness up to failure (D^R). This relationship serves as the failure criterion in the S-VECD model. Figure 1 presents four material functions used in the S-VECD model: the dynamic modulus master curve and time–temperature (t–T) shift factor determined by AASHTO T 378, *Standard Method of Test for Determining the Dynamic Modulus and Flow Number for Hot Mix Asphalt (HMA) Using the Asphalt Mixture Performance Tester (AMPT)*, and R 84, *Developing Dynamic Modulus Master Curves for Asphalt Mixtures Using the Asphalt Mixture Performance Tester (AMPT)*, specifications and the damage characteristic curve and pseudoenergy-based failure criterion characterized by the TP 107 specification.^(9,10)

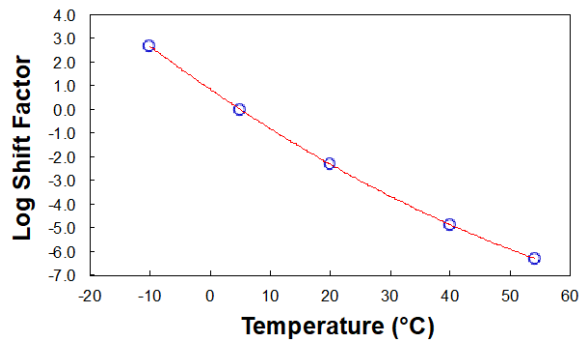
One of the major strengths of the S-VECD model over empirically-based methods is that both the damage characteristic curve and the D^R -based failure criterion are independent of loading condition and temperature. The unique relationships between the amount of damage and the material's integrity (i.e., the damage characteristic curve) and between the energy input and the fatigue failure strongly suggest that the damage characteristic curve captures the material's fundamental behavior. This loading history and temperature independence means that these engineering properties can be determined at a single condition and that the model can predict the performance of the mixture under other conditions (e.g., different stress and strain levels, temperatures, loading frequencies, or even under complex loading histories where these conditions change randomly). The comprehensive characterization of the fatigue performance of a mixture under a wide range of loading and temperature conditions is time-consuming for more

empirically-based approaches due to the number of tests required for characterization, but the mechanistic nature of the S-VECD model reduces the fatigue testing time by orders of magnitude. This increased efficiency in testing and the ability of the S-VECD model to capture the fundamental behavior of asphalt mixtures makes the model especially suitable for practical applications (discussed later in the Material Characterization subsection of the Practical Significance section).



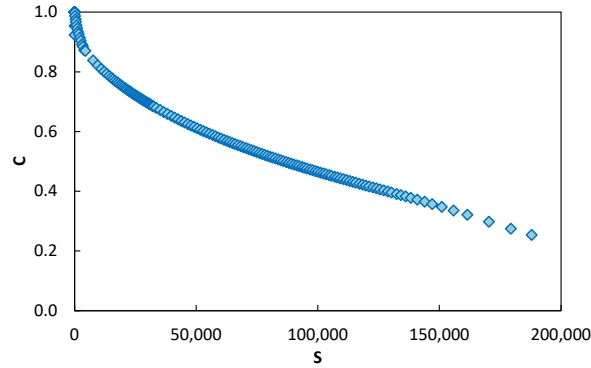
Source: FHWA.
1 MPa = 145.04 psi.

A. Dynamic modulus master curve.



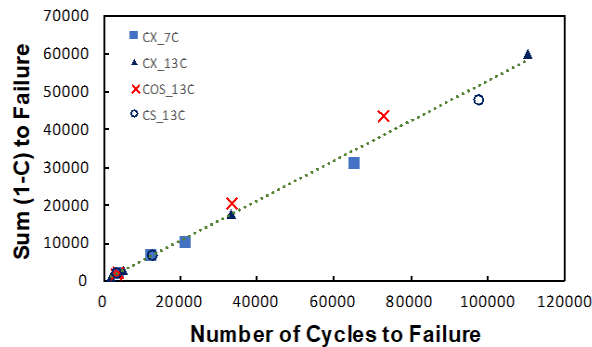
Source: FHWA.
0°C = 32°F.

B. t-T shift factor.



Source: FHWA.

C. Damage characteristic curve.



Source: FHWA.

D. Pseudoenergy-based failure criterion.⁽¹¹⁾

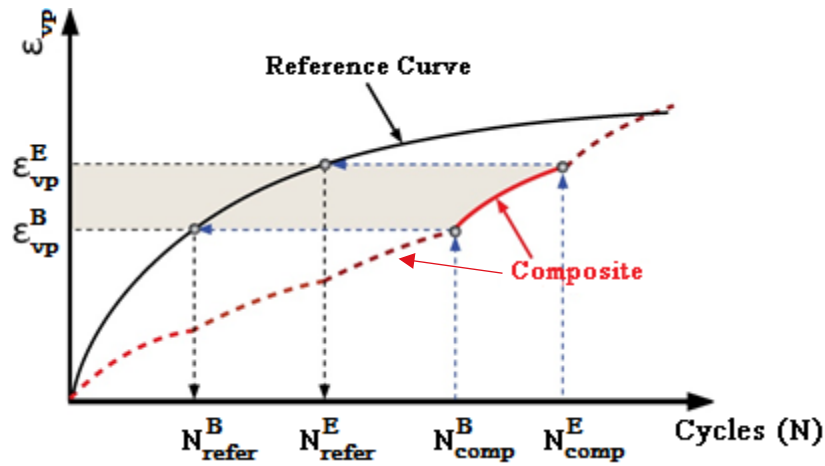
Figure 1. Graphs. Four material functions used in the S-VECD model.

Shift Model for Rutting Performance

Adequate rutting models for asphalt mixtures should be able to account for the effects of the stress state, temperature, and loading time. As is the case for fatigue cracking characterization, experimentally evaluating the effects of these variables on rutting would be too time-consuming for State highway agencies to implement in their routine mixture evaluations and pavement analyses. In this research, the shift model was developed by simplifying the rigorous viscoelastic model previously developed at North Carolina State University.⁽¹²⁾ The shift model accounts for the changes in permanent deformation that occur due to changes in loading time and temperature, as well as the difference between the applied vertical stress and the confining stress (known as deviatoric stress). Longer loading times, higher temperatures, and higher deviatoric stress levels result in more permanent deformation.

The shift model is based on the concept that a standard set of conditions will produce a relationship between permanent deformation and the number of load cycles. Equivalent levels of permanent deformation will develop at a different number of cycles for loading conditions that differ from the reference condition, or reference curve, as depicted in figure 2. Using the data obtained from various combinations of deviatoric stress and temperature, the model calculates

the amount of shifting that is required for each combination to match the reference curve. This shifting takes into account the effects of the differences caused by both the deviatoric stress and the test temperature by having separate shift factors for each effect.



© 2013 Road Materials and Pavement Design. (DTFH61-08-H-00005)

Figure 2. Illustration. Linking permanent strains developed under composite loading history to those developed in the reference test.⁽¹³⁾

Once these shift factors are determined from the experimental data, shift factor functions can be developed. Then, the model can estimate the response of the material under any combination of deviatoric stress and temperature by applying the shift factor equations along with the shift model.

Characterizing the shift model requires the material’s behavior under different temperatures and stress levels. The triaxial stress sweep (TSS) test was developed for this purpose. Details of the shift model and TSS test development are presented in chapter 4. Further simplifying the original TSS test protocol resulted in the simplified TSS, known as the Stress Sweep Rutting (SSR) test method. The SSR test protocol employs cyclic triaxial tests in the AMPT with three loading groups of different deviatoric stresses at high and low temperatures. Chapter 4 describes SSR development efforts.

Healing Model

Healing occurs in asphalt concrete mixtures and binders. Due to the healing process, existing microcracks in the asphalt layers of pavement caused by the previous load cycles can be “cured,” and thus the mixture can either partially or completely regain its strength, leading to rest periods increasing the fatigue life of asphalt concrete.

This research developed a mechanistic healing model by extending the continuum damage theory and t–TS principle with growing damage to include the material’s recovery that occurs due to healing during rest periods. The healing model is based on a percent healing concept in which the percentage of healing increases as the temperature and length of the rest period increase and decreases as damage becomes greater. The research team developed a healing test protocol using cyclic tests in which a group of load cycles is followed by a rest period, and this load–rest

combination of groups is repeated three times during the fatigue life of the test specimen. The team then developed a percent healing master curve from the test results, and, combined with the damage characteristic curve from the S-VECD model, can be used to predict the strain responses obtained from the pulse-rest loading history, which is similar to field loading conditions.

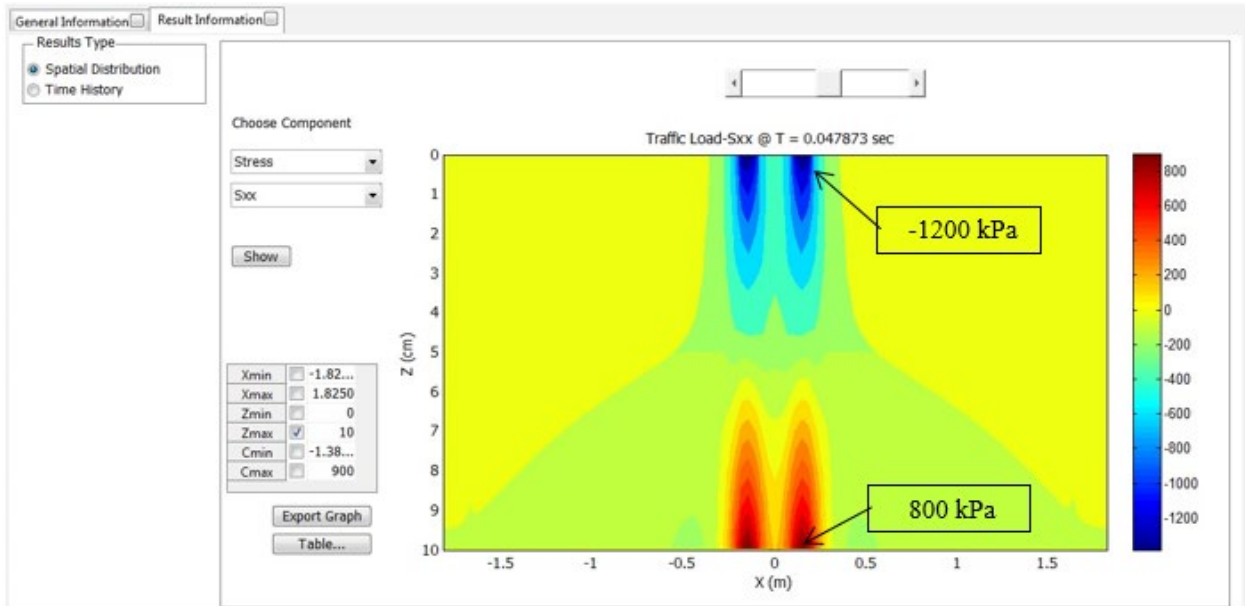
THE FLEXMAT™ PROGRAM FOR MIXTURE LEVEL DATA ANALYSIS

The dynamic modulus test, the cyclic fatigue test, and the SSR test were designed to be easily performed using the AMPT. The research team developed a Microsoft® Excel-based data analysis program, called FlexMAT, to characterize the performance models using data files generated by the AMPT. Upon selection of the proper data files, FlexMAT performs the complex analysis algorithms to generate the dynamic modulus master curve, calibrate the S-VECD model, and calibrate the shift model, and then generates the output files that can be readily used in the pavement performance analysis program, FlexPAVE. The user manual for the FlexMAT program is provided in Appendix C.

THE FLEXPAVE PROGRAM

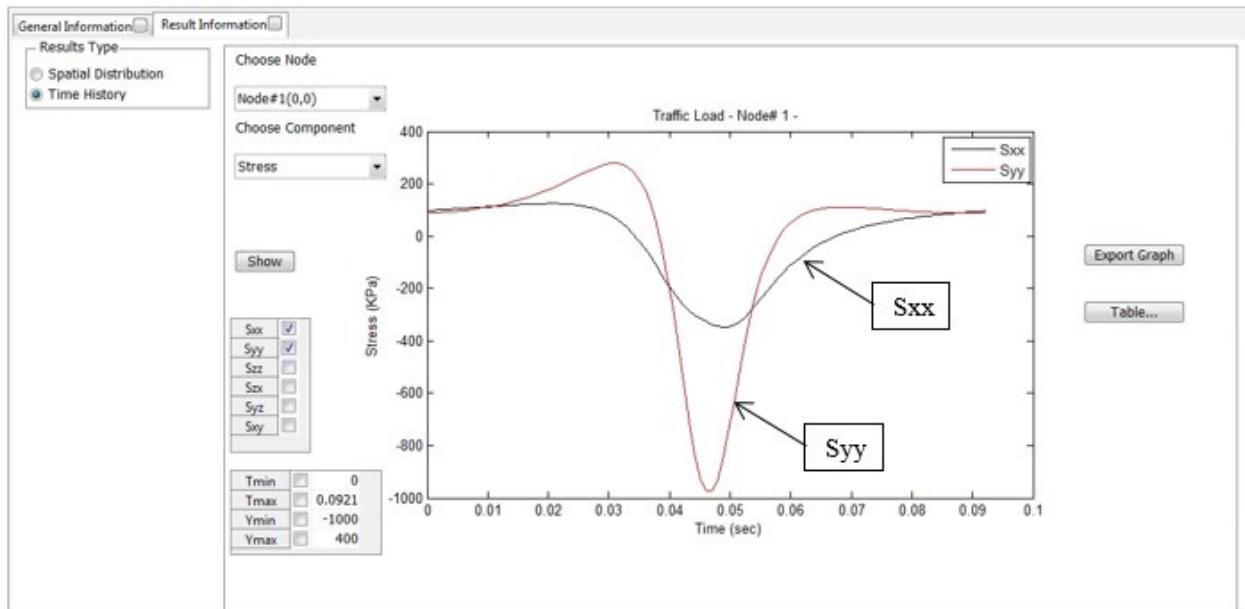
To apply the material models developed in this research to a pavement performance analysis software package useful for practitioners and researchers, the research team developed and verified the FlexPAVE software program (formerly known as the Layered Viscoelastic Pavement Design for Critical Distresses, or the LVECD, program) during this research. The FlexPAVE program is a structural model that employs the VECD theory to account for the effects of loading rate and temperature on the response and distress mechanisms present in asphalt pavements. The research team applied Fourier transform and reasonable assumptions for simplification to the program to enhance its computing efficiency. Chapter 5 presents theoretical details on the FlexPAVE program, and Appendix A provides guidance on use of the *FlexPAVE User Manual, Version 1.1*. FHWA retains a royalty-free, nonexclusive license to reproduce, publish, or otherwise use the FlexMAT and FlexPAVE programs and all associated data for Federal Government purposes, and authorizes others to do so.

The FlexPAVE program features a graphical user interface that allows the creation of pavement structures that consist of asphalt concrete and unbound materials. Each asphalt concrete layer can be assigned various material properties that can be measured using the test methods developed in this research. These material properties are input into the FlexPAVE program by selecting output files that are generated from FlexMAT. The software gives considerable control to the user to select the traffic conditions and design vehicle configurations, and the program has several options for selecting the environmental conditions at the site. The first option is to choose from various preselected cities throughout the United States. Once selected, the software uses Enhanced Integrated Climatic Model information to determine the temperature gradients throughout the pavement depth throughout the year. Another set of options for controlling the environmental conditions of the site are by providing a text input file or selecting an isothermal condition. For analysis, the program can provide either the pavement's response to the passing of a single axle or distress prediction information with time. These results can be represented in the form of contour plots or a time history graph for a selected point (figure 3 through figure 6).



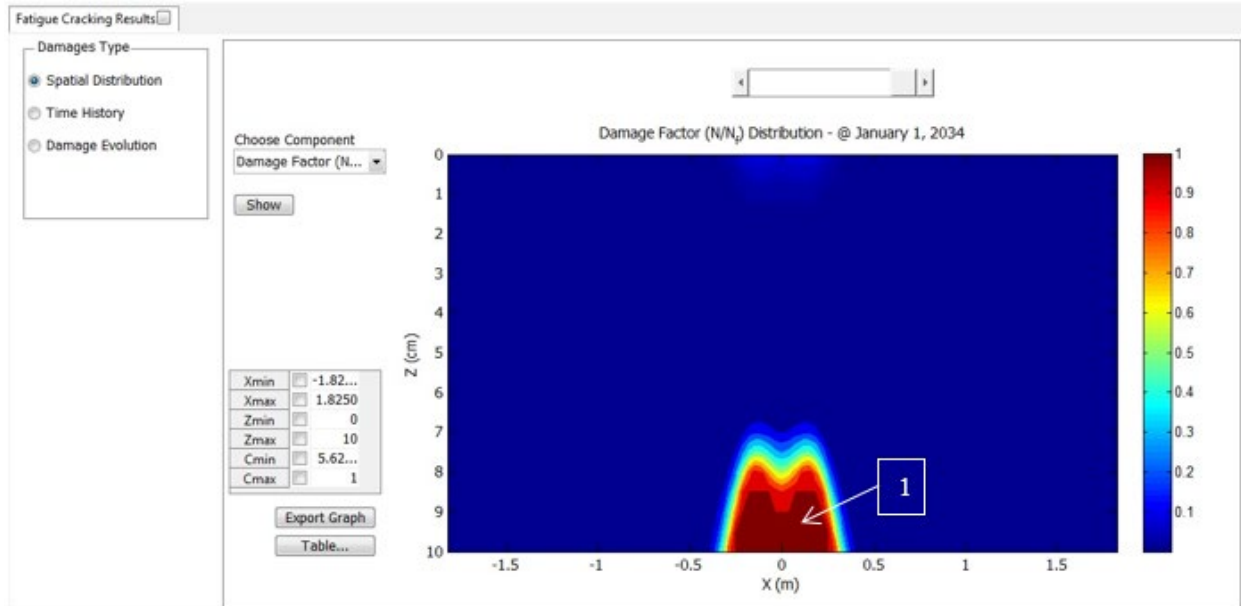
Source: FHWA.

Figure 3. Screenshot. S_{xx} (transverse stress) distribution (contour plot) at peak stress time.



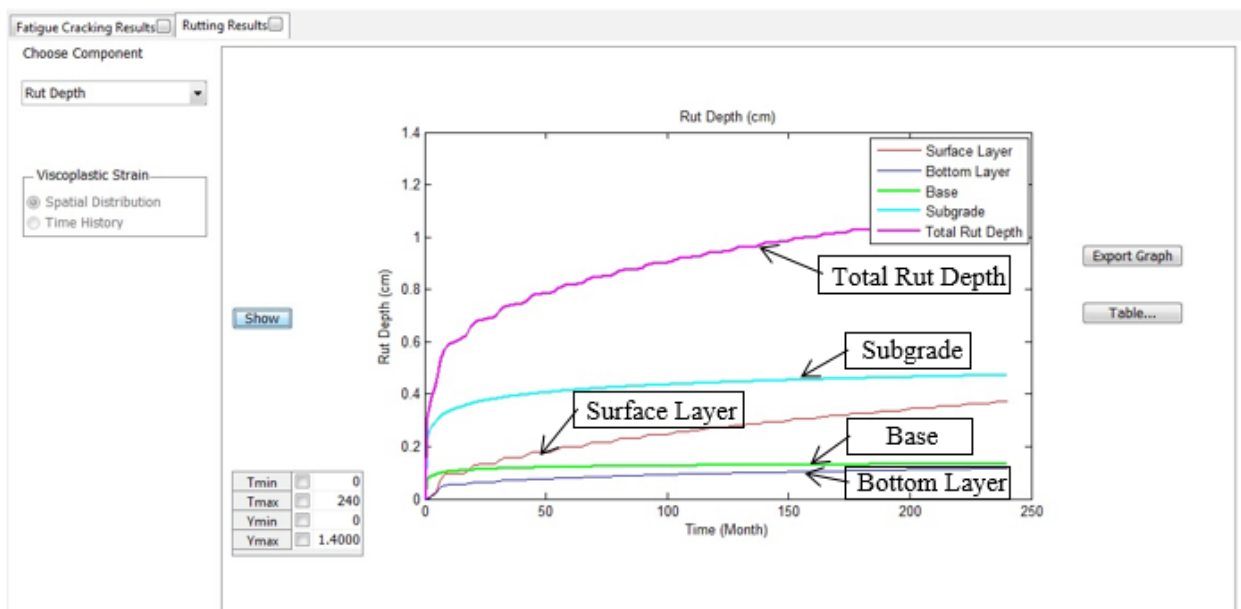
Source: FHWA.

Figure 4. Screenshot. Stress history plot at center of wheel path.



Source: FHWA.

Figure 5. Screenshot. Damage factor distribution after 20-yr simulation.



Source: FHWA.

Figure 6. Screenshot. Rut depth development.

FIELD VALIDATION

To validate the performance models and the FlexPAVE software, this study tested asphalt mixtures from different pavement projects. The field projects included FHWA's Accelerated Load Facility test sections, the National Center for Asphalt Technology test track, the Korea Expressway Corporation test road, the Manitoba Infrastructure and Transportation test roads for reclaimed asphalt pavement (RAP) and warm-mix asphalt studies, as well as roadways under the

authority of the New York State Department of Transportation (NYSDOT), the Louisiana Department of Transportation and Development (LaDOTD), and the city of Binzhou in China. Pavement condition survey data were not available from NYSDOT and LaDOTD; therefore, the research team only conducted mixture-level characterization using the mixtures from those two projects. In addition, test results for asphalt mixtures with various RAP contents and virgin binder grades that were used in the New England RAP Pooled Fund study were also used in this project. In total, the research tested 60 asphalt mixtures and analyzed 47 different pavement structures. The laboratory-measured material properties of these pavements' mixtures were input into the FlexPAVE program with section-specific traffic and climatic conditions to predict the performance of the asphalt pavements.

Chapter 6 discusses the research team's results obtained from the material characterization efforts, and Chapter 7 presents the FlexPAVE program simulations of the field projects. The results reveal that the FlexPAVE program predicts field performance with reasonable accuracy in terms of ranking and evolution trends; however, it has some limitations related to the nature of the unbound-material permanent deformation model. Specifically, when using the AASHTOWare® Pavement ME Design unbound material-permanent deformation model, the model's predictions for permanent deformation in unbound layers do not accurately represent the actual permanent deformation of these layers in the field (AASHTOWare® v2.6, 2020; available from <https://me-design.com/MEDesign/>). Program users should keep this limitation in mind when utilizing rutting test results. The research efforts under National Cooperative Highway Research Program (NCHRP) Project 01-53 are designed to develop enhanced unbound material models for mechanistic-empirical pavement design. The FlexPAVE program will implement the NCHRP 01-53 models once these models become publicly available, improving the prediction accuracy of permanent deformation in unbound layers.

Chapter 8 summarizes performance model development, the experimental and computational work and results from this project. It also provides suggestions for the research's future direction.

PRACTICAL SIGNIFICANCE

Given the technical ramifications surrounding the theories behind the S-VECD model, the shift model, and the FlexPAVE program, it is easy to lose sight of the overall practical benefits of the methodologies and models developed in this project. The combination of the S-VECD model, the shift model, and the FlexPAVE program provide major benefits in two main areas: material characterization and performance prediction. These two areas are subdivided into various practical applications of interest to practitioners and engineers in the private and public sectors.

Material Characterization

Material characterization can be broken down into two levels: determining the index properties and determining the engineering properties.

Index Properties

The rutting and fatigue tests discussed in this report can be used as simple pass/fail tests. Although pass/fail tests are generally empirical in nature, the S-VECD and shift models, along

with their corresponding test methods, have solid mechanistic underpinnings. These advantages may lead to more reliable index properties than a torture test run under a standard test condition.

Engineering Properties

The power of the methodologies developed in this research is realized by moving beyond index properties and using the measured engineering properties of the materials to predict the behavior of an asphalt mixture under a wide range of conditions. The models used in this research can predict the behavior of materials under various loading and environmental conditions outside of those used for material characterization. Therefore, by running a limited set of tests in the lab, the models can predict the material behavior under a wide range of conditions. This capability allows more efficient and better determination of material suitability than individual index properties for a limited number of conditions. Moreover, when these characterizations are combined with appropriate models, the models can make performance predictions, which is true for both simulations of lab tests (i.e., fatigue testing under complex loading histories) and in the field (i.e., when a pavement structure is subjected to traffic and climatic variations).

Performance Prediction

The research team developed a reliable pavement performance–prediction system so the system could serve as the basis for the asphalt mixture-performance-related specifications (AM-PRS). This system could be used during pavement construction to assess the constructed pavement and compare the as-constructed pavement to the as-designed pavement. The models and tests described in this report enabled the development of PRS for asphalt pavements as part of a performance-focused quality assurance (QA) system. By providing the ability to compare constructed pavements to designed pavements in terms of expected pavement performance, these PRS constitute a fair and logical way to assure the materials the highway agencies receive are the same quality as those they have paid for, while reassuring the traveling public that their tax dollars were spent responsibly and efficiently. The owner agency can also use the PRS to develop pay factors that relate to the increase or decrease in the expected pavement life for the materials produced in the project. Mix producers can test their various mixtures and seek to optimize the mixtures’ performance by making any necessary adjustments, limiting the risk of penalties and maximizing the potential for bonuses. Thus, the AM-PRS serves not only to reliably predict pavement performance but also to provide financial incentives that ensure quality construction and increase public confidence in the overall pavement network.

The performance tests and models developed and employed in this research support a PRS framework, with performance tests that can be conducted using asphalt mixtures with various acceptance quality characteristics (AQC) measured during a given paving project for QA purposes. The measured performance properties obtained from asphalt mixtures with different AQC can be input into the FlexPAVE program to simulate pavement cracking and rutting over time. The difference between the predicted development of distress in the as-constructed pavement and the predicted development of distress in the as-designed pavement can be used to determine the difference in the life of the as-constructed and as-designed pavements due to the variations in the AQC measured during construction. The life difference then can be used to determine incentives and disincentives by applying agency-specific cost models. The benefit of

this approach represents a more fair and legally robust methodology for determining pay factors than what is currently in place.

Asphalt Mixture Design

The efficient test methods and powerful models developed in this research provide a strong foundation for a performance-engineered mix design method. Rather than solely focusing on volumetric design, as is the current Superior Performing Asphalt Pavements practice, various State agencies can conduct additional testing to ensure quality mixture performance. Generally, these tests rely on index parameters for pass/fail decisions. A more rigorous approach can be taken using the test methods and performance prediction models developed in this project that allow the designer to determine the capability of a given mixture to perform well over time in a real pavement structure. For States where mixtures are designed after a project has been awarded (i.e., a pavement design has been completed and is available), this approach may best optimize mixtures for the project. For States where mix designs are preapproved and verified prior to the construction of any given project, this approach would involve approving mixtures based on preselected structures. These preselected structures vary depending on the considered mixture (e.g., mixtures intended for low-volume roadways would be verified using a different structure than mixtures intended for high-volume roadways) and would be related to the most critical condition that the mixture is expected to experience.

Pavement Design

Another possible application area for the results of this research is pavement structural design. By using materials representative of those expected to be used in a given project, the FlexPAVE program can propose and try multiple pavement designs, compare the predicted performance of these designs, and allow the pavement engineer to make determinations about the number of layers to use. The program also provides a pavement engineers with guidance on which materials to select and their relative placement in the pavement structure, as well as evaluate the effects of different traffic and environmental conditions. Not only does FlexPAVE employ the S-VECD and shift models that are efficient for testing, but it also predicts a material's performance under a wide range of loading and environmental conditions. Thus, FlexPAVE offers several advantages over other programs that are currently advanced for pavement design. FlexPAVE uses VECD principles, which lead to improved predictions over elastic analysis programs. Additionally, FlexPAVE uses material properties from all the asphalt layers and determines how each layer affects the cracking and rutting performance of a pavement using mechanistic principles. In this framework, it is not necessary to assume a priori location of macrocrack initiation, nor the path of macrocrack evolution. Not having to make such assumptions is an essential feature of FlexPAVE in evaluating top-down cracking in complex pavement structures under a wide range of loading and environmental conditions. The flexible nature of the FlexPAVE modeling technique allows cracks to initiate and propagate wherever the fundamental material law suggests. As a result, the FlexPAVE program accomplishes much more realistic and accurate top down–cracking simulation than was previously possible.

Pavement Management

Lastly, the ability of the FlexPAVE program to predict pavement performance provides additional benefits for highway agencies. More accurate predictions of pavement life and distresses help with the development of pavement-management strategies and the planning of future maintenance and rehabilitation projects. As agencies work toward meeting the goals of transportation-performance management, knowing the expected pavement condition over time while a project is being constructed provides insights on how that project will impact the overall pavement condition numbers for a corridor or region in the future

CHAPTER 1. INTRODUCTION

PROBLEM STATEMENT

Asphalt pavement, one of the largest infrastructure components in the United States, is a complex system that involves multiple layers of different materials, various combinations of irregular traffic loading, and various environmental conditions. Specifications for hot-mix asphalt (HMA) pavements have continued to evolve since late 1800's when bitumen from Trinidad Lake was used for pavement construction. Initial HMA pavement specifications took the form of warranties or guarantees, and the contractor carried much of the performance responsibility. As pavement construction technology and knowledge increased, and as litigation burdens due to poor pavement performance grew, agencies began to adopt "recipe" specifications whereby the agency explicitly stated the materials and processes the contractor should use to ensure their compliance. By implementing such specifications, the burden of responsibility for ensuring properly performing pavements shifted completely to the agency and its personnel and away from contractors. However, evolving technology and increasing demands revealed shortcomings in recipe-type specifications for HMA pavements. In the early 1960s, motivated by congressional oversight of highway construction and results from the American Association of State Highway and Transportation Officials road tests, the industry began to move away from this type of specification and more toward statistically-based quality assurance (QA) methods.⁽¹⁴⁾ Currently, QA-based methods are the prevalent practice in the United States.^(14,15)

Other, more cutting-edge techniques include warranty, design-build, and performance-based specifications, which are growing in popularity but still face resistance from both contractors and agency partners. As an alternative to these end-result specifications, intermediate performance-related specifications (PRS) have been the focus of substantial national efforts in the last 20 to 30 yr⁽¹⁴⁻¹⁹⁾ PRS are QA specifications that base acceptance on desired levels of key materials and construction quality characteristics found to correlate with fundamental engineering properties.⁽²⁰⁻²²⁾ These acceptance quality characteristics (AQC) are amenable to acceptance testing at the time of construction.

As with any QA specifications, PRS also require contractor quality management and agency acceptance throughout the production and placement of the product. Final acceptance of the product is usually based on random statistical sampling of the measured quality level on a lot-by-lot basis for the specified AQC. PRS use mathematical models to quantify the relationship between these AQCs and subsequent product performance. The performance prediction models are used to provide reasonable pay adjustments based on an assessment of the measured quality and variability of the product. The pay adjustments are typically related to the difference between the as-designed and as-constructed expected performance or lifecycle costs (LCC). PRSs aim to enhance pavement quality through reasonable pay adjustments determined by the accurate performance prediction of asphalt pavement. However, predictions made on a lot-by-lot basis typically require a large amount of sampling and testing.

The WesTrack PRS project and National Cooperative Highway Research Program (NCHRP) 9-22 project developed simple and fast prediction methods like performance-predictive equations and closed-form solutions based on *Mechanistic-Empirical Pavement Design Guide* (MEPDG)

simulations.⁽²³⁾ However, the accuracy of these performance prediction methods was limited. As a result, agencies were hard pressed to defend the pay factors used to account for substandard pavement performance. The WesTrack project PRS, although reasonable, introduced many unknown factors that may not have been explicitly related to the quality of the product delivered by the contractor for a particular project. This shortcoming led other researchers to adopt other techniques. The NCHRP 9-22 project was based on the use of linear viscoelastic properties to evaluate performance using simplification procedures. Although NCHRP 9-22A used field studies to demonstrate the Quality-Related Specification Software (QRSS) methodology, some limitations remain. For example, QRSS uses linear viscoelastic properties to characterize cracking and rutting distresses governed by highly nonlinear behavior. Other limitations include the software's reliance on equivalent single-axle loads (ESAL) and its lack of consideration for the use of modified binders.

With the goal of accurate pavement performance evaluation and prediction, the research team has been developing advanced models for asphalt concrete under complex loading conditions. Over the past few decades, they have successfully developed material models that accurately capture various critical phenomena like microcrack-induced damage that is critical in fatigue modeling, strain-rate temperature interdependence, permanent deformation behavior that is critical for high-temperature modeling, and damage reduction during rest periods between loads. The resulting models are mechanistic models that can evaluate fatigue cracking, permanent deformation (rutting), and healing, and are referred to as the simplified viscoelastic continuum damage model, the shift model, and the healing model, respectively.

These mechanistic models required PRS characterization using simple and fast test methods. The research team proposed robust and efficient test methods. All the tests and corresponding specifications are designed to use the asphalt mixture performance tester (AMPT) because the AMPT is a widely-distributed test machine in the United States and readily available in most States. In the testing scheme developed under this project, the material properties necessary for the predictions of cracking and permanent deformation (rutting) can be measured within only 1 to 2 d of testing time for each type of prediction (i.e., cracking or rutting). Using one AMPT, the entire mixture characterization takes 3 d of testing time. Sample preparation time is not included in the time estimates because it would differ among different laboratories depending on their setups. Then, the power of the mechanistic performance models allows the prediction of mixture performance under a wide range of loading and environmental conditions.

To predict the performance of real pavement structures, the research team advanced the mechanistic models into a structural model to consider the vehicle loads and climatic conditions as well as the boundary conditions. The finite-element method was best suited for this purpose due to its ability to handle nonlinear, inelastic material behavior of materials used in asphalt pavements. The research team developed an in-house, finite-element code, referred to as the FlexPAVE™ program. The FlexPAVE program is a pavement performance–prediction engine used by the asphalt mixture PRS software known as PASSFlex™. In addition to calculating pavement responses, it computes pavement performance (i.e., fatigue cracking and permanent deformation or rutting) under moving loads using three-dimensional analysis. This FlexPAVE program was calibrated against the observed performance data from 47 in-place pavements composed of 60 different asphalt mixtures, including warm-mix asphalt and reclaimed asphalt pavement mixtures.

OBJECTIVES

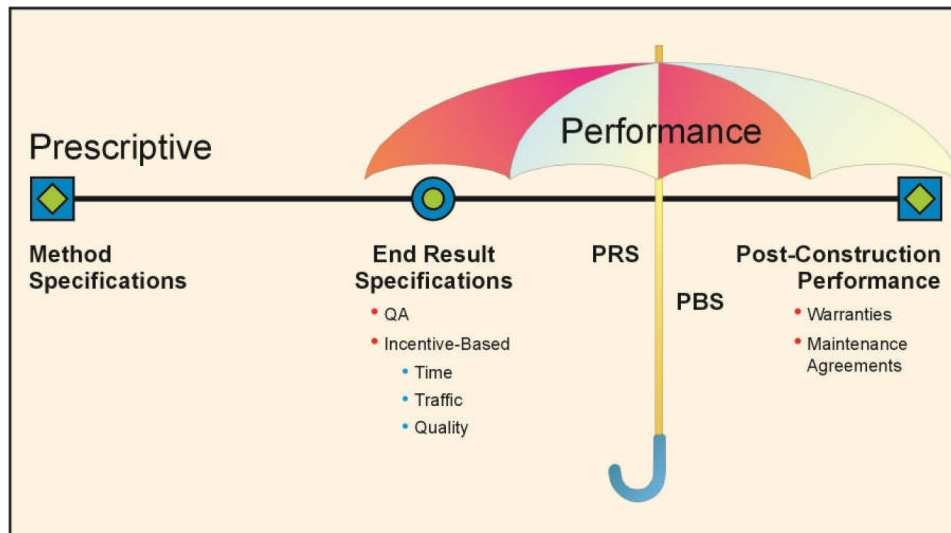
The primary goal of this project was to develop asphalt mixture-level and asphalt pavement structural models that can be used as the basis of the PASSFlex program, which supports the development of asphalt mixture-PRS.

The following are the objectives of this research:

- To develop mechanistic performance models for fatigue cracking, permanent deformation (rutting), and healing of asphalt pavement.
- To develop reasonable test methods to support the proposed performance models.
- To develop asphalt pavement performance–prediction tools.

CHAPTER 2. HISTORICAL EFFORT TO IMPLEMENT PRS

To enhance the quality of asphalt pavement performance, performance-related specifications (PRS) aim to motivate contractors by transferring more responsibility to them. Figure 7 shows types of specifications along a continuum of increasing contractor responsibility for performance. On one end are the traditional method-type specifications for which the agency retains primary responsibility for pavement performance. On the other end are post-construction performance provisions, which are designed to monitor and hold the contractor accountable for the actual performance of the pavement over time.



© 2013 Transportation Research Board. (DTFH61-08-H-00005)
PBS = performance-based specifications.

Figure 7. Illustration. Continuum of highway specifications.⁽²²⁾

Material and method specifications require the contractor to use specified materials in definite proportions as well as specific types of equipment and methods to place the material. Each step is directed by the overseeing agency. Historically, this recipe-type approach obligates the agency to accept the completed work regardless of quality.

Performance specifications is an umbrella-style term that includes end-result specifications, PRS, performance-based specifications (PBS), and warranty and long-term maintenance provisions. Performance specifications describe how the finished product should perform over time. End-result specifications require the contractor to take complete responsibility for supplying a product or an item for construction. The buyer either accepts or rejects the final product or applies a pay adjustment commensurate with the degree of compliance with the specifications, as established through sampling and testing of the final in-place product. PBS prescribe the desired levels of fundamental engineering properties (e.g., resilient modulus, creep properties, and fatigue properties) that predict performance and appear in primary predictive relationships (i.e., models that can be used to predict pavement stress, distress, or performance from combinations of predictors that represent traffic, environmental, roadbed, and structural conditions). PRS require acceptance quality characteristics (AQC), which can be or correlate to fundamental engineering

properties. Ultimately, AQC are used to evaluate the actual performance of pavement, and thus, PRS require performance models. Warranty specifications are another type of performance specification that seek to guarantee the integrity of a product by assigning responsibility for the repair or replacement of defects to the contractor rather than assessing the expected long-term performance at construction completion.

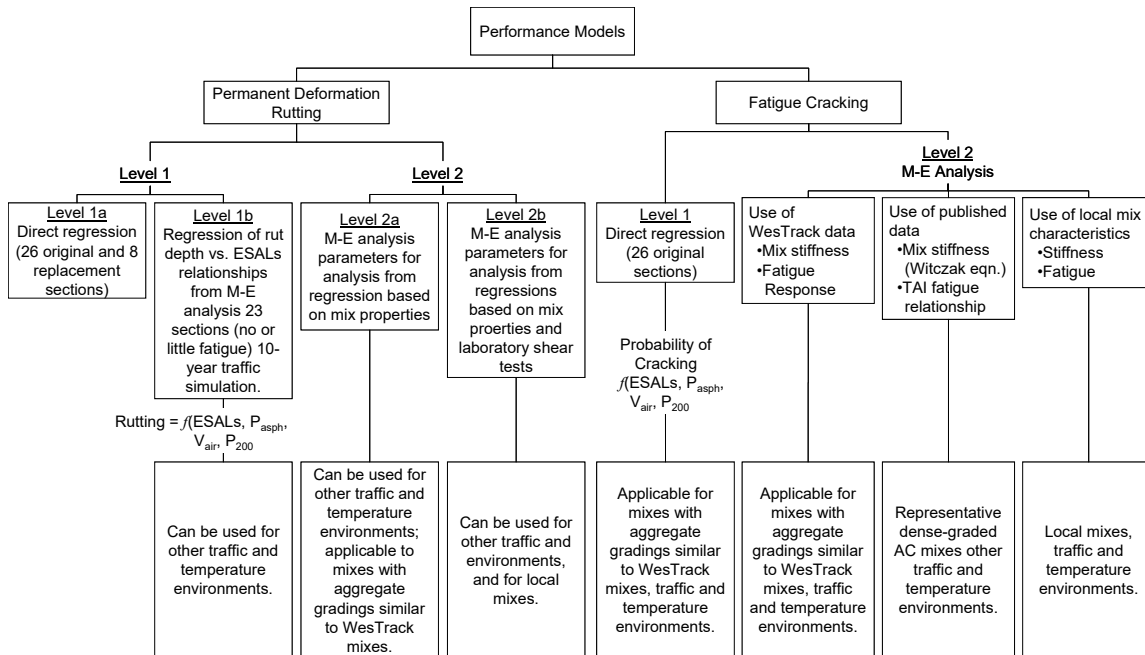
PRS should provide contractors with the tools they need to design as well as control the quality of the asphalt pavement based on the pavement's performance. Pavement performance evaluation usually can be conducted on a lot-by-lot basis. The number of tests and predictions required for such evaluation is significant; therefore, prediction accuracy and efficiency both play a key role in PRS. To account for these considerations, PRS projects are now aimed to develop performance models that can predict performance with reasonable accuracy within a reasonable time. This chapter reviews the historical effort to achieve both accuracy and efficiency.

WESTRACK PROJECT PERFORMANCE-RELATED SPECIFICATIONS

The groundwork for PRS development through the WesTrack project was established by Shook et al., who identified the primary materials and construction factors that are related to asphalt pavement.⁽²⁴⁾ When used to control quality, these factors are termed AQC and include air void content, asphalt content, and aggregate gradation.

The outcome of the WesTrack project is a prototype PRS with a hierarchical structure of complexity and accuracy. To address the need for performance models, researchers in the WesTrack project adopted two levels of complexity. Level 1 was considered the least complex and level 2 was more advanced. This numbering scheme is opposite to the way the different analysis levels are defined in the AASHTOWare® Pavement ME Design software and in this report (AASHTOWare v2.6, 2020; available from <https://me-design.com/MEDesign/>).

The WesTrack PRS primarily considers rutting and fatigue cracking, as these are the two distresses most often cited for degrading pavement performance. A summary of these models is given in figure 8. The WesTrack project researchers also adopted a procedure that considers the stochastic nature of specifications as well as materials and construction parameters. The following section presents a summary of the procedure adopted by the WesTrack research team. The report frames the discussion in the context of level 1 modeling; however, level 2-type models could be incorporated in a similar fashion with proper consideration of the statistical factors.



AC = asphalt concrete; M-E = mechanistic–empirical; TAI = The Asphalt Institute.

Figure 8. Illustration. WesTrack performance prediction model hierarchy.⁽¹⁷⁾

Procedures

The WesTrack research team, informed by general framework developed in previous work, divided the PRS process into a series of steps. The primary goal of these steps was to analyze the expected performance of the designed pavement and then use these expectations (or predictions) to assess pay factors (or bonuses) for deviations from the as-constructed pavement.

Step 1—Acquire Required Inputs for the As-Designed Pavement

Inputs for the WesTrack PRS included mean and standard deviations of AQC as independent variables in the performance prediction models like layer thickness, asphalt content, air void content, and gradation. The inputs also included, either directly or through surrogate relationships, parameters for base and subbase thicknesses and moduli. The inputs also required external factors like design traffic (initial level and growth rates) and a maintenance and rehabilitation decision tree. This final factor was necessary because LCC were being calculated for the full pavement design life, including the projected rehabilitation strategy.

Step 2—Estimate Mean LCC of the As-Designed Pavement Structure

To account for allowable variability in the as-designed pavement specifications (i.e., the lack of a deterministic design from a specification standpoint), the WesTrack research team devised an iterative analysis technique that applied Monte Carlo methods to create multiple pavement simulations using randomly selected values based on the designed mean and allowable tolerances of the AQCs. The research team determined the LCC for each of these simulations, and after

generating a population of LCC, the team then determined mean and standard deviations of these expected, as-designed costs.

Step 3—Estimate Preconstruction Pay Factor Equation

The specific nature of individual pavement projects motivated the WesTrack researchers to develop a preconstruction pay factor equation as part of the primary PRS output. Monte Carlo simulations based on assumed means and standard deviations for AQC resulted in a population of expected LCC. Comparisons between the LCC of each individual simulation and the mean LCC of the as-designed pavement provided a population of expected pay factors. Statistical analysis of this population resulted in a pay factor equation similar to the one shown in equation 1. Such an equation should allow contractors to determine, through sensitivity analysis, the strategy that would best maximize their cost–benefit ratio.

$$\begin{aligned}
 PF = & 1.0087 - 0.11877 * z_{Vair} + 0.13160 * z_{TH} - 0.00126 * z_{P200} + 0.3485 * z_{Pasp} \\
 & - 0.00082 * (z_{P200})^2 - 0.00391 * (z_{TH})^2 - 0.00457 * (z_{Pasp})^2 \\
 & + 0.00573 * z_{Vair} * z_{Pasp} + 0.00340 * z_{Vair} * z_{TH} + 0.00305 * z_{Vair} * z_{P200} \\
 & - 0.00831 * z_{TH} * z_{Pasp} - 0.00130 * z_{TH} * z_{P200} - 0.00395 * z_{Pasp} * z_{P200}
 \end{aligned} \tag{1}$$

Where:

PF = contractor pay factor.

z_{Vair} = factor representing variance of air void content.

z_{TH} = factor representing variance of hot-mix asphalt thickness.

z_{Pasp} = factor representing variance of asphalt content.

z_{P200} = factor representing variance of percent passing the No. 200 sieve.

Step 4—Adjust Post-Construction Pay Factor

The final step in the WesTrack PRS was to determine the true pay factor adjustment after construction completion. The research team used results from the quality assurance (QA) performed during the actual construction phase as inputs at this stage. The team developed a population of probable pavement LCC based on the probabilistic determinations of the QA parameters, which was compared with the as-designed mean LCC. Finally, to provide flexibility to agencies, the WesTrack team included a methodology by which uncertainty factors, specific to an agency and local contractors, could be included.

Performance Models

Level 1 analysis includes regression models based on WesTrack measurements. Performance characteristics (i.e., fatigue cracking and rutting) were measured at 26 original sections and 8 replacement sections in the WesTrack test sections and were used to develop level 1 models. Level 2 analysis includes mechanistic–empirical models.

Fatigue Model

Equation 2 presents the level 1 regression models for fatigue cracking.

$$\begin{aligned}
 \text{FC (\%)} &= [1.2313 + 0.071655 \cdot \log(ESAL) && \text{(for fine mix)} \\
 &+ 0.2358 \cdot \log(\varepsilon_t) + 0.061193 \cdot \log(|E^*|) - 0.034086 P_{asp} \\
 &0.0074593 \cdot V_{air} - 0.014954 P_{200}]^{154.04} \\
 \text{FC (\%)} &= [1.2850 + 0.07478 \cdot \log(ESAL) && \text{(for coarse mix)} \\
 &+ 0.2461 \cdot \log(\varepsilon_t) + 0.06386 \cdot \log(|E^*|) - 0.0336791 \cdot P_{asp} \\
 &0.002761 \cdot V_{air}]^{147.73}
 \end{aligned} \tag{2}$$

Where:

$ESAL$ = number of 80-kN ESAL.

P_{200} = percent aggregate finer than 0.075-mm (No. 200) sieve.

V_{air} = air void content (percent).

P_{asp} = asphalt content (percent).

ε_t = maximum tensile strain in asphalt layer.

$|E^*|$ = dynamic modulus of asphalt mixture.

The research team developed the mechanistic–empirical models for fatigue cracking based on flexural fatigue testing and an assumed multilayered elastic system. Performance measurements of only original pavement sections were utilized and classified into three different mixtures: fine, fine plus, and coarse, as reflected in equation 3.

$$\begin{aligned}
 \ln(N_f) &= -27.0265 - 0.14739 \cdot V_{air} + 0.4148 \cdot P_{asp} - 4.6894 \cdot \ln(\varepsilon_t) && \text{(for fine mix)} \\
 \ln(N_f) &= -27.3409 - 0.1431 \cdot V_{air} + 0.4219 \cdot P_{asp} - 4.6918 \cdot \ln(\varepsilon_t) && \text{(for fine plus mix)} \\
 &+ 0.0128 \cdot T_{90} \\
 \ln(N_f) &= -27.6273 - 0.0941 \cdot V_{air} + 0.6540 \cdot P_{asp} - 4.5402 \cdot \ln(\varepsilon_t) && \text{(for coarse mix)} \\
 &+ 0.0331 \cdot T_{90}
 \end{aligned} \tag{3}$$

Where:

T_{90} = 90th percentile air temperature during the period for which the rut depth was measured.

Rutting Model

Equation 4 presents the regression models for the fine and coarse mixtures, respectively.

$$\begin{aligned}
\ln(rd) &= -5.257 + 0.357 \cdot \ln(ESAL) + 0.185P_{exp} && \text{(for fine mix)} \\
&\quad + 0.041V_{air} + 0.916P_{200} + 0.005T \\
\ln(rd) &= -4.939 + 0.212 \cdot \ln(ESAL) + 0.439P_{exp} && \text{(for coarse mix)} \\
&\quad + 0.044V_{air} + 0.034T
\end{aligned}
\tag{4}$$

Where R_D is rut depth (inches).

The mechanistic–empirical models assume that rutting in the asphalt pavement is controlled by shear deformation. The rutting model can be calibrated by means of a repeated simple shear test at a constant height, as shown in equation 5.

$$\gamma^e = a \cdot \exp(b\tau \gamma^e n^c)
\tag{5}$$

Where:

τ = shear stress calculated at 50-mm depth using elastic analysis.

γ^e = corresponding elastic shear strain.

N = number of load repetitions.

a, b, c = regression coefficients.

The performance models developed in the WesTrack PRS project were based on a limited number of mixtures used in the WesTrack test sections. Even though the models predicted the performance of the WesTrack sections properly, they were not necessarily valid for other different mixtures and loading conditions (i.e., climate regions and traffic levels). The insistence on full LCC analysis as the primary basis for the pay factor adjustment was an additional concern with the approach adopted by the WesTrack research team. Although seemingly rational, the approach nevertheless could introduce many unknown factors that may not be explicitly related to the quality of the product delivered by the contractor for a particular project. These shortcomings of the WesTrack PRS project led other researchers (i.e., the NCHRP 9-22 project researchers) to adopt other techniques.

NCHRP 9-22 PROJECT QUALITY RELATED SPECIFICATION SOFTWARE

The follow-up project to the WesTrack project was aimed at further developing the PRS methodology for asphalt mixtures, but it adopted a somewhat different approach to both modeling and pay factor assessment to address previously identified challenges and perceived shortcomings. This more recent work (i.e., the NCHRP 9-22 project) strongly advocated analysis techniques used in the NCHRP 1-37A MEPDG.⁽²⁵⁾ Thus far, these modeling efforts can best be compared to WesTrack level 1 analysis because of its use of surrogate as opposed to primary factors (e.g., shear strength, tensile strength, subsoil moduli) for pavement performance predictions.

Performance Models (Closed-Form Solutions)

The module of the NCHRP 9-22 PRS, referred to as QRSS, relates to the performance models of the MEPDG. One of the critical objectives of PRS is to predict performance using a calibrated performance model on a lot-by-lot basis, which means conducting performance tests as well as predicting performance for each lot. However, it is not possible to calibrate all the MEPDG performance models, such as thermal cracking, fatigue cracking, and rutting models, for each possible lot. The following sections describe how the research team overcame this difficulty in QRSS.

Rutting Model

The NCHRP 9-22 research team developed closed-form solutions of individual performance models by running thousands of MEPDG simulations. The research team assumed that the dynamic modulus was related to fatigue cracking and rutting to simplify the performance models. The model obtained the Witczak dynamic modulus ($|E^*|$) values by calculating the effective temperature and frequency for a given project site. The dynamic modulus values at the effective temperature and frequency were related to the rut depths the MEPDG predicted. Equation 6 shows the relationship between rut depth and dynamic modulus. Traffic speed, traffic level, and asphalt layer thickness correct the predicted rut depth.

$$R_D = a(|E^*|)^b \quad (6)$$

Where:

$|E^*|$ = dynamic modulus at effective temperature and effective frequency.

a, b = regression coefficients.

Similar to the closed-form solution for rutting, the research team developed a fatigue cracking model using the MEPDG simulation database. The simplified fatigue model is expressed as equation 7. Equation 7 implies that fatigue is related to the asphalt layer, the modulus, the void filled with bitumen, and the unbounded layers (i.e., the base layer and subgrade). Among these factors, the dynamic modulus is a mechanistic property of asphalt mixtures.

$$\begin{aligned}
\log N_f = 8.3014 - & \left[(b_1 \log(h_{ac})^2 + b_2 \log(h_{ac}) + b_3) \cdot \log(|E^*|) \right. \\
& + (b_4 \log(h_{ac})^2 + b_5 \log(h_{ac}) + b_6) \cdot \log(|E_{cf}|)^2 \\
& + (b_7 \log(|E^*|)^2 + b_8 \log(|E^*|) + b_9) \cdot \log(|E_{cf}|) \\
& + (b_{10} \log(h_{ac})^2 + b_{11} \log(h_{ac}) + b_{12}) \cdot \log(VFB)^2 \\
& + (b_{13} \log(h_{ac})^2 + b_{14} \log(h_{ac}) + b_{15}) \cdot \log(VFB) \\
& \left. + b_{16} \log(|E^*|)^2 + (b_{17} \log(h_{ac})^2 + b_{18} \log(h_{ac}) + b_{19}) \cdot \log(|E^*|) + b_{20} \right] \quad (7)
\end{aligned}$$

Where:

h_{ac} = thickness of asphalt pavement layer (inches).

E_{cf} = composite foundation modulus.

VFB = void filled with bitumen.

Thermal Cracking Model

The research team newly developed a thermal cracking model because of a coding error in the thermal model in the MEPDG and difficulty in developing a closed-form solution. The model calculated thermal stress using the pavement temperature and the temperature gradient at the surface. The stress-to-strength ratio results in incremental thermal cracking, which is related to thermal cracking in the field, is shown in equation 8.

$$C_f = \beta_1 N \left(\frac{\log C / D}{\sigma} \right) \quad (8)$$

Where:

C_f = observed amount of thermal cracking in ft./500 ft.

N = standard normal distribution.

C = crack depth.

σ = standard deviation of the log of the depth of the crack in the pavement.

β_1 = regression coefficient obtained by field calibration (353.5).

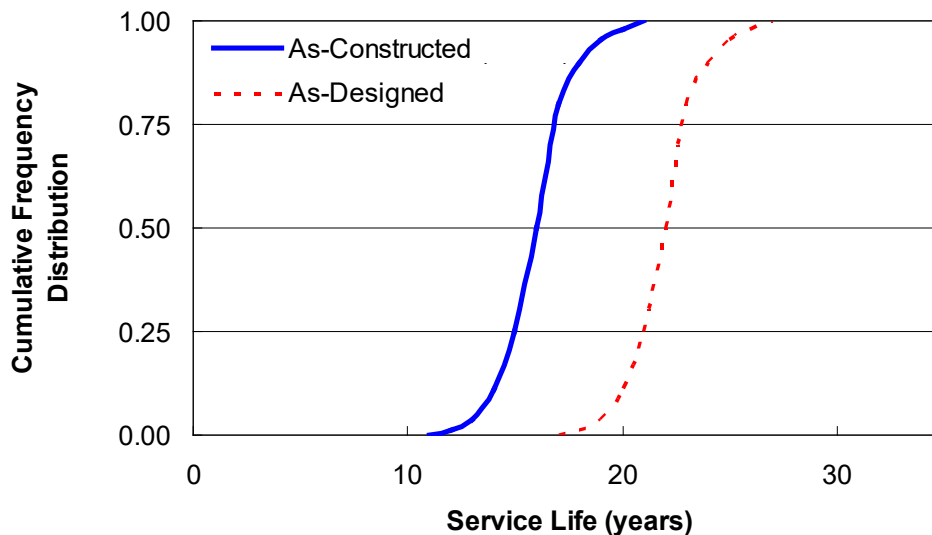
Pay Adjustment Factor

For QA purposes, a pavement project is divided into smaller lots of materials assumed to have stochastic characteristics. From each of these lots, surrogate factors necessary for performance predictions are obtained from a mean and standard deviation. The mean and standard deviations of these surrogate factors are used with the Witczak dynamic modulus ($|E^*|$) predictive equation in combination with Monte Carlo simulations to predict possible dynamic modulus values of the given lot ($|E^*|_n$) and performance at the design load application number (N_{Design}) thereby combining closed-form solutions with the effective frequency and temperature.

The user can employ the MEPDG resilient-to-permanent strain model to investigate rutting performance. The model calculates the actual number of ESAL applications to failure (i.e., the number of applications that it takes for a given lot to reach the selected failure criterion) and denotes the outcome as N_{actual} . Finally, based on various factors, the model can predict the actual service life (i.e., the number of years until a lot reaches critical rut depth). At the end of this step, the model provides the user with a number (up to 1,000) of statistically possible service life values, mean service life, and variance of service life for each lot in a given project.

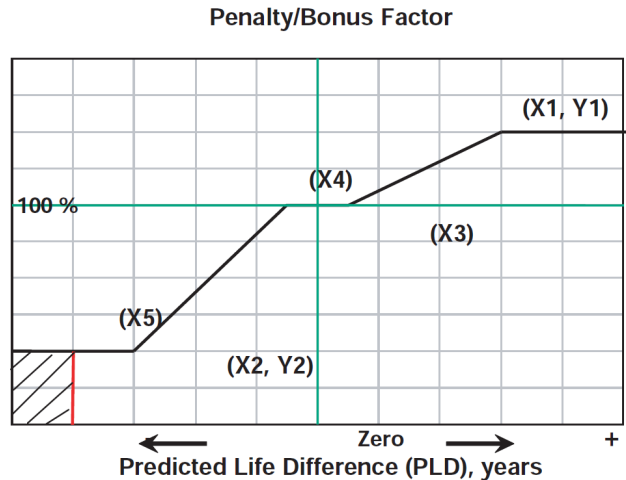
It is also necessary that the user predict the expected service life of the as-designed pavement. The user applies the mean and historical variances of the job mix formula values for the materials in the given project for this purpose. The Monte Carlo technique can then predict a statistically valid set of possible dynamic modulus values. The user can predict the mean and variance in the design life from this set of values using the same methodology used to determine the expected life of the field mixtures.

If the user enters a target life, the model creates cumulative frequency distributions for the individual lots. Such a plot provides information about the probability that a pavement will reach a certain service life. For example, in the sample plot shown in figure 9, the as-designed pavement structure has a 50-percent probability of reaching a design life of 22 yr, but the as-constructed lot only has a life of 15 yr at 50-percent probability. The predicted life difference (PLD) becomes -7 yr; that is, the difference between the as-constructed 15 yr and the as-designed 22 yr. The agency and contractor should predetermine the penalty and bonus factors during contract discussions (figure 10). Then, the PLD is used to determine the penalty and bonus factors. The PLD also can be used in reference to fatigue cracking and thermal cracking to determine final penalty and bonus factors.



Source: FHWA.

Figure 9. Graph. Example of cumulative frequency distribution for NCHRP 9-22 rutting module.



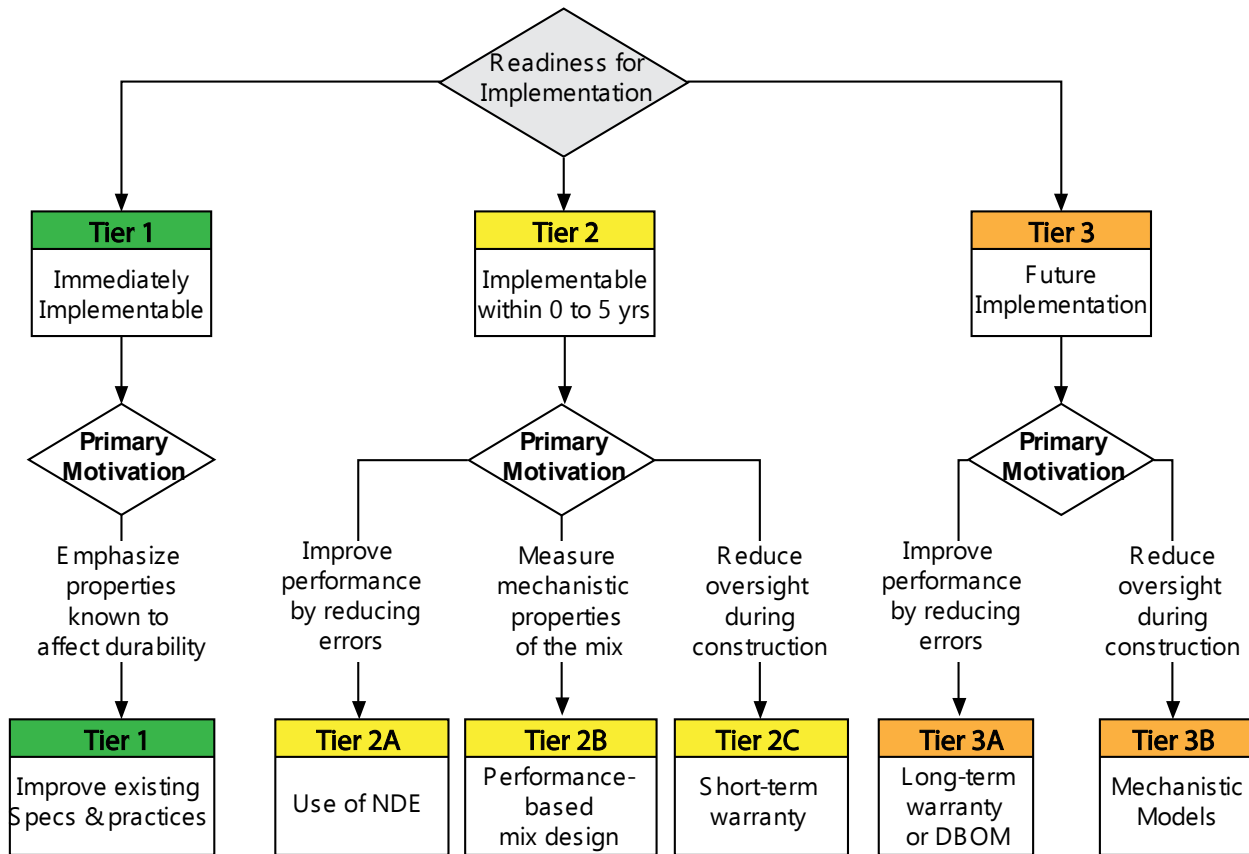
© 2011 Transportation Research Board. (DTFH61-08-H-00005)

Figure 10. Graph. Example of penalty/bonus factor predetermined by agency and contractors.⁽²³⁾ (Note: The horizontal line from (X1, Y1) extends beyond the graph boundary, indicating that the maximum bonus factor is capped at Y1.)

SHRP2 RENEWAL PROJECT R07

The second Strategic Highway Research Program (SHRP2) R07 project, *Performance Specifications for Rapid Highway Renewal*, described the concept and general application of performance specifications but it did not detail performance specifications.⁽²²⁾ This project also introduced AQC and measuring methods according to their applicability in terms of time. Regarding future technology, the project’s research team suggested nondestructive continuous measuring methods for material properties and integrity of as-constructed asphalt pavement.

The SHRP2 R07 project suggested three tiers of AQC based on current technology and business practices for both portland concrete cement (PCC) and asphalt pavements.⁽²²⁾ Tier 1 represents the currently available technologies, and tier 3 recommends future technologies to determine mechanical properties. Figure 11 presents these different tiers and the motivation for implementing them for pavement specifications. This current asphalt mixture PRS project may fall within tier 3 in terms of performance models but belongs to tier 2 in terms of measuring mechanical properties. As expressed in figure 11, the crux of PRS is mechanistic predictive models that can evaluate a pavement’s future performance.



© 2013 Transportation Research Board. (DTFH61-08-H-00005)

NDE = nondestructive evaluation; DBOM = design build operate maintain.

Figure 11. Illustration. Acceptance characteristics tiers for asphalt pavement.⁽²²⁾

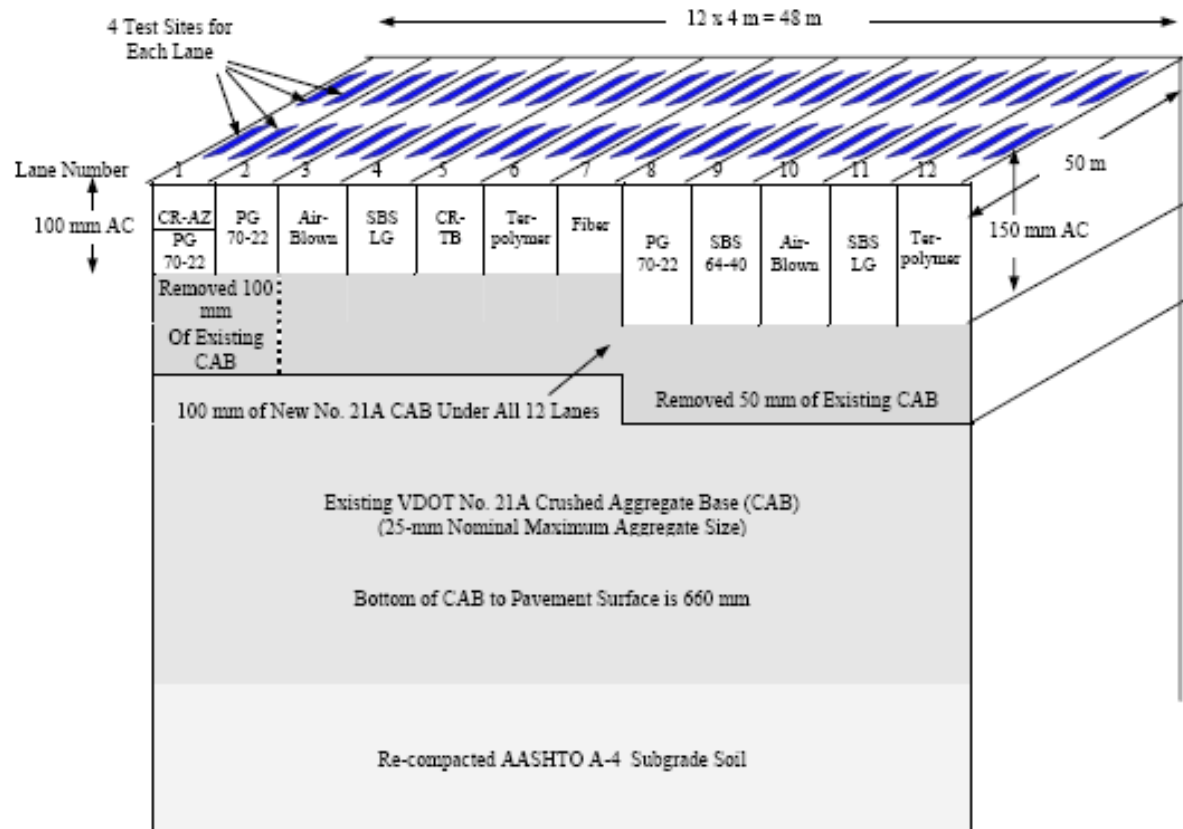
CHAPTER 3. MATERIALS USED IN THE PROJECT

OVERVIEW

Developing performance models and verifying them in realistic conditions requires asphalt pavements in service constructed with a wide range of asphalt materials and pavement structures; original materials and information (e.g., job mix formula); and as-constructed information like in situ density, layer thicknesses, unbound base and subgrade moduli; and traffic, climate, and condition survey data in time histories. The project team selected various field sections that satisfy these conditions for use in this project. These pavements include the Federal Highway Administration (FHWA) Accelerated Load Facility (ALF) sections, National Center for Asphalt Technology (NCAT) Test Track pavements, Manitoba Infrastructure and Transportation (MIT) facilities, Korea Expressway Corporation (KEC) test road pavement sections, perpetual pavements constructed by the New York State Department of Transportation (NYSDOT), and the second Strategic Highway Research Program (SHRP2) 2 R07 pavements constructed by the LaDOTD. In addition, the research team added test results for asphalt mixtures used in the New England RAP Pooled Fund study to the material database to develop and verify models. Including these mixtures allowed the research team to evaluate the performance of asphalt mixtures with various RAP contents and virgin binder grades. The team tested a total of 60 asphalt mixtures for dynamic modulus tests, cyclic fatigue tests, and triaxial stress sweep (TSS) rutting tests, with the FlexPAVE program predicting performance of 47 different pavement sections by using field, climate, traffic, structure, and boundary conditions. The following sections describe each of the selected projects.

FHWA ALF

FHWA ALF tests involved 12 lanes of unmodified, polymer-modified, air-blown, and fiber-reinforced asphalt mixtures. The facility finished accelerated testing of these sections in 2012. Each lane was large enough to contain four different test sites: two for rutting and two for fatigue cracking testing under the ALF loading. The research team performed fatigue and rutting tests on sections that had both 100- and 150-mm thicknesses, as shown in figure 12. Each of these sections comprised an asphalt layer resting on top of 560 or 510 mm of crushed aggregate base, which in turn rested on an AASHTO A-4 subgrade. The temperature remained constant during testing: 19°C for the cyclic fatigue tests and 45, 64, and 74°C for the rutting tests. The load applied to the pavement was a 425/64R22.5 (super-single) with tires moving at 17 km/h (10.5 mph). The applied load was 73.8 kN (16.6 kip) with contact pressure of 827 kPa (120 psi) for the cyclic fatigue tests and 44 kN (10 kip) with contact pressure of 689 kPa (100 psi) for the rutting tests. This project used the four mixtures listed in table 1. Detailed information about the project mixtures and binders can be found elsewhere in this report.⁽²⁴⁾



Source: FHWA.

1 m = 3.28 ft; 1 mm = 0.4 inch.

AC = asphalt concrete; CAB = crushed aggregate base; CR-AZ = crumb rubber-Arizona; CR-TB = crumb rubber-terminal blend; SBS = styrene butadiene styrene.

Figure 12. Illustration. FHWA ALF experiment overview.⁽²⁶⁾

Table 1. FHWA ALF hot-mix asphalt materials information.

Mixture Name	Description	Asphalt Binder	G (mm)	NMAS (mm)	Layer Thickness (mm)	Test Air Voids* for E* and Fatigue (%)	Test Air Voids* for Rutting Top/Bottom (%)
Control	Unmodified	PG 70-22	2.715	12.5	100/150	4	8.1
SBS	SBS-modified	PG 70-28	2.713	12.5	100/150	4	7.7/5.5
CR-TB	Crumb rubber	PG 70-28	2.714	12.5	100/150	4	7.7/5.2
Terpoly	Terpolymer	PG 70-28	2.708	12.5	100/150	4	7.0/4.6

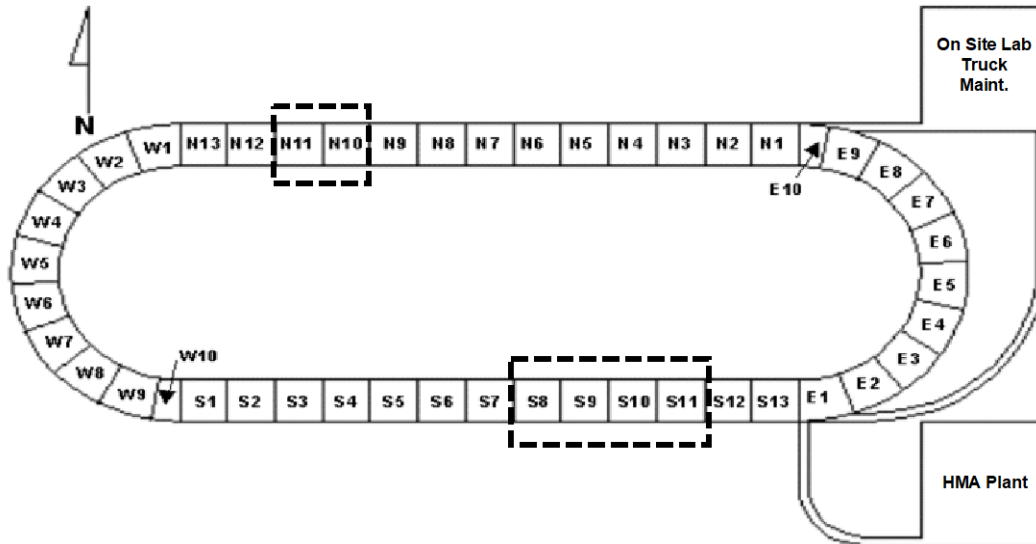
1 mm = 0.04 inch.

CR-TB = crumb rubber-terminal blend; NMAS = nominal maximum aggregate size; PG = performance grade; SBS = styrene butadiene styrene.

*Determined based on the method presented in the Sample Fabrication section.

NCAT Test Track

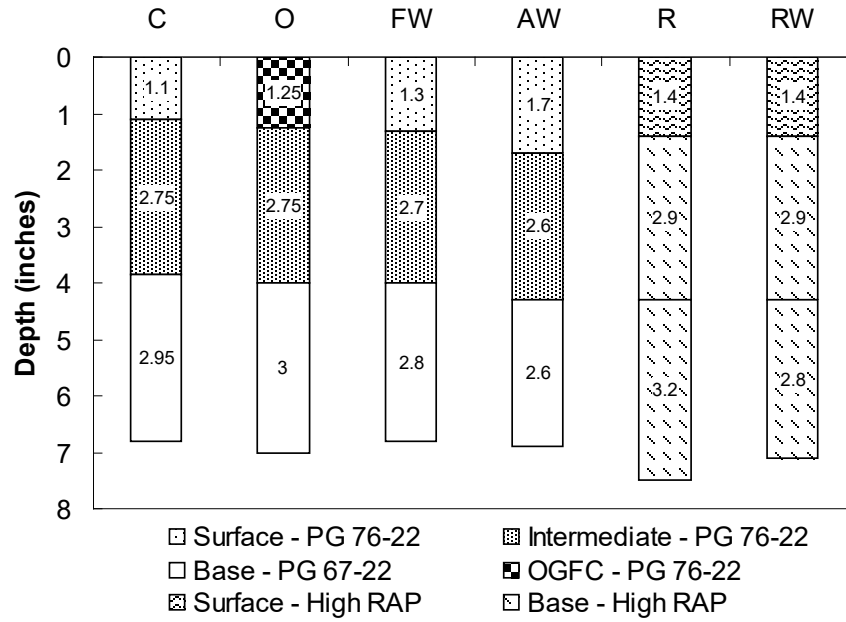
The NCAT Test Track is located near Auburn University in Opelika, AL. The track consists of a 1.7-mi oval divided into 46 different 200-ft test sections, as seen in figure 13. To expedite loading, tractor trailers continuously circulate the test track, which has produced about 10 million ESAL after 2 yr of circulation.



© 2010 NCAT. Section additions modified by NCSU. (DTFH61-08-H-00005)

Figure 13. Illustration. NCAT Test Track layout.⁽²⁷⁾

The asphalt mixtures used in this project were part of a project referred to as the Group Experiment, which had a goal of assessing the performance and structural responses of pavements constructed with warm-mix asphalt (WMA) technologies, high percentages of RAP, a combination of WMA and high RAP content, and a porous friction course.⁽²⁸⁾ The sections used in this project are marked by the rectangles with dashed lines in figure 13 and presented in figure 14. Each section is composed of three layers: surface, intermediate, and base. The layers are numbered: the surface layer is 1, the intermediate layer is 2, and the base layer is 3. For example, C1 stands for the control mixture at the surface layer. The mixtures' letter designations (C, O, FW, AW, R, and RW) are explained in table 2. The designed thicknesses are 1.25, 2.75, and 3.00 in for the surface, intermediate, and base layers, respectively. The constructed pavement structures are shown in figure 14, and the test conditions for the mixtures are presented in table 2.



Source: FHWA.

1 in = 25.4 mm.

OGFC = open-graded friction course; PG = performance grade.

Figure 14. Illustration. NCAT Test Track pavement sections with different thicknesses (inches) and mixture combinations.

Table 2. NCAT Test Track asphalt mixture information.

Label	NMAS (mm)	Binder Grade	Air Void (%)	Asphalt Content (%)	Description	NCAT Section
NCAT-C1	9.5	PG 76-22	4.3	6.1	A	S8
NCAT-C2	19.0	PG 76-22	6.1	4.4	A	S8
NCAT-C3	19.0	PG 67-22	7.4	4.7	A	S8
NCAT-O1	9.5	PG 76-22	18.3	5.1	B	S9
NCAT-O2	19.0	PG 76-22	5.1	4.4	B	S9
NCAT-O3	19.0	PG 67-22	8.3	4.7	B	S9
NCAT-FW1	9.5	PG 76-22	4.9	6.1	C	S10
NCAT-FW2	19.0	PG 76-22	6.0	4.7	C	S10
NCAT-FW3	19.0	PG 67-22	7.7	4.7	C	S10
NCAT-AW1	9.5	PG 76-22	3.9	6.4	D	S11
NCAT-AW2	19.0	PG 76-22	6.2	4.6	D	S11
NCAT-AW3	19.0	PG 67-22	6.1	5.0	D	S11
NCAT-R1	9.5	PG 67-22	4.7	6.0	E	N10
NCAT-R2	19.0	PG 67-22	6.1	4.4	E	N10
NCAT-R3	19.0	PG 67-22	5.0	4.7	E	N10
NCAT-RW1	9.5	PG 67-22	5.0	6.1	F	N11
NCAT-RW2	19.0	PG 67-22	5.8	4.7	F	N11
NCAT-RW3	19.0	PG 67-22	5.8	4.6	F	N11

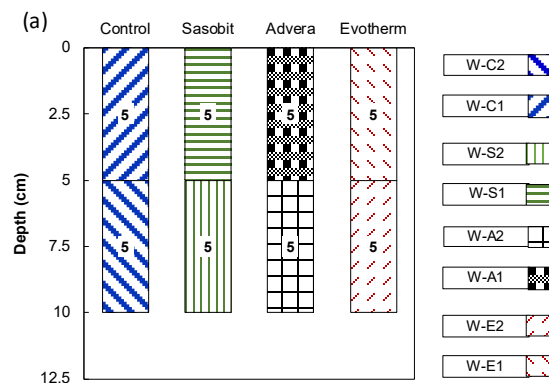
1 mm = 0.04 inch.

A = Control; B = Open-graded friction course surface with control intermediate/base; C - Control mixtures using foamed asphalt WMA; D = Control mixtures using Advera additive WMA; E = 50-percent RAP mixture; F = 50-percent RAP mixture using foamed asphalt WMA; NMAS = nominal maximum aggregate size; PG = performance grade.

MIT Project

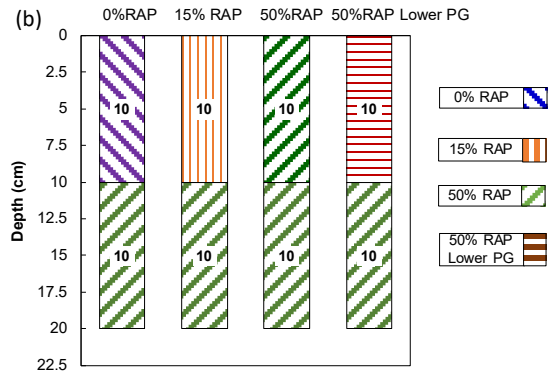
For the purposes of this research, the project team constructed two separate sections (one for RAP pavements and the other for WMA pavements) in Manitoba, Canada. These pavements are located on Provincial Highway 8 (between Gimli and Hnaua) and Provincial Highway 14 (from Winkler toward Plum Coulee), respectively, and were constructed between 2009 and 2010. These pavement sections were well-suited for correlating the laboratory evaluations of field-produced WMA and RAP mixtures and comparing the findings with actual field performance. The WMA overlay project contains eight different mixtures placed in four sections, and the RAP full-depth paving project contains four mixtures placed in four sections. The research team designed the WMA project to evaluate the effects of the following WMA technologies: Advera, Sasobit, and Evotherm (W-A, W-S, and W-E, respectively) as shown in figure 15-A. All the mixtures used for the surface layers (W-A1, W-S1, and W-E1) had the same gradation and binder as the control mixture (W-C1), but different warm-mix additives. The bottom layer mixtures (W-A2, W-S2, and W-E2) contained 35-percent RAP with the same gradation and binder as the control mixture (W-C2). The RAP project consisted of two 2-in layers with conventional HMA (R-C), 15-percent RAP (R-15R), 50-percent RAP (R-50R), and RAP with a soft binder (R-50RSB), as shown in figure 15-B.

Table 3 and table 4 provide a summary of the MIT test mixes for WMA and RAP mixes, respectively.



Source: FHWA.
1 cm = 0.4 inch.

A. WMA pavement sections.



Source: FHWA.
 1 cm = 0.4 inch.
 PG = performance grade.

B. RAP pavement sections.

Figure 15. Illustrations. MIT pavement sections.

Table 3. MIT WMA asphalt mixture information (NMAS 16 mm).

Mixture	Additive	RAP Content (%)	Binder Grade	Layer	Test Air Voids* (%)	Compaction Temperature (°C)
W-C1	None	0	PG 58-28	Surface	6.1	129
W-C2	None	35	PG 58-28	Bottom	5.5	139
W-S1	Sasobit	0	PG 58-28	Surface	5.2	106
W-S2	Sasobit	35	PG 58-28	Bottom	5.5	118
W-E1	Evotherm	0	PG 58-28	Surface	5.9	106
W-E2	Evotherm	35	PG 58-28	Bottom	6.1	117
W-A1	Advera	0	PG 58-28	Surface	4.7	108
W-A2	Advera	35	PG 58-28	Bottom	6.1	106

0°C = 32°F.

PG = performance grade.

*Determined based on the method presented in the Sample Fabrication section.

Table 4. MIT RAP asphalt mixture information (NMAS 16 mm).

Mixture	Additive	RAP Content (%)	Binder Grade	Layer	Test Air Voids* (%)	Compaction Temperature (°C)
R-C	None	0	PG 58-28	Surface	7.0	134
R-15R	None	15	PG 58-28	Surface	6.4	134
R-50R	None	50	PG 58-28	Surface/bottom	7.6	134
R-50RSB	None	50	PG 52-34	Surface	7.4	129

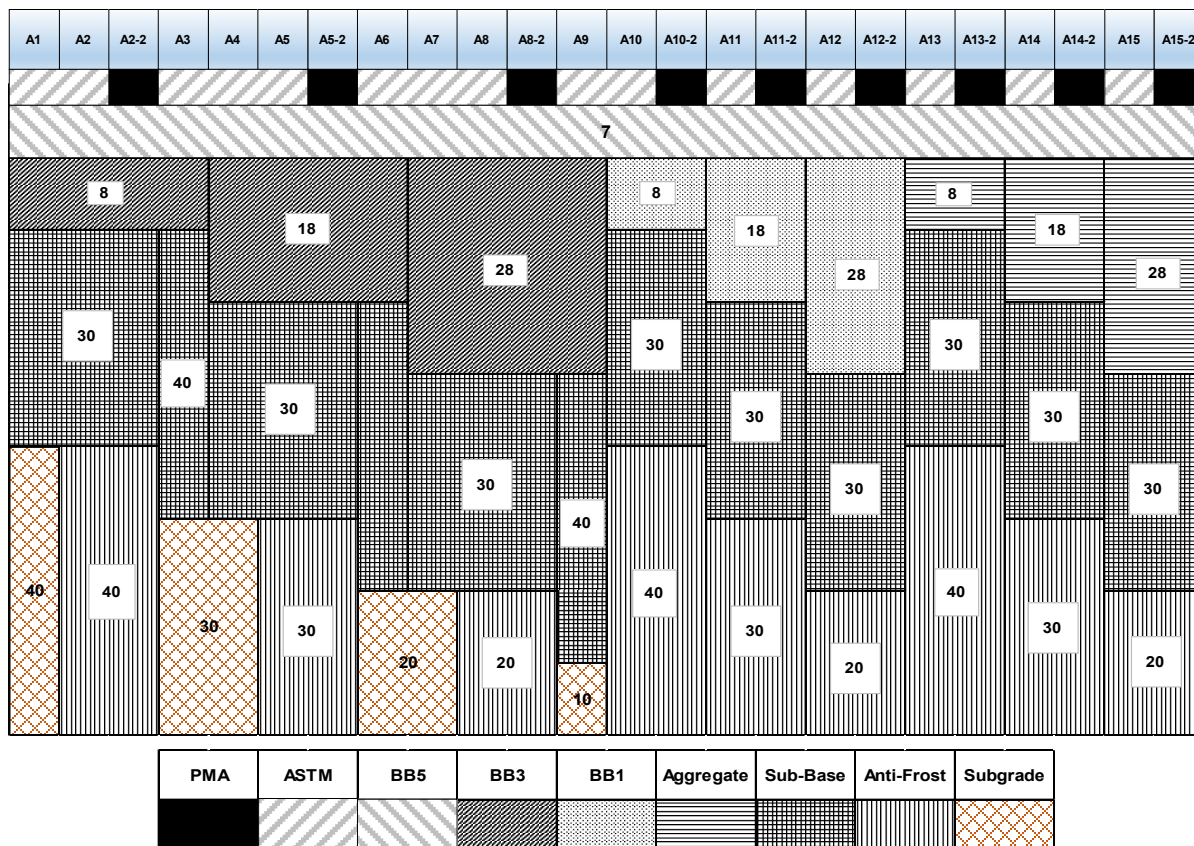
0°C = 32°F.

PG = performance grade.

*Determined based on the method presented in the Sample Fabrication section.

KEC Test Road

The KEC test road was constructed in December 2002. This test road was composed of 24 types of asphalt pavement; figure 16 schematically presents the KEC pavement structures. The field performance data the test road provided allowed researchers to compare different types of pavement structures and different mixtures under various climate conditions and real traffic loads. KEC conducted annual pavement condition surveys of the test road using Automatic Road Analyzer, ROADWARE.⁽²⁹⁾ Asphalt overlays were applied to some of the pavement sections in 2006. Therefore, the research team used the performance data obtained in 2005 for the FlexPAVE program analysis, because direct comparisons between field measurements and FlexPAVE program predictions are only possible using performance data prior to overlay construction.



Source: FHWA.

1 cm = 0.4 inch.

Note: The numbers in the figure are all in cm.

Figure 16. Illustration. Layout of KEC test sections.

For this study, the research team performed experiments using five laboratory-produced mixtures. Of these mixtures, two types of asphalt mixtures were used at the surface to compare rutting and crack propagation; these mixtures were an ASTM mix and a 19-mm nominal maximum aggregate size (NMAS) polymer-modified styrene butadiene styrene (SBS) mixture (hereinafter referred to as PMA). The intermediate layer consisted of a 25-mm NMAS BB5

mixture with 70-mm thickness. The research team used mixtures designated as BB1 (25-mm NMA) and BB3 (40-mm NMA), which are frequently used in South Korea, for the base layers.

Table 5 and table 6 summarize the general mixture information and the gradations of the mixtures used in the KEC test road sections, respectively. The sublayers below the base layer are mostly composed of subbase and antifrost layers placed on top of the subgrade. An antifrost layer often is used to compensate for the level difference due to the base; however, the research team omitted the antifrost layer from some sections for comparative purposes to evaluate the effectiveness of antifrost layers on pavement performance. Figure 16 schematically presents the KEC pavement structures.

Table 5. KEC test road mixture information.

Type	Surface	Surface	Base	Base	Intermediate
Mixture	ASTM	PMA	BB1	BB3	BB5
Binder type	Unmodified	SBS	Unmodified	Unmodified	Unmodified
Binder grade	PG 64-22	PG 76-22	PG 64-22	PG 64-22	PG 64-22
Binder content (%)	5.2	4.9	4.2	4.4	4.3
NMA (mm)	19	19	25	40	25
Test air voids (fatigue %)	5.9	5.9	5.7	7.6	7.5
Test air voids (rutting %)	5.9	5.9	6.0	8.0	9.9

1 mm = 0.04 inch.

PG = performance grade.

Table 6. Gradations of the KEC test road mixtures.

Sieve Size	ASTM	PMA	BB1	BB3	BB5
37.5 mm	100	100	100	100	100
25.0 mm	100	100	100	88.6	100
19.0 mm	99.6	99.6	92.5	71	91
12.5 mm	84.9	84.9	72.9	51.1	67.5
9.5 mm	71.1	71.1	63.9	44.1	55.1
4.75 mm	49.3	49.3	48.5	38.1	31.2
2.36 mm	36.2	36.2	36.1	29.1	23
0.60 mm	18.1	18.1	18	15.1	12.8
0.30 mm	11.6	11.6	11.6	10.1	9.2
0.15 mm	7.4	7.4	7.3	6.8	6.7
0.075 mm	4.4	4.4	4.2	4.4	4.6

NYSDOT Project

The NYSDOT pavement sections have three layers: surface, intermediate, and base. The intermediate layer is composed of two lifts. The research team tested four mixtures from the

NYSDOT project to accommodate the surface layer, two lifts of the intermediate layer, and the base layer. Table 7 presents the volumetric properties for the four NYSDOT mixtures used in the project.

Table 7. NYSDOT mixture information.

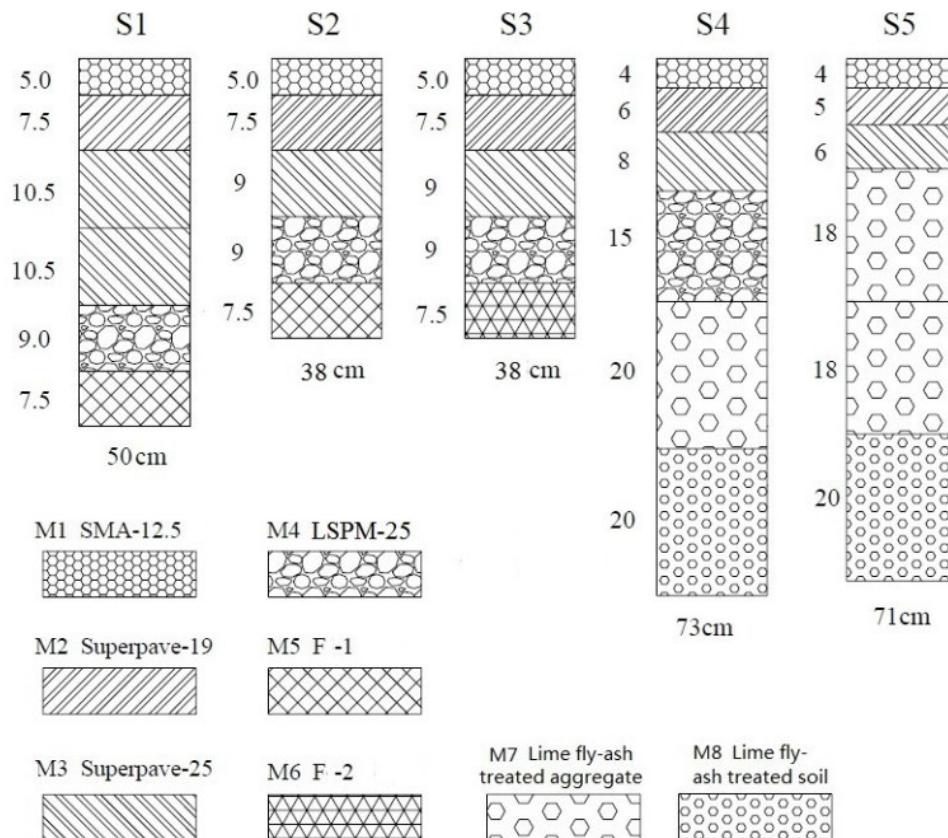
Mixture Label	Description	Mixture Label	G (mm)	Thickness (mm)	Test Air Voids* (%) Fatigue	Test Air Voids* (%) Rutting
NY9.5	Surface	NY9.5	2.410	100	3.2	5.4
NY19 L5	Inter.-Lift 2	NY19 L5	2.462	100	5.0	6.0
NY19 L3	Inter.-Lift 1	NY19 L3	2.467	100	6.1	6.1
NY25	Base	NY25	2.490	100	6.2	6.2

1 mm = 0.04 inch.

*Determined based on the method presented in the Sample Fabrication section.

Binzhou, China Perpetual Pavement Project

The Binzhou perpetual pavement project in China consisted of five test sections of varying thicknesses and material compositions (figure 17). Six asphalt mixtures were used in these sections, and their descriptions are given in table 8. For each section, the top three layers are the same: 12.5-mm NMAS stone matrix asphalt (SMA), 19.0-mm NMAS dense-graded mixture, and 25.0-mm NMAS dense-graded mixture, respectively. The thickness of each of these layers differs between sections as do the support layers for these mixtures. Section 5 adopts a flexible pavement design with semirigid base layers widely used in China. The major problem with this type of pavement is reflective cracking that initiates in the semirigid base and propagates through the asphalt layers above. Section 4 is an upgrade of Section 5 in that an absorbing layer of large stone porous mixture (LSPM) has been inserted between the conventional asphalt mixtures and the semirigid base. LSPMs have been field proven in China to reduce reflective cracking as well as drain water from pavement structures. Sections 1 through 3 are full-depth asphalt pavements that were designed based on traditional perpetual pavement principles. Each section contains a highly fatigue-resistant mixture on top of the base or subgrade and a layer of LSPM just above the bottom fatigue layer. The pavement structure layout of each section is illustrated in figure 17. The six different asphalt mixtures are described in table 8.



© 2016 Journal of Traffic and Transportation Engineering. (DTFH61-08-H-00005)
1 cm = 0.4 inch.

Figure 17. Illustration. Binzhou pavement structure layout for each section.⁽³⁰⁾

Table 8. HMA material description.

Mixture ID	Mixture Name	Description
M1	SMA-12.5	SMA (PG 76-22, MAC modified)
M2	Superpave-19	19-mm NMAS Superpave (PG 76-22, MAC modified)
M3	Superpave-25	25-mm NMAS Superpave (PG 64-22)
M4	LSPM-25	25-mm LSPM (PG 70-22, MAC modified)
M5	F-1	12.5-mm NMAS fatigue layer (PG 64-22)
M6	F-2	12.5-mm NMAS fatigue layer (PG 76-22, SBS modified)

1 mm = 0.04 inch.

MAC = multigrade asphalt cement; NMAS = nominal maximum aggregate size; PG = performance grade.

LaDOTD SHRP2 R07 Project

The LaDOTD's US 90 Frontage Roads project pavement has two layers: a top layer and a bottom layer. Table 9 presents the volumetric properties for the two LaDOTD mixtures used in this project.

Table 9. LaDOTD mixture information.

Mixture Name	Description	Asphalt Binder	G (mm)	NMAS (mm)	Test Air Voids* (%) Fatigue	Test Air Voids* (%) Rutting
Surface	Top layer	PG 64-22	2.494	12.5	4.9	7.4
Bottom	Bottom layer	PG 64-22	2.504	19	3.5	5.6

1 mm = 0.04 inch.

PG = performance grade.

*Determined based on the method presented in Section 3.2.

New England RAP Mixtures

The nine mixtures from the New England RAP Pooled Fund study are 12.5-mm laboratory-produced mixtures. The study team systematically varied the RAP contents and the binder contents to create these nine mixtures. The objective of this study was to investigate the effects of the changes of the RAP content and binder content on the fatigue properties of the New England asphalt mixtures. Table 10 presents detailed information about these mixtures.

Table 10. New England RAP mixture information.

Mixture Name	PG Binder	RAP (%)	Binder Content (%)
NH5820-opt	58-28	20	Optimum-0.5
NH5840-opt	58-28	40	Optimum-0.5
NH6400-opt	64-28	0	Optimum-0.5
NH6420-opt	64-28	20	Optimum-0.5
NH6440-opt	64-28	40	Optimum-0.5
NH6400opt	64-28	0	Optimum
NH6420opt	64-28	20	Optimum
NH6440opt	64-28	40	Optimum
NH6440+opt	64-28	40	Optimum+0.5

PG = performance grade.

SAMPLE FABRICATION

The sample fabrication process for the PRS field verification sections is documented in this section.

Field Simulation and Test Air Void Determination

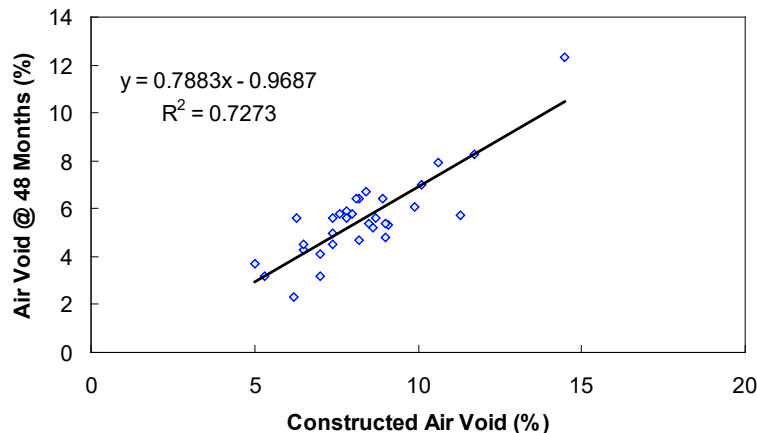
The goal of this PRS project was to develop performance models and verify them using field performance measurements. The research team considered field conditions, such as air void content, for the sample fabrication stage.

To simulate field performance, the air void contents of the specimens should be representative of the field air void contents. Air void content has a significant effect on the rutting and fatigue cracking of asphalt pavement. Tests used to verify the rutting potential of a mixture should use the initial air void content because rutting generally occurs within the first 2 yr of the pavement life. The challenge with using only the initial air void content comes from the fact that fatigue cracking does not occur until 5 yr or later in the pavement life.

The NCAT, under the auspices of the NCHRP 9-9 project, conducted a comprehensive study to examine this issue by measuring the air void content of asphalt pavements after 3, 6, 24, and 48 mo of service.⁽³¹⁾ A total of 40 different pavements from 15 different States were sampled. The pavements were mostly high volume (ESAL between 10 and 30 million) but included some lower volume (ESAL less than 80,000) and extremely high volume (ESAL of approximately 100 million) cases. The basic conclusion from this work is that asphalt pavements densify relatively

quickly and ultimately reach their final density after 2 to 4 yr of service. Most of this density is gained in the first 3 to 6 mo.

After extracting the relevant data compiled during the NCHRP 9-9 project, a weak but noticeable correlation was found to exist between initial air void (AV_{ini}) and final air void (AV_f) contents. The regression model fit is shown in figure 18. This relationship is quite simple, as efforts to cross-correlate this relationship with traffic level, climate, or other factors did not improve the predictability. The inability to improve the predictions with these additional factors suggests that other unknown factors, such as construction quality, measurement inconsistencies, material characteristics, etc., mask all but the most important factor, which is the initial air void content.



Source: FHWA.

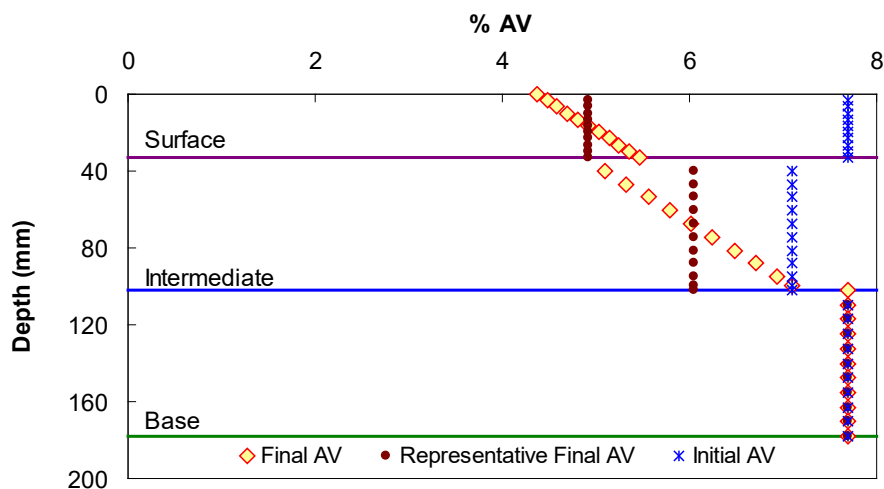
Figure 18. Graph. Relationship between as-constructed and in-service air void contents.

Because the relationship between the initial and final air void contents had been established, the research team could adjust each mixture to a new air void content. The air void reduction is not as simple as using the relationship shown in figure 18 for all layers because most densification occurs in the top 100 mm. The NCHRP 9-9 researchers referenced a single study, Blankenship et al. 1993, that addresses this particular issue.⁽³²⁾ In this study, the researchers concluded that not much of a relationship exists between traffic and densification below a depth of approximately 100 mm. Based on these findings and the aforementioned observations, the research team proposed the following steps for this PRS study to determine the air void contents for different layers:

1. Use the relationship derived from the NCHRP 9-9 project to predict the air void content at 22 mm from the pavement surface (the average lift thickness of the NCHRP 9-9 project cores was 44 mm).
2. Compute the change in air void content at this depth by subtracting the predicted long-term air void content from the initial construction air void content.
3. Fix the air void content for depths greater than or equal to 100 mm in the pavement structure at a value equal to the as-constructed value.
4. Assume a linear variation in air void content between 22 mm and 100 mm and compute the change in air void content as a function of depth between 0 mm and 100 mm.

5. Compute the long-term air void content by subtracting the reduction in air void content from the initial as-constructed air void content.
6. Compute the averaged (representative) air void content of a given layer by numerically integrating and averaging the computed air void distribution throughout the section depth.

An example of this procedure can be seen in figure 19. The greatest air void reduction occurs at the surface. The intermediate section air void reduction with depth does not align with the surface air void reduction with depth because these layers start with different initial air void contents, but the change in air void content versus depth (slope) remains the same. The base layer does not exhibit any air void changes. This finding suggests that the base mixture will perform worse than the intermediate mixture in both rutting and cyclic fatigue tests due to the high air void content, if all other conditions are the same.

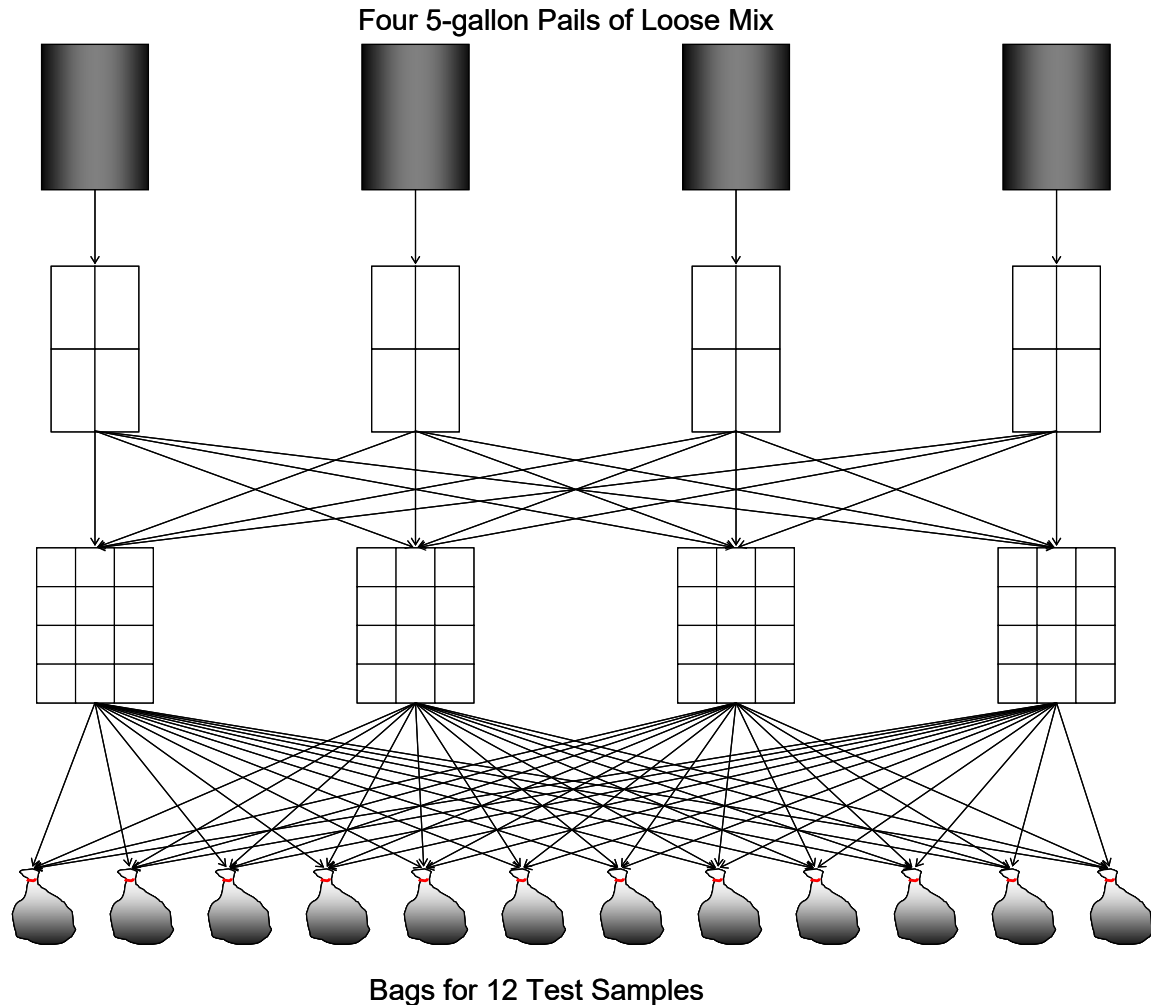


Source: FHWA.
 1 mm = 0.04 inch.
 AV = air void.

Figure 19. Illustration. Example of calculating air void-content reduction (NCAT-FW section).

Sample Fabrication Procedure

Because this PRS project required significant testing of plant-mixed materials that were sampled in the asphalt mixing plant, stored in 5-gal pails and sent to the research team, the process required an effective and efficient means of dividing the materials for sampling and storage. Because of the number of tests required to build the necessary material property databases, the method had to be repeatable and easy to perform, as existing commercial equipment for this purpose was found to be cumbersome and expensive. Instead, the research team devised a plan that followed, in principle, the guidelines laid out in ASTM D979, *Standard Practice for Sampling Bituminous Paving Materials*; ASTM D3665, *Standard Practice for Random Sampling of Construction Materials*; and ASTM C702, *Standard Practice for Reducing Samples of Aggregate to Testing Size*.⁽³³⁻³⁵⁾ A schematic diagram of the sampling procedure is shown in figure 20.



Source: FHWA.
1 gal = 3.785 L.

Figure 20. Illustration. Loose mix sampling schematic.

The sampling procedure begins with four 5-gal pails of material (approximately 100 lb) and reduces the quantity to 12 test samples. To accomplish this, the buckets are first heated to 10 degrees below the plant discharge temperature for 2 h. Then, each of the four buckets is quartered by pouring the contents into the center of a pan that holds four smaller subpans. The contents are poured so that one-fourth of the total content of each bucket fills each subpan. These subpans are then randomly selected and poured into one of a second set of four pans. Once the contents of all four original buckets are quartered, each of the second pans contain approximately one-fourth of each original bucket. The contents of each of these pans are thoroughly mixed by hand using a scoop and small rake and spread into layers of equal thickness. Once the material is mixed and spread, the pan is placed on top of a box with 12 subboxes inside. Each pan in the second set has a sliding bottom that can be removed to allow the contents to drop into these subboxes. These subboxes contain approximately one-fourth of the mass needed for a test specimen. Each subbox is randomly sampled and dumped into 1 of 12 cloth sacks prepared beforehand. This final step is repeated for each of the remaining three pans. Finally, the 12 cloth bags are sealed and placed in an unlit cabinet until needed for testing.

The gyratory-compacted specimens were made according to AASHTO T 312, *Standard Method of Preparing and Determining the Density of Asphalt Mixture Specimens by Means of the Superpave Gyratory Compactor*, which included the short-term aging process.⁽³⁶⁾ The gyratory-compacted specimens were cored to a 100-mm diameter and cut to 130 or 150 mm in length, which are the dimensions required for the AMPT and by AASHTO TP 107.⁽³⁷⁾ A specimen that is any longer and thinner than these dimensions could not be used due to the height limitations of the Superpave gyratory compactor and the representative volume entity (RVE). The RVE is a material sample with minimal dimensions so the material is large enough to represent the global properties of the test material. The goal of the experimental project is to maintain the same structure, aggregate gradation, and air void content, as well as asphalt binder content and grade for each section.

All the specimens were fabricated from loose or plant mixtures. To compact the loose mixture, the research team developed a procedure that provided a sample with enough mass (i.e., 8,000 g) to compact a specimen in the gyratory compactor to a height of 178 mm and a diameter of 150 mm. Test specimens were cored from these gyratory-compacted specimens to reduce the effects of nonuniform air void distribution in the gyratory-compacted specimens.

CHAPTER 4. PERFORMANCE MODELS AND CALIBRATION METHODS

The PRS project used structural models to estimate pavement responses due to loading. However, to estimate the strains more accurately, a basic relationship must be defined between the stresses and strains in the various model layers that are as similar as possible to the relationship between the in situ values of the stresses and strains. Because asphalt concrete is a viscoelastoplastic material, the actual responses have elastic, plastic, and viscous—or time- or rate-dependent—components and are dependent on a variety of factors, such as temperature, load level, loading time, and strain level. As such, it is essential to provide mixture-specific linear viscoelastic properties for accurate response analysis.

Performance evaluation also plays a key role in the PRS project. As discussed, the existing performance models were mainly developed in an empirical manner. The research team made an effort to develop mechanistic performance models of asphalt concrete so asphalt pavement performance can be more accurately and reasonably calculated than is possible with structural models alone.

LINEAR VISCOELASTIC MODEL

The dynamic modulus is an important variable in characterizing the material's linear viscoelastic properties. This section documents the material model and characterization method.

Introduction

Asphalt concrete is a linear viscoelastic material at small strain levels (i.e., between 50 and 75 microstrains). Asphalt materials are also thermorheologically simple (TRS), which implies that the effects of loading frequency and temperature can be combined into a single parameter called reduced frequency to produce a single curve to describe the dynamic modulus ($|E^*|$). Dynamic modulus values can be predicted for any reduced frequency within the measured parameters and extrapolated for values outside the measured range. In AASHTO T 342, *Standard Method of Test for Determining Dynamic Modulus of Hot Mix Asphalt (HMA)*, the single curve that describes the dynamic modulus as a function of temperature and frequency is called the master curve.⁽³⁷⁾ The master curve is represented by the sigmoidal functional form given in equation 9.

$$\log |E^*| = a + \frac{b}{1 + \frac{1}{e^{d+g \cdot \log(f_r)}}} \quad (9)$$

Where:

e = Euler's number.

a , b , d , and g = optimized constants.

f_r = reduced frequency.

The time–temperature superposition (t–TS) principle states that unit response functions (e.g., the dynamic modulus) in TRS materials, such as asphalt mixtures, can be shifted in the time or frequency domain (i.e., along the horizontal axis) to produce a single continuous master curve.

The shifted frequency, also known as the reduced frequency, is calculated by multiplying the measured frequency by a shift factor. The equation for the reduced frequency can be obtained from equations 10 and 11, and the shift factor is represented by a quadratic equation.

$$f_r = a_T f \tag{10}$$

$$\log(a_T) = a_1 T^2 + a_2 T + a_3 \tag{11}$$

Where:

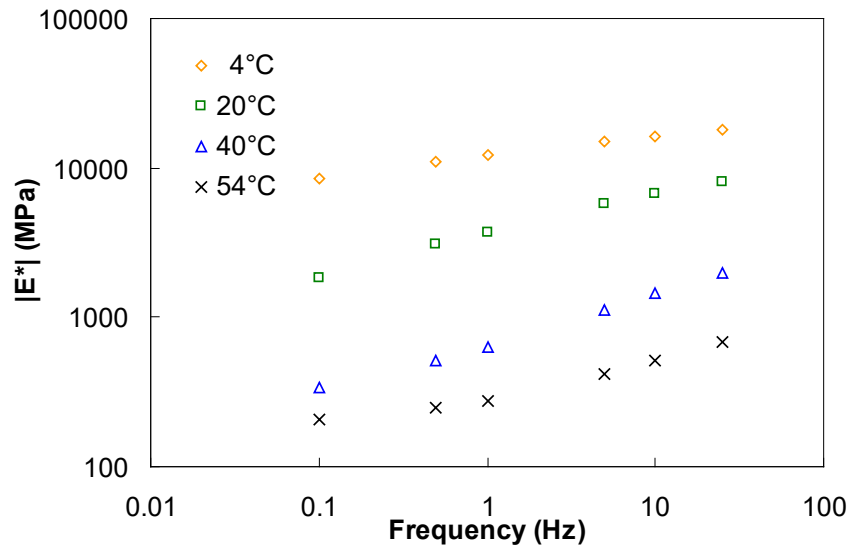
a_T = t-T shift factor.

f = loading frequency in Hz.

a_1 , a_2 , and a_3 = shift factor coefficients.

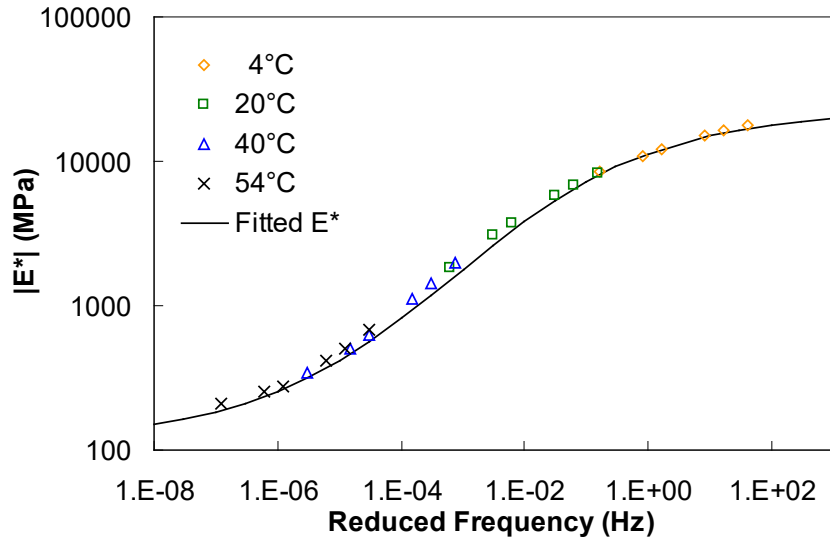
T = temperature.

An example of dynamic modulus values at different frequencies and temperatures is given in figure 21 through figure 23.



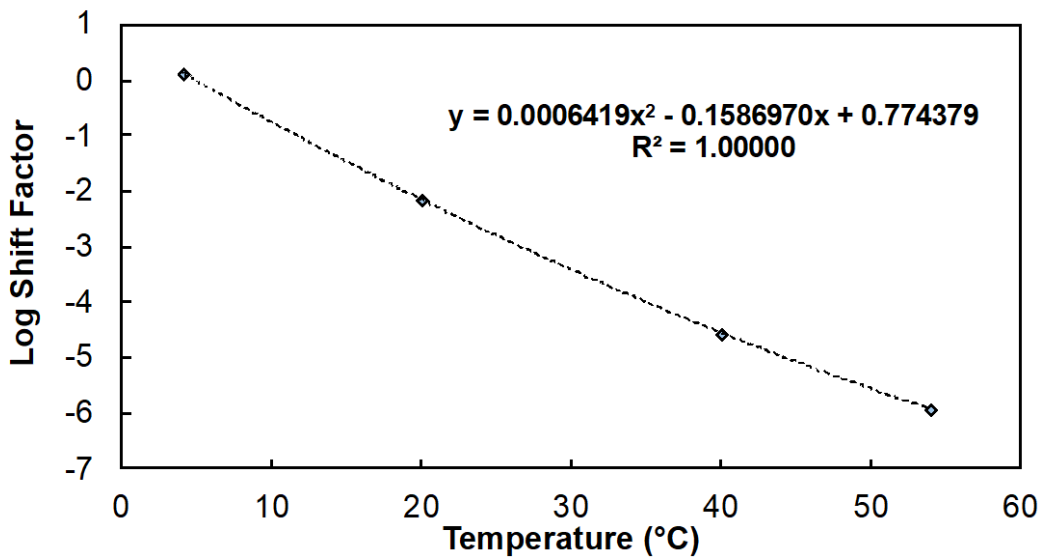
Source: FHWA.
 0°C = 32°F; 1 MPa = 145.04 psi.

Figure 21. Graph. Example of measured dynamic modulus values at different frequencies and temperatures.



Source: FHWA.
 0°C = 32°F; 1 MPa = 145.04 psi.

Figure 22. Graph. Dynamic modulus master curve.



Source: FHWA.
 0°C = 32°F.

Figure 23. Graph. Example of a t-T shift factor curve.

The benefit of measuring dynamic modulus values over measuring other stiffness measurements, such as the resilient modulus (M_R), is that the dynamic modulus values combined with the phase angle (ϕ)— also known as the complex modulus (E^*) —provides a constitutive relationship between the stress and strain for steady-state sinusoidal loading. Because the complex modulus describes a constitutive relationship, it can be mathematically transformed from a frequency-dependent property to a time-dependent property like the relaxation modulus ($E(t)$) and creep compliance ($D(t)$). The relaxation modulus, with appropriate mathematical

considerations, can be used to predict the stress response to any applied strain. The creep compliance can be used to predict the strain response to any stress history. The predicted responses are accurate as long as the applied histories remain in the linear viscoelastic range. The relaxation modulus can be expressed using the Prony series representation given in equation 12.

$$E(t) = E_{\infty} + \sum_{i=1}^m E_i e^{-\frac{t}{\rho_i}} \quad (12)$$

Where:

E_{∞} = elastic modulus.

t = time.

m = number of Maxwell elements.

E_i = modulus time of the i th Maxwell element.

ρ_i = relaxation time of the i th Maxwell element.

Equation 12 has two components that determine the material response. The first component, E_{∞} , represents the elastic response. The summation of the Maxwell elements, $E_i e^{-t/\rho_i}$, represents the viscoelastic response. To represent the real and imaginary components of the complex modulus (i.e., the storage moduli (E') and loss moduli (E'')), equation 12 can be transformed, as shown in equation 13 and equation 14, where ω_r is the reduced angular frequency ($2\pi f_r$).

$$E'(\omega_r) = E_{\infty} + \sum_{i=1}^m \frac{\omega_r^2 \rho_i^2 E_i}{\omega_r^2 \rho_i^2 + 1} \quad (13)$$

$$E''(\omega_r) = \sum_{i=1}^m \frac{\omega_r \rho_i E_i}{\omega_r^2 \rho_i^2 + 1} \quad (14)$$

The storage and loss moduli values can be calculated from the dynamic modulus and phase angle values using equation 15 and equation 16, respectively.

$$E'(\omega_r) = |E^*(\omega_r)| \cos(\phi(\omega_r)) \quad (15)$$

$$E''(\omega_r) = |E^*(\omega_r)| \sin(\phi(\omega_r)) \quad (16)$$

Conversely, the dynamic modulus values can be calculated from the storage and loss moduli values using equation 17. Park et al. provide details for calculating and transforming this information from the frequency domain to the time domain.⁽³⁸⁾

$$|E^*(\omega_r)| = \sqrt{(E'(\omega_r))^2 + (E''(\omega_r))^2} \quad (17)$$

Impact Resonance Test

$|E^*|$ master curves provide a fingerprint of the linear viscoelastic behavior of asphalt concrete, which then allows the user to predict the responses of asphalt concrete to any loading history or temperature within the linear viscoelastic range. The AASHTOWare Pavement ME Design

developed by NCHRP Project 1-37A also uses dynamic modulus values as inputs.⁽²⁵⁾ In this project, the research team evaluated the impact resonance (IR) test as a fast and simple method to determine the dynamic modulus of asphalt concrete.

In response to the need for a more practical dynamic modulus test method than AASHTO T 342-11, researchers developed alternative methodologies to estimate the dynamic modulus values of asphalt mixtures.^(37,39) One alternative to determining dynamic modulus values is estimating them using a predictive equation. Several predictive equations are available, and most of them are empirical and rely on mixed volumetric properties and binder characteristics. The most widely used predictive equation was developed by Witczak.⁽³⁹⁾ Witczak derived the Witczak predictive equation based on nonlinear regression analysis of dynamic modulus data from 205 mixtures. However, the Witczak predictive equation's accuracy has been found to be questionable.⁽³⁹⁾

Another alternative methodology to conventional dynamic modulus testing is the IR test.⁽⁴⁰⁾ The IR test is more advantageous than the conventional dynamic modulus test because the IR test's setup is simpler, more efficient, and significantly less expensive. The IR test method induces an excitation by striking a mass (usually a steel ball) onto a specimen and measuring the sample's natural vibration, which can then be used to determine the material properties of the specimen. The IR test is also nondestructive, so the IR test specimens can be used for other tests following test completion. The IR tests determine the dynamic modulus values based on the resonant frequency obtained from the measured response curve in the frequency domain. The resonant frequency is the frequency that corresponds to the highest peak in amplitude, which is often referred to as the first resonance frequency. The resonant frequency can be obtained using the fast Fourier transform of the waveform and is used alongside the relationship between wave velocity and density to calculate the modulus value.

Researchers have used the IR test method to measure portland concrete cement (PCC) mixture properties, and ASTM C 215, *Standard Test Method for Fundamental Transverse, Longitudinal and Torsional Resonant Frequencies of Concrete Specimens*, provides a standard procedure for this process.⁽⁴¹⁾ Researchers in the asphalt pavement community have built upon PCC work to enable the measurement of asphalt concrete dynamic modulus values using IR testing and have found promising results. Kweon and Kim and LaCroix and Kim concluded that IR tests using long cylindrical specimens could be an alternative test method for determining the dynamic modulus and phase angle of asphalt mixtures.^(40,42) However, the geometry (100 mm in diameter by 150 mm in height) of the cylindrical specimens used in these tests prohibited applying IR testing to field cores because individual pavement layers are generally thinner than 100 mm.

The research team tested beam-shaped specimens (380 × 60 × 60 mm) to determine their resonant frequencies by applying resonant acoustic spectroscopy to obtain frequency response functions.^(43,44) However, it is difficult to obtain for the laboratory because they are normally fabricated from slabs; additionally, it is difficult to obtain from the field because of the required sawing operation. This sawing is significantly more difficult than coring.

The advantages of IR tests as well as the need to test field cores led researchers to consider performing IR testing on thin, disk-shaped specimens. The use of thin disk specimens allows researchers to test both standard gyratory-compacted specimens and field cores. In addition, the

use of thin disk specimens requires only sawing the specimens from gyratory-compacted samples, whereas standard dynamic modulus test specimens require both sawing and coring; thus, the use of thin disk specimens helps provide further efficiency in testing.

Ryden applied IR testing for thin disk asphalt concrete specimens and used the fundamental antisymmetric flexural mode and the fundamental symmetric longitudinal mode of vibration to determine two different resonant frequencies.⁽⁴⁵⁾ Ryden estimated Poisson's ratio from the elastic modulus, conducted the IR tests at multiple temperatures, and constructed the dynamic modulus master curves by optimizing the Williams-Landel-Ferry shift factor function and the dynamic modulus sigmoidal function. Ryden then compared the master curves determined from these IR tests with the master curve predicted from Witczak's predictive equation.

Researchers have more actively applied the IR test to the characteristic of PCC than to asphalt concrete. ASTM E 1876-09, *Standard Test Method for Dynamic Young's Modulus, Shear Modulus and Poisson's Ratio by Impulse Excitation of Vibration*, is a standard method for using IR testing to determine the elastic properties of PCC thin disks.⁽⁴⁶⁾ This method considers two modes of vibration: antiflexural vibration and axisymmetric flexural vibration. The main advantage of the ASTM E 1876-09 method is that it measures Poisson's ratio using the ratio of two resonant frequencies obtained from two natural vibrations. Leming et al. conducted another study that focuses on determining the elastic modulus of concrete disks using the IR test.⁽⁴⁷⁾ Leming et al.'s work uses Hutchinson's solution for the axisymmetric flexural vibration of a thick free circular plate to determine the fundamental frequency, which is then used to determine the elastic modulus of PCC.⁽⁴⁸⁾

This study considers the strengths and weaknesses of different modes of conventional IR testing when applying them to asphalt concrete. The work presented in this report builds upon the foundations laid by previous researchers to determine the optimal testing parameters for efficiently and accurately obtaining the dynamic modulus properties of asphalt mixtures using thin disk specimens. The research team investigated the ASTM E 1876-09 method and the method suggested by Leming et al. to propose a better method that can produce consistent and accurate IR test results for asphalt mixtures. The team obtained dynamic modulus values from IR tests and compared them with conventional dynamic modulus test results to assess the accuracy of the proposed methodology.

The research team identified two objectives of this IR test study. The first objective was to develop an IR test procedure for thin disk specimens to determine the dynamic modulus and phase angle values of asphalt mixtures. The second objective was to verify the dynamic modulus values measured from thin disk IR tests by comparing them to the dynamic modulus values measured from IR tests of long cylindrical specimens and the dynamic modulus values obtained from the commonly used AASHTO T 342-11 test procedure.⁽³⁷⁾ Appendix B presents the research efforts taken to accomplish these objectives.

Although the dynamic modulus values determined by the IR tests agree with the dynamic modulus values determined by the axial compression tests, the IR test's inability to measure the dynamic modulus of asphalt mixtures at high temperatures prevents the research team from including this test method in the PRS framework.

FATIGUE PERFORMANCE MODEL

The research team used the S-VECD model to determine the material's fatigue behavior and to predict the material's fatigue performance. This section introduces the background of this model.

Introduction

The continuum damage theory can be used to characterize material using macroscale observations while ignoring microscale behavior. The two essential parameters that the continuum damage theory quantifies are effective stiffness and damage. Pseudostiffness represents the material's structural integrity and can be easily assessed in the form of the instantaneous secant modulus and measured in experiments, whereas damage is sometimes difficult to quantify and generally relies on rigorous theories. One such theory is the work potential theory developed by Schapery for elastic materials with growing damage based on the thermodynamics of irreversible processes.⁽⁴⁹⁾ This theory quantifies damage by an internal state variable (ISV) that accounts for microstructural changes in the material. For viscoelastic material, the theory applies the correspondence principle first to uncouple the time dependency associated with viscoelasticity. After transforming the physical strain to the pseudostrain, the same formula used for elastic materials can model the viscoelastic problem. The viscoelastic continuum damage (VECD) theory is composed of the basic equations detailed in this section.

The pseudostrain energy density function, the stress–pseudostrain relationship, and the damage evolution law are defined as equation 18, equation 19, and equation 20, respectively.

$$W^R = f(\varepsilon^R, S) \quad (18)$$

$$\sigma = \frac{\partial W^R}{\partial \varepsilon^R} \quad (19)$$

$$\frac{dS}{dt} = \left(-\frac{\partial W^R}{\partial S}\right)^\alpha \quad (20)$$

Where:

W^R = pseudostrain energy density.

ε^R = pseudostrain.

S = damage parameter (ISV).

α = damage evolution rate.

Equation 21 computes the uniaxial mode of loading and can be written as:

$$W^R = \frac{1}{2}(\varepsilon^R)^2 C \quad (21)$$

Where:

C (the pseudostiffness) is the only variable that is a function of damage S .

When equation 21 is substituted into equation 20, the damage evolution law becomes equation 22.

$$\frac{\partial S}{\partial t} = \left(-\frac{1}{2}(\varepsilon^R)^2 \frac{\partial C}{\partial S}\right)^\alpha \quad (22)$$

Lee and Kim used the chain rule (equation 23) to solve the damage evolution law by substituting it into equation 22.⁽¹³⁾

$$\frac{dC}{dS} = \frac{dC}{dt} \frac{dt}{dS} \quad (23)$$

After simplification, the damage calculation equation for each time increment i is given as equation 24. In this equation, the reduced time interval ($\Delta \xi$) replaces the time step term (Δt) due to verifying the t-TS principle with growing damage.

$$dS_i = \left(-\frac{1}{2}(\varepsilon^R)_i^2 \Delta C_i\right)^{\frac{\alpha}{1+\alpha}} \times (\Delta \xi)_i^{\frac{1}{1+\alpha}} \quad (24)$$

S-VECD Model

A requirement of the rigorous VECD model is calculating and tracking the pseudostrain, pseudostiffness, and damage for the entire loading history. This requirement necessitates a computationally expensive procedure for cyclic loading. An average test with 10,000 cycles to failure and 100 data points per cycle would require analyzing 1,000,000 data points. Although this task is not impossible using advanced computers, it is cumbersome and time-consuming. In addition, experimental difficulties like data storage can lead to significant errors.

In response to this problem, Underwood developed the S-VECD model for the cyclic-loading application.⁽⁵⁰⁾ First, Underwood defined a common set of variables to avoid confusion, as summarized in figure 24. This figure depicts two pseudostiffness terms: a total pseudostrain-based value (\bar{C}) and a cyclic magnitude-based value (F). Equation 25 and equation 26 provide the mathematical definition of each value. Figure 24 and equation 27 graphically and mathematically depict the relationship between these pseudostiffness values, respectively.

$$\bar{C} = \frac{\sigma_{0,ta}}{\varepsilon_m^R * I} = \frac{\sigma_{0,ta}}{(\varepsilon_{0,ta}^R + \varepsilon_s^R) * I} \quad (25)$$

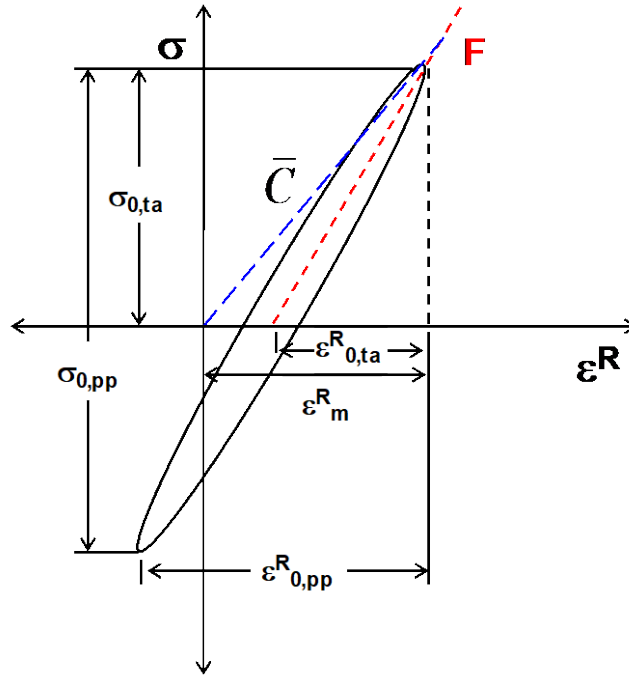
$$F = \frac{\sigma_{0,ta}}{\varepsilon_{0,ta}^R * I} = \frac{\sigma_{0,pp}}{\varepsilon_{0,pp}^R * I} = \frac{\sigma_{0,ta}}{(\varepsilon_m^R - \varepsilon_s^R) * I} \quad (26)$$

$$\bar{C} = F \frac{\varepsilon_m^R - \varepsilon_s^R}{\varepsilon_m^R} \quad (27)$$

Where:

ε_m^R = absolute pseudostrain at peak.

- $\varepsilon_{0,ta}^R$ = pseudostrain tension amplitude.
- $\varepsilon_{0,pp}^R$ = peak-to-peak pseudostrain amplitude.
- ε_s^R = permanent pseudostrain.
- $\sigma_{0,pp}$ = peak-to-peak stress amplitude.
- I = specimen-to-specimen variability factor.



© 2010 International Journal of Pavement Engineering. (DTFH61-08-H-00005)

Figure 24. Illustration. Schematic view of stress, pseudostrain, and pseudostiffness definitions.⁽⁵⁰⁾

The S-VECD model the research team employed in this study combines both a rigorous and simplified approach. The team suggests that, within the model, pseudostrain should be calculated piecewise, whereby the rigorous calculation is used for the first loading path. This portion of the loading history is important because damage growth can be substantial in this first loading path. However, the research team used the simplified calculation (i.e., equation 28) for all other cycles. The simplified calculation only evaluated pseudostiffness at each cycle instead of at each data point because damage usually does not propagate much during one cycle under fatigue loading. As a result of pseudostrain's piecewise definition, the pseudostiffness is also piecewise, as defined in equation 28.

$$\varepsilon^R = \begin{cases} \varepsilon^R = \frac{1}{E_R} \int_0^{\xi} E(\xi - \tau) \frac{d\varepsilon}{d\tau} d\tau & \xi \leq \xi_p \\ \varepsilon_{0,ta}^R = \frac{1}{E_R} \cdot \frac{A_{tension} + 1}{2} ((\varepsilon_{0,pp}) \cdot |E^*|_{LVE}) & \xi > \xi_p \end{cases} \quad (28)$$

Where:

E_R = reference modulus.

$$C = \begin{cases} C = \frac{\sigma}{\varepsilon^R \cdot DMR} & \xi \leq \xi_p \\ \bar{C} = \frac{\sigma_{0,ta}}{\varepsilon_{0,ta}^R \cdot DMR} & \xi > \xi_p \end{cases} \quad (29)$$

For a similar reason, and because significant damage can occur along the first loading path, the research team used the rigorous calculation shown in equation 30 for the damage calculation but then used the simplified calculation after the first loading cycle. This document refers to the first portion of the damage calculation as the transient calculation ($dS_{Transient}$) and the remaining calculations as the cyclic calculations (dS_{Cyclic}). The simplified calculation implicitly assumes that the pseudostrain is constant within a cycle. The research team adjusted the errors of this assumption by multiplying by K_1 , an adjustment factor valid when damage growth within an individual cycle is small.

$$dS = \begin{cases} (dS_{Transient})_{timestep j} = \left(-\frac{1}{2} (\varepsilon^R)_j^2 \frac{\partial C}{\partial S} \right)^\alpha \cdot (d\xi)_j & \xi \leq \xi_p \\ (dS_{Cyclic})_{cycle i} = \left(-\frac{1}{2} (\varepsilon_{0,ta}^R)_i^2 \frac{\partial C^*}{\partial S} \right)^\alpha \cdot (d\xi_p) \cdot (K_1) & \xi > \xi_p \end{cases} \quad (30)$$

Where:

$$K_1 = \frac{1}{\xi_f - \xi_i} \int_{\xi_i}^{\xi_f} (f(\xi))^{2\alpha} d\xi \quad (31)$$

Where:

ξ_i = starting time of a cycle.

ξ_f = ending time of a cycle.

The rigorously defined pseudostiffness (C) is approximately the same as F , except that F is defined as a single quantity for a given cycle, whereas for theoretical rigor C will evolve during a cycle. Also, F should be very similar to \bar{C} (equation 29), but F is calculated by using the complete time history pseudostrain.

The research team performed displacement controlled crosshead (CX) cyclic fatigue tests at 10 Hz at different temperatures based on the binder performance grade (PG) to determine the

viscoelastic damage characteristics. They performed all tests at three to four different strain amplitudes (high to low amplitudes) and made specific strain amplitude selections to create a spread of numbers of cycles to failure (N_f) across the range of 1,000 to 100,000 cycles. The team then conducted fingerprint dynamic modulus tests to check the variability of the test specimens before running the CX cyclic fatigue tests.

The dynamic modulus value this test measures is specified as $|E^*|_{fingerprint}$, and equation 32 uses it to calculate the dynamic modulus ratio (DMR). $|E^*|_{LVE}$ is the linear viscoelastic dynamic modulus of the material at the test's particular temperature and frequency. A DMR value in the range of 0.9 to 1.1 guarantees effective use of the linear viscoelastic properties the dynamic modulus tests provide in S-VECD analysis. The research team used the DMR to reduce variability through equation 32.

$$DMR = \frac{|E^*|_{fingerprint}}{|E^*|_{LVE}} \quad (32)$$

The research team used Reese's approach, which is based on the change in phase angle behavior, to determine the fatigue failure for each of the specimens tested in the CX cyclic tests.⁽⁵¹⁾ The phase angle increases until strain localization occurs and then drops suddenly. This sharp decrease occurs around the failure point, which makes determining N_f accurate and consistent in laboratory testing. AASHTO TP 107 provides the detailed testing procedures for calibrating the S-VECD model.⁽³⁷⁾

Fatigue Failure Criteria

Fatigue cracking is one of the major distresses in asphalt pavements. A good fatigue model should be able to evaluate the fatigue properties of asphalt mixtures and predict the pavement's fatigue life under realistic loading history and environmental conditions. As researchers have recently begun applying mechanistic–empirical pavement analysis more, they have also begun using fatigue models to predict the pavement life to help practitioners design pavement and implement pavement maintenance and rehabilitation efforts more efficiently. Over the past few decades, researchers have expended considerable effort to develop fatigue models for asphalt mixtures.^(52–57)

The VECD model and its simplified version, the S-VECD model, are among these fatigue models. The advantage of the VECD and S-VECD models is that they show the change in modulus value as the fatigue damage grows based on the pseudostrain energy input history (See references^{5, 6, 7, 50, 58}) However, in its original form, the VECD theory can only capture the relationship between stress and strain as microcracks initiate and propagate and does not describe the ultimate failure of the material. Developing a failure criterion that is based on the same VECD theory will overcome this limitation.

One of the existing failure criteria for asphalt concrete is if the modulus value reduces to 50 percent in the fatigue tests. The test and the analysis can easily measure and compute the modulus value of the mixture, respectively. However, it has been proven that the correlation between the 50-percent modulus value–reduction indicator and the real failure of the material is questionable.⁽⁵⁹⁾ Researchers believe the drop in the phase angle is a more reliable failure

indicator than the 50-percent modulus value–reduction.⁽⁵¹⁾ Zhang et al. found that the fitting discrepancy that occurs from using a sinusoidal function on the distorted strain signal after the macrocracking localization causes the drop in phase angle.⁽⁵⁹⁾ However, actual fatigue tests can only measure the drop in phase angle as a failure indicator. Predictive models like structural models cannot use it as a failure criterion to predict failure. Some literature suggests referring to the failure indicator (used during testing) and failure criterion (used during modeling) as the experimental failure criterion and model failure criterion, respectively.⁽⁶⁰⁾

Model failure criterion should be derived from the fundamental variables used in tests (i.e., strain, stress, and strain energy) to allow predictive models to implement those variables. This derivation would allow fatigue-failure prediction under a variety of loading conditions, such as those typically experienced in pavement simulations. Researchers have conducted studies to find fundamental variables that indicate fatigue failure and have performed evaluations based on dissipated strain or pseudostrain energy using asphalt concrete. Shen and Carpenter defined “plateau value” based on the stable region of the ratio of dissipated energy change and found a correlation between the plateau value and N_f .⁽⁶¹⁾ However, a later study by Chiangmai and Buttler found this relationship to be dependent on loading mode.⁽⁶²⁾ Previous studies have also applied the concept of dissipated pseudostrain energy (DPSE).⁽⁵³⁾ The elastic-viscoelastic correspondence principle can better determine DPSE due to damage in viscoelastic materials. A benefit of the correspondence principle is that it separates the strain energy that dissipates due to viscous damping and the strain energy that dissipates due to fatigue damage evolution from the total lost energy. Unfortunately, researchers can only apply this method in experiments for which they know the histories of stress, strain, and phase angle in advance.⁽⁵⁹⁾ In 2010, Hou et al. presented a failure criterion for the S-VECD model that assumes failure occurs when C reduces to a critical value, C_f .⁽⁶³⁾ However, these researchers observed high variability from their experiments. Therefore, the research team does not consider this parameter as a reliable failure criterion for use in the VECD and S-VECD models.

Development of New Failure Criteria

Due to the limitations associated with existing failure criteria, the research team developed two new failure criteria, G^R and D^R criteria, for use with the S-VECD model during the research project. The team developed these criteria from data provided by dynamic modulus and cyclic fatigue tests conducted according to AASHTO T 378 and AASHTO TP 107, respectively.^(9,8,37) The control mode used in the cyclic fatigue tests recommended in TP 107 controls actuator displacement and is referred to as CX mode. Beyond this recommendation, the research team performed tests under control stress (CS) mode and control on-specimen strain (COS) mode on some mixtures. The team performed all the cyclic tests at 10 Hz at different amplitudes to cover a wide range of N_f (from 1,000 to 100,000).

The research team determined the fatigue life of the specimens under all loading modes by observing the drop-in phase angle. The phase angle remains nearly constant throughout the whole fatigue life of the specimen when the team used COS mode. Therefore, using the phase angle drop as the failure indicator is not as accurate for tests the team conducted in COS mode compared with CX or CS modes. For consistency, this study determined the failure of the material under the COS test mode by observing the phase angle drop as best as possible. The research team observed some discrepancies in the material behavior between the COS mode and

other loading modes that might be related to the ambiguity associated with determining the phase angle drop in the COS test mode.

The following describes the theory behind these two new failure criteria, as well as their validation, detailing their strengths, weaknesses, and potential for use.

Supporting Theory: Dissipated Pseudo Strain Energy in Cyclic Tension Testing

When asphalt concrete is under CX cyclic loading, sinusoidal functions, as shown in equation 33 and equation 34, describe the stress (σ) and strain (ε) at cycle i .

$$\varepsilon = \varepsilon_i \sin(\omega t) \quad (33)$$

$$\sigma = \sigma_i \sin(\omega t + \phi_i) \quad (34)$$

Where:

- ω = angular frequency.
- σ_i = stress amplitude measured at cycle i .
- ε_i = strain amplitude measured at cycle i .
- ϕ_i = phase angle measured at cycle i .

When the research team plotted against strain, the area of the formed hysteresis loop represented the total energy dissipated in this cycle. Two different factors cause the energy dissipation: viscous damping due to viscoelasticity and the creation of new microcrack surfaces during the fatigue damage evolution. According to the correspondence principle, replacing physical strain with pseudostrain eliminates the effect of viscoelasticity from the total dissipated energy, as presented in equation 35.⁽⁶⁴⁾ Expressing pseudostrain amplitude at cycle i as equation 36 after the test enters the quasistatic state simplifies the computation.

$$\varepsilon^R(t) = \int_0^t E(t-\tau) \frac{d\varepsilon}{d\tau} d\tau \quad (35)$$

$$\varepsilon_i^R = |E^*| \cdot \varepsilon_i \cdot \sin(\omega t + \phi) \quad (36)$$

Where:

- $\varepsilon^R(t)$ = pseudostrain at time t .
- ε_i^R = pseudostrain amplitude at cycle i .
- $E(t)$ = relaxation modulus of the asphalt mixture.
- $|E^*|$ = dynamic modulus value at the corresponding frequency and temperature.

The area of the newly obtained hysteresis loop in the stress–pseudostrain space represents the DPSE (W^R_i). Equation 37 and equation 38 compute DPSE and pseudostiffness, respectively.

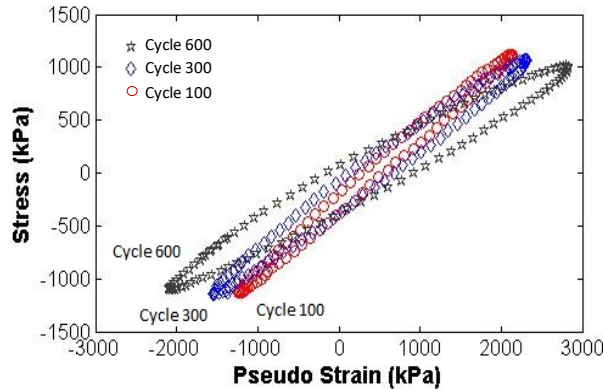
$$W_i^R = \pi \sigma_i \varepsilon_i^R \sin(\phi_i - \phi) \quad (37)$$

Where:

π = Archimedes' constant, approximately equal to 3.14159.

$$C = \frac{\sigma_i}{\varepsilon_i^R} \quad (38)$$

Figure 25 presents the change in hysteresis loop during fatigue loading under CX loading mode. As shown, the incline of the loop changes due to the reduction in pseudostiffness, and the enclosed area of the hysteresis loop increases as the phase angle increases. Researchers consider damage as the cause of the reduction in pseudostiffness. Alternatively, instead of calculating the DPSE directly, researchers can evaluate the dissipated energy using only the reduction in pseudostiffness. This method is presented in the following section.



© 2019 International Journal of Pavement Engineering. (DTFH61-08-H-00005)
 1 MPa = 145.04 psi.
 1 kPa = 0.145 psi.

Figure 25. Graph. Pseudohysteresis loops for controlled CX cyclic tests.⁽¹¹⁾

During cyclic loading, the maximum stored pseudostrain energy (W_{max}^R) at each cycle reflects the material's current damage status because W_{max}^R at each cycle appears at the point of peak stress, and this point also corresponds to the maximum pseudostrain and maximum damage experienced at that cycle. Therefore, using this definition of C , researchers can estimate W_{max}^R at one specific cycle using equation 39.

$$\begin{aligned}
 W_{\max}^R &= \frac{1}{2}(\sigma_{0,ta})(\varepsilon_{0,ta}^R) \\
 &= \frac{1}{2}C \cdot (\varepsilon_{0,ta}^R)^2
 \end{aligned}
 \tag{39}$$

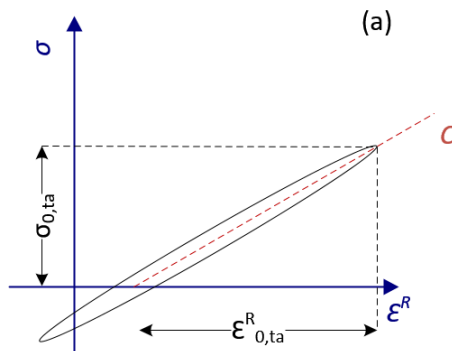
Where:

$\sigma_{0,ta}$ = tension amplitude of the stress.

$\varepsilon_{0,ta}^R$ = pseudostrain amplitude for the duration of the stress being in tension.

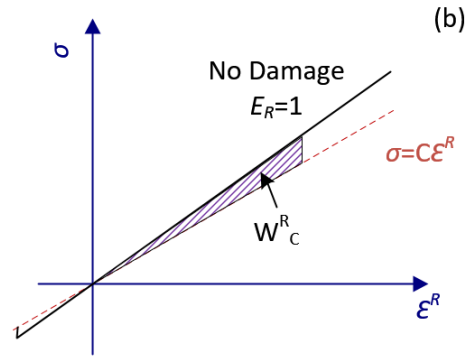
As the damage accumulates, the material loses the capacity to store energy. The difference between the current stored W_{\max}^R and the corresponding undamaged state is the total dissipated pseudostrain energy (W_C^R). Equation 40 presents the formula to calculate the W_C^R at one specific cycle, and figure 26 presents the method explicitly.

$$W_C^R = \frac{1}{2}(1-C)(\varepsilon_{0,ta}^R)^2
 \tag{40}$$



© 2019 International Journal of Pavement Engineering. (DTFH61-08-H-00005)

A. Representation of pseudostiffness in the S-VECD model.



© 2019 International Journal of Pavement Engineering. (DTFH61-08-H-00005)

B. Representation of total dissipated pseudostrain energy in the S-VECD model.

Figure 26. Schematics. Representation of pseudostiffness and total dissipated pseudostrain energy in the S-VECD model.⁽¹¹⁾

Furthermore, the theory that underlies the S-VECD model shows that this total DPSE is related to the current state of damage. Equation 41 presents the damage evolution law in the S-VECD model.

$$\frac{dS}{dt} = \left(-\frac{\partial W^R}{\partial S} \right)^\alpha = \left(-\frac{\partial W_{\max}^R}{\partial S} \right)^\alpha \quad (41)$$

According to Schapery, this ISV is “associated with *distributed damage* or, what may be a better term, *microstructural changes*;” thus, these changes may include not only microcracking but also dislocation motion and generation, as well as local plastic deformation.⁽⁶⁴⁾

Researchers have also found to have a monotonic relationship with pseudostiffness, as presented in equation 42.

$$1 - C = aS^b \quad (42)$$

Where a and b are regression coefficients.⁽⁵⁾

This relationship is independent of loading mode, temperature, and stress and strain amplitude. If equations 41 and 42 are combined, and both sides of the equation integrated after separating S and t , produces equation 43.

$$S^{\alpha+1} = \frac{b^\alpha}{(\alpha+1)} \int_0^t \left(\frac{1}{2} (1-C) (\varepsilon^R)^2 \right)^\alpha dt \quad (43)$$

When written in a discrete form for cyclic loading (details can be found in Underwood et al.), equation 43 becomes equation 44 and equation 45.⁽⁵⁰⁾

$$S^{\alpha+1} = \frac{b^\alpha}{(\alpha+1)} \sum_1^N \left(\frac{1}{2} (1-C_i) (\varepsilon_{0,ta}^R)_i^2 \right)^\alpha K_{1,i} t_i \quad (44)$$

$$S^{\alpha+1} = \frac{b^\alpha}{(\alpha+1)} \sum_1^N (W_{C,i}^R)^\alpha K_{1,i} t_i \quad (45)$$

Where:

$(\varepsilon_{0,ta}^R)_i$ = pseudostrain amplitude in tension at cycle i .

C_i = pseudostiffness at cycle i .

t_i = loading time at cycle i .

$K_{1,i}$ = shape function related to the loading pattern.

The left side of equation 45 is the current state of damage at cycle i and is related to the entire loading history before the current cycle, according to the right side of the equation. Moreover, the summation of the total DPSE, after it is raised to the power of α , is related to the damage at that cycle. The moduli term, $(1 - C)$, represents the material's capacity to accumulate damage. The following sections discuss the relationship between the total DPSE and damage as well as their application in creating failure criteria.

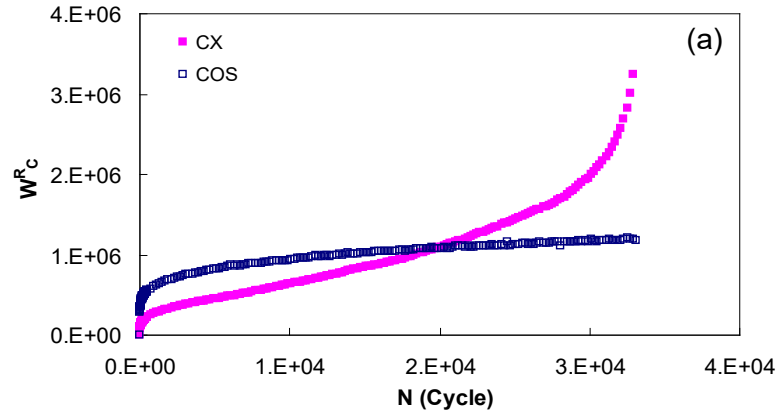
G^R Failure Criterion

Sabouri and Kim proposed the G^R (pseudostrain energy release rate) approach, which evaluates energy in a cumulative sense.⁽⁶⁵⁾ During cyclic loading, the maximum stored pseudostrain energy at each cycle appears at the point of peak stress, which is also the point that corresponds to the maximum pseudostrain and maximum damage experienced at that cycle. Hence, W_{max}^R reflects the material's current damage state as well as its ability to store energy.

W_C^R is affected by two factors: the pseudostrain amplitude in tension ($\varepsilon_{0,ta}^R$) and the reduction in C . So, W_C^R is considered to be a comprehensive energy measure that quantifies the dissipated energy using both the external loading and the material itself.

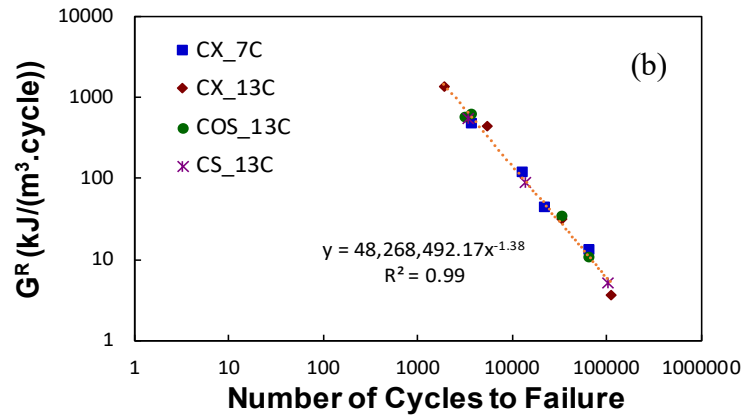
Figure 27 presents the cyclic fatigue test data of a Vermont asphalt mixture with 30-percent RAP under different loading modes. Comparing the W_C^R histories of the two CX and COS displacement mode tests—which resulted in about the same N_f as shown in figure 27-A indicates that, in the case of the CX mode, more energy is released at the end of the loading history when the material is rapidly losing its structural integrity. However, the specimen is forced to experience more COS from the beginning of the test in the COS mode, so more energy is released at the outset. Thus, an ideal failure criterion should be able to capture the effect of the whole loading history. Therefore, the new term, G^R , represents the rate of change of the averaged released pseudostrain energy (per cycle) throughout the entire history of the test, as computed in equation 46. The G^R still depends on the pseudostrain energy's rate of change, but it also captures the effect of the whole loading history.

$$G^R = \frac{\int_0^{N_f} W_C^R dN}{N_f} = \frac{\int_0^{N_f} \frac{1}{2}(1-C)(\varepsilon_{0,ta}^R)^2 dN}{N_f} \quad (46)$$



© 2019 International Journal of Pavement Engineering. (DTFH61-08-H-00005)

A. W_C^R versus N for CX and COS modes with similar N_f .



© 2019 International Journal of Pavement Engineering. (DTFH61-08-H-00005)
 $1 \text{ m}^3 = 35.314 \text{ ft}^3$.

B. G^R versus N_f for CS, COS, and CX modes.

Figure 27. Graphs. Illustration for the G^R failure criteria.⁽¹¹⁾

Because the G^R approach characterizes the overall rate of damage accumulation during fatigue testing, the research team hypothesizes that a correlation must exist between G^R and the final fatigue life (N_f), because the faster the damage accumulates (i.e., reaches a higher W_C^R value during fewer numbers of cycles) the more quickly the material fails.

Phenomenologically, N_f tested at different load amplitudes in different loading modes and the G^R in each test has a high correlation with a power function. This relationship is presented in

equation 47 as well as in figure 27-B.⁽⁶⁵⁾ In the legend of figure 27-B, the first part of the name stands for the loading mode and the second part is the test temperature in degrees Celsius.

$$G^R = \gamma N_f^\delta \quad (47)$$

As the graph shows, not only does the G^R method highly correlate with the N_f (high R^2 values) for all cases but the lines of the CX, CS, and COS modes also collapse well, showing this characteristic G^R curve is independent from loading mode and temperature. Therefore, the research team considers this curve to be independent of both temperature and loading at the same time. However, because the research team obtained the model parameters via linear regression in log-log scale, the test variability highly impacts the deterministic fitted model coefficients. Gudipudi and Underwood conducted a subsequent study about the questionable reliability of such test methods.⁽⁶⁰⁾ Moreover, Wang et al. encountered problems in their study when they used the G^R failure criterion to predict the pavement performance.⁽⁶⁶⁾ In real pavements, the number of load cycles in a pavement's lifetime could be in the millions; thus, both the number of load cycles and the G^R values in the field were beyond the laboratory testing range shown in figure 27, so the study had to extrapolate. Extrapolating a power function is highly sensitive to the power term (δ) in this model. In addition, because G^R is the rate of the average DPSE per cycle, the N_f predictions the study obtained using extrapolation were found to be very sensitive to the accuracy of the G^R versus N_f relationship in log-log scale. Therefore, when the study implemented the G^R failure criterion for pavement life predictions, the extrapolation exaggerated the uncertainty the test variability caused. It is this shortcoming of the G^R failure criterion that necessitated developing a more forgiving failure criterion in terms of test variability.

D^R Failure Criterion

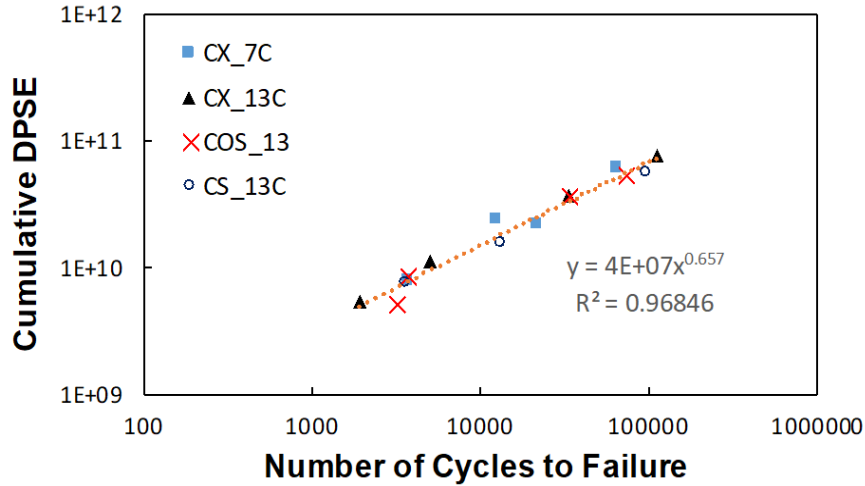
The research team developed the newly proposed failure criterion presented in this section to alleviate the sensitivity involved in extrapolation without compromising the G^R failure criterion's strength. Equation 46 and equation 47 can be rearranged to become equation 48.

$$\int_0^{N_f} \frac{1}{2} (1-C) (\epsilon_{0,ta}^R)^2 dN = \gamma N_f^\lambda \quad (48)$$

Where $\lambda = \delta + 2$.

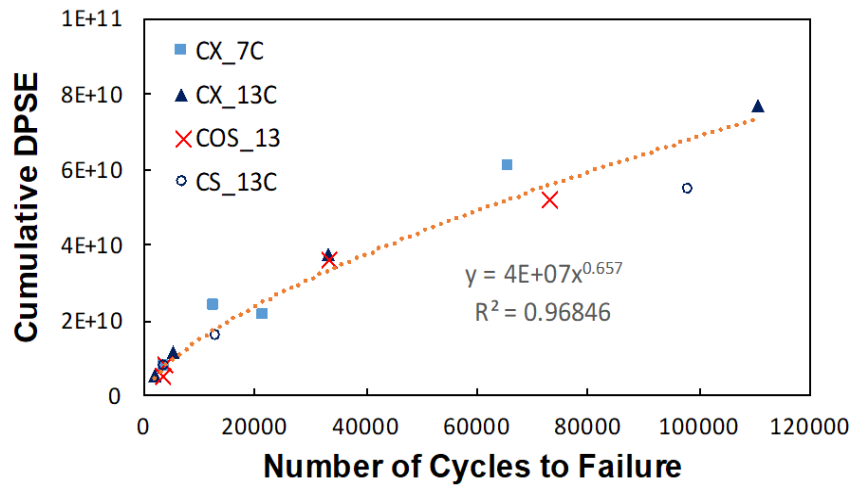
The same data shown in figure 27-B for different loading modes and temperatures are presented in figure 28 to depict the relationship shown in equation 48 in log-log scale. The high R^2 value (approximately 0.97) suggests that the power relationship in equation 48 is valid under different loading modes and temperatures.

Equation 48 and its verification shown in figure 28 confirm that the fatigue life of asphalt mixtures is solely determined by the cumulative DPSE up to failure, regardless of loading mode and temperature. Another material function the research team found to be independent of loading mode and temperature is the damage characteristic relationship, which is presented in equation 42.



© 2019 International Journal of Pavement Engineering. (DTFH61-08-H-00005)

A. Relationship between the cumulative W_C^R and number of cycles to failure under different test modes and temperatures in log-log scale.



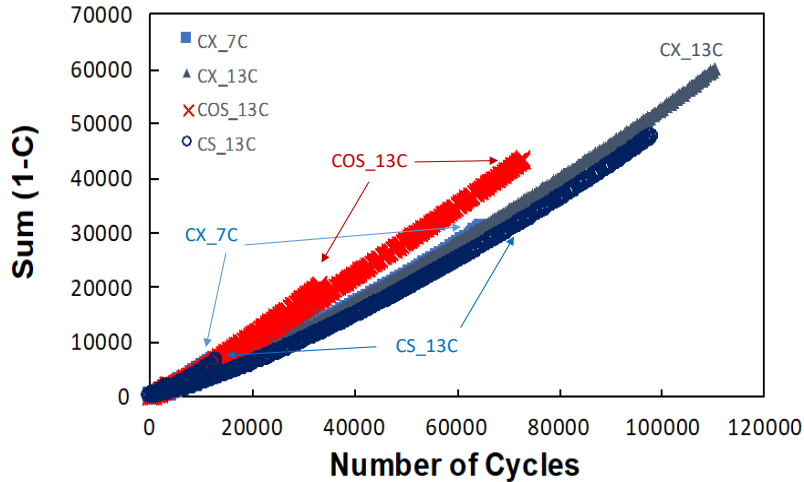
© 2019 International Journal of Pavement Engineering. (DTFH61-08-H-00005)

B. Relationship between the cumulative W_C^R and number of cycles to failure under different test modes and temperatures in arithmetic scale.

Figure 28. Graphs. Relationship between the cumulative W_C^R and number of cycles to failure under different test modes and temperatures.⁽¹¹⁾

The damage characteristic relationship in equation 42 defines how the damage grows as the material is loaded, whereas the relationship shown in equation 48 defines when fatigue failure occurs. Since the $(1 - C)$ term appears in both relationships, the research team investigated this term further. The same data shown in figure 28 were plotted between cumulative $(1 - C)$ (denoted as “*Sum*($1 - C$)” in the figure) and the number of loading cycles. Figure 29 shows that the trends between the cumulative $(1 - C)$ and the number of loading cycles are similar among the different loading and temperatures.

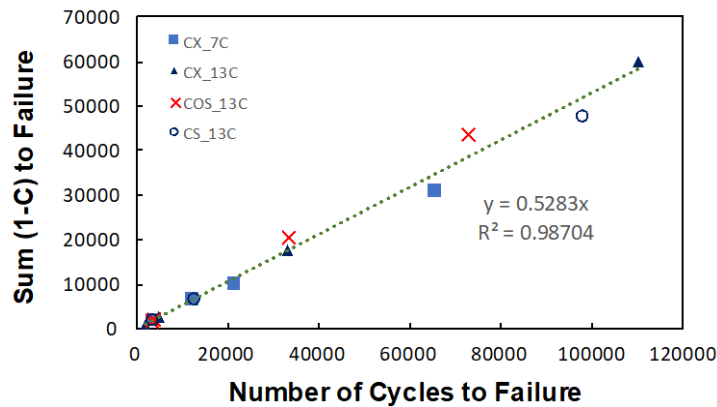
Because this investigation’s objective was to identify a failure criterion independent of loading mode, stress and strain amplitudes, and temperature, the research team plotted the data in figure 29 using only the data at failure. In the plot, each point represents one fatigue test performed under one initial strain level, one specific loading mode, and one temperature.



© 2019 International Journal of Pavement Engineering. (DTFH61-08-H-00005)

Figure 29. Graph. Relationship between the cumulative (1 – C) and number of cycles under different test modes and temperatures.⁽¹¹⁾

The research team made three important observations from figure 30. First, the $Sum(1 - C)$ values under different loading modes and temperatures correlate well with the N_f values. Second, the $Sum(1 - C)$ versus N_f relationship is linear in arithmetic scale. This fact reduces the sensitivity that was present in the G^R criterion in log-log scale due to experimental variability. Third, the $Sum(1 - C)$ versus N_f relationship passes through the origin, thus reducing the number of fitting coefficients in the linear regression from two (i.e., slope and intercept) to one (i.e., slope). This reduction in the number of fitting coefficients may result in a greater accuracy in characterizing the failure criterion for a given mixture using the same number of tests.



© 2019 International Journal of Pavement Engineering. (DTFH61-08-H-00005)

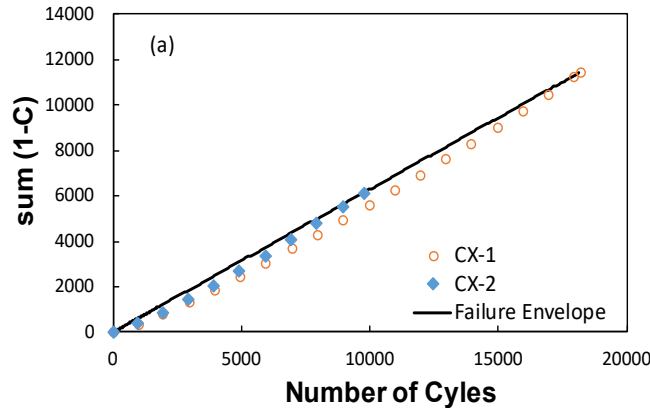
Figure 30. Graph. Relationship between $Sum(1 - C)$ to failure and N_f .⁽¹¹⁾

The linear relationship between $\text{Sum}(1 - C)$ and N_f , which passes through the origin, suggests that the slope in the relationship between $\text{Sum}(1 - C)$ and N_f is the material property that defines the failure of the material. This slope is denoted as D^R and defined in equation 49.

$$D^R = \frac{\int_0^{N_f} (1 - C) dN}{N_f} \quad (49)$$

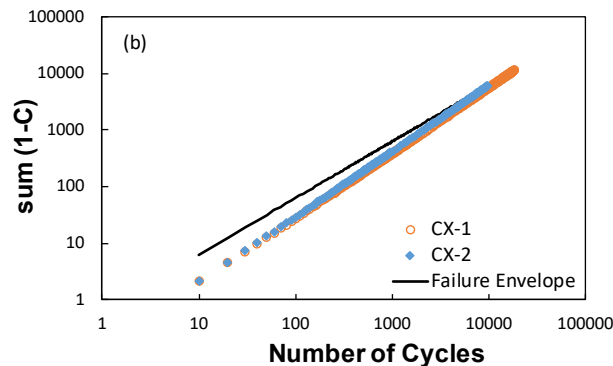
Where D^R is the average reduction in C up to failure.

Figure 31 depicts how the D^R failure criterion defined by the $\text{Sum}(1 - C)$ versus N_f line works to define the failure in the cyclic fatigue test data. As a study applies cyclic loading to a specimen, $\text{Sum}(1 - C)$ grows following the points denoted as CX-1 and CX-2 for two different CX displacement amplitudes. The load cycle at which the point meets the $\text{Sum}(1 - C)$ versus N_f line, which is defined by the slope D^R , is defined as N_f .



© 2019 International Journal of Pavement Engineering. (DTFH61-08-H-00005)

A. Failure identification using the D^R criterion in arithmetic scale.



© 2019 International Journal of Pavement Engineering. (DTFH61-08-H-00005)

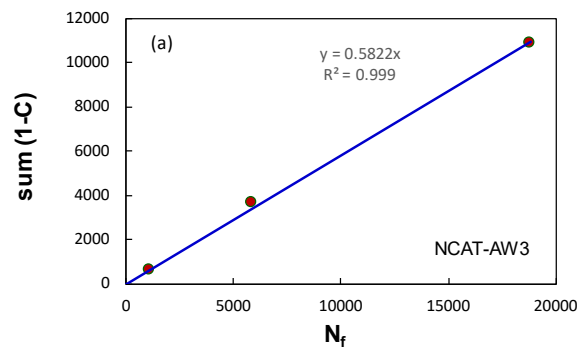
B. Failure identification using the D^R criterion in log-log scale.

Figure 31. Graphs. Failure identification using the D^R criterion in arithmetic and log-log scale.⁽¹¹⁾

Test Results and Discussion

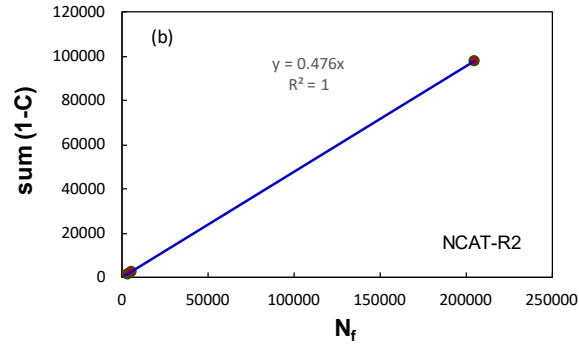
The research team applied the proposed failure criterion to the different mixtures described in chapter 3. As mentioned previously, those mixtures consisted of different gradations: NMAS, binder grades, RAP contents, and binder modifiers. Figure 32 presents the results of the implementing the failure criterion for four mixtures as examples. The slope of the $Sum(1 - C)$ versus N_f curve is the D^R value of the given mixture. The research team obtained three mixtures shown in figure 32-A through figure 32-C from the NCAT Test Track: the bottom layer WMA mixture, the intermediate layer mixture with high RAP content, and the open-graded friction course (OGFC) mixture, respectively. The mixture shown in figure 32-D is a North Carolina surface mixture with polymer-modified binder.⁽⁶⁷⁾ The research team observed from the large number of tested mixtures that the $Sum(1 - C)$ versus N_f relationship formed by multiple strain levels is linear with a high R^2 value (i.e., the D^R value is constant regardless of the strain level). The D^R value, which is the slope of the linear regression equation in figure 32, also varied from 0.3 to 0.8 among the different asphalt mixtures.

Some of the fatigue test results for the O1 and R2 mixtures, as shown in figure 32-B and figure 32-C, indicate N_f values much higher than the typical N_f values recommended in TP 107, as shown in figure 32-A and figure 32-D. The research team conducted these long fatigue tests to check the linearity of the $Sum(1 - C)$ versus N_f relationship at high N_f values so that the extrapolation from typical fatigue tests to large N_f values remains valid.



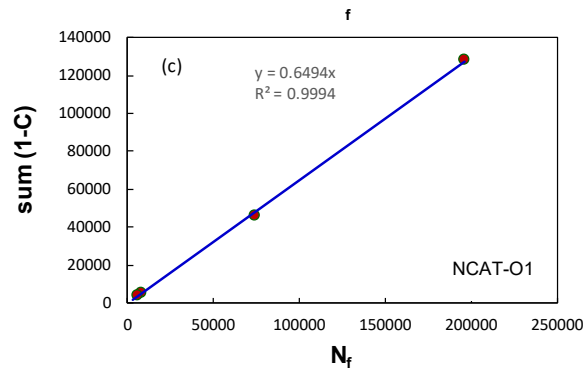
© 2019 International Journal of Pavement Engineering. (DTFH61-08-H-00005)

A. D^R failure criterion of the NCAT-AW3 mixture.



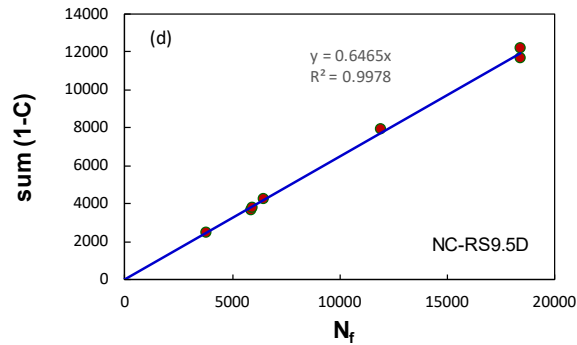
© 2019 International Journal of Pavement Engineering. (DTFH61-08-H-00005)

B. D^R failure criterion of the NCAT-R2 mixture.



© 2019 International Journal of Pavement Engineering. (DTFH61-08-H-00005)

C. D^R failure criterion of the NCAT-O1 mixture.



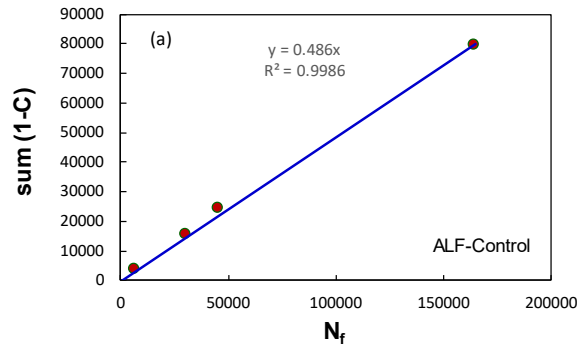
© 2019 International Journal of Pavement Engineering. (DTFH61-08-H-00005)

D. D^R failure criterion of the NC-R9.5D mixture.

Figure 32. Graphs. Implementation of new failure criterion using different mixtures.⁽¹¹⁾

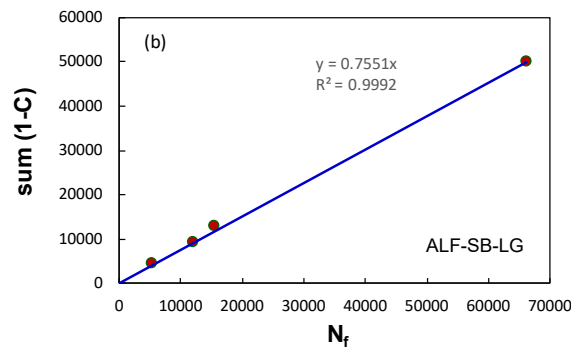
Figure 33 presents the test results for the four different mixtures used in the FHWA ALF study. Among the four ALF mixtures, one is the control mixture and the other three contain modified binders.

Figure 34 presents the test results for another four mixtures the research team obtained from the MIT test road. The mixtures shown in figure 34-A through figure 34-D are the control mixture (0-percent RAP); a mixture containing 15-percent RAP; a mixture containing 50-percent RAP; and a mixture containing 50-percent RAP with a soft binder.



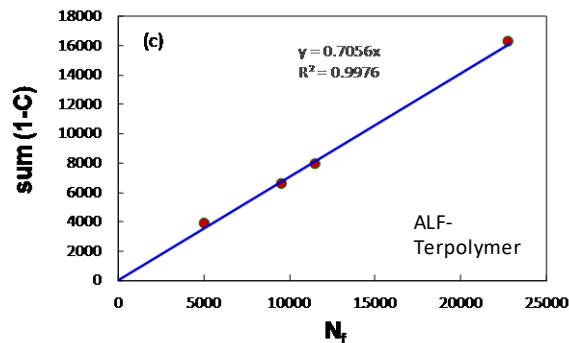
© 2019 International Journal of Pavement Engineering. (DTFH61-08-H-00005)

A. D^R failure criterion of the ALF control mixture.



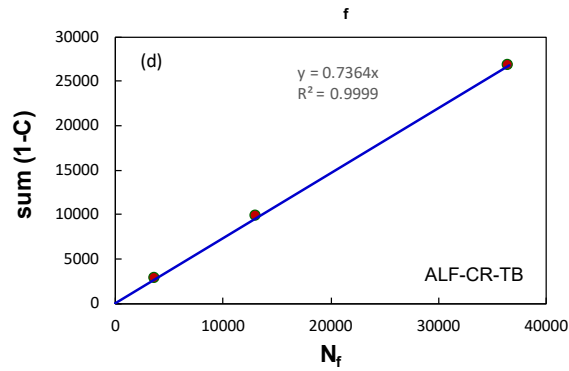
© 2019 International Journal of Pavement Engineering. (DTFH61-08-H-00005)

B. D^R failure criterion of the ALF-SB-LG mixture.



© 2019 International Journal of Pavement Engineering. (DTFH61-08-H-00005)

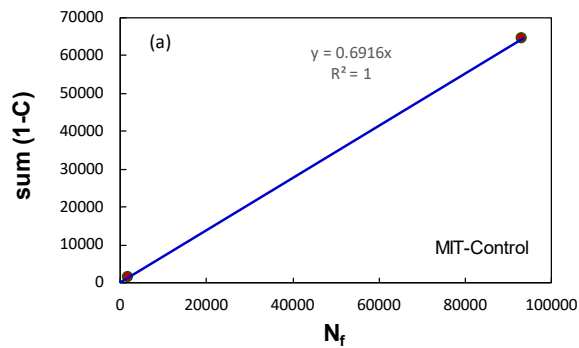
C. D^R failure criterion of the ALF-Terpolymer mixture.



© 2019 International Journal of Pavement Engineering. (DTFH61-08-H-00005)

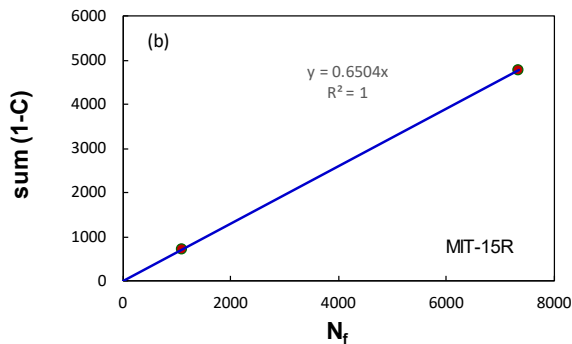
D. D^R failure criterion of the ALF-CR-TB mixture.

Figure 33. Graphs. Implementation of new failure criterion using ALF mixtures.⁽¹¹⁾



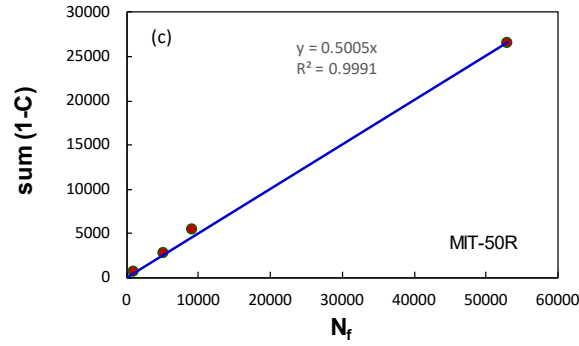
© 2019 International Journal of Pavement Engineering. (DTFH61-08-H-00005)

A. D^R failure criterion of the MIT control mixture.



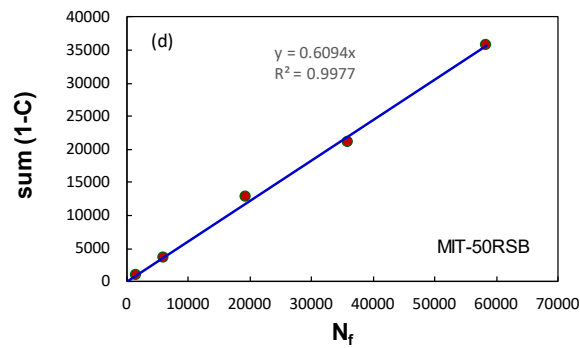
© 2019 International Journal of Pavement Engineering. (DTFH61-08-H-00005)

B. D^R failure criterion of the MIT-15R mixture.



© 2019 International Journal of Pavement Engineering. (DTFH61-08-H-00005)

C. D^R failure criterion of the MIT-50R mixture.



©2019 International Journal of Pavement Engineering. (DTFH61-08-H-00005)

D. D^R failure criterion of the MIT-50RSB mixture.

Figure 34. Graphs. Implementation of new failure criterion using MIT mixtures with different RAP contents.⁽¹¹⁾

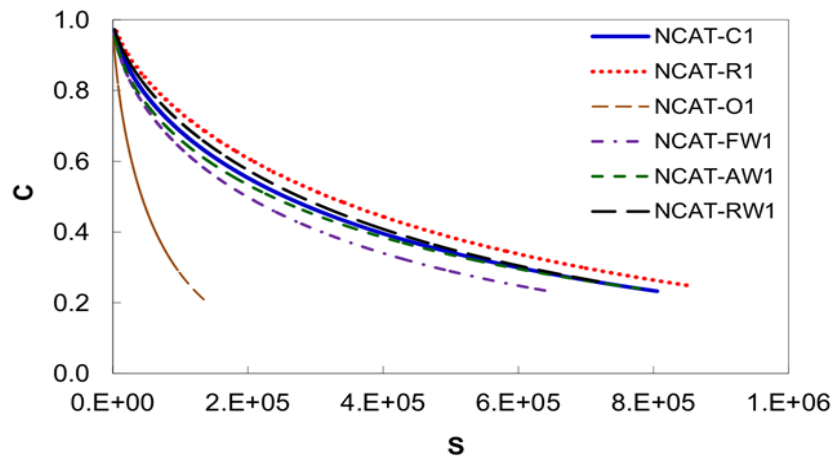
Table 11 summarizes the D^R values for all the study mixtures. According to the ALF data presented in table 11, the mixtures with modified binders have significantly higher D^R values than the control mixture. The MIT-RAP data also show that the D^R value decreases as the RAP content increases.

Table 11. Summary of D^R values for study mixtures.

Project	Mixture	D^R
NCAT	OGFC1	0.649
NCAT	R2	0.476
NCAT	AW3	0.582
NCDOT	RS9.5D	0.618
ALF	Control	0.473
ALF	SBS	0.743
ALF	Terpolymer	0.706
ALF	CR-TB	0.735
MIT-RAP	Control	0.702
MIT-RAP	15R	0.649
MIT-RAP	50R	0.501
MIT-RAP	50R-SB	0.614

NCDOT = North Carolina Department of Transportation.

Despite these good trends, the D^R criterion alone cannot compare the fatigue performance of different asphalt mixtures. As shown in table 11, the OGFC mixture has a D^R value of 0.649, which is relatively high. Nonetheless, as presented in figure 35, the pseudostiffness value dramatically decreases as the damage grows compared with the other NCAT surface mixtures, which indicates that this OGFC mixture has extremely low capacity to resist damage. The field performance data also show substantial top-down cracking from the OGFC section in the field.⁽²⁸⁾ As for the other mixtures, the C versus S curves are at about the same level; thus, the pseudoductility can be used as a preliminary measure to estimate the material's fatigue resistance. Structural simulations that are dependent on the traffic level, climate, pavement structure, and other material properties (i.e., the dynamic modulus, damage characteristic curve, and failure criterion) provide the actual ranking and evaluation of the material's fatigue behavior.



© 2019 International Journal of Pavement Engineering. (DTFH61-08-H-00005)
 Note: S is the ISV in VECD theory that indicates the amount of damage that has accumulated under fatigue loading.

Figure 35. Graph. Damage characterization curves of NCAT surface mixtures.⁽¹¹⁾

Statistical Analysis of Test Results

This section describes the statistical analyses the research team performed to find the best method to determine the D^R value for a given mixture. The team used two statistical methods to obtain D^R values from the test data. The section presents the pseudoductility confidence intervals the methods measured (and discusses the advantages and disadvantages of the two methods later on). This section presents data from two tested mixtures as examples. The first mixture is the bottom layer control mixture from the NCAT Test Track, and the other mixture is from the New England RAP project, which has 20-percent RAP and PG 64-28 binder (hereinafter referred to as the NE6420 mixture). Table 12 presents the test data and demonstrates that D^R values for the NCAT-C3 mixture samples show less variability than the NE6420 mixture samples. The level of variability that the NE6420 mixture shows for its D^R values is above average for all the mixtures in the research team’s asphalt mixture database.

Table 12. Test data for two representative asphalt mixtures.

Mixture	Sample ID	Nf	Sum(1 – C)	D^R
NCAT-C3	1600	5,646	3,249	0.575
NCAT-C3	1400	13,081	7,574	0.579
NCAT-C3	1200	37,593	21,675	0.577
NE6420	1800	6,844	3,252	0.475
NE6420	1500	17,605	8,685	0.493
NE6420	1200	65,433	33,914	0.518

Statistical Analysis Using Linear Regression

A fatigue test can measure or compute $Sum(1 - C)$ and N_f . The research team used data from several tests to perform linear regression between $Sum(1 - C)$ and N_f performed using equation 49. The estimated slope of the linear regression line should be computed using equation 50 since the origin has been passed. The standard error of the estimated slope is computed using equation 51 and equation 52.

$$\hat{\beta}_1 = \frac{\sum x_i y_i}{\sum x_i^2} \quad (50)$$

$$S_{\hat{\beta}_1} = \frac{S_\varepsilon}{\sqrt{\sum x_i^2}} \quad (51)$$

$$S_\varepsilon = \sqrt{\frac{\sum (y_i - \beta_1 x_i)^2}{n-1}} \quad (52)$$

Where:

$\hat{\beta}_1$ = estimated slope, which is the estimated D^R value.

x_i = measured x value used in the linear regression (in this report, N_f).

y_i = measured y value used in the linear regression (in this report, $Sum(1 - C)$).

$S_{\hat{\beta}_1}$ = standard error of the estimated slope.

S_ε = residual standard error.

n = number of samples.

Equation 53 computes the confidence interval at one confidence level.

$$CI = \left(\hat{\beta}_1 - S_{\hat{\beta}_1} \cdot t_{n-1, \alpha/2}, \hat{\beta}_1 + S_{\hat{\beta}_1} \cdot t_{n-1, \alpha/2} \right) \quad (53)$$

Where:

CI = confidence interval.

$t_{n-1, \alpha/2}$ = the t -value of the two-tail Student's t -test with degree of freedom $(n-1)$ and probability level of α .

Table 13 presents the statistical analysis results the research team obtained using the linear regression method. The team first performed the analysis based on data obtained from three fatigue tests for each mixture. Then they conducted an analysis based on two of these three tests, using the two tests with the highest difference in D^R values to be conservative. The team selected samples 1400 and 1600 of the NCACT-C3 mixture and samples 1800 and 1200 of the NE6420 mixture from table 13 for the study. The results show that, regardless of the number of tests, calculating the D^R value using linear regression provided a high confidence level for both mixtures. The research team also carried out sensitivity studies of the pavement performance analysis using the S-VECD model with the D^R failure criterion. The team found that the fatigue damage of the pavements—with a variation of ± 0.04 in the D^R value and as predicted by FlexPAVE—did not differ significantly. If the difference between the upper (or lower) endpoint

of the confidence interval and beta value presented in table 13 is less than 0.04, the research team considered the variability among the tests acceptable. Based on this criterion, the team could not obtain a 95-percent confidence level for the NE6420 mixture using data from only two fatigue tests, as indicated by italicized values in table 13.

Another observation the research team made from table 13 is based on equation 50. The higher the N_f measured from the test, the higher the $Sum(1 - C)$ and the greater the product of N_f and $Sum(1 - C)$. Therefore, tests with more cycles to failure contribute more to the computing the D^R value than tests with fewer cycles to failure. As equation 50 shows, the weight of each test in terms of its contribution to calculating the estimated slope is proportional to N_f^2 in the test. If the N_f in one test is higher than the N_f in the other tests, then the results from the tests with low N_f values would affect the estimated slope or D^R value less.

Table 13. Statistical analysis of test data using linear regression method.

Mixture	No. of Samples	Sample ID	Beta	Residual Standard Error	Standard Error of Estimated Slope	DF	% CI	Two-tail t-value	Upper Endpoint of CI	Lower Endpoint of CI
NCAT-C3	3	1600	0.577	22.2	0.0006	2	95	4.3	0.579	0.574
NCAT-C3	3	1400	0.577	22.2	0.0006	2	90	2.9	0.578	0.575
NCAT-C3	3	1200	0.577	22.2	0.0006	2	70	1.4	0.578	0.576
NCAT-C3	2	1600	0.579	30.1	0.0021	1	95	12.7	0.605	0.552
NCAT-C3	2	1400	0.579	30.1	0.0021	1	90	6.3	0.592	0.565
NCAT-C3	2	1400	0.579	30.1	0.0021	1	70	2.0	0.583	0.574
NE6420	3	1800	0.516	360.0	0.0053	2	95	4.3	0.539	0.493
NE6420	3	1500	0.516	360.0	0.0053	2	90	2.9	0.532	0.501
NE6420	3	1200	0.516	360.0	0.0053	2	70	1.4	0.524	0.509
NE6420	2	1800	0.518	293.3	0.0045	1	95	12.7	0.575	0.461
NE6420	2	1200	0.518	293.3	0.0045	1	90	6.3	0.546	0.490
NE6420	2	1200	0.518	293.3	0.0045	1	70	2.0	0.527	0.509

DF = degree of freedom.

Statistical Analysis Assuming Normal D^R Value Distribution

Table 12 presents a D^R value calculation based on the data from each fatigue test using equation 49. Equation 54 calculates the mean of the D^R value of each mixture by assuming the D^R value has a normal distribution.

$$\bar{y} = \frac{1}{n} \sum y_i \quad (54)$$

Where \bar{y} is the mean of the measured values, y_i , and is the mean of the D^R value obtained from each replicate. Equation 55 and equation 56 calculate the confidence intervals because the standard deviation is unknown.

$$s = \sqrt{\frac{1}{n-1} \sum_{i=1}^n (y_i - \bar{y})^2} \quad (55)$$

$$CI = \left(\bar{y} - t_{n-1, \alpha/2} \cdot \frac{STD}{\sqrt{n}}, \bar{y} + t_{n-1, \alpha/2} \cdot \frac{STD}{\sqrt{n}} \right) \quad (56)$$

Table 14 presents the statistical analysis results using this normal distribution assumption method. The table shows that, to generate the same confidence intervals as the linear regression method, analysis using this method provides a lower confidence level than the linear regression method. Additionally, using ± 0.04 for the D^R value as a tolerance to the variation and using data from three fatigue tests for the mixture with greater test variability produces a 90-percent confidence level, whereas performing only two fatigue tests produces only a 70-percent confidence level.

Using this method, in terms of the mean value, data from each fatigue test will equally contribute regardless of the N_f in the test, which is different from the linear regression method that gives more weight to test results indicating more cycles to failure. Abnormal flaws, such as large air pockets, will cause earlier-than-expected failure of a specimen under cyclic loading, which does not reflect the true performance of the material. This study verified the performance based on the experimental data, showing D^R values at low N_f values tend to have greater variability and deviate from mixture-specific D^R values more than D^R values at high N_f values. Additionally, the number of load cycles under actual field conditions was much higher than typical numbers of load cycles in laboratory fatigue tests. Based on these two observations and the statistical analysis results, the research team recommends the linear regression method for obtaining mixture-specific D^R values.

RESEARCH FINDINGS UPDATE

Since this report was first written, the ongoing research effort has led to a change in the way the mixture's representative D_R value is determined. Rather than the linear regression method that is presented in this report, the research team has found that averaging the D_R values obtained from individual cyclic fatigue tests for the given mixture is a more effective method based on findings from the ongoing research. This change is due to improvements made in the cyclic fatigue test method during follow-up research projects, and the improvements include a refined strain selection guideline and rejection of cyclic fatigue tests that result in fewer than 2,000 cycles to failure.

In the new, revised cyclic fatigue test standards, only the tests that result in 2,000 to 80,000 cycles to failure are accepted, thus removing the problems associated with very early failures (which was one of the main reasons that the linear regression method was recommended originally in this report). In addition, the refined strain selection guideline has reduced the potential for very short cyclic fatigue tests (fewer than 2,000 cycles) or very long tests (more than 80,000 cycles). These changes have been implemented in AASHTO TP 107-22 for the 100-mm diameter specimen geometry and AASHTO TP 133-21 for the 38-mm diameter specimen geometry.

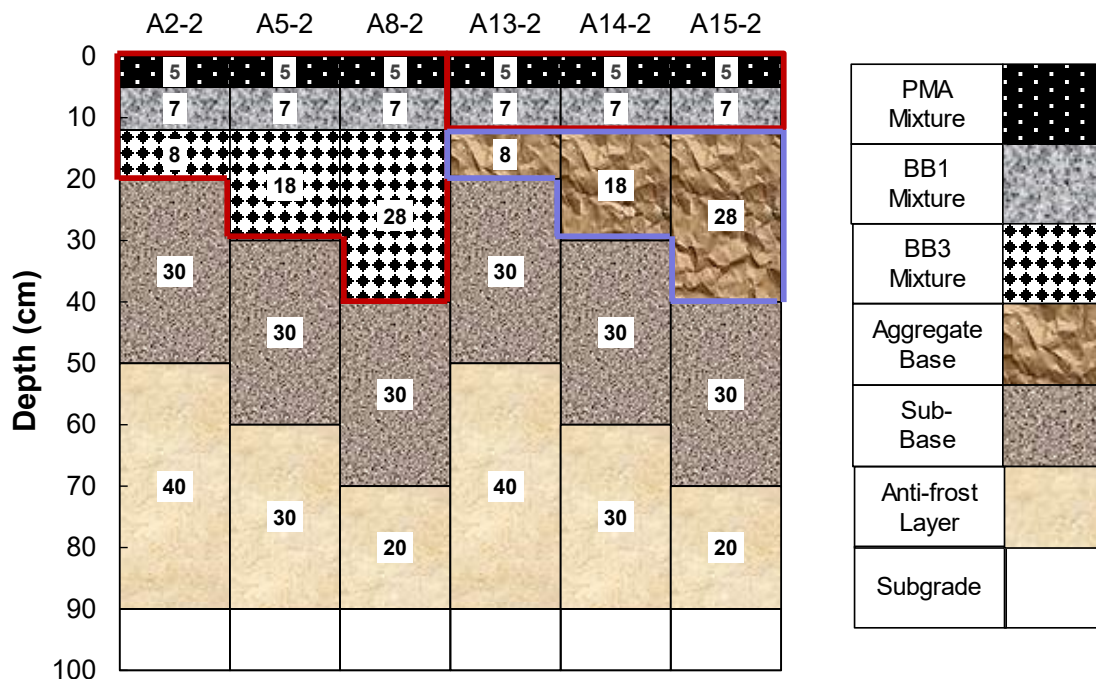
Table 14. Statistical analysis of test data assuming normal D^R value distribution.

Mixture	No. of Samples	Sample ID	Mean	Standard Deviation	DF	% CI	Two-tail t-value	Upper Endpoint of CI	Lower Endpoint of CI
NCAT-C3	3	1600	0.577	0.0018	2	95	4.3	0.582	0.572
NCAT-C3	3	1400	0.577	0.0018	2	90	2.9	0.580	0.574
NCAT-C3	3	1200	0.577	0.0018	2	70	1.4	0.279	0.576
NCAT-C3	2	1600	0.577	0.0025	1	95	12.7	0.600	0.554
NCAT-C3	2	1400	0.577	0.0025	1	90	6.3	0.589	0.566
NCAT-C3	2	1400	0.577	0.0025	1	70	2.0	0.581	0.574
NE6420	3	1800	0.496	0.0216	2	95	4.3	0.549	0.442
NE6420	3	1500	0.496	0.0216	2	90	2.9	0.532	0.459
NE6420	3	1200	0.496	0.0216	2	70	1.4	0.513	0.478
NE6420	2	1800	0.497	0.0305	1	95	12.7	0.770	0.223
NE6420	2	1200	0.497	0.0305	1	90	6.3	0.633	0.361
NE6420	2	1200	0.497	0.0305	1	70	1.963	0.5390	0.454

DF = degree of freedom.

Use of D^R Criterion in Pavement Performance Predictions

This section briefly presents the results and explains the advantages of using the D^R criterion for pavement performance predictions, and uses one field project, the KEC test road, as an example. The KEC team designed the project to evaluate the effects of different asphalt materials and structures on pavement performance. Figure 36 presents the KEC test road's structural layout and materials. In this example, sections A2-2, A5-2, and A8-2 are full-depth pavements with three asphalt layers, whereas sections A13-2, A14-2, and A15-2 are pavements with aggregate base courses (ABCs). In full-depth pavements, the total thickness of the asphalt layers varies from 20 cm to 40 cm. For the ABC pavements, the total asphalt layer thickness is 12 cm, but the thickness of the base layers varies from 8 to 28 cm.

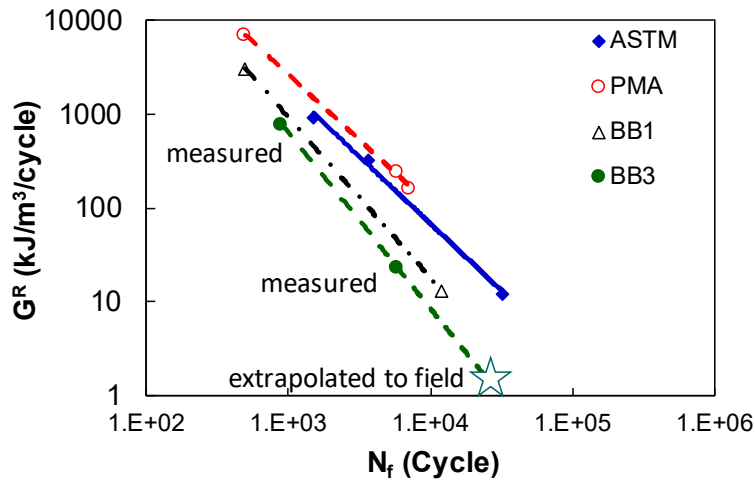


Source: FHWA.
1 cm = 0.4 inch.

Figure 36. Illustration. Schematic of pavement structures for representative sections at the KEC test road.

Chapter 5 will introduce and detail FlexPAVE, the main program used in this study. FlexPAVE simulates the fatigue performance of these pavements using the material properties measured by the laboratory tests. However, the difference between the loading conditions in the lab and conditions in the field leads to inaccuracies in predictions. In the field, the materials fail after years of a high number of traffic loadings with small loading amplitudes. By contrast, laboratory tests apply thousands to tens of thousands of loading cycles with high-loading amplitudes applied. Therefore, researchers must apply an extrapolation strategy to simulate the fatigue life of an asphalt mixture under actual traffic loading. For instance, if the G^R failure criterion is used to predict the fatigue life of the BB3 mixture under a certain traffic load in the field, N_f can be obtained by extrapolation from two data points measured under laboratory test conditions, as

illustrated in figure 37. However, this extrapolation is performed in log-log scale; thus, any variability in the laboratory test may lead to a significant difference in the predicted fatigue life. Nevertheless, the D^R failure criterion can minimize the inaccuracies in the fatigue life predictions caused by extrapolation because extrapolation is only conducted in arithmetic scale.

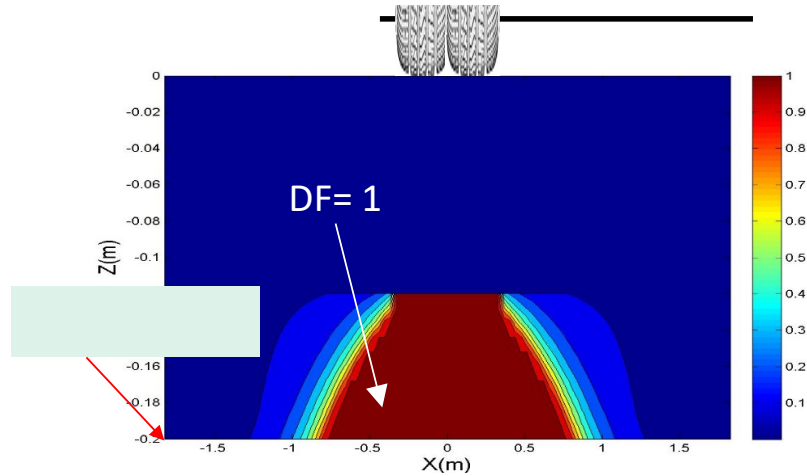


© 2018 Transportation Research Record. (DTFH61-08-H-00005)
 1 m³ = 35.314 ft³.

Figure 37. Graph. G^R failure criterion for the asphalt mixtures used in the KEC test road.⁽⁶⁸⁾

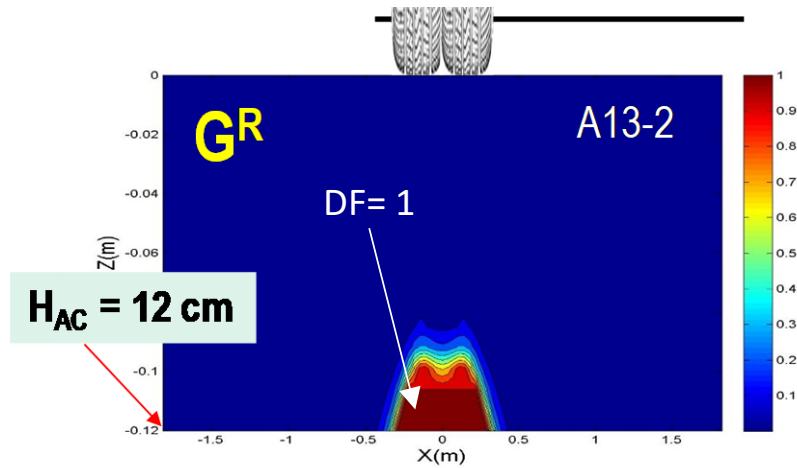
Figure 38 presents the damage contours for Sections A2-2 and A13-2 after 6 yr of loading as predicted by FlexPAVE, and figure 39 presents the predicted damage area as a percent of the full-depth pavement sections (A2-2, A5-2, and A8-2) and the ABC pavement sections (A13-2, A14-2, and A15-2). According to figure 38 and figure 39, the full-depth pavements experience more fatigue damage than the ABC pavements when the predictions use the G^R failure criterion. However, these prediction results differ from the field measurements, and this discrepancy is due to carrying out the extrapolation in log-log scale using the G^R criterion defined by two data points. Conducting more tests to more accurately define the G^R criterion can minimize this problem, but the research team does not recommend this approach because it increases testing time.

Figure 38 and figure 39 show the D^R failure criterion predicting the greater damage area for the ABC projects compared with the full-depth pavements, and the predicted ranking matches the field measurements well. The research team obtained the model coefficients for the D^R criterion from the same test data used to determine the G^R criterion. Therefore, the D^R criterion better predicts the true fatigue resistance performance than the G^R failure criterion because the variability in the material testing the extrapolation in numerical simulations affects the predictions less.



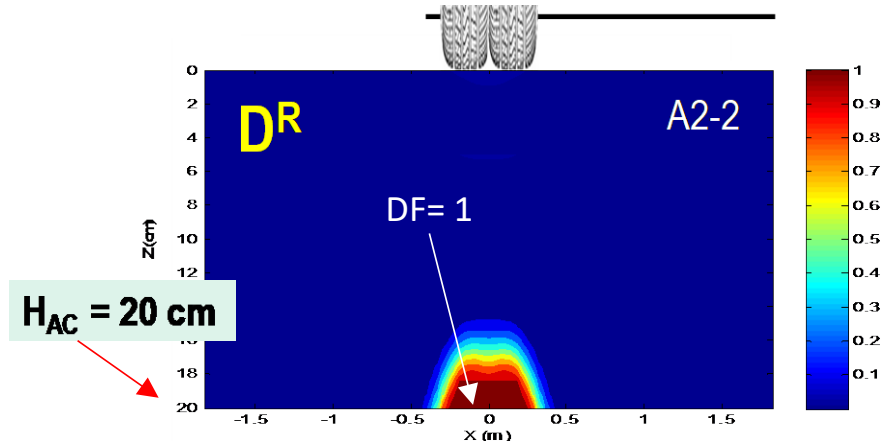
© 2018 Transportation Research Record.
 1 cm = 0.4 in; 1 m = 3.28 ft.
 DF at 1 = failure.
 DF = damage factor.

A. Damage contour predicted using G^R failure criterion for the 20-cm-thick pavement.



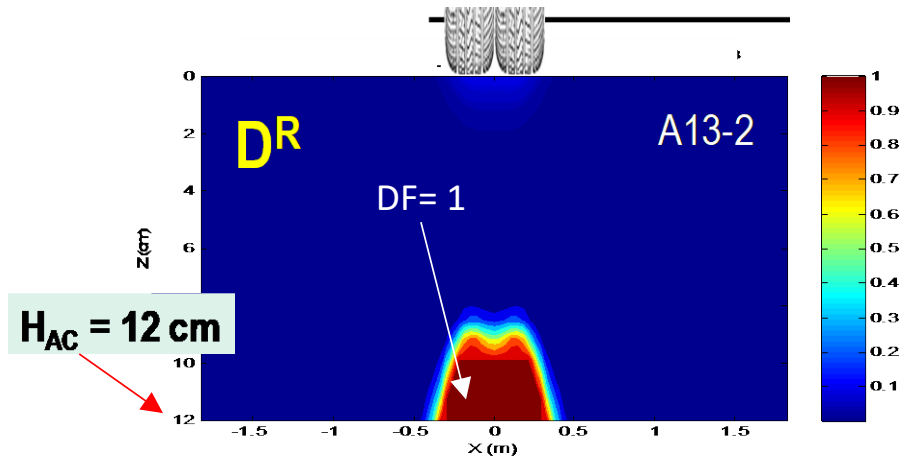
© 2018 Transportation Research Record. (DTFH61-08-H-00005)
 1 cm = 0.4 in; 1 m = 3.28 ft.
 DF at 1 = failure.
 DF = damage factor.

B. Damage contour predicted using G^R failure criterion for the 12-cm-thick pavement.



© 2018 Transportation Research Record. (DTFH61-08-H-00005)
 1 cm = 0.4 in; 1 m = 3.28 ft.
 DF at 1 = failure.
 DF = damage factor.

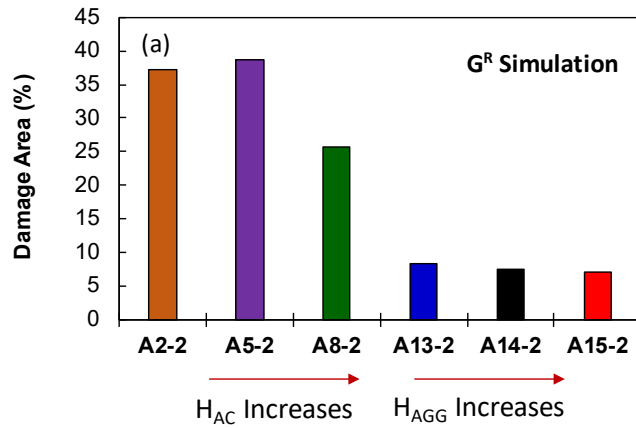
C. Damage contour predicted using D^R failure criterion for the 20-cm-thick pavement.



© 2018 Transportation Research Record. (DTFH61-08-H-00005)
 1 cm = 0.4 inch; 1 m = 3.28 ft.
 DF at 1 = failure.
 DF = damage factor.

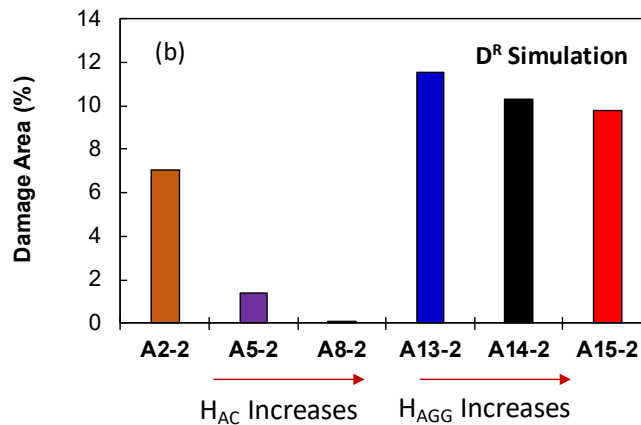
D. Damage contour predicted using D^R failure criterion for the 12-cm-thick pavement.

Figure 38. Graphs. Damage contours predicted using the two different failure criteria.⁽⁶⁸⁾



Source: FHWA.

A. Predicted percent damage area for the KEC test sections using the G^R failure criterion.



Source: FHWA.

B. Predicted percent damage area for the KEC test sections using the D^R failure criterion.

Figure 39. Graphs. Predicted percent damage area for the KEC test sections using the two failure criteria.

In conclusion, the research team found the D^R criterion has the following main advantages over the G^R criterion:

- The D^R value is measured in arithmetic scale rather than in log-log scale; therefore, the results are not as affected by test variability, which is the case for the G^R failure criterion. This measurement is particularly important for predicting pavement fatigue resistance under realistic traffic loading (which involves many more load cycles than accelerated laboratory testing) because of the sensitivity of extrapolation in log-log scale.
- The D^R value can be computed for each fatigue test and used to check the sample-to-sample variability for each test.

PERMANENT DEFORMATION MODEL

Permanent deformation is a significant type of pavement distress. This section introduces the shift model, which characterizes the asphalt mixture's permanent deformation behavior under traffic loading.

Introduction

Permanent deformation (or rutting) in roadways leads to traffic accidents, especially in rainy or snowy weather conditions. Rain causes dangerous driving hazards, such as hydroplaning, and large amounts of water spray hinder visibility. Snow causes similar problems because snow and ice collect in the rutted wheel path. Various models can predict the amount and rate of rutting to predict permanent deformation of asphalt pavements, with these models fall into two categories: mechanistic (visco-) plastic models and power law-type models.

Mechanistic (visco-) plastic models are based on classical plasticity. Desai et al. and Gibson applied hierarchical single-surface yield criteria and a Perzyna-type flow rule to predict the three-dimensional behavior of asphalt concrete in compression. Their models, however, were limited in their ability to simulate rate-dependent behavior, such as rate-dependent softening, of asphalt mixtures.⁽⁶⁹⁻⁷¹⁾ Darabi et al. introduced the concept of a memory surface to overcome the limitations associated with rate-dependent behavior.⁽⁷²⁾ However, this model could not describe the effects of temperature despite the temperature sensitivity of asphalt concrete. Yun and Subramanian adopted viscoelastic concepts, such as the convolution integral, to explain the time-dependent viscoplastic behavior of asphalt concrete.^(12,73)

The concepts developed by Yun and Subramanian are complex for practicing engineers to thoroughly and easily apply, even though these models can predict permanent strain in various loading conditions like stress, load time, and/or temperature, and may be able to shed light on the three-dimensional performance of a pavement structure through numerical implementation. Applying viscoelastic concepts also incurs high calibration and computing costs. Therefore, mechanistic (visco-) plastic models have not been widely accepted by agencies, despite providing good predictions.

In contrast, power law-type models are relatively simple and easily implemented. The representative model, shown in equation 57, is a strain ratio model from the MEPDG.

$$\frac{\varepsilon_p}{\varepsilon_r} = \beta_1 T^{\beta_2} N^{\beta_3} \quad (57)$$

Where:

ε_p = permanent strain.

ε_r = resilient strain.

N = number of cycles.

$\beta_1, \beta_2, \beta_3$ = regression parameters.

This model describes the effects of temperature and stress on permanent strain. The resilient strain calculated from the dynamic modulus and the stress calculated based on the theory of

elasticity represent the effect of stress. The model assumes that the difference in dynamic modulus values represents the rutting properties for different mixtures. However, Von Quintus et al. report that this assumption increases error (i.e., the dynamic modulus itself is important but cannot predict the plastic deformation characteristics for an entire range of mixtures and climates).⁽⁷⁴⁾ In addition, the model cannot describe the behavior of the primary region because the functional form of equation 57 applies only to the behavior of the secondary region.

The research team and their colleagues conducted permanent deformation modeling research, resulting in a viscoplastic model based on viscoelastic convolution integrals for explaining the behavior of asphalt concrete in compression under repeated loading.⁽¹²⁾ The team further reduced this model to a simplified form known as the incremental model, which is an advanced power law-type model that represents the permanent strain-growth behavior of both the primary and secondary regions of asphalt concrete.⁽⁷⁵⁾

Based on the research team’s previous work, this document suggests a simple, mechanistic permanent-deformation model and accompanying test protocol for this PRS project. The model represents the effects of load time, stress, and temperature on the permanent deformation of asphalt concrete and has been verified by complex loading histories and field-measured rut depths at various sites.

Testing Program—Triaxial Repeated Load Permanent Deformation Test

The Triaxial Repeated Load Permanent Deformation (TRLPD) test is a cyclic compression test conducted under constant confining pressure that employs a haversine load pulse followed by a rest period. This project used the TRLPD test because constant cyclic loading can provide the permanent deformation characteristics for a specific test condition. In order to obtain true permanent strain levels, the research team applied 100 s as the rest period, and measured the permanent strains at the end of the rest period. The team used two mixtures, FHWA ALF control mixture (hereinafter referred to as the FHWA mixture) and NY9.5B mixture, with three different load times and three different deviatoric stress levels at two temperatures to capture the effects of load time, deviatoric stress, and temperature. The research team applied constant confining pressure during the initial development of the models to avoid complexity. Table 15 presents the mixture information and TRLPD test conditions used to determine the features of permanent deformation in this project. Choi et al.’s research provides detailed information about this model.⁽⁷⁵⁾

Table 15. Mixture information and test conditions for TRLPD tests.

TRLPD Tests	Details	FHWA ALF	NY9.5B
Mixture information	Aggregate type	Diabase	Crushed gravel
Mixture information	NMAS	12.5 mm	9.5 mm
Mixture information	Asphalt grade	PG 70-22	PG 64-22 (modified)
Mixture information	Percent air voids	4.0 percent	5.4 percent
Testing conditions	Load time (s)	0.1, 0.4*, 1.6	0.1, 0.4, 1.0 at 37°C 0.1, 0.4, 1.6 at 47°C
Testing conditions	Rest period (s)	100	100

TRLPD Tests	Details	FHWA ALF	NY9.5B
Testing conditions	Deviatoric stress (kPa)	620, 827, 1,034 (90, 120, 150 psi)	482, 689, 896 (70, 100, 130 psi)
Testing conditions	Confining pressure (kPa)	140 (20 psi)	70 (10 psi)
Testing conditions	Temperature (°C)	40, 54	37, 47
Testing conditions	Load shape	Haversine	Haversine

0°C = 32°F; 1 cm = 0.4 inch; 1 kPa = 0.145 psi.

*Data are not available for 0.4-s load time tests with 620 kPa (90 psi) and 1,034 kPa (150 psi) deviatoric stress levels at 40°C.

Incremental Model

Choi et al. introduced the incremental model, expressed as equation 58, to describe the permanent deformation behavior of asphalt concrete.⁽⁷⁵⁾

$$\varepsilon_{vp} = \frac{A_0 + \varepsilon_0 \cdot N}{(N_I + N)^\beta} \quad (58)$$

Where:

$1-\beta$ = slope of the log-log relationship between the permanent strain and the number of loading cycles and is related to the hardening evolution.

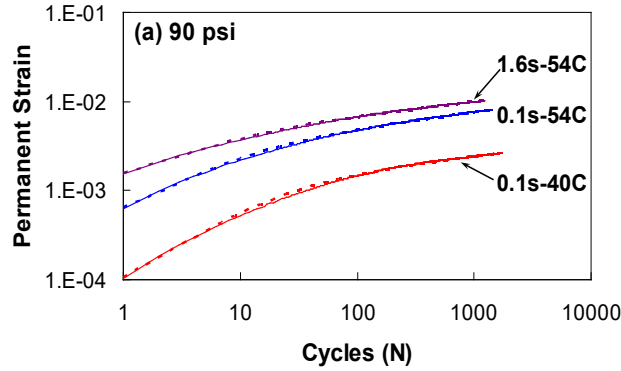
A_0 and N_I govern the permanent strain behavior in the primary region.

ε_0 and β are model coefficients that control the secondary region development.

A_0 = the initial permanent strain.

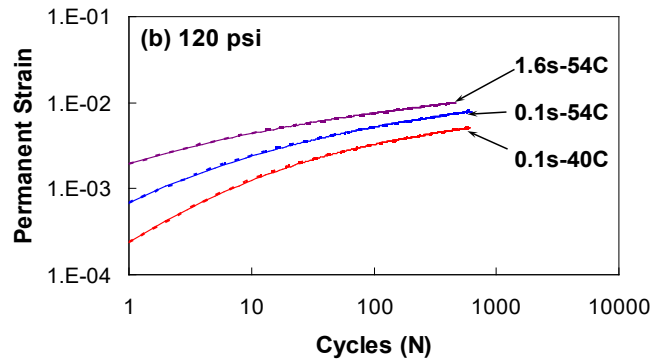
N_I = the number of cycles where the transition from the primary region to the secondary region occurs.

One of the incremental model's strengths is that it fits both the primary and secondary regions regardless of loading conditions (figure 40).



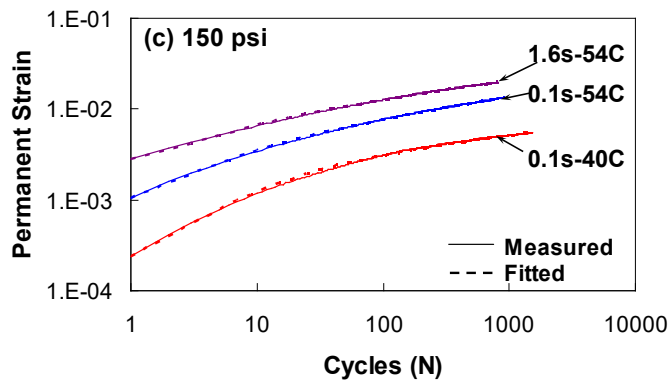
© 2013 Road Materials and Pavement Design. (DTFH61-08-H-00005)
 0°C = 32°F.

A. Fitting results of the incremental model for the FHWA mixture at 90 psi.



© 2013 Road Materials and Pavement Design. (DTFH61-08-H-00005)
 0°C = 32°F.

B. Fitting results of the incremental model for the FHWA mixture at 120 psi.



© 2013 Road Materials and Pavement Design. (DTFH61-08-H-00005)
 0°C = 32°F.

C. Fitting results of the incremental model for the FHWA mixture at 150 psi.

Figure 40. Graphs. Fitting results of incremental model for FHWA mixture.⁽¹³⁾

A summary of the characteristics of Choi et al.'s incremental model follows:⁽⁷⁵⁾

- The permanent strain behavior of asphalt concrete under significant viscoplastic strain verifies the t -TS principle.
- The reduced load time evaluates the behavior of asphalt materials using the t -TS principle instead of using temperature and load time separately.
- The slope of the secondary region in the log-log scale is constant regardless of the reduced load time and deviatoric stress; thus, β is a material constant.
- The regression coefficients, A_0 , ε_0 , and N_I , change according to reduced load time (i.e., as a function of temperature and load time) and deviatoric stress.

The slope of the secondary region remains constant regardless of the test conditions enacted by the incremental model. At high and intermediate temperatures, the secondary region of the FHWA and NY9.5B mixtures showed a constant slope. The slopes of the secondary region for the two mixtures were different at the low temperature; however, the constant slope assumption did not produce a significant difference in the permanent strain prediction of the asphalt pavement because most of the deformation occurred at the higher temperatures. Von Quintus et al. conducted an exploratory program using TRLPD tests and concluded that the average slope is approximately the same for the different test temperatures.⁽⁷⁴⁾ Therefore, the constant slope assumption seems to be reasonable considering the simplicity it provides for developing the permanent strain model.

Permanent Deformation Model (Shift Model)

A single constant slope can horizontally shift the permanent strain curves of the different reduced load times and deviatoric stress levels along the number of loading cycles on the x-axis. If the focus is on the secondary region, all the permanent strain values can be translated to construct one strain evolution curve in log-log space because they have the same slope. The strain curve after the horizontal shift is called the permanent strain master curve, and the amount of translation is called the shift factor.

This shifting strain approach is conceptually the same as the approach for deriving the dynamic modulus master curve and its predictions using the shift function. The approach is known as the shift model and is helpful in characterizing permanent deformation behavior using fewer experimental requirements. Because the t -TS principle's applicability already has been proven by many researchers, the following sections describe the time-stress superposition (t -SS) principle, which forms the basis for the shift model and the experimental verification of the shift model.⁽⁷⁶⁻⁷⁹⁾

t-SS Principle

The incremental model characterization's findings provided a phenomenological basis for shifting the permanent strain curves, and is furthered by a literature review that briefly investigates theoretical support for this approach.

It is important to understand the t-TS principle to understand the t-SS principle. The t-TS principle is a characteristic of TRS materials. Asphalt concrete is one of the TRS materials, and researchers often apply the t-TS principle when assessing the behavior of this material in the viscoelastic range. The t-TS principle is also a viable tool when significant viscoplasticity and damage are present. The single integral nonlinear viscoelastic constitutive equation proposed by Schapery, presented as equation 59, shows the theoretical basis for these findings.⁽⁸⁰⁾

$$\begin{aligned}\varepsilon(t) &= g_0 D_0 \sigma(t) + g_1 \int_0^t D(\psi - \psi') \frac{dg_2 \sigma}{d\tau} \\ \psi &\equiv \int_0^t dt' / a_\sigma(\sigma(t')) \\ \psi' &\equiv \psi'(\tau) \equiv \int_0^\tau dt' / a_\sigma(\sigma(t'))\end{aligned}\quad (59)$$

Where:

- D = creep compliance.
- D_0 = elastic portion of creep compliance.
- ψ' = integration variable.
- t' = integration variable.
- g_0, g_1, g_2 = material constants.
- a_σ = function of stress.

Equation 59 reduces to a standard linear viscoelastic equation when g_0, g_1, g_2 , and a_σ equal one. That is, these factors represent the nonlinear behavior of viscoelastic material. In the case of a square-shaped creep loading input, equation 59 simplifies to equation 60. This simplified equation then suggests that the measured incremental creep compliances (ΔD_n) at different stress levels can be made to overlap by translation along the logarithmic scale of time (t). To superpose the curves, the vertical distance is defined as the difference between the $\log(g_1 \times g_2)$ of the two different stress levels, and the horizontal distance is defined as $\Delta \log(a_\sigma)$ of the two creep compliance curves. In this scenario, a_σ is the time-stress shift factor. If $g_1 \times g_2 = 1$ (i.e., $\log(g_1 \times g_2) = 0$), the plot does not need to be shifted vertically. Schapery showed one example where only horizontal shifting was necessary by using experimental data from glass-reinforced phenolic resin.⁽⁸⁰⁾ Many researchers have adopted the nonlinear equation to explain the viscoelastic behavior of asphalt materials.⁽⁸¹⁻⁸⁴⁾

$$\varepsilon(t) = g_0 D_0 \sigma + g_1 g_2 D \left(\frac{t}{a_\sigma} \right) \sigma \quad (60)$$

Other researchers have proven the t-SS principle using a free volume concept.⁽⁸⁵⁻⁸⁹⁾ Free volume changes with time, temperature, and stress in a viscoelastic material under loading as these three factors are related to one another such that they are interchangeable. This phenomenon is the underlying mechanism that also explains the t-TS principle. Therefore, the t-SS principle applies to viscoelastic materials. Only Wenbo et al. suggested horizontal and vertical shifting where the vertical shift indicates the effects of stress-induced microstructural changes on the material properties.⁽⁸⁸⁾ Other researchers used only horizontal shifting (i.e., time-scale shifting) to

generate creep compliance master curves using creep test results at different stress levels. Azari and Mohseni introduced the TP variable (i.e., $TP = \text{temperature } (^{\circ}\text{C}) \times \text{deviatoric stress (MPa)}$) and used it on the horizontal axis to successfully construct a minimum strain rate (MSR) master curve from flow number test results for asphalt materials.⁽⁹⁰⁾ Their work indicates that deviatoric stress is interchangeable with temperature, and thus, the MSR master curve could be evidence of the t -SS correspondence principle at work.

The literature suggests that the t -SS principle applies to viscoelastic materials. Some cases require vertical shifting (i.e., translating the curve along the creep compliance axis) to represent the nonlinearity or the stress-induced microstructural changes of the materials. Other cases only need horizontal shifting. Determining which shift process is necessary for a given material depends on the material behavior observed through well-orchestrated experiments.

Shiftability Validation Using TRLPD Tests

Experiment observations and the two superposition principles (t -TS and t -SS) support the notion that permanent strain levels at different temperatures and deviatoric stress levels can translate and create a permanent strain master curve. However, this hypothesis had never been proven for asphalt concrete by applying it to experimental data. This study used a series of TRLPD tests to verify the assumption. Three factors were used for model development: deviatoric stress, load time, and temperature. In this approach, reduced load time encompasses temperature and load time, leaving only two factors to characterize: reduced load time and deviatoric stress. Therefore, the hypothesis underlying the shift approach can be proven using these two factors.

Reduced Load-Time Shifting

Asphalt material permanently deforms more as the load time increases under the same stress conditions. For general plasticity, for which the hardening function does not change dramatically, the permanent strain grows in proportion to the length of the load time or cumulative load time if the stress conditions are constant. However, Yun found that the apparent incremental strain rate, defined as the incremental strain of one cycle divided by the load time, decreases as the load time increases.⁽⁷³⁾ This observation suggests that the amount of permanent strain is not directly proportional to the length of the load time. This lack of proportionality is due to hardening during loading and softening during unloading. As a result, only experimentation can determine the effect of load time.

The load-time shift factor quantifies the effect of reduced load time on permanent strain. The number of cycles directly relates to the cumulative load time for the TRLPD tests, and thus, horizontal shifting of the permanent strain curves along the number of load cycles axis for different load times can represent the effect of load time at the same deviatoric stress levels. Equation 61 expresses this horizontal load-time shift. The load-time shift factor is defined as the logarithmic horizontal distance between the reference strain curve and the strain curve in cases where the deviatoric stress levels are the same, as depicted in figure 41.

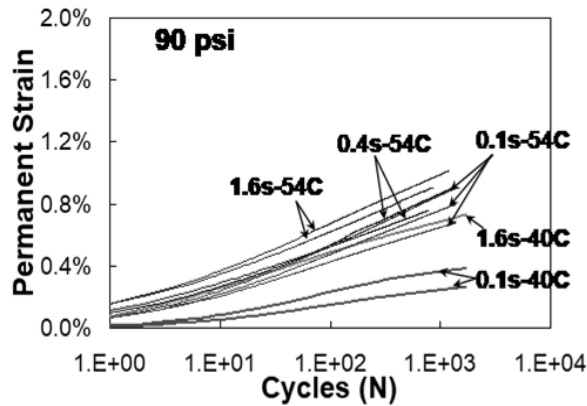
$$N_{red} = N \times 10^{a_{\xi p}} \quad (61)$$

Where:

N_{red} = the reduced number of cycles after load-time shifting.

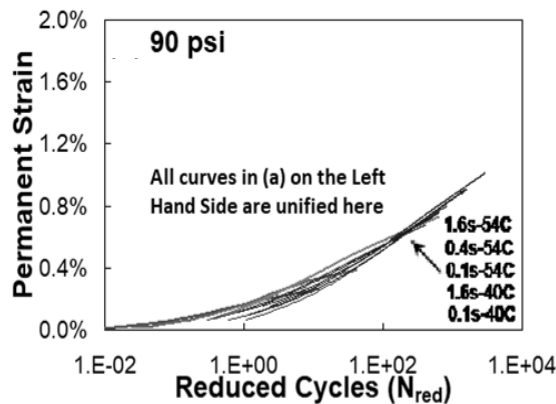
$a_{\xi p}$ = the reduced load-time shift factor.

Figure 41 shows the reduced load-time shift. Figure 41-A through figure 41-C represent the strains before translation, and figure 41-D through figure 41-F show the same data after horizontal load-time shifting. The research team used the average strain of the 0.4-s load-time test at each deviatoric stress level as the reference curve to make one representative curve. The strain evolution curves overlap relatively well after horizontal load-time shifting. The research team also found the same degree of success for the NY9.5B mixture. The shift shown in figure 41 is not perfect; however, as is seen later in the verification study, this amount of error from horizontal shifting is acceptable from an engineering standpoint.



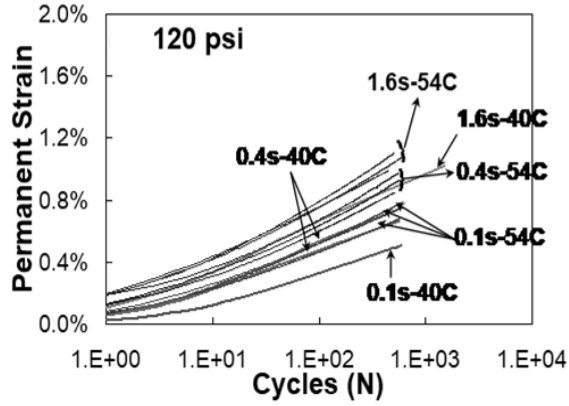
© 2013 Road Materials and Pavement Design. (DTFH61-08-H-00005)
 0°C = 32°F; 1 psi = 6.89 kPa.

A. Permanent strain growth as number of cycles increase loaded at 90 psi.



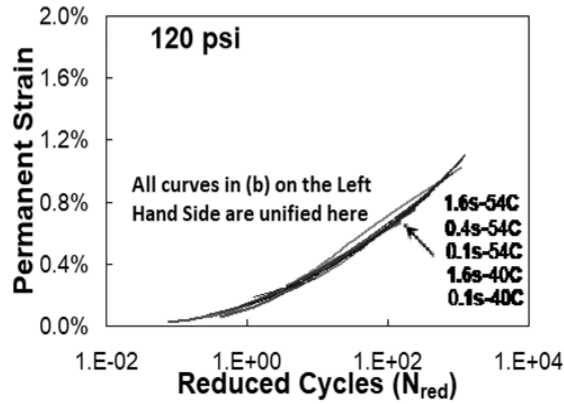
© 2013 Road Materials and Pavement Design. (DTFH61-08-H-00005)
 0°C = 32°F; 1 psi = 6.89 kPa.

B. Unified permanent strain curves at 90 psi.



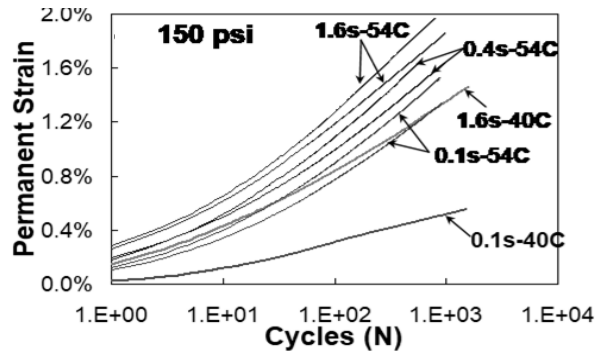
© 2013 Road Materials and Pavement Design. (DTFH61-08-H-00005)
 0°C = 32°F; 1 psi = 6.89 kPa.

C. Permanent strain growth as number of cycles increase loaded at 120 psi.



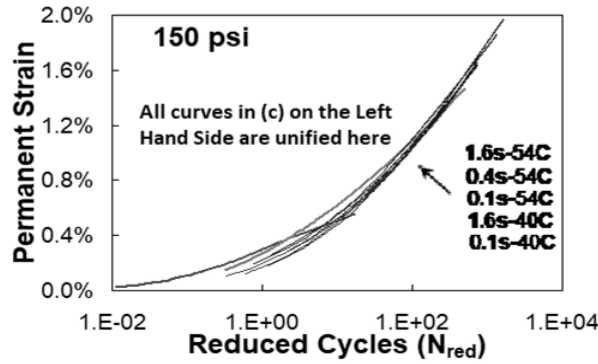
© 2013 Road Materials and Pavement Design. (DTFH61-08-H-00005)
 0°C (32°F); 1 psi = 6.89 kPa.

D. Unified permanent strain curves at 120 psi.



© 2013 Road Materials and Pavement Design. (DTFH61-08-H-00005)
 0°C = 32°F; 1 psi = 6.89 kPa.

E. Unified permanent strain curves at 150 psi.



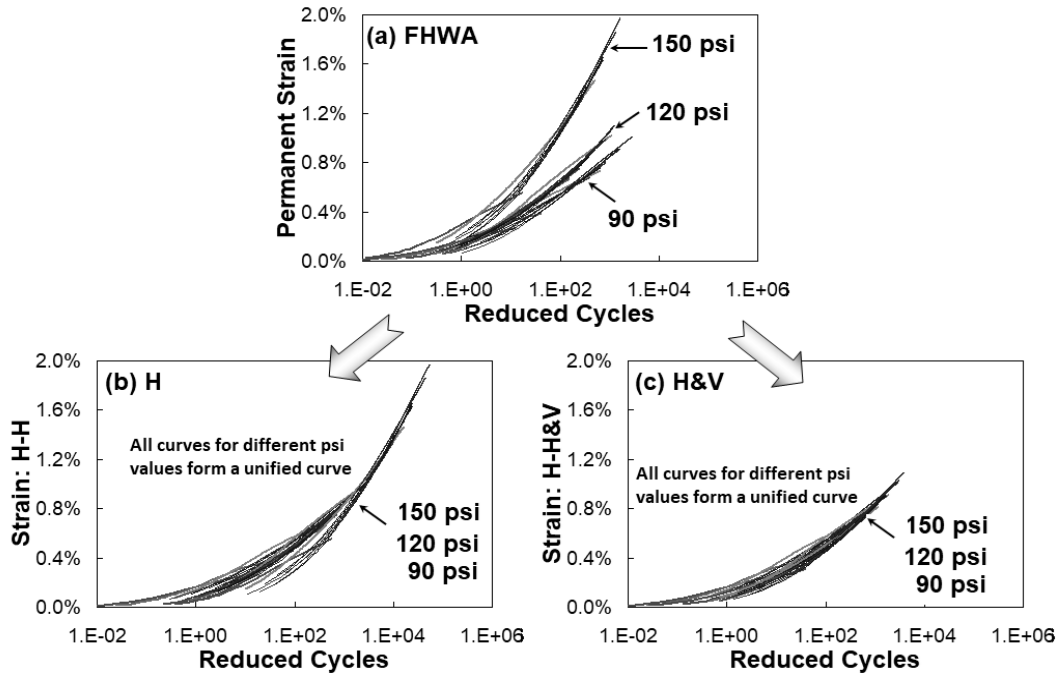
© 2013 Road Materials and Pavement Design. (DTFH61-08-H-00005)
 0°C = 32°F; 1 psi = 6.89 kPa.

F. Unified permanent strain curves at 150 psi.

Figure 41. Graphs. Verification of load time shifting for FHWA mixture.⁽¹³⁾

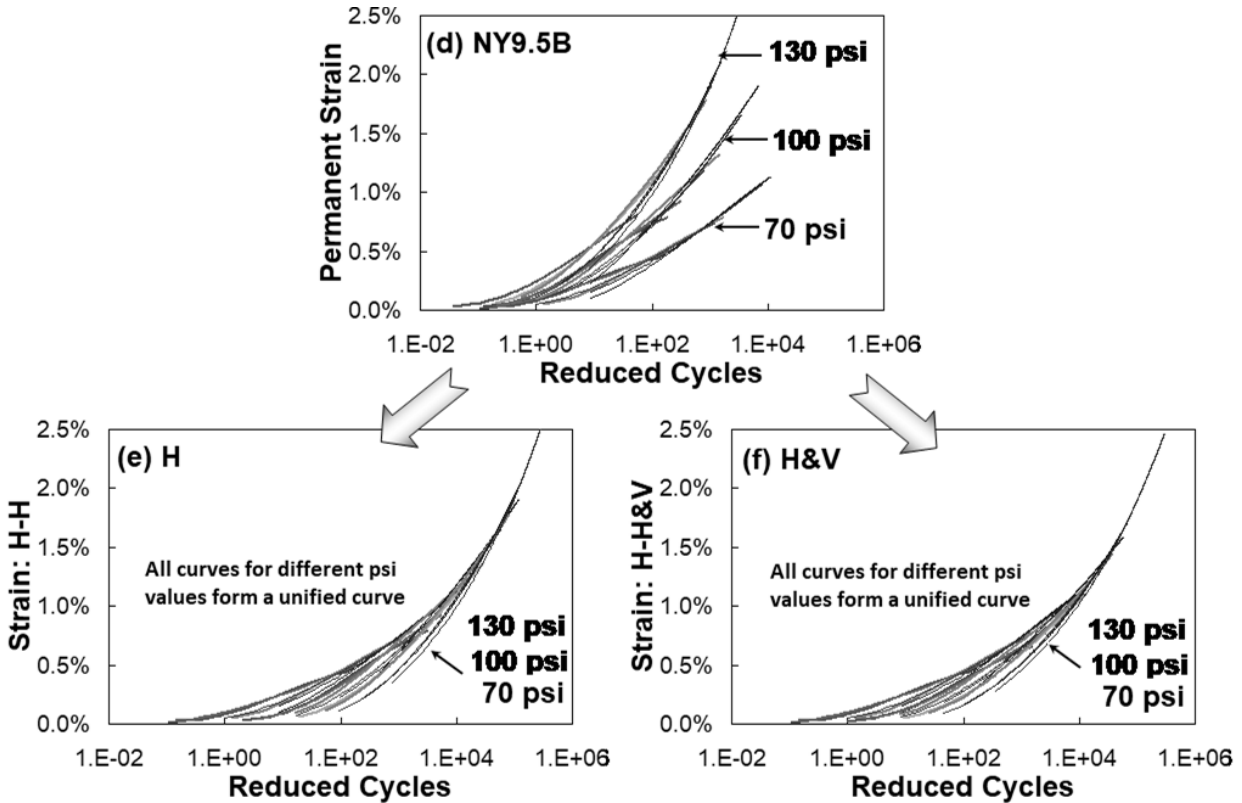
Stress Shifting

Researchers suggest using the t -SS principle to model asphalt concrete behavior at different stress levels. As the literature indicates, the possible shift combinations are horizontal-only shifting and both horizontal and vertical shifting. The research team investigated these two approaches to verify the t -SS principle and to find the best shifting approach for the study mixtures. They applied the same approach used for the reduced load-time shifting. The research team visually translated the cluster of strains that developed after the load-time shift to build the strain master curve. The team determined the stress shift factor (a_{od}) based on the logarithmic distance between the cluster of strains of the individual deviatoric stress levels and the reference curve. Figure 42 indicates that, regardless of the stress shift direction, the strain versus number of cycle curves for the individual deviatoric stresses overlap one another fairly well after shifting. There are some discrepancies at lower strain levels, but they are small and appear mostly within the primary region, which is expected because of the one constant β assumption. The research team selected the horizontal-only shifting approach for applying the t -SS principle to the viscoplastic strain of asphalt concrete to model asphalt concrete behavior at different stress levels.



© 2013 Road Materials and Pavement Design.
1 psi = 6.89 kPa.

A. Verification of stress shifting for the FHWA mixture.



© 2013 Road Materials and Pavement Design. (DTFH61-08-H-00005)
1 psi = 6.89 kPa.

B. Verification of stress shifting for the NY9.5B mixture.

Figure 42. Graphs. Verification of stress shifting for the FHWA mixture and the NY9.5B mixtures.⁽¹³⁾

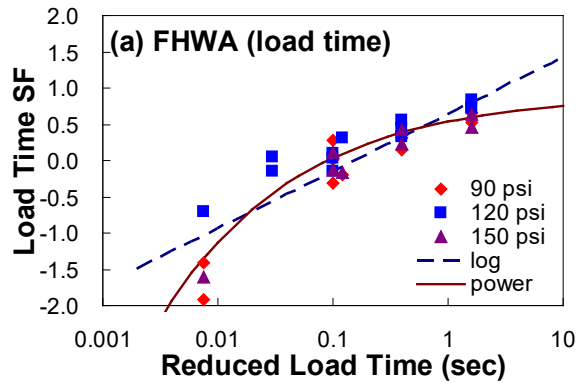
Characteristics of Shift Factors

Shift factor is one of the key elements in the shift model. Shift factors characterize the effects of loading amplitude, loading time, and loading temperatures on permanent strain.

Reduced Load-Time Shift Factors

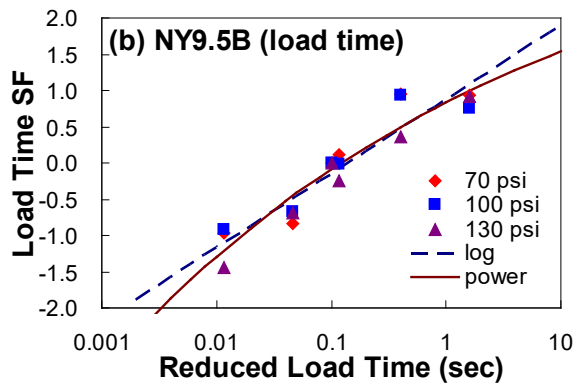
The horizontal distance between a certain strain curve and the reference curve in logarithmic scale under the same deviatoric stress is defined as the load-time shift factor. It is the ratio of the number of cycles between two load-time conditions that produce the same amount of permanent strain. Figure 43 depicts the shift factors measured by horizontal-only shifting. There is no clear trend in deviatoric stress in figure 43-A and figure 43-B. The shift factors at 120 psi for the FHWA mixture are slightly higher than those for the other stress conditions. However, considering the specimen-to-specimen variability and the sequence of the deviatoric stress levels, the research team found it reasonable to conclude that deviatoric stress does not affect the load-time shift factors. The NY9.5B mixture more clearly shows this random behavior in figure 43-B. Thus, the research team concluded that the load-time shift factor is only a function of the reduced load time. This conclusion implies that load-time shift factors can be determined by only one

stress condition, instead of three different deviatoric stress levels, when various load times are applied to the sample.



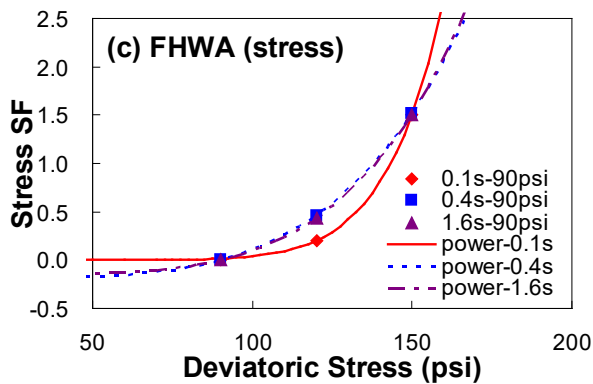
© 2013 Road Materials and Pavement Design. (DTFH61-08-H-00005)
1 psi = 6.89 kPa.

A. Load-time shift factor of the FHWA mixture.



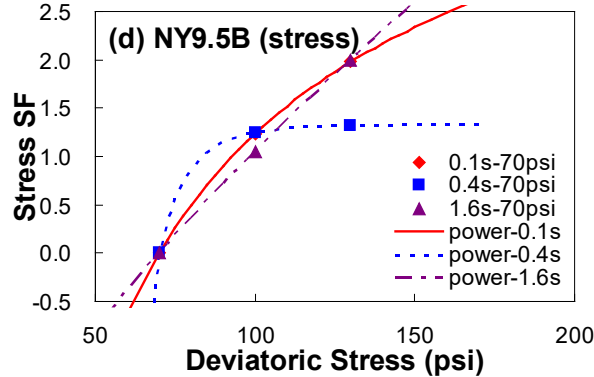
© 2013 Road Materials and Pavement Design. (DTFH61-08-H-00005)
1 psi = 6.89 kPa.

B. Load-time shift factor of the NY9.5B mixture.



© 2013 Road Materials and Pavement Design. (DTFH61-08-H-00005)
1 psi = 6.89 kPa.

C. Deviatoric stress shift factor of the FHWA mixture.



© 2013 Road Materials and Pavement Design. (DTFH61-08-H-00005)
1 psi = 6.89 kPa.

D. Deviatoric stress shift factor of the NY9.5B mixture.

Figure 43. Graphs. Load-time shift factors and deviatoric stress shift factors of the FHWA and NY9.5B mixtures.⁽¹³⁾

The load-time shift factor explains the effect of load time on permanent strain, especially the load time–dependent hardening effect that Yun found.⁽⁷³⁾ When hardening is independent of the load-time length, the reduced load–time shift factor linearly increases in arithmetic scale because permanent strain develops proportionally to the load-time length. However, figure 43-A and figure 43-B demonstrate that the shift factor increases linearly in semilogarithmic scale, not in arithmetic scale, which indicates that hardening evolves during the load time, and thus, the permanent strain is not proportional to the load-time length.

The research team needed a functional form of this shift factor for modeling purposes. Because the shift factor linearly increases in semilogarithmic scale as the reduced load time lengthens, the team investigated both logarithmic and power function expressions. Figure 43-A and figure 43-B illustrate the results of fitting using these two models. The power form fits the results slightly better than the logarithmic expression; however, considering the overall trend and the need for simplicity, the logarithmic form explains the load-time behavior better than the power form. The power form may also cause more error outside of the tested range depending on its curvature.

Stress Shift Factors

Translating strain clusters after load-time shifting to construct a master curve provides stress shift factors. Because this process involves moving the strain clusters for the individual deviatoric stress conditions, the research team only calculated three stress shift factors, as depicted in figure 43-C and figure 43-D, but used different loading times as the reference. For example, the “0.4s-90psi” data in the graphs indicate that the reference loading condition is a 0.4-s load time and 90 psi is the deviatoric stress.

Due to the relatively large specimen-to-specimen variability, the shift factor for the NY9.5B mixture using the 0.4-s, 70-psi data appears to be an outlier at 130 psi. Thus, the research team

excluded the 0.4-s load time for the NY9.5B mixture in the detailed analysis. Otherwise, the stress shift factors are similar to one another.

The stress shift factors illustrate the effect of deviatoric stress on permanent deformation. Von Quintus et al. reported that permanent strain exponentially rather than linearly increases as deviatoric stress increases.⁽⁷⁴⁾ The deviatoric stress shift factors demonstrate this phenomenon. The FHWA mixture shows such exponential increments clearly; however, the stress shift factors of the NY9.5B mixture increase linearly. The stress shift factor dramatically increases when 150 psi or higher deviatoric stress is applied to the NY9.5B mixture, which is why the research team initially selected the power form to explain the behavior of the stress shift factors.

In summary, the model that employs shift factors comprises the reference curve, the load-time shift function, and the stress shift function. The reference curve is the permanent strain growth curve obtained from a single TRLPD test under the reference loading condition. In contrast to the construction of a dynamic modulus master curve, the reference curve is obtained by a separate test to determine the datum line. The incremental model fits the permanent strain and then becomes the final reference curve form, which is the permanent strain master curve. Strains provided by the TRLPD tests translate horizontally for load-time shifting and again for stress shifting to construct the reference curve; accordingly, the total shift factor is a summation of

these two shift factors (i.e., $a_{Total} = a_{\xi_p} + a_{\sigma_d}$).

Equations 62 to 64 express the preliminary shift model form.

$$\varepsilon_{vp} = \frac{\varepsilon_0 \cdot N_{red}}{(N_I + N_{red})^\beta}, \quad (62)$$

$$a_{\xi_p} = p_1 \log(\xi_p) + p_2, \quad (63)$$

$$a_{\sigma_d} = d_1 (\sigma_v / P_a)^{d_2} + d_3. \quad (64)$$

Where:

ε_{vp} = viscoplastic strain.

$N_{red} = N \times 10^{a_{Total}}$,

$p_1, p_2, d_1, d_2,$ and d_3 = model coefficients.

P_a = atmospheric pressure used to normalize the stress.

The research team later changed the form of the equation for the stress shift factor in equation 64 to the same logarithmic expression used for the time shift-factor function. Not only did the logarithmic function fit the nonlinear properties of the stress shift factors but this function also satisfied the condition that when the vertical stress is zero the stress shift factor is zero. This condition prevents permanent strain development when no stress is present, and the research team found the condition to be critical in FlexPAVE's pavement performance predictions. Also, the deviatoric stress-based shift model is reformulated using vertical stress, which is the sum of the deviatoric and confining stresses. Equations 65 to 67 express this revised form of the shift model with the vertical stress shift factor (a_{σ_v}).

$$\varepsilon_{vp} = \frac{\varepsilon_0 N_{red}}{(N_I + N_{red})^\beta} \quad (65)$$

$$a_{\xi_p} = p_1 \log(\xi_p) + p_2 \quad (66)$$

$$a_{\sigma_v} = d_1 \log(\sigma_v / P_a) + d_2 \quad (67)$$

Further research showed that d_1 and d_2 in equation 67 are not independent and both of those are functions of temperature. Equation 68 expresses the final form of vertical stress shift factor. The research team developed parameter Q in equation 68 to capture the temperature dependency of the vertical stress shift factor. Equation 69 presents the final form of reduced number of cycles (N_{red}).

$$a_{\sigma_v} = Q \times \left(\log\left(\frac{\sigma_v}{P_a}\right) - 0.877 \right) \quad (68)$$

Where:

$$Q = d_1 \times T + d_2 \text{ for } T \geq \frac{-d_2}{d_1} \text{ and } Q = 0 \text{ for } T < \frac{-d_2}{d_1}$$

$$N_{red} = A \cdot N \cdot (\xi_p)^{p_1} \left(\frac{\sigma_v}{P_a} \right)^Q \quad (69)$$

Where:

$$A = 10^{P_2} \cdot 10^{-0.877Q}$$

Q = vertical stress shift factor coefficient.

T = temperature, °C.

Composite Loading Block Test with State Variable

The proposed shift model simulates the effect of three major factors on permanent strain: load time, vertical stress, and temperature. The model requires at least five (generally nine) different loading conditions for the TRLPD test to calibrate the model. Considering the number of replicates needed to reduce variability, the shift model demands a large effort. Therefore, the research team proposed a composite loading block test with a state variable to reduce the testing effort and the number of required samples.

State Variable

A state variable is a quantity that marks the state of the material. Therefore, no matter what its stress or strain history may be, its current value affects the development of the permanent strain at any given instant. The state variable defines the condition of the materials in the permanent deformation model. If different specimens have the same state variable value, the same amount of incremental strain occurs due to the same load, even though their past loading histories may be different.

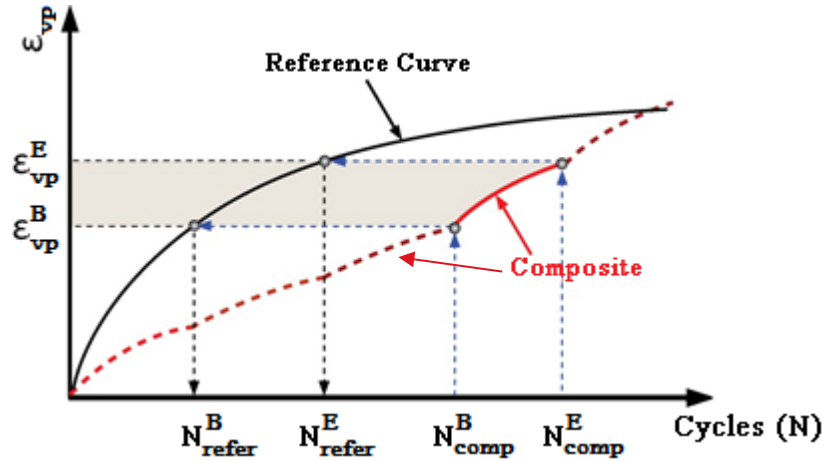
Permanent strain is a good indicator for characterizing the state of viscoplastic behavior because it is simple and provides intuition about the viscoplastic state. For general plasticity, the yield criterion and hardening function based on the plastic strain illustrate the state of the material, which is complex and could require additional calibration and testing. As such, the research team did not consider the yield criterion and hardening function acceptable for this simple model development. Additionally, the MEPDG uses permanent strain as the state variable to evaluate rutting. Gibson also used volumetric permanent strain as a state variable by combining yield functions.⁽⁷⁰⁾ Based on these observations, the research team applied permanent strain as the state variable for shift model calibration and prediction.

Composite Loading Block Test

The proposed models are built on TRLPD tests and demand at least five (generally nine) different conditions for calibration. The research team investigated an alternative method for model calibration, the composite loading block test, to reduce the number of tests required. This test is composed of several loading blocks that each represents one of the conditions needed to characterize the model.

Figure 44 provides a schematic representation of the composite loading test. The schematic assumes the entire results from any individual TRLPD test can be reliably captured using only a small amount of data at that condition by applying the state variable concept. Thus, for example, it is not necessary to perform 0.1-s pulse tests at 90 psi for thousands of cycles to characterize the model—only a few hundred is sufficient.

The composite loading block test performs only a part of the TRLPD test, so it requires a fitting process to extract the entire TRLPD test behavior from the small loading block available to it. Figure 44 illustrates this linking procedure using the state variable (i.e., permanent strain). Assume a small block (composite line) of the composite test has loading conditions that are the same as the entire TRLPD test (reference curve). Because the research team used permanent strain as a state variable, they found the equivalent number of cycles in the TRLPD test to cause the same permanent strain increase due to the small block of loading in the composite loading test. This process is illustrated in figure 44, which denotes the equivalent number of cycles for the beginning and end of the composite loading test loading block as N_{refer}^E and N_{refer}^B , respectively. The research team fitted the portion of permanent strain provided by the composite loading block test and the equivalent number of cycles using the incremental model form to extract the behavior for the entire TRLPD test.



© 2013 Road Materials and Pavement Design Road. (DTFH61-08-H-00005)

Figure 44. Illustration. Linking the composite loading test to the TRLPD test.⁽¹³⁾

However, this approach demands as many TRLPD tests as there are number of loading conditions in the composite loading test. So, the research team used only one TRLPD test to create a permanent strain curve reference to reduce the testing effort instead of several TRLPD tests. Because a loading block can represent an entire TRLPD test, horizontal shifting calculates the total shift factor, which is the sum of the reduced load–time shift factor and vertical stress shift factor. Figure 44 also illustrates this process of calculating the total shift factor, and the TRLPD test provides the reference strain curve. Equation 70 calculates the total shift factor by matching a loading block from the composite test with a reference strain curve. The research team then separated the total shift factor into two shift factors by applying the assumption that the load-time shift factor is independent of the vertical stress shift factor. They then determined the model parameters using the reduced load time and vertical stress shift factors.

$$a_{total} = \log \left(\frac{\Delta N_{ref}}{\Delta N_{comp}} \right) \quad (70)$$

Where:

a_{total} = total shift factor.

$\Delta N_{ref} (= N_{ref}^E - N_{ref}^B)$ = incremental number of cycles at reference curve.

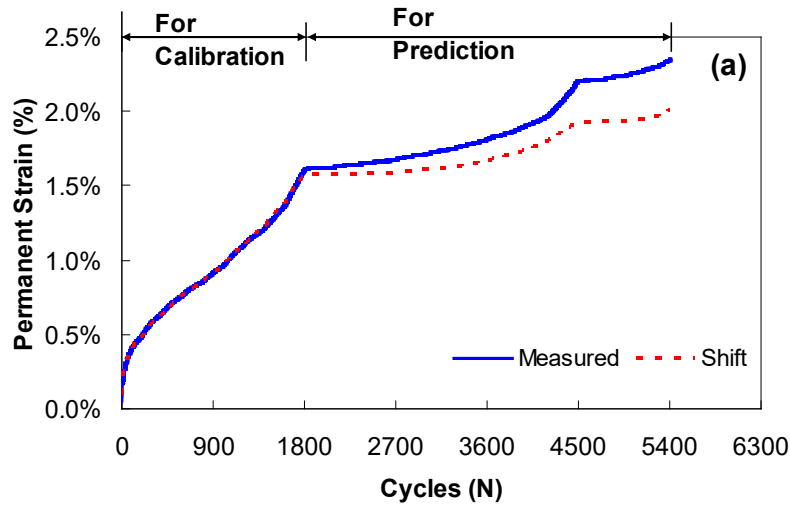
$\Delta N_{comp} (= N_{comp}^E - N_{comp}^B)$ = incremental number of cycles for composite loading test.

Proposed Model Verification

To verify the composite loading block test with the state variable, the research team applied nine loading blocks to one sample. The detailed test conditions and verification results can be found elsewhere.⁽⁹¹⁾ The research team used the first loading group (nine loading blocks) to calibrate the shift model so it could predict the permanent strain of two additional groups, as shown in figure 45-A. Figure 45-A shows that the model can predict the composite loading history well,

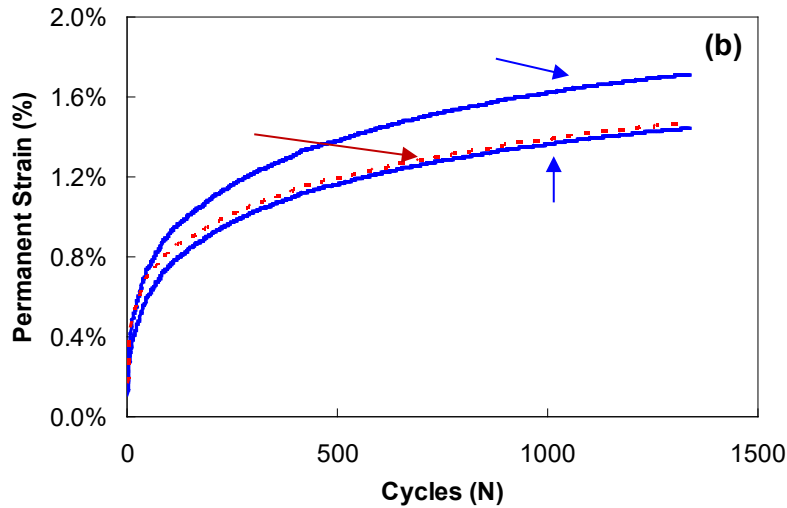
even though the difference between the measured and shifted values increases in the second and third groups.

For further verification, the research team used a random loading history with changes to the vertical stress, load time, and temperature. In this approach, the random loading history mimics actual field conditions with changing load times and deviatoric stress levels. Thus, a good prediction for the random loading history is essential for a model to be applied for pavement performance predictions. Figure 45-B shows that the permanent strains predicted by the shift model calibrated by the composite loading block test (figure 45-A) match the random loading test results. In summary, the shift model calibrated by the composite loading block test predicts permanent strain growth under various complex loading histories reasonably well. These reasonable prediction results provide evidence that the model, the composite loading test method, and the state variable approach together capture the permanent deformation behavior of asphalt mixtures.



© 2013 Transportation Research Record. (DTFH61-08-H-00005)

A. Prediction for composite loading test.



© 2013 Transportation Research Record. (DTFH61-08-H-00005)

B. Prediction for random loading test.

Figure 45. Graphs. Predictions by the shift model calibrated using the composite test.⁽¹⁾

Suggested TSS Testing Protocol

The research team developed the TSS test for the calibration of the shift model, with the TSS test verified through random loading testing. The research team utilized the composite loading block test combined with the state variable (the permanent strain) to reduce the testing time and number of samples.

Effect of Stress

The shift model assumes constant confining pressure; thus, the effects of the stress state on the permanent strain growth originate from deviatoric stress only. To characterize the stress effects (i.e., to determine the deviatoric stress shift factors), tests should be carried out for at least three different deviatoric stress conditions.

The NCHRP 9-30A project found that confining pressure reduces permanent strain substantially, but the report did not clearly define the threshold for confining pressure.⁽⁷⁴⁾ Considering the importance of confining pressure and the NCHRP 9-30A project's recommendation (70 psi and 10 psi for deviatoric stress and confining pressure, respectively), the research team used 10 psi confining pressure as the standard confined condition for the proposed test protocol.

Deviatoric stress is directly related to the tire contact pressure. This pressure depends on many factors, such as tire type, tire structure, and loading conditions.⁽⁹²⁾ Under free rolling conditions and assuming an 18-kN load, the contact pressure distribution is from 60 psi to 120 psi.⁽⁹³⁾ Based on this finding, the research team chose three deviatoric stress levels for the testing protocol: 482 kPa (70 psi), 689 kPa (100 psi), and 896 kPa (130 psi). An additional deviatoric stress level, such as 1,034 kPa (150 psi) or higher, may be applied for heavy trucks, which allows the

deviatoric stress shift function to more clearly the effects of heavy vehicles on permanent deformation.

Effect of Reduced Load Time

At least three reduced load time conditions are needed to determine the reduced load time shift function. Because the reduced load time is a function of temperature and physical load time, data for the different reduced loading times can be obtained in two ways: (1) tests using three different physical load times at one temperature or (2) tests using one physical load time at three temperatures. The first method provides only a limited range of reduced load times, for example, 0.1 s to 1.6 s; otherwise, the testing time is too lengthy. This narrow range of reduced load times cannot represent a sufficiently wide range of interest in the permanent deformation modeling of asphalt pavement. Because of this limitation, the research team chose the second approach for this study. To generate sufficiently high permanent strain levels within a practical length of test time, the load time selected for the calibration tests was 0.4 s. Moreover, a 0.4-s pulse allows a testing machine to reach the target peak stress easier and follow the haversine shape better than a 0.1-s pulse.

Effect of Temperature

The research team determined that three temperatures should be used for the proposed testing protocol to obtain three different reduced load times, including the entire range of temperatures that can affect permanent deformation that would be an ideal scenario, but practically very difficult. Therefore, the research team explored reasonable ways to determine the test temperatures, which are presented in the following paragraphs.

Azari and Mohseni compared protocols used for flow number testing.⁽⁹⁰⁾ The temperatures selected for these protocols were based on 50-percent reliability for a high pavement temperature, as determined by the LTPPBind software.⁽⁹⁴⁾ LTPPBind was designed for binder grade selection and therefore provides only minimum and maximum pavement temperatures. The minimum temperature is usually below 0°C, at which permanent strain would not develop. Therefore, this temperature cannot be used in permanent deformation test protocols, so this approach for choosing test temperatures is not adequate for this project despite its simplicity.

The Enhanced Integrated Climatic Model (EICM) (NCHRP 1-37A), which was implemented in the MEPDG, can be used to determine test temperatures. The EICM is a one-dimensional coupled heat and moisture flow model that has been improved and integrated with other climate models. The EICM generates pavement temperatures with respect to pavement depth every hour. The distribution of temperature within a pavement structure is important to include in permanent deformation modeling because of the temperature sensitivity of asphalt concrete. The number of occurrences of a particular temperature is also important for rut depth calculations. Low temperatures produce very low strain levels; however, low temperatures occur frequently, so the cumulative strain due to low temperatures may not be insignificant. As such, both the distribution and number of occurrences of temperatures should be considered simultaneously.

For this study, the research team selected the rutting model from the MEPDG to determine the cumulative permanent strains at a given temperature because of the model's simplicity and

ability to account for temperature and number of load applications, as expressed in equation 71. This rutting model can calculate the contribution of each temperature to the evolution of the rut depth.

$$\frac{\varepsilon_p}{\varepsilon_r} = 10^{k_1} T^{k_2} N^{k_3} \quad (71)$$

Where:

ε_p = permanent strain.

ε_r = resilient strain ($=\sigma/|E^*(T)|_{@fr}$).

k_1, k_2, k_3 = nonlinear regression parameters.

$|E^*(T)|_{@fr}$ = the dynamic modulus at the frequency and the temperature of the sublayer for the given time increment of the analysis.

σ = the stress induced by a vehicle on the pavement structure.

To evaluate the contribution of only the pavement temperature, the research team assumed that the other conditions—frequency and stress—remain constant. They used a frequency of 10 Hz based on an assumed 0.1-s pulse. Considering the gradients of temperature and stress with respect to pavement depth, the research team divided the pavement into sublayers at 2.54 cm intervals and the analysis on the top 10.16 cm because most rutting occurs in the top 4 inches. They determined the stress at each sublayer through layered viscoelastic analysis (LVEA).⁽⁹⁴⁾ The research team used pavement temperatures determined using the EICM and a 10-Hz loading assumption to determine the dynamic modulus values. The team also used the resilient strain calculated from the stress and the dynamic modulus values to calculate the permanent strain using equation 72.

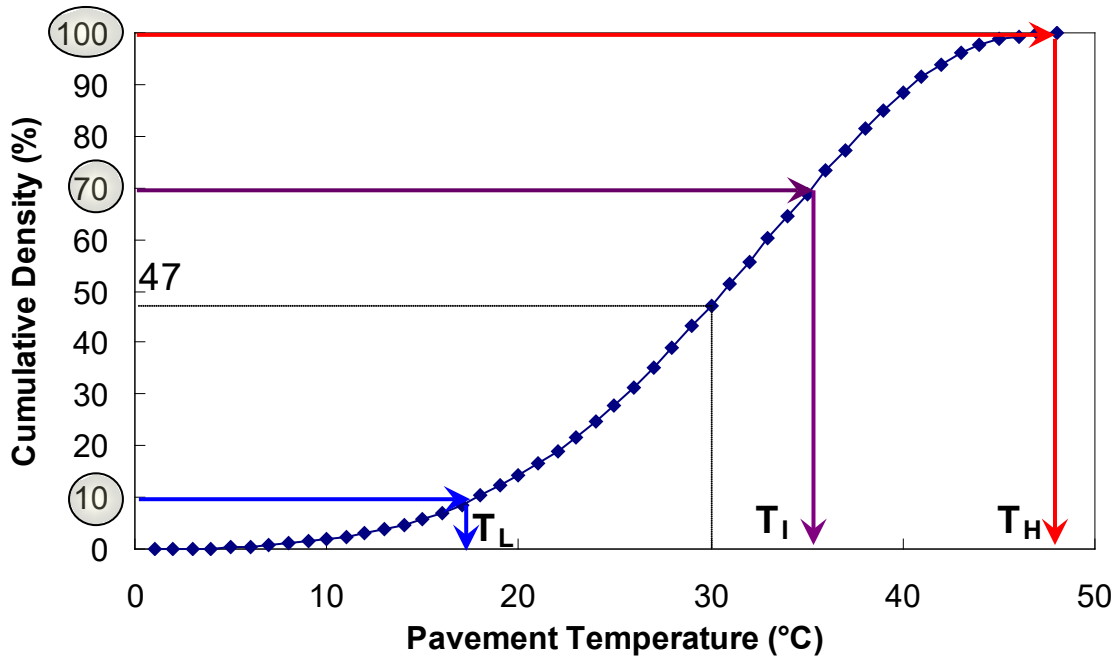
$$T_H = \begin{cases} T_{100} & T_{100} \leq 54^\circ \text{C} \\ 54 & T_{100} > 54^\circ \text{C, increased load time} \end{cases} \quad (72)$$

Where T_{100} is the temperature at 100-percent cumulative density. The main reason to keep the maximum temperature of T_H at 54°C is that the maximum temperature AMPT could reach at the time of developing the TSS test protocol was 54°C. If the calculated T_H is greater than 54°C, the load time is increased using the t–T shift factor so the reduced load time of the increased load time at 54°C is equal to that of the 0.4-s load time at 54°C.

The research team carried out the analysis for the entire duration for which climatic data were available. To determine the contribution of different temperatures on the permanent strain development, the team separated the permanent strains by temperature in 1°C increments. They ignored temperatures lower than 0°C by assuming that no permanent strain develops at such temperatures.

The research team created a cumulative density graph by accumulating permanent strain with respect to pavement temperature, as shown in figure 46. This graph illustrates the contribution of temperature to the permanent strain evolution. For example, 30°C corresponds to the 47th

percentile (see the dotted line in figure 46), which explains that temperatures below 30°C contribute to 47 percent of the total cumulative permanent deformation.



© 2013 Transportation Research Record. (DTFH61-08-H-00005)
 0°C = 32°F.

Figure 46. Graph. Example of a cumulative density function of permanent strain according to pavement temperatures at Angelica, NY.⁽¹⁾

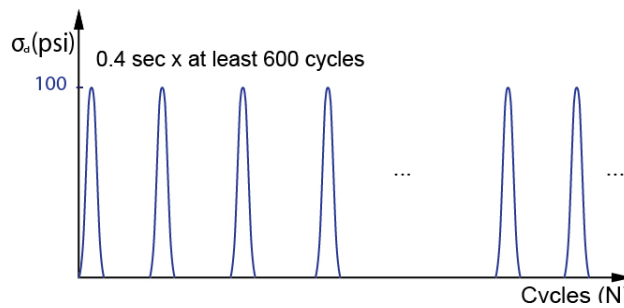
To select the test temperatures, ideally the upper and lower boundaries should be the 100th and 0th percentiles, respectively. However, permanent strain does not develop much at low temperatures. Therefore, the research team chose the temperature that corresponds to the 10th percentile as the low temperature (T_L). Because high temperatures induce significant permanent deformation, they chose the 100th percentile for the high temperature (T_H), the highest pavement temperature found during the analysis period, which is usually about 10 yr. For a similar reason, the temperature corresponding to a range from the 60th to 80th percentile, rather than the 50th percentile, would be effective as an intermediate temperature (T_I) for protocol testing. Thus, the research team recommended the 70th percentile temperature as the intermediate temperature.

TSS Test Protocol Determination

This report proposes a new test protocol on the basis of the aforementioned test conditions and the applicability of the composite loading test. Multiple stress levels can be applied to one sample to obtain the stress shift factor. This composite test has three loading blocks in which the deviatoric stress levels—482 kPa (70 psi), 689 kPa (100 psi), and 896 kPa (130 psi) with a constant 0.4-s load time—and is referred to as the TSS test. The test is performed at three different temperatures to obtain a reduced load-time shift factor. To obtain a reference strain curve, the TRLPD test (hereinafter referred to as the reference test) is needed in addition to TSS testing. The reference test is conducted under reference loading conditions. The high temperature

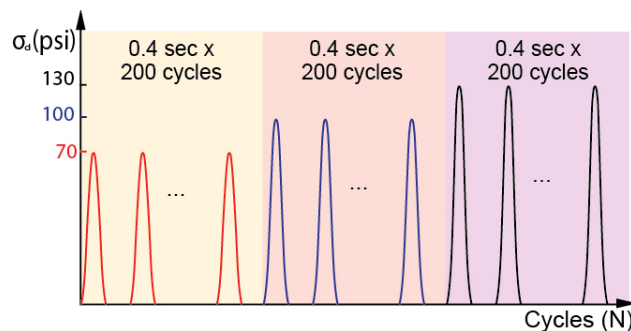
(T_H) is the reference temperature because it causes high enough permanent strain levels that cover a wide range of strain levels. The reference deviatoric stress becomes 689 kPa (100 psi). In brief, the test protocol consists of one reference test at the high temperature (T_H) and three TSS tests at each of the three temperatures (low, intermediate, and high), as shown in figure 47.

To capture the true permanent strain after each load cycle, the rest period must be long enough to avoid the effects of viscoplastic softening and viscoelastic recovery.⁽⁷³⁾ However, too long a rest period will result in an impractical amount of testing time. In this study, the research team found the shortest rest periods for the three calibration temperatures (i.e., T_H , T_I , and T_L) by conducting numerous TRLPD tests with various rest periods. The team compared the permanent strain growth results against those from the 100-s rest period to determine the shortest rest periods that would statistically yield the same permanent strain growth results as the 100-s rest period tests. They found that 1.6 s was long enough for T_I and T_L , whereas 10 s was needed for T_H .



© 2013 Transportation Research Record. (DTFH61-08-H-00005)
1 psi = 6.89 kPa.

A. Reference test at high temperature.



© 2013 Transportation Research Record. (DTFH61-08-H-00005)
1 psi = 6.89 kPa.

B. TSS tests at all three temperatures.

Figure 47. Illustrations. Schematic diagram of proposed testing protocol.⁽¹⁾

TSS Test Protocol Verification

In this section, the research team used random loading histories to evaluate the prediction accuracy of the developed TSS test protocol.

Calibration Test

The research team selected the NY9.5B mixture to verify the model and test protocol. This mixture is a dense-graded mixture with polymer-modified PG 64-22 binder and an NMAS of 9.5 mm. Detailed information about both of the mixtures (i.e., NY9.5B and FHWA) used in this study can be found elsewhere.⁽⁷⁵⁾ The research team determined the three temperatures (i.e., T_H , T_I , and T_L) as 47°C, 37°C, and 17°C, respectively. The reference test conditions were 0.4-s load time and 689 kPa (100 psi) at 47°C, and table 16 presents the TSS test conditions. The first three loading blocks shown in table 16 represent the proposed testing protocol, and the research team used blocks 4 to 20 to verify the proposed testing protocol. The three rightmost columns in table 16 indicate the final testing blocks for each temperature.

The random loading history test is another test the research team used to verify the combination of the test protocol and shift model. They performed the random loading test at the high temperature, 47°C. The team selected the load times and deviatoric stress levels randomly; the load-time distribution ranging from 0.1 to 1.6 s, and the deviatoric stress levels ranged from 482 kPa (70 psi) to 896 kPa (130 psi) at 69-kPa (10-psi) intervals.

Figure 48 depicts the random loading history.

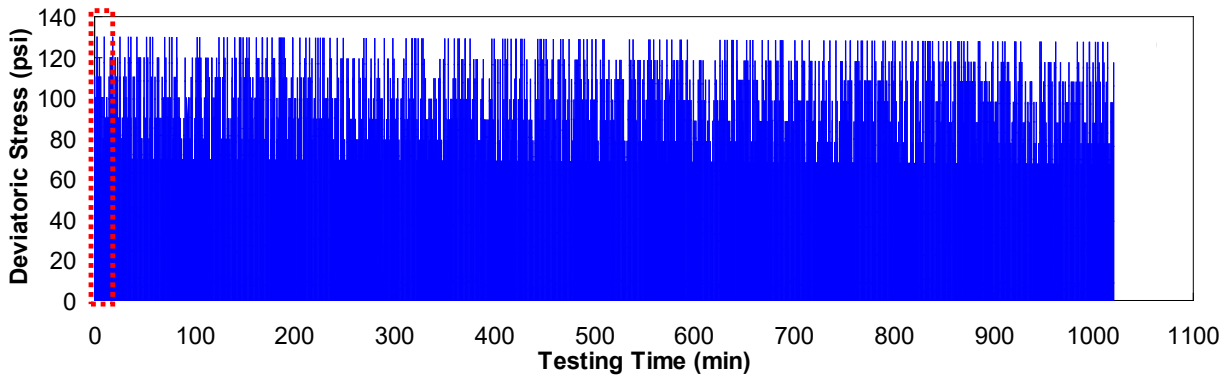
Table 16. Testing plan for verifying the proposed testing protocol.

No.	Dev. Stress (kPa/psi)	Load Time (s)	Cycles	Cumulative Cycles	TH (°C)	TI (°C)	TL (°C)	Purpose
1*	482/70	0.4	200	200	47	37	17	TP
2*	689/100	0.4	200	400	47	37	17	TP
3*	896/130	0.4	200	600	47	37	17	TP
4	482/70	0.1	200	800	47	37	17	MV
5	482/70	1.6	200	1,000	47	37	17	MV
6	689/100	0.1	200	1,200	47	37	17	MV
7	689/100	1.6	200	1,400	47	37	17	MV
8	896/130	0.1	200	1,600	47	37	17	MV
9	896/130	1.6	200	1,800	47	37	17	MV
10	689/100	0.1	50	1,850	47	37	-	MV
11	826/120	0.4	30	1,880	47	37	-	MV
12	620/90	1.6	25	1,905	47	37	-	MV
13	482/70	0.8	30	1,935	47	37	-	MV
14	689/100	0.4	40	1,975	47	37	-	MV
15	1,034/150	0.4	40	2,015	47	37	-	MV
16	689/100	0.1	60	2,075	47	37	-	MV
17	413/60	0.4	50	2,125	47	-	-	MV
18	482/70	1.6	60	2,185	47	-	-	MV
19	689/100	0.5	100	2,285	47	-	-	MV
20	551/80	0.4	50	2,335	47	-	-	MV

Note: *These three loading blocks represent the proposed testing protocol.

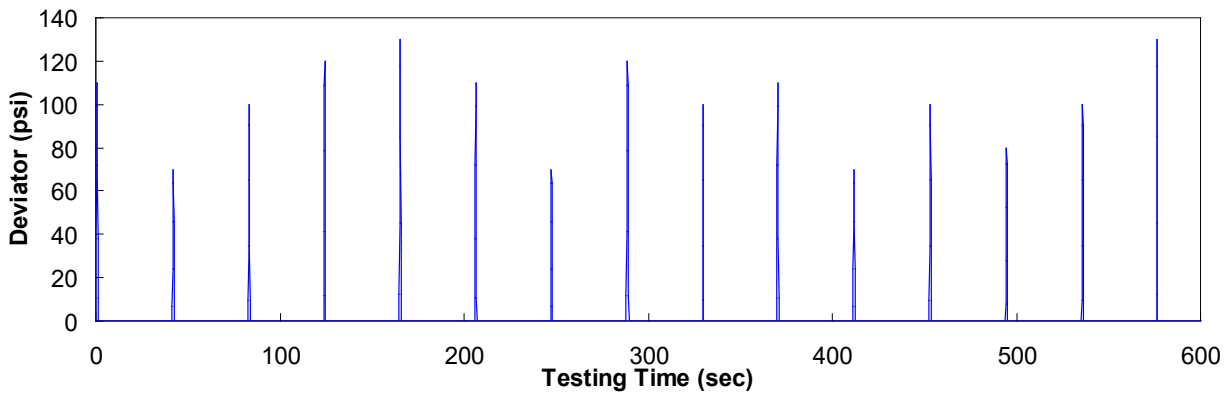
0°C = 32°F; 1 kPa = 0.145 psi; 1 psi = 6.89 kPa.

MV = model verification; TP = testing protocol.



© 2013 Transportation Research Record. (DTFH61-08-H-00005)
 1 psi = 6.89 kPa

A. Whole random loading history of random loading history at 47°C.



© 2013 Transportation Research Record. (DTFH61-08-H-00005)
 1 psi = 6.89 kPa.

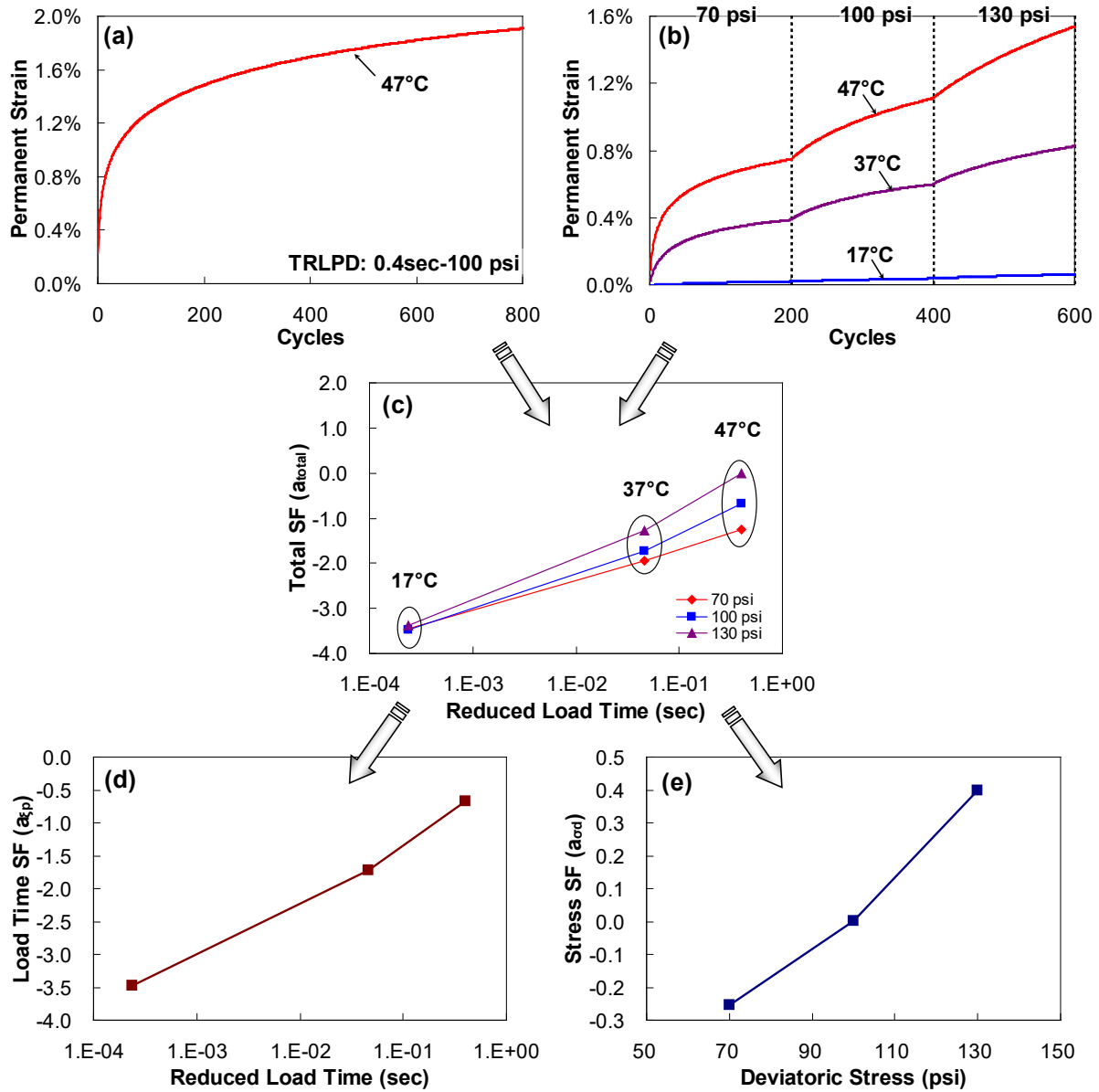
B. Beginning portion of random loading history marked in figure A by the rectangle with dashed line.

Figure 48. Graphs. Random loading history at 47°C.⁽¹⁾

Figure 49-A and figure 49-B present the results of the protocol testing. Horizontally translating the strains of the individual loading blocks in the TSS tests to the reference permanent strain curve provides the total shift factor, shown in figure 49-C. Because the load-time shift factor is independent of the vertical stress shift factor, the research team divided the total shift factors into load-time shift factors and deviatoric stress shift factors, which are shown in figure 49-D and figure 49-E. Then, they characterized the shift functions and reference strain curve shown in figure 49-A, which became the permanent strain master curve for the NY9.5B mixture with a 0.4-s load time and deviatoric stress of 689 kPa (100 psi) at 47°C.

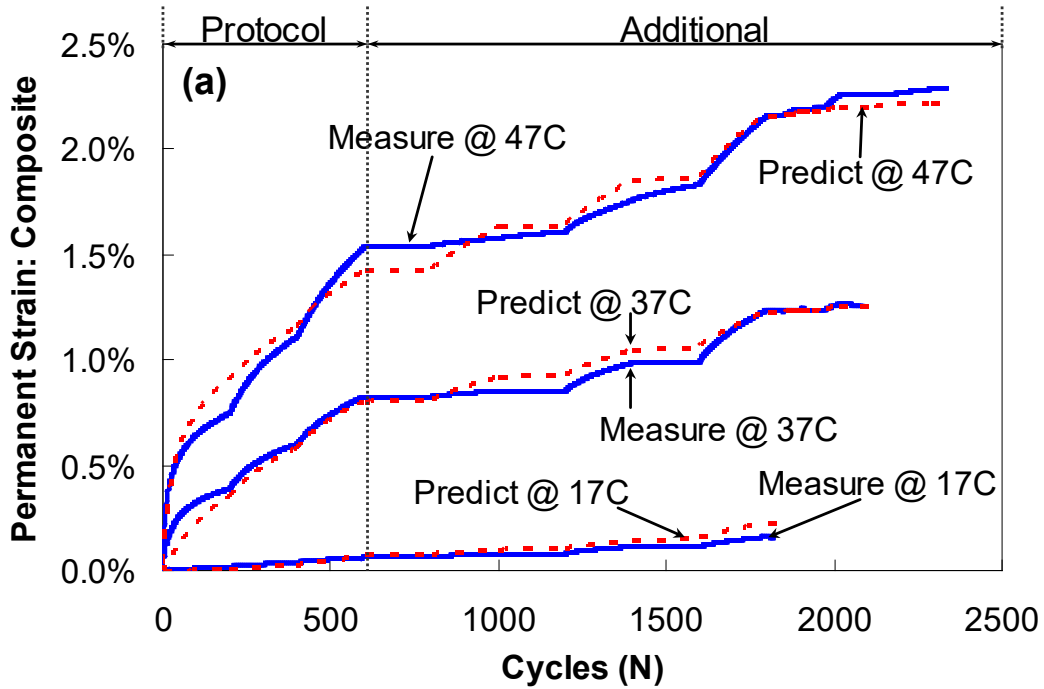
As shown in figure 50-A, the predictions match not only the loading blocks of the test protocol but also the randomly added loading blocks at the three different temperatures. These reasonable predictions prove that the model and test protocol together can evaluate permanent strain development for all study temperatures. In addition, the research team performed a random

loading history and used the calibrated model to further confirm the model and protocol. A random loading history is similar to a traffic loading history encountered with in-service pavements. The research team found agreement between the experimental strain and predicted strain, as shown in figure 50-B, indicating the shift model's potential to predict rutting under realistic conditions with the proposed calibration test protocol.



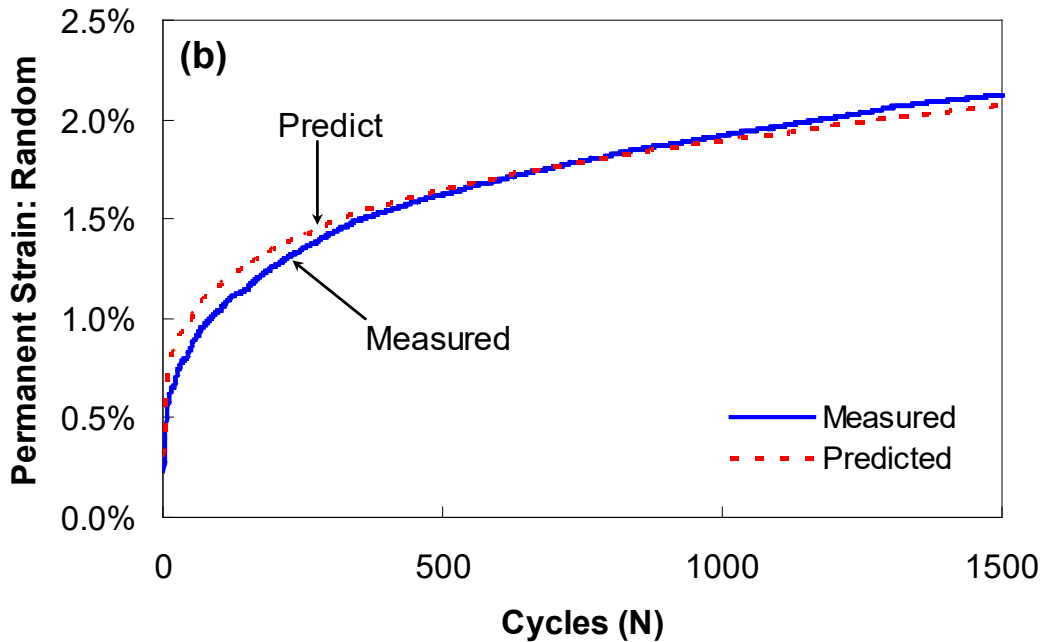
© 2013 Transportation Research Record. (DTFH61-08-H-00005)
 0°C = 32°F; 1 psi = 6.89 kPa.

Figure 49. Graph. Calibration process with protocol testing for the NY9.5B mixture.⁽¹⁾



© 2013 Transportation Research Record. (DTFH61-08-H-00005)
 0°C = 32°F.

A. Prediction of composite loading history.



© 2013 Transportation Research Record. (DTFH61-08-H-00005)

B. Prediction of random loading history.

Figure 50. Graphs. Predictions of the model calibrated by protocol testing.⁽¹⁾

Specifications for Proposed TSS Testing Protocol

Table 17 summarizes the details of the TSS test.

Table 17. Summary of TSS test protocol.

Testing Method	Reference	Stress Sweep Test
Number of tests	1 (T_H)	3 (T_H , T_I , and T_L)
Pulse time (s)	0.4	0.4
Rest period (s)	10 (T_H)	10 (T_H) and 1.6 (T_I and T_L)
Confining pressure (kPa/psi)	68.9/10	68.9/10
Deviatoric stress (kPa/psi)	689/100	482/70, 689/100, and 896/130
Number of cycles	600	200
Parameters	ε_0 , N_I , and β	p_1 , p_2 , d_1 , d_2 , and d_3
Total samples	2	6
Total testing time (h)	3.5	4.8

1 kPa = 0.145 psi; 1 psi = 6.89 kPa.

Note: d_1 , d_2 , and d_3 were calculated using equation 64.

This section provides detailed specifications for performing the calibration tests using the AMPT. Based on AASHTO T 378 and use of the AMPT, the testing procedure is composed of six steps: specimen preparation; temperature conditioning in a separate environmental chamber; installation of the specimen in the AMPT; specimen pressurizing and additional temperature conditioning; fingerprint testing; and main protocol testing.⁽⁹⁾

During step 4 (specimen pressurizing and additional temperature conditioning), the sample should reach a stabilized state in accordance with the pressure and temperature. The research team investigated the time needed for the sample to reach this stabilized state. They measured the sample's deformation while it was being pressurized. The team found the radial strain, which indicates horizontal deformation, to be higher than the axial strain. This observation may indicate that the specimen had more axial resistance than horizontal resistance because it was compacted in the axial direction. The research team found most of the deformation caused by the added pressure to occur within 30 min. The incremental strain between 30 and 60 min was less than 60 $\mu\epsilon$ for the axial strain and less than 120 $\mu\epsilon$ for the radial strain. Therefore, the research team selected 30 min as the pressurizing time.

To accelerate the testing, the research team conducted temperature conditioning in a separate environmental chamber. They also performed an additional temperature conditioning procedure because of the temperature drop that occurs when a specimen is placed in the AMPT chamber. This process took place at the same time as the pressurizing process. The research team installed two thermocouple wires in the center and on the surface of a dummy specimen that was 100 mm in diameter and 150 mm in height. They tracked the temperature for 5 min after opening the cell against three different target temperatures: 20, 40, and 54°C. The temperature reached the target temperatures (within $\pm 0.5^\circ\text{C}$) within about 30 to 40 min. Since the results were dependent on the room temperature and the research team applied no confinement for the tests, 60 min is the time recommended for additional temperature conditioning as well as 1 h is recommended for pressurizing and temperature conditioning.

Taking into consideration all of the aforementioned test conditions, the total test time becomes 2.9 h for the high temperature test in which the rest period is 10 s, and 1.5 h for the low and intermediate temperature tests in which the rest period for both tests is 1.6 s. This results in about a day to complete one set of calibration tests. As such, within 2 to 3 d of testing, depending on the number of replicates tested, the calibrated shift model can predict the permanent strain growth in asphalt concrete for different temperatures, load times, and deviatoric stress levels.

SIMPLIFIED TSS TEST METHOD

Although 2 to 3 d of testing for the complete characterization of permanent deformation behavior of asphalt mixture using the TSS test is significant, the research team made additional efforts to further simplify the test procedure. These efforts resulted in a simplified TSS test procedure known as the Stress Sweep Rutting (SSR) test.

Testing Plan

The current TSS test requires four tests (one reference and three stress sweep) and recommends two replicates to eliminate variability so the total testing time, including temperature conditioning, is 2 d for a single mixture. To reduce the TSS test requirements, each of the parameters that affect the shift model first need to be examined because the TSS test is an optimized test protocol for calibrating the shift model. The shift model contains three factors that play important roles in predicting the permanent strains of asphalt mixtures: temperature, deviatoric stress, and load time. The research team explored the possibility of using fewer temperatures, fewer deviatoric stress levels, and shorter load times. The second TSS test protocol eliminated the reference test, which not only shortened the testing time to half of the original TSS test but also reduced the number of total samples from six to four. The research team introduced the reversed loading block (689, 482, and 896 kPa or 100, 70, and 130 psi) for the high temperature (T_H) so they could use the first loading block to generate the reference curve. The team also considered the length of the rest period in the simplification because it is directly related to the total testing time. The research team conducted TSS tests with 10-, 5-, and 3-s rest periods and compared the permanent deformations obtained from FlexPAVE analysis to explore the effect of the rest period. Lastly, the team considered using actuator displacement to collect permanent strain data, which substantially simplified the instrumentation system as installing linear variable differential transformers (LVDTs) on the specimen takes considerable effort.

Specimen Preparation

To accomplish the goal of simplifying the TSS test, the research team used an RS9.5B mixture with varying test conditions, as shown in table 18. The team obtained this loose mixture from Knightdale, NC, and prepared all of the specimens in accordance with AASHTO R 83, *Standard Practice for Preparation of Cylindrical Performance Test Specimens Using the Superpave Gyrotory Compactor (SGC)*.⁽⁹⁶⁾ The research team cut and cored cylindrical specimens 100 mm in diameter by 150 mm in height for the TSS test from gyrotory-compacted specimens originally 150 mm in diameter by 178 mm in height. After obtaining specimens of the appropriate dimensions, the research team took air void measurements via the vacuum bag method. The air void content of a given sample fell within the target range of 6.0 ± 0.5 percent. The research team used greased double latex to reduce the friction between the samples and loading platens

and latex sheets to encase specimens for confined tests using an O-ring seal. The team conducted all tests on the AMPT.

Table 18. Summary of various tests performed in this study on RS9.5B mixture.

Deviatoric Stress (kPa/psi)	Temperature (°C)	Pulse-Rest (s)	Number of Replicates	Test Time (h)	Remarks
689/100 (Reference)	Reference	0.4–10	8	8.3	Original TSS
482/70, 689/100, 896/130 (T_H)	T_H	0.4–10	8	8.3	Original TSS
482/70, 689/100, 896/130 (T_I)	T_I	0.4–1.6	8	8.3	Original TSS
482/70, 689/100, 896/130 (T_L)	T_L	0.4–1.6	8	8.3	Original TSS
689/100, 482/70, 896/130 (T_H)	T_H	0.4–10	4	4.1	Reversed block
482/70, 689/100, 896/130 (T_L)	T_L	0.4–1.6	4	4.1	Reversed block
689/100, 482/70, 896/130 (T_H),	T_H	0.4–5	4	2.5	None
482/70, 689/100, 896/130 (T_L)	T_L	0.4–1.6	4	2.5	None
689/100, 482/70, 896/130 (T_H)	T_H	0.4–3	4	1.8	None
482/70, 689/100, 896/130 (T_L)	T_L	0.4–1.6	4	1.8	None
275/40, 896/130 (Random)	T_H and T_I	Pulse: 0.1-1.6 Rest: 10s	4	1.8	Random Loading

0°C = 32°F; 1 kPa = 0.145 psi; 1 psi = 6.89 kPa.

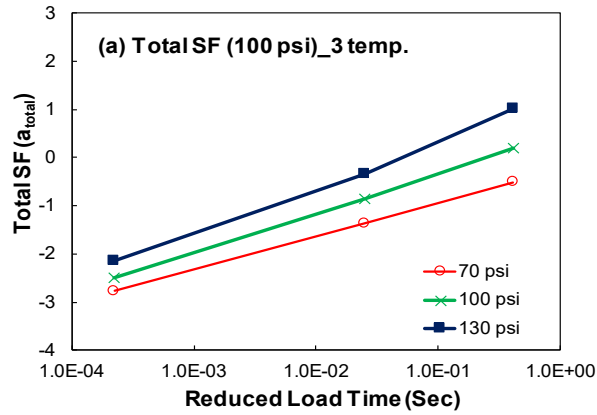
Effects of Test Parameters on the Shift Model

The research team identified temperature, deviatoric stress, and loading time as critical factors to include in the shift model. This section documents the effects of these test parameters on permanent strain.

Temperature

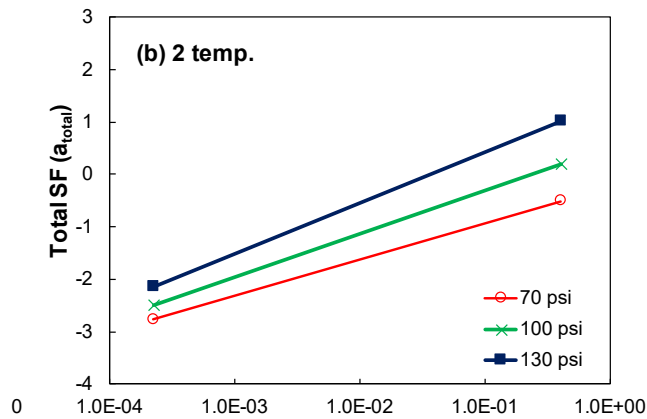
The current TSS test employs the results of three temperatures to define the reduced load time shift factor, as shown in equation 66, which has two variables. The research team determined if they could obtain the reduced load-time shift factor from two test temperatures, they could significantly reduce the testing requirements. The reduced load-time shift factor is a linear logarithmic equation defined based on two data points obtained from two temperatures. The most logical temperature to eliminate is the intermediate temperature because the shift factors from T_H and T_L cover a wider temperature range. The research team found in this investigation that the reduced load-time shift factor and the vertical stress shift factor they obtained from two

temperatures and three temperatures were in good agreement, as shown in Figure 51-C and Figure 51-D. Figure 51-A and Figure 51-B show the total shift factors obtained from three temperatures (T_H , T_I , and T_L) and two temperatures (T_H and T_L), respectively.



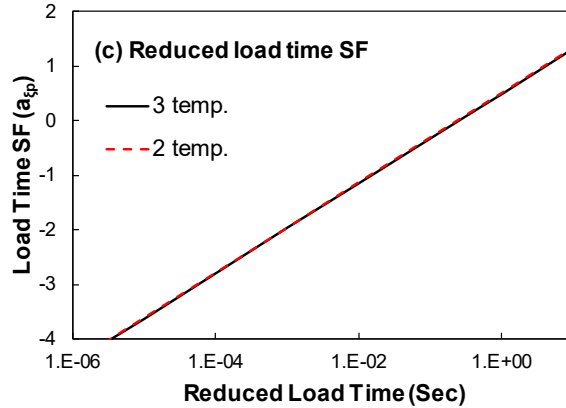
© 2017 Construction and Building Materials. (DTFH61-08-H-00005)
 1 psi = 6.89 kPa.
 SF = shift factor.

A. Effect of three temperatures on total shift factors.



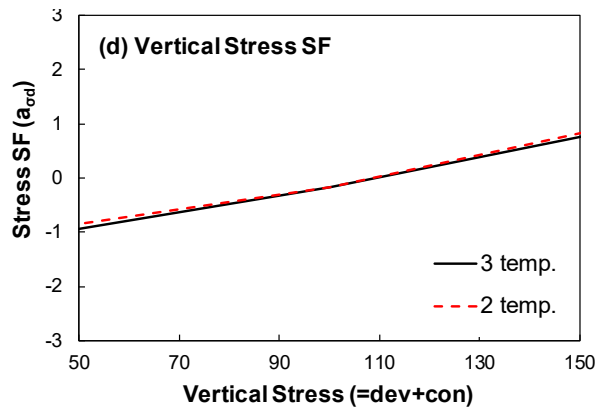
© 2017 Construction and Building Materials. (DTFH61-08-H-00005)
 1 psi = 6.89 kPa.
 SF = shift factor.

B. Effect of two temperatures on total shift factors.



© 2017 Construction and Building Materials. (DTFH61-08-H-00005)
SF = shift factor.

C. Effect of number of temperatures on reduced load time shift factor.

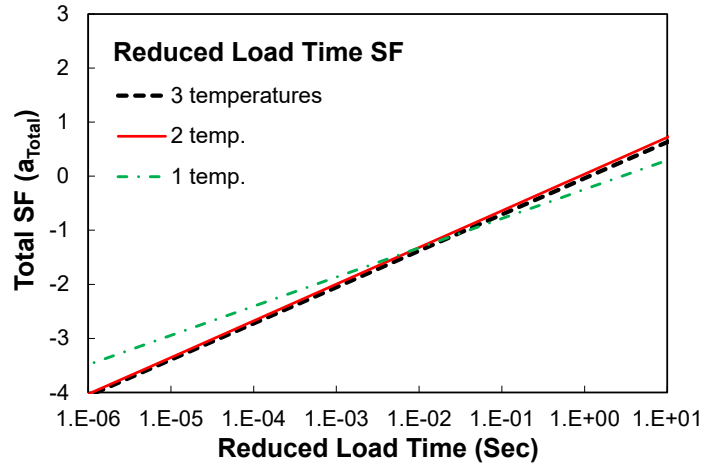


© 2017 Construction and Building Materials. (DTFH61-08-H-00005)
SF = shift factor.

D. Effect of number of temperatures on vertical stress shift factor.

Figure 51. Graphs. Effect of number of temperatures on shift factors.⁽⁹⁷⁾

One step the research team took to simplify the TSS protocol further was eliminating both the intermediate and low temperatures. However, a linear equation cannot be defined using one data point from a single temperature. One method this report presents is applying a fixed reduced load time shift factor; the research team derived this factor from TSS data based on a total of 27 mixtures (i.e., 8 MIT mixtures, 18 NCAT mixtures, and a North Carolina RS9.5B mixture), as shown in figure 52. The reduced load-time shift factor defined by two temperatures is almost identical to the one defined by three temperatures, as the fixed function has a less steep slope and higher y -intercept than the other lines, as compared in figure 52. The shift factor defined by two temperatures can represent the mixture-specific information, whereas the fixed shift factor from a single temperature cannot. Based on this observation, the research team recommends using two temperatures (T_H and T_L) to define the reduced load-time shift factor.



© 2017 Construction2017Construction and Building Materials. (DTFH61-08-H-00005)
SF = shift factor.

Figure 52. Graph. Averaged reduced load time shift factor from PRS database.⁽⁹⁷⁾

Properly selecting test temperatures is another area in which the research team could simplify the testing procedure. The original procedure for selecting the testing temperatures utilizes EICM software by combining the permanent strain obtained from the strain ratio model in the MEPDG.⁽⁷⁵⁾ Accumulating the permanent strain with respect to the pavement temperature obtained from the EICM produces the cumulative density graph for a specific section. However, this method is somewhat complicated and requires extra EICM program runs by users.

Mohseni and Azari proposed a simple procedure for the effective temperature, which is defined as a single testing temperature, to simulate the rutting of asphalt mixtures in the field.⁽⁹⁸⁾ This method employs the degree-days (DD) parameter from LTPPBind. Researchers can use the DD parameter where the materials will be placed to calculate effective temperatures. Mohseni and Azari developed this method based on the loading frequency of 10 Hz, which is equal to the 0.1-s loading time. The loading time is 0.4 s in the SSR test, and therefore the effective temperature Mohseni and Azari proposed needs to be modified using the t -TS principle to make the reduced loading time in the SSR test the same as that of the 0.1-s loading time used in determining Mohseni and Azari's effective temperature. The research team used the data generated in this research to investigate this correction, which resulted in the multiplication factor of 87 percent to Mohseni and Azari's model to reflect the effect of difference in loading times between Mohseni and Azari's test and the TSS test. Equation 73 shows the final form of the model.

$$T_H = 58 + 7 \times DD - 15 \times \log(H + 45) \quad (73)$$

Where:

T_H = high temperature, °C.

DD = degree-days $>10^\circ\text{C}$ ($\times 1,000$) from LTPPBind V 3.1.

H = depth of layer, mm (0 for surface layer).

The research team selected five sections in the United States and Canada to compare the test temperatures obtained from the two different methods, as shown in table 19. The effective temperatures (T_{eff}) gained from the DD parameter were very similar to those obtained from the TSS method for high temperatures (T_H). Thus, the high temperature selection method from Mohseni and Azari's work can be used to facilitate and simplify the TSS temperature selection method.

Equation 74 determines the low testing temperature.

$$T_L = \frac{T_{HPG,98\%} + T_{LPG,50\%}}{2} + 4 \quad (74)$$

Where:

T_L = low temperature, °C.

$T_{HPG,98\%}$ = high climatic PG temperature based on 98-percent reliability, °C.

$T_{LPG,50\%}$ = low climatic PG temperature based on 50-percent reliability, °C.

Equation 75 calculates the testing temperature if intermediate testing is needed.

$$T_I = \left(\frac{T_H + T_L}{2} \right) + 3 \quad (75)$$

Table 19. Comparison of testing temperature selection methods.

State	City	Teff TH	TSS TH	TSS TI	TSS TL	TSS TH_Test	SSR TH	SSR TL
NY	Angelica	49	47	35	15	47	43	18
AL	Auburn	60	61	45	19	54	52	30
AZ	Phoenix	69	64	49	31	54	60	38
NC	Raleigh	58	55	40	23	54	50	29
MB	Manitoba	47	48	36	19	48	41	16

Deviatoric Stress

To reduce the testing requirements, the research team investigated the deviatoric stress shift factor. The deviatoric stress shift factor needs at least two different stress levels to be defined. The total testing time can be shortened by eliminating the intermediate stress level. However, the extra effort for running three different stress levels is fairly small due to the fact that it only requires adding one loading block during the test procedure. Because the samples are already prepared and the temperature conditioned, the extra time required is only what is needed to run the test during that loading block. Considering all these factors together, the research team found the three deviatoric stress levels selected for the TSS test protocol to be reasonable. As such, the team recommends that the SSR test use three deviatoric stress levels for further tests.

Load Time

The shift model uses reduced load time, which is a function of physical load time and temperature, by applying the t-TS principle. The research team used an equivalent 80-kN single-axle load with a single tire to determine a reasonable load time for a real pavement. They selected 2.6-m spacing between the two single tires. The tire contact area depends on the contact pressure, which the team calculated as 0.0522 m² for a single tire based on a tire pressure of 758 kPa. The research team converted the contact area to an equivalent rectangular area 0.29-m long and 0.18-m wide. Another important factor that affects load time is vehicle speed, which is directly related to the load duration on the pavement. A lower speed will lead to a longer loading duration than a higher speed and thus produce a greater rut depth in the pavement surface. To suggest a reasonable pulse time for the SSR test, the research team converted the same reduced load time at various temperatures to different physical times by applying t-T shift factors, as shown in table 20. The team utilized the averaged PRS mixture shift factor function in this study, as shown in equation 76. This equation is for the reference temperature of 54°C.

$$\log(a_T)_{avg,mixture} = 0.00064T^2 - 0.1564T + 5.2315 \quad (76)$$

An example of this operation is as follows:

The physical load time is 0.01 s when a vehicle with a 0.29-m contact length with a speed of 30 m/s passes a specific point. If the pavement under consideration is 65°C, a t-T shift will be needed to correct the load time used in the SSR test. Using equation 76, the research team determined that 0.08 is the physical pulse time at 54°C that produces the same reduced pulse time of the 0.01-s pulse at 65°C. As such, the 0.01 pulse time at 65°C is equivalent to the 0.08 pulse at 54°C. The team conducted the same protocol using 46°C. They found that the pulse time for this temperature was 0.4 s. Note that some test equipment cannot properly simulate the load at less than 0.1 s.⁽⁹⁹⁾ Additionally, 0.4 s can generate sufficiently large permanent deformation within a practical testing time. Therefore, the research team selected the 0.4-s pulse time for further SSR testing. Table 20 shows the equivalent pulse times at different temperatures.

Table 20. Pulse time at different temperatures.

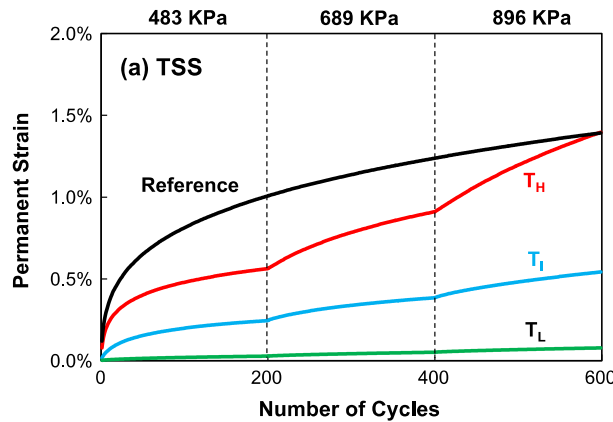
Temperature (°C)	Pulse Time (s)
65	0.01
54	0.08
46	0.4

0°C = 32°F.

Reference Curve

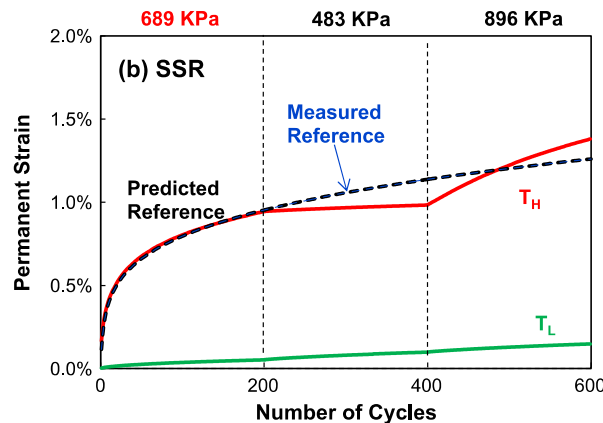
The reference test is one type of the Repeated Loading Permanent Deformation test, which applies a repeated load at a constant frequency (load time) to a test specimen for many repetitions and measures the specimen's permanent deformation. The shift model requires a reference test to characterize the representative strain development curve, referred to as the permanent strain master curve, as discussed earlier in the Permanent Deformation Model section. To eliminate the reference test, Kim focused on methods for predicting a strain master curve

from the first block of the TSS test obtained under 482 kPa (70 psi), because the current TSS test employs increasing stress blocks with 482, 689, and 896 kPa (70, 100, and 130 psi), and only the first block has information from both the primary and secondary regions.⁽¹⁰⁰⁾ Kim's work shows the importance of obtaining a strain master curve under 100 psi.⁽¹⁰⁰⁾ Therefore, the research team introduced a reversed block protocol (689, 482, 896 kPa or 100, 70, 130 psi) in this study. The reversed block idea originated from the possibility of using the strain levels of the first block as the reference curve instead of conducting separate reference tests or predicting the reference curve by other means if the stress level of the first block is 689 kPa (100 psi). To verify the possibility of this proposal, the research team used the reversed block protocol on the RS9.5 mixture. Figure 53-A and figure 53-B compare the details of the TSS and SSR test protocols, respectively.



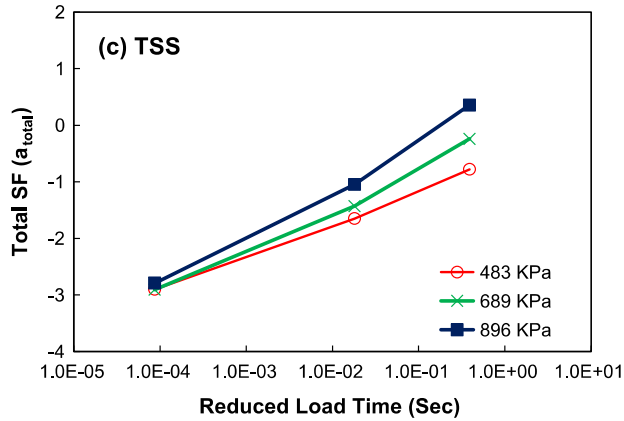
© 2017 Construction and Building Materials. (DTFH61-08-H-00005)
1 psi = 6.89 kPa.

A. Test protocol in TSS test.



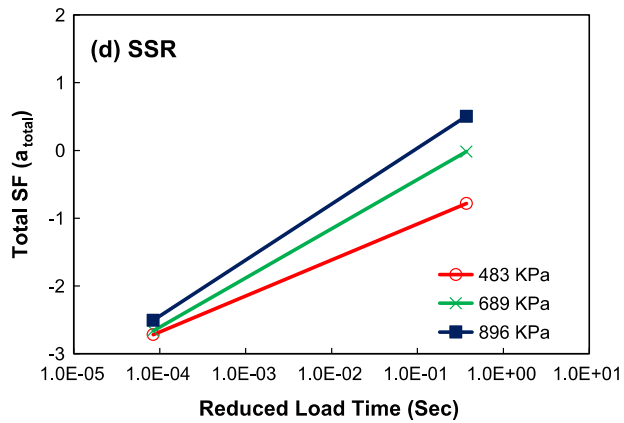
© 2017 Construction and Building Materials. (DTFH61-08-H-00005)
1 psi = 6.89 kPa.

B. Test protocol in SSR test.



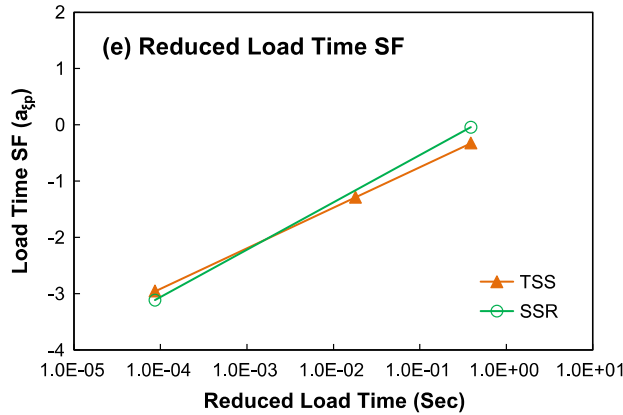
© 2017 Construction and Building Materials. (DTFH61-08-H-00005)
 1 kPa = 0.145 psi.
 SF = shift factor.

C. Total shift factors for TSS test.



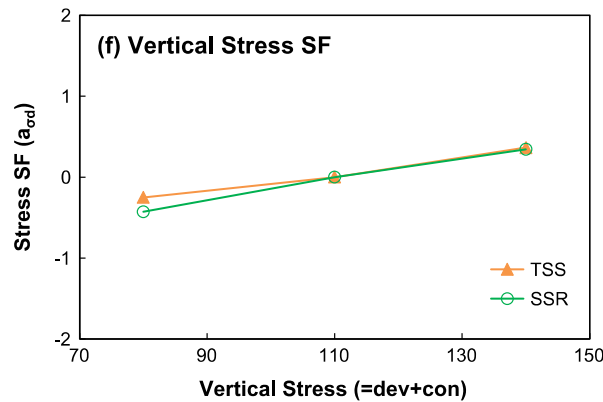
© 2017 Construction and Building Materials. (DTFH61-08-H-00005)
 1 kPa = 0.145 psi.

D. Total shift factors for SSR test.



© 2017 Construction and Building Materials. (DTFH61-08-H-00005)
SF = shift factor.

E. Reduced load time shift factor.



© 2017 Construction and Building Materials. (DTFH61-08-H-00005)
SF = shift factor.

F. Vertical stress shift factor (RS9.5B mixture).

Figure 53. Graphs. Comparison of calibration processes for TSS and SSR protocols.⁽⁹⁷⁾

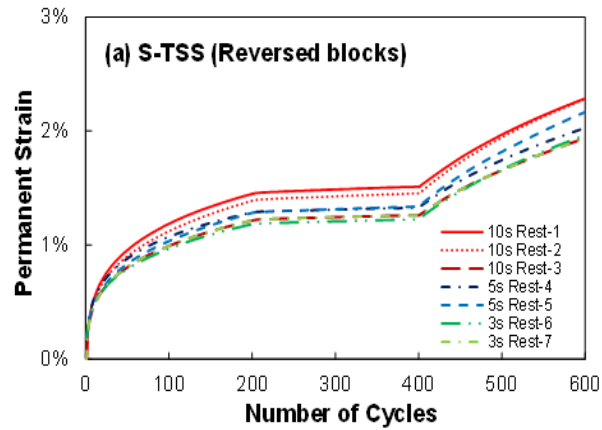
The TSS test requires four different tests (reference, T_H , T_L , and T_L) with increasing loading blocks of 482, 689, and 896 kPa (70, 100, and 130 psi), detailed in figure 53-A. The SSR test requires only two tests (T_H and T_L); the high temperature (T_H) employs the reversed loading blocks of 689, 482, and 896 kPa (100, 70, and 130 psi); and the low temperature (T_L) uses increasing loading blocks of 482, 689, and 896 kPa (70, 100, and 130 psi). The reference curve for the SSR test comes from the first block of the high temperature results (T_H), detailed in figure 53-B. The original reference curve applies to TSS test runs up to 600 cycles, as shown in figure 53, but the first block of the SSR test stops at 200 cycles. Therefore, the research team extrapolated the remaining cycles, from 200 to 600, from the incremental model obtained from the first block of the SSR test, which is shown in figure 53-B as a separate line. The reference curves from the TSS and SSR tests are in good agreement, as shown in figure 53. The main advantage of this approach is that the first block of the SSR test can be used as a reference curve without any correction, which significantly reduces the testing time and the required number of

specimens. Figure 53-C through figure 53-F detail the calibration procedure of the shift model using the TSS and SSR tests. The research team horizontally shifted the strains at the end of each block to match the equal strains on the reference curve. They used these shifts for each block to produce the total shift factors, as shown in figure 53-C and figure 53-D, and divided the total shift factors into the reduced load-time shift factors shown in figure 53-E and the vertical stress shift factors shown in figure 53-F, respectively. Overall, the reduced load-time shift factors and the vertical stress shift factors from the two different test methods are similar. The reduced load-time shift factors from the SSR test tend to be higher than those obtained from the TSS test at the high reduced load time, but these factors become very similar at the low reduced load time. The research team calculated the vertical stress shift factors by subtracting the reduced load-time shift factor from the total shift factors. The vertical stress shift factors from the SSR test are exactly the same at high vertical stress levels and tend to be lower at low vertical stress levels.

Rest Period

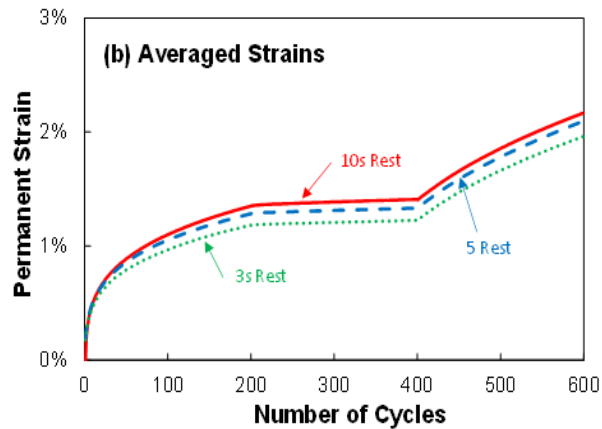
The rest period is directly related to the total testing time, and thus, should be considered for reducing the original TSS test's testing demand. The TSS test utilizes a 10-s rest period for the high temperature. This long rest period makes the testing time impractical for users, given that 0.9 s is the general flow number test. Therefore, the research team used the reversed loading block with shorter rest periods (10, 5, and 3 s) for the high temperature specimens to determine the effect of the rest period on the permanent strain development. For the low temperature, the team employed the 1.6-s rest period used in the TSS test protocol for further SSR testing. Figure 54 shows that the permanent strain levels of the three different rest periods are close to each other and their difference is minimal. This difference is smaller than the variability between the samples. This result suggests the possibility of using a rest period shorter than 10 s to reduce the overall testing time. Because the measured permanent strains are similar, as shown in figure 54-B, the research team selected the shortest possible rest period using proper verification procedures: a random loading history comparison and rut depth predictions in the structural model using FlexPAVE, as discussed in the following paragraph.

Figure 54 describes the detailed calibration procedure of the shift model using the SSR test protocol. Table 21 presents the individual shift model coefficients from different rest periods. Overall, the slope of the permanent strain master curve ($1 - \beta$) is consistent, but slightly decreases as the rest period decreases.



© 2017 Construction and Building Materials. (DTFH61-08-H-00005)

A. Individual samples showing permanent strain with reversed loading blocks.



© 2017 Construction and Building Materials. (DTFH61-08-H-00005)

B. Averaged samples showing permanent strain with reversed loading blocks.

Figure 54. Graphs. Effect of rest periods on permanent strains with reversed loading blocks.⁽⁹⁷⁾

Table 21. Coefficients for shift model.

Test	Deviatoric Stress (kPa/psi)	Pulse-Rest (s)	Reference Curve β	Reference Curve ϵ_0	Reference Curve NI	Load Time SF p1	Load Time SF p2	Vertical Stress SF d1	Vertical Stress SF d2
TSS	S1	0.4–10	0.700	0.003	2.159	0.719	-0.036	2.499	-2.119
SSR	S2	0.4–10	0.697	0.003	1.203	0.824	0.290	3.073	-2.674
SSR	S2	0.4–5	0.710	0.003	1.248	0.816	0.291	3.340	-2.903
SSR	S2	0.4–3	0.712	0.003	1.285	0.803	0.288	3.473	-3.016

1 kPa = 0.145 psi; 1 psi = 6.89 kPa.

SF: shift factor

S1 = 482, 689, 896 kPa/70, 100, 130 psi; S2 = 689, 482, 896 kPa/100, 70, 130 psi (T_H); 482, 689, 896 kPa/70, 100, 130 psi (T_L).

Note: d_1 and d_2 were obtained from equation 67.

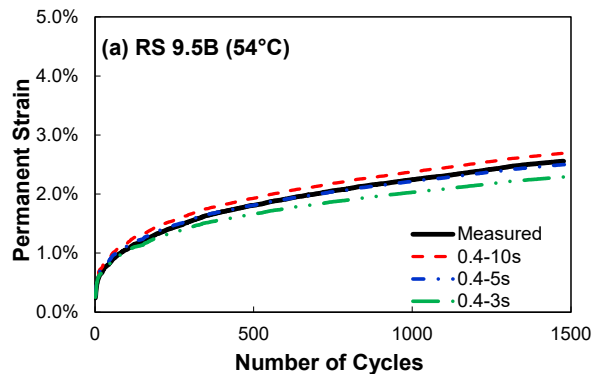
Verification of Shift Model Calibrated by SSR

To verify the SSR test with the reversed loading block, the research team conducted a test with a random loading history. A good prediction of the random loading history using the shift model calibrated by the SSR test would verify the test protocol and the calibration procedure.

Random Loading History

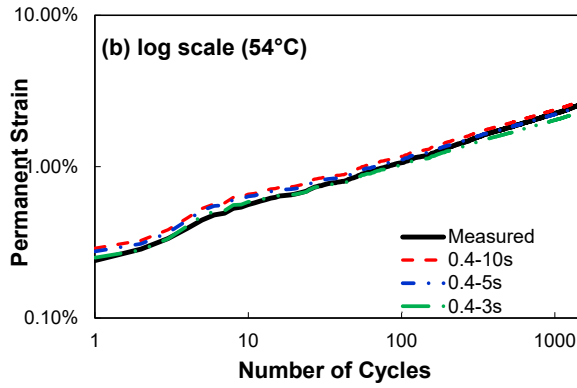
The random loading history changes the stress levels and load time, which simulates the actual field conditions of various traffic loading by changing the load times and deviatoric stress levels. The research team performed the random load test for the 9.5B mixture at a high temperature (54°C) and an intermediate temperature (40°C) at which the asphalt mixture significantly deforms. The load-time distribution is from 0.1 to 1.6 s, and the deviatoric stress levels range from 70 to 130 psi with a 5-s rest period. The research team selected the loading history randomly, using the “RAND” function in MATLAB®.⁽¹²⁰⁾ (2018; <https://www.mathworks.com/products/matlab.html>)

Overall, the predicted strains from the different rest periods show good correlations with the measured permanent strains, as shown in figure 55. At 54°C, the best agreement was found between the experimental strain and predicted strain using the 5-s rest period, as shown in figure 55-A and figure 55-B. Additionally, at 40°C, the prediction with the 5-s rest period showed better results than the others, as shown in figure 55-A and figure 55-B.



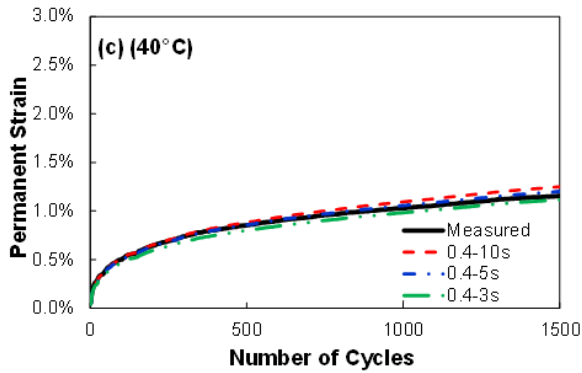
© 2017 Construction and Building Materials. (DTFH61-08-H-00005)
0°C = 32°F.

A. Comparison between measurements and predictions on random loading history with various rest periods at 54°C in arithmetic scale.



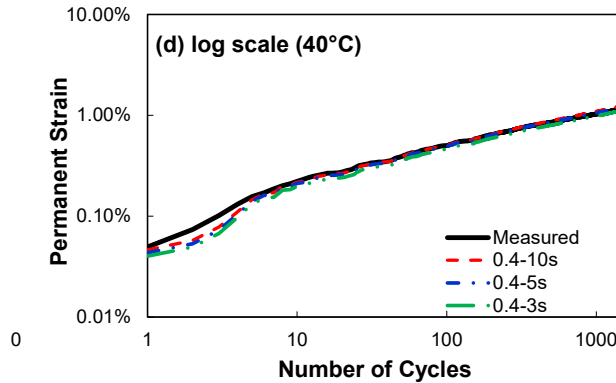
© 2017 Construction and Building Materials. (DTFH61-08-H-00005)
 0°C = 32°F.

B. Comparison between measurements and predictions on random loading history with various rest periods at 54°C in semi-log scale.



© 2017 Construction and Building Materials. (DTFH61-08-H-00005)
 0°C = 32°F.

C. Comparison between measurements and predictions on random loading history with various rest periods at 40°C in arithmetic scale.



© 2017 Construction and Building Materials. (DTFH61-08-H-00005)
 0°C = 32°F.

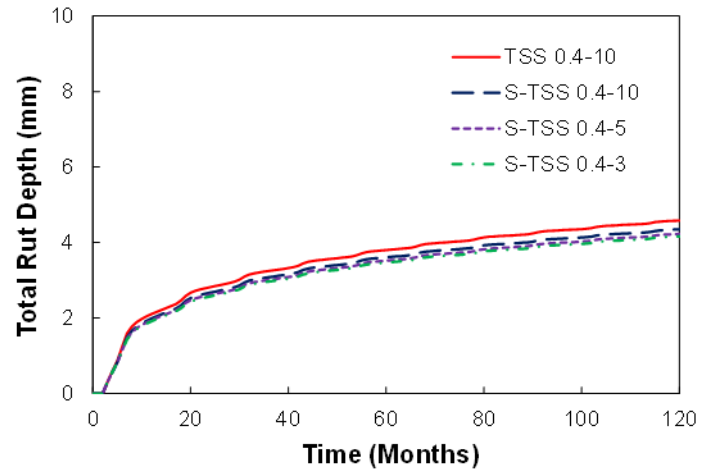
D. Comparison between measurements and predictions on random loading history with various rest periods at 40°C in semi-log scale.

Figure 55. Graphs. Random loading history predictions with various rest periods for RS9.5B.⁽⁹⁷⁾

Prediction Using FlexPAVE

The purpose of this study is to develop a simple test method that predicts reasonable asphalt pavement compared with those predicted by the original TSS test. To select and verify the best SSR test method, the rut depths predicted by the original TSS test and the SSR test with different rest period options should be compared. First, the research team used different methods to predict the reference curve of materials and calibrate the shift model. They then put all rutting parameters from each method into the FlexPAVE program to calculate the rut depths of asphalt pavements. The program calculated the linear viscoelastic pavement responses under moving loads using fast Fourier transforms (FFTs). The team then used pavement responses in the shift model to predict rutting performance. The inputs required for the FlexPAVE simulations are design time, structural layout, traffic, and climate. The research team assumed the design period for this study to be 10 yr. The structural layout for the simulations was a 10-cm asphalt layer on top of an aggregate base and subgrade layer, with the team assuming a single tire with standard loading of 80 kN at the center of the pavement and an average annual daily truck traffic of 700.

Figure 56 shows the comparison of the predicted rut depths from the original TSS test and the SSR test with different rest periods. In this figure, the SSR uses two tests with reversed blocks at the high temperature and the TSS employs four tests with increasing loading blocks. The predicted rut depths from the different rest periods of the SSR test are almost identical to each other. The research team observed slightly lower permanent strains from all of the SSR tests than the strains predicted by the original TSS method, as shown in figure 56. However, the differences between the rut depth predictions are less than 5 percent after 10 yr of simulation, which is not significant given that the SSR test requires about half the time and number of replicates compared with the TSS test requirements. Using a 3-s rest or 5-s rest makes almost no difference in the predicted rut depths. The research team selected the 3.6-s rest period because it makes one cycle of a pulse and rest period 4.0 s in the SSR test.



© 2017 Construction and Building Materials. (DTFH61-08-H-00005)
1 mm = 0.04 inch.

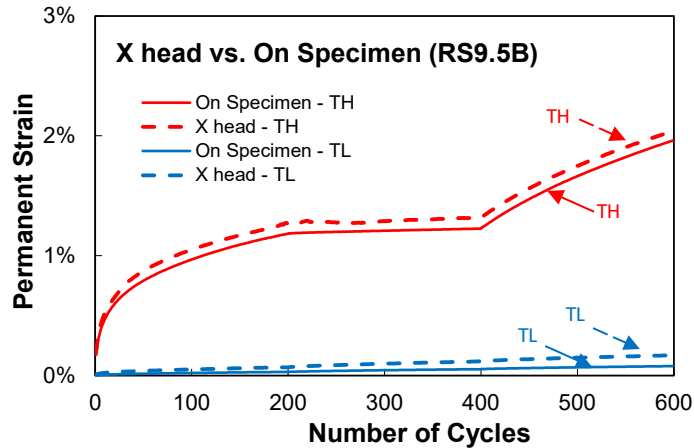
Figure 56. Graph. Effect of rest period in the rut depth prediction from the SSR test.⁽⁹⁷⁾

Use of Actuator Displacement

The research team obtained all strain measurements in the TSS and SSR test data presented in this report from four LVDTs equally spaced around the circumference of the specimen. However, installing loose-core LVDTs is time-consuming when positioning the test specimen and is generally not practical for routine testing. Therefore, one of the research team's ideas for reducing test requirements was to use actuator displacement instead of on-specimen LVDTs. This method resulted in a substantially simpler test setup and similar precision compared with the specimen-mounted system.⁽⁷⁴⁾

This study compared the permanent strains based on the actuator displacement with those based on loose-core LVDTs and the research team then used each of those strain levels to calibrate the shift model to evaluate the rut depth prediction using the FlexPAVE structural model. They then converted the actuator displacement to strain by dividing the displacement by the specimen length of 150 mm. The team converted the data from the specimen-mounted LVDTs to strain by dividing by the gauge length of 70 mm. Figure 57 shows a plot indicating the permanent strains from the actuator displacement (CX) to be generally greater than those from LVDTs (with a 70-mm gauge length).

The difference between the permanent strains from the loose-core LVDTs and the actuator displacement was caused by the compliance of the system (machine). At a relatively high temperature, the modulus value of an asphalt mixture is low and much softer than that of the equipment; therefore, the deformation due to machine compliance is negligible. However, at a low temperature, the modulus value of the asphalt sample is high and very close to that of the equipment; as a result, the deformation due to machine compliance is no longer negligible. If the system compliance of the test machine can be reliably and accurately characterized, then the actual deformation in the sample can be easily computed by subtracting the system's displacement in the testing equipment from the total displacement experienced by the actuator.



© 2017 Construction and Building Materials. (DTFH61-08-H-00005)

Figure 57. Graph. Comparison of RS9.5B mixture permanent strains based on actuator displacement and loose-core LVDTs.⁽⁹⁷⁾

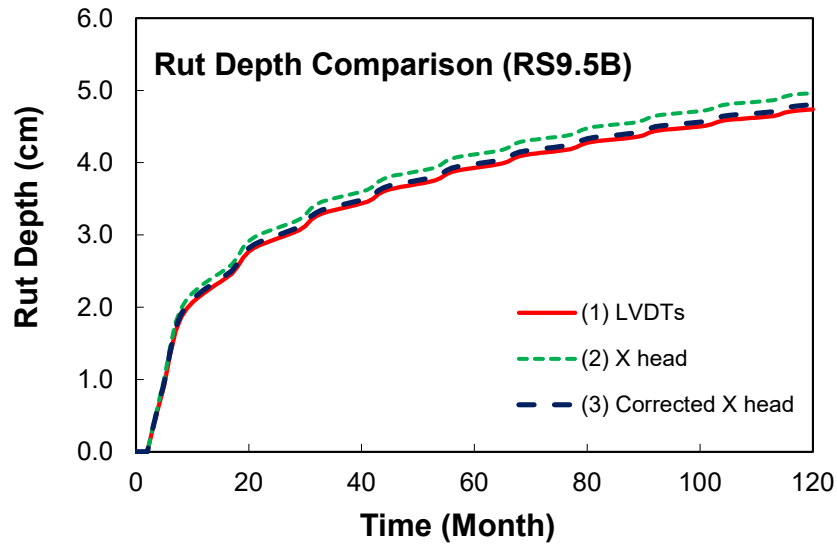
The research team employed one method, which uses an aluminum specimen, to account for the effect of system compliance. The actual deformation in the specimen can be computed by subtracting the machine's displacement in the testing equipment (including the membrane's displacement) from the total displacement experienced by the actuator. The detailed steps are as follows:

- Run the SSR test using the asphalt specimen at the desired temperatures (T_L and T_H) and calculate the strains based on the actuator displacement ($\epsilon_{actuator}$).
- Prepare a 100-mm (4-in) diameter by 150-mm (6-in)-high aluminum specimen with the same end treatment (greased double latex) as the asphalt specimen.
- Run the SSR test using the aluminum specimen at the test temperatures (T_L and T_H) and calculate the strains based on the actuator displacement ($\epsilon_{actuator}$).
- Subtract the machine's strain ($\epsilon_{machine}$) from the actuator's strain ($\epsilon_{actuator}$) to calculate the strains on the specimen ($\epsilon_{on-specimen}$).

Tests using an aluminum specimen should be conducted at exact testing temperatures (T_H and T_L for the SSR test method) with the same end treatment. This procedure allows for isolating the displacement of the sample from the actuator displacement by removing the effect of machine compliance.

The research team verified the procedure by comparing the rut depth predictions from FlexPAVE, as given in figure 58. In this figure, the predicted rut depths from the corrected actuator displacement show rut depths almost identical to those from the on-specimen LVDTs. The research team believes that if the system compliance of the testing fixture can be reliably and accurately characterized, the predicted rut depths of the pavement structure would be similar to those predicted by LVDTs. In general, the predicted rut depths from the actuator displacement are slightly higher than those from the on-specimen LVDTs. This outcome is because the

relatively high machine compliance at a low temperature causes the high total shift factors at the low reduced frequency, which results in the high rut depth predictions in the analysis. However, the difference between the rut depths from two measurements is less than 3 percent, which is negligible. Therefore, the permanent strains from the actuator displacement can be used without any correction for practical purposes.



© 2017 Construction and Building Materials. (DTFH61-08-H-00005)
1 cm = 0.4 inch.

Figure 58. Graph. Rut depth prediction of RS9.5B using FlexPAVE based on loose-core LVDTs, actuator displacement, and corrected strains.⁽⁹⁷⁾

Comparison Among SSR, TSS, and Flow Number Tests

Table 22 compared the details of the permanent deformation test protocols (SSR, TSS, and flow number). The proposed SSR test requires 6 h of conditioning and testing time and four specimens for a single mixture, which is about 40 percent of the TSS test requirements but 50 percent more than the flow number test requirements. The SSR testing for a single mixture, including temperature conditioning and pressurizing, can be completed within a day, which is not significant if the advantages of the SSR test method are considered. Specifically, the SSR test protocol can be used to predict the rut depths of pavements, whereas the flow number test can only rank materials. The proposed SSR test protocol requires a shorter testing time and fewer specimens than the TSS test without losing accuracy in predicting rut depths in pavements.

Table 22. Comparison of permanent deformation testing methods.

Test Method	SSR	TSS	Flow Number
Strain measure	Machine displacement	On-specimen LVDTs	Machine displacement
Number of reference tests	None	1 (T_H)	1 (T_H)
Number of TSS tests	2 (T_H and T_L)	3 (T_H , T_I , and T_L)	1 (T_H)
Total samples	4	8	3
Total testing time including conditioning time (h)	6	16	4
Pulse time (s)	0.4	0.4	0.1
Rest period (s)	3.6 (T_H) and 1.6 (T_L)	10 (T_H) and 1.6 (T_I and T_L)	0.9
Deviatoric stress (kPa/psi)	689/100, 482/70, and 896/130 (T_H) 482/70, 689/100, and 896/130 (T_L)	482/70, 689/100, and 896/130	482/70
Number of cycles	200	200	1,000

1 kPa = 0.145 psi; 1 psi = 6.89 kPa.

Summary

The TSS test is a test protocol for calibrating a permanent deformation model (the shift model). The TSS test is advantageous over other existing models because it simulates the effect of temperature, load time, and deviatoric stress. However, the TSS test protocol requires eight specimens and 2 d of testing for a single mixture, which is significant for agencies and contractors. Therefore, the research team proposes the SSR test in this document, as this protocol reduces the testing time and number of specimens. The research team explored the effect of each parameter, which includes temperature, deviatoric stress, and load time; these parameters in turn affect the shift model coefficients and testing requirements. The team investigated each parameter to reduce the test requirements of the TSS test and predict relatively accurate permanent deformations. They recommend two temperatures (T_H and T_L) for the SSR test, eliminating the intermediate temperature used in the TSS test and specifying a simpler temperature selection method. The SSR test recommends a 0.4-s pulse time and a 3.6-s rest period with the reversed loading block of 689, 482, and 896 kPa (100, 70, and 130 psi) to employ the first block as a reference curve using machine displacement to calibrate the shift model.

In conclusion, the research conducted in this study found that the proposed SSR test requires a shorter testing time with fewer replicates than the TSS test but still produces accurate permanent deformation.

HEALING MODEL

In this project, the research team investigated how S-VECD theory applies to loading histories with rest periods and developed a healing model that accounts for the effects of temperature, rest period, and the damage state on the healing potential of a mixture. The characteristic test protocol also needed to be efficient enough for State highway agencies to adopt the healing model in their specifications and design methods. This section documents the research efforts for developing the healing model and associated test protocol.⁽¹⁰¹⁾

Introduction

One of the main distresses in asphalt pavements is fatigue cracking. This type of distress occurs due to the repeated loading of traffic. Small cracks (i.e., microcracks) begin to appear shortly after traffic loading begins. These microcracks densify and coalesce after many cycles to form larger cracks (i.e., macrocracks). A deep and thorough understanding of asphalt concrete constitutive behavior under realistic traffic loading conditions is critical for comprehending the processes of crack initiation and crack propagation.

Furthermore, for asphalt concrete modeling, a true constitutive relationship must reflect the viscoelasticity of the matrix—the fatigue damage growth and subsequent healing that occurs during rest periods between the applications of load cycles. Since healing does occur in asphalt mixtures and binders, existing microcracks in the body of a pavement that were caused from the previous load cycle can be “cured,” and the mixture can partially or completely regain its strength. There are several different expressions and definitions for healing in the literature; the terminology includes reversal of microdamage or microcracks, increase in the stiffness and integrity of the material, and increase in the fatigue life. Healing the microdamage of an asphalt

mixture is a function of several factors, such as temperature, rest period, the physical and chemical properties of the binder, properties of the mixture itself, the amount of damage that occurred prior to the rest period, the number of rest period applications, aging, and pressure.

In S-VECD theory, the pseudostiffness (C) of the material represents the overall integrity of the mixture, and an ISV (S) represents the overall damage within a specimen. The relationship between C and S is unique for a given mixture regardless of loading rate, stress–strain amplitude, and temperature. Because the S-VECD model can be used to characterize fatigue damage in asphalt mixtures and healing is defined as the partial or complete reversal of induced damage due to previous loading, the S-VECD model can be adapted to model microcrack healing. As such, the ISV value will decrease and the pseudostiffness of the material will increase when a rest period is applied to the material.

The primary objectives of the healing model research were to:

- Develop a procedure to quantify the healing potential of asphalt mixtures based on reducing the damage parameter, S , or possibly stiffness recovery during the rest period by applying S-VECD theory.
- Present a functional form that relates the healing potential of a mixture to rest period, temperature, and pseudostiffness.
- Suggest a simple test method that can be completed within a reasonable time to calibrate the proposed healing model.

Testing Program

This section documents the materials and the protocols the research team used to develop the healing model.

Materials

The first mixture the research team used in the healing study was a prepared RS9.5B loose mixture with an NMAS of 9.5 mm and that contained 30-percent RAP material. The binder grade of the mixture was PG 64-22. The team compacted all specimens using a Superpave gyratory compactor to a height of 178 mm and a diameter of 150 mm. To obtain specimens of uniform quality, the research team cored and cut the fabricated samples to a diameter of 75 mm and a height of 150 mm for testing. They took air void measurements using the vacuum sealing method, and stored the specimens in sealed bags until testing to avoid aging the material. The target air void content was 4.0 percent, and the air void contents for all the samples in this healing study were between 3.5 and 4.5 percent. The research team tested all specimens within 2 w after fabrication to maintain consistency among the test conditions.

Test Conditions

The primary factors that can affect the healing behavior of asphalt materials are temperature, rest period duration, and damage status. The research team designed tests for studying the effect of

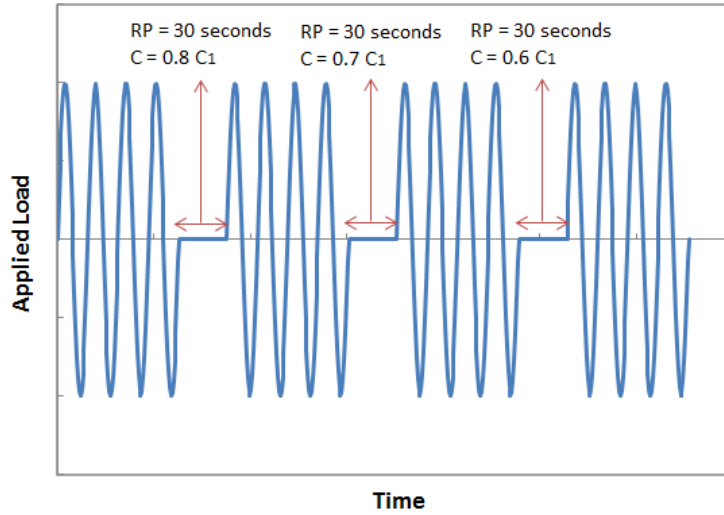
these factors by modifying the original cyclic fatigue test conditions that support the S-VECD model because the healing model aims to link to that model.

The test conditions comprised four different rest period durations and three temperatures with a 0.1-s haversine-shaped pulse. The rest period durations were 10, 30, 90, and 270 s, and the temperatures were 10, 20, and 30°C. According to Prowell et al., for a pavement design life of 40 yr and a total of 20 million ESAL applications, the average rest period between load applications for actual pavements is about 60 s (i.e., 40 yr divided by 20 million ESAL).⁽¹⁰²⁾ The research team decided to use four different rest periods, two of which were less than 60 s (10 and 30 s) and two of which were more than 60 s (90 and 270 s).

Depending on the different ways that rest periods are applied during a test, the following types of healing tests can be considered and conducted:

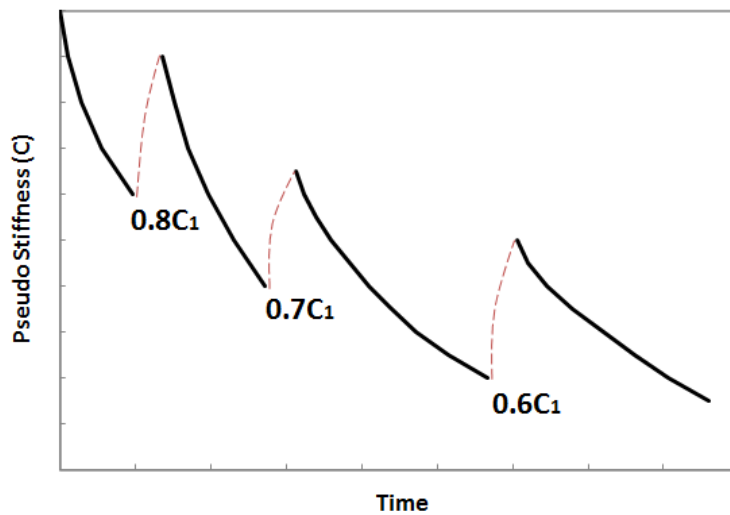
- **Group-rest healing (interrupted loading).** This test is a “short” healing test in which the rest periods are applied in the middle of continuous fatigue testing at predefined cycles. Different lengths of rest periods are inserted at different pseudostiffnesses to determine a modulus or energy recovery value as a function of rest period and pseudostiffness.
- **Pulse-rest healing (intermittent loading).** This test is a “long” healing test in which a single rest period is applied after each load cycle. This healing test reflects a more realistic traffic loading history than the shorter healing test because there is a rest period between the load applications of the successive axles of passing vehicles for actual pavements.

Figure 59 shows a schematic of a group-rest healing test that can be used to evaluate the functional form of healing. As the figure indicates, rest periods interrupted the stress-controlled, tension-compression cyclic test at different levels of reduction in specimen stiffness. This type of test makes it possible to monitor healing potential change with respect to the pseudostiffness as well as capture the effects of temperature and rest period on the healing potential because the tests are conducted at different temperatures and rest periods. Finally, by combining the results of these tests at different temperatures and rest periods applied at various pseudostiffnesses of tested specimens, a healing model can be developed as a function of rest period, temperature, and pseudostiffness.



Source: FHWA.

A. Loading pattern with 30-s rest period.



Source: FHWA.

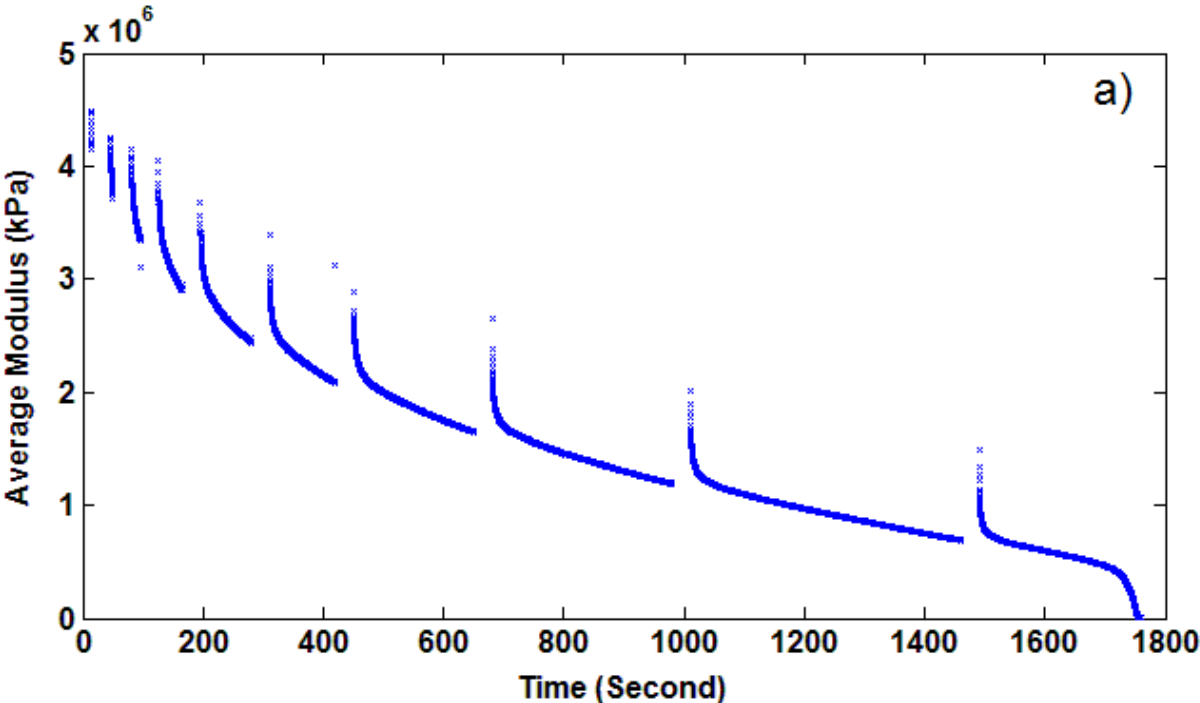
B. Response of pseudostiffness under loads with 30-s rest period.

Figure 59. Graphs. Typical group-rest healing test with 30-s rest period.

Characteristics of Healing

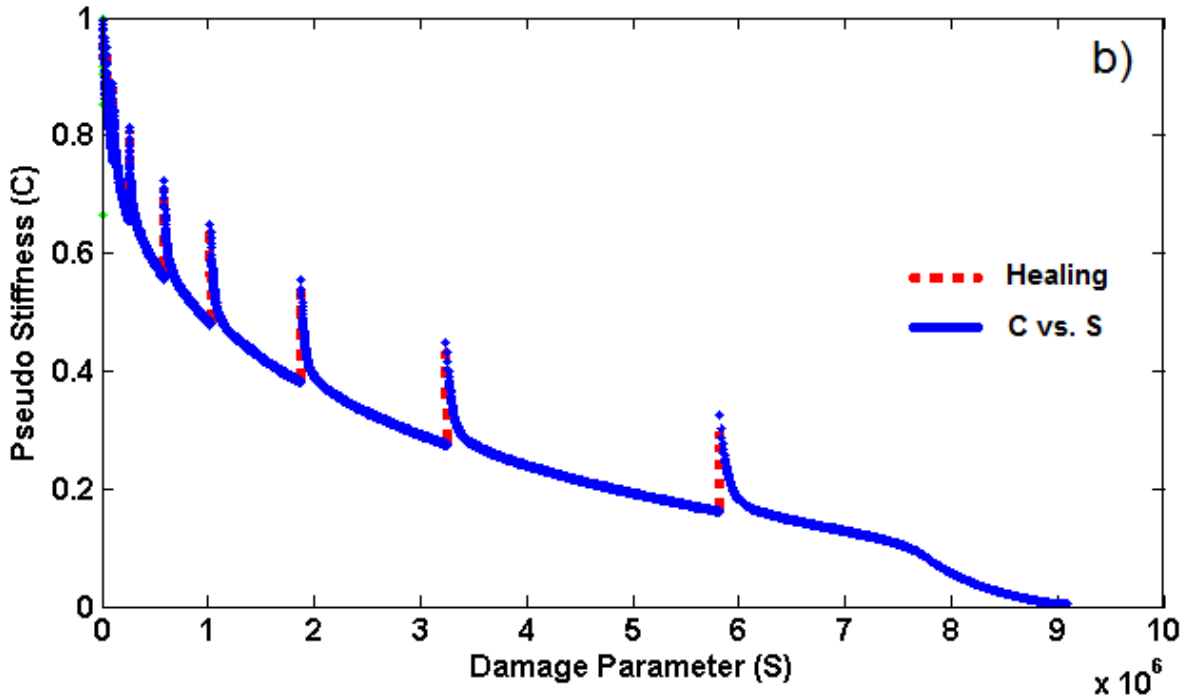
During each healing period, the material partially regains its strength. Figure 60 shows an example of a group-rest healing test at 30°C with 30 s of rest. There is an increase in the modulus value of the specimen after each rest period, as the research team expected. Comparing the original damage characteristic curve and the damage characteristic curve after each rest period shows the damage growth is faster after each rest period until the pseudostiffness become similar to the pseudostiffness before the rest period. This fast damage phenomenon implies that the increase in modulus value due to the crack closure during the rest period does not guarantee the material has regained its strength and that some fraction of the modulus recovery comes from the

weak joints between the crack faces during the resting time. Some of the microcracks in the tested specimen only partially during the rest period, and these weak bonds reopen faster during reloading, which results in the faster rate of damage growth.



Source: FHWA.
1 kPa = 0.145 psi.

A. Modulus changes in group-rest healing tests.



Source: FHWA.

B. Pseudostiffness changes in group-rest healing test.

Figure 60. Graphs. Results of group-rest healing test at 30°C with 30-s rest period.

Percent Healing Definition

Healing is affected by the duration of the rest period, the level of damage before the rest period, and temperature. Quantitative variables that can define the level of healing are essential for developing a healing model. Healing is defined as a reverse change in damage, and damage is defined as the change in modulus. Therefore, the stiffness ratio of the current modulus value to the initial modulus value can be applied to express damage, as illustrated in equation 77. The stiffness of the intact material before running the test is measured by the fingerprint test, a dynamic modulus test that uses 10 Hz at the target test temperature. As the number of cycles in the fatigue test increases, the damage increases and the modulus value of the specimen decreases; accordingly, the normalized pseudostiffness also decreases. The pseudostiffness starts from unity and then decreases until the specimen fails.

$$C = \frac{E}{E_0} \tag{77}$$

Where:

C = pseudostiffness before applying rest period.

E = modulus of specimen before applying rest period.

E_0 = initial modulus of intact specimen (from the fingerprint test).

During the rest period, the damaged specimen heals, and thus, the modulus value increases. During reloading, the modulus value rapidly decreases to the pseudostiffness before the rest period, and the specimen tends to become damaged as usual, similar to the continuous cyclic testing case. The incremental number of cycles during reloading (until the specimen reaches the same pseudostiffness as before the rest period) has a direct effect on the incremental increase of the fatigue life, as shown in figure 61-A. As the rest period is applied for a longer duration and/or the number of rest periods increases, the fatigue life also becomes longer due to the incremental number of cycles (ΔN).

However, because the relationship between C and S expresses the damage characteristic curve, it would be convenient for modeling if healing was also by C and S . Therefore, the research team introduced the percentage of the amount of healing (figure 61-B), or percent healing (defined by equation 78). After applying each rest period, the damage characteristic curve shifts to the right and the amount of the horizontal shift (ΔS) of the damage characteristic curve is due to the healing caused by applying the rest period. The material can last longer before the failure, as much as that of the horizontal shift, which is equivalent to the incremental number of cycles, ΔN . Eventually, applying that specific rest period causes an increase in the fatigue life (N_f) of the specimen by the incremental number of cycles. The damage parameter value at the moment of the rest period application (S_0) is related to the pseudostiffness at the beginning of the rest period.

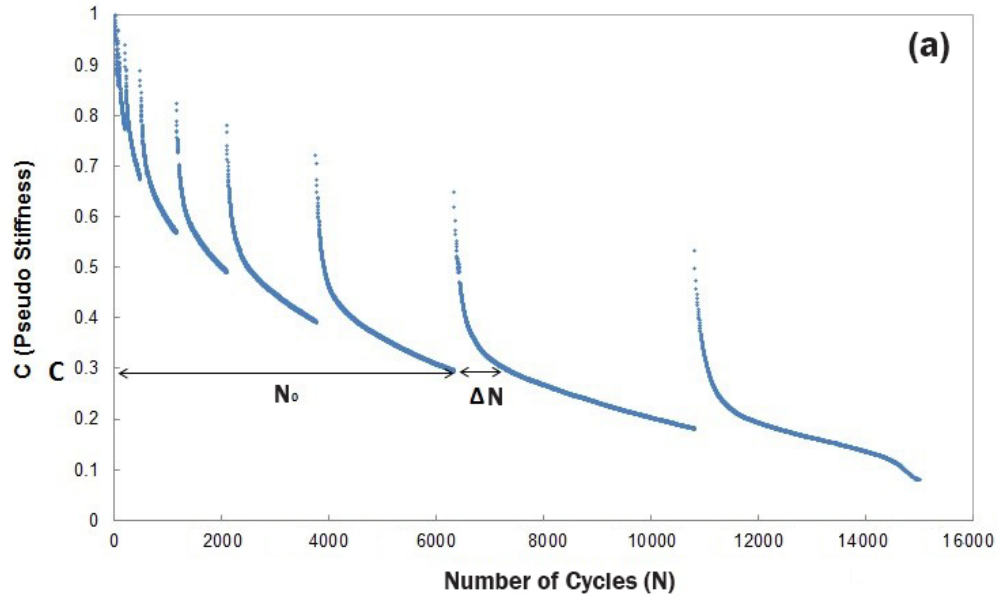
$$\%H_s = \frac{\Delta S}{S_0} \times 100 \quad (78)$$

Where:

$\%H_s$ = healing potential, which is the percentage of healing of the material due to an applied rest period.

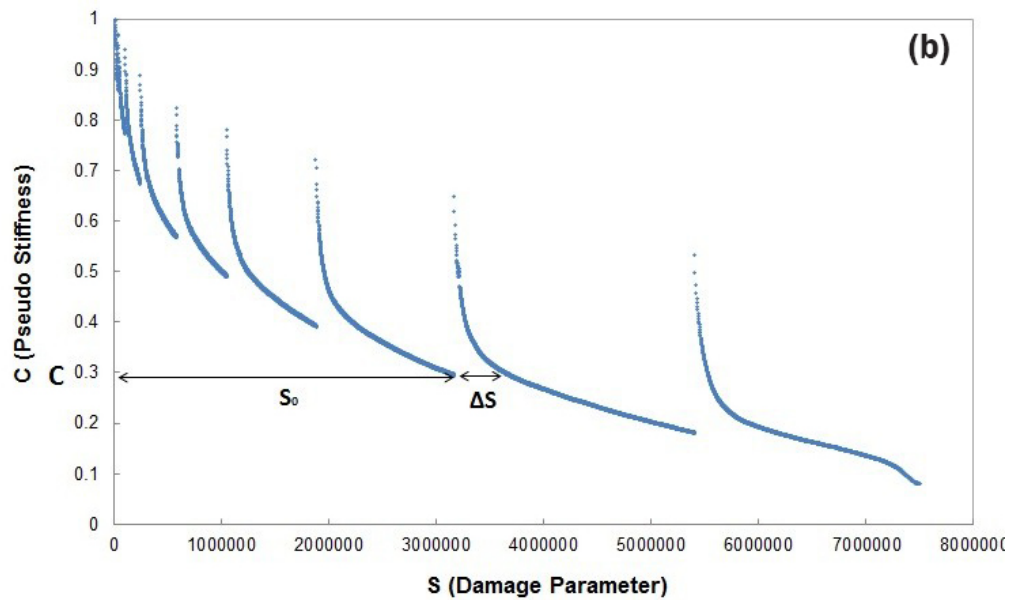
ΔS = horizontal shift of the damage characteristic ($C(S)$) curve due to the healing caused by applying the rest period.

S_0 = damage parameter value at the moment of the rest period application.



Source: FHWA.

A. Pseudostiffness changes with number of cycles.



Source: FHWA.

B. Pseudostiffness changes with damage parameter.

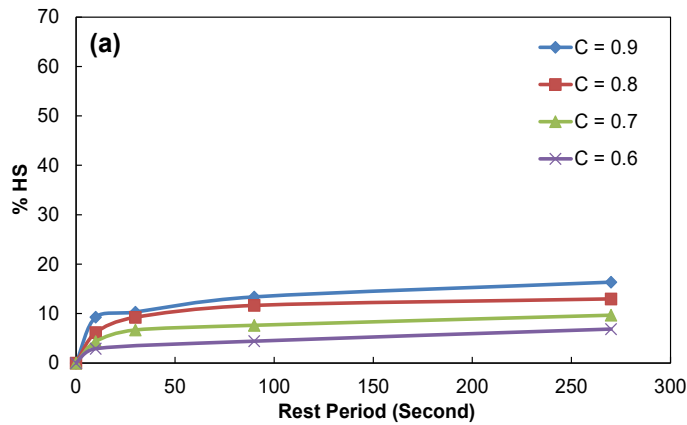
Figure 61. Graphs. Parameters for calculating pseudostiffness and percent healing.

Curves at Specific Pseudostiffnesses

Even though the research team applied the rest periods at a certain number of cycles estimated to be equivalent to pseudostiffnesses of 0.9, 0.8, 0.7, and so on, the pseudostiffnesses of the specimens were slightly different from the target values. To compare the healing curves at

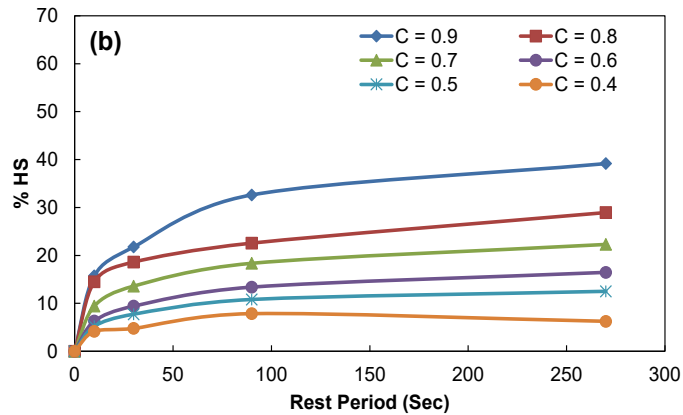
specific pseudostiffnesses, the research team linearly interpolated the measured pseudostiffness and healing potential.

Figure 62 shows the calculated actual healing potential of the material using equation 78 (schematically in figure 61) as a function of rest period and pseudostiffness prior to the rest period at the three test temperatures. The healing potential (%*H_s*) increases as the rest period lengthens and the specimen is more intact (less damaged). Temperature also plays a key role in healing potential—the higher the temperature, the more the specimen heals. Figure 62 proves that, as the research team expected, healing is a function of rest period duration, pseudostiffness, and temperature.



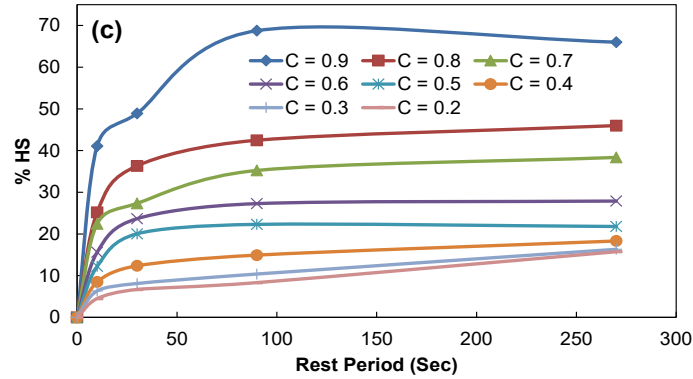
Source: FHWA.

A. Percent healing at 10°C.



Source: FHWA.

B. Percent healing at 20°C.



Source: FHWA.

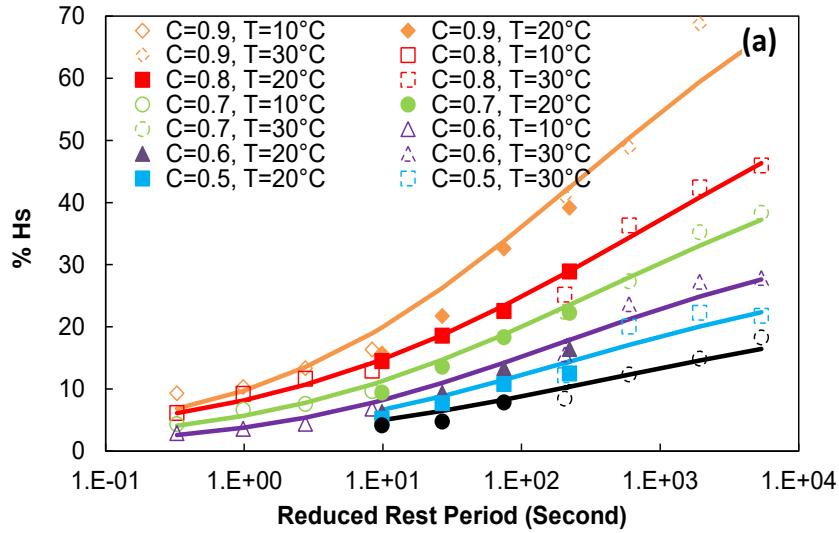
C. Percent healing at 30°C.

Figure 62. Graphs. Percent healing according to pseudostiffness and rest period.

The time and temperature effects on the healing had not previously been commonly combined using the t–TS principle. Previous research proved that the t–TS principle is viable in linear viscoelastic, damaged, and even permanent strain ranges. Thus, the research team assumed that the principle could apply to healing as well. For this study, the research team suggested a reduced rest period duration (RP_{Red}), calculated by equation 79, which applies the t–T shift factor (i.e., a_T) from dynamic modulus testing.

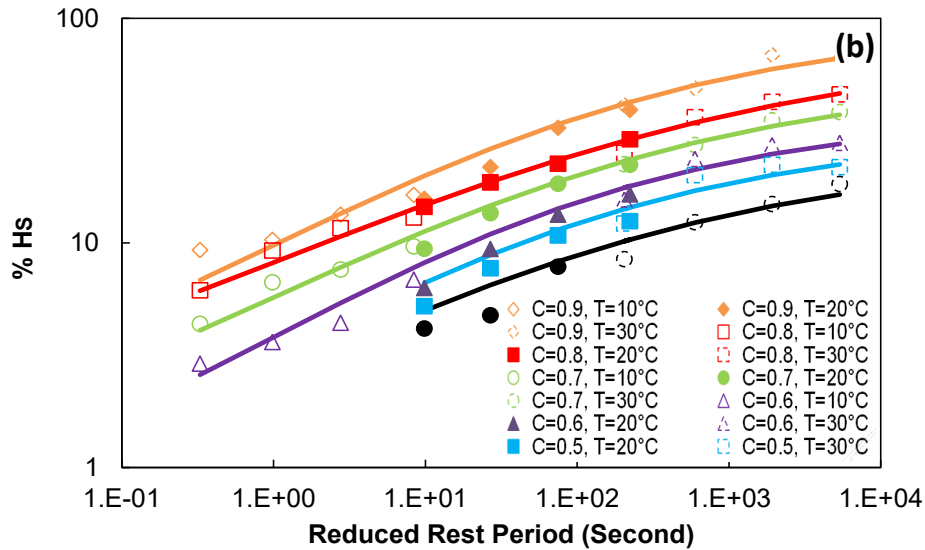
$$RP_{Red} = \frac{RP}{a_T} \quad (79)$$

Figure 63 illustrates that the t–TS principle is viable even for healing because one healing master curve can be constructed for different pseudostiffnesses. The repetitions of each symbol in the figure represents the same pseudostiffness at the different temperatures. The percent healing overlaps at the same reduced rest period, creating a single healing master curve for each pseudostiffness. The next approach would be to find an appropriate functional form of the healing master curve at different pseudostiffnesses. Moreover, the fitting parameters of the master curve can be expressed in terms of pseudostiffness. The final master curve equation shows the dependency of healing on the reduced rest period and pseudostiffness.



Source: FHWA.
 0°C = 32°F.

A. Relationship between percent healing and reduced rest period in semi-log scale.



Source: FHWA.
 0°C = 32°F.

B. Relationship between percent healing and reduced rest period in log-log scale.

Figure 63. Graphs. Relationship between percent healing and reduced rest period.

The research team fitted the healing master curves at different pseudostiffnesses to the sigmoidal functional form (equation 80). The second-order polynomial obtained from dynamic modulus tests of this mixture represents the relationship between shift factor and temperature. The research team used the Solver function in Microsoft Excel® to determine the sigmoidal

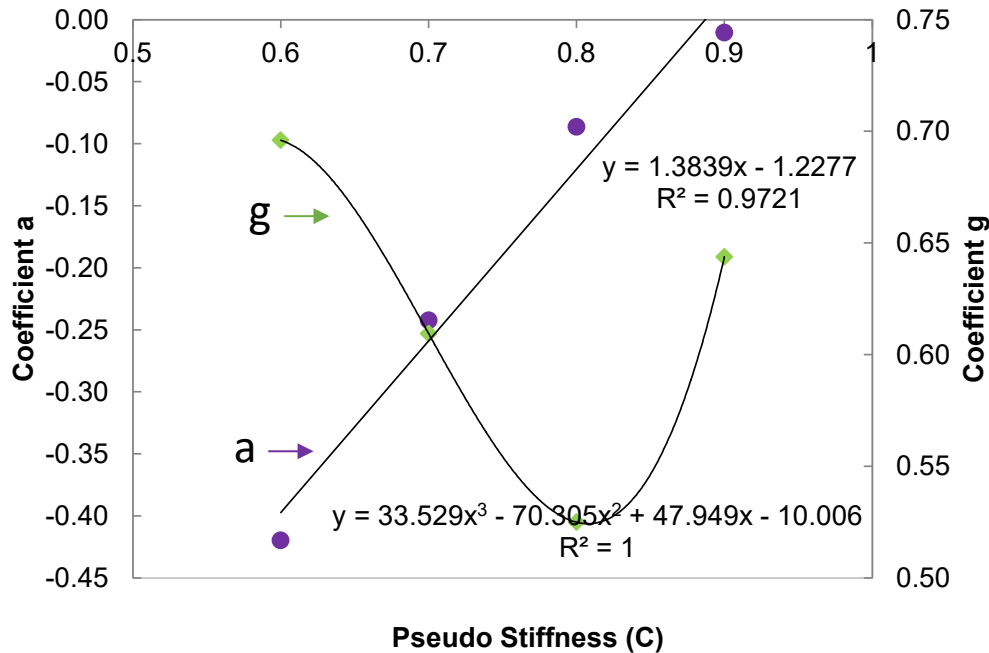
coefficients by minimizing the error between equation 80 and the measured data. The team took the reference temperature as the median test temperature (20°C). They could then find the percent healing at any temperature and rest period combination by using the coefficients of equation 80 in equation 79.

$$\log | \%H_s | = a + \frac{b}{1 + \frac{1}{e^{d+g*\log(RP_{Red})}}} \quad (80)$$

The solid lines in figure 63 show the healing potential master curve for each pseudostiffness. The percent healing values are not available for the pseudostiffness of 0.5 and below 10°C because the specimens failed at a C value higher than 0.5 at the low temperature. To develop a relationship between the parameters of the master curve and the pseudostiffness, the research team plotted the parameters of the healing master curve (a , b , d , g) against the pseudostiffness, as shown in figure 64. Table 23 shows the calibrated parameters as well. Through optimization, b and d turned out to be constant values: 2.00 and 0.0, respectively. Table 23 also presents the model parameters, and the trend is shown in figure 64. Equation 81 expresses the model parameters (a and g) with the master curve of equation 80.

$$\begin{aligned} a &= 1.38391C - 1.2277, \\ g &= 33.529C^3 - 70.305C^2 + 47.949C - 10.006, \end{aligned} \quad (81)$$

Where C is the pseudostiffness before starting the rest period.



Source: FHWA.

Figure 64. Graph. Fitting parameters for percent healing master curves with pseudostiffness.

Table 23. Fitting parameters for percent healing master curves.

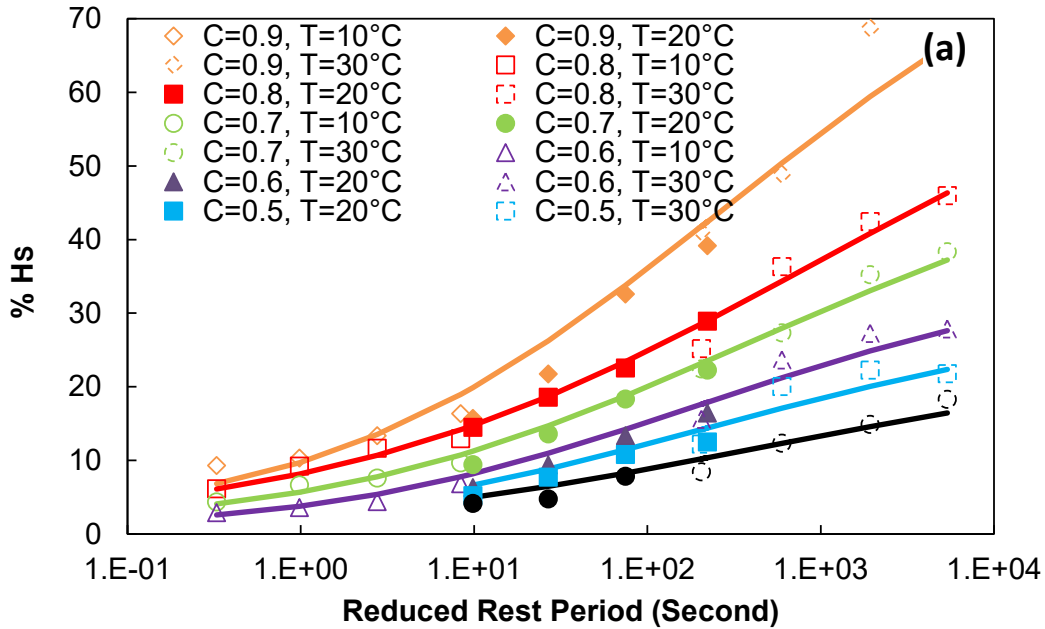
Pseudostiffness (C)	a	b	d	g
0.9	-0.011	2.00	0.00	0.644
0.8	-0.086	2.00	0.00	0.525
0.7	-0.242	2.00	0.00	0.609
0.6	-0.420	2.00	0.00	0.696

Characteristic Protocol

The testing matrix the research team used to develop the healing model is composed of 12 tests (three temperatures at four rest periods), which demands 4 d of testing. Because the team successfully created the healing potential master curve via the t-TS principle, they were able to reduce all 12 tests. As such, fewer combinations of temperatures and rest periods could provide enough information about healing when used along with the t-TS principle.

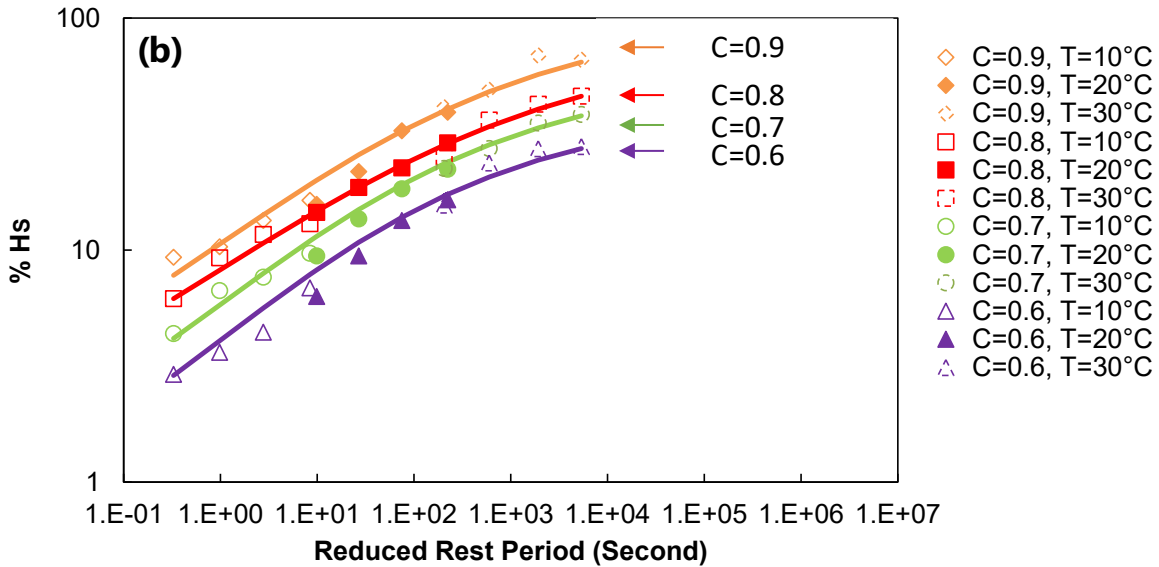
The research team only needed three conditions to create the healing potential master curve. To cover a wide range of reduced rest periods, they selected a low temperature with a short rest period (10°C with 10 s), high temperature with a long rest period (30°C with 270 s), and an intermediate condition (20°C with 30 s). The research team had already tested these conditions and had calibrated the suggested healing model using these three test conditions.

Figure 65 shows the characteristic curves using the three different test conditions. The healing potential master curves match the measured percentages of healing, which are presented in the figure as various symbols. These results imply that the three healing test conditions could properly calibrate the suggested healing model (i.e., instead of 12 rigorous tests, only three conditions are required to evaluate the healing behavior of asphalt materials). The corresponding three tests demand only 1 d of testing time.



Source: FHWA.
0°C = 32°F.

A. Healing master curves fitted using three selective tests in semi-log scale.



Source: FHWA.
0°C = 32°F.

B. Healing master curves fitted using three selective tests in log-log scale.

Figure 65. Graphs. Healing master curves fitted using three selective tests.

Damage Evolution Prediction

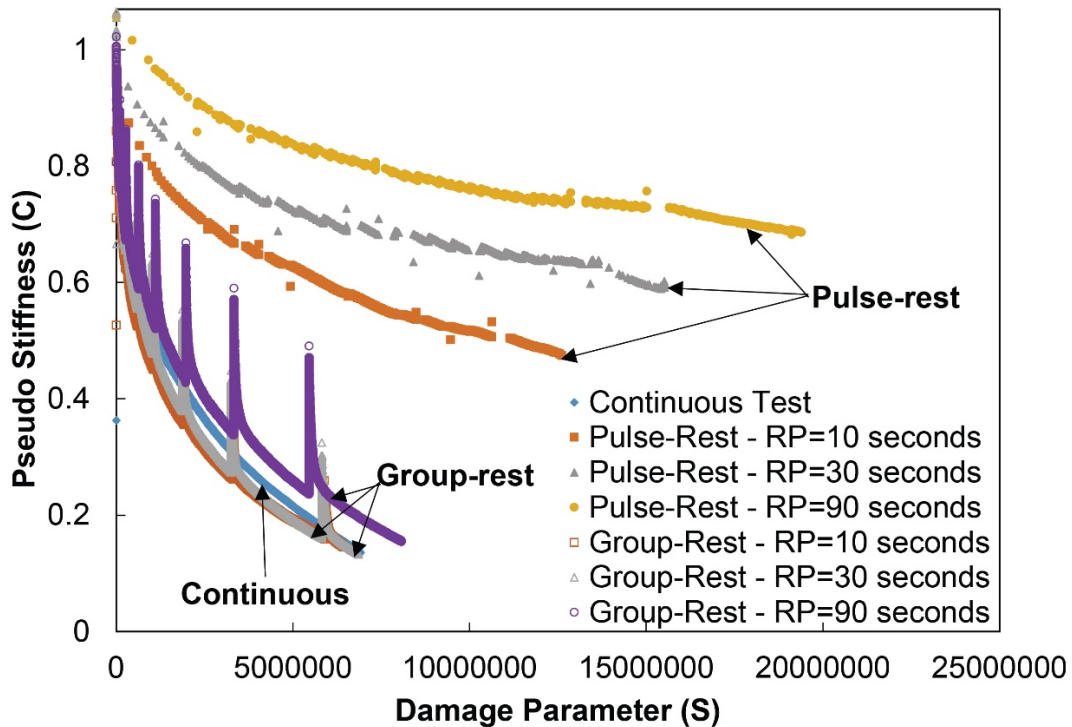
The research team developed the healing model and test protocol based on group-rest tests. As discussed, the group-rest test is composed of continuous loading blocks followed by a rest period

of a particular duration. However, asphalt pavement typically experiences loading followed by unloading, which can be considered a rest period. In this sense, the pulse-rest test seems to be a better choice for simulating pavement conditions in the field than a group-rest test. This section suggests a way to link the short group-rest test and long pulse-rest test. This way, by conducting only short group-rest healing tests and using the damage characteristic curves of these tests, the research team can determine the characteristic curves for the longer pulse-rest healing tests.

Relationships Among Different Loading Conditions

Comparing the damage characteristic curves among the different loading conditions for the group-rest, pulse-rest, and continuous loading tests can provide meaningful information regarding the healing behavior of asphalt concrete. Figure 66 presents the damage characteristic curves for the different loading conditions. The pulse-rest test conditions appear to heal the specimen the most out of all the test conditions. As the rest period increases, the effect of healing also increases. The continuous loading test (i.e., without a rest period) has a curve similar to the curves seen for the group-rest tests. This result is due to the similar loading conditions for the continuous test and group-rest tests, except for the several rest periods the research team applied in the group-rest tests.

Plotting the characteristic curves in other spaces may then be helpful. For this purpose, the research team examined the best functional forms to fit to these curves. Two functional forms fit the damage characteristic curves of the continuous fatigue tests. Equation 82 and equation 83 show these two functions with their fitting parameters.



Source: FHWA.

Figure 66. Graph. Damage characteristic curves for all the tests at 30°C.

$$C = e^{(-aS^b)} \quad (82)$$

$$C = 1 - C_{11}S^{C_{12}} \quad (83)$$

Where a , b , C_{11} , and C_{12} are the fitting parameters, and a and b should be larger than zero.⁽¹⁰³⁾

The research team then rearranged equation 82 and equation 83 into the forms of equation 84 and equation 85, respectively.

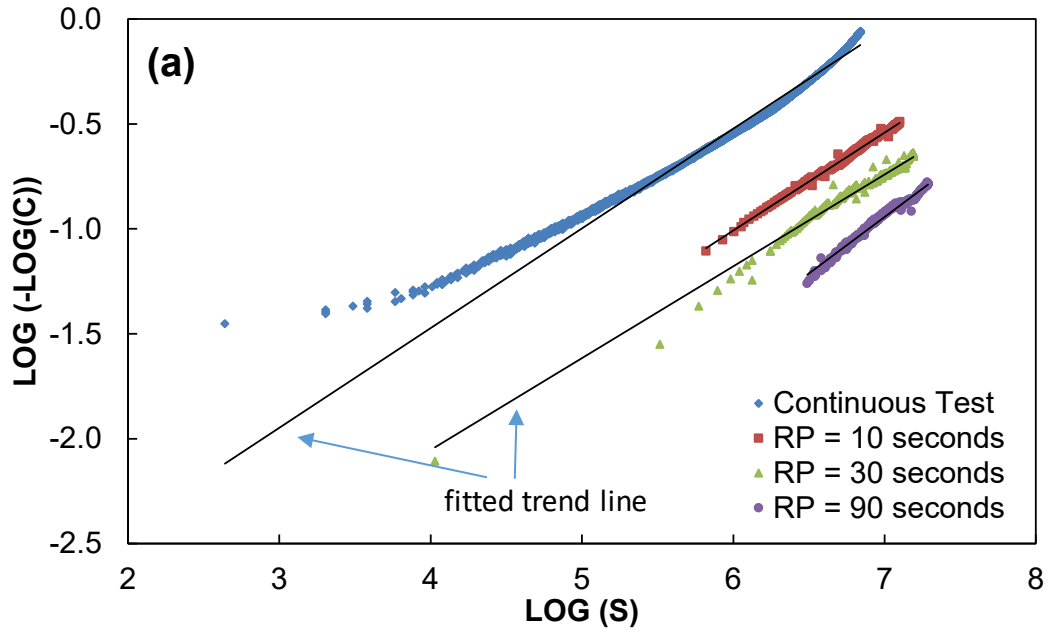
$$\log(-\log(C)) = \log(\log(e)) + \log(a) + b \times \log(S) \quad (84)$$

$$\log(1 - C) = \log(C_{11}) + C_{12} \times \log(S) \quad (85)$$

Thus, the damage characteristic curves are approximately linear in $\log(-\log(C))$ versus $\log(S)$ and $\log(1 - C)$ versus $\log(S)$ spaces. Figure 67-A and figure 67-B show the damage characteristic curves for the continuous fatigue test and the three pulse-rest healing tests (rest periods of 10, 30, and 90 s at 30°C) for the RS9.5B mixture in these two new coordinate systems, respectively. The research team fitted the lines to these curves using Microsoft Excel.

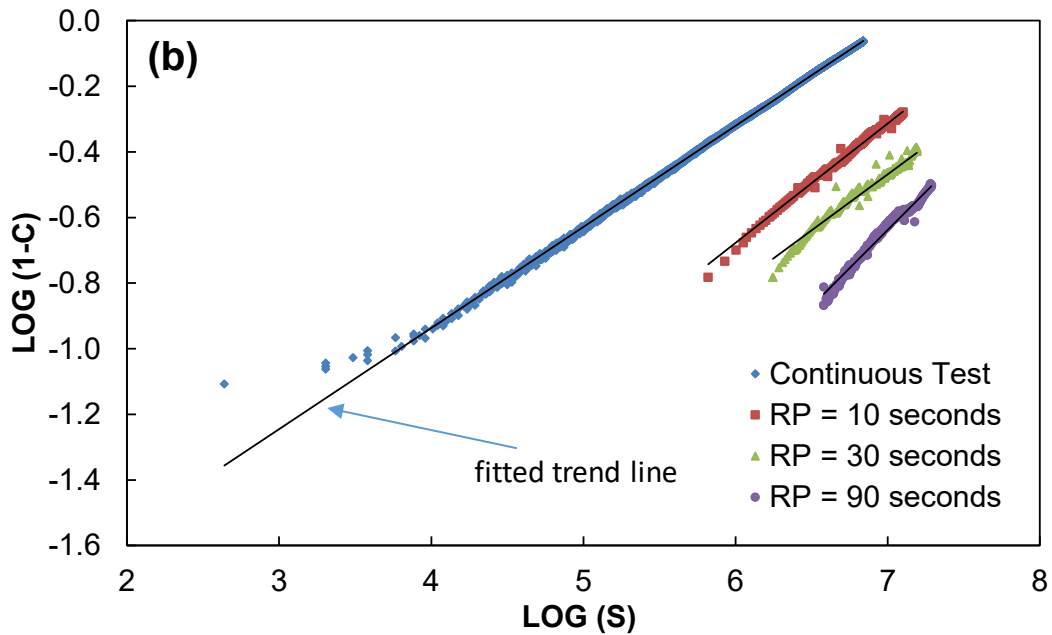
These two figures show that the linear approximation in the $\log(1 - C)$ versus $\log(S)$ space is more valid because the relationship in figure 67-B is more linear than the relationship in figure 67-A. Furthermore, figure 67-B shows more parallel lines, making it easier to find a correlation between these curves. Because the lines in figure 67-B are approximately parallel, the initial approach for generating the pulse-rest test curves from the continuous test curve would be to shift them along the horizontal axis, which is $\log(S)$, and try to fit them into a single line. This approach stems from the fact that asphalt concrete material in the linear viscoelastic range is TRS, so the damage characteristic curves for different durations of rest periods would create one representative curve via the superposition of the rest period.

Figure 68 is the result of shifting the pulse-rest healing test curves along the $\log(S)$ axis. Because the research team's objective is to develop damage characteristic curves for the pulse-rest healing tests using the curve for the continuous fatigue test, they considered the damage characteristic curve from the continuous cyclic fatigue test to be the reference relationship.



Source: FHWA.

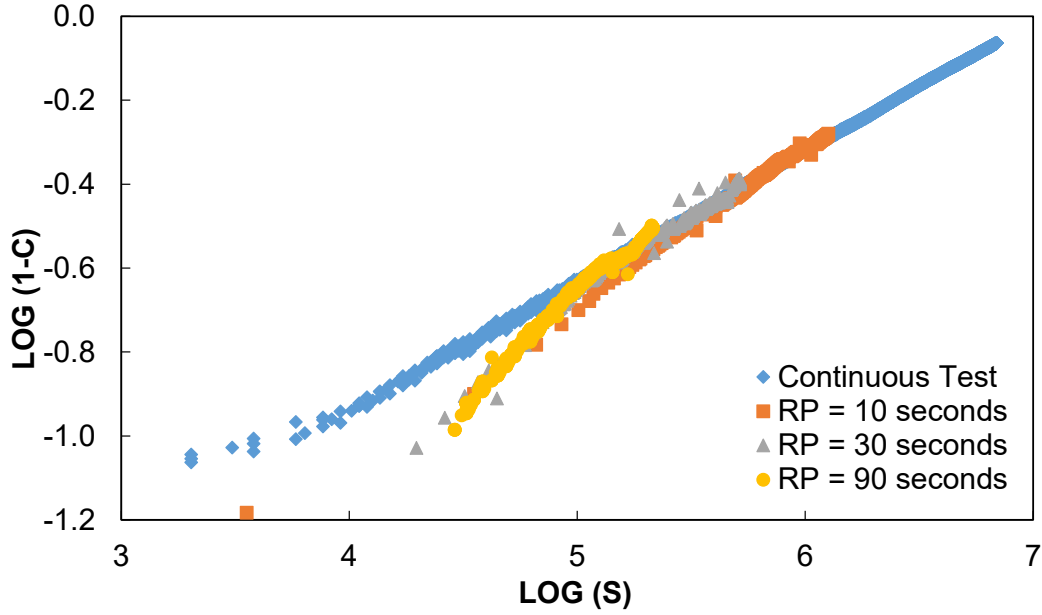
A. Damage characteristic curves for continuous fatigue test and pulse-rest healing tests at 30°C in the $\log(-\log(C)) - \log(S)$ space.



Source: FHWA.

B. Damage characteristic curves for continuous fatigue test and pulse-rest healing tests at 30°C in the $\log(1 - C) - \log(S)$ space.

Figure 67. Graphs. Damage characteristic curves for continuous fatigue test and pulse-rest healing tests at 30°C.



Source: FHWA.

Figure 68. Graph. Damage characteristic curves for continuous fatigue test and pulse-rest healing tests in the $\log(1 - C) - \log(S)$ space after shifting at 30°C.

The research team horizontally shifted the damage characteristic curves for the different rest periods, as shown in figure 68. Figure 68 also shows that horizontal shifting alone could not provide a good collapse of the damage characteristic curves from no rest to rest periods with varying durations and that the curves need to be rotated as well. The research team followed a trial and error method to collapse the damage characteristic curves. They developed equation 86 by applying a new parameter called $(h(C, RP_R))^{1/1+\alpha}$, which they assumed to be a function of pseudostiffness and reduced rest period.

$$S \cong (h(C, RP_R))^{1/1+\alpha} \sum_{i=1}^N \left[\frac{I}{2} (\varepsilon_i^R)^2 (C_{i-1} - C_i) \right]^{\alpha/1+\alpha} (t_i - t_{i-1})^{1/1+\alpha} \quad (86)$$

Using trial and error, the research team found the dependency of this newly introduced parameter on pseudostiffness and reduced rest period in the form of equation 87 and equation 88.

$$(h(C, RP_R))^{1/1+\alpha} = \frac{1}{a_{RP}} \quad (87)$$

$$a_{RP} = S^{H(C, RP_R)} \quad (88)$$

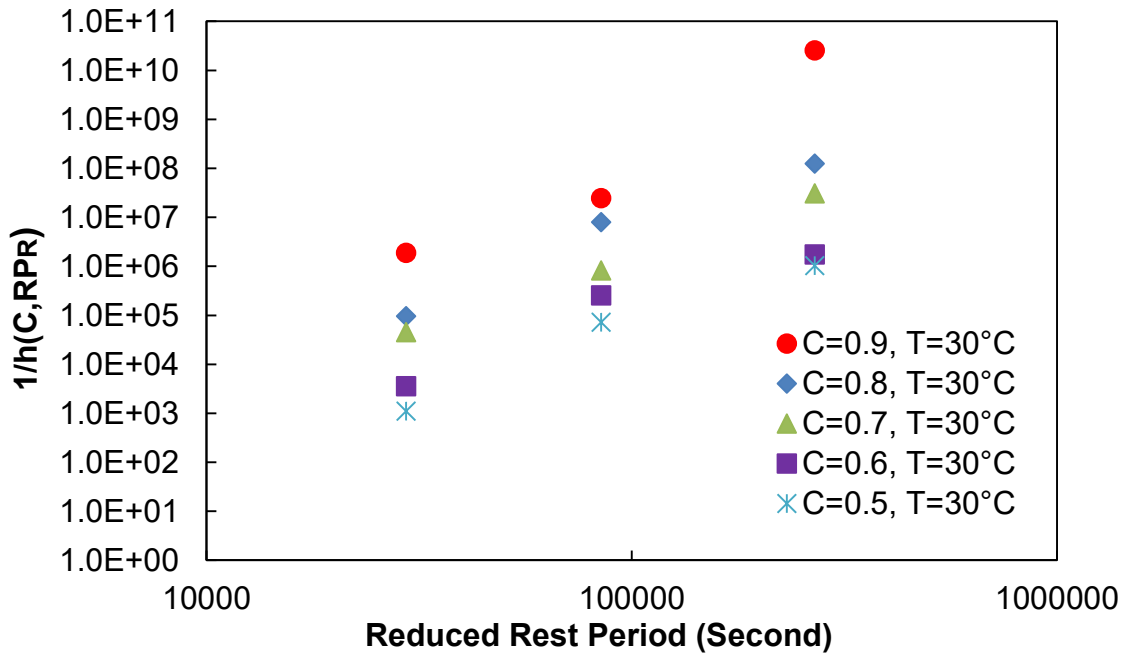
Where:

a_{RP} = rest period shift factor.

S = damage parameter at different C values in a continuous test.

$h(C, RP_R)$ = healing index as a function of C and RP_R .

Figure 69 shows the dependency of $h(C, RP_R)$ on pseudostiffness and reduced rest period. To show the dependency in a clearer graph, the figure plots $1/h(C, RP_R)$ instead of $h(C, RP_R)$.



Source: FHWA.
 $0^{\circ}\text{C} = 32^{\circ}\text{F}$.

Figure 69. Graph. $1/h(C, RP_R)$ as a function of pseudostiffness and reduced rest period.

The research team derived the following equation for $h(C, RP_R)$ by substituting equation 88 into equation 87.

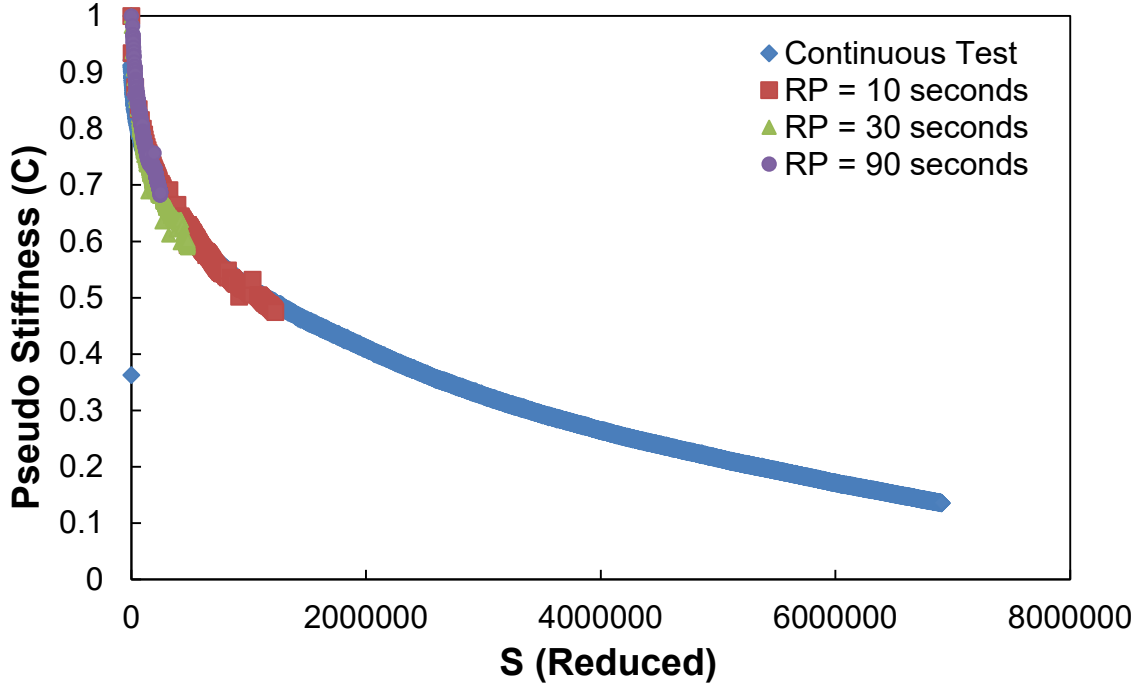
$$h(C, RP_R) = S^{-H(C, RP_R)(1+\alpha)} \quad (89)$$

Using equation 86 to compute the damage parameter in all of the tests collapses the damage characteristic curves for the continuous fatigue test and the three pulse-rest tests, as shown in figure 70. Figure 70 proves that rotational shifting works and that a single healing master curve, which is a continuous loading curve, can be created. For clarity, the damage value computed from the new numerical scheme shown in equation 86 is designated as S_{New} in equation 90.

$$S_{New}(C) = S_{Continuous}(C) \quad (90)$$

where $S_{Continuous}$ is the S value from the continuous test.

Therefore, in the case of the continuous fatigue test ($RP = 0$), no healing occurs ($\%H = 0$), and equation 89 results in $h(C, RP_R) = 1$, meaning there is no shifting of the continuous loading curve (i.e., the reference curve). As such, the results derived from the continuous fatigue test (equation 86) and the damage characteristic curves from the pulse-rest tests are identical.



Source: FHWA.

Figure 70. Graph. Damage characteristic curves for continuous fatigue test and pulse-rest tests using the new scheme.

The research team obtained the following relationship by combining equation 86 and equation 87.

$$S \cong \frac{1}{a_{RP}} \sum_{i=1}^N \left[\frac{I}{2} (\varepsilon_i^R)^2 (C_{i-1} - C_i) \right]^{\alpha/1+\alpha} (t_i - t_{i-1})^{1+\alpha} \quad (91)$$

$$S_{Reduced} = S_{Continuous} = \frac{S_{Pulse-Rest}}{a_{RP}} \quad (92)$$

Where $S_{Reduced}$ and $S_{Pulse-Rest}$ are the S values in the healing mastercurve and from the pulse-rest test, respectively.

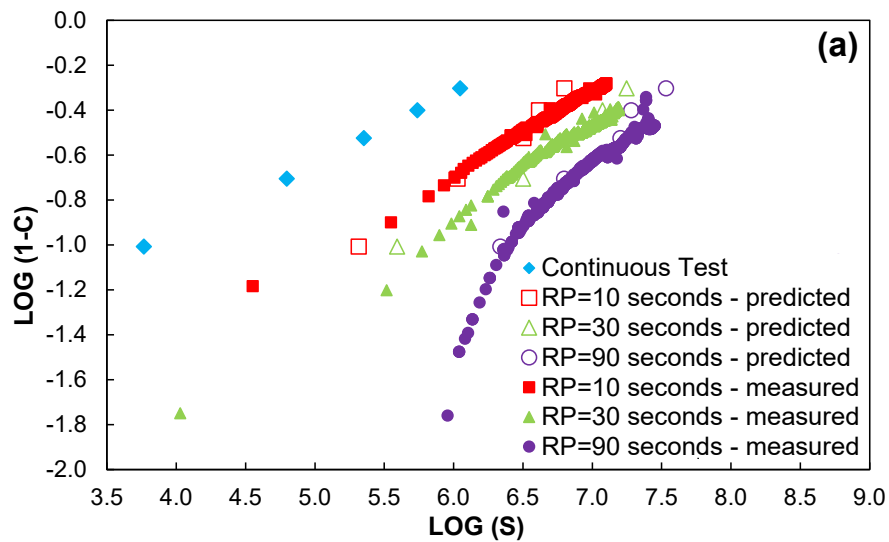
The research team obtained the following relationship from equation 92 and equation 88.

$$S_{Pulse-Rest} = S_{Continuous} \times a_{RP} = S_{Continuous}^{[H(C,RP_r)+1]} \quad (93)$$

Once the research team established the damage characteristic curve for the continuous loading test for a mixture, they were able to find the corresponding damage values at the same pseudostiffness for the pulse-rest healing tests (at any reduced rest period) using equation 93 and predict the damage characteristic curve for any pulse-rest healing test conducted on the same mixture.

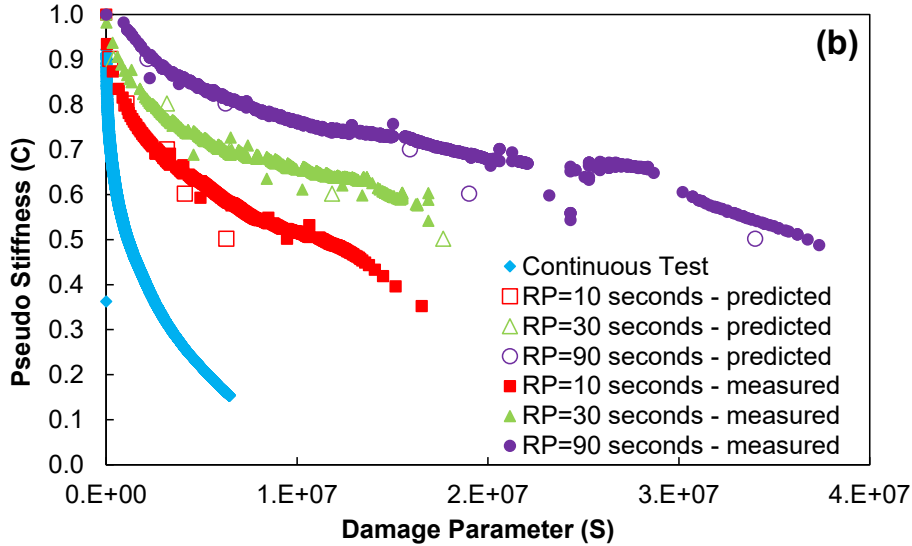
Group-Rest and Pulse-Rest Healing Tests

The previous Relationships among Different Loading Conditions section discussed the relationship between the continuous loading test, which is a typical fatigue test, and the pulse-rest healing test, which uses typical loading conditions found in the field. However, using pulse-rest healing tests to calibrate the healing model may take hours or even many days, depending on the test temperature and the length of the rest period. As described for the development of the healing model, the group-rest healing test reduces the testing time and requires only 1 d of testing. To apply the group-rest test to the calibration method, the research team verified the test method by predicting the healing behavior of the pulse-rest test using the model calibrated by the group-rest test. Figure 71 shows the results of applying the percent healing values from the group-rest healing tests, which are the prediction, and test results of the pulse-rest healing tests. As these plots indicate, there is good agreement between the predicted points and the actual test data. The figures show the proposed method for predicting damage characteristic curves for the pulse-rest healing tests reasonably in the arithmetic space as well as logarithmic space. Therefore, the group-rest test can be used as a test method for calibrating the proposed healing model.



Source: FHWA.

A. Comparison of damage characteristic curves from actual pulse-rest healing tests and shifting procedure at 30°C in the $\log(1 - C)$ versus $\log(S)$ space.



Source: FHWA.

B. Comparison of damage characteristic curves from actual pulse-rest healing tests and shifting procedure at 30°C using damage characteristic curves.

Figure 71. Graphs. Comparison of damage characteristic curves from actual pulse-rest healing tests and shifting procedure at 30°C.

Model and Protocol Verification

As described in the previous section, the research team had proposed a method for developing damage characteristic curves for the pulse-rest healing tests. The team used the continuous loading test—a typical fatigue test (i.e., the cyclic fatigue test)—as the reference test, and the group-rest tests for calibrating the healing model. They successfully predicted the pulse-rest healing test results using the results from the continuous loading test and the group-rest test and the suggested healing model for the RS9.5B mixture.

However, to fully examine the capacity of the model and calibration method, it was critical the research team also verify the model and test method’s applicability to other mixtures. They selected the SBS mixture used in the FHWA ALF test sections as a second mixture because they knew the mixture had relatively good healing potential compared with other mixtures in the FHWA ALF sections, as the SBS mixture uses binder that contains a polymer-modified SBS modifier.

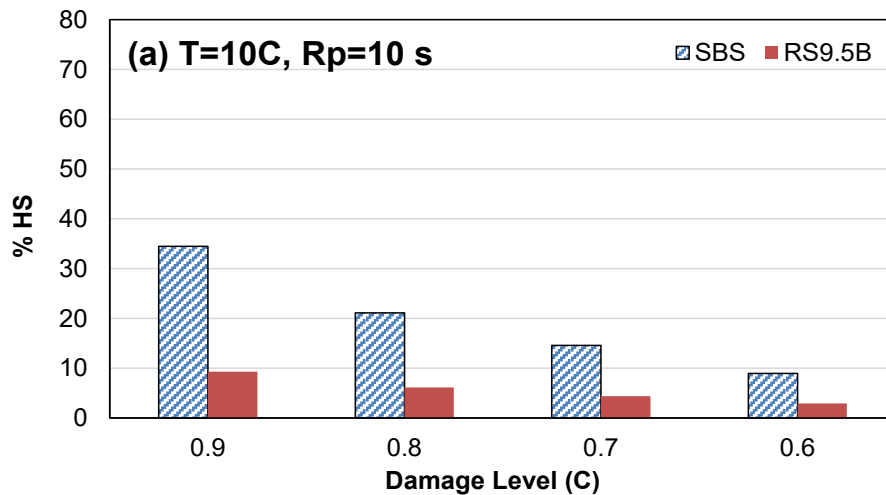
According to the proposed test protocol, the research team performed three characteristic group-rest healing tests on specimens of the SBS mixture, and calculated the percent healing at different pseudostiffnesses. The team chose the temperatures and rest periods for these three tests following the suggested protocol. Table 24 shows the conditions for these three tests.

Table 24. Characteristic test conditions for SBS mixture (group-rest test).

Test ID	Temperature (°C)	Rest Period (s)
1	10	10
2	20	90
3	30	270

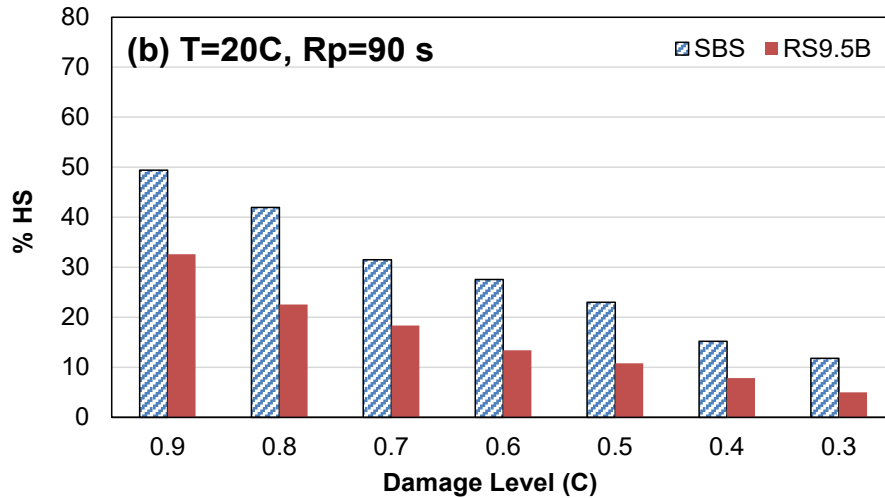
0°C = 32°F.

The research team compared the healing potentials of the SBS and RS9.5B mixtures to understand the characteristics of the healing process in terms of mixtures and binders, as shown in figure 72. The healing potential of the SBS mixture is shown in the graphs as a bar that is always higher than that of the RS9.5B mixture. This trend indicates that the percent healing can quantify the healing potential and indirectly proves that the SBS mixture experiences the least fatigue cracking among the FHWA ALF mixtures. The SBS mixture also seemed different from the RS9.5B mixture in terms of healing, and thus, if the model and protocol are applicable to the SBS mixture, the model along with the suggested test protocol is valid for estimating the healing behavior of asphalt concrete.



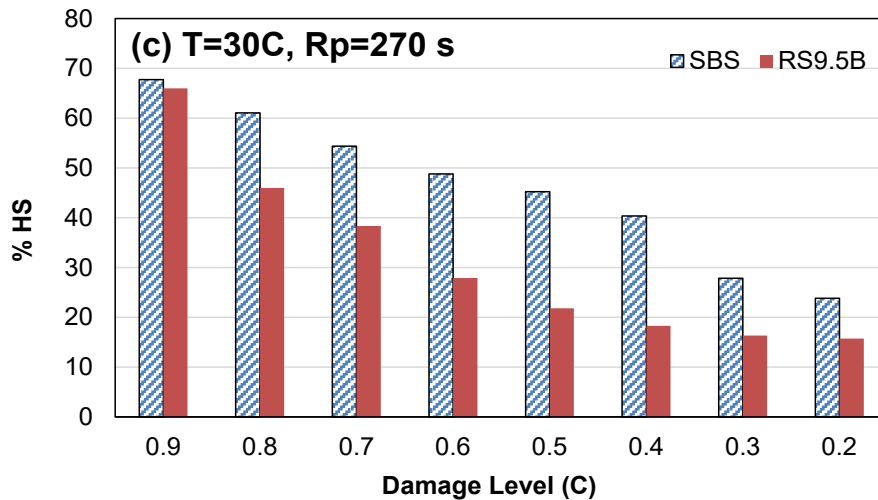
Source: FHWA.
0°C = 32°F.

A. Comparison of healing properties between SBS and RS9.5B mixtures at different temperatures and rest periods at 10°C with a 10-s rest period.



Source: FHWA.
0°C = 32°F.

B. Comparison of healing properties between SBS and RS9.5B mixtures at different temperatures and rest periods at 20°C with a 90-s rest period.



Source: FHWA.
0°C = 32°F.

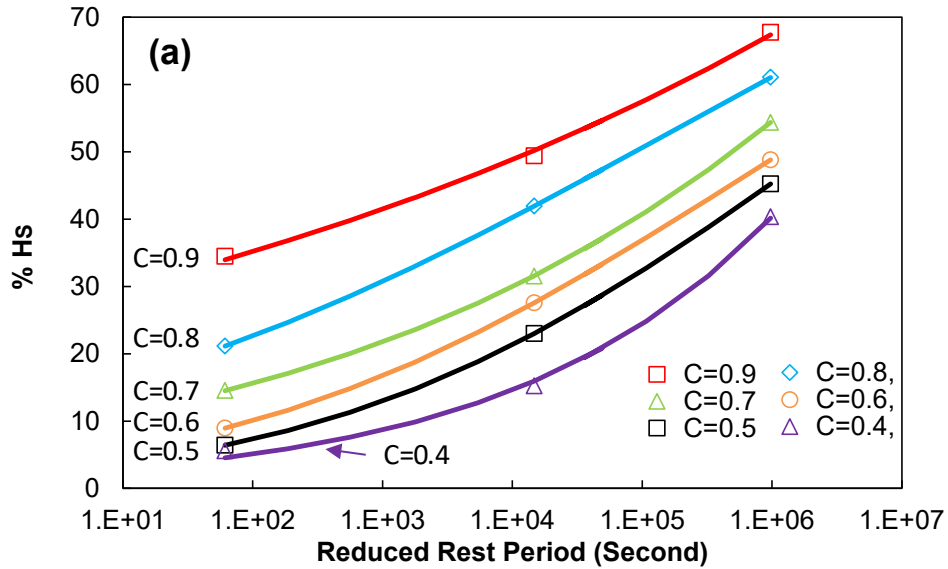
C. Comparison of healing properties between SBS and RS9.5B mixtures at different temperatures and rest periods at 30°C with a 270-s rest period.

Figure 72. Graphs. Comparison of healing properties between SBS and RS9.5B mixtures at different temperatures and rest periods.

Model Calibration

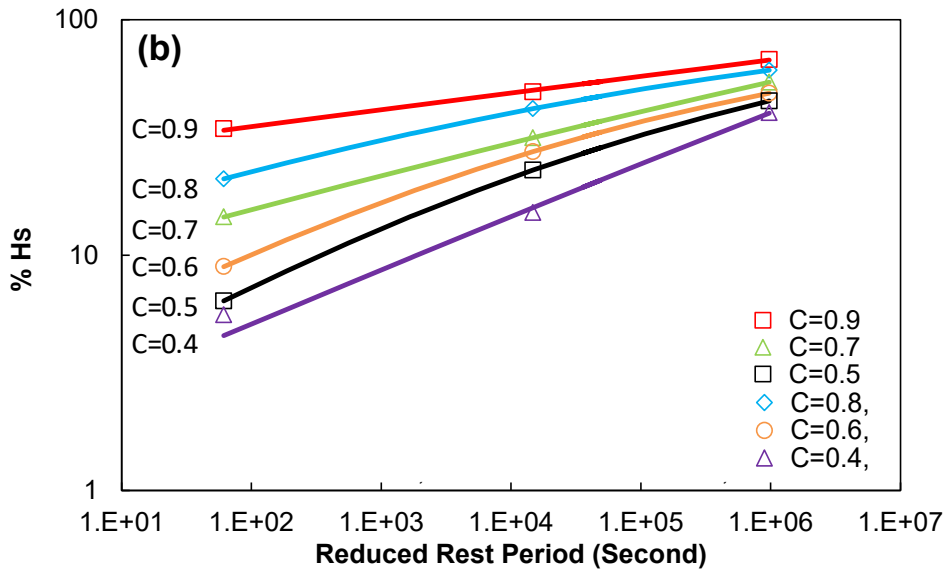
The research team applied the healing model calibration procedure developed from the RS9.5B mixture to the SBS mixture. They calculated the percentages of healing at each pseudostiffness from three group-rest healing tests and fitted them using a sigmoidal functional form to create

healing master curves. Figure 73 presents the healing master curves. As the research team expected, the percentage of healing is higher for longer reduced rest periods. Any healing master curve with a larger C value (less damage) lies above the other master curves that have smaller C values (more damage).



Source: FHWA.

A. Healing master curves of SBS mixture in semi-log scale.



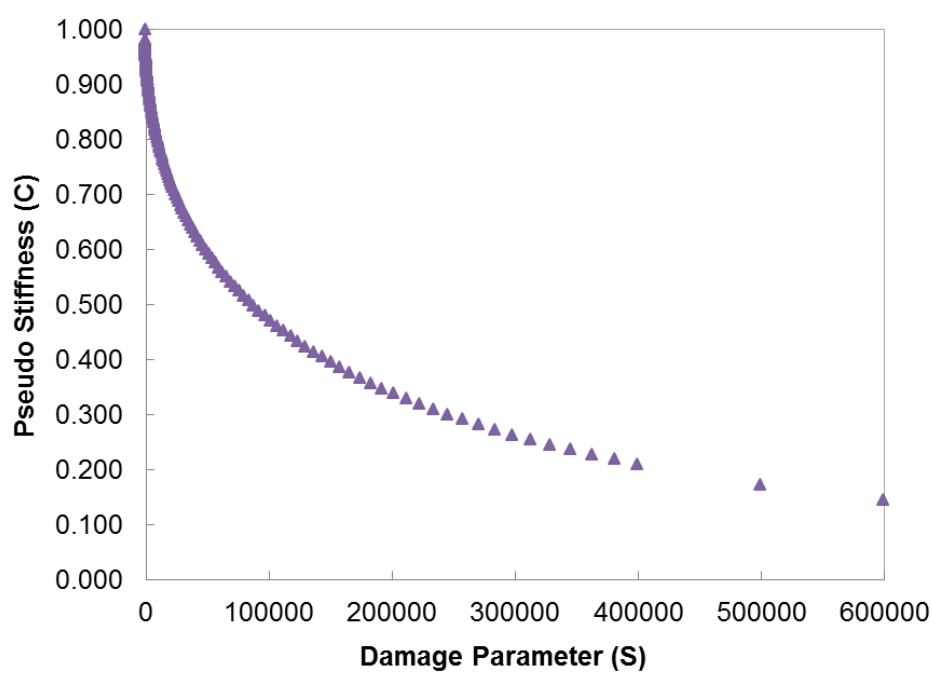
Source: FHWA.

B. Healing master curves of SBS mixture in log-log scale.

Figure 73. Graphs. Healing master curves of SBS mixture.

Group-rest tests characterize the relationship between the “percent healing potential with damage” level and the rest period. The ultimate goal of the healing model is to predict healing in

the field where a pulse (i.e., loading) is followed by a period of rest. As such, the healing model requires a continuous fatigue test to obtain a reference damage characteristic curve, which can then be used to estimate the fatigue performance of a given mixture. The continuous loading fatigue test is part of the healing test protocol, not an additional test. Figure 74 shows a characteristic curve of a continuous fatigue test for the SBS mixture.



Source: FHWA.

Figure 74. Graph. Damage characteristic curve for continuous fatigue test.

Healing Model Verification

This section details the verification of the developed healing model by predicting the damage evolution and strain development from the pulse-rest test.

Damage Evolution of Pulse-Rest Test

The research team performed three pulse-rest healing tests to verify the capacity and reasonableness of the proposed healing model. Table 25 shows the test conditions for verification, which are different from the test conditions for the healing model characteristic.

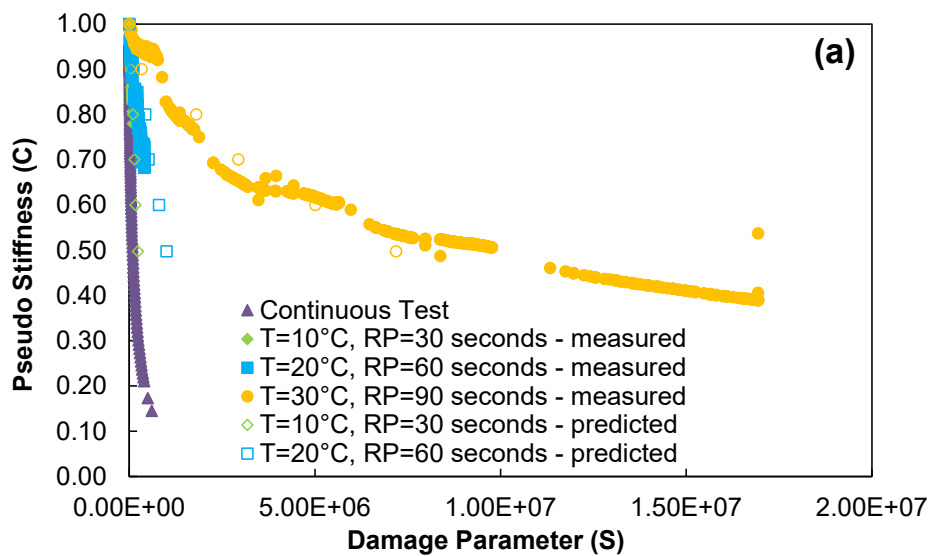
Table 25. Verification test conditions for SBS mixture.

Test ID	Temperature (°C)	Rest Period (s)
1	10	30
2	20	60
3	30	90

0°C = 32°F.

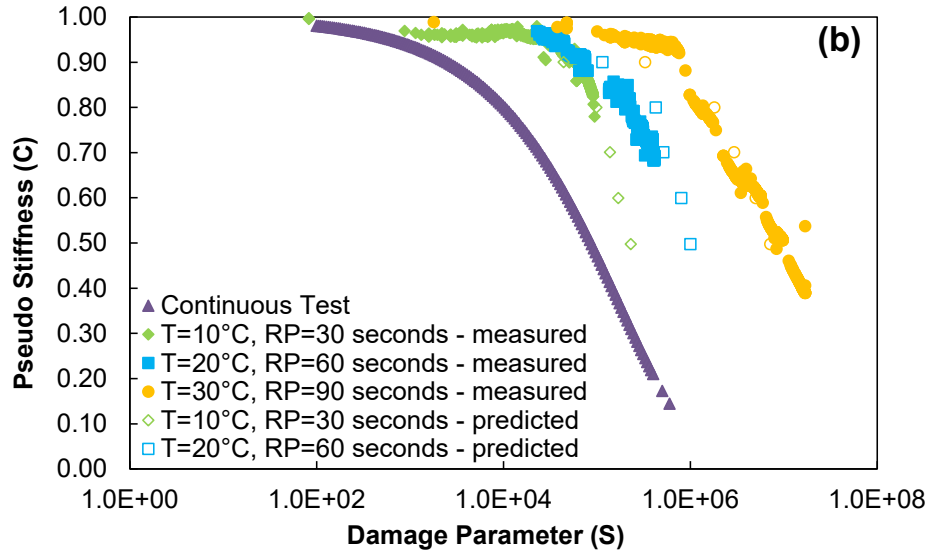
The research team predicted the damage characteristic curves for the pulse-rest healing tests using the damage characteristic curve for the continuous fatigue test and the healing master curves for the SBS mixture. $S_{Pulse-Rest}$ (refer to equation 93) comes from the damage characteristic curve of the continuous test, and H in the exponent comes from the healing master curve, both of which are provided via the healing model test protocol.

The calibrated healing model along with equation 93 can predict the damage evolution in the pulse-rest tests. Figure 75-A and figure 75-B plot a comparison of these predictions with the test results in arithmetic scale and semi-log scale, respectively. In these figures, the hollow symbols represent the predicted damage characteristic curves for the pulse-rest test conditions from the proposed healing model. As shown in figure 75, the model along with the protocol predicts the pulse-rest test results, which proves the capacity of the proposed healing model.



Source: FHWA.

A. Comparison of damage characteristic curves for actual pulse-rest healing tests and predictions in arithmetic scale.



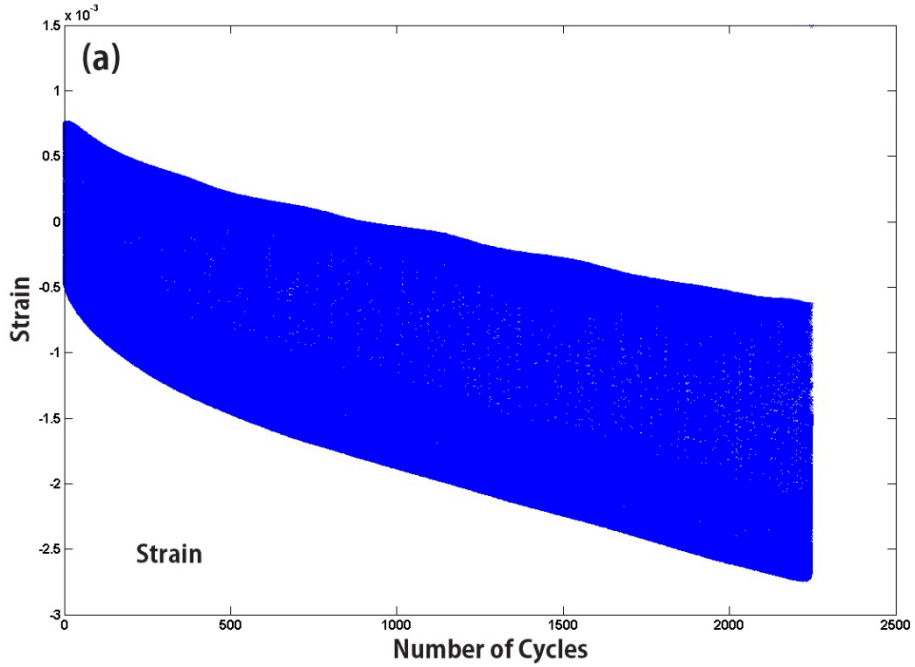
Source: FHWA.

B. Comparison of damage characteristic curves for actual pulse-rest healing tests and predictions in semi-log scale.

Figure 75. Graphs. Comparison of damage characteristic curves for actual pulse-rest healing tests and predictions.

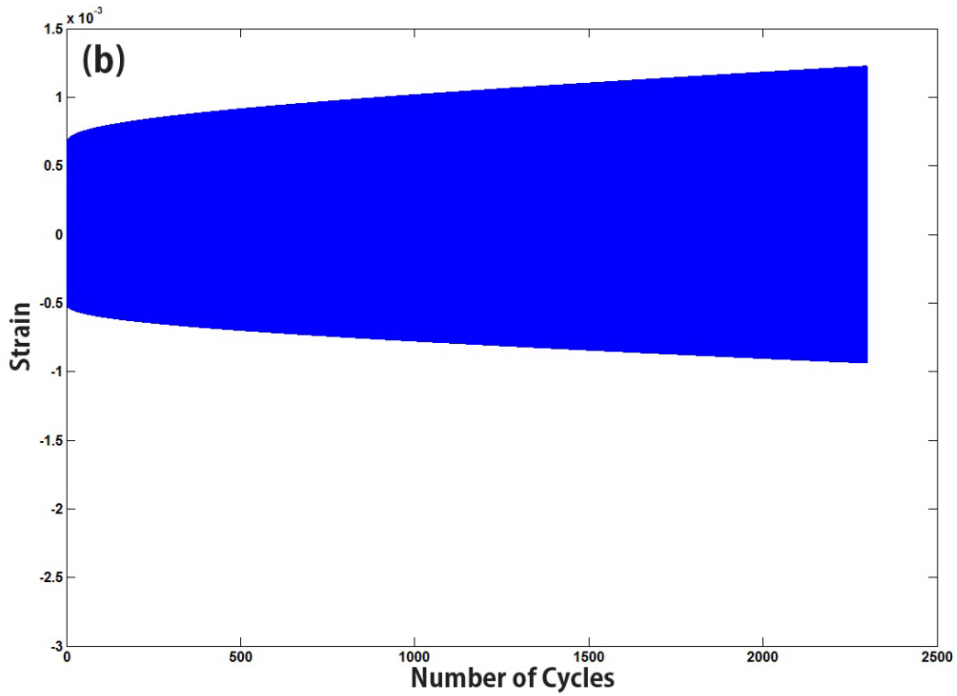
Strain Prediction

Healing affects the change in stiffness of the material during a rest period, and thus, predicting the damage evolution should be enough to verify the healing model. However, if the healing model combined with the S-VECD model could better predict the stress-strain behavior, then the healing model would have more capacity to describe the performance of asphalt pavement. Furthermore, the damage parameter does not have a clear physical meaning. As such, a predicted quantity, which has a sensible physical meaning, should be compared to the same quantity in an actual test. Because the explained procedure provides the predicted damage characteristic curve, the strains can be backcalculated using the predicted damage characteristic curve and the results can be compared with the actual strains of samples used in the pulse-rest tests. Figure 76 shows the results of such analysis for a pulse-rest test using the RS9.5B mixture. Permanent strain used in the laboratory tests, shown in figure 76-B, causes the overall trend to decrease with the number of cycles. For a more reasonable comparison, the research team plotted and compared the strain amplitudes, which are the peak-to-peak strains, in figure 77, which does not contain permanent strain. The predicted and measured strain amplitudes are similar to one another. Therefore, it is likely that the healing model combined with the S-VECD model can predict the strain history if the test does not reasonably generate permanent strain.



Source: FHWA.

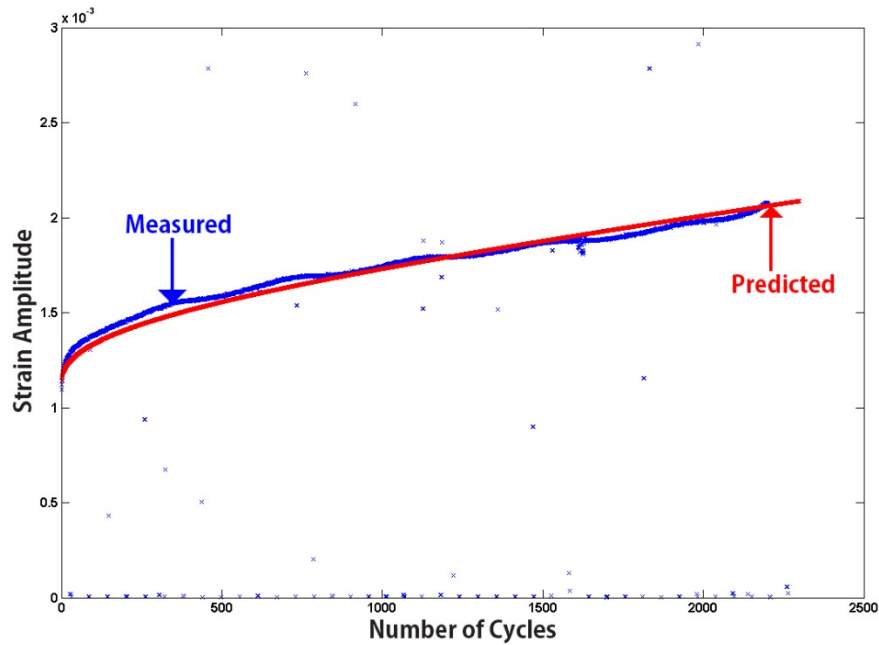
A. Measured strain history of pulse-rest test.



Source: FHWA.

B. Predicted strain history of pulse-rest test from backcalculation.

Figure 76. Graphs. Strain history of pulse-rest test.



Source: FHWA

Figure 77. Graph. Comparison between measured and predicted strain amplitudes.

Proposed Test Protocol for Healing

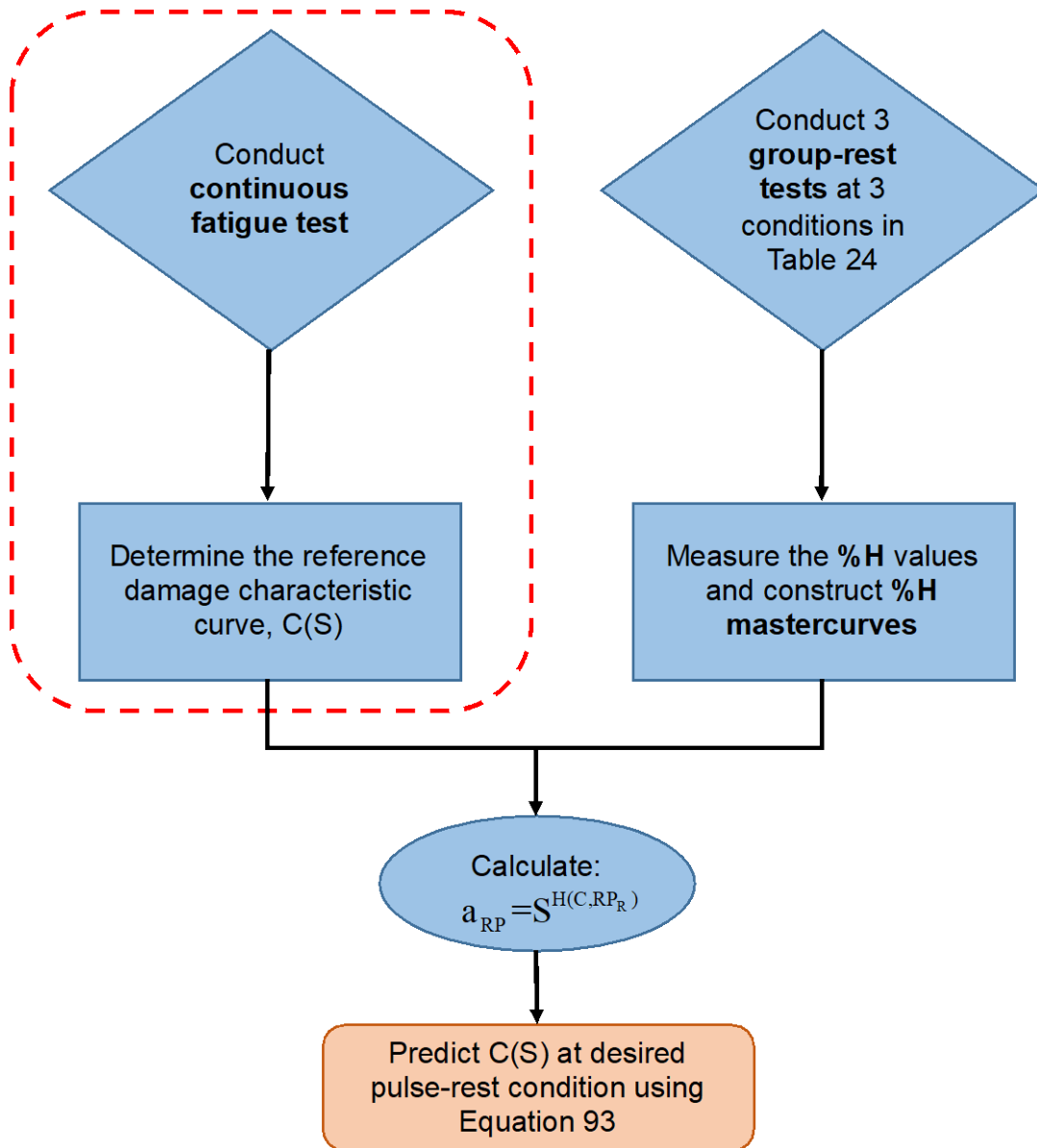
The protocol for characterizing the proposed healing model is composed of three group-rest tests at different conditions and one continuous loading test, which is a typical AMPT Cyclic Fatigue test. Therefore, the overall healing test protocol actually requires only three group-rest tests in addition to the continuous loading test that is needed for fatigue characterization without rest periods.

Table 26 presents the amount of time the proposed characteristic protocol saves. As the table shows, the testing time needed to conduct the characteristic tests (including the replicate testing and analysis) is 3 d, whereas 60 d of testing is needed to conduct the pulse-rest tests. Three group-rest healing tests and one continuous fatigue test are needed for the proposed protocol, which is a total of four tests. In this example, the research team assumed needing damage characteristic curves for only five different pulse-rest tests.

Table 26. Example showing the amount of time saved using proposed protocol.

Item	Proposed Protocol (Group-Rest Test)	Empirical Protocol (Pulse-Rest Test)
Number of tests	3	5
Number of replicates	3	3
Total number of tests	9	15
Required time (d)	3	60

Figure 78 presents a flowchart summarizing the proposed test protocol and analysis procedure for obtaining the damage characteristic curves for the pulse-rest tests using the damage characteristic curve of the continuous test and the percent healing data from the group-rest tests.



Source: FHWA.

Figure 78. Illustration. Flowchart of proposed protocol for healing model.

Findings from the Healing Model

Testing and analysis of the fatigue test data with rest periods resulted in the following findings, which led to the healing model developed in this study:

- The percent healing concept characterizes the healing behavior of asphalt material during a rest period.

- The percent healing of asphalt material increases as test temperature, rest period duration, and pseudostiffness increase, which indicates a less damaged material heals more.
- The $t-TS$ concept applies to asphalt concrete material not only in the viscoelastic range but also during rest periods when the material heals. Therefore, a percent healing master curve can be developed by combining the rest period with temperature.
- A healing model based on the percent healing master curve and damage function was developed in this study.
- The proposed test protocol for the characterization of the healing model consists of three group-rest healing tests and the continuous cyclic fatigue test.
- The healing model that is characterized by the group-rest healing tests and a continuous cyclic fatigue test predicts the damage characteristic curve for pulse-rest test conditions reasonably well, which are similar to the field loading conditions.
- The proposed healing model and test protocol were verified using two different mixtures.
- The healing model combined with the S-VECD model can predict strain history and the predicted strain levels match the measured strain levels.

Although the developed healing model and test protocol provide an accurate evaluation of the healing potential of asphalt mixtures, the research team acknowledges that including the healing test in the PRS framework would cause the PRS testing program to be too lengthy for State highway agencies to adopt. Therefore, the research team recommends delaying implementing the developed healing test and model into the PRS framework until State highway agencies have become fully familiar with the AMPT cyclic fatigue and SSR tests.

SUMMARY OF TEST METHODS AND MODELS FOR PRS METHODOLOGY

The acceptance of PRSs by State highway agencies and contractors requires test equipment and associated hardware and software to be readily available, test methods to be efficient and standardized, and performance prediction models to be accurate and reliable. In this project, the research team developed the direct tension cyclic fatigue test (AASHTO TP 107) further and revised the SSR test to evaluate asphalt pavement fatigue cracking and rutting, respectively.⁽³⁷⁾ These test methods, in addition to the already available dynamic modulus test (AASHTO T 378), constitute the primary asphalt mixture characterization test methods for PRS methodology.⁽⁹⁾

The major strength of these test methods and associated models is that they can predict the cracking and rutting performance of the asphalt mixture of interest under a wide range of loading and climatic conditions in only 3 d of conditioning and testing. Additionally, the Excel-based data analysis program, FlexMAT, allows the seamless and automatic processing of AMPT-generated test results and the creation of input files for FlexPAVE's pavement performance predictions. The combined power of the AMPT performance test methods and seamless integration of the performance prediction models, FlexMAT and FlexPAVE, allow for efficient asphalt mixture characterization using various AQC's (e.g., volumetrics) and accurate

prediction of cracking and rutting performance of asphalt mixtures in pavement structures. The strengths of the AMPT performance test methods and associated models and programs provide the very foundation for the AM-PRS.

CHAPTER 5. FLEXPAVE PROGRAM

INTRODUCTION

Reasonable stress–strain analysis is a key component in pavement design and predicting pavement life. Given the complexity of variables like pavement life, traffic loading, and temperature variations, various approximation methods can predict pavement performance. Despite differing assumptions, these prediction methods aim to reduce analysis that takes millions of cycles over several years to a few hundred analyses for a single cycle of loading.

One such predictive analysis method is the three-dimensional finite-element method (3D FEM), which is a sophisticated tool for pavement performance analysis that can model the responses of 3D pavement under a moving load.^(104,105) Although the 3D FEM is capable of including the viscoelasticity and nonlinearity of pavement layers, fatigue cracking, and rutting, its computational cost is prohibitively expensive. Therefore, more practical approaches are often used to conduct pavement performance analyses.

The most basic method is layered elastic analysis (LEA), in which the pavement is idealized as a layered elastic system under a stationary axisymmetric load. In this method, the normal and radial stresses and strains are often computed using a Fourier-Bessel transform.⁽¹⁰⁶⁾ However, LEA can lead to inaccurate responses because traffic loading (i.e., tire pressure) is neither stationary nor circular and asphalt concrete exhibits significant viscoelastic behavior, especially under moving loads.

Layered viscoelastic moving-load analysis (LVEMA) is an improvement over LEA because it efficiently handles viscoelasticity and moving load effects with the help of Fourier transforms. LVEMA is more appealing than LEA for pavement stress analysis, although it still does not capture the stress redistribution effects due to damage. Taking LVEMA into consideration, the research team developed a 3D layered viscoelastic FEM code with moving loads to calculate the responses and performance of asphalt pavement and designated this software program the FlexPAVE program. The advantages of the FlexPAVE program include:

- Asphalt concrete shows a significant amount of viscoelasticity, and thus, the behavior of asphalt concrete depends on both loading frequency and temperature. Pavements undergo wheel loading at a vast range of frequencies as well as different temperature distributions throughout the depth of the pavement over the lifetime of the pavement, such that the whole structural behavior of the pavement significantly over time. The FlexPAVE program accounts for the effects of loading frequency and temperature that change along pavement depth on pavement performance.
- The FlexPAVE program can assign each pavement layer its own material and structural properties. For granular material, the FlexPAVE program can assume anisotropic elasticity with the axis of symmetry in the depth direction.
- The FlexPAVE program takes advantage of Fourier transform assumptions and time-scale separation to reduce computational costs. The 3D moving load layer analysis

considers damage (rutting and fatigue) and can still complete a simulation within a relatively short time compared with other viscoelastic analysis programs.

- The FlexPAVE program's graphical user interface (GUI) is designed to facilitate the processes of data inputs and outputs.

The research team performed the pavement simulations presented in this report using FlexPAVE version 1.1. Although FlexPAVE version 1.1 provides an efficient way to perform viscoelastic structural modeling under moving loads using MATLAB, the approach has the following limitations:

- FlexPAVE version 1.1 cannot capture the effect of load redistribution due to the reduced modulus of the pavement in the damaged region given its layered analysis approach.
- MATLAB is inherently less efficient than programming languages like C++, although the research team explored several avenues for increasing computational efficiency.

The research team is currently working on FlexPAVE version 2.0, which remedies these shortcomings of FlexPAVE version 1.1 by implementing the Fourier finite element (FFE) method in a highly efficient C++ language. FlexPAVE version 2.0 will be able to capture load redistribution as well as possibly include nonlinear models for aggregate base and subgrade and models for thermal and reflective cracking.

SIMPLIFYING IDEA

Most of the relevant existing analysis tools are built on elastic analysis even though asphalt concrete is a viscoelastic material. Viscoelastic analysis would be more sophisticated than elastic analysis and would increase the accuracy for both the responses and the performance of asphalt pavement. However, LVEA requires huge computing expenditures, especially in terms of runtime. Therefore, reducing the run-time without losing accuracy has been a goal of developing LVEA software.

The research team used reasonable assumptions to develop appropriate software, with the proposed framework based on an approach that includes various assumptions and observations regarding the pavement's structure, material properties of the pavement layers, thermal variations, and traffic variations. The assumptions and the rationale are as follows:

- Pavement length (in the traffic direction) and width are both large areas compared with the size of the tire and pavement thickness. Thus, if the approach ignores the effects of fatigue cracking and rutting on the material's properties and pavement structure, it can approximate the pavement as an infinite layered system in which the material properties only in terms of depth. The distresses (fatigue cracking and rutting) in the program result from the previous steps taken to update the distresses in the next steps, not from changing the stress and strain distributions due to material and geometric changes.
- Temperature variation is only captured in terms of pavement depth and is assumed to be constant over the entire plane at a given depth, because the temperature variation along

the length of the pavement is not significant, and the material properties are assumed to be isotropic on the plane perpendicular to the depth direction.

- The pavement temperature profile (throughout the pavement depth) is assumed to be cyclic within a period of 1 yr. Although the yearly variations can be modeled with a corresponding increase in computational cost, the variation is not significant given that the stress redistribution effects due to damage are not considered in the analysis.
- Temperature variations are captured using hourly data. Although thermal variation at a finer time increment can be captured, it is unnecessary given the approximate nature of the analysis.
- Traffic load is idealized as a cyclic load with a constant shape (tire footprint) and speed.
- Traffic loading varies by seconds, whereas temperature varies by hours. The temperature profile and the resulting effects on the material properties are assumed to be fixed for the traffic analysis of a given segment.
- The base and subgrade, despite their nonlinear nature, are idealized as linear elastic materials because the effects of nonlinearity are not significant compared with the approximations inherent in the modeling of traffic and temperature variations.

Time-Scale Separation

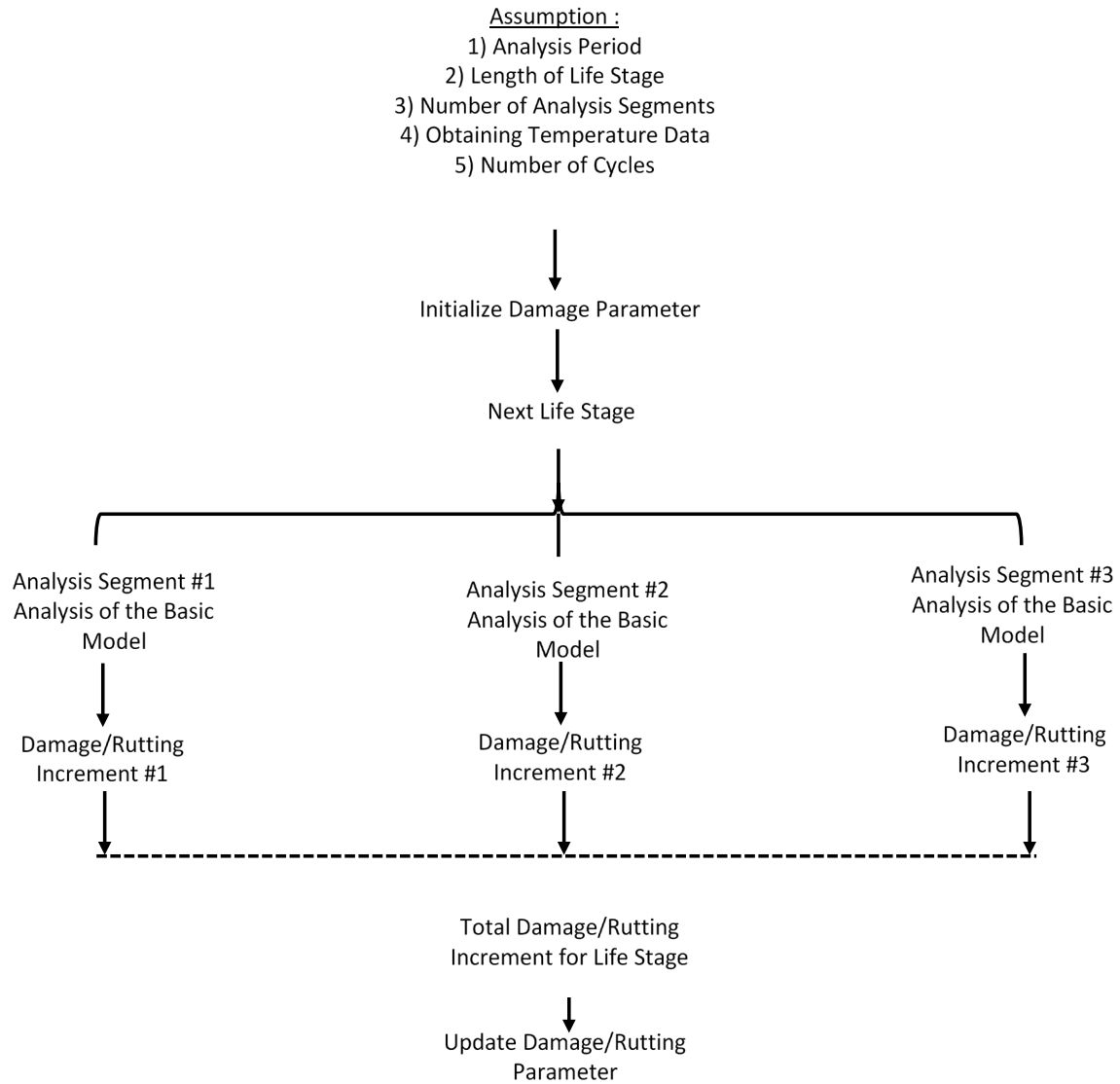
The observations and assumptions presented in the previous section allow the analysis to be reduced from millions of load cycles to fewer than 100 independent analyses by using a segmented analysis scheme.⁽¹⁰⁷⁾ The intention was to divide the pavement life into different stages, with each stage characterized by seasonal or monthly variations in temperature. The FlexPAVE program updates the damage at the end of each life stage and uses this updated value for the next stage. The typical length of a life stage is between 2 weeks and a few months, depending on the desired level of accuracy. Because the yearly variations in temperature are ignored by the program, the stage division is restricted to the first year of pavement life, and the research team assumed the pavement responses during that stage repeat within the remainder of that pavement's life. Additionally, they divided each life stage further into analysis segments, whereby an analysis segment is assumed to have a constant temperature as well as a constant traffic load level and frequency. Typically, an analysis segment is a block of a few hours per day over the life stage. The number of segments depends on the desired level of accuracy and the hourly variations of temperature and traffic (figure 79).

The program computes thermal and traffic stress values for each analysis block during the first year of the pavement life. It computes the thermal stress levels using standard thermal analysis that employs the Enhanced Integrated Climatic Model (EICM) temperature history.

The pavement's response to traffic and thermal loading depends on three-dimensional coordinates (x , y , and z) as well as the time domain. The FFE method is used in the FlexPAVE program to eliminate the time dimension as well as the spatial dimension in the direction of traffic (y). In addition, the FlexPAVE program conducts Fourier transform in the width direction

(x) of the pavement system. As a result of using Fourier transform, the pavement analysis reduces from four dimensions (x , y , z , and t) to one dimension (z).

Due to this simplification made by reducing the dimensions, the FFE method is more efficient than the direct 3D FEM by orders of magnitude. This difference can be justified by comparing the large amount of memory needed to analyze and store the results of dynamic moving load data to that of one-dimensional analysis. The Fourier transform helps the FlexPAVE program decrease the number of analyses required while simultaneously capturing the 3D effects accurately.



Source: FHWA.

Figure 79. Illustration. Pavement performance analysis framework in the FlexPAVE program.

Three time scales are associated with a pavement's responses and performance during the lifetime of the pavement. The first scale is related to traffic loading, which varies in the order of seconds. The second scale is related to temperature and thermal stress, which varies in the order of hours. The last scale is pavement performance, which varies in the order of months. Considering these three scales, the research team found it rational to assume that pavement distress is approximately constant when performing traffic and thermal stress analyses.

This approach can simulate the effect of millions of cycles of traffic loading on a pavement using a few hundred independent stress analyses at different levels of distresses and temperatures, which means the basic building block for pavement performance modeling is performing stress analysis under a single cycle of traffic loading and at a given temperature profile. The FlexPAVE program updates distresses based only on the previous steps regarding distress. There is no change in stress and strain distribution due to distress.

Segments

At the beginning of each analysis segment, the FlexPAVE program extracts the expected traffic data for the whole segment. The program considers the annual growth rate in the traffic data. The FlexPAVE program assumes some functions for wheel loading and performs Fourier transform for the traffic and width directions to obtain loading vectors for the different values of frequencies and wave numbers.

The FlexPAVE program assumes a constant temperature profile (i.e., the average temperature of the segment) to perform pavement analysis under the moving load during a segment. The program performs analysis assuming a single wheel and then calculates the pavement response under a moving vehicle using interpolation. Superposing the loads results in the pavement's response due to traffic loading.

The program used hourly changes in temperature for the thermal analysis. It performs Fourier transform in the time domain to find the temperature distribution in the frequency domain. After analyzing the pavement layer system under thermal loading, the program applies an inverse Fourier transform to obtain the response in the time domain.

According to the definition of segment analysis, damage (fatigue cracking and rutting) is assumed to be constant in each segment. The FlexPAVE program superposes the stress and strain components induced by traffic loading and thermal loading. The program assumes that an undamaged material is isotropic and damage is symmetrically in the direction of the maximum experienced principal stress. As such, the damaged material is transversely anisotropic with the local axis of symmetry that coincides with the maximum experienced stress. After finding the maximum principal stress, the FlexPAVE program uses standard transformation to determine the local stress from the stress vector in the x - y - z coordinate system.

FlexPAVE calculates the change in pseudostiffness (ΔC) for one pass of traffic loading. The program uses this value, which is calculated for all analysis segments, to compute the induced damage for each life stage.

For the rutting analysis, the FlexPAVE program calculates the viscoplastic strain increment at each step for the viscous layers. This approach is based on a reduced experienced number of

cycles at each segment. The program uses the temperature profile, vertical stress from the response analysis, and load time (or pulse time) to convert the experienced number of cycles into the reduced number of cycles. Then, it calculates the permanent strain. The FlexPAVE program utilizes the same permanent deformation models as the MEPDG to estimate the rut depths of granular layers.

Life Stage

The life stage is a short period of a pavement's service life, and the distresses of the previous life stage are used as the initial distresses of the current life stage in the FlexPAVE program. All damage effects must be summed up at the end of the last segment in each life stage.

FlexPAVE calculates the average pseudostiffness value at the end of each life stage for all points within the pavement section. Predicting the ratio of the experienced number of load cycles (N) to the maximum allowable cycles of loading (N_f), which is designated as the damage factor, demands knowing a failure criterion a priori. FlexPAVE uses either the D^R or G^R criterion to calculate the remaining life of the given pavement section at each stage.

In the D^R -based formulation, FlexPAVE calculates the ratio of the difference between the intact material pseudostiffness and the average absorbed pseudostiffness for the experienced number of cycles to the absorbed pseudostiffness up to failure. It defines the damage factor as equal to this ratio in D^R -based methodology.

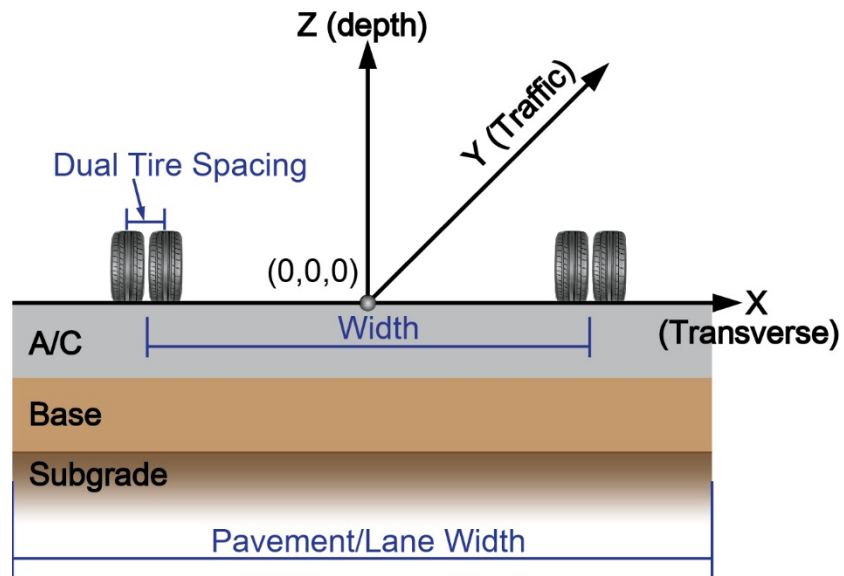
In the G^R -based formulation, FlexPAVE calculates the released pseudostrain energy for a large number of load cycles ($N > 1$). It obtains the maximum allowable cycle of loading by intersecting the released pseudostrain energy and the number of load cycles using the G^R criterion.⁽⁶⁵⁾ G^R -based methodology considers the damage factor to be equal to the ratio of N to N_f .

For the fatigue cracking analysis, the FlexPAVE program calculates the weighted average of the pseudostiffness decrement for each segment. It uses nonlinear extrapolation to find the pseudostiffness evolution at the last cycle of the current life stage. This value is used for the analysis segments at the next stage. For the rutting analysis, the FlexPAVE program sums up all the reduced experienced number of cycles in the current life stage to find the final viscoplastic strain increment. It then integrates this viscoplastic strain throughout the pavement depth to calculate the rut depth.

LAYERED VISCOELASTIC MOVING LOAD ANALYSIS

Layered viscoelastic moving load analysis considers an infinite pavement under a traffic load that is moving with a constant speed (V). It uses the coordinate x for the transverse direction ($-\infty < x < +\infty$), y for the traffic direction ($-\infty < y < +\infty$), and z for the depth direction ($0 < z < z_{\max}$; $z = 0$ is the top surface). The spatial distribution of the load at $t = 0$ is given by $p(x,y)$.

The FlexPAVE program uses a rod element with three degrees of freedom at each node. Figure 80 presents the direction convention used in the FlexPAVE program.



Source: FHWA.

Figure 80. Illustration. Coordinate definition in the FlexPAVE program.

The FlexPAVE program uses zero continuity in its finite element discretization, and thus, the strain and stress values may not be continuous. It will use the averages of the corresponding stress and strain values as the final results. The program indicates the Fourier transform of any variable with a hat shape on top of the variable. The pavement system may have both viscous and elastic layers depending on the properties and assumptions of each layer; therefore, the FlexPAVE program uses two different material models to make the stiffness matrix: an elastic layer and a viscoelastic layer.

Elastic Layer

The FlexPAVE program considers transverse anisotropy in addition to elastic isotropic properties for elastic layers. Equation 94 shows the stress-strain relationships used in the FlexPAVE program. For the elastic state, the equation only uses the same value for the elastic modulus and Poisson's ratio for all directions.

$$\begin{Bmatrix} \sigma_{xx} \\ \sigma_{yy} \\ \sigma_{zz} \\ \sigma_{yz} \\ \sigma_{zx} \\ \sigma_{xy} \end{Bmatrix} = \begin{bmatrix} \frac{1-\nu_{pz}\nu_{zp}}{E_p E_z \Delta} & \frac{\nu_p + \nu_{pz}\nu_{zp}}{E_p E_z \Delta} & \frac{\nu_{zp} + \nu_p \nu_{zp}}{E_p E_z \Delta} & 0 & 0 & 0 \\ \frac{\nu_p + \nu_{pz}\nu_{zp}}{E_p E_z \Delta} & \frac{1-\nu_{pz}\nu_{zp}}{E_p E_z \Delta} & \frac{\nu_{zp} + \nu_p \nu_{zp}}{E_p E_z \Delta} & 0 & 0 & 0 \\ \frac{\nu_{pz} + \nu_p \nu_{pz}}{E_p^2 \Delta} & \frac{\nu_{pz}(1+\nu_p)}{E_p^2 \Delta} & \frac{1-\nu_p^2}{E_p^2 \Delta} & 0 & 0 & 0 \\ 0 & 0 & 0 & 2G_{zp} & 0 & 0 \\ 0 & 0 & 0 & 0 & 2G_{zp} & 0 \\ 0 & 0 & 0 & 0 & 0 & 1-2\nu_p \end{bmatrix} \begin{Bmatrix} \varepsilon_{xx} \\ \varepsilon_{yy} \\ \varepsilon_{zz} \\ \varepsilon_{yz} \\ \varepsilon_{zx} \\ \varepsilon_{xy} \end{Bmatrix} \quad (94)$$

Where:

E_p = elastic modulus in the x - y symmetry plane.

ν_{pz} = Poisson's ratio in the x - y symmetry plane.

ν_{zp} = Poisson's ratio in the y - x symmetry plane.

ν_p = Poisson's ratio in the x direction.

E_z = elastic modulus in the z direction.

G_{zp} = shear modulus in the x - y symmetry plane.

$$\Delta = \frac{(1+\nu_p)(1-\nu_p-2\nu_{pz}\nu_{zp})}{E_p^2 E_z}$$

Viscoelastic Layer

The FlexPAVE program also considers the isotropic viscoelastic properties for asphalt layers, as shown in equation 95.

$$\sigma = \begin{Bmatrix} \frac{1}{(1+\nu)(1-2\nu)} \int E(t-\tau) \left[(1-\nu) \frac{\partial \varepsilon_{xx}}{\partial \tau} + \nu \frac{\partial \varepsilon_{yy}}{\partial \tau} + \nu \frac{\partial \varepsilon_{zz}}{\partial \tau} \right] d\tau \\ \frac{1}{(1+\nu)(1-2\nu)} \int E(t-\tau) \left[\nu \frac{\partial \varepsilon_{xx}}{\partial \tau} + (1-\nu) \frac{\partial \varepsilon_{yy}}{\partial \tau} + \nu \frac{\partial \varepsilon_{zz}}{\partial \tau} \right] d\tau \\ \frac{1}{(1+\nu)(1-2\nu)} \int E(t-\tau) \left[\nu \frac{\partial \varepsilon_{xx}}{\partial \tau} + \nu \frac{\partial \varepsilon_{yy}}{\partial \tau} + (1-\nu) \frac{\partial \varepsilon_{zz}}{\partial \tau} \right] d\tau \\ \frac{1}{1+\nu} \int E(t-\tau) \frac{\partial \varepsilon_{yz}}{\partial \tau} d\tau \\ \frac{1}{1+\nu} \int E(t-\tau) \frac{\partial \varepsilon_{zx}}{\partial \tau} d\tau \\ \frac{1}{1+\nu} \int E(t-\tau) \frac{\partial \varepsilon_{xy}}{\partial \tau} d\tau \end{Bmatrix} \quad (95)$$

Where:

ν = Poisson's ratio.

ε_{xx} = strain component in the xx plane.
 ε_{yy} = strain component in the yy plane.
 ε_{zz} = strain component in the zz plane.
 ε_{xy} = strain component in the xy plane.
 ε_{yz} = strain component in the yz plane.
 ε_{zx} = strain component in the zx plane.

The complex modulus depends on the temperature and reduced frequency. The FlexPAVE program applies Fourier transform to the compliance matrix and calculates this matrix for the whole range of frequencies. After defining the layer geometry by meshing all the layers and using the material properties to build the compliance matrix, the FlexPAVE program calculates the stiffness matrices for all existing layers, shown in equation 96.

$$\hat{\sigma} = \begin{Bmatrix} \hat{\sigma}_{xx} \\ \hat{\sigma}_{yy} \\ \hat{\sigma}_{zz} \\ \hat{\sigma}_{yz} \\ \hat{\sigma}_{zx} \\ \hat{\sigma}_{xy} \end{Bmatrix} = \begin{Bmatrix} \frac{i\omega E^*(\omega)}{(1+\nu)(1-2\nu)} ((1-\nu)\hat{\varepsilon}_{xx} + \nu(\hat{\varepsilon}_{yy} + \hat{\varepsilon}_{zz})) \\ \frac{i\omega E^*(\omega)}{(1+\nu)(1-2\nu)} ((1-\nu)\hat{\varepsilon}_{yy} + \nu(\hat{\varepsilon}_{xx} + \hat{\varepsilon}_{zz})) \\ \frac{i\omega E^*(\omega)}{(1+\nu)(1-2\nu)} ((1-\nu)\hat{\varepsilon}_{zz} + \nu(\hat{\varepsilon}_{xx} + \hat{\varepsilon}_{yy})) \\ \frac{i\omega E^*(\omega)}{(1+\nu)} (\hat{\varepsilon}_{yz}) \\ \frac{i\omega E^*(\omega)}{(1+\nu)} (\hat{\varepsilon}_{zx}) \\ \frac{i\omega E^*(\omega)}{(1+\nu)} (\hat{\varepsilon}_{xy}) \end{Bmatrix} \quad (96)$$

Where:

$E^*(\omega)$ = complex modulus in frequency domain.

$i = \sqrt{-1}$.

over-hat = the variables in complex domain.

FLEXPAVE PROGRAM ENGINES

All input parameters for pavement analysis and outputs can be operated and monitored through the FlexPAVE program's GUI. The GUI's environment is similar to that of the AASHTOWare Pavement ME, allowing agencies, asphalt engineers, and practitioners to quickly become familiar with the FlexPAVE program and run it with ease (AASHTOWare® v2.6, 2020; available from <https://me-design.com/MEDesign/>).

Users can obtain the stress, strain, and displacement of the pavement structure for the pavement response analysis within a couple of minutes using the program. For the pavement performance analysis, users can evaluate performance (i.e., rut depth and fatigue cracking) for 20 yr within 30

to 40 min. The FlexPAVE program is composed of several solvers that can efficiently calculate the responses and performance of asphalt pavements.

Solvers

This section individually describes different solvers used in the FlexPAVE program.

Load Solver

The FlexPAVE program performs Fourier transform in the traffic and width directions and solves for the pavement layers for a whole set of frequency/wave numbers. It performs this analysis for only one tire and uses inverse Fourier transform to capture the pavement's response in the time domain.

Thermal Solver

The FlexPAVE program assumes the plane strain condition in the traffic direction for the thermal analysis. The temperature profile for 1 yr is an input for the FlexPAVE program and is repeated for performance simulations that are longer than 1 yr. The program only performs Fourier transform in the time domain, and analyzes the pavement section for different values of frequency. It also uses inverse Fourier transform to find the pavement's thermal response in the time domain.

Damage (Fatigue) Solver

Damage increases as the number of cycles increases according to the damage characteristic curve. Based on the simplifying idea (discussed in the Simplifying Idea section), the FlexPAVE program extrapolates the damage for the sake of efficient simulation. As damage grows, an asphalt element will fail when the element reaches the ultimate state. The ultimate state is defined based on either the D^R criterion or the G^R criterion. The FlexPAVE program finds the maximum number of cycles to failure (N_f) based on the applied traffic and thermal loading. The damage index value is defined as the actual experienced number of cycles to the maximum capacity of the pavement obtained from the D^R curve. The damage index values are calculated at the end of each life. The damage index is calculated for each nodal point and varies between zero (no damage) and one (failure).

Rutting Solver

A modified version of the shift model, which is a permanent deformation model, utilizes the response results (vertical stress and pulse time) and inputs (temperature) to calculate the viscoplastic strain at a certain element.⁽¹⁾ It then calculates the rut depth by integrating the plastic strain throughout the pavement depth.

Traffic Analysis

Given that the material properties and geometry do not vary with t , x , and y ; the material properties are linear; and t , x , and y are unbounded, Fourier transform can be applied to reduce the problem dimension.

The FlexPAVE program performs Fourier transform on geometric discretization using equation 97.

$$\hat{u} = \sum_{j=1}^{Node\ Number} N_j(z) \hat{u}_j \quad (97)$$

Where:

z = pavement depth.

N_j = rod element shape function for node j .

\hat{u}_j = nodal displacement value for node j .

Equation 98 calculates the strain–displacement matrix (L).

$$\varepsilon = Lu \rightarrow \begin{Bmatrix} \hat{\varepsilon}_{xx} \\ \hat{\varepsilon}_{yy} \\ \hat{\varepsilon}_{zz} \\ \hat{\varepsilon}_{yz} \\ \hat{\varepsilon}_{zx} \\ \hat{\varepsilon}_{xy} \end{Bmatrix} = \begin{Bmatrix} ik_x & 0 & 0 \\ 0 & ik_y & 0 \\ 0 & 0 & \frac{\partial}{\partial z} \\ 0 & \frac{\partial}{\partial z} & ik_y \\ \frac{\partial}{\partial z} & 0 & ik_x \\ ik_y & ik_x & 0 \end{Bmatrix} \begin{Bmatrix} \hat{u}_x \\ \hat{u}_y \\ \hat{u}_z \end{Bmatrix} \rightarrow \hat{\varepsilon} = \hat{L}\hat{u} \quad (98)$$

Where:

k_x, k_y = wave number in the x and y directions.

u_x, u_y, u_z = displacement component in the $x, y,$ and z directions.

Calculating the total potential energy (π) of the system (equation 99) can give the element's stiffness matrix.

$$\delta\pi(\omega, k_x, z) = \int_{\Omega} \sigma \delta\hat{\varepsilon}^T dz = \int_{\Omega} N^T L^T i\omega L N dx dy \quad (99)$$

Where:

Ω is the domain of analysis.

Superscript T represents transpose of an operator/matrix.

To calculate the force vector p , the FlexPAVE program assumes a certain function for wheel load distribution. After calculating the load distribution function (equation 100), the FlexPAVE program performs Fourier transform on it to obtain load values in the frequency/wave number domains.

$$p(k_x, k_y, z, \omega) = \int_{-\infty}^{\infty} \int_{-\infty}^{\infty} \int_{-\infty}^{\infty} p(x, y - vt) e^{-ik_x x} e^{-ik_y y} e^{-i\omega t} dx dy dt \quad (100)$$

Applying $\bar{t} = t - y / V$ to equation 100 leads to equation 101.

$$p(k_x, k_y, z, \omega) = \int_{-\infty}^{\infty} \int_{-\infty}^{\infty} \int_{-\infty}^{\infty} p(x, \bar{t}) e^{-ik_x x} e^{-i(k_y + \frac{\omega}{V})y} e^{-i\omega \bar{t}} dx dy d\bar{t} \quad (101)$$

Equation 101 is nonzero if and only if $k_y = -\omega / v$.

The FlexPAVE program needs to know the pavement length and vehicle velocity to calculate the passing time (t) and determine the frequency range. The maximum frequency for the load analysis is calculated as $2\pi/(t/n_t)$. In this equation, n_t is the number of points in the time domain. The maximum wave number frequency for the load analysis is calculated as $2\pi/(w/n_x)$, n_x is the number of points in the width direction, and w is the pavement width.

For each frequency (ω) and wave number (k_x), the FlexPAVE program builds a stiffness matrix and vector force. Based on these two factors, the FlexPAVE program calculates the pavement response for any frequency and wave number set.

Thermal Analysis

The second step in each analysis segment is determining the thermal response of the pavement layers. The first assumption in thermal analysis is that pavement temperature varies only as a function of pavement depth and is constant in the traffic or transverse directions. The second assumption is that thermal displacement is zero in the traffic direction because the pavement is infinite. Therefore, the thermal stress levels can be determined using the plane strain problem (equation 102) with the pavement cross-section.

$$\varepsilon = \begin{Bmatrix} \varepsilon_{xx} \\ \varepsilon_{zz} \\ \varepsilon_{zx} \end{Bmatrix} = \begin{bmatrix} \frac{\partial}{\partial x} & 0 \\ 0 & \frac{\partial}{\partial z} \\ \frac{\partial}{\partial z} & \frac{\partial}{\partial x} \end{bmatrix} \begin{Bmatrix} u_x \\ u_z \end{Bmatrix} = Lu \xrightarrow{FT} \begin{bmatrix} ik_x & 0 \\ 0 & \frac{\partial}{\partial z} \\ \frac{\partial}{\partial z} & ik_x \end{bmatrix} \begin{Bmatrix} \hat{u}_x \\ \hat{u}_z \end{Bmatrix} = \hat{L}\hat{u} \quad (102)$$

Where FT stands for Fourier transform.

The compliance matrix is the same as the matrices used in traffic analysis. Because the FlexPAVE program considers the plane strain condition in the traffic direction, all rows and

columns in the compliance matrix that correspond to ε_{xx} , ε_{yy} , and ε_{zy} should be omitted to obtain the compliance matrix for thermal analysis.

Equation 103 uses the thermal expansion coefficient (α) and the temperature increment (ΔT) to determine the body force vector.

$$f = \begin{Bmatrix} f_x \\ f_z \end{Bmatrix} = -\int_0^t \frac{E(t-\tau)}{1-2\nu} \alpha \begin{bmatrix} \frac{d(\Delta T)}{dx} \\ \frac{d(\Delta T)}{dz} \end{bmatrix} d\tau \xrightarrow{FT} \bar{f} = \frac{E^*(\omega)}{1-2\nu} \alpha \begin{bmatrix} ik_x \Delta T \\ \frac{d(\Delta T)}{dz} \end{bmatrix} \quad (103)$$

Where:

f_x is the force component in the x direction and f_y is the force component in the y direction.

$E^*(\omega)$ = complex modulus in frequency domain.

$E(t)$ = relaxation modulus.

The rest of the formulation is similar to that of traffic loading. The problem set in equation 103 can be solved using an efficient one-dimensional finite-element method within the pavement depth for a given wave number (k_x) and frequency (ω). The thermal stress in the traffic direction can be determined after finding the stress in the pavement section.

Damage Calculation

The FlexPAVE program can evaluate fatigue cracking using the VECD model in which asphalt concrete is modeled as a viscoelastic material with microcrack-induced damage.⁽¹⁰⁸⁾ The VECD model can represent the effect of damage on the material stiffness, where S is the damage parameter and ε^R is the pseudostrain.⁽⁹³⁾ Then, laboratory cyclic testing can provide the damage characteristic curve.

Equation 104 calculates the damage evolution law.

$$\frac{ds}{dt} = \left(-\frac{\partial W^R}{\partial s} \right)^\alpha = \left(-\frac{1}{2} \frac{\partial c}{\partial s} (\varepsilon^R)^2 \right)^\alpha \quad (104)$$

The current model can be extended to the multiaxial case using the definition for pseudostrain energy density function, reflected in equation 105.

$$W^R = \frac{1}{2} \left[A_{11} e_v^2 + A_{22} e_d^2 + 2A_{12} e_d e_v + A_{66} (e_s)^2 \right] \quad (105)$$

Where:

$$e_v = \varepsilon_{11}^R + \varepsilon_{22}^R + \varepsilon_{33}^R$$

$$e_d = \varepsilon_{33}^R - \frac{e_v}{3}$$

$$e_s = \varepsilon_{11}^R - \varepsilon_{22}^R.$$

$A_{11}, A_{22}, A_{12}, A_{66}$ are the components of the normalized modulus tensor that captures the Poisson's effect among other things.

For the multiaxial state of stress, the damage evolution law can be written as expressed in equation 106.

$$\frac{\partial S}{\partial t} = \frac{1}{2^\alpha} \left(-\frac{\partial C}{\partial S} \right)^\alpha \left(\frac{1}{3} e_v^R + e_d^R \right)^{2\alpha} \quad (106)$$

Equation 107 uses the chain rule integrated with respect to time to calculate the change in the normalized stiffness value in a single cycle.

$$\Delta S = \frac{1}{2^\alpha} \left(-\frac{\partial C}{\partial S} \right)^\alpha \int_0^{T_{cycle}} \left(\frac{1}{3} e_v^R + e_d^R \right)^{2\alpha} dt \quad (107)$$

Where T_{cycle} is the period of the cyclic moving load, and ΔS is the change in damage parameter.

The FlexPAVE program calculated the damage increment for each segment assuming constant pseudostiffness at the beginning of each stage. Then, the research team conducted nonlinear extrapolation by solving the ordinary differential equation in equation 108 to calculate the damage during the stage.

$$\Delta C = \sum_{i=1}^{N_{segments}} \left(\frac{dC}{ds} \right) \left(\frac{ds}{dt} \right),$$

$$\frac{\partial C}{\partial n} = \Delta C \left(\frac{1-C}{1-C_0} \right)^{\alpha(1-\frac{1}{b})}, \quad (108)$$

Where:

C_0 = pseudostiffness at the start of each life stage.

n = a cycle in each analysis segment.

$N_{segments}$ = total number of cycles at the end of each analysis segment.

In the G^R -based methodology, FlexPAVE calculates the C value for a large N and then calculates W_R^C , as show in equation 109.

$$W_R^C = \frac{1}{2} (1-C) W^R \quad (109)$$

The FlexPAVE program can find the evolution of the pseudostrain energy as the number of cycles increases. This relationship between W_R^C and N can then be used to calculate the number

of cycles at failure (N_f) by intersecting the failure criterion that the user entered as a material property.

In the D^R -based methodology, FlexPAVE calculates the value of equation 110 at the end of each life stage.

$$\begin{aligned} \frac{N}{N_f} &= \frac{C_{intact} - C_{average}^{current}}{C_{intact} - C_{average}^{failure}} \\ C_{average}^{current} &= \frac{\int C dN}{N} \\ C_{average}^{failure} &= 1 - D^R \end{aligned} \quad (110)$$

Where C_{intact} , $C_{average}^{current}$, and $C_{average}^{failure}$ are average pseudostiffnesses in the intact condition, at the current time, and at failure, respectively.

Rutting Calculation

The FlexPAVE program implements the shift model, a permanent deformation model, to evaluate the rut depth of asphalt pavement.⁽¹⁾ The shift model can simulate the effects of temperature, load time and vertical stress on permanent deformation, and number of cycles. The following three sections discuss these four parameters.

Temperature

Pavement temperature has a significant effect on rutting and is an input in the FlexPAVE program. The FlexPAVE program provides a pavement temperature database of about 450 climate sections calculated by the EICM software. Users can enter the pavement temperature, and the FlexPAVE program uses the average temperature for each segment of analysis as the temperature for the rut depth calculation.

Vertical Stress and Load Time

Vertical stress plays a major role in rut depth. The shift model is a uniaxial model and thus assumes constant confining pressure of 10 psi (70 kPa), given that 10 psi might be considered an average confining pressure of the whole depth of an asphalt pavement. The research team applied the vertical stress (σ_{zz}) obtained from the FlexPAVE program response analysis to the shift model.

The research team used the vertical stress history over time to calculate the load time, or pulse time (t_p), at a given nodal point. The stress-time history was fitted with a haversine function, and the period of the function is the load time. Reduced load time can be calculated by combining the time and temperature through t -TS at the given nodal point.

The FlexPAVE program analysis for various conditions results in a normalized relationship between load time and pavement depth, which is expressed as equation 111.

$$\frac{t_p}{t_p^{surface}} = 0.172 \times \text{pavement depth} + 0.849 \quad (111)$$

Where $t_p^{surface}$ is the pulse time at the surface of an asphalt pavement and is calculated from the vehicle speed and tire contact area.

Instead of fitting all the vertical stress levels to obtain the load time, the research team implemented equation 111 into the FlexPAVE program analysis for computational efficiency.

Using vertical stress and reduced load time, equations 112 and 113 calculate the stress shift factor and reduced load time shift factors, respectively.

$$a_{\sigma_v} = Q \times \left(\log\left(\frac{\sigma_v}{P_a}\right) - 0.877 \right) \quad (112)$$

$$a_{\xi_p} = p_1 \log\left(\frac{\xi}{\xi_p}\right) + p_2 \quad (113)$$

Number of Cycles

Vertical stress and reduced load time are important factors in the current rutting model. After calculating the required shift, equation 114 calculates the reduced number of cycles (N_{red}). The permanent strain master curve calculates permanent strain (refer to equation 114) using N_{red} , and the FlexPAVE program then calculates the rut depth using cumulative summation of the permanent strain level at each node multiplied by the element length.

$$N_{red} = N \times 10^{(a_{\xi_p} + a_{\sigma_v})} \quad (114)$$

Extrapolation

This section describes methods for extrapolating damage and permanent strain.

Damage Extrapolation

The total damage increment due to traffic and thermal loading should be calculated at the end of each stage. The FlexPAVE program uses weighted averages of the damage increments of all the segments in each stage using equation 115.

$$\Delta C_{comb} = \frac{\sum_i^{Segments} N_i \Delta C_i(C_0)}{\sum_i^{Segments} N_i} \quad (115)$$

Where ΔC_{comb} is the change in pseudostiffness due to combined effect of traffic and thermal loading.

Equation 116 calculates the final damage value for each point using the nonlinear extrapolation formula. There is no need to extrapolate C ; the C values only need to be calculated at the end of

the last cycle of loading. The FlexPAVE program finds the final C value for the mesh points. Because all the output data should be shown for the evaluation points, the FlexPAVE program uses interpolation to find the damage values.

$$\frac{\partial c}{\partial t} = \Delta C_{comb} \left(\frac{1-c}{1-c_0} \right)^{\alpha \left(1 - \frac{1}{b}\right)} \quad (116)$$

Rutting Extrapolation

Similar to damage, the total rut depth due to all traffic loading for each stage should be calculated. The FlexPAVE program uses weighted averages to calculate the net value for N , here in equation 117 and equation 118.

$$\Delta N_{combo,j} = \frac{\sum_{i=1}^{Num\ of\ Segments} N_{i,j} \Delta N_{i,j}}{\sum_{i=1}^{Num\ of\ Segments} N_{i,j}} \quad (117)$$

Where:

$\Delta N_{combo,j}$ = number of loading cycles for stage j .

$N_{i,j}$ = number of traffic loading cycles for segment i in stage j .

$\Delta N_{i,j}$ = reduced number of loading cycles for segment i in stage j .

$$N_t = \sum_{j=1}^{Current\ stage-1} N_j \Delta N_{combo,j} + N_{Current\ Stage} \Delta N_{Current\ Stage} \quad (118)$$

Where:

N_t = total number of loading cycles from the beginning of traffic opening until the end of the current stage.

$N_{Current\ Stage}$ = number of loading cycles for the current stage.

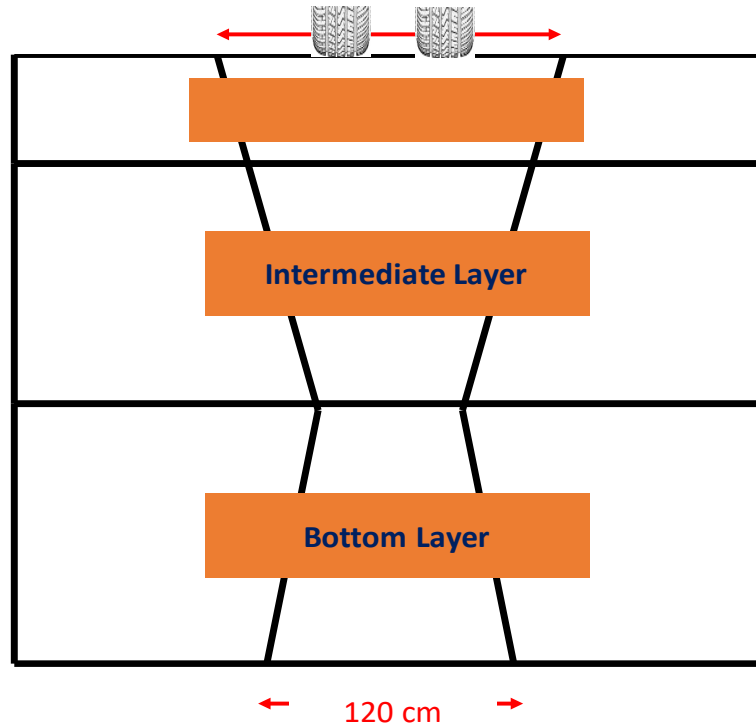
$\Delta N_{Current\ Stage}$ = total number of reduced cycles of loading for the current stage.

Then equation 65 calculates the permanent strain.

Percent Damage Definition

FlexPAVE 1.1 uses two overlapping triangles to form a reference area within which the damage evolution can be considered. The top inverted triangle has a 170-cm-wide base located at the top of the surface layer and a vertex located at the bottom of the bottom asphalt layer. The 120-cm-wide base of the second triangle is located at the bottom of the bottom asphalt layer and its vertex is positioned at the surface layer. Figure 81 presents the final shape of these overlapping triangles. The research team determined the shape and dimensions of the reference area based on an investigation into the many damage contours generated in this project for various mixtures and pavement structures. As such, the research team has not observed any

damage outside of this area. Therefore, including the area outside this reference area would cause the changes in the damaged areas to appear less sensitive once the percent damage is calculated.



© 2018 KSCE Journal of Civil Engineering. (DTFH61-08-H-00005)
1 cm = 0.4 inch.

Figure 81. Illustration. Reference area for percent damage definition.⁽¹⁰⁹⁾

The research team defined the percentage of damage (referred to as percent damage) as the ratio of the sum of the damage factors within the reference cross-section area to the reference cross-section area, as shown in equation 119.

$$\text{Percent Damage} = \frac{\sum_{i=1}^M (\text{Damage Factor})_i \times A_i}{\sum_{i=1}^M A_i} \quad (119)$$

Where:

- i = nodal point number for nodes located within the given reference cross-section.
- M = total number of nodal points located within the given reference cross-section in finite-element mesh.
- A_i = area represented by nodal point i in the finite-element mesh.
- $\sum A_i$ = reference area.

The damage factor in equation 119 is defined using the D^R criterion in FlexPAVE, as shown in the equation 120:

$$Damage\ Factor = \frac{0.8 - C_{avg}}{-0.2 + D^R} \quad (120)$$

Where C_{avg} is the average pseudostiffness per cycle up to the current number of loading cycles. Therefore, the damage factor defined by the D^R criterion is the ratio of $(0.8 - C_{avg})$, which represents the average reduction in pseudostiffness per cycle up to the current number of load cycles, to D^R , which represents the average reduction in pseudostiffness per cycle up to failure.

FLEXPAVE PROGRAM FEATURES

This section describes the various features included in the FlexPAVE program.

General Information

The User Manual for the FlexPAVE program, presented in Appendix A, details the features of the program. The FlexPAVE program offers the following two types of analysis:

- **Response analysis.** The FlexPAVE program analyzes the pavement's response under one cycle of loading at a certain temperature distribution. The total time required for this analysis is about a minute.
- **Performance analysis.** The FlexPAVE program analyzes pavement performance (fatigue cracking and rutting) for the entire period of the pavement's design life. The average total run time for the analysis is less than an hour. Users can select "Pavement Response Analysis" or "Pavement Performance Analysis," as shown in figure 82. If the user selects the performance analysis option, they can then also select performance models. The current version of the FlexPAVE program does not include an aging model but future versions most likely will.

The screenshot displays two main panels. The left panel, titled 'Analysis Options', contains two radio buttons: 'Pavement Response Analysis' (unselected) and 'Pavement Performance Analysis' (selected). Below these are two sub-sections: 'Fatigue Options' with checkboxes for 'Fatigue Cracking', 'Thermal Stress', 'Healing', and 'Aging' (all checked); and 'Rutting Options' with a checked checkbox for 'Rutting'. The right panel, titled 'Pavement Construction Timeline', features three rows of date and duration inputs: 'Pavement Construction Date' (January, 2014), 'Traffic Opening Date' (January, 2014), and 'Pavement Design Life (years)' (20).

Source: FHWA.

Figure 82. Illustration. Pavement performance analysis and design life.

Materials and Structure

This section describes analytical representations of asphalt layers and unbound layers.

Viscoelastic Analysis

The FlexPAVE program offers three options for importing the dynamic modulus values of asphalt layers: the dynamic modulus test, the master curve of the dynamic modulus, and the Prony series.

The FlexPAVE program uses the Prony series in its engine. It converts dynamic modulus values and master curves data into Prony series coefficients. To convert test data into a Prony series, the FlexPAVE program first converts the data into a master curve. The program characterizes all Prony series coefficients by fitting the master curve and Prony series form in the frequency domain.

Isotropic and Anisotropic Elastic Material

The FlexPAVE program can consider the following two types of material for the base and sublayers:

- **Isotropic elastic material.** Users must enter two coefficients: the elastic modulus and Poisson's ratio.
- **Anisotropic elastic material.** Users must enter five coefficients.

Fatigue and Rutting

This section provides the required parameters for performance analysis of a pavement layer.

The FlexPAVE program offers the following two options for crack determination:

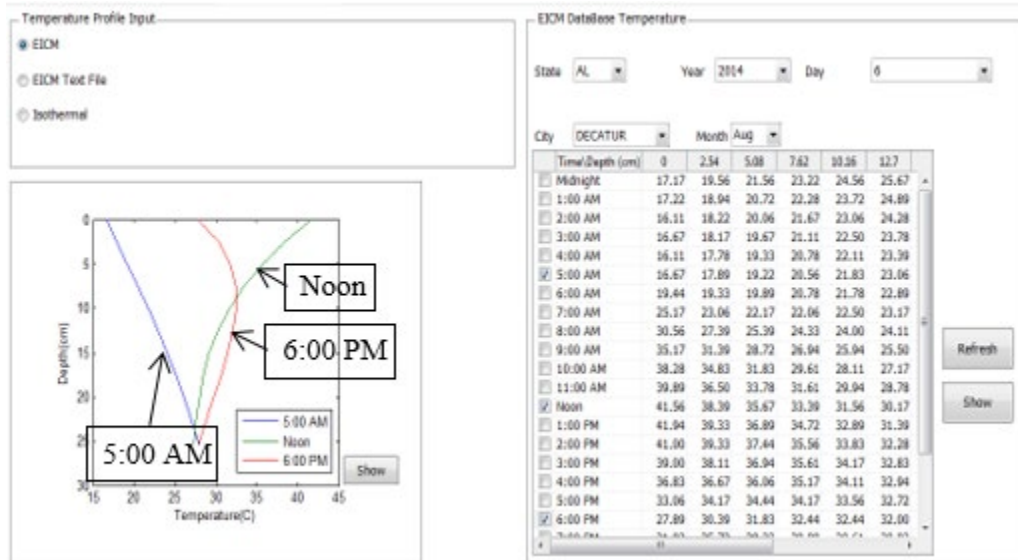
- **Static.** The FlexPAVE program determines the crack direction for the first cycle of loading, and applies the direction to all the other steps. The three modes of static crack types are:
 - **Auto.** The FlexPAVE program determines the maximum principal pseudostrain direction for the first segment and uses this direction for all other segments.
 - **Transverse.** The FlexPAVE program assumes that cracks propagate in the transverse direction.
 - **Traffic.** The FlexPAVE program uses traffic direction as the crack propagation direction.

- **Dynamic.** The FlexPAVE program updates the crack direction for each segment of analysis. This update is based on the direction of the maximum principal pseudostrain direction, and is the default setting in the FlexPAVE program.

Climate

The FlexPAVE program offers the following three options for importing temperature data:

- **EICM.** The FlexPAVE program provides a pavement temperature database of about 450 weather stations in the United States. The user can select a project site by choosing its State and city, and then the FlexPAVE program automatically loads the pavement temperature data. If the simulation period is longer than 1 yr, that 1 yr of temperature data will repeat as the 1-yr temperature during the required simulation length. An example of temperature data from EICM is shown in figure 83.
- **EICM text file.** The user can enter a user-defined temperature history. For example, the user can input the measured pavement history after establishing the data according to the text file format the FlexPAVE program requires.
- **Isothermal.** For special cases, such as FHWA ALF test sections, the program will keep the temperature constant during testing. By choosing the “Isothermal” condition, the user can enter a constant temperature and simulate the response and performance analyses under that constant pavement temperature.

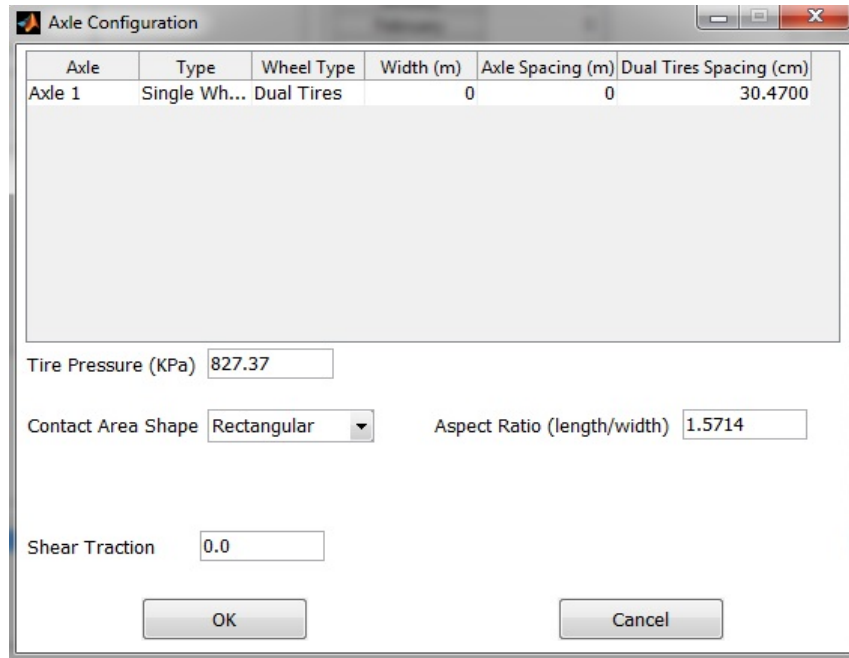


Source: FHWA.

Figure 83. Screenshot. Example of temperature input (EICM case).

Traffic

The FlexPAVE program considers two different contact shapes: circular and rectangular. The program simulates contact pressure distribution using a 3D haversine shape, constant shape, smoothed constant exponential shape, and smoothed constant cubical shape. ESAL analysis is a default traffic input; however, user-defined traffic inputs according to truck type and load enable users to simulate various kinds of traffic loads. Figure 84 shows the screenshot of the axle configuration user interface.



Source: FHWA.

Figure 84. Screenshot. Determining contact area shape for wheels in the FlexPAVE program.

The FlexPAVE program can calculate the volume under the wheel load (according to the selected load distribution) and then divide the wheel load by input pressure to find the average area. Based on the input, the program can determine the contact shape or radius. The program uses the aspect ratio for the rectangular contact shape.

Equations 121 and 122 show the pressure distribution and radius of the circular contact shape and haversine distribution.

$$p = \begin{cases} p_0 & |x| \leq (1 - \sigma) \frac{x_0}{2} \\ p_0 \cos\left(\frac{\pi}{\sigma x_0} \left(|x| - (1 - \sigma) \frac{x_0}{2}\right)\right)^2 & |x| > (1 - \sigma) \frac{x_0}{2} \text{ and } |x| \leq \frac{x_0}{2} \\ 0 & \frac{x_0}{2} \end{cases} \quad (121)$$

$$r = \sqrt{\frac{8\pi}{\pi^2 - 4} * \frac{\text{load}}{\text{pressure}}} \quad (122)$$

Where p_0 is maximum pressure and x_0 is radius of the load.

Equations 123 and 124 show the pressure distribution and radius for the circular contact shape and constant distribution.

$$p = p_0 \quad (123)$$

$$r = \sqrt{\frac{4}{\pi} * \frac{load}{pressure}} \quad (124)$$

Equations 125 and 126 show the pressure distribution and radius for the circular contact shape and smoothed constant cubic distribution.

$$p = \begin{cases} p_0, & |x| \leq (1-\sigma)\frac{x_0}{2} \\ p_0 \left(\frac{-1}{\left(\frac{\sigma x_0}{2}\right)^2} (x - (1-\sigma)\frac{x_0}{2})^2 + 1 \right), & |x| > (1-\sigma)\frac{x_0}{2} \text{ and } |x| \leq \frac{x_0}{2} \\ 0, & \frac{x_0}{2} \end{cases} \quad (125)$$

$$r = \sqrt{\frac{24}{\pi(\sigma^2 - 4\sigma + 6)} * \frac{Load}{pressure}} \quad (126)$$

Equation 127 shows the dimensions for the rectangular contact shape and haversine distribution.

$$a' = \sqrt{\frac{4}{AspectRatio} * \frac{Load}{Pressure}}$$

$$b' = AspectRatio * a' \quad (127)$$

Equation 128 shows the dimensions for the rectangular contact shape and smoothed constant cubic distribution.

$$\begin{cases} aw = 1 - \frac{1}{3}\sigma_1 \\ bw = 1 - \frac{1}{3}\sigma_2 \end{cases} \rightarrow \begin{cases} a' = \sqrt{\frac{1}{AspectRatio * aw * bw} * \frac{Load}{Pressure}} \\ b' = AspectRatio * a' \end{cases} \quad (128)$$

Where:

aw and bw = intermediate variables.

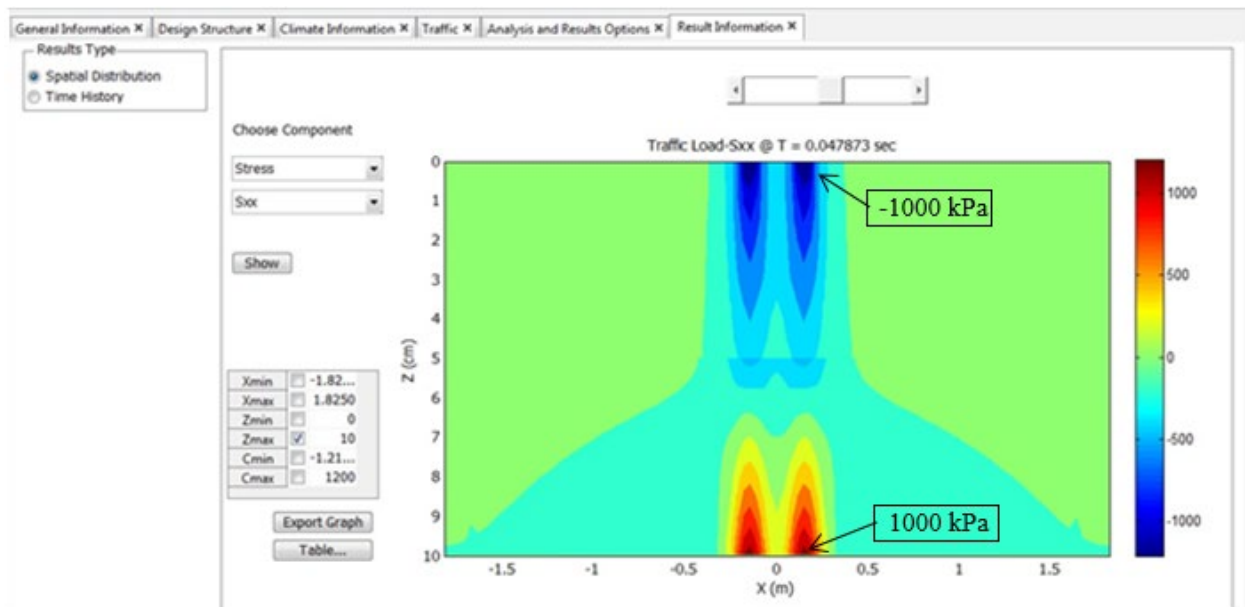
σ_1 and σ_2 = shape parameters in width and length directions, respectively.

Output and Analysis Options

The user should select the output parameters from the “Output and Analysis Options” tab. To obtain contour plots for the pavement response and performance, the user should create evaluation points. The user can automatically make evaluation points by determining the number of steps and increments in the x and z directions. The program evaluates the pavement response and performance at finite-element mesh nodal points.

After running the response analysis, the user can view the response output via the “Results” tab.

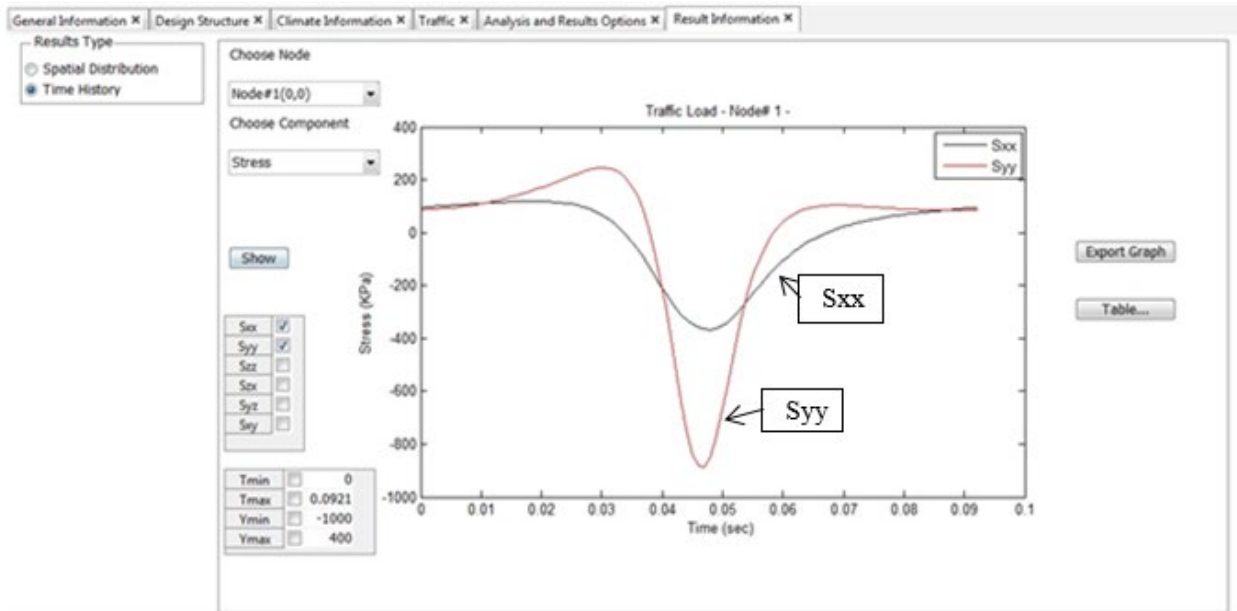
The user can choose the transverse normal stress (S_{xx}) under the “Spatial Distribution” option (i.e., the contour plot) (figure 85) and investigate the stress distribution by scrolling the bar. Figure 85 presents the transverse stress distribution at the peak stress time. By choosing the “Time History” option, the user can plot the strain, stress, and displacement values at predefined nodes (figure 86).



Source: FHWA.

1 cm = 0.4 in; 1 kPa = 0.145 psi; 1 m = 3.28 ft.

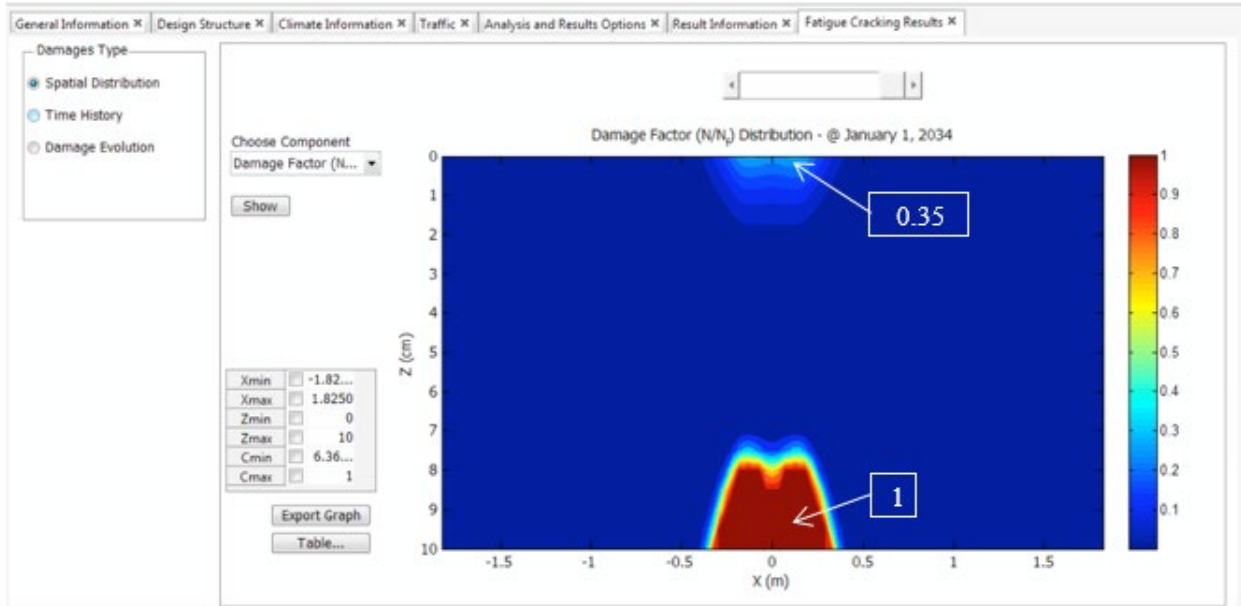
Figure 85. Screenshot. S_{xx} distribution at peak stress time.



Source: FHWA.
 1 kPa = 0.145 psi.

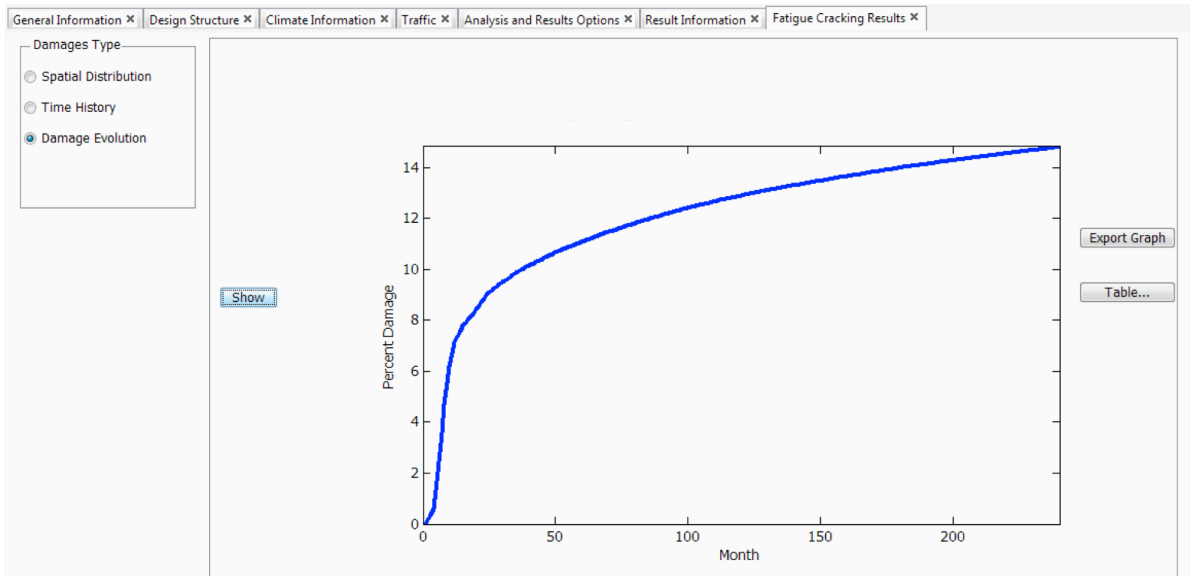
Figure 86. Screenshot. Stress history plot at center of wheel path.

Users can also plot the C values (i.e., the modulus after damage) as a contour at a given time or history at a predetermined node. They can also plot the damage factor as a fatigue cracking indicator, as shown in figure 87. The damage factor distribution is defined as N/N_f . When the damage factor becomes 1.0, the program considers the asphalt element to be completely cracked. Figure 88 shows the evolution of percent damage as defined in equation 119. It also provides rut depth development over time as shown in figure 89.



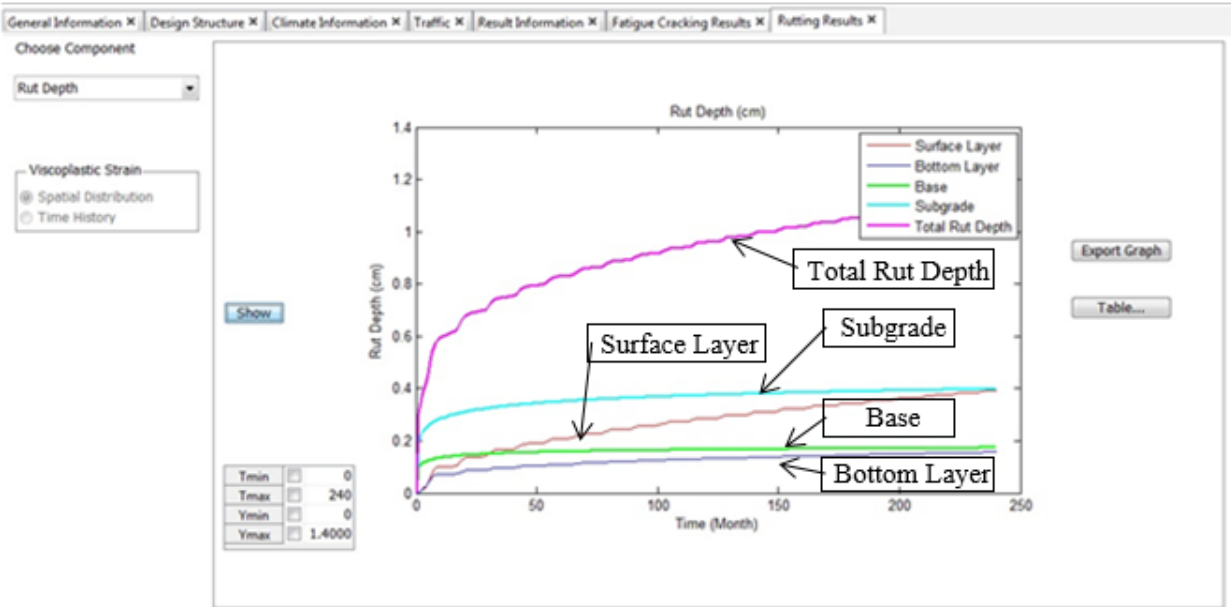
Source: FHWA.
 1 cm = 0.4 in; 1 m = 3.28 ft.

Figure 87. Screenshot. Damage factor distribution after 20-yr simulation.



Source: FHWA.

Figure 88. Screenshot. Percent damage evolution.



Source: FHWA.
1 cm = 0.4 inch.

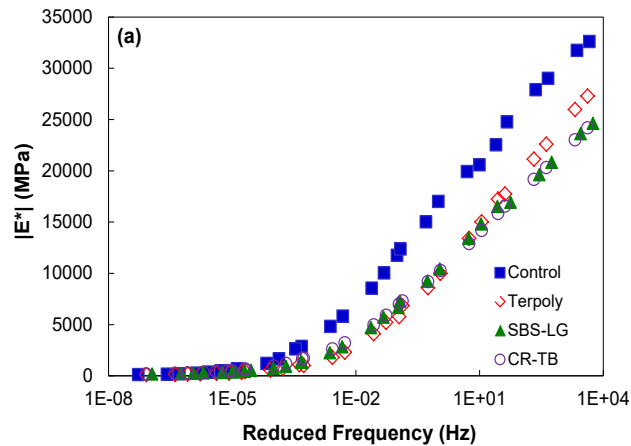
Figure 89. Screenshot. Rut depth development.

CHAPTER 6. PERFORMANCE EVALUATION OF ASPHALT MIXTURES

As described in chapter 4, linear viscoelastic properties, damage evolution and failure criteria, and permanent deformation properties should be characterized through proposed testing protocols to evaluate performance. The research team applied AASHTO PP 62, *Standard Practice For Developing Dynamic Modulus Master Curves For Hot Mix Asphalt*, to obtain the linear viscoelastic properties like the dynamic modulus values and t-T shift factors.⁽¹¹⁰⁾ The team used AASHTO TP 107 for S-VECD model characterization with failure criteria and applied the SSR test for rutting characterization.⁽³⁷⁾

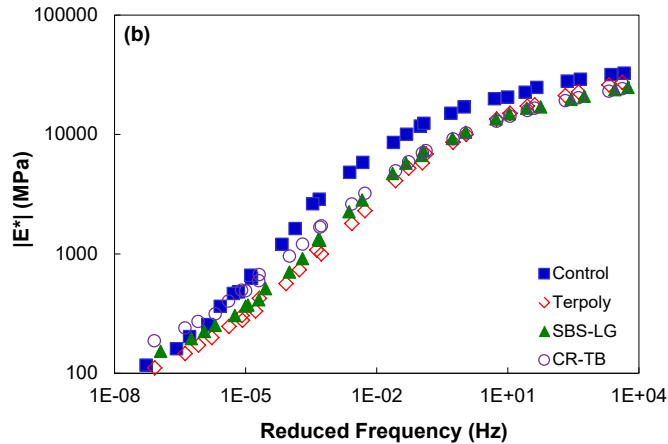
FHWA ALF

Figure 90 shows comparisons of the linear viscoelastic characteristics of the FHWA ALF mixtures and averaged dynamic modulus master curves for all mixtures in both semi-log and log-log scales. The figure shows that at high reduced frequencies (low temperatures), the control mixture shows substantially higher stiffness values than the polymer-modified mixture, whereas the control mixture shows lower stiffness values at low reduced frequencies. The SBS, crumb rubber (CR-TB), and terpolymer mixtures show similar trends and values.



© 2017 International Journal of Pavement Engineering. (DTFH61-08-H-00005)
1 MPa = 145.04 psi.

A. Linear viscoelastic characteristic curves for FHWA ALF mixtures in semi-log space.



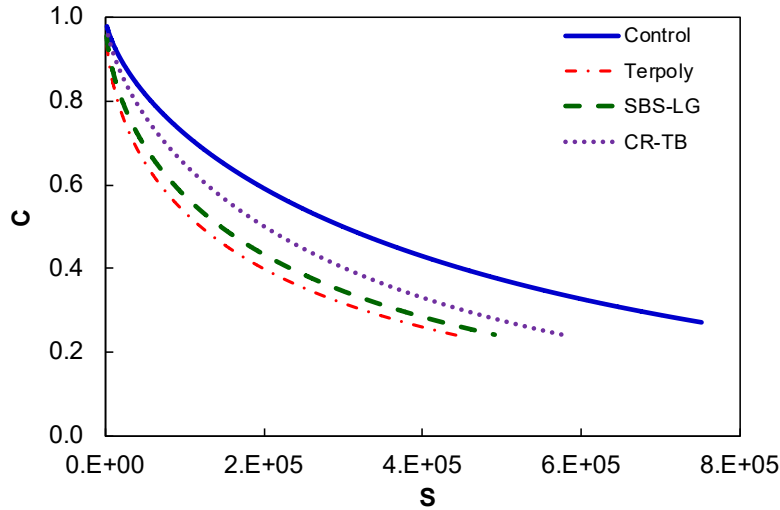
© 2017 International Journal of Pavement Engineering. (DTFH61-08-H-00005)
 1 MPa = 145.04 psi.

B. Linear viscoelastic characteristic curves for FHWA ALF mixtures in log-log space.

Figure 90. Graphs. Linear viscoelastic characteristic curves for FHWA ALF mixtures.⁽¹¹¹⁾

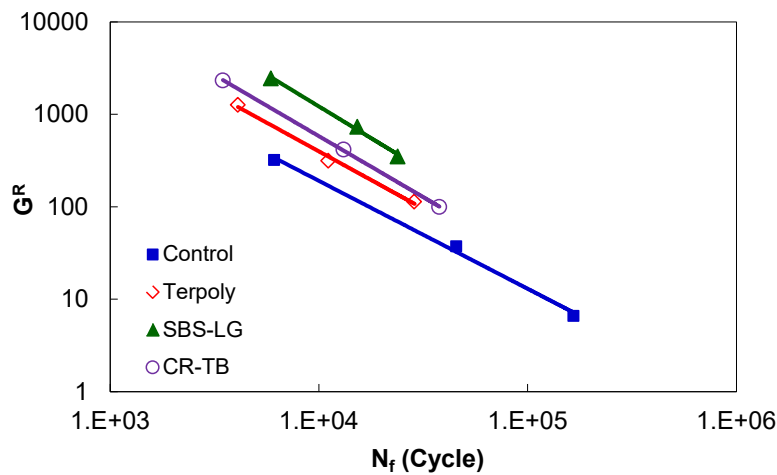
Figure 91 illustrates the damage characteristic curves for the FHWA ALF mixtures. The control mixture lies at the top because of its high stiffness values, as presented in figure 91. The damage characteristic curves alone, however, do not explain the fatigue behavior properly. The control mixture seems to have a longer fatigue life than the other mixtures because of the control mixture curve's high position. However, the failure criterion (C_f) for the control mixture is also greater than that of the modified mixtures; thus, the fatigue life of the polymer-modified mixtures could be longer than that of the unmodified mixture (the control mix). The failure criterion shown in figure 92 illustrates the fatigue life better. In figure 92, the control mixture curve is the lowest one, which implies it has the shortest fatigue life. As such, the SBS mixture exhibits the strongest fatigue resistance of all the mixtures.

Table 27 presents the D^R values. The research team observed that the control mixture has lower D^R values than the mixtures with modified binders. This low D^R value may also suggest a short fatigue life. However, complete assessment of the fatigue performance of different mixtures must account for the mixtures' time- and temperature-dependent stiffness characteristics, damage evolution, and failure criterion. For example, even though the control mixture's stiffness values and damage characteristic curves suggest better fatigue resistance than the other mixtures, the control mixture shows the worst fatigue resistance of all the mixtures in terms of the failure criterion. Therefore, the best way to evaluate the fatigue performance of these mixtures is to run the FlexPAVE program simulations using the damage characteristic curves and the fatigue failure curves together in a few representative pavement systems.



© 2017 International Journal of Pavement Engineering. (DTFH61-08-H-00005)

Figure 91. Graph. Damage characteristic curves for FHWA ALF mixtures.⁽¹¹¹⁾



© 2017 International Journal of Pavement Engineering. (DTFH61-08-H-00005)

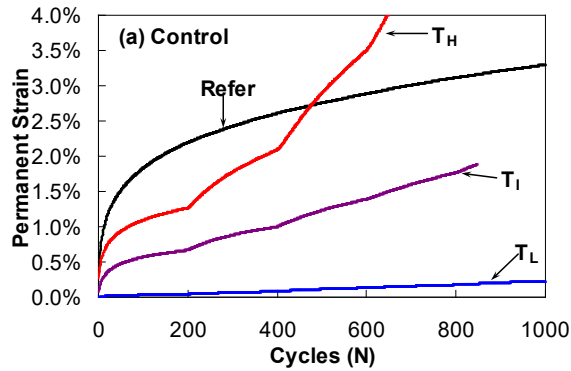
Figure 92. Graph. Failure criterion curves for FHWA ALF mixtures.⁽¹¹¹⁾

Table 27. D^R values for FHWA ALF mixtures.

Mixture	D^R
Control	0.486
CR-TB	0.733
Terpolymer	0.677
SBS	0.755

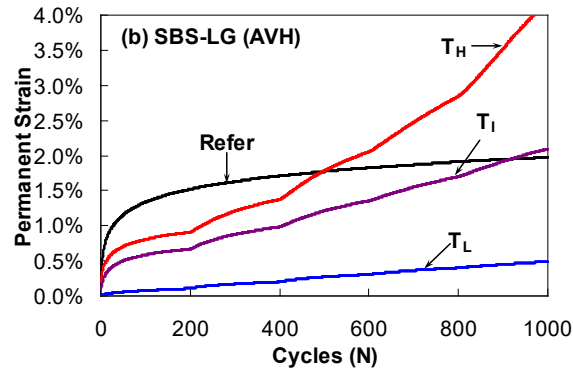
Figure 93 presents the permanent deformation behavior of the FHWA ALF mixtures. Initial air void content after construction affects permanent deformation. The top lift shows a higher air void content than the lower lift. Therefore, the research team fabricated the specimens using two different air void contents: a high air void content (AVH) and low air void content (AVL) for the

top and bottom lifts, respectively. The control mixture shows high permanent strain, and the other modified mixtures show similar permanent strain levels. This observation illustrates the effect of modified binder on rutting resistance.



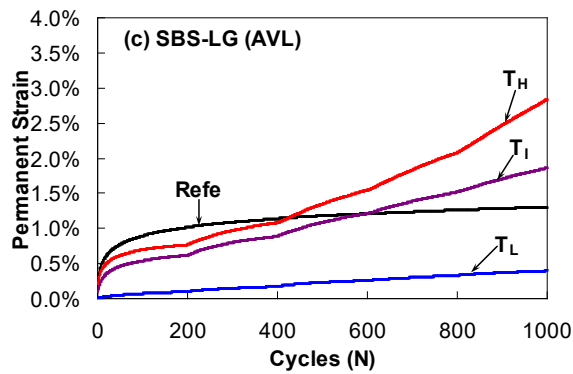
© 2014 Road Materials and Pavement Design. (DTFH61-08-H-00005)

A. Permanent deformation results from TSS tests of FHWA ALF control mixtures.



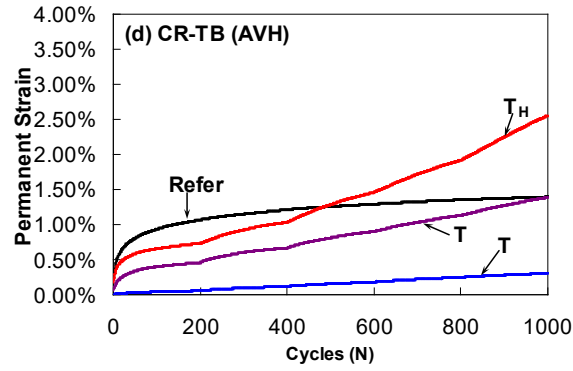
© 2014 Road Materials and Pavement Design. (DTFH61-08-H-00005)

B. Permanent deformation results from TSS tests of FHWA ALF-SB-LG (AVH) mixtures.



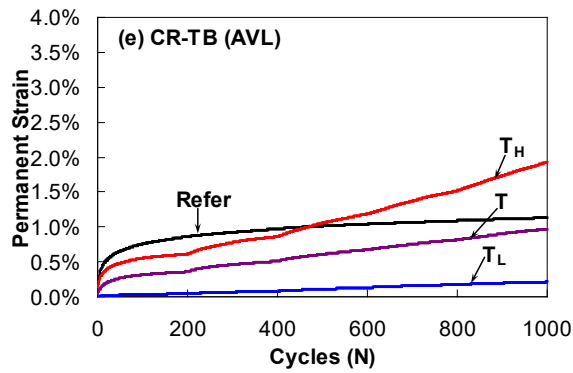
© 2014 Road Materials and Pavement Design. (DTFH61-08-H-00005)

C. Permanent deformation results from TSS tests of FHWA ALF-SBS-LG (AVL) mixtures.



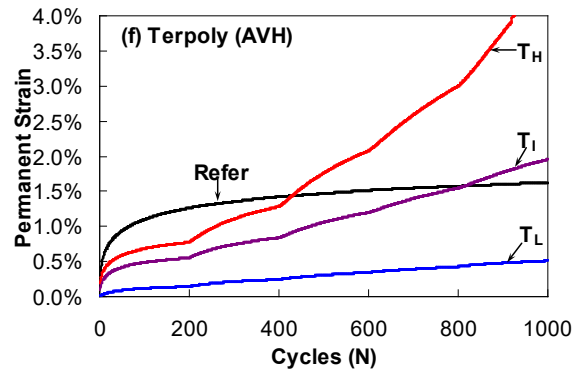
© 2014 Road Materials and Pavement Design. (DTFH61-08-H-00005)

D. Permanent deformation results from TSS tests of FHWA ALF-CR-TB (AVH) mixtures.



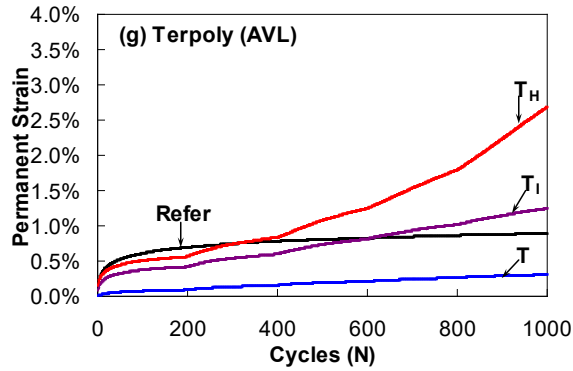
© 2014 Road Materials and Pavement Design. (DTFH61-08-H-00005)

E. Permanent deformation results from TSS tests of FHWA ALF-CR-TB (AVL) mixtures.



© 2014 Road Materials and Pavement Design. (DTFH61-08-H-00005)

F. Permanent deformation results from TSS tests of FHWA ALF-Terpolymer (AVH) mixtures.



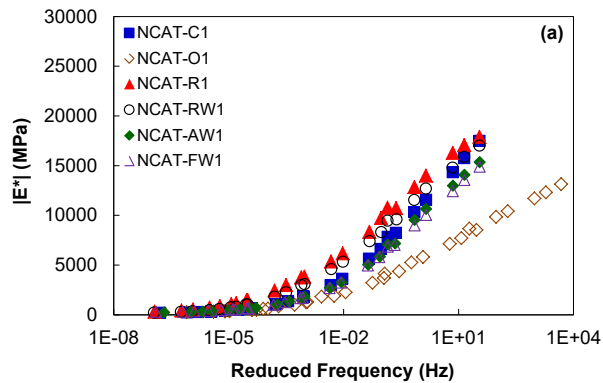
© 2014 Road Materials and Pavement Design. (DTFH61-08-H-00005)

G. Permanent deformation results from TSS tests of FHWA ALF-Terpolymer (AVL) mixtures.

Figure 93. Graphs. Permanent deformation results from TSS tests of FHWA ALF mixtures.⁽⁹⁹⁾

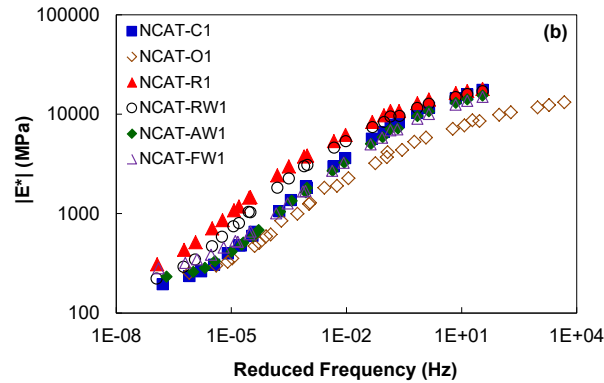
NCAT TEST TRACK

Figure 94 shows the results of the linear viscoelastic characteristics for the National Center for Asphalt Technology (NCAT) mixtures. The modulus ranking from stiffest to softest mixture is R1, RW1, C1, FW1, AW1, and O1. Several factors contributed to the modulus value of each NCAT mixture. The first factor is the difference between the virgin mixtures and the mixtures with 50-percent RAP. The research team expected that the aged RAP would increase the modulus value of the mixture. In some instances, shown in figure 94, the modulus value for the high RAP mixture is nearly double the modulus value for a nearly equivalent non-RAP mixture.



© 2017 International Journal of Pavement Engineering. (DTFH61-08-H-00005)
1 MPa = 145.04 psi.

A. Linear viscoelastic characteristic curves for NCAT surface mixtures in semi-log scale.

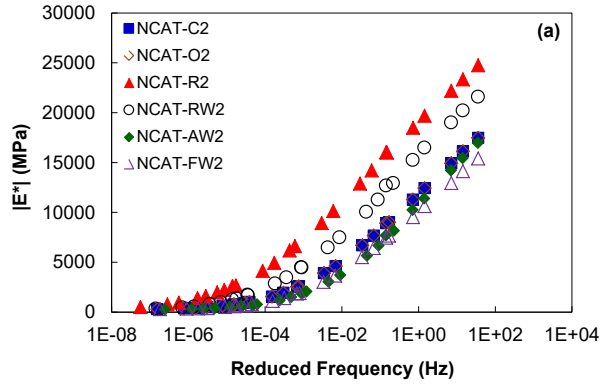


© 2017 International Journal of Pavement Engineering. (DTFH61-08-H-00005)
 1 MPa = 145.04 psi.

B. Linear viscoelastic characteristic curves for NCAT surface mixtures in log-log scale.

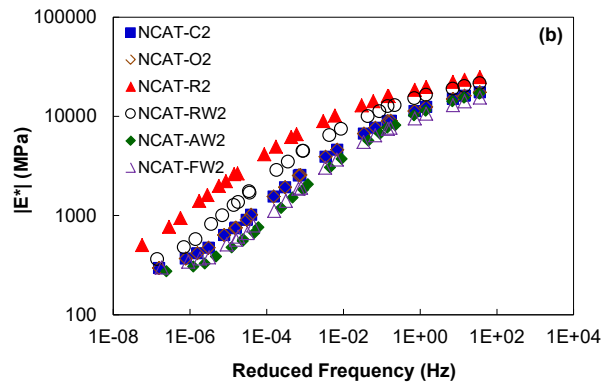
Figure 94. Graphs. Linear viscoelastic characteristic curves for NCAT surface mixtures.⁽¹¹¹⁾

Another factor that affects the modulus of the mixtures is the type of warm-mix asphalt (WMA) technology. Adding the WMA did not significantly change the dynamic modulus values of the mixtures for the virgin materials (FW1 and AW1), whereas the foam WMA used for the RAP mixture decreased the stiffness value. Figure 95 and Figure 96 show similar rankings among the mixtures for the intermediate and base layers. The high RAP content mixtures show even higher dynamic modulus values at high reduced frequencies (equivalent to low temperatures) when compared with the surface mixtures. A reasonable explanation for these higher modulus values is the higher percentage of RAP binder for the base mixtures. The amount of RAP aggregate was the same, but there was less total binder content, so the percentage of RAP binder increased from 37 percent for the R1 mixture and 50 percent for the R2 and R3 mixtures. The effect of air void content also can be observed by comparing the C2 and O2 mixes. The mixtures are the same mixture and from the same batch, but were compacted at different air void contents (6.1 and 5.1 percent, respectively). There is a slight increase in the dynamic modulus values for the mixture with the lower air void content, so this trend is consistent with less dense mixtures having lower dynamic modulus values.



© 2017 International Journal of Pavement Engineering. (DTFH61-08-H-00005)
 1 MPa = 145.04 psi.

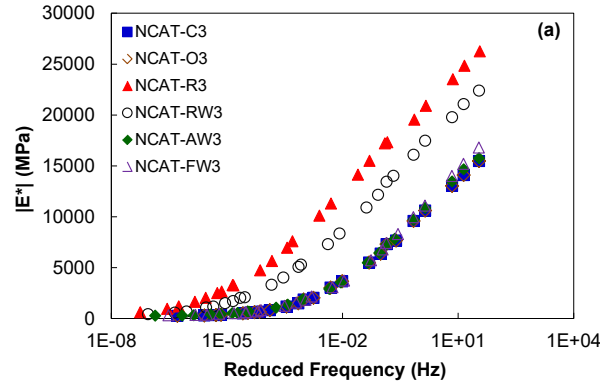
A. Linear viscoelastic characteristic curves for NCAT intermediate mixtures in semi-log scale.



© 2017 International Journal of Pavement Engineering. (DTFH61-08-H-00005)
 1 MPa = 145.04 psi.

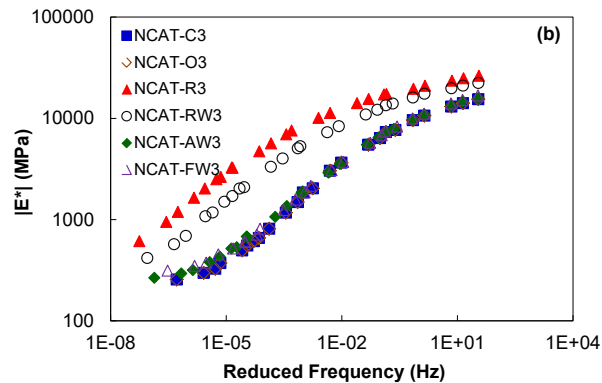
B. Linear viscoelastic characteristic curves for NCAT intermediate mixtures in log-log scale.

Figure 95. Graphs. Linear viscoelastic characteristic curves for NCAT intermediate mixtures.⁽¹¹¹⁾



© 2017 International Journal of Pavement Engineering. (DTFH61-08-H-00005)
1 MPa = 145.04 psi.

A. Linear viscoelastic characteristic curves for NCAT base mixtures in semi-log scale.



© 2017 International Journal of Pavement Engineering. (DTFH61-08-H-00005)
1 MPa = 145.04 psi.

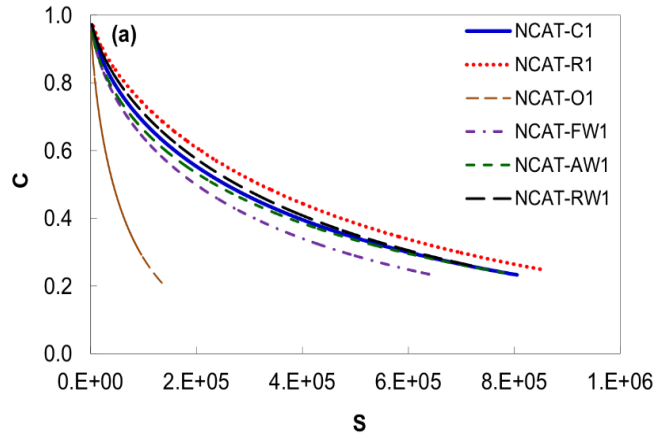
B. Linear viscoelastic characteristic curves for NCAT base mixtures in log-log scale.

Figure 96. Graphs. Linear viscoelastic characteristic curves for NCAT base mixtures.⁽¹¹¹⁾

Figure 97 shows the S-VECD fatigue characteristic curves for each layer. The results show a similar ranking trend as dynamic modulus master curves. As the modulus value of the mixture increases, the C -value at failure increases. These results confirm Hou et al.'s observations that suggest the inclusion of RAP increases the C -value at failure, though not to the same degree.⁽⁶³⁾ The surface mixtures without RAP have an average C_f of 0.18, whereas the RAP mixtures have an average C_f of 0.23. The higher C_f value suggests that RAP mixtures tolerate less damage before cracking than mixtures without RAP.

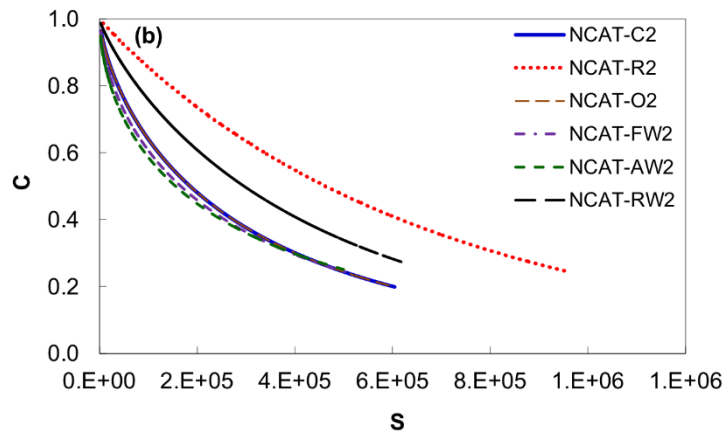
Figure 98 shows the results of characterizing the failure criterion based on the G^R versus N_f curves. One of the benefits of characterizing this failure criterion is it can predict failure for different temperatures and strain levels without testing at different temperatures. The research team performed all cyclic fatigue tests at different strain levels at 19°C but the relationship between the G^R and N_f remains about the same as long as the viscoplastic strain level remains low. For a given strain level, the control and WMA mixtures have a longer fatigue life than the

RAP mixtures in the surface layers. The intermediate layers trend the same, as seen in figure 98-B. However, the bottom layer mixtures behave differently. The R3 and RW3 mixtures, which contain high percentages of RAP, seem to be more fatigue resistant than the other mixtures with no RAP, as observed in figure 98-C.



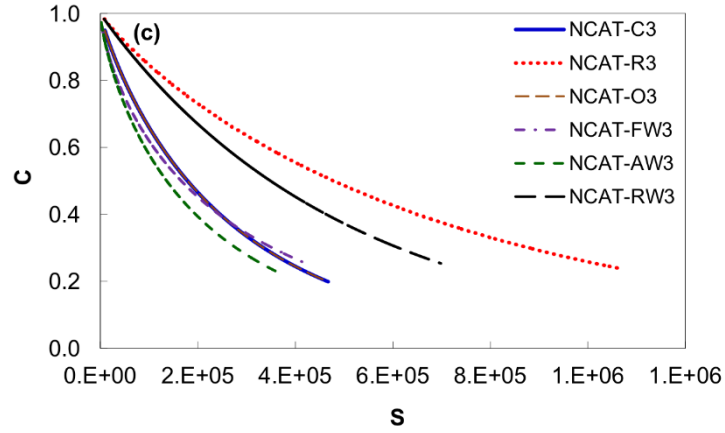
© 2017 International Journal of Pavement Engineering. (DTFH61-08-H-00005)

A. Damage characteristic curves for NCAT surface-layer mixtures.



© 2017 International Journal of Pavement Engineering. (DTFH61-08-H-00005)

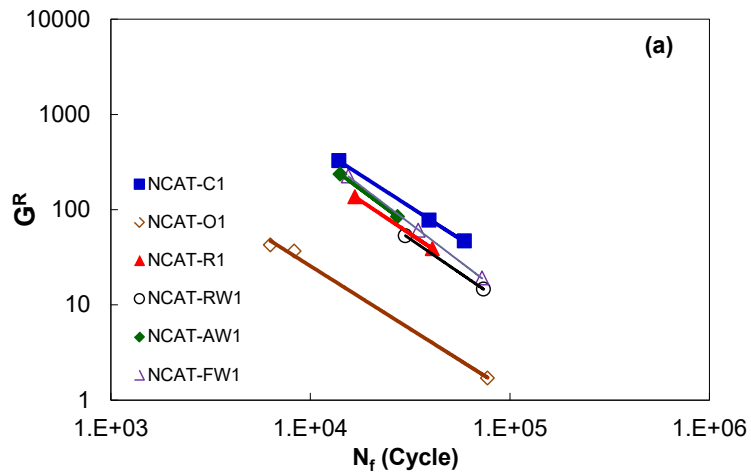
B. Damage characteristic curves for NCAT intermediate-layer mixtures.



© 2017 International Journal of Pavement Engineering. (DTFH61-08-H-00005)

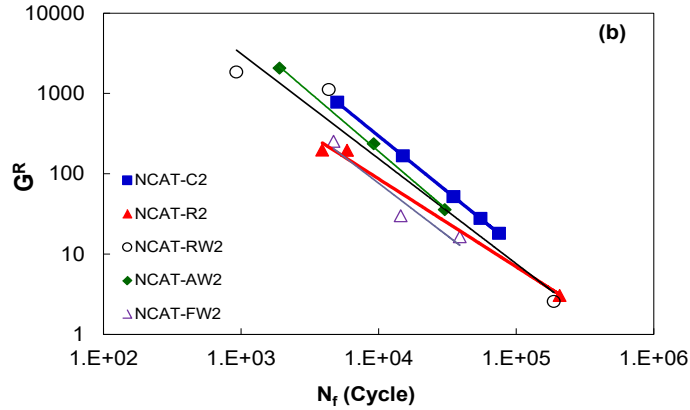
C. Damage characteristic curves for NCAT base-layer mixtures.

Figure 97. Graphs. Damage characteristic curves for NCAT mixtures.⁽¹¹¹⁾



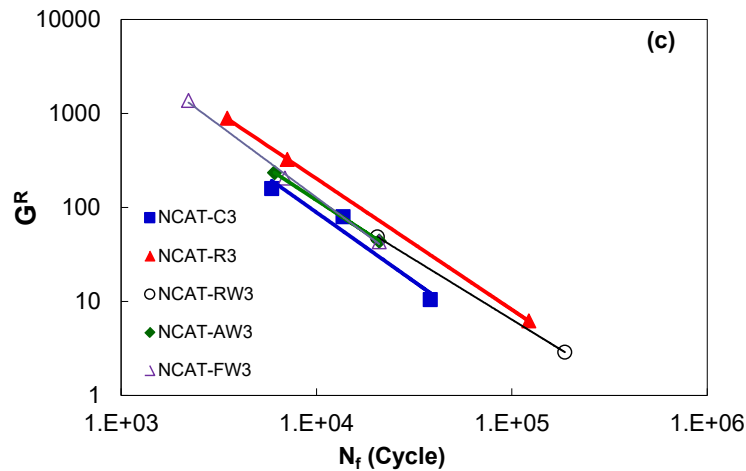
© 2017 International Journal of Pavement Engineering. (DTFH61-08-H-00005)

A. G^R versus N_f curves for NCAT surface-layer mixtures.



© 2017 International Journal of Pavement Engineering. (DTFH61-08-H-00005)

B. G^R versus N_f curves for NCAT intermediate-layer mixtures.



© 2017 International Journal of Pavement Engineering. (DTFH61-08-H-00005)

C. G^R versus N_f curves for NCAT base-layer mixtures.

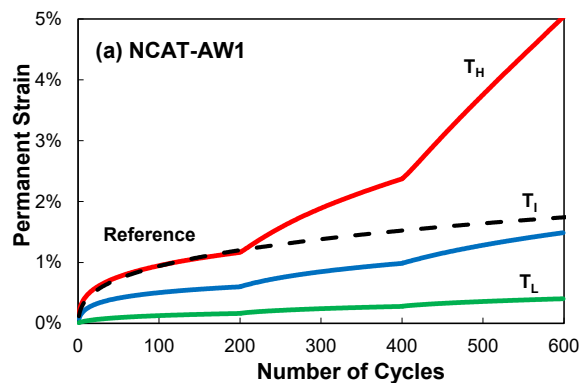
Figure 98. Graphs. G^R versus N_f curves for NCAT mixtures.⁽¹¹¹⁾

Table 28 presents the NCAT mixtures' D^R values. As shown, the R and RW mixtures have low D^R values, which indicates using RAP materials reduces the ductility, or the D^R value, of the mixture. However, Figure 96 and figure 97 show RAP materials with high RAP contents have high modulus values and high damage evolution curves. Because the fatigue life of the mixtures is a combination of the mixture properties (i.e., stiffness and ductility), other factors like pavement structure and climate must be taken into account in a pavement structural analysis program to rank the field performance of the materials properly.

Table 28. D^R values for NCAT Test Track mixtures.

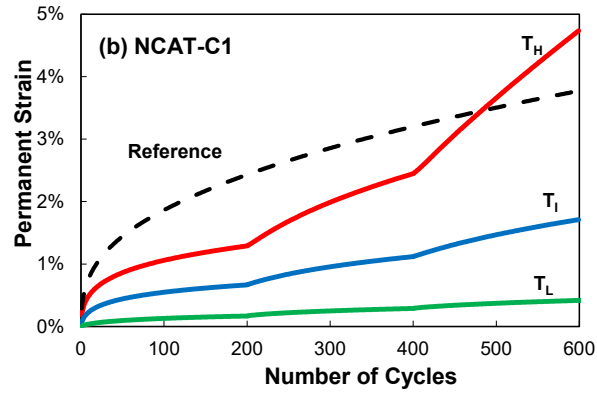
Mixture	D^R
AW1	0.686
AW2	0.587
AW3	0.582
C1	0.711
C2	0.522
C3	0.577
FW1	0.712
FW2	0.618
FW3	0.559
R1	0.475
R2	0.476
R3	0.540
RW1	0.575
RW2	0.472
RW3	0.499
O1	0.649

Figure 99 and figure 100 present the permanent strain growths for the individual NCAT surface and intermediate mixtures, respectively. The virgin surface mixtures in figure 99 have high reference test permanent deformation levels. The O1 mixture shows a higher strain level than the C1 mixture, but performs well considering it has an 18.3-percent air void content. Adding foamed WMA appears to increase the permanent deformation (FW1 versus C1) with a 0.8-percent increase in air void content. The AW1 mixture is similar to the C1 mixture with a 0.6-percent decrease in air void content. All the FW mixtures show a similar trend of increasing permanent strain compared to the C mixtures. The AW mixtures show similar trends to the C mixtures.



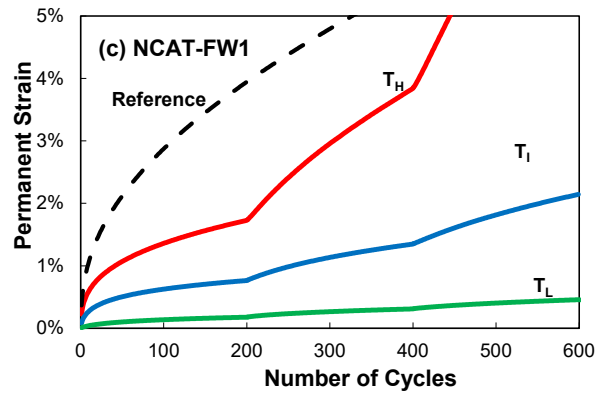
Source: FHWA.

A. TSS test results for NCAT-AW1 surface mixture.



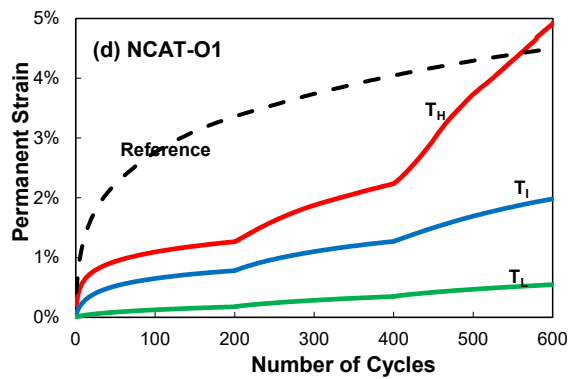
Source: FHWA.

B. TSS test results for NCAT-C1 surface mixture.



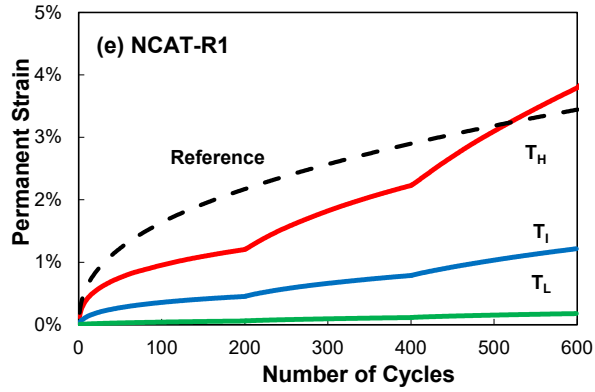
Source: FHWA.

C. TSS test results for NCAT-FW1 surface mixture.



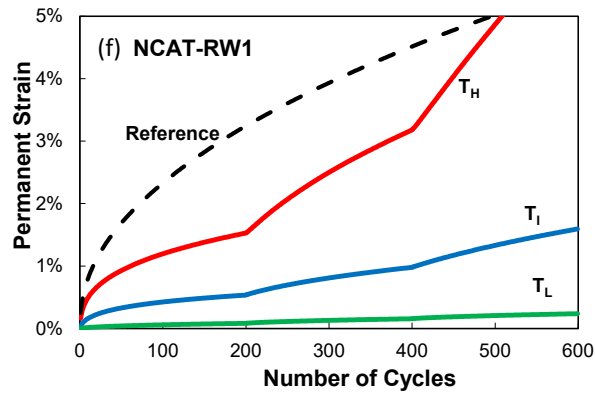
Source: FHWA.

D. TSS test results for NCAT-O1 surface mixture.



Source: FHWA.

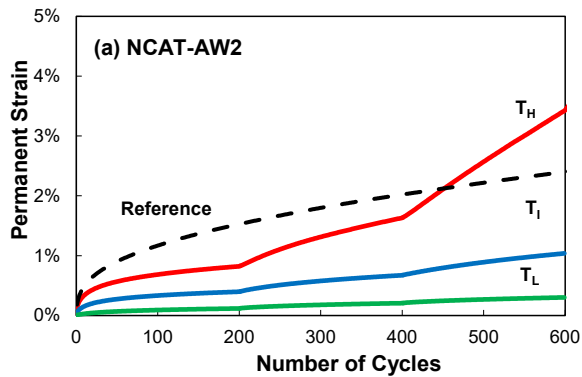
E. TSS test results for NCAT-R1 surface mixture.



Source: FHWA.

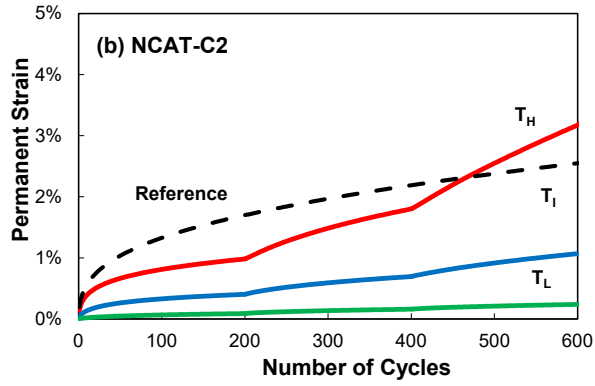
F. TSS test results for NCAT-RW1 surface mixture.

Figure 99. Graphs. TSS test results for NCAT surface mixtures.



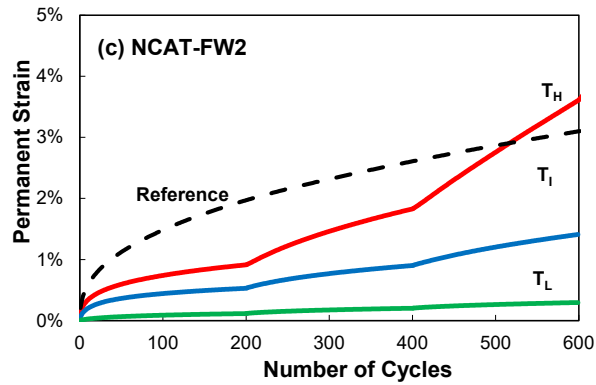
Source: FHWA.

A. TSS test results for NCAT-AW2 intermediate mixture.



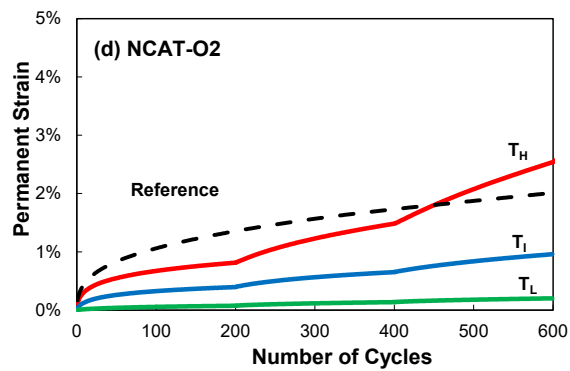
Source: FHWA.

B. TSS test results for NCAT-C2 intermediate mixture.



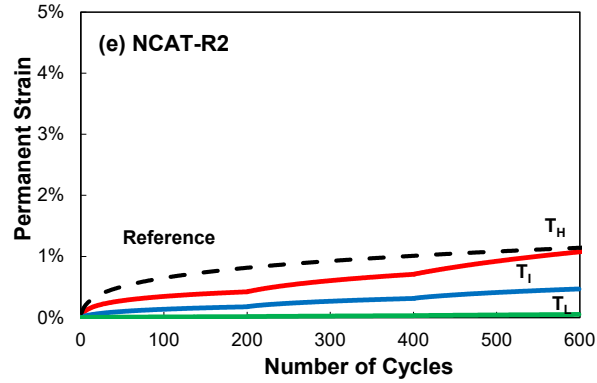
Source: FHWA.

C. TSS test results for NCAT-FW2 intermediate mixture.



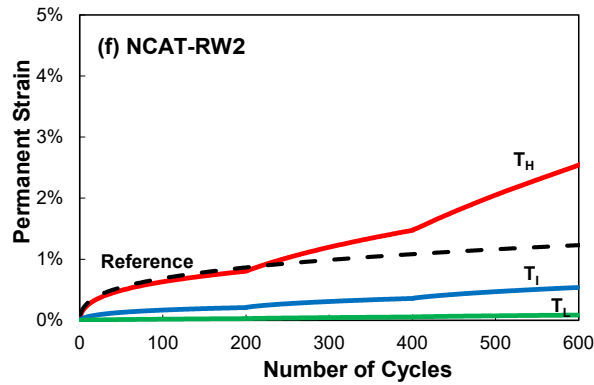
Source: FHWA.

D. TSS test results for NCAT-O2 intermediate mixture.



Source: FHWA.

E. TSS test results for NCAT-R2 intermediate mixture.

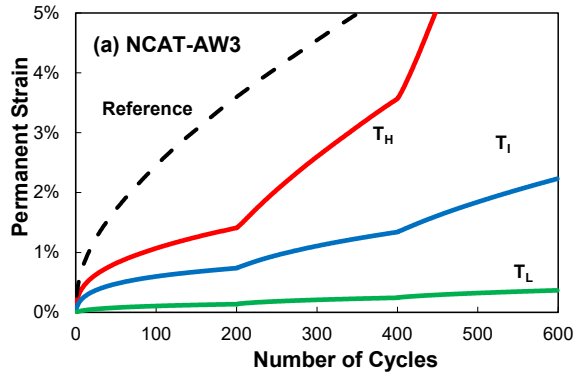


Source: FHWA.

F. TSS test results for NCAT-RW2 intermediate mixture.

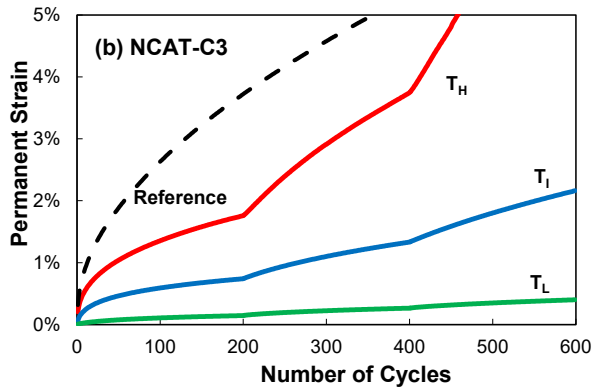
Figure 100. Graphs. TSS test results for NCAT intermediate mixtures.

The base mixtures displayed in figure 101 show more permanent deformation than the surface layer (figure 99) and intermediate layer (figure 100) mixtures. Some of the surface and base mixtures exceed the scale of 5-percent strain within 300 cycles. The scale is limited to 5 percent because that is the maximum measurement that can be made using on-specimen LVDTs.



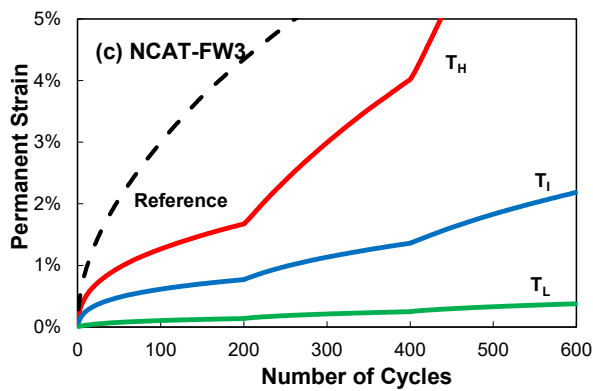
Source: FHWA.

A. TSS test results for NCAT-AW3 base mixture.



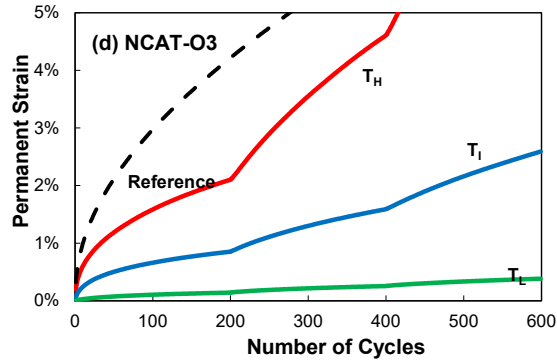
Source: FHWA.

B. TSS test results for NCAT-C3 base mixture.



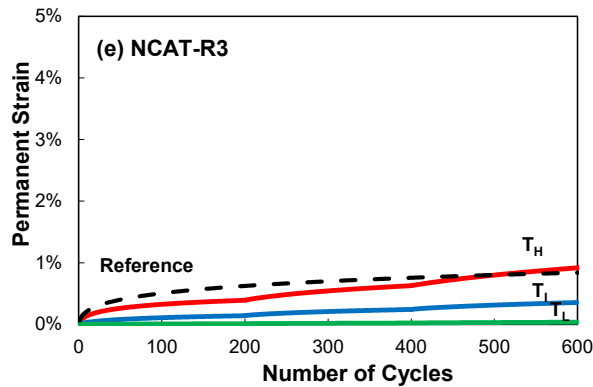
Source: FHWA.

C. TSS test results for NCAT-FW3 base mixture.



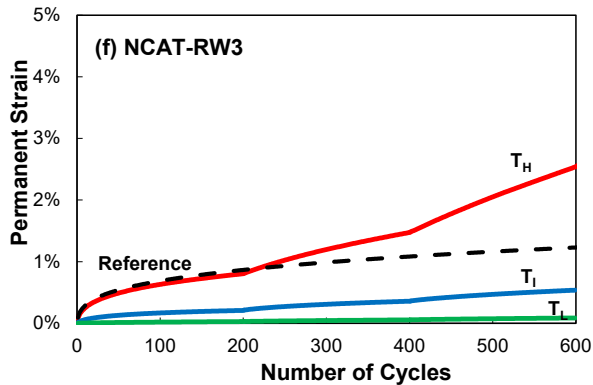
Source: FHWA.

D. TSS test results for NCAT-O3 base mixture.



Source: FHWA.

E. TSS test results for NCAT-R3 base mixture.



Source: FHWA.

F. TSS test results for NCAT-RW3 base mixture.

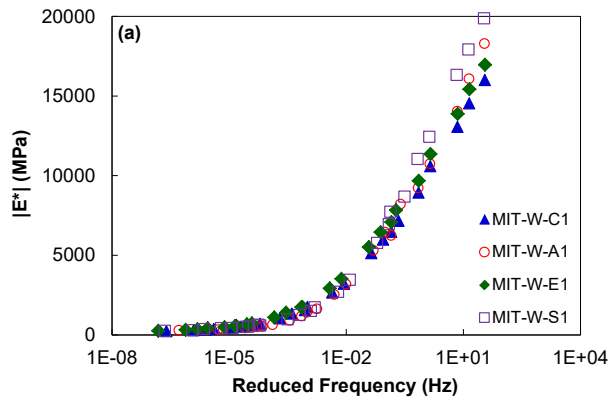
Figure 101. Graphs. TSS test results for NCAT base mixtures.

Given the base layer is the bottom 3 in of the pavement, the research team found it reasonable to use a lower PG binder (PG 67-22) instead of the polymer-modified binder (PG 76-22) used in the

surface and intermediate layers. The team determined the high temperature as the highest temperature at the surface of the pavement, so the temperature is extreme for the base layers. Therefore, the research team found the more permanent deformation of the base layer mixtures to be reasonable. The intermediate and base layers have the same aggregate type, gradation, and binder content but different binder grades. These results provide strong evidence of the benefit of polymer modification for rutting resistance. Even though the base layer shows relatively weak rutting resistance, the stress state and temperature are not as severe as in the upper layers, so the permanent strain level of the base layer would become relatively low but still present.

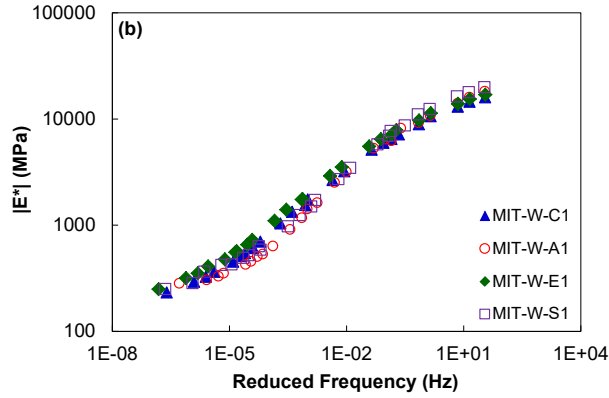
MIT-WMA PROJECT

Figure 102 and figure 103 present the dynamic modulus values of the top and bottom layers in the WMA sections in the MIT project (MIT-WMA), respectively. There is no clear trend depending on the variability of the warm-mix additive.



© 2017 Construction and Building Materials. (DTFH61-08-H-00005)
1 MPa = 145.04 psi.

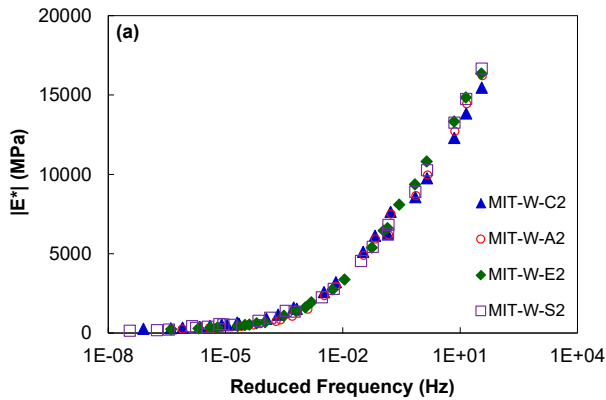
A. Linear viscoelastic characteristic curves for MIT-WMA surface-layer mixtures in semi-log scale.



© 2017 Construction and Building Materials. (DTFH61-08-H-00005)
 1 MPa = 145.04 psi.

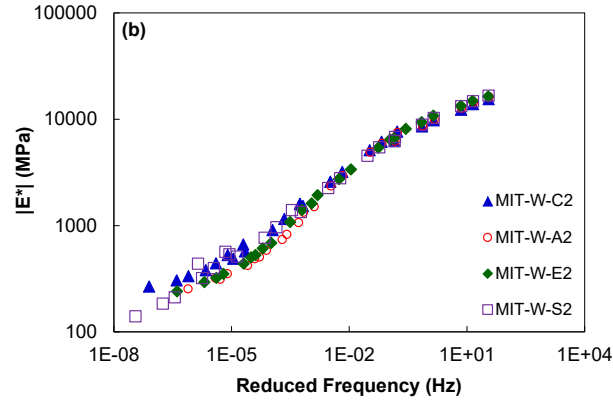
B. Linear viscoelastic characteristic curves for MIT-WMA surface-layer mixtures in log-log scale.

Figure 102. Graphs. Linear viscoelastic characteristic curves for MIT-WMA surface-layer mixtures.⁽¹¹²⁾



© 2017 Construction and Building Materials. (DTFH61-08-H-00005)
 1 MPa = 145.04 psi.

A. Linear viscoelastic characteristic curves for MIT-WMA bottom-layer mixtures in semi-log scale.

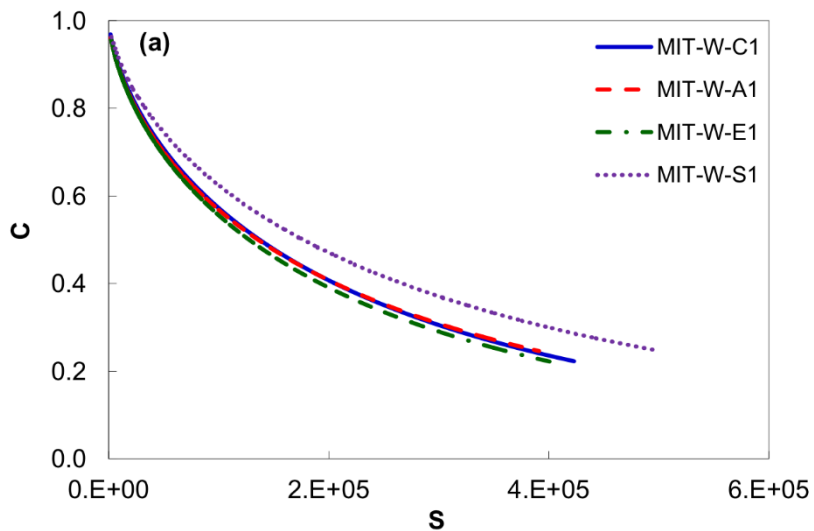


© 2017 Construction and Building Materials. (DTFH61-08-H-00005)
 1 MPa = 145.04 psi.

B. Linear viscoelastic characteristic curves for MIT-WMA bottom-layer mixtures in log-log scale.

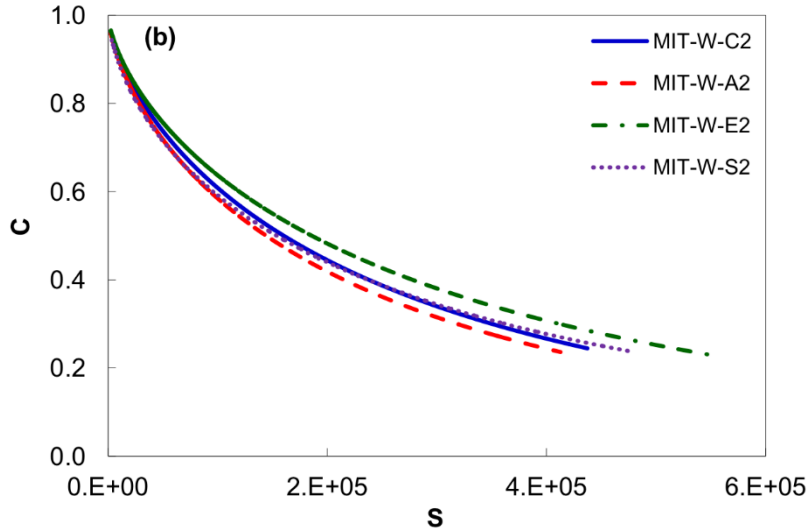
Figure 103. Graphs. Linear viscoelastic characteristic curves for MIT-WMA bottom-layer mixtures.⁽¹¹²⁾

Figure 104 shows the damage characteristic curves for the MIT-WMA mixtures. Similar to the dynamic modulus curves, the damage characteristic curves of the mixtures behave similarly to one another. It is possible that there would not be a significant difference in fatigue behavior among the different WMA additives. However, it is also possible that the damage characteristic curves alone may not be able to discern fatigue resistance clearly.



© 2017 Construction and Building Materials. (DTFH61-08-H-00005)

A. Damage characteristic curves for MIT-WMA surface-layer mixtures.

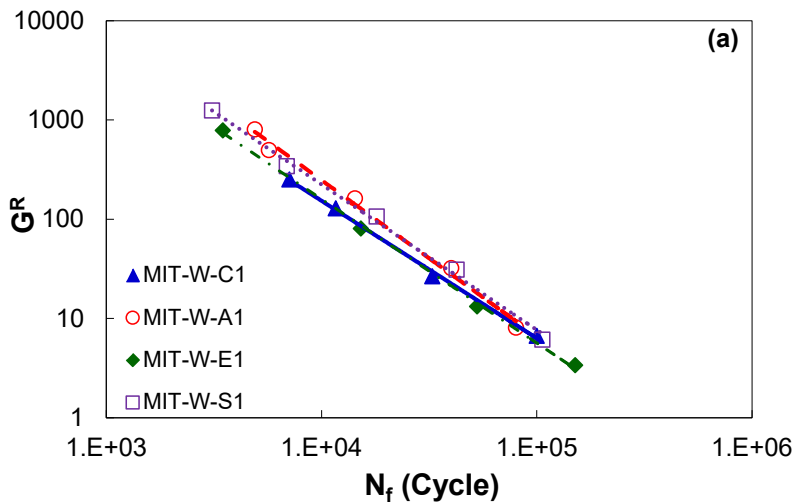


© 2017 Construction and Building Materials. (DTFH61-08-H-00005)

B. Damage characteristic curves for MIT-WMA bottom-layer mixtures.

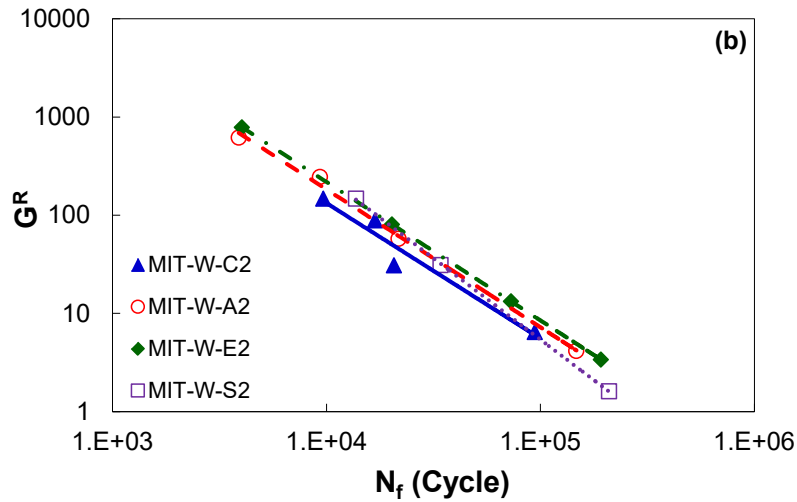
Figure 104. Graphs. Damage characteristic curves for MIT-WMA mixtures.⁽¹¹²⁾

Figure 105 shows the failure criterion curves of the MIT-WMA mixtures. Again, there is no clear trend among the additives between the surface and bottom layers. Table 29 presents the D^R values of the MIT-WMA mixtures, and similarly to the dynamic modulus and damage characteristic curves, there are no significant differences between the D^R values of the four mixtures. Therefore, the effects of the additives (i.e., Advera, Sasobit, and Evotherm) on fatigue cracking are insignificant based on the dynamic modulus, damage characteristic, and failure criterion values and curves. However, this observation needs to be verified by the field-measured results.



© 2017 Construction and Building Materials. (DTFH61-08-H-00005)

A. G^R versus N_f curves for MIT-WMA surface-layer mixtures.



© 2017 Construction and Building Materials. (DTFH61-08-H-00005)

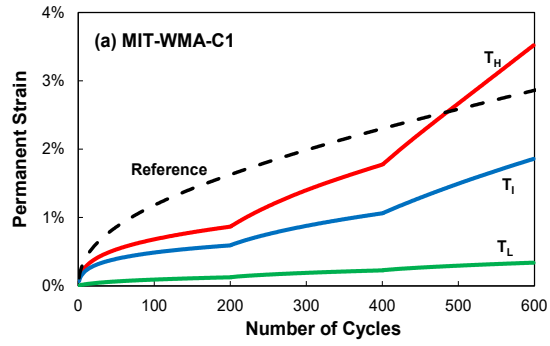
B. G_R versus N_f curves for MIT-WMA bottom-layer mixtures.

Figure 105. Graphs. G^R versus N_f curves for MIT-WMA mixtures.⁽¹¹²⁾

Table 29. D^R values for MIT-WMA mixtures.

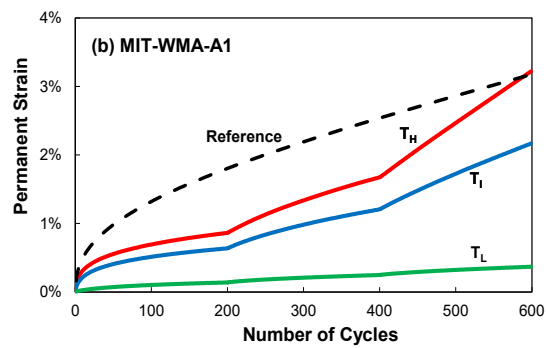
Mixture	D^R
C1	0.551
C2	0.494
S1	0.541
S2	0.572
E1	0.550
E2	0.543
A1	0.541
A2	0.555
F1	0.569
F2	0.558

The research team conducted TSS tests to evaluate rutting for the MIT-WMA mixtures. Figure 106 presents the averaged TSS test results for the MIT mixtures for the WMA surface layer, and figure 107 shows the averaged TSS test results for the WMA bottom layer. The Sasobit (W-S1) mixture behaved very similarly to the Advera (W-A1) mixture in the reference tests, but the permanent strains of the Sasobit mixture are higher than those of the control mixture (W-C1) and lower than those of the Evotherm mixture (W-E1). The TSS test results show that the Evotherm W-E1 and W-S1 mixtures exhibit similar high permanent deformation values, which are higher than the W-A1 permanent deformation values. The W-E1 mixture exhibits the highest permanent deformation values for both the reference and TSS tests. These results agree with the findings of Porrás et al. (i.e., the Evotherm mixture exhibited the lowest flow number at the effective pavement temperature among the surface WMA mixtures in MIT sections).⁽¹¹³⁾



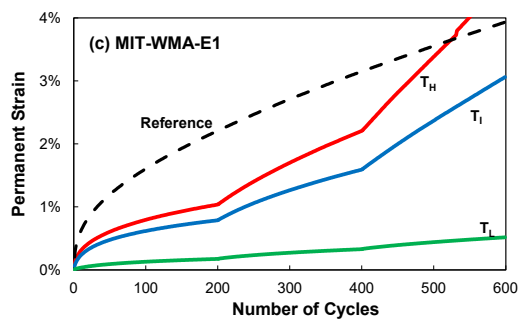
Source: FHWA.

A. Permanent strain levels of MIT-WMA C1 surface-layer mixture.



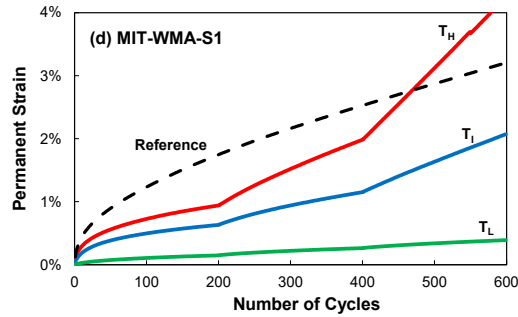
Source: FHWA.

B. Permanent strain levels of MIT-WMA A1 surface-layer mixture.



Source: FHWA.

C. Permanent strain levels of MIT-WMA E1 surface-layer mixture.

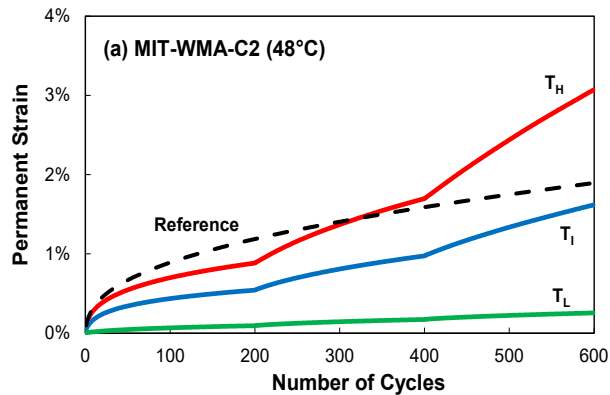


Source: FHWA.

D. Permanent strain levels of MIT-WMA S1 surface-layer mixture.

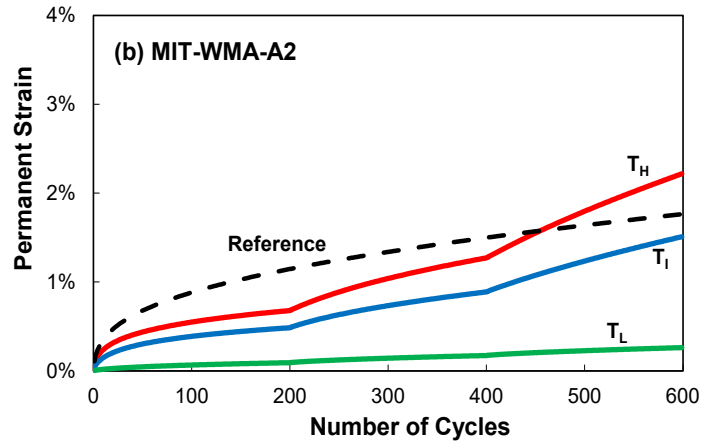
Figure 106. Graphs. Permanent strain levels of MIT-WMA surface-layer mixtures.

Figure 107 presents the results of the TSS tests of the four different MIT-WMA mixtures with 35-percent RAP for the base layer. The permanent strain levels of the mixtures with 35-percent RAP are much lower than for those with no RAP, as shown in figure 106 and figure 107, respectively. The research team tested the control mixture (MIT-W-C2) at 48°C, which is different from the other test temperature (42°C). The team took this difference into account when obtaining the shift model coefficients and confirmed it did not affect the FlexPAVE program analysis for predicting the mixtures' rutting resistance. The Sasobit mixture (MIT-W-S2) shows better rutting resistance than the Advera (MIT-W-A2) and Evotherm (MIT-W-E2) mixtures, as shown in figure 107.



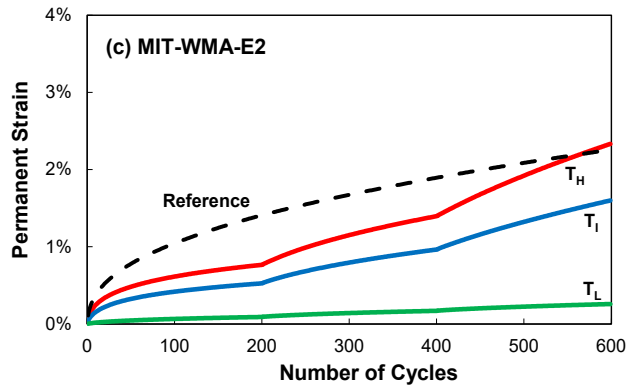
Source: FHWA.

A. TSS test results for MIT-WMA C2 mixture with 35-percent RAP.



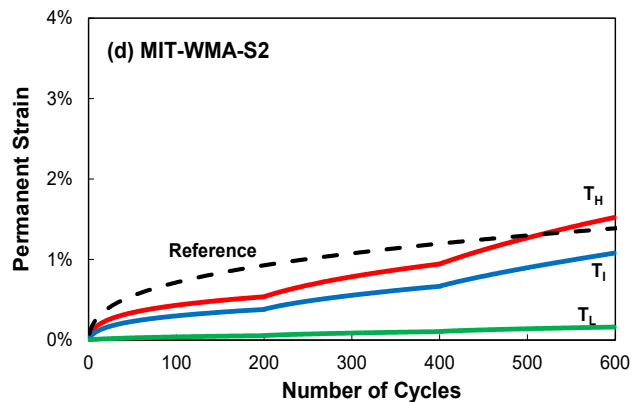
Source: FHWA.

B. TSS test results for MIT-WMA A2 mixture with 35-percent RAP.



Source: FHWA.

C. TSS test results for MIT-WMA E2 mixture with 35-percent RAP.



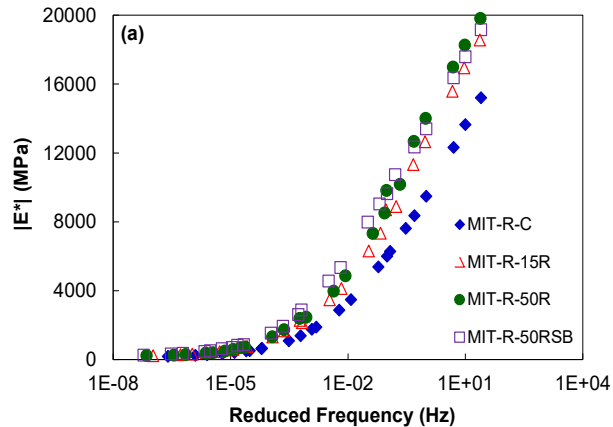
Source: FHWA.

D. TSS test results for MIT-WMA S2 mixture with 35-percent RAP.

Figure 107. Graphs. TSS test results for MIT-WMA mixtures with 35-percent RAP.

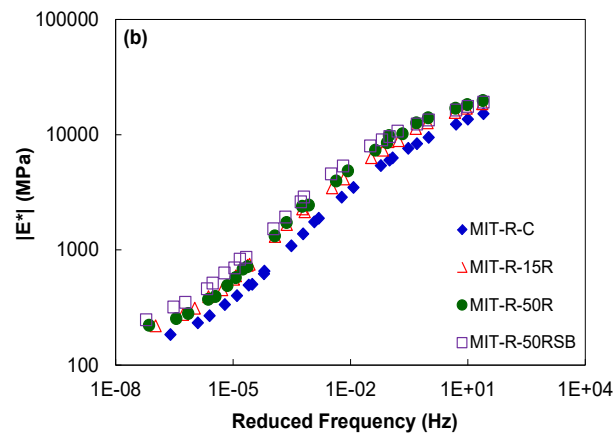
MIT-RAP PROJECT

Figure 108 shows the results of the linear viscoelastic characteristic for the MIT-RAP mixtures. The research team expected the aged RAP to increase the modulus value of the mixtures. As a result, the control mixture (MIT-R-C) that has no RAP shows less stiffness than the other RAP mixtures.



© 2017 Construction and Building Materials. (DTFH61-08-H-00005)
1 MPa = 145.04 psi.

A. Linear viscoelastic characteristic curves for MIT-RAP mixtures in semi-log scale.

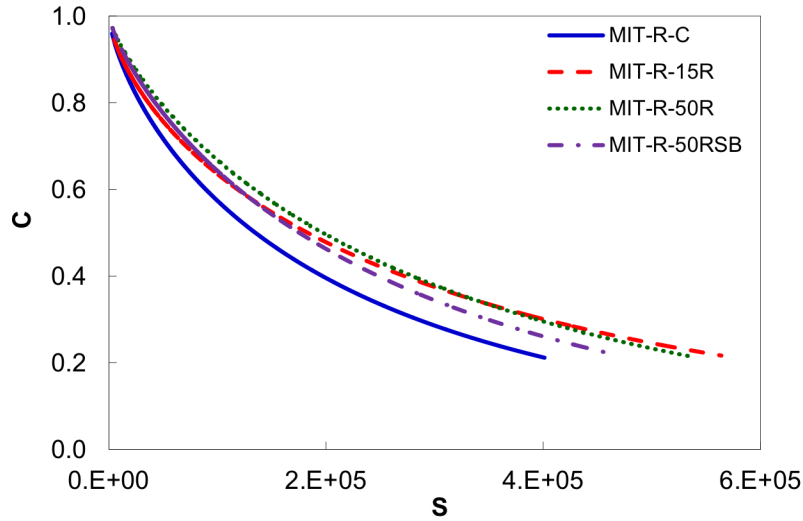


© 2017 Construction and Building Materials. (DTFH61-08-H-00005)
1 MPa = 145.04 psi.

B. Linear viscoelastic characteristic curves for MIT-RAP mixtures in log-log scale.

Figure 108. Graphs. Linear viscoelastic characteristic curves for MIT-RAP mixtures.⁽¹¹²⁾

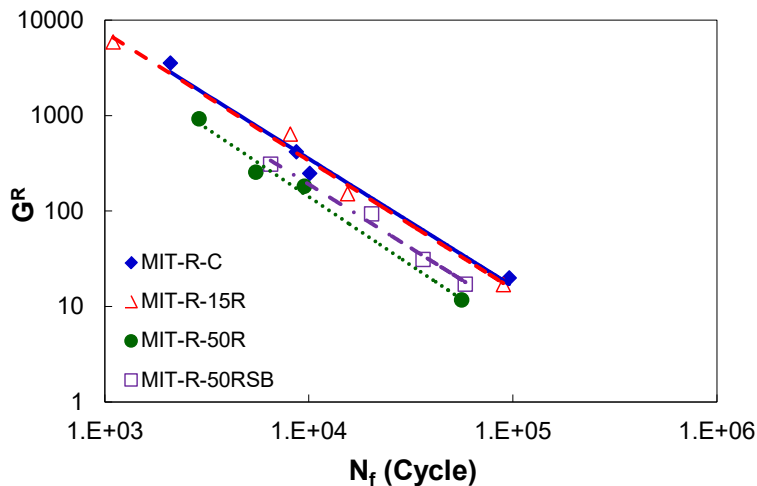
Figure 109 shows that the non-RAP mixture (MIT-R-C) and the mixture with the soft binder (MIT-R-50RSB) experience decreased material integrity relatively faster than the other mixtures with 15-percent and 50-percent RAP contents. The last point on each curve indicates the C_f value at failure (C_f). The RAP mixtures show slightly higher C_f values, which indicates the RAP mixtures cannot tolerate as much damage before failure as the non-RAP mixtures. As such, the RAP content makes the mixture more brittle.



© 2017 Construction and Building Materials. (DTFH61-08-H-00005)

Figure 109. Graph. Damage characteristic curves for MIT-RAP mixtures.⁽¹¹²⁾

Figure 110 demonstrates that high RAP content weakens the mixture's fatigue resistance. The failure criterion line for the MIT-R-15R mixture is slightly below that of the virgin mixture (MIT-R-C), but the line for the MIT-R-50R (50-percent RAP) mixture deviates from these two mixtures. At the same G^R value, the MIT-R-50R mixture results in fewer cycles to failure. However, high RAP content also increases the mixture stiffness, causing the tensile strain at the bottom of the pavement to decrease, which induces smaller G^R values. Table 30 presents the D^R values of the MIT-RAP mixtures. There is a clear trend that indicates the D^R value decreases as the RAP content increases, and increases when the research team applied a soft binder. The team investigated the combined effect via FlexPAVE analysis for a more accurate comparison.



© 2017 Construction and Building Materials. (DTFH61-08-H-00005)

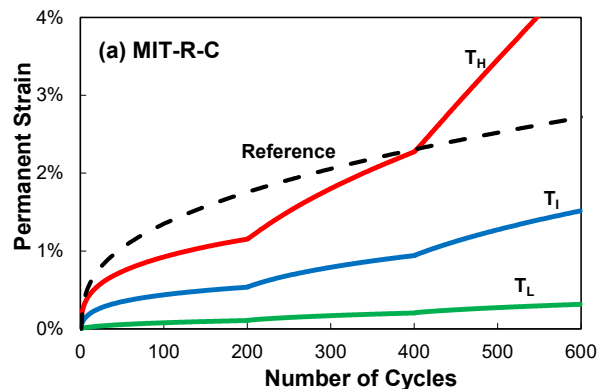
Figure 110. Graph. G^R versus N_f curves for MIT-RAP mixtures.⁽¹¹²⁾

Table 30. D^R values for MIT-RAP mixtures.

Mixture	D^R
C	0.702
15R	0.649
50R	0.501
50RSB	0.614

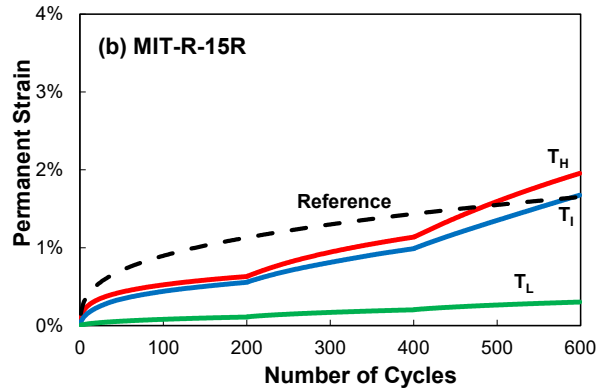
Figure 110 also indicates that using the softer binder (PG 52-34) improves fatigue resistance, as the line for the MIT-R-50RSB mixture (softer binder with 50-percent RAP) stays lower than the line of the MIT-R-C mixture and higher than that of the MIT-R-50R mixture. This result suggests that using softer binder in high RAP content mixes compensates for the decrease in fatigue resistance. Additionally, as the research team expected, the MIT-R-C mixture—which has the lowest stiffness and damage characteristic curves among all the MIT mixtures with the same base binder—seems to show the best fatigue resistance. Again, further analysis is needed to draw conclusions about fatigue resistance.

Figure 111 presents the TSS test results for the RAP mixtures, with the permanent strain values for different RAP contents plotted in figure 112. Although it is expected that permanent deformation decreases as RAP content increases, the 50-percent RAP mixtures produced higher permanent strain levels than the 15-percent RAP mixtures. This result likely stems from the difference in air void content between the two mixtures. The air void content of the 15-percent RAP mixture was 6.4 percent and the 50-percent RAP mixture was 7.6 percent. The 1.2-percent-higher air void content of the 50-percent RAP mixture causes more permanent deformation than the 15-percent RAP mixture. The difference in permanent strain levels at the end of the test was less than 1 percent. If the research team had tested these two mixtures using the same initial air void content, the 15-percent RAP mixture might have produced more or similar permanent deformation as the 50-percent RAP mixture. In this case, the ranking for rutting resistance from most resistant to least resistant would be 50-percent RAP (MIT-R-50R), 15-percent RAP (MIT-R-15R), 50-percent RAP with soft binder (MIT-R-50RSB), and 0-percent RAP (MIT-R-C) mixtures.



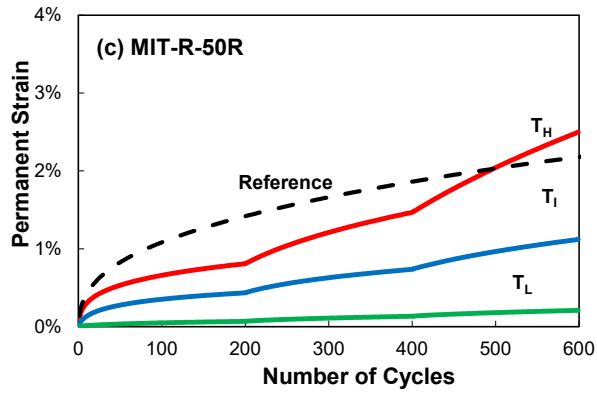
Source: FHWA.

A. TSS test results for the MIT-RAP-C mixture.



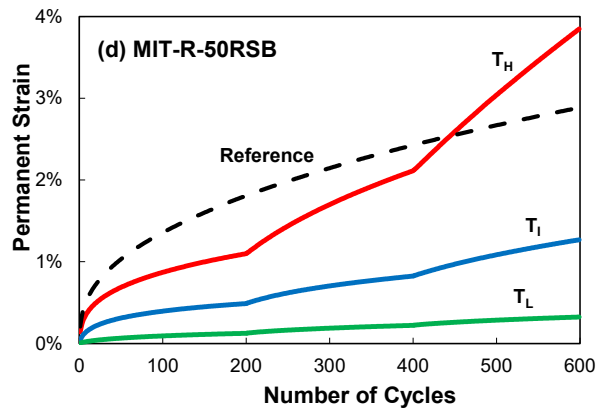
Source: FHWA.

B. TSS test results for the MIT-RAP-15R mixture.



Source: FHWA.

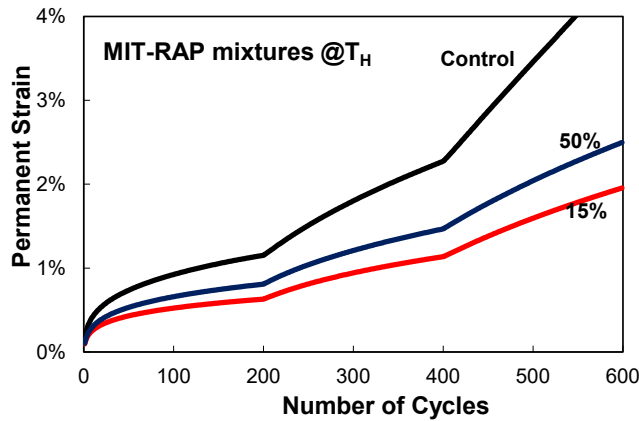
C. TSS test results for the MIT-RAP-50R mixture.



Source: FHWA.

D. TSS test results for the MIT-RAP-50RSB mixture.

Figure 111. Graphs. TSS test results for MIT-RAP mixtures.



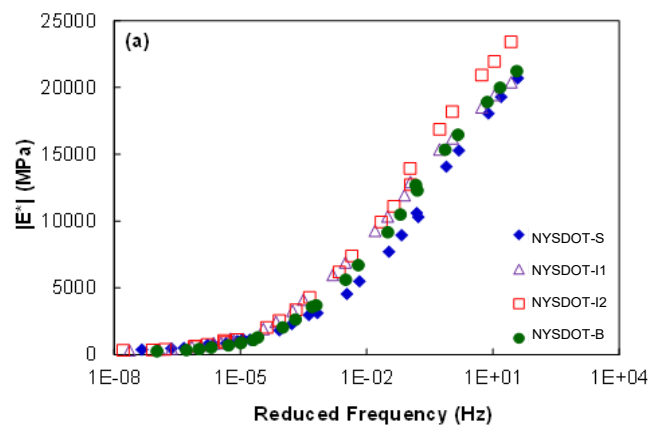
Source: FHWA.

Figure 112. Graph. Comparison of permanent strain levels for MIT-RAP mixtures at the high temperature.

These test results indicate that adding RAP improves rutting resistance, but more than 15 percent RAP does not make much difference. The content of 0-percent RAP (R-C) shows a similar level of permanent strain to that of the 50-percent RAP mixture with a soft binder (R-50RSB). This finding verifies that using aged binder in RAP, especially for mixtures with high RAP contents, may compensate for a one-grade-lower high PG of a virgin binder. However, these observations are based on limited test results of mixtures with different RAP contents.

NYSDOT PERPETUAL PAVEMENT PROJECT

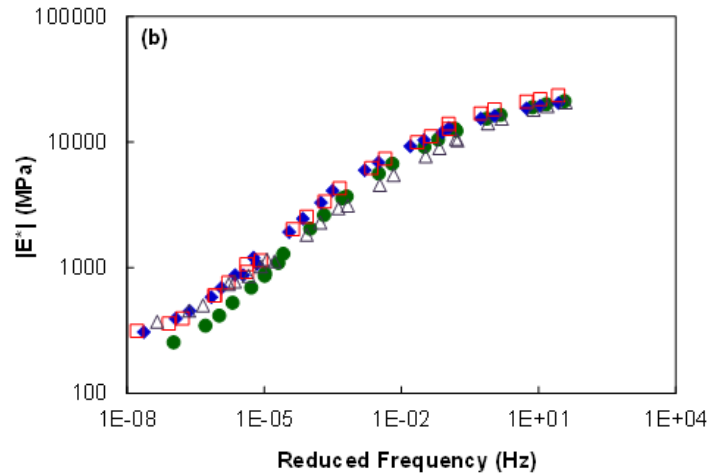
Figure 113 presents the dynamic modulus master curves for the NYSDOT mixtures. The different aggregate gradations seem to have an insignificant effect on the dynamic modulus values for this case.



Source: FHWA.

1 MPa = 145.04 psi.

A. Linear viscoelastic characteristic curves for NYSDOT mixtures in semi-log scale.

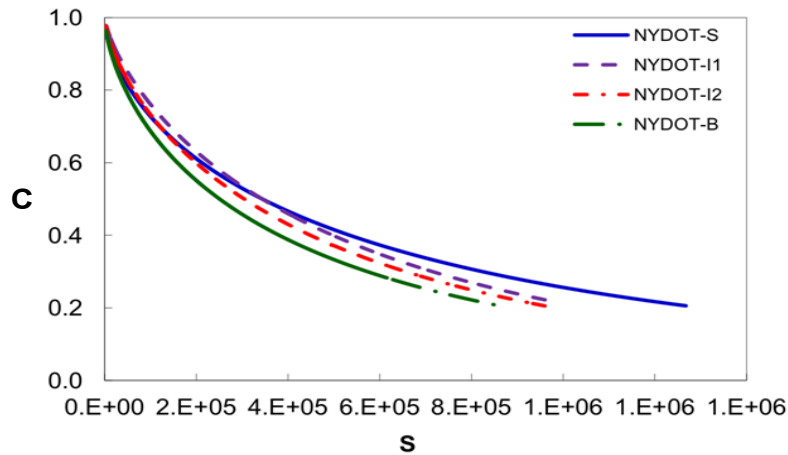


Source: FHWA.
 1 MPa = 145.04 psi.

B. Linear viscoelastic characteristic curves for NYSDOT mixtures in log-log scale.

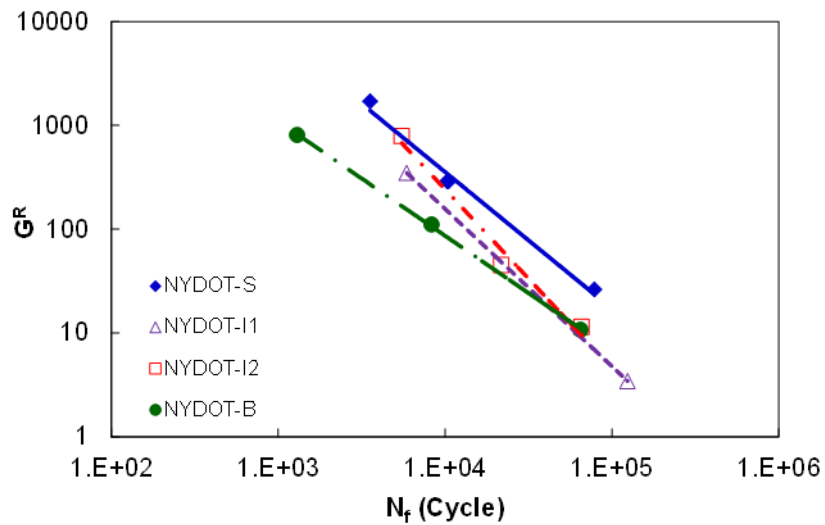
Figure 113. Graphs. Linear viscoelastic characteristic curves for NYSDOT mixtures.

Figure 114 and figure 115 show the attributes of the damage characteristic curves and the G^R versus N_f curves for all NYSDOT mixtures, respectively. The research team conducted cyclic fatigue testing at 18°C for all mixtures. The surface layer mixture (NYSDOT-S) exhibits more fatigue resistance than the bottom and intermediate layer mixtures. The NYSDOT-S and NYSDOT-B mixtures have similar slopes with different intercepts, as seen in figure 115. NY19-I1 and NY19-I2 have steeper slopes compared with the other two mixtures. As table 31 presents, the four mixtures do not show significant differences in the D^R values. However, there is a weak trend whereby as the mixtures change from the surface layer mixture to the bottom layer mixture, the D^R values decrease slightly.



Source: FHWA.

Figure 114. Graph. Damage characteristic curves for NYSDOT mixtures.



Source: FHWA.

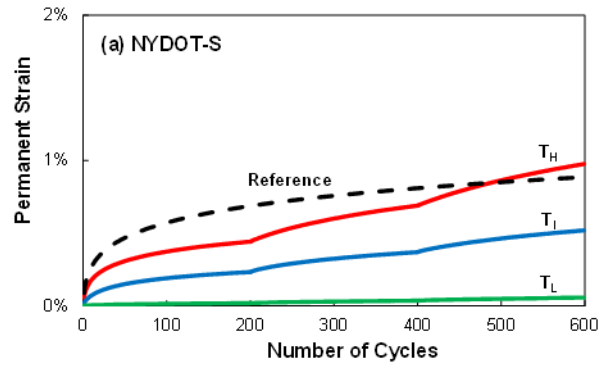
Figure 115. Graph. Failure criterion curves for NYSDOT mixtures.

Table 31. D^R values for NYSDOT mixtures.

Mixture	D^R
NYSDOT-S	0.599
NYSDOT-I1	0.508
NYSDOT-I2	0.497
NYSDOT-B	0.484

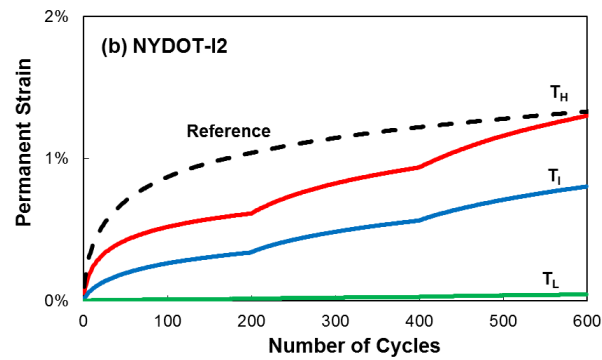
The test temperatures for the NYSDOT mixtures are 15°C for the low temperature (T_L), 35°C for the intermediate temperature (T_I), and 47°C for the high temperature (T_H). The intermediate layer mixtures (I1 and I2) indicate a high level of permanent deformation for the reference tests, as

shown in figure 116. The surface mixture shows less permanent deformation than the base and intermediate layer mixtures. The research team used the averaged permanent strain levels presented in figure 116 to characterize the shift model.



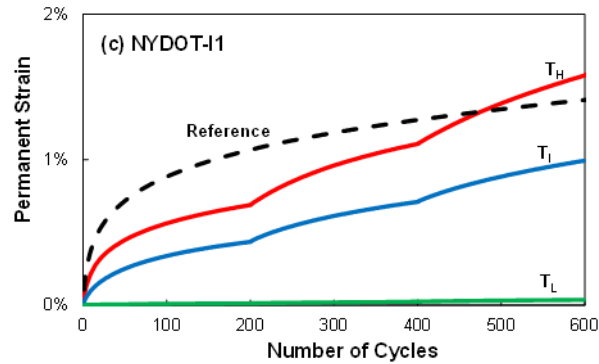
Source: FHWA.

A. TSS test results for NYSDOT-S.



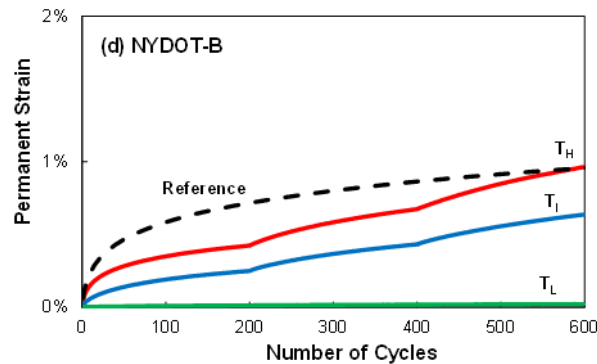
Source: FHWA.

B. TSS test results for NYSDOT-I2.



Source: FHWA.

C. TSS test results for NYSDOT-I1.



Source: FHWA.

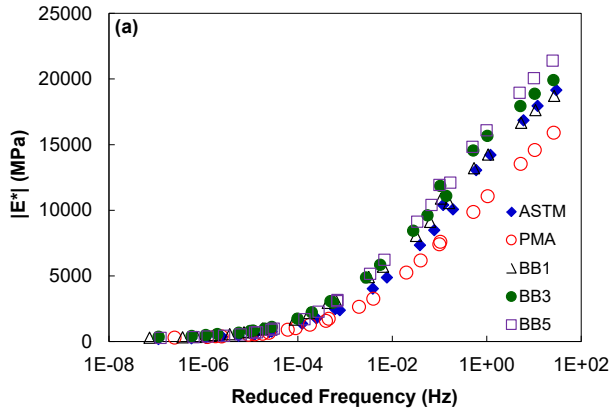
D. TSS test results for NYSDOT-B.

Figure 116. Graphs. TSS test results for NYSDOT mixtures.

KEC TEST ROAD

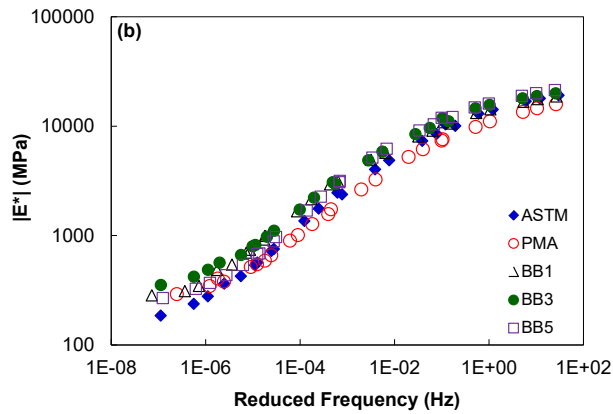
Figure 117 presents the dynamic modulus master curve results for the Korea Expressway Corporation (KEC) mixtures. The PMA mixture is the only polymer-modified mixture (SBS); however, the PMA mixture has lower modulus values than the ASTM mixture, which has the same aggregate gradation as the PMA mixture but uses unmodified binder. The research team also observed this finding for the FHWA ALF mixtures (figure 90). The control mixture, which is an unmodified mixture, shows higher dynamic modulus values than the modified mixtures.

The damage characteristic curves for the KEC mixtures, which are plotted in figure 118, illustrate the difference in the damage evolution of the different mixtures with different aggregate sizes. Overall, the ASTM and PMA mixture curves lie over the other curves, and the curves for the BB3 and BB5 mixtures are located just below the curves of the surface mixtures. The BB1 mixture lies below the other mixtures. As such, the research team interpreted that damage in the BB1 mixture increased a little faster than in the other mixtures. However, this observation needs to be verified using failure criteria and FlexPAVE program simulations.



© 2016 Journal of Materials and Structures. (DTFH61-08-H-00005)
 1 MPa = 145.04 psi.

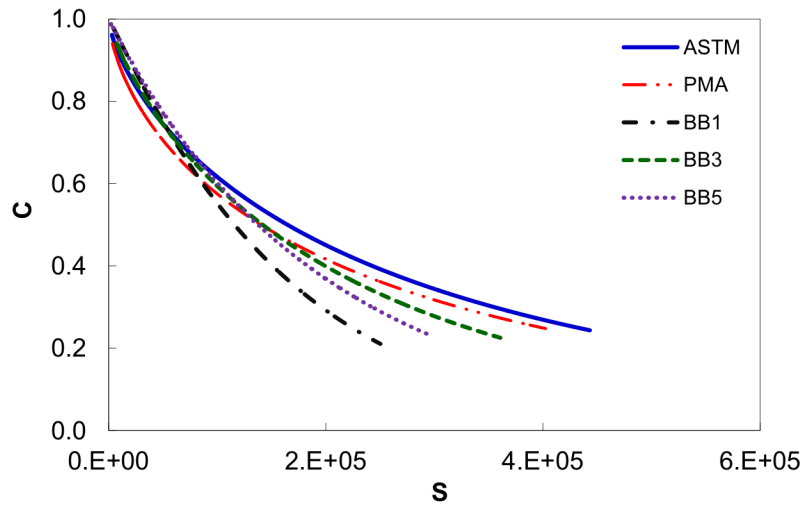
A. Linear viscoelastic characteristic for KEC mixtures in semi-log scale.



© 2016 Journal of Materials and Structures. (DTFH61-08-H-00005)
 1 MPa = 145.04 psi.

B. Linear viscoelastic characteristic for KEC mixtures in log-log scale.

Figure 117. Graphs. Linear viscoelastic characteristic for KEC mixtures.⁽¹¹⁴⁾

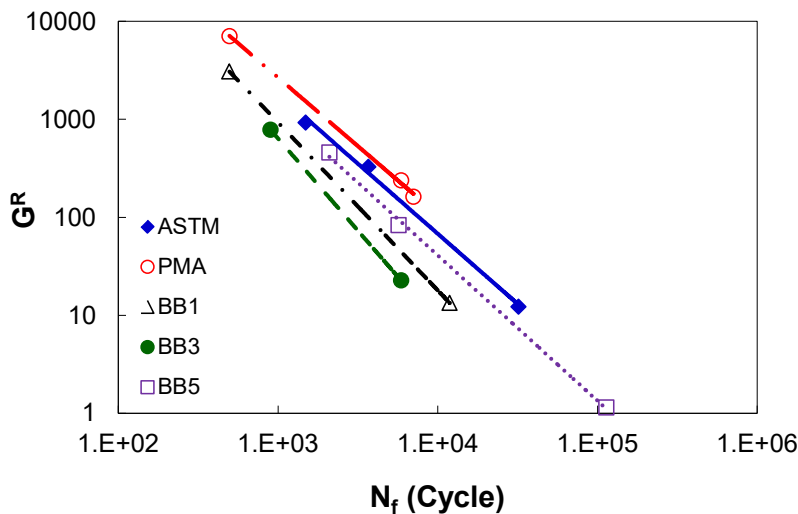


© 2016 Journal of Materials and Structures. (DTFH61-08-H-00005)

Figure 118. Graph. Damage characteristic curves for KEC mixtures.⁽¹¹⁴⁾

Figure 119 describes the failure criterion for the KEC mixtures. The PMA mixture curve is parallel to the ASTM mixture curve, which is likely due to the fact that the only difference between them is their binders. The BB5 mixture curve is higher than the BB1 and BB3 mixture curves. This finding indicates that for the same G^R value, the BB5 mixture has a greater number of cycles to failure (N_f), or a longer fatigue life. However, the G^R value also is related to the stiffness of the material and the pavement structure. Therefore, to evaluate fatigue life accurately, FlexPAVE simulations should be performed as well.

Table 32 shows the D^R values of the five KEC mixtures. The PMA mixture, which contains modified binder, exhibits the highest D^R value. However, unlike the trend the G^R criterion indicates, the BB3 mixture shows reasonable fatigue properties; thus, the research team does not predict the sections containing this mixture to exhibit extremely poor fatigue resistance. Chapter 4 discusses the discrepancy between the G^R and D^R criteria.



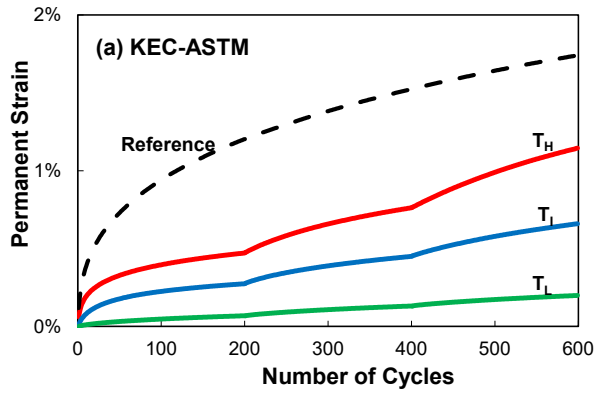
© 2016 Journal of Materials and Structures. (DTFH61-08-H-00005)

Figure 119. Graph. Failure criterion curves for KEC mixtures.⁽¹¹⁴⁾

Table 32. D^R values for KEC mixtures.

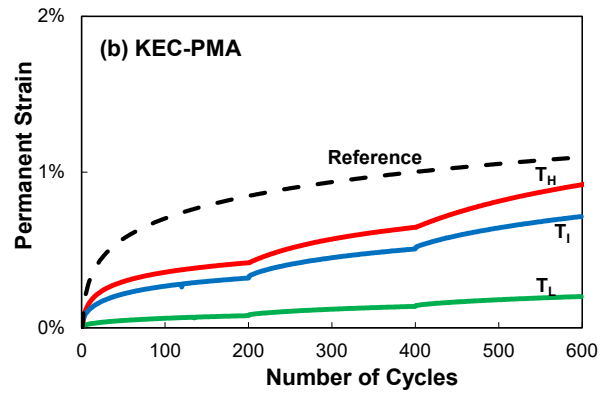
Mixture	D^R
ASTM	0.563
PMA	0.626
BB1	0.545
BB3	0.449
BB5	0.439

The TSS test temperatures used for the KEC mixtures are 22, 36, and 46°C for the low, intermediate, and high temperatures, respectively. Figure 120 presents the results of the TSS tests. The dotted lines show the reference curves and the solid lines correspond to the averaged permanent strains of the MSS tests at each temperature. An important observation about the surface mixtures is the difference in permanent strain levels between the ASTM and PMA mixtures. The corresponding curves for the ASTM mixture indicate higher permanent deformation levels than the PMA mixture because the PMA mixture contains SBS-modified asphalt binder (PG 76-22). Additionally, the temperature susceptibility of the PMA mixture, which kx evaluated by the amount of increase in the permanent strain from the low to intermediate to high temperatures, is much less than for all the other mixtures. These observations provide strong evidence for the benefits of polymer modification for rutting resistance. For the base layer (BB1 mixture and BB3 mixture) comparison, the BB1 mixture exhibits lower permanent deformation levels than the BB3 mixture due to the BB1 mixture's smaller aggregate particles (25 mm) and lower target air void content than the BB3 mixture. The research team used the averaged permanent strain values presented in figure 120 to characterize the shift model. The team then applied the model coefficients to the FlexPAVE program to evaluate the rutting performance of a pavement structure.



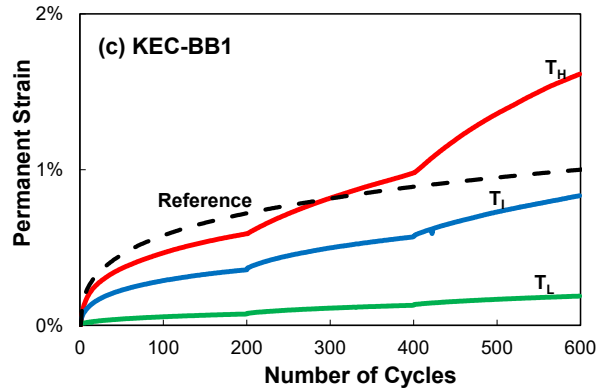
© 2016 Journal of Materials and Structures. (DTFH61-08-H-00005)

A. TSS test results for the KEC-ASTM mixture.



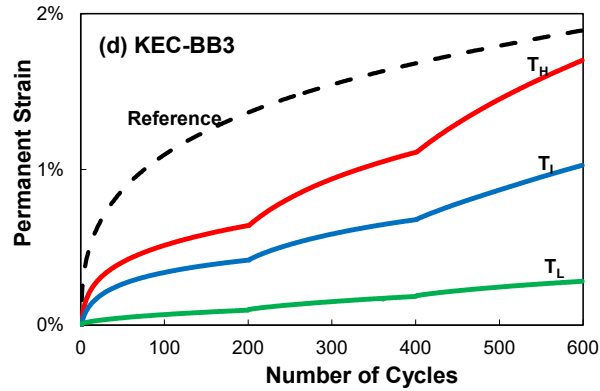
© 2016 Journal of Materials and Structures. (DTFH61-08-H-00005)

B. TSS test results for the KEC-PMA mixture.



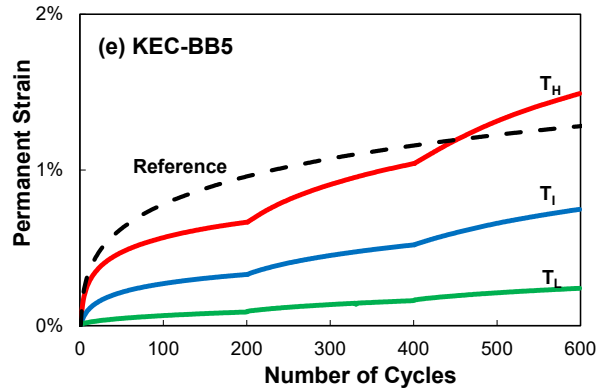
© 2016 Journal of Materials and Structures. (DTFH61-08-H-00005)

C. TSS test results for the KEC-BB1 mixture.



© 2016 Journal of Materials and Structures. (DTFH61-08-H-00005)

D. TSS test results for the KEC-BB3 mixture.



© 2016 Journal of Materials and Structures. (DTFH61-08-H-00005)

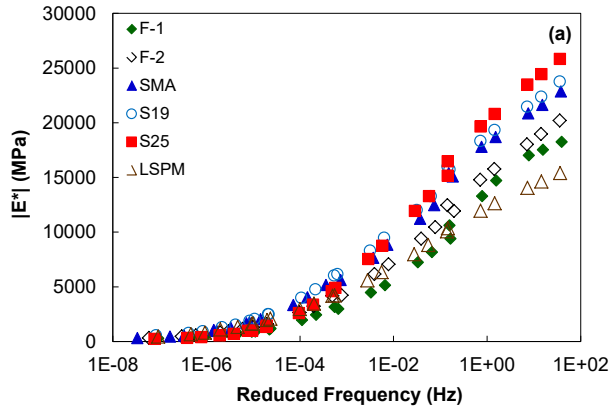
E. TSS test results for the KEC-BB5 mixture.

Figure 120. Graphs. TSS test results for the KEC mixtures.⁽¹¹⁴⁾

BINZHOU PERPETUAL PAVEMENT PROJECT

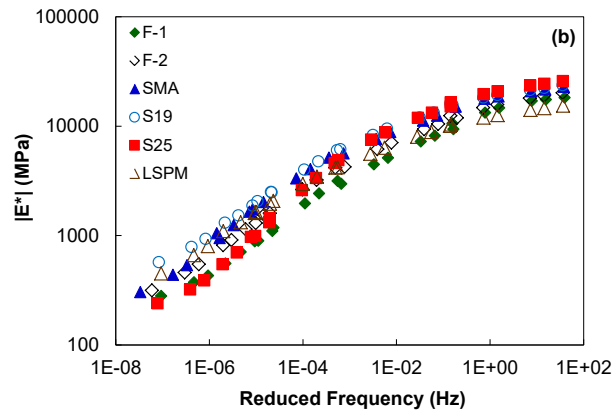
Figure 121 provides a summary of the dynamic modulus data for all Binzhou (China) mixtures. The key observations from these plots include the following:

- The large stone porous mixture (LSPM) is much softer than the other five mixtures at high reduced frequencies (physically representing cool temperatures and fast loading frequencies), which could be attributed to the high air void content (15.1 percent) in the LSPM.
- The LSPM is as stiff as the SMA and S19 mixtures at low reduced frequencies (physically representing high temperatures and slow loading frequencies). This difference in behavior, which the research team observed between the low and high reduced frequencies, could be attributed to the high degree of internal structure and particle-to-particle interaction within the LSPM. This particle interaction effect is more likely to appear under conditions in which the asphalt mastic is soft and less viscous (i.e., at low reduced frequencies), whereas a stiff mastic may diminish the effect (i.e., at high reduced frequencies).
- The S-25 mixture becomes much softer than the other mixtures at low reduced frequencies. This behavior may be attributable to differences in volumetrics between the materials as well as the fact that the S-25 mixture uses PG 64-22 binder whereas the other mixtures use PG 76-22 asphalt binder.
- The overall ranking from stiffest to softest mixture is S25, S19, SMA, F-2, F-1, and LSPM at high reduced frequencies and S19, LSPM, SMA, F-2, F-1, and S25 at low reduced frequencies.
- The S25 mixture shows a higher degree of elasticity than the other mixtures at low reduced frequencies, but a lower degree of elasticity at high reduced frequencies. This effect may be due to the fact that the S25 mixture uses a lower grade binder than the other materials.
- The LSPM shows the greatest sensitivity to stress state, followed by the SMA, S25, and S19 mixtures. This ranking may be related to the same issues identified in the first bullet point.



© 2016 Journal of Traffic and Transportation Engineering. (DTFH61-08-H-00005)
 1 MPa = 145.04 psi.

A. Linear viscoelastic characteristic curves for Binzhou mixtures in semi-log scale.

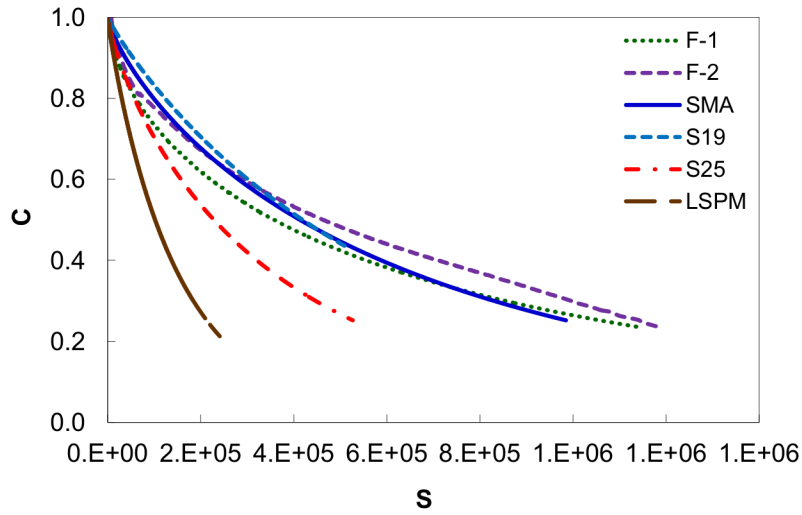


© 2016 Journal of Traffic and Transportation Engineering. (DTFH61-08-H-00005)
 1 MPa = 145.04 psi.

B. Linear viscoelastic characteristic curves for Binzhou mixtures in log-log scale.

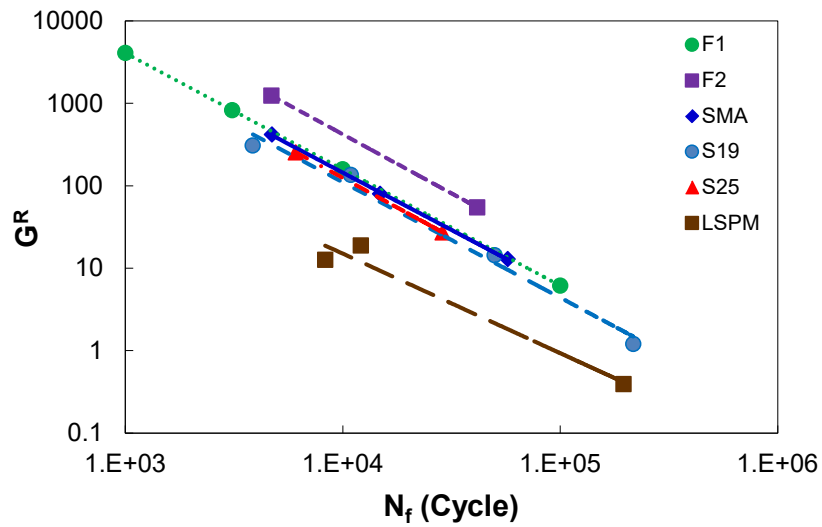
Figure 121. Graphs. Linear viscoelastic characteristic curves for Binzhou mixtures.⁽³⁰⁾

Figure 122 and figure 123 present the damage characteristic curve and the fatigue failure criterion lines for the Binzhou perpetual pavements, respectively. The F2 mixture seemingly performs better than the F1 mixture, which is mainly due to the SBS-modified binder in this mixture. In addition, the NMAS of the F2 mixture is smaller than the other mixtures; therefore, the research team concluded the F2 mixture should perform better than the other mixtures. As presented in figure 121, the S19 and S25 mixtures have similar dynamic modulus values at both the low and high temperatures; however, the corresponding failure criterion for the S25 mixture has a steeper slope than the S19 mixture. As such, the S25 mixture is likely to perform worse than the S19 mixture, probably due to its greater aggregate size and higher binder grade. As expected, the LSPM, due to its specific structure, shows the worst fatigue life among the mixtures. Table 33 presents the D^R values of those mixtures.



© 2016 Journal of Traffic and Transportation Engineering. (DTFH61-08-H-00005)

Figure 122. Graph. Damage characteristic curves for Binzhou mixtures.⁽³⁰⁾



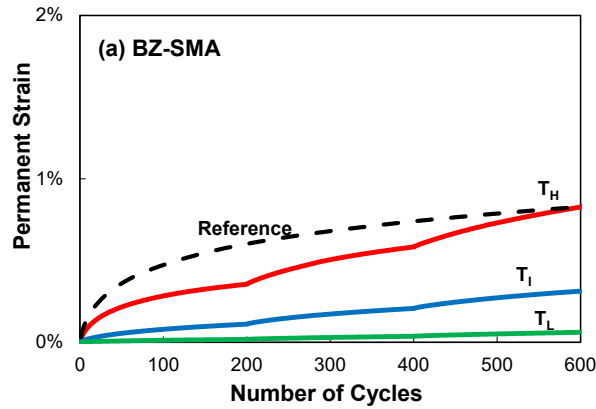
© 2016 Journal of Traffic and Transportation Engineering. (DTFH61-08-H-00005)

Figure 123. Graph. Failure criterion curves for Binzhou mixtures.⁽³⁰⁾

Table 33. D^R values for Binzhou mixtures.

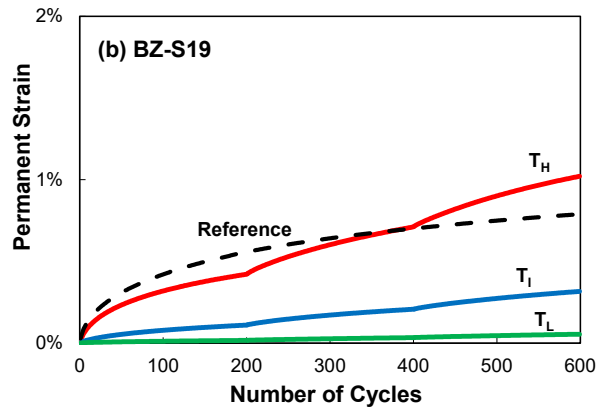
Mixture	D^R
F1	0.569
F2	0.558
S25	0.446
LSPM	0.466
S19	0.432
SMA	0.494

The test temperatures used for the Binzhou mixtures were 26, 36, and 46°C. Figure 124 shows the rutting resistance of the Binzhou mixtures. The SMA mixture shows good rutting resistance compared with the other mixtures because it contains coarse aggregate particles that interlock to form a stone skeleton that resists permanent deformation. The S25 mixture shows a higher permanent strain level than the other mixtures. Again, this result is likely due to the S25 mixture using a lower grade binder (PG 64-22) than the other materials (PG 76-22).



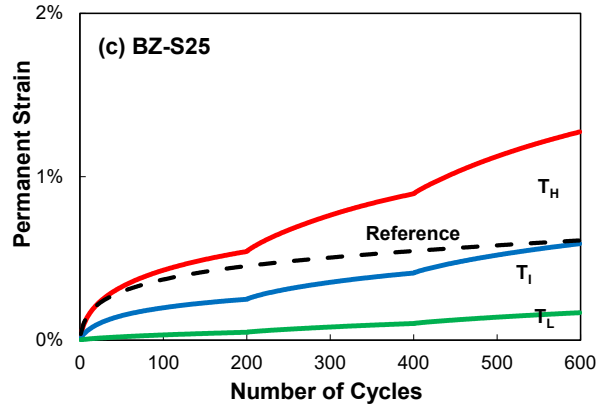
Source: FHWA.

A. TSS test results for the Binzhou SMA mixture.



Source: FHWA.

B. TSS test results for the Binzhou S19 mixture.



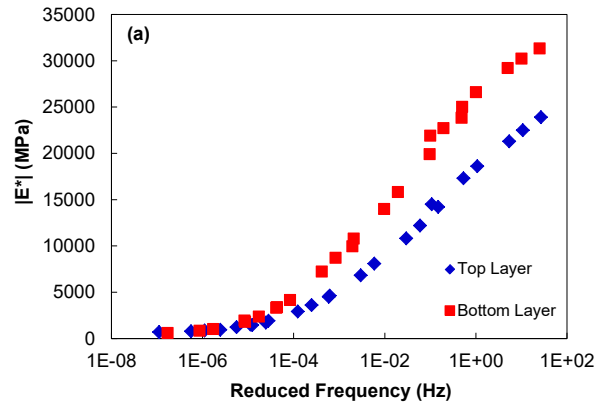
Source: FHWA.

C. TSS test results for the Binzhou S25 mixture.

Figure 124. Graphs. TSS test results for the Binzhou mixtures.

LADOTD PAVEMENTS

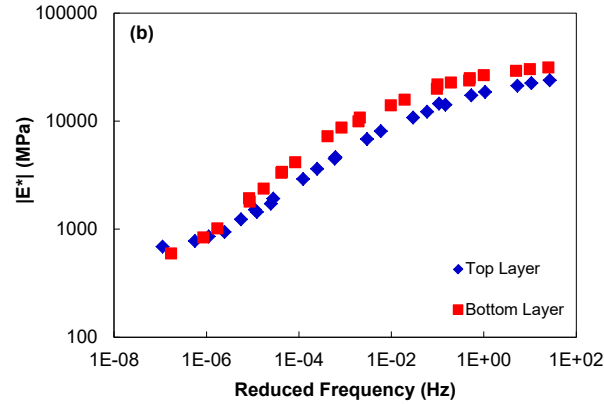
Figure 125 and figure 126 present the dynamic modulus master curves and damage characteristic curves for the LaDOTD mixtures, respectively. As shown, the surface layer (top layer) mixture has lower modulus values than the bottom layer mixture. One probable reason for this result could be the smaller aggregate size of the top layer with an NMAS of 12.5 mm compared with 19 mm for the bottom layer, and a higher air void content in the top layer. In addition, table 34 shows the D^R values of the mixtures.



Source: FHWA.

1 MPa = 145.04 psi.

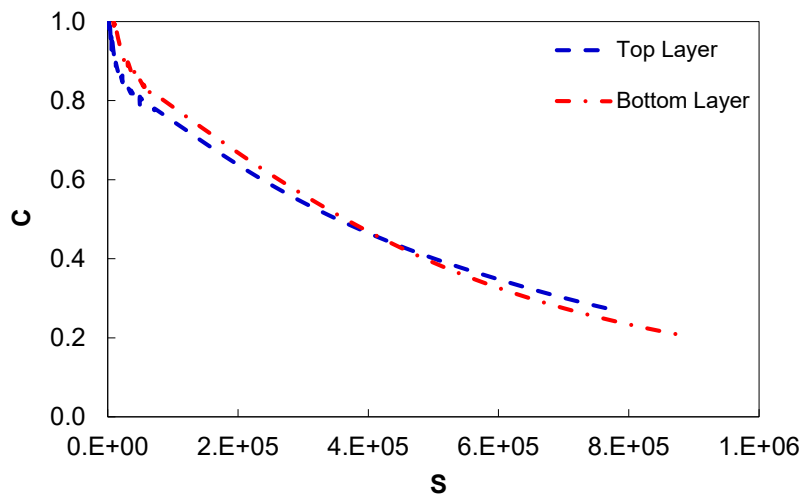
A. Linear viscoelastic characteristic curves for LaDOTD mixtures in semi-log scale.



Source: FHWA.
1 MPa = 145.04 psi.

B. Linear viscoelastic characteristic curves for LaDOTD mixtures in log-log scale.

Figure 125. Graphs. Linear viscoelastic characteristic curves for LaDOTD mixtures.



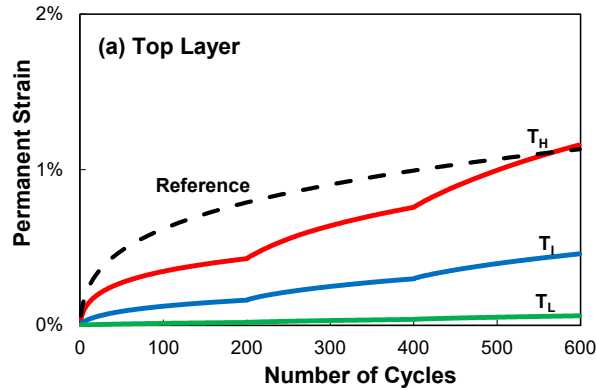
Source: FHWA.

Figure 126. Graph. Damage characteristic curves for LaDOTD mixtures.

Table 34. D^R values of LADOTD mixtures.

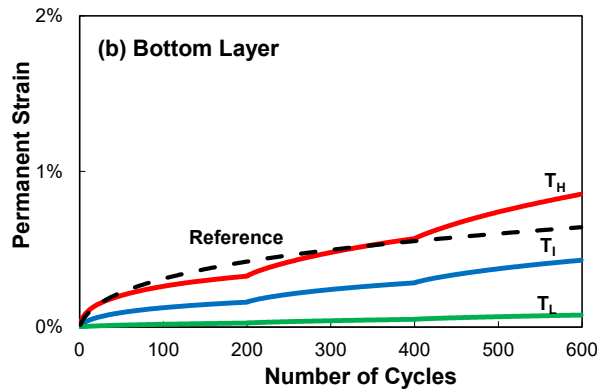
Mixture	D^R
Bottom	0.417
Top	0.496

The TSS test temperatures the research team used for the LaDOTD mixtures were 21, 35, and 49°C. Figure 127 presents the permanent strain levels of the top and bottom layers, which indicates the bottom layer mixture exhibits lower permanent deformation levels than the top layer mixture, because the bottom layer mixture has larger (19-mm NMAS) aggregate particles and a lower target air void content than the top layer mixture. As such, the interlocking of the aggregate particles in the bottom layer mixture increases its rutting resistance.



Source: FHWA.

A. TSS test results for the LaDOTD top-layer mixture.



Source: FHWA.

B. TSS test results for the LaDOTD bottom-layer mixture.

Figure 127. Graphs. TSS test results for the LaDOTD mixtures.

SUMMARY OF THE CHAPTER

As discussed in chapter 6, the research team used AMPT performance test methods to characterize 60 different asphalt mixtures with a wide range of mixture factors. The performance trends these mixtures showed agree with the expected trends based on common understanding of the effects of different mixture factors on the mixtures' cracking and rutting performance.

Chapter 7 details how the research team input the material properties obtained from these tests to FlexPAVE to evaluate the performance of the asphalt pavements and validate the reasonableness of the AM-PRS methodology.

CHAPTER 7. FIELD VERIFICATION

BACKGROUND

Thus far, the research team has proposed the fatigue cracking model (i.e., the S-VECD model) and the permanent deformation model (i.e., the shift model), along with their calibration methods, as an integral part of this PRS project. The research team has also implemented these models into the three-dimensional FEM program (i.e., the FlexPAVE program) to evaluate field performance. The ultimate goal of the performance models and the numerical program is predicting the performance of asphalt pavements in reality. This chapter details how the research team verified the FlexPAVE program, together with the performance models, through field-measured data. The team used the calibrated models for each mixture discussed in chapter 6 for the predictions.

FATIGUE CRACKING PREDICTIONS

This section first defines fatigue damage and damage factor. Then, it compares the FlexPAVE-predicted percent damage for various pavement sections against the field-measured percent cracking to demonstrate the reasonableness of the FlexPAVE prediction.

Fatigue Damage Calculation

Miner's law, as expressed by equation 129, represents the cumulative damage in a pavement due to repeated wheel loading and thermal stresses.

$$\sum_{i=1}^T D_i = \frac{N_i}{N_{fi}} \quad (129)$$

Where:

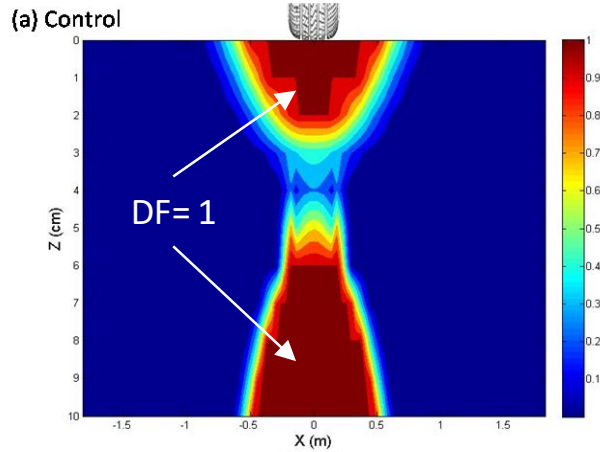
D_i = damage accumulated during period i .

T = total number of periods.

N_i = traffic for period i .

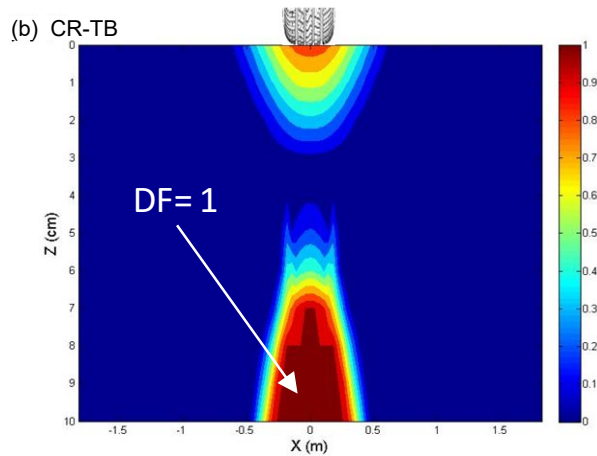
N_{fi} = allowable failure repetitions under the conditions that prevail in period i .

The damage factor, defined as N/N_f , starts from zero in an intact condition and increases as the level of damage increases. The value of $N/N_f = 1$ generally corresponds to the point at which the strains localize and the material fails. Figure 128 presents the damage factor contours for the four FHWA ALF pavements. A high damage factor represents the areas with high levels of damage. To better quantify the simulation results for fatigue damage, the research team defined an index value (i.e., percent damage area). The team calculated this index by determining the percentage of the damage points across the pavement cross-section that have a damage factor equal to 1 ($N/N_f = 1$) over the total nodes in the pavement structure.



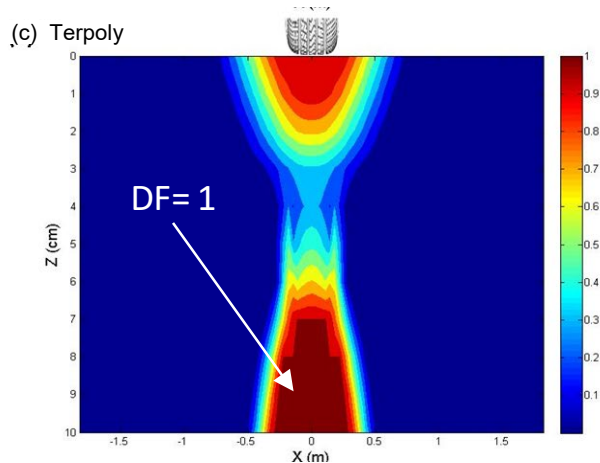
© 2018 Transportation Research Record. (DTFH61-08-H-00005)
 1 cm = 0.4 inch; 1 m = 3.28 ft.
 DF at 1 = failure.
 DF = damage factor.

A. Damage factor for 20-yr simulation of the FHWA ALF control section.



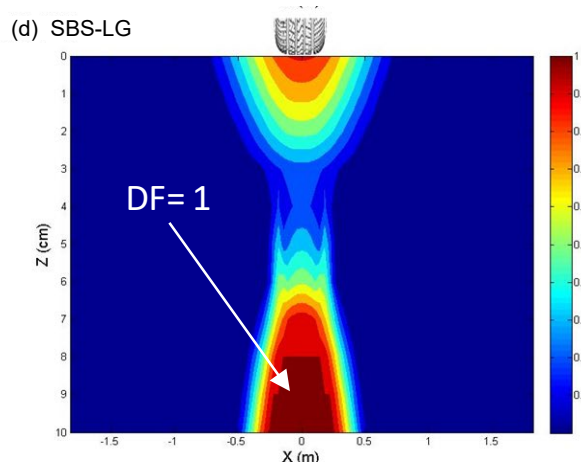
© 2018 Transportation Research Record. (DTFH61-08-H-00005)
 1 cm = 0.4 inch; 1 m = 3.28 ft.
 DF at 1 = failure.
 DF = damage factor.

B. Damage factor for 20-yr simulation of the FHWA ALF crumb rubber-terminal blend (CR-TB) section.



© 2018 Transportation Research Record. (DTFH61-08-H-00005)
 1 cm = 0.4 inch; 1 m = 3.28 ft.
 DF at 1 = failure.
 DF = damage factor.

C. Damage factor for 20-yr simulation of the FHWA ALF terpolymer section.



© 2018 Transportation Research Record. (DTFH61-08-H-00005)
 1 cm = 0.4 inch; 1 m = 3.28 ft.
 DF at 1 = failure.
 DF = damage factor.

D. Damage factor for 20-yr simulation of the FHWA ALF SBS-LG section.

Figure 128. Contours. Damage factors of 20-yr simulations of FHWA ALF sections.⁽⁶⁸⁾

The research team used real traffic data expressed in terms of ESALs for the pavement performance simulations. To convert the field measurements into a single index, the team adopted equation 130 to define a representative index of fatigue performance. Because of the different degrees of cracking (low, medium, and high intensity) and multiple test sections with different lengths, equation 131 estimates the parameters in equation 130. The next subsections present and compare the results for the percentage of damage area the research team obtained

from the FlexPAVE program simulations and the percentage of crack area they obtained from the field measurements for the different projects.

$$Crack\ area\ (\%) = 40 \times \left[\left(\frac{\%Low}{350} \right) + \left(\frac{\%Med}{200} \right) + \left(\frac{\%High}{75} \right) \right] \quad (130)$$

Where:

%Low = percentage of interval length, low severity.

%Med = percentage of interval length, medium severity.

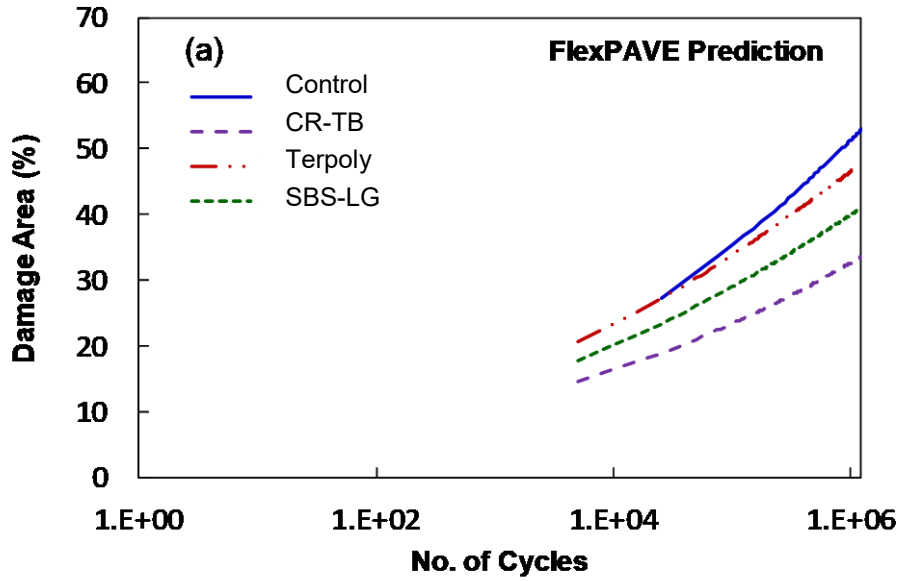
%High = percentage of interval length, high severity.

$$\text{percent interval}(\%) = \frac{\text{length of respective longitudinal cracking}}{\text{section length}} \times 100\% \quad (131)$$

FHWA ALF

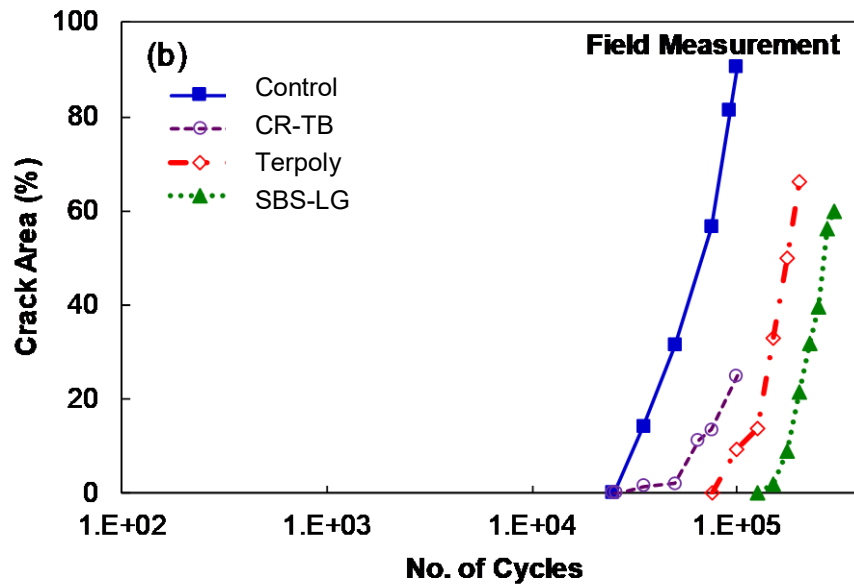
Figure 128 presents the damage contours for the FHWA ALF asphalt pavement sections and figure 129 presents the percent predicted damage area and percent cracking area measured from the field. The research team calculated the percent predicted damage area based on the definition given in the Percent Damage Definition section in Chapter 5.

According to figure 128 and figure 129, both the predicted damage area and the measured cracking area indicate that the sections with modified binder performed better than the control section. Among the three test sections built using modified binder, the section with the SBS binder performed the best according to the field measurements, but the predicted results indicate that the SBS section is the second best test section in terms of resistance to fatigue damage. However, if the research team only counted the failed points with damage factors equal to one in the damage contour, the SBS section would be considered to perform the best of the three sections. Given that the research team found problems with the quality of the material in the terpolymer section, the ranking of the fatigue resistance the FlexPAVE program predicted is in relatively good agreement with that measured from the field, as presented in figure 130. In addition to ranking the pavement sections that contain different mixtures, the overall trend of the fatigue cracking evolution appears to be similar to trends the research team observed in the field.



© 2018 Transportation Research Record. (DTFH61-08-H-00005)

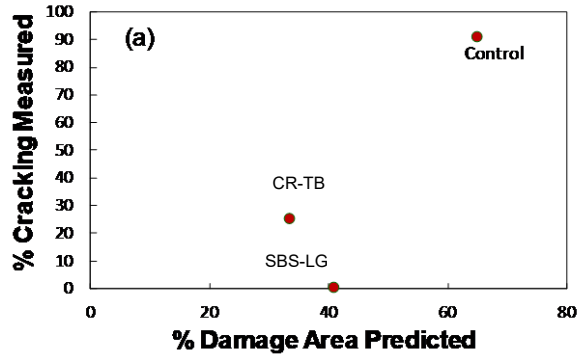
A. FlexPAVE-predicted cracking evolution in FHWA ALF sections.



© 2018 Transportation Research Record. (DTFH61-08-H-00005)

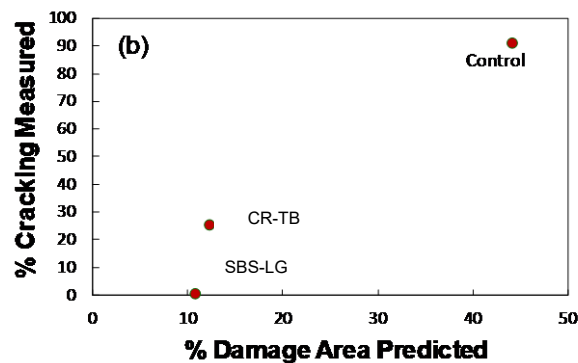
B. Field-measured cracking evolution in FHWA ALF sections.

Figure 129. Graphs. Cracking evolution in FHWA ALF sections.⁽⁶⁸⁾



© 2018 Transportation Research Record. (DTFH61-08-H-00005)

A. Measured cracking area versus predicted damage area counting all points with damage.



© 2018 Transportation Research Record. (DTFH61-08-H-00005)

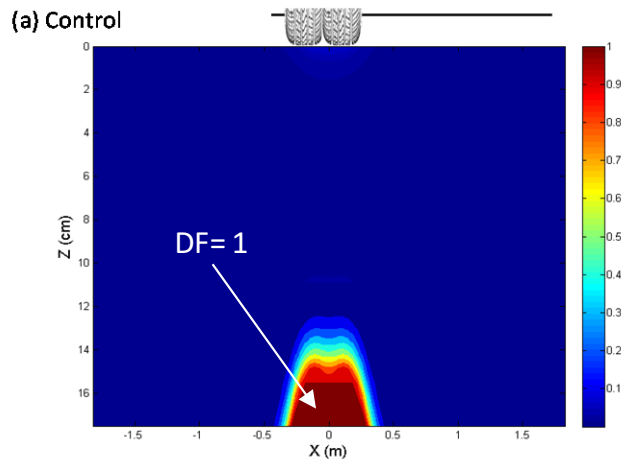
B. Measured cracking area versus predicted damage area counting only failure points.

Figure 130. Graphs. Measured cracking area versus predicted damage area.⁽⁶⁸⁾

NCAT Test Track

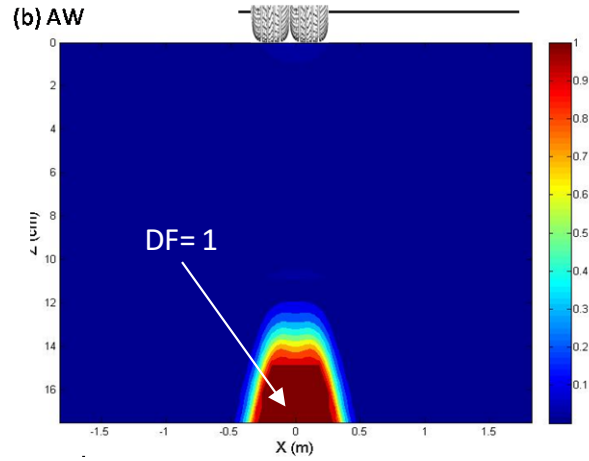
Figure 131 presents the predicted damage contours for the NCAT Test Track sections, and figure 132 and figure 133 illustrate the percent predicted damage area and percent measured cracking area in the field. The figures show the predicted fatigue damage for those sections is in agreement with the field measurements. The section that uses the OGFC mixture as the surface mixture has the greatest cracking area according to the field-measured results. Moreover, the cracking area in the field grew dramatically after a certain number of loads had passed. The FlexPAVE simulations predicted this behavior well. The predicted growth rate of the damage evolution in the OGFC section accelerates after a number of loading passes. This section ranks first after 20 million ESAL in terms of percent damage area. Moreover, the damage contours in figure 131 show the presence of top-down cracking. The current version of FlexPAVE does not yet include an aging model, nor does it update the stiffness values of the asphalt layers as damage accumulates in those layers in the fatigue simulations. Therefore, the amount of predicted damage will increase after those features are added in the next version of FlexPAVE. However, FlexPAVE did predict the low amount of damage for the RW and R sections in the field. Furthermore, the amount of fatigue damage of both WMA sections, AW and FW, is greater than that of the control section in both the predicted and measured results.

The research team expected the section with the OGFC mixture to show more cracking on the surface because the mixture is a coarse-graded mixture and contains a high percentage of air voids. Though a common assumption is pavement sections containing a high proportion of RAP materials will exhibit more cracking because of the preaged brittle material, this was not the case according to the field observations of the NCAT Test Track sections. The good agreement between the results from FlexPAVE and the field measurements indicates the discrepancy between the common assumption and the field observations from the RAP sections can be predicted by the mechanistic models employed in FlexPAVE in conjunction with the laboratory data measured using the TP 107 procedure.⁽³⁷⁾ Based on the material test results presented in chapter 6, the mixtures that contain high percentages of RAP have high modulus values as well. When those materials are placed on the road, the mechanical responses under the traffic load, such as tensile strain and shear stress, have much lower values than those responses under other materials softer than RAP mixtures. Therefore, the research team observed low amounts of cracking even though the mixtures with high RAP contents were brittle.



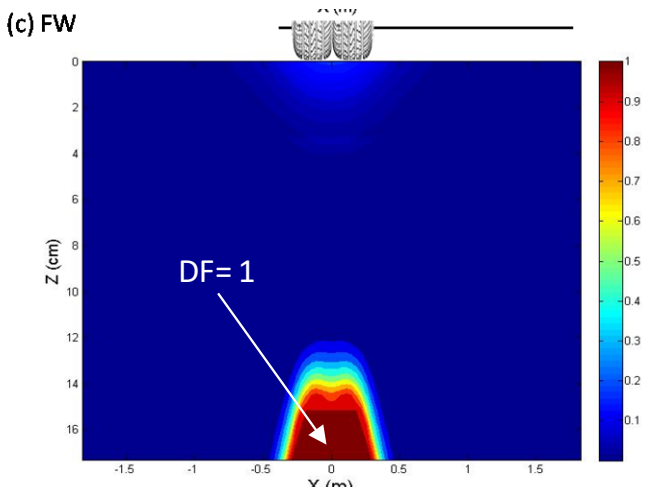
© 2018 Transportation Research Record. (DTFH61-08-H-00005)
 1 cm = 0.4 inch; 1 m = 3.28 ft.
 DF at 1 = failure.
 DF = damage factor.

A. Four-year FlexPAVE simulation results for the NCAT control mixture.



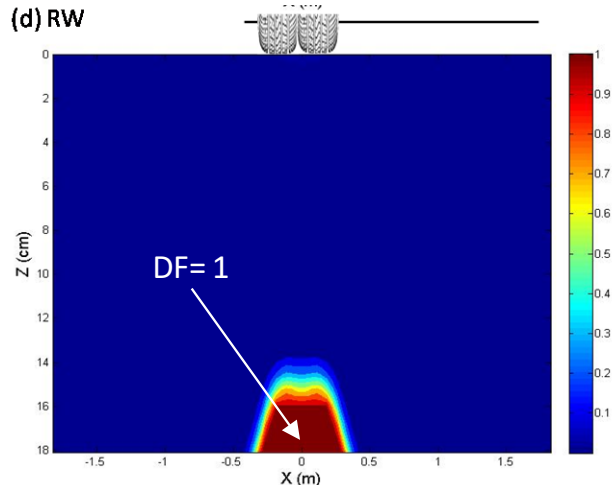
© 2018 Transportation Research Record. (DTFH61-08-H-00005)
 1 cm = 0.4 inch; 1 m = 3.28 ft.
 DF at 1 = failure.
 DF = damage factor.

B. Four-year FlexPAVE simulation results for the NCAT-AW mixtures.



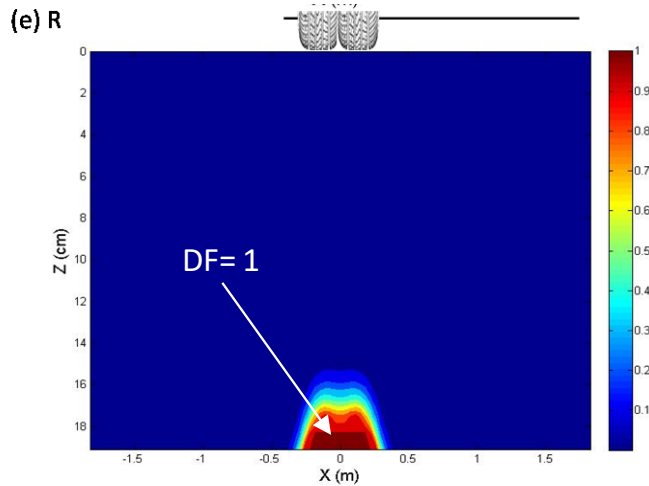
© 2018 Transportation Research Record. (DTFH61-08-H-00005)
 1 cm = 0.4 inch; 1 m = 3.28 ft.
 DF at 1 = failure.
 DF = damage factor.

C. Four-year FlexPAVE simulation results for the NCAT-FW mixtures.



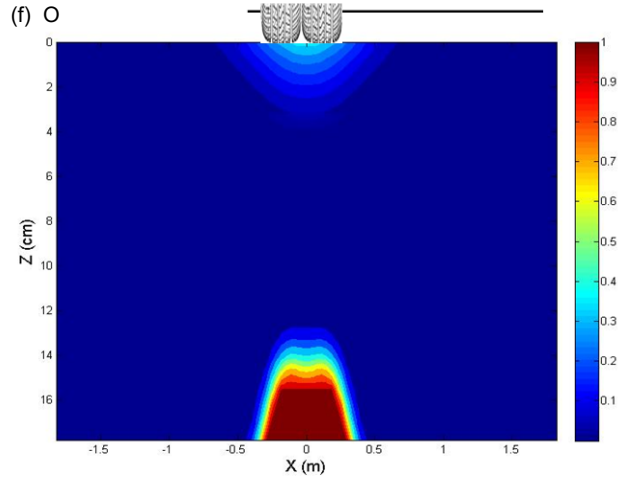
© 2018 Transportation Research Record. (DTFH61-08-H-00005)
 1 cm = 0.4 inch; 1 m = 3.28 ft.
 DF at 1 = failure.
 DF = damage factor.

D. Four-year FlexPAVE simulation results for the NCAT-RW mixtures.



© 2018 Transportation Research Record. (DTFH61-08-H-00005)
 1 cm = 0.4 inch; 1 m = 3.28 ft.
 DF at 1 = failure.
 DF = damage factor.

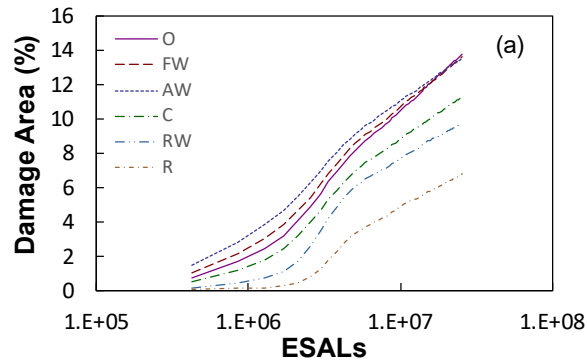
E. Four-year FlexPAVE simulation results for the NCAT-R mixtures.



© 2018 Transportation Research Record. (DTFH61-08-H-00005)
 1 cm = 0.4 inch; 1 m = 3.28 ft.
 DF at 1 = failure.
 DF = damage factor.

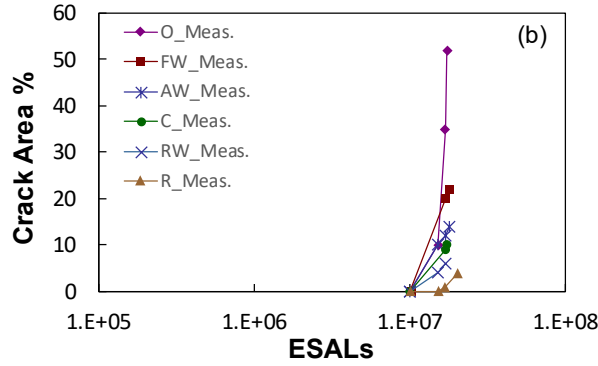
F. Four-year FlexPAVE simulation results for the NCAT-O mixtures.

Figure 131. Contours. Four-year FlexPAVE simulation results for NCAT mixtures.⁽⁶⁸⁾



© 2018 Transportation Research Record. (DTFH61-08-H-00005)

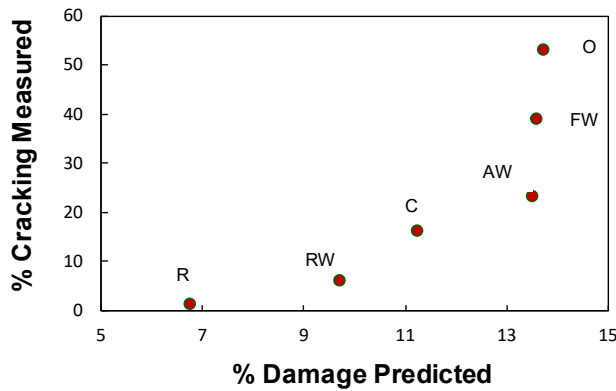
A. FlexPAVE-predicted cracking evolution in NCAT Test Track sections.



© 2018 Transportation Research Record. (DTFH61-08-H-00005)

B. Field-measured cracking evolution in NCAT Test Track sections.

Figure 132. Graphs. Cracking evolution in NCAT Test Track sections.

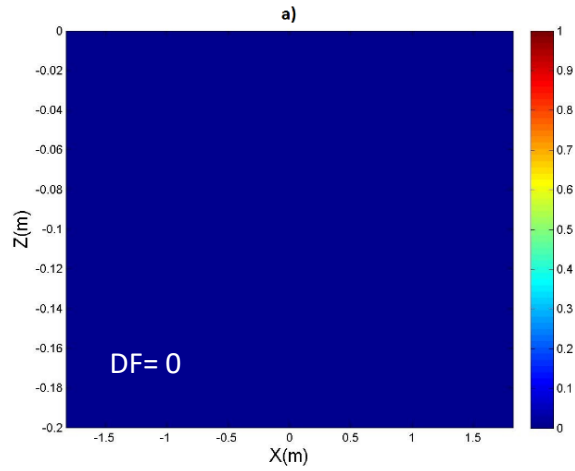


© 2018 Transportation Research Record. (DTFH61-08-H-00005)

Figure 133. Graph. Measured cracking area versus predicted damage area for NCAT Test Track sections.⁽⁶⁸⁾

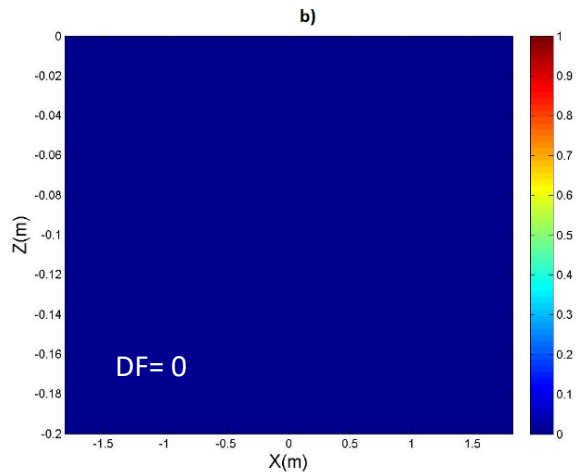
MIT-RAP

The FlexPAVE program results shown in figure 134-E through figure 134-H for the MIT-RAP project indicate no major differences in fatigue cracking. Using a damage factor of $N/N_f = 1$, the FlexPAVE predicts no cracking, which fits well with the field observations.



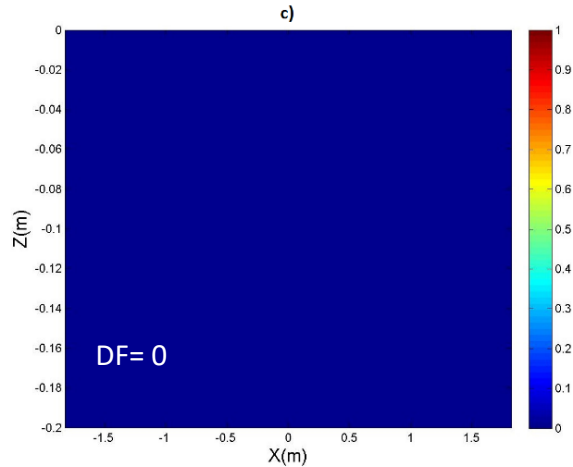
Source: FHWA.
 1 cm = 0.4 inch; 1 m = 3.28 ft.
 DF at 1 = failure.
 DF = damage factor.

A. Twenty-year FlexPAVE simulation results for the MIT-RAP control mixture.



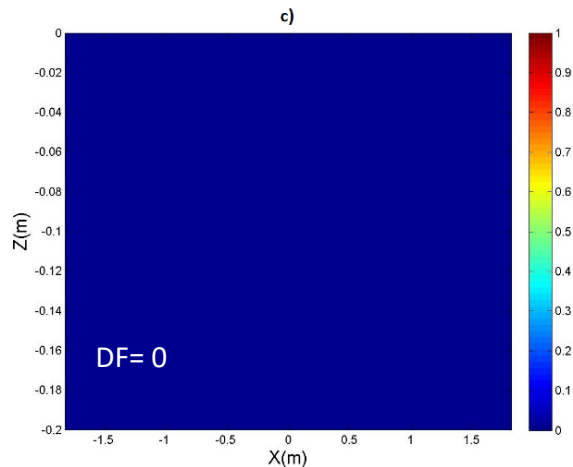
Source: FHWA.
 1 cm = 0.4 inch; 1 m = 3.28 ft.
 DF at 1 = failure.
 DF = damage factor.

B. Twenty-year FlexPAVE simulation results for the MIT-RAP 15R mixture.



Source: FHWA.
 1 cm = 0.4 inch; 1 m = 3.28 ft.
 DF at 1 = failure.
 DF = damage factor.

C. Twenty-year FlexPAVE simulation results for the MIT-RAP 50R mixture.



Source: FHWA.
 1 cm = 0.4 inch; 1 m = 3.28 ft.
 DF at 1 = failure.
 DF = damage factor.

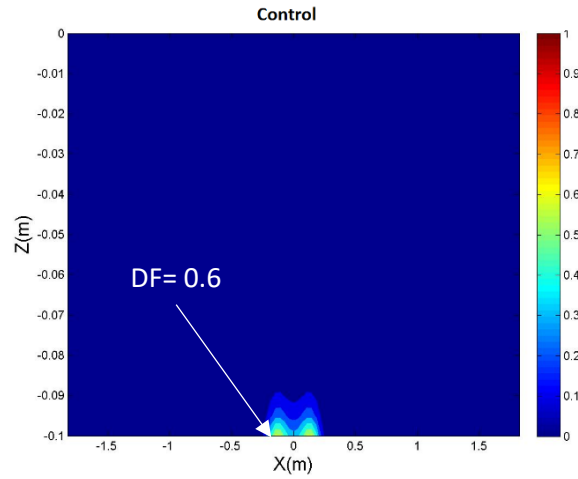
D. Twenty-year FlexPAVE simulation results for the MIT-RAP 50RSB mixture.

Figure 134. Contours. Twenty-year FlexPAVE simulation results for MIT-RAP mixtures.

MIT-WMA

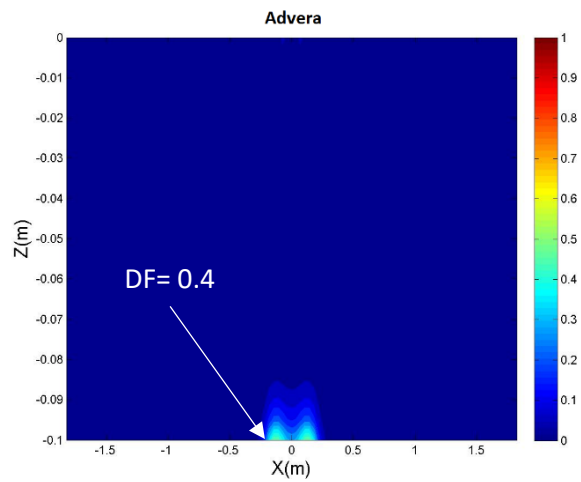
Figure 135 presents the effects of three different WMA technologies on the MIT mixtures, respectively. Since there was no damage in the short term, due to extremely low traffic levels, the simulation ran for 20 yr to emphasize the difference in performance between the sections. As shown, utilizing Evotherm led to improved predicted performance, which is in contrast to the

observations made from the NCAT sections, as seen in figure 129 and figure 131. Including Advera slightly reduced predicted damage, whereas Sasobit increased the predicted damage in the MIT pavement sections. The research team observed no significant cracking in the field for any section. The simulations fit well with the field observations; however, effects due to aging mean that the predictions of very little damage at 20 yr may not be true in reality.



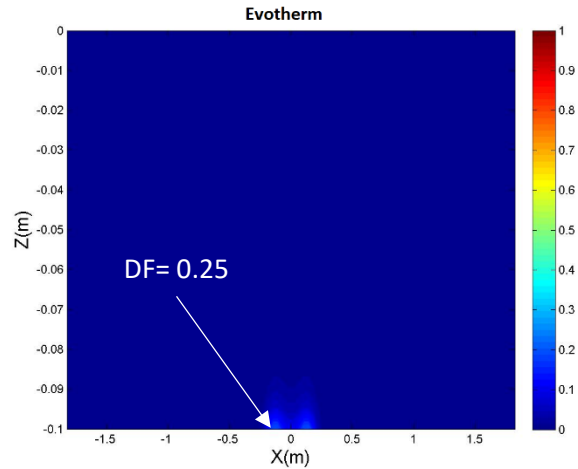
Source: FHWA.
 1 cm = 0.4 inch; 1 m = 3.28 ft.
 DF at 1 = failure.
 DF = damage factor.

A. Twenty-year FlexPAVE simulation results for the MIT-WMA control mixture.



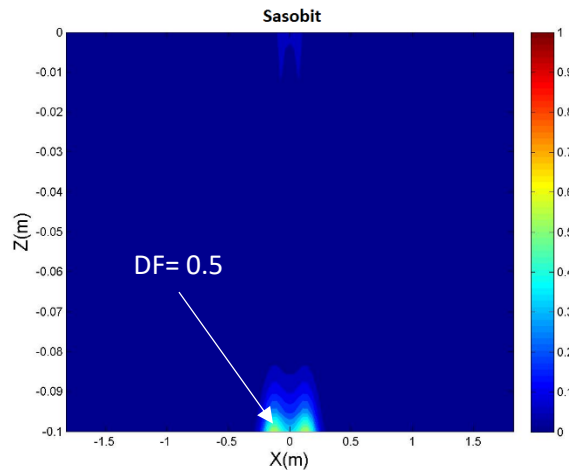
Source: FHWA.
 1 cm = 0.4 inch; 1 m = 3.28 ft.
 DF at 1 = failure.
 DF = damage factor.

B. Twenty-year FlexPAVE simulation results for the MIT-WMA Advera.



Source: FHWA.
 1 cm = 0.4 inch; 1 m = 3.28 ft.
 DF at 1 = failure.
 DF = damage factor.

C. Twenty-year FlexPAVE simulation results for the MIT-WMA Evotherm mixture.



Source: FHWA.
 1 cm = 0.4 inch; 1 m = 3.28 ft.
 DF at 1 = failure.
 DF = damage factor.

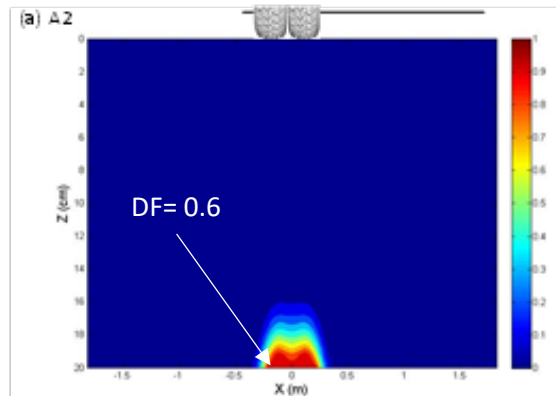
D. Twenty-year FlexPAVE simulation results for MIT-WMA Sasobit.

Figure 135. Contours. Twenty-year FlexPAVE simulation results for MIT-WMA mixtures.

KEC

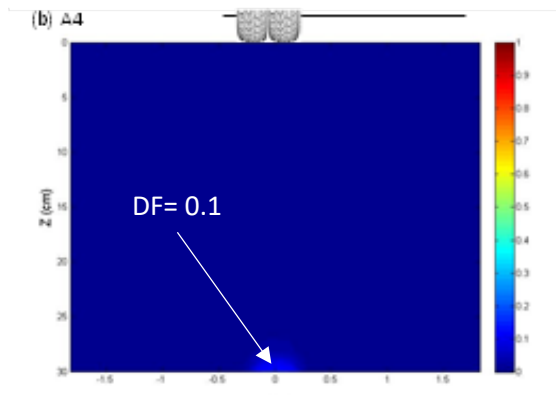
The FlexPAVE simulations for the KEC pavements are shown in figure 136. In general, most of the predicted simulation results for the KEC mixtures indicate reasonable agreement with the field performance observations. A direct comparison of the KEC simulations and field observations is not as straightforward as similar comparisons made for the other projects because the research team did not know accurate traffic and climatic conditions for the KEC test road.

Other factors like in-place material properties and construction variability increase this complexity. As such, the field measurements show high variability and indicate sections with subtle differences in material types or structure may experience extremely different field performance. This variability means that, to check reasonableness of FlexPAVE predictions, the user should not exclusively focus on how well the predictions match the field but instead look at the overall ranking of the predicted performance of the sections. In doing this, the user can make several conclusions about the FlexPAVE predictions (figure 137-A).



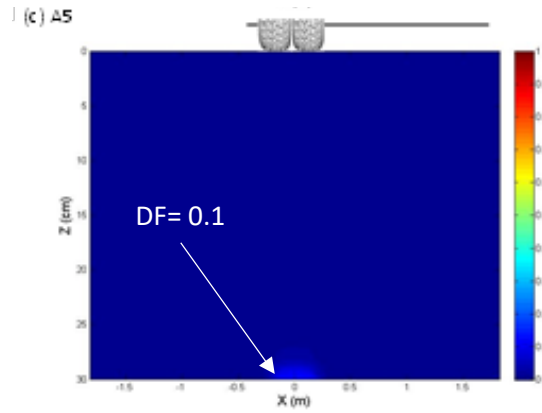
Source: FHWA.
 1 cm = 0.4 inch; 1 m = 3.28 ft.
 DF at 1 = failure.
 DF = damage factor.

A. Six-year FlexPAVE simulation results for the KEC A2 test road section.



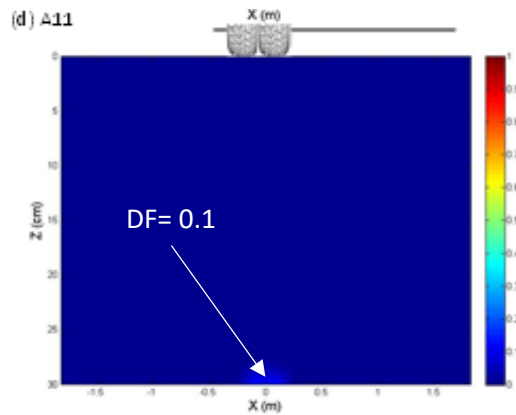
Source: FHWA.
 1 cm = 0.4 inch; 1 m = 3.28 ft.
 DF at 1 = failure.
 DF = damage factor.

B. Six-year FlexPAVE simulation results for the KEC A4 test road section.



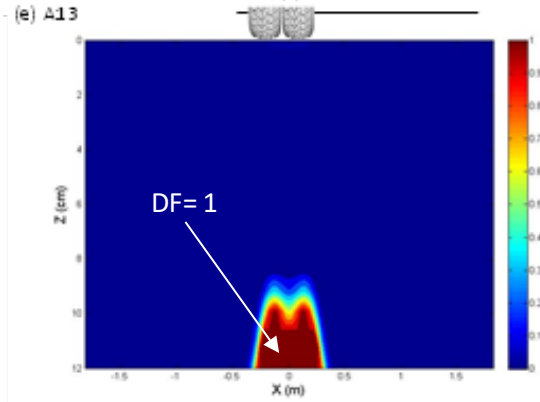
Source: FHWA.
 1 cm = 0.4 inch; 1 m = 3.28 ft.
 DF at 1 = failure.
 DF = damage factor.

C. Six-year FlexPAVE simulation results for KEC the A5 test road section.



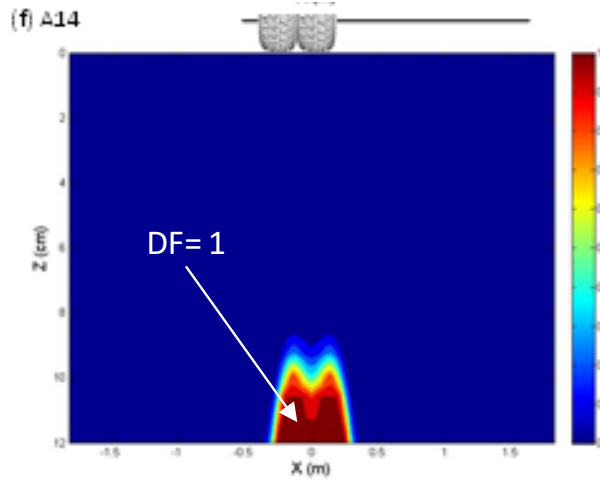
Source: FHWA.
 1 cm = 0.4 inch; 1 m = 3.28 ft.
 DF at 1 = failure.
 DF = damage factor.

D. Six-year FlexPAVE simulation results for the KEC A11 test road section.



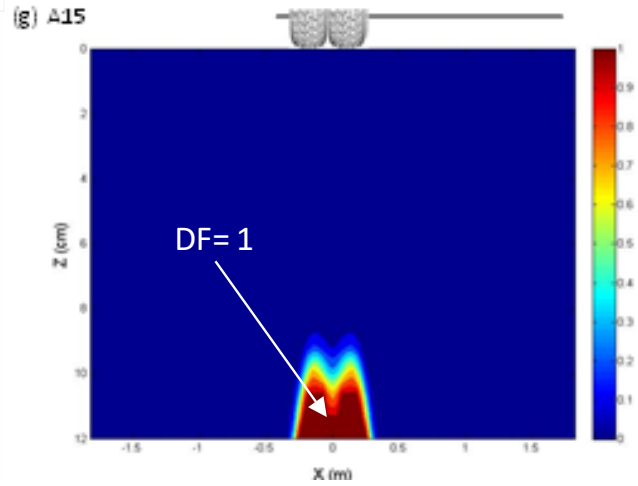
Source: FHWA.
 1 cm = 0.4 inch; 1 m = 3.28 ft.
 DF at 1 = failure.
 DF = damage factor.

E. Six-year FlexPAVE simulation results for the KEC A13 test road section.



Source: FHWA.
 1 cm = 0.4 inch; 1 m = 3.28 ft.
 DF at 1 = failure.
 DF = damage factor.

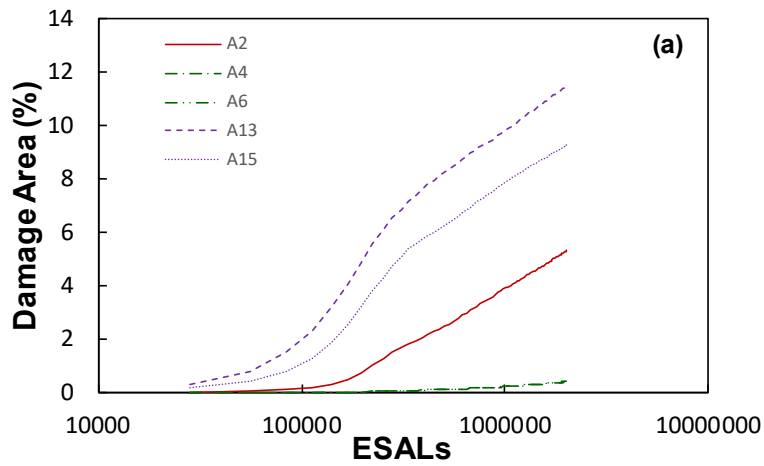
F. Six-year FlexPAVE simulation results for the KEC A14 test road section.



Source: FHWA.
 1 cm = 0.4 inch; 1 m = 3.28 ft.
 DF at 1 = failure.
 DF = damage factor.

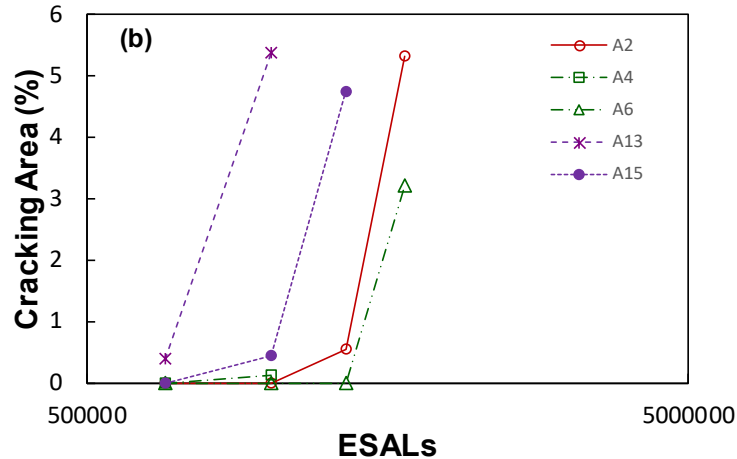
G. Six-year FlexPAVE simulation results for the KEC A15 test road section.

Figure 136. Contours. Six-year FlexPAVE simulation results for KEC test road sections.



© 2018 Transportation Research Record. (DTFH61-08-H-00005)

A. FlexPAVE-simulated damage area percent in KEC sections.



© 2018 Transportation Research Record. (DTFH61-08-H-00005)

B. Field-measured cracking evolution in KEC sections.

Figure 137. Graphs. Damage and cracking evolution in KEC test sections.⁽⁶⁸⁾

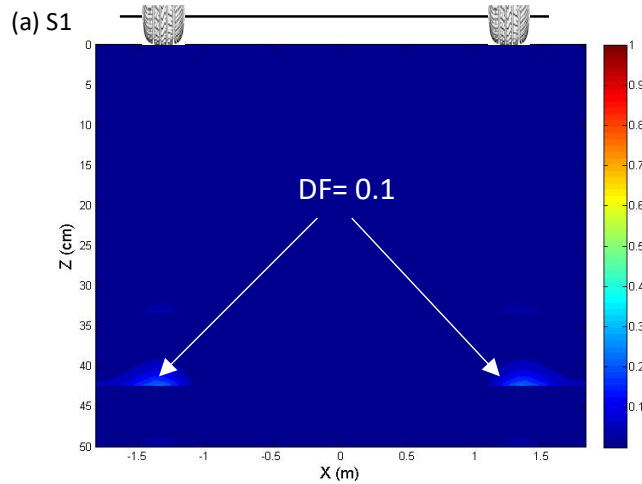
Binzhou

The Binzhou project’s main goal was to evaluate different perpetual pavement designs. Several pavement sections were included in this study, three of which (sections 1, 2, and 3) had fatigue-resistant layers as their bottom asphalt layers. The other two pavement sections were thinner and did not contain fatigue-resistant layers as their bottom asphalt layers. Unfortunately, no detailed field-cracking information was available for the Binzhou project. The only fatigue-related information the research team knew was that section 5 failed within 5 yr and was replaced by the transportation authority in Shandong, China.⁽¹¹⁵⁾

For the purposes of FlexPAVE model verification, the research team ran an 8-yr FlexPAVE simulation to compare the performance among the various test sections and determine their reasonableness regarding engineering judgement. As such, the predicted ranking among all the Binzhou sections from superior to inferior was sections 1, 3, 2, 4, and 5. As the research team expected, this sequence follows the general ranking of asphalt pavement. Section 1 is the thickest and thus demonstrated the best fatigue performance at the end of the 8-yr simulation. In this section, there is some damage in the Superpave-19 layer, as shown in figure 138-A. Section 3 exhibits slightly better predicted performance than section 2, as there was reduced damage in both the bottom asphalt layer and the layer directly above it in section 3. This damage level was a result of the SBS-modified binder in the bottom asphalt layer. Section 4 experienced high damage in the bottom asphalt layer due to its lower quality of material (LSPM). Section 5 was a conventional design of semirigid asphalt pavement and exhibits the worst predicted performance at the end of 8 yr. As shown in figure 138-F, the damage was concentrated at the bottom of this relatively thin asphalt pavement. This worst prediction was in line with the early failure and replacement of section 5 in the field.

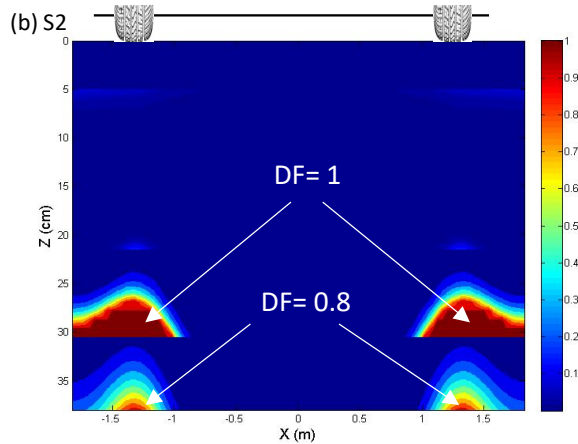
Figure 139 presents the FlexPAVE prediction of percent damage area for the five Binzhou pavements. While these results cannot be used to calibrate the model, they provide evidence that FlexPAVE differentiates between poorer performing sections and better performing sections.

Furthermore, FlexPAVE's ability to determine the location of the damage in the pavement structure due to the quality of the materials used (fatigue-resistant versus nonfatigue-resistant) helps inform proper perpetual pavement design, which requires extremely low damage levels in the bottom asphalt layers.



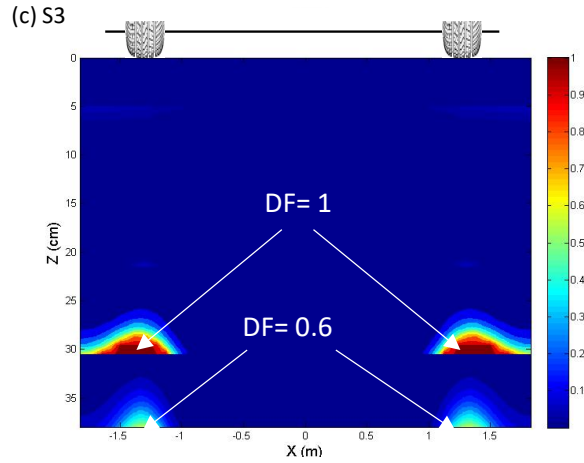
© 2018 Transportation Research Record. (DTFH61-08-H-00005)
 1 cm = 0.4 inch; 1 m = 3.28 ft.
 DF at 1 = failure.
 DF = damage factor.

A. Fifteen-year FlexPAVE simulation results for the Binzhou S1 test road section.



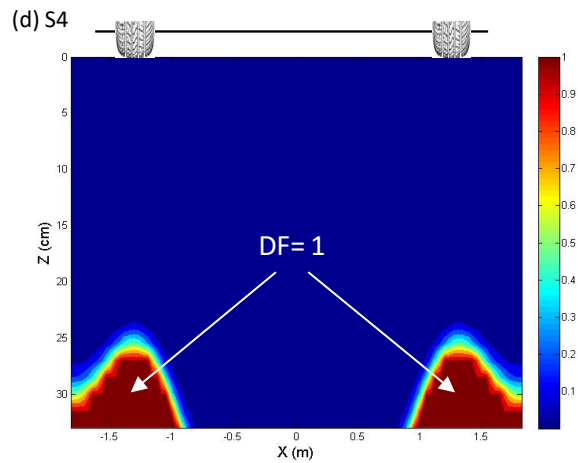
© 2018 Transportation Research Record. (DTFH61-08-H-00005)
 1 cm = 0.4 inch; 1 m = 3.28 ft.
 DF at 1 = failure.
 DF = damage factor.

B. Fifteen-year FlexPAVE simulation results for the Binzhou S2 test road section.



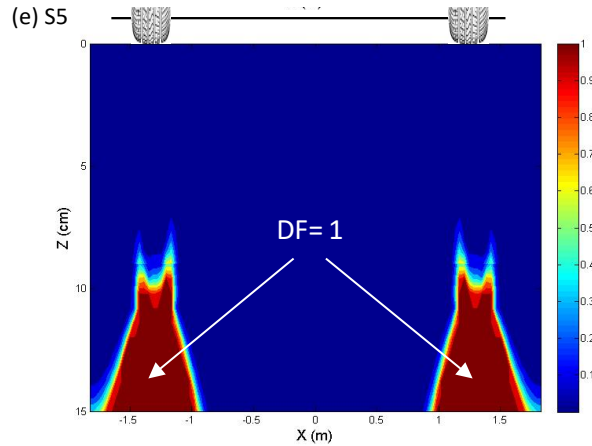
© 2018 Transportation Research Record. (DTFH61-08-H-00005)
 1 cm = 0.4 inch; 1 m = 3.28 ft.
 DF at 1 = failure.
 DF = damage factor.

C. Fifteen-year FlexPAVE simulation results for the Binzhou S3 test road section.



© 2018 Transportation Research Record. (DTFH61-08-H-00005)
 1 cm = 0.4 inch; 1 m = 3.28 ft.
 DF at 1 = failure.
 DF = damage factor.

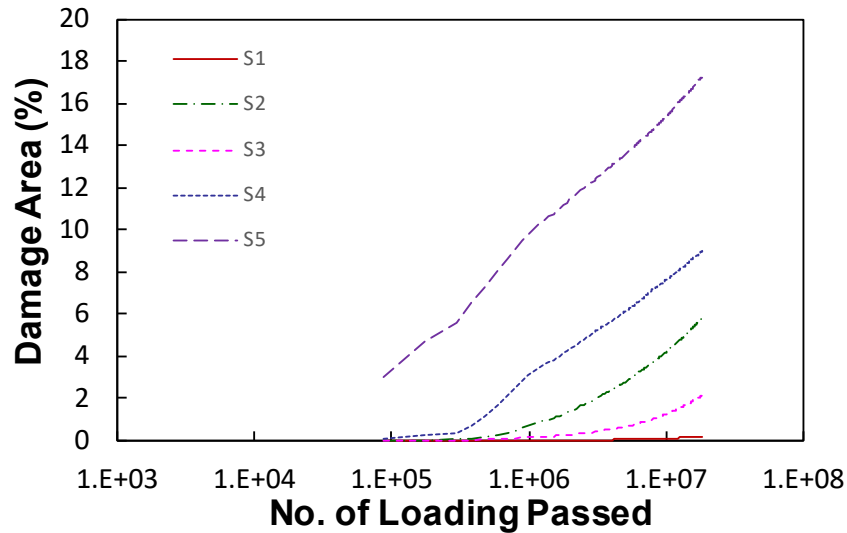
D. Fifteen-year FlexPAVE simulation results for the Binzhou S4 test road section.



© 2018 Transportation Research Record. (DTFH61-08-H-00005)
 1 cm = 0.4 inch; 1 m = 3.28 ft.
 DF at 1 = failure.
 DF = damage factor.

E. Fifteen-year FlexPAVE simulation results for the Binzhou S5 test road section.

Figure 138. Contours. Fifteen-year FlexPAVE simulation results for the Binzhou test road sections.⁽⁶⁸⁾



© Transportation Research Record. (DTFH61-08-H-00005)

Figure 139. Graph. FlexPAVE prediction of percent damage area increase for the Binzhou pavements.⁽⁶⁸⁾

PERMANENT DEFORMATION PREDICTIONS

This section discusses selected NCAT test track, FHWA ALF, MIT, KEC, and Binzhou pavement rut depth predictions using TSS test results, the shift model, and FlexPAVE. The research team used the shift model and TSS tests predicted permanent deformation (rutting) for these pavements. Once the team calibrated the shift model, implementation was similar to that of the strain ratio model. They divided each pavement layer into 10 sublayers and calculated the

deviatoric stress and load time underneath the center of the wheel at the middle of individual sublayers using FlexPAVE. The research team also calculated the reduced load-time shift factor based on temperature and load time, which both change with depth, and the deviatoric stress underneath the center of the wheel using the layered viscoelastic model. Vertical stress levels are required for calculating vertical stress shift factor.

One complication with this effort is the material model FlexPAVE used for the unbound layers. Early versions of FlexPAVE used material coefficients from Tseng and Lytton's model.⁽¹¹⁶⁾ Later versions of FlexPAVE used the updated version of this model as modified in NCHRP 1-37A for use in the MEPDG.⁽²⁵⁾ These respective models provide differing results, making it difficult to judge which provides a more realistic total rut depth prediction as well as the ratio of the permanent deformation developed in the bituminous layers to that of the permanent deformation developed in the unbound layers. As such, results for both the original unbound layer model as well as the MEPDG unbound layer model, are shown in this section.

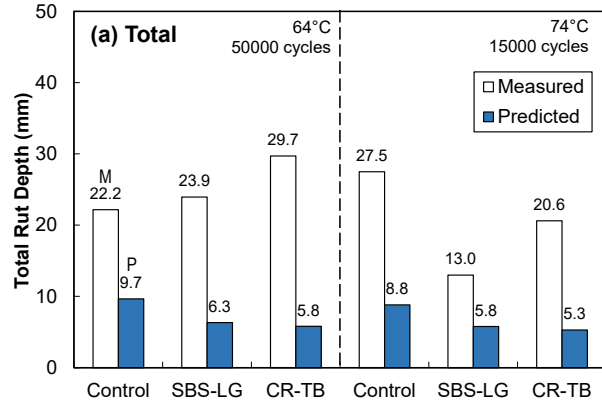
The research team hopes providing both results will offer insight for future researchers into the possible effect of implementing more accurate unbound layer models on the trends observed in this research.

FHWA ALF

The terpolymer rutting section with 100-mm thickness had significant issues with nonuniform lime distribution within the mixture. What are known as lime nuggets formed, with some nearly 1 inch in diameter. As a such, the research team did not use the field measurements from this section for comparison, only the control, SBS, and CR-TB mixtures. The research team performed FlexPAVE program analysis for four cases: 100-mm-thick pavement at 64°C and 74°C, and 150-mm-thick pavement at 45°C and 64°C.

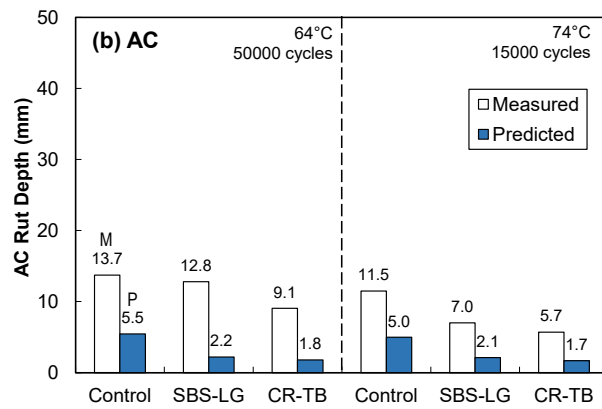
Figure 140 shows the FlexPAVE prediction using the original unbound layer permanent deformation model compared with the field measurements. At 64°C, the ranking of the field measurements in this figure shows the control section having the lowest total rut depth, the SBS-LG section showing intermediate rut depth, and CR-TB showing the highest total rut depth.

The FlexPAVE predictions of total rut depth are completely the opposite. At 74°C, the rankings based on field measurements change with control having the highest rut depth, CR-TB having an intermediate total rut depth, and SBS-LG having the lowest rut depth. The rankings for the FlexPAVE-predicted of total rut depth in this condition are the same as the predictions for the previous condition. Additionally, the measured rut depths are significantly higher than the predicted value.



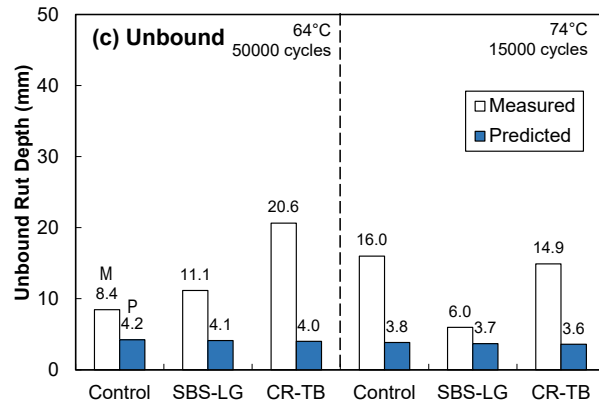
Source: FHWA.
 0°C = 32°F; 1 mm = 0.04 inch.

A. Total rut depth comparison of FHWA test sections using the original unbound material model.



Source: FHWA.
 0°C = 32°F; 1 mm = 0.04 inch.

B. Asphalt layer rut depth comparison of FHWA test sections using the original unbound material model.



Source: FHWA.
 0°C = 32°F; 1 mm = 0.04 inch.

C. Unbound layer rut depth comparison of FHWA test sections using the original unbound material model.

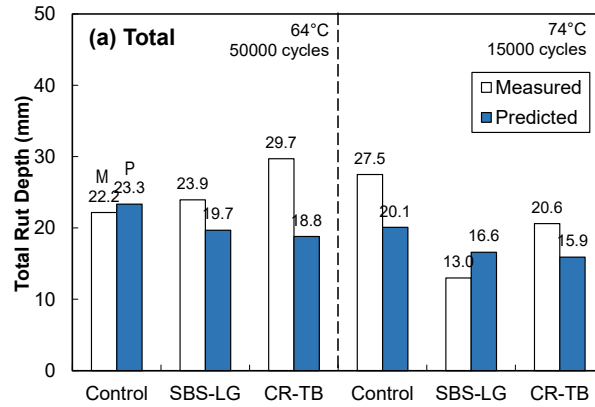
Figure 140. Graphs. Rut depth comparisons of FHWA test sections using the original unbound material model.

The reason for this poor predictive ability of FlexPAVE with the original unbound layer permanent deformation model is better understood by assessing the relative components of the total rut depth. If a user compares just the rutting experienced in the bituminous layers, the field measurements show the control section had the highest permanent deformation, followed by the SBS-LG section, and then the CR-TB section. This trend is true for both the 64 and 74°C conditions. FlexPAVE is able to predict this ranking, even though the total deformation is underpredicted. The problem arises in the permanent deformation prediction in the unbound layers. Using the original unbound layer permanent deformation model, all sections exhibit similar permanent deformation development in the unbound layers as shown in figure 140-C. In the field, there are dramatic differences in unbound-layer deformation from section to section. These differences in unbound layer permanent deformation between sections mask the predicted ranking of the asphalt material deformation.

Using the MEPDG unbound layer permanent deformation model, the deformation in the unbound materials increases significantly, whereas the deformation in the asphalt concrete layers remains the same (figure 141). As figure 141-A shows, the total predicted magnitude of permanent deformation is closer to that measured in the field, but the trend of the predicted total rut depth among the sections still does not match the field rankings. Figure 141-B shows FlexPave-predicted rankings of the different asphalt mixtures well, but the predictions in figure 141-C do not capture rankings based on the field unbound layer deformation. The results shown in figure 140 and figure 141 suggest the urgent need for more accurate permanent deformation models for unbound materials.

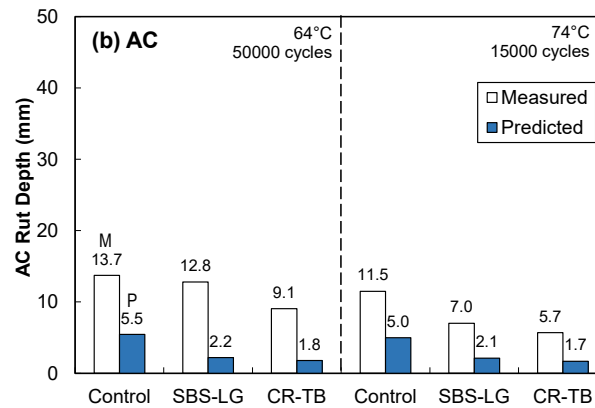
New permanent deformation models for unbound materials have been developed as part of the NCHRP 01-53 project, *Proposed Enhancements to Pavement ME Design: Improved Consideration of the Influence of Subgrade and Unbound Layers on Pavement Performance*.⁽¹¹⁷⁾ Upon the completion of testing and adoption of the NCHRP 01-53 project's models by the

AASHTO, the research team will implement those models into FlexPAVE and check their validity.



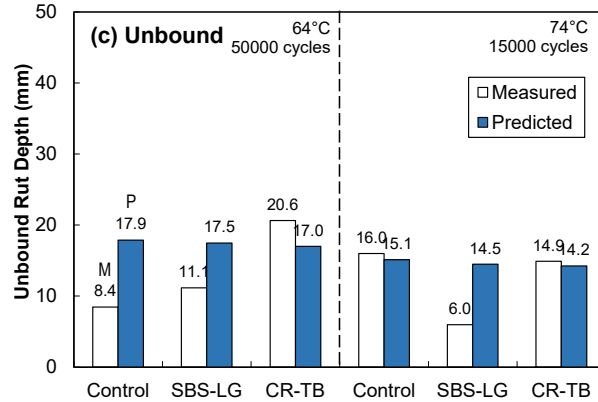
Source: FHWA.
 0°C = 32°F; 1 mm = 0.04 inch.

A. Total rut depth comparison of FHWA test sections using the MEPDG unbound material model.



Source: FHWA.
 0°C = 32°F; 1 mm = 0.04 inch.

B. Asphalt layer rut depth comparison of FHWA test sections using the MEPDG unbound material model.



Source: FHWA.
 0°C = 32°F; 1 mm = 0.04 inch.

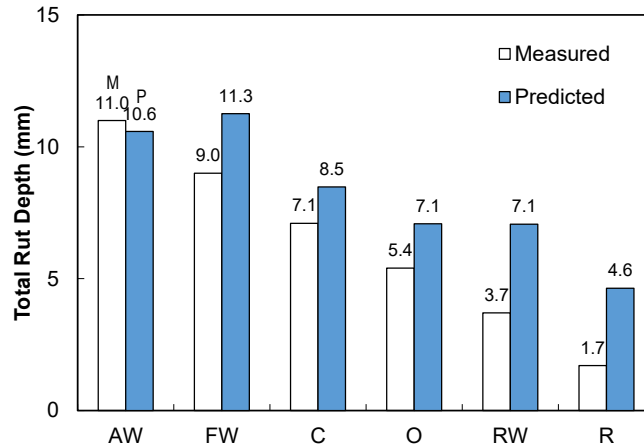
C. Unbound layer rut depth comparison of FHWA test sections using the MEPDG unbound material model.

Figure 141. Graphs. Rut depth comparisons of FHWA test sections using the MEPDG unbound material model.

In summary, the FlexPAVE program, the shift model and TSS test protocol were able to predict the ranking of the permanent deformation in the FHWA ALF bituminous layer; however, they underestimated the amount of rutting developed in the AC layers. This underestimation was likely due to the excessive shear flow caused by very severe loading conditions at the ALF Facility (high temperatures and channelized loading). The FlexPAVE program was also not able to capture the trend of the permanent deformation of the unbound layers, and was unable to accurately rank the total rut depth compared with the field measurements. This inability could possibly be explained by unknown variability in the unbound layers in the field.

NCAT

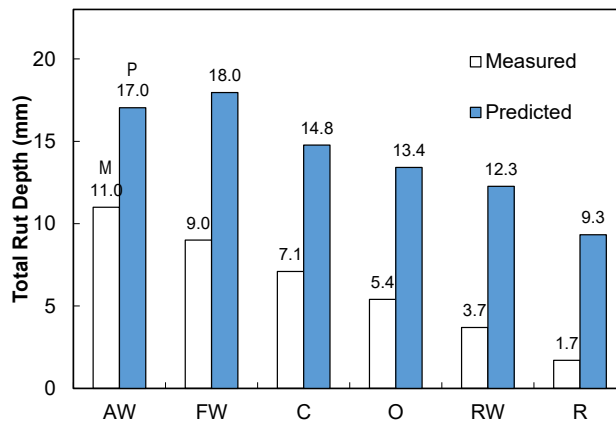
The research team measured the rut depths at the NCAT Test Track after 2 yr of trafficking. Figure 142 depicts the test track measurements and predicted rut depths using the original unbound layer permanent deformation model, with EICM climate information for that site. The predicted ranking matches field observations well, with only the ranking of the AW and FW sections being switched. However, the difference in total magnitude is within a few millimeters without applying any correction factor, though the predicted rut depth values are generally higher than the measured ones. This outcome may be partially explained by the research team not including aging—which occurred in the test track pavements for 2 yr and reduced the amount of permanent deformation—in the FlexPAVE simulations. Another possible reason for this outcome could have been wheel-wandering of the trailers, because the current FlexPAVE program simulates channelized loading. NCHRP 1-37A (the MEPDG manual) assumes the standard deviation of truck-traffic wander is 10 in and determines the number of axle load applications over a prediction point to consider vehicle wandering.⁽²⁵⁾ This assumption leads to about 20-percent reduction in total ESAL even though it does not simulate nonlinearity.⁽¹¹⁸⁾ The 20-percent reduction in total ESAL lowers the rut depth by about 9 percent; then, the predictions will become closer to the measurements.



Source: FHWA.
1 mm = 0.04 inch.

Figure 142. Graph. Original unbound material model measured versus predicted rut depths for NCAT Test Track sections after 2 yr of traffic.

The ranking of these sections using the MEPDG unbound layer permanent deformation model remains the same, but now the model predicts a significantly higher permanent deformation, with nearly double the measured values. Higher predicted rutting in the unbound layers causes this difference (figure 143). Comparing the difference between the original and MEPDG model predictions shows the critical importance of having an accurate unbound layer model.



Source: FHWA.
1 mm = 0.04 inch.

Figure 143. Graph. MEPDG unbound material model measured versus predicted rut depths for NCAT Test Track sections after 2 yr of traffic.

In summary, the NCAT Test Track test conditions are closer to in-service asphalt pavement conditions than FHWA ALF conditions, except for the relatively constant loading of tractor trailers. The test track simulates traffic loading, wandering, actual climate change, actual pavement structure (including base layer and subgrade), aging effects, etc. The research team found the FlexPAVE program analysis to predict rut-depth rankings under these realistic field

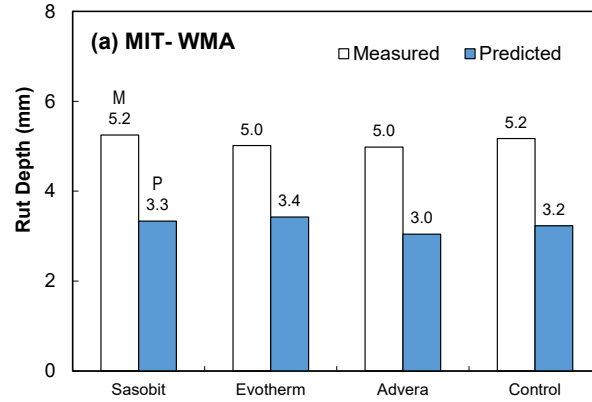
conditions, but the total magnitude of these predictions was highly dependent on the unbound-material permanent deformation model used. This finding verifies that the prediction methodology used in this study (i.e., the TSS test as the material characteristic test, the shift model for the material permanent deformation model, and the FlexPAVE program for the pavement analysis) has the capacity to predict rut depth in bituminous layers fairly well. Including aging, wandering, and a more accurate unbound layer permanent deformation model will improve predictability in the future.

MIT

Figure 144 presents comparisons of the predicted rut depths using the original unbound layer permanent deformation model and the measured rut depth values for the MIT sections at the end of 5 yr for the WMA sections and 6 yr for the RAP sections. The rutting performance of the various WMA and RAP sections was still excellent after 36 mo of service, as evidenced by very low rut depth measurements (less than 6 mm). All WMA sections using different WMA technologies show similar rutting performance based on the 0.2-mm maximum rut depth difference in the field. The predicted rut depths from FlexPAVE program simulations capture this trend, even though there is some variation in ranking and the FlexPAVE predictions are lower than the measured values by approximately 1 mm. (Note that the WMA and RAP projects were overlay projects on top of a cracked 2.8-inch asphalt pavement layer.) The research team did not model the cracked layer since no information about this layer was available. Therefore, the research team expected lower rut depth predictions from FlexPAVE compared to the field measurements.

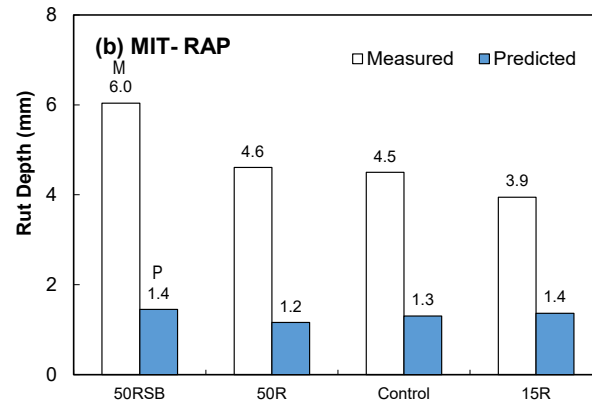
The RAP sections shown in figure 144-B exhibit a decreasing trend in rut depth values in the field from the 50-percent RAP SB section down to the 15-percent RAP section. However, the FlexPAVE program using the original unbound layer model was not able to predict this tendency well, although the predicted rut depth of the 50-percent RAP SB mixture is the highest. The material-level TSS test results for the 50-percent RAP SB mixture show relatively low permanent strains in the lab, and the predicted rut depths from FlexPAVE program analysis using a low traffic volume of 30 ESAL per day may not represent the trends present if the program had used more accurate traffic information. The magnitude of the rut depths predicted using FlexPAVE with low traffic volume tends to be very low compared with the rut depths measured in the field. Thus, the rutting performance predicted from FlexPAVE should be calibrated against the field rutting performance data. These findings suggest the need to develop a laboratory-to-field transfer function.

The research team made similar observations for the FlexPAVE predictions using the MEPDG unbound layer permanent deformation model (figure 145). Just as with the original version of the model, all FlexPAVE predictions are close to one another. However, the predicted rut depths significantly increased using the MEPDG unbound layer permanent deformation model. This increase results in overpredicting the rut depths in the WMA sections and matching the rut depths in some of the RAP sections fairly well. This finding is further proof of the critical need to develop an accurate unbound layer model. The research team expected the rut depth predictions in the WMA sections to be higher than the reported values in this section when the existing cracked AC layer in the WMA sections is properly modeled.



Source: FHWA.
1 mm = 0.04 inch.

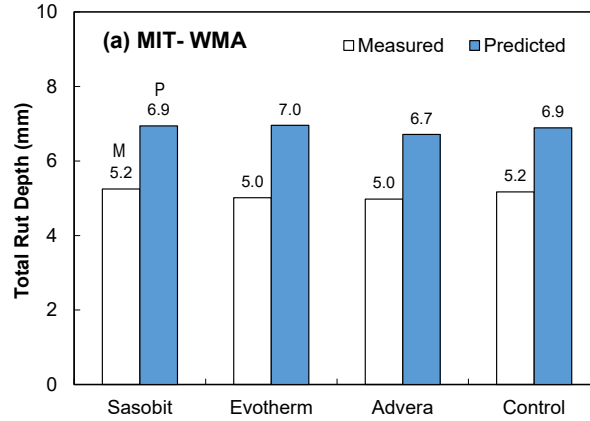
A. Original unbound material model measured versus predicted rut depths for the MIT-WMA sections.



Source: FHWA.
1 mm = 0.04 inch.

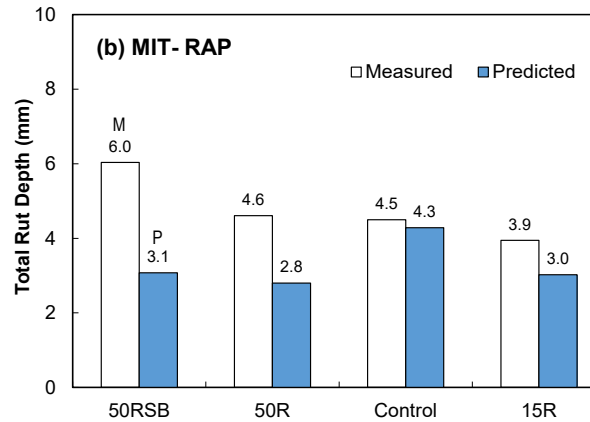
B. Original unbound material model measured versus predicted rut depths for the MIT-RAP sections.

Figure 144. Graphs. Original unbound material model measured versus predicted rut depths for MIT sections.



Source: FHWA.
1 mm = 0.04 inch.

A. MEPDG unbound material model measured versus predicted rut depths for the MIT-WMA sections.



Source: FHWA.
1 mm = 0.04 inch.

B. MEPDG unbound material model measured versus predicted rut depths for the MIT-RAP sections.

Figure 145. Graphs. MEPDG unbound material measured versus predicted rut depths for MIT sections.

KEC

The KEC test road was constructed by Korea Expressway Corporation (KEC) to better understand the behavior of pavements with different structures. The test road contains more than 20 sections composed of various structures. As figure 16 illustrates, the layout of all sections designed with asphalt layers include surface (ASTM and PMA) layers, base (BB1, BB3, and aggregate) layers, base layers (8, 18, and 28 cm), and subbase layers (30 and 40 cm). The rut depths measured by KEC before traffic opening are not zero because of construction traffic that occurred prior to opening the road to vehicular traffic. Therefore, a direct comparison of the measured and predicted rut depths at the same period of time is not meaningful. Instead, the

research team compared rut depths measured right before maintenance work began, which was 40 mo after the traffic opening, and those predicted after 20 yr by the FlexPAVE program to investigate the reasonableness of the predictions.

The research team compared the FlexPAVE rutting simulation results using the original unbound layer permanent deformation model for KEC sections with the measured rut depths in the field, as described in the following subsections for each parameter.

Surface Layer Type

Figure 146-A presents both the measured and predicted rut depths using the original unbound layer permanent deformation model and indicates better rutting resistance of the polymer-modified mixture than the ASTM mixture. The magnitude of these predictions is slightly lower than those observed in the field.

Base Layer Type and Base Layer Thickness

Figure 146-B presents the rut-depth comparison of the different base-layer types (BB1, BB3, and aggregate base) using the original unbound layer permanent deformation model. As shown, the 8-cm aggregate base layer exhibits extreme rutting deformation in the field, whereas an increase in thickness to 18 cm resulted in significant rut-depth decrease. However, increasing thickness to 28 cm did not lessen rut depth compared with the 18-cm layer. This outcome led to the conclusion that a thicker aggregate base layer provides additional rutting resistance for a pavement, but the rate of increase in rutting resistance due to increase in aggregate base layer thickness decreases as the aggregate base layer becomes thicker. The research team believes the FlexPAVE program using the original unbound layer permanent deformation model was unable to simulate the poor performance of the thinner aggregate base layer because the rutting coefficient inputs in the program were not accurate enough to capture the true performance of the aggregate base.

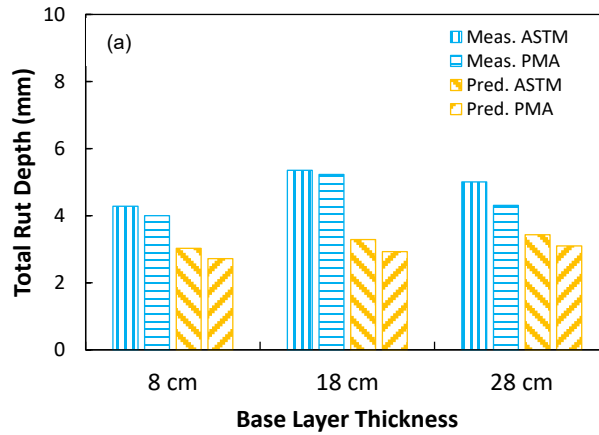
As for bituminous based layers, in the field the asphalt base mixtures (BB1 and BB3) provided better rutting resistance than the aggregate base layers. Overall, the BB1 mixture showed better rutting resistance than the BB3 mixture, as demonstrated in figure 146-B. FlexPAVE was not able to predict these rankings and consistently predicted lower rut depths than the research team observed in the field.

Subgrade Layer Thickness

The subgrade and antifrost layers constituted the sublayers of the asphalt sections. The research team selected three sections (1, 3, and 6) out of six that have no antifrost layer (2, 4, and 8) and compared their rut depths against sections with an antifrost layer. Figure 146 illustrates the effects (or lack thereof) of an antifrost layer on rutting performance. In the field, there were slightly greater rut depths in sections that had an antifrost layer. The FlexPAVE predictions using the original unbound layer permanent deformation models also show a slight increase in rut depth for the antifrost sections.

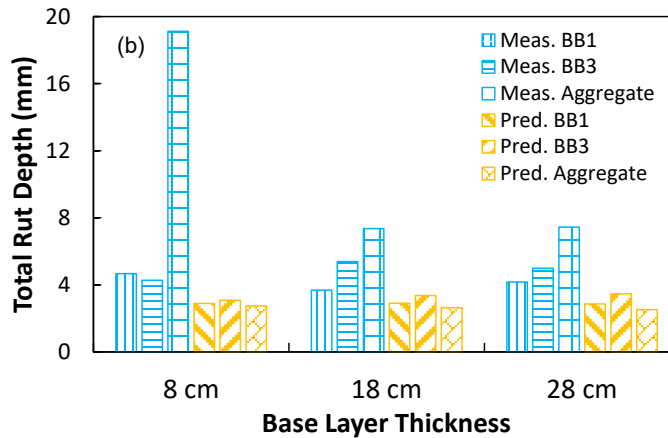
Subbase Layer Thickness

Figure 146-D presents the effect of the subbase layer thickness on the rutting performance of sections without an antifrost layer. Although the rut depth values in the 30-cm subbase layer are slightly greater than those in the 40-cm subbase layer, there is no significant relationship regarding subbase layer thickness. The FlexPAVE predictions using the original unbound layer permanent deformation model show that the rut depths of the 30- and 40-cm subbase layers are nearly the same.



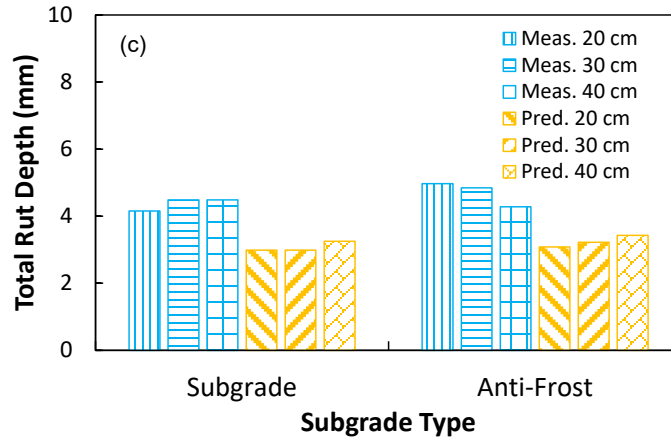
Source: FHWA.
1 cm = 0.4 in; 1 mm = 0.04 inch.

A. Effects of different surface layer thicknesses on rutting performance of KEC sections using the original unbound material model.



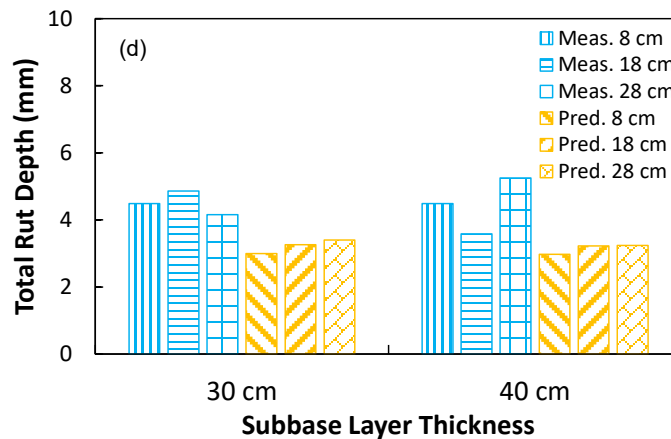
Source: FHWA.
1 cm = 0.4 in; 1 mm = 0.04 inch.

B. Effects of different surface layer thicknesses on rutting performance of KEC sections using the original unbound material model.



Source: FHWA.
 1 cm = 0.4 in; 1 mm = 0.04 inch.

C. Effects of different subgrade layer thicknesses on rutting performance of KEC sections using the original unbound material model.

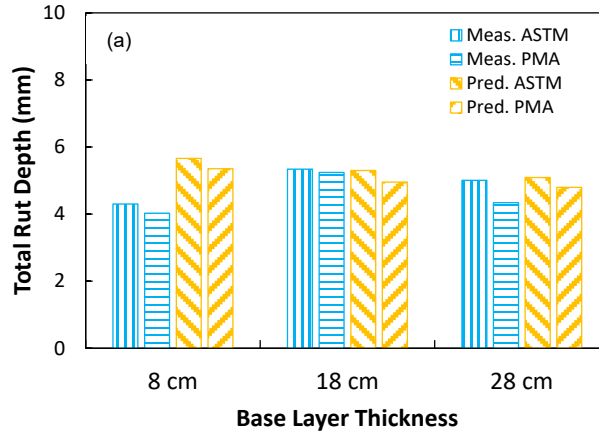


Source: FHWA.
 1 cm = 0.4 in; 1 mm = 0.04 inch.

D. Effects of different subbase layer thicknesses on rutting performance of KEC sections using the original unbound material model.

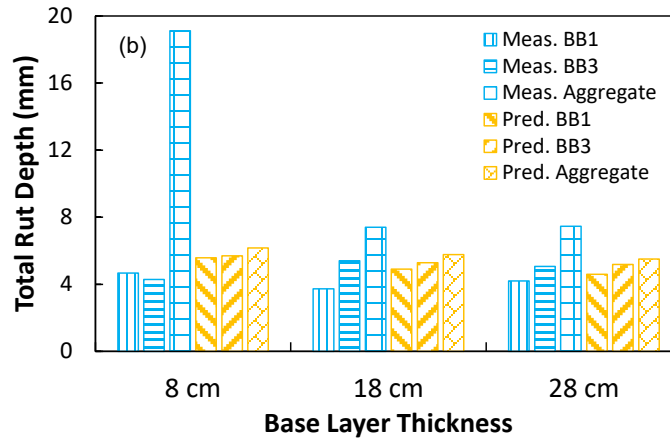
Figure 146. Graphs. Effects of different parameters on rutting performance for KEC sections using the original unbound material model.

Using the MEPDG unbound-material permanent deformation model, most of the trends from the figure 146 still hold true (Figure 147). One main difference using this model is FlexPAVE predicts a slight decrease in permanent deformation as base layer thickness increases. All predicted rut depths, in most cases, are reasonably close to the measured values.



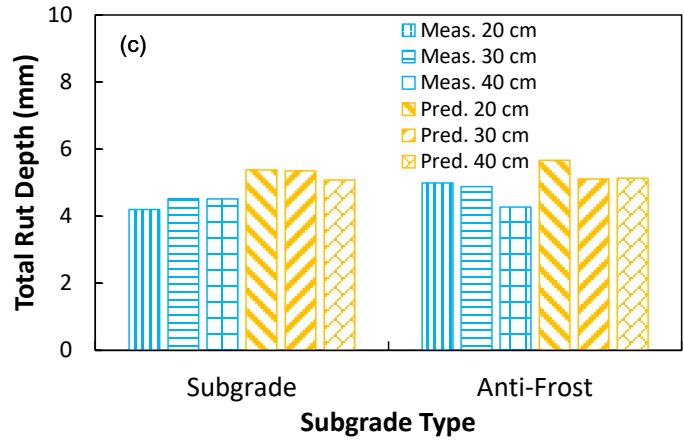
Source: FHWA.
1 cm = 0.4 in; 1 mm = 0.04 inch.

A. Effects of different surface layer thicknesses on rutting performance of KEC sections using the MEPDG unbound material model.



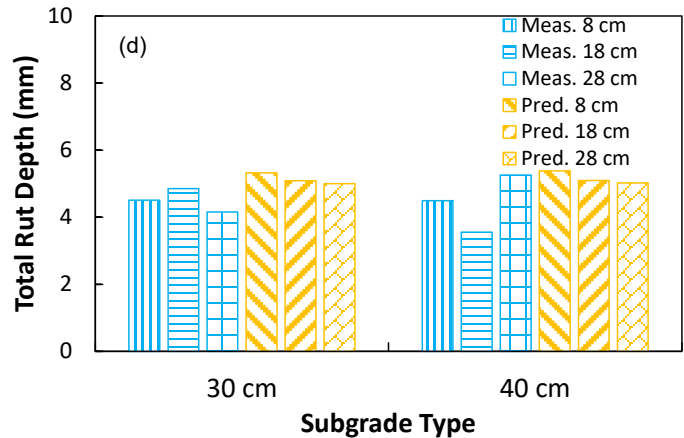
Source: FHWA.
1 cm = 0.4 inch; 1 mm = 0.04 inch.

B. Effects of different base layer thicknesses on rutting performance of KEC sections using the MEPDG unbound material model.



Source: FHWA.
1 cm = 0.4 inch; 1 mm = 0.04 inch.

C. Effects of anti-frost layer on rutting performance of KEC sections using the MEPDG unbound material model.



Source: FHWA.
1 cm = 0.4 inch; 1 mm = 0.04 inch.

D. Effects of different subbase layer thicknesses on rutting performance of KEC sections using the MEPDG unbound material model.

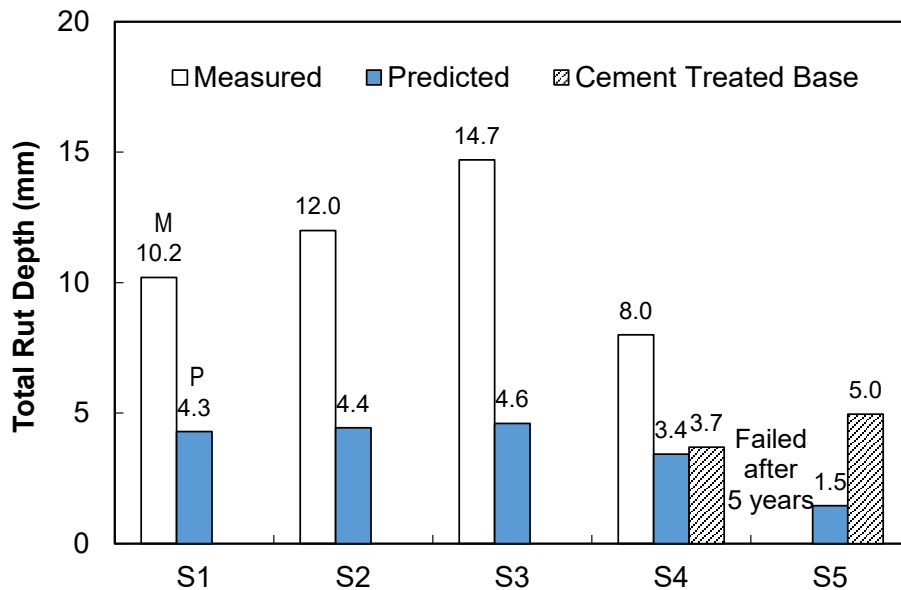
Figure 147. Graphs. Effects of different parameters on rutting performance for KEC sections using the MEPDG unbound material model.

Binzhou

Limited traffic information was available for the Binzhou project. Some mixtures were also not available in sufficient quantities to perform permanent deformation testing. Therefore, the research team did not perform these tests on the LSPM, F1, and F2 mixtures. The rutting model coefficients for those mixtures were instead replaced by the coefficients of BB3, ASTM, and ASTM in the KEC project, respectively. The research team selected the substitutive coefficients based on the similarity of the NMA5 and behaviors between the corresponding mixtures. Since

these three mixtures were all located deep in the pavement, the research team assumed approximating the rutting coefficients would not significantly impact prediction results.

The research team compared model prediction rankings with the rankings in the field to determine their reasonableness. Figure 148 and figure 149 show the results after 8 yr of simulated traffic. The team compared these results with field measurements. FlexPAVE predictions using both the original and the MEPDG unbound layer model predicted the same trend the research team observed in the field but experience drastically different total magnitudes, with the original model significantly underpredicting and the new model slightly underpredicting the field measurements. Due to the traffic-level and material-property assumptions for some of the layers, these underpredictions do not carry any significant meaning. As such, these sections cannot be used to develop transfer functions. The research team performed an additional investigation, treating the cement-treated base as an unbound layer with a high modulus. These predictions show high permanent deformation for the MEPDG model and low deformation for the original unbound layer model.



Source: FHWA.
1 mm = 0.04 inch.

Figure 148. Graph. Original unbound material model measured versus predicted rut depths of Binzhou sections.

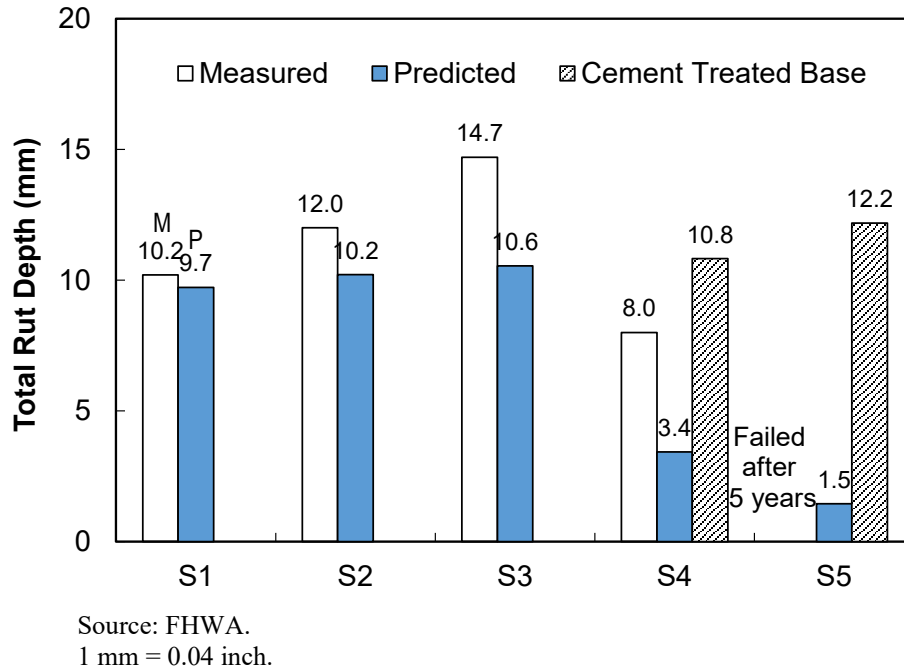


Figure 149. Graph. MEPDG unbound material model measured versus predicted rut depths of Binzhou sections.

CONCLUSIONS

The current FlexPAVE 1.1 version released to alpha testers includes fatigue cracking and permanent deformation models (i.e., the S-VECD model and the shift model, respectively). The research team developed laboratory test protocols to characterize the performance models that aim to use the nationally distributed AMPT.

The study found that FlexPAVE and the fatigue cracking models can predict pavement field performance with acceptable accuracy, given that these predictions do not use transfer functions (table 35). In general, FlexPAVE predicted the ranking of the study mixtures well. However, fatigue cracking predictions require a transfer function to predict the amount of surface cracking in the field based on the FlexPAVE-computed damage factors.

FlexPAVE predicted the rut depth ranking and permanent deformation level with an acceptable difference considering the limitations of the current unbound material model and the lack of a transfer function (table 36). The program underestimated the rut depths with severe loading conditions, due to excessive shear flow more quickly accelerating rutting than FlexPAVE could simulate. Nonetheless, under general loading conditions, FlexPAVE reasonably estimates rut depths in the field.

Table 35. Summary of fatigue predictions.

Project	Agreement with Field Results	Limitations of Dataset	Remarks
FHWA ALF	Good	Not applicable	None
NCAT	Fair	Not applicable	None
MIT-RAP	Good	Low traffic, low distress	None
MIT-WMA	Good	Low distress	None
KEC	Fair	Traffic and climate data unavailable	None
Binzhou	Not applicable	Traffic and climate data unavailable; field cracking data unavailable	Cracking ranks well with results expected from engineering judgement

Table 36. Summary of rutting predictions.

Project	Agreement with Field Ranking	Agreement with Field Magnitude	Limitations of Dataset	Remarks
FHWA ALF	Good	Good	Terpolymer section had material quality issues and was not used	Only rutting in the asphalt layers was considered
NCAT	Good	Overpredicts	Not applicable	None
MIT-RAP	Poor	Underpredicts	Not applicable	None
MIT-WMA	Good	Fair	It is an overlay project—underlying pavement layers are not modeled	Over- and underpredicts depending on the unbound layer model used
KEC	Fair	Good	Traffic and climate information unavailable	None
Binzhou	Good	Underpredicts	Traffic and climate information unavailable; and SSR data not available for all mixtures	For layers without SSR data; SSR data from similar mixtures were used

CHAPTER 8. CONCLUSIONS AND FUTURE WORK

CONCLUSIONS

A PRS is an enhanced, performance-driven QA system that provides contractors with more responsibility and opportunity, thus incentivizing contractors to improve pavement quality through enhanced mix designs, construction quality, etc. In PRS, performance is the key for all procedures.

This report documents the development of tests, performance models, and software for pavement analysis to predict asphalt pavement performance (i.e., cracking and permanent deformation) based on viscoelastic analysis. The research team adopted an approach to characterize asphalt concrete over a wide range of temperatures and loading rates encountered in the field divides the problem into two components: characterizing the viscoelastic response and characterizing the viscoplastic response. The S-VECD model describes the time-dependent behavior of asphalt concrete with growing microcrack damage in a simplified manner. The permanent deformation (or shift) model describes the irrecoverable (whether time-dependent or -independent) strain. The research team also investigated the healing (considered to be the reverse behavior of damage) and aging asphalt pavement experiences in addition to primary cracking and rutting distresses, which were the focus of these two representative models. The team incorporated healing into the S-VECD model, while also integrating these models into the FlexPAVE program to predict the overall performance of asphalt pavement. Aging inclusion is covered under the ongoing FHWA project DTFH61-13-C-00025, *Develop and Deploy PRS for Pavement Construction*. Each model is briefly referenced in the following paragraphs.

The research team adopted the S-VECD model as a damage model to predict fatigue cracking. Developing a failure criterion based on the energy-release rate enhanced the S-VECD model's applicability and predictive ability. The characterization test protocol from AASHTO TP 107 allowed the research team to determine both the damage characteristic curve and the energy-based failure criterion using only three dynamic modulus tests and three AMPT cyclic fatigue tests.⁽³⁷⁾

The research team developed the shift model, which is based on the t-TS and t-SS principles, as a permanent deformation model for asphalt mixtures. The team derived the incremental form of the shift model from a more rigorous viscoplastic rate model and found the model to be sufficient for simulating both the primary region and secondary region of the permanent strain growth curve. They also found the slopes for permanent strain and number of cycles on the log-log scale to be relatively constant regardless of the loading conditions using TRLPD tests under various loading conditions (deviatoric stress, load time, temperature). This constant slope is evidence of the effectiveness of the t-TS and t-SS principles. The research team used the shift model to shift the permanent strain growth curves among different temperatures, load times, and stress levels. The team developed the TSS test protocol, which is composed of eight tests (two replicate tests for each reference test and stress sweep tests at three temperatures), to calibrate the shift model. They then simplified the TSS test protocol further to derive the SSR test protocol that requires only four specimens (two specimens for each of the high and low temperatures) for characterization without losing prediction accuracy.

Healing is one of the major mechanisms that affects the properties of asphalt concrete. Healing occurs during rest periods, and pseudostiffness, rest period duration, and temperature define and quantify healing potential. The t - TS principle is also a viable way to define and quantify healing potential; thus, the suggested healing model can be characterized by only a few test conditions. The research team thus proposed this simple test protocol requiring little effort to calibrate the healing model as part of the PRS. Laboratory test results prove the capability of the healing model and the testing protocol.

The research team developed the FlexPAVE program, which is based on VECD analysis and Fourier transform, to evaluate the responses and performance of asphalt pavements using field conditions. The team verified the FlexPAVE program together with the developed performance models through field-measured performance data. For this verification, they characterized the models using the AASHTO T 378 dynamic modulus test, the TP 107 cyclic fatigue test, and the SSR test.⁽⁹⁾ The FlexPAVE program predicts performance trends among various pavements with acceptable accuracy.

Mechanistic-empirical pavement analysis methods require transfer functions to convert the mechanistic prediction of pavement damage into distress intensities commonly measured by State highway agencies. In this project, the research team tried to develop transfer functions for cracking and rutting by comparing the observed performance data and the performance predicted by FlexPAVE. However, because only a limited number of test sections were available and the traffic loading characteristics were different among the test road projects (i.e., accelerated loading versus normal live traffic loading), the team was unable to develop reliable transfer functions. In addition, the unbound layer permanent deformation model incorporated in FlexPAVE needs further evaluation. As such, this research effort fell short in developing the necessary transfer functions. Future research should predict and calibrate a sufficient number of pavement sections in the United States to develop such transfer functions.

CURRENT RESEARCH EFFORTS

The research team is currently working on a follow-up PRS project, Develop and Deploy PRS for Pavement Construction (DTFH61-13-C-00025), for deployment. Enhancing and implementing the PRS and performance models will address the following challenges the research team encountered in this study:

- FlexPAVE version 1.1 is based on a layered viscoelastic finite-element program; thus, the program does not properly capture the effect load redistribution due to damage it has on cracking. In response, the research team is developing an FFE method that can capture the effect of load redistribution due to damage under the follow-up project. This program will be in C++ instead of MATLAB and will have an Excel-based GUI to provide a user-friendly interface for users.
- Pavement performance needs to be evaluated in terms of performance life; for example, acceptable rut depth criteria should be set for a certain design life and roadway classification, which should be predetermined by the agency and contractor. Then, the performance life of the as-constructed pavement would be required to meet or exceed the design life as predicted by the asphalt mixture PRS software. The research team has

already completed this approach to obtain fatigue life and will be developing it for rutting performance characteristics as well.

- Other variables related to material quality (i.e., binder type and quality, RAP quality, moisture susceptibility, etc.) need to be verified at the mix design stage using mixture performance tests because performance predictions based on volumetric AQC's would be used to develop pay tables for the PRS. Thus, the research team is developing a performance engineered–mix design method as part of the follow-up research project.
- The state-of-the-practice asphalt mix design uses volumetric properties only without performance testing. Performance-volumetric relationships and rules of thumb developed during this research will aid contractors and agencies in designing mixtures that best meet the performance criteria in performance-engineered mix design.
- FlexPAVE needs aging and thermal cracking models added to its performance models.
- FlexPAVE needs functionalities related to mixed traffic and reliability.

FUTURE WORK

Developing performance models, which are the engines of this PRS project, was the focus of this study. Ongoing research continues to address gaps preventing model application in an implementable performance-related specification methodology for highway agencies. For future work, the following items would enhance what the research team has already developed:

- Improved models for characterizing permanent deformation of unbound materials. Ongoing research at Texas A&M University is developing these models. Once developed, these models should be included in the FlexPAVE software to improve the accuracy of the rutting prediction.
- Transfer functions for FlexPAVE to more accurately predict the amount of fatigue cracking and rutting although the cracking and rutting trends for the various pavements, as predicted by FlexPAVE, matched the measured trends quite well. This goal requires the identification of a wide range of pavement sections with available original paving materials and good performance data.
- Predictive equations based on the volumetric properties of mixtures that can provide the mechanical properties to enable performance predictions. However, the development of such predictive equations applicable to a wide range of mixtures under a wide range of volumetric conditions would require a larger database of FlexPAVE predictions from laboratory tests and field-measured performance than currently exists.

APPENDIX A. USER MANUAL FOR FLEXPAVE VERSION 1.1

INTRODUCTION

The FlexPAVE version 1.1 program is a pavement performance analysis tool based on an efficient framework developed by combining time-scale separation and LVEA. First, using the time-scale differences among temperature variations, traffic frequency variations, and fatigue and rutting evolution reduces the number of pavement response analyses from millions of cycles to only a few dozen runs. Then, the program can perform stress–strain analysis using Fourier transform–based layered structural analysis. This analysis tool efficiently captures the effects of the pavement material’s viscoelasticity, temperature (thermal stress and changes in viscoelastic properties), and moving nature of the traffic load. Eslaminia et al. provide details of this analysis framework.⁽¹¹⁹⁾ Once the program determines the pavement responses, it can predict the pavement’s fatigue cracking and rutting performance using the VECD model and the shift model, respectively (See references 1–6, 8, 12, 50, 59, 63, 65, 68, 75, 91, 99, 105, 109, 111, 112, 114, and 118.)

The manual detailed in this section describes features of the GUI and the data input and output processes necessary for carrying out FlexPAVE pavement analyses. This user guide also includes three examples of pavement analysis to explain the various features of FlexPAVE.

SOFTWARE RELEASE

To obtain a copy of the FlexPAVE version™ v 1.1 software, currently in alpha testing, please contact the point of contact listed in <https://www.fhwa.dot.gov/pavement/asphalt/analysis/>.

GETTING STARTED

The research team developed and tested the FlexPAVE version 1.1 program using computers with the following specifications:

- Operating system—Windows 7 (64-bit) or newer.
- Processor—2 GHz or faster.
- RAM—4 GB or higher.
- Hard disk space—400 MB to install FlexPAVE software and 1 GB to install MATLAB Compiler Runtime (MCR).⁽¹²⁰⁾
- Screen resolution—1,366 × 768 pixels or higher.

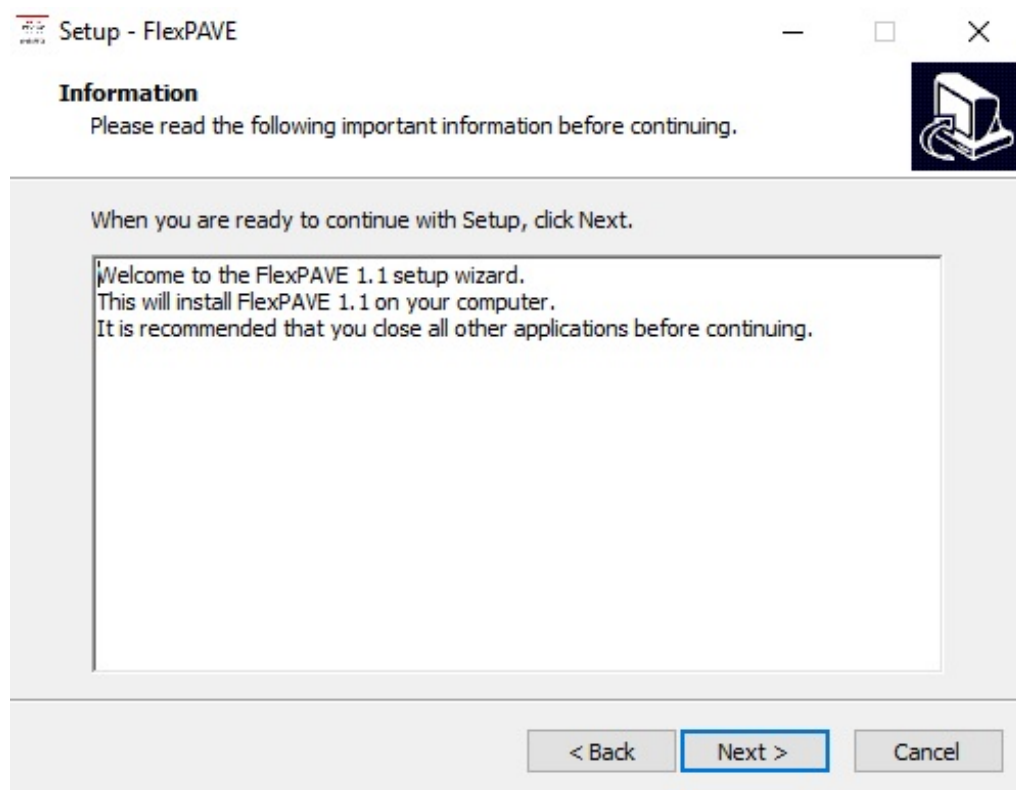
Installation

The research team built FlexPAVE version 1.1 for the 64-bit version of Windows 7 or newer. The user must have administrative rights to run the installer. Please contact the system administrator with any questions.

Step 1—Run FlexPAVE Setup

After checking the minimum system requirements, the FlexPAVE installer is ready to be run. Figure 150 shows a screenshot of the dialogue box the user will see when running the installer “FlexPAVE.exe.” Clicking Next will prompt the installation procedure to proceed.

If installing FlexPAVE a second (or subsequent) time, remove all components from the earlier versions prior to reinstallation.

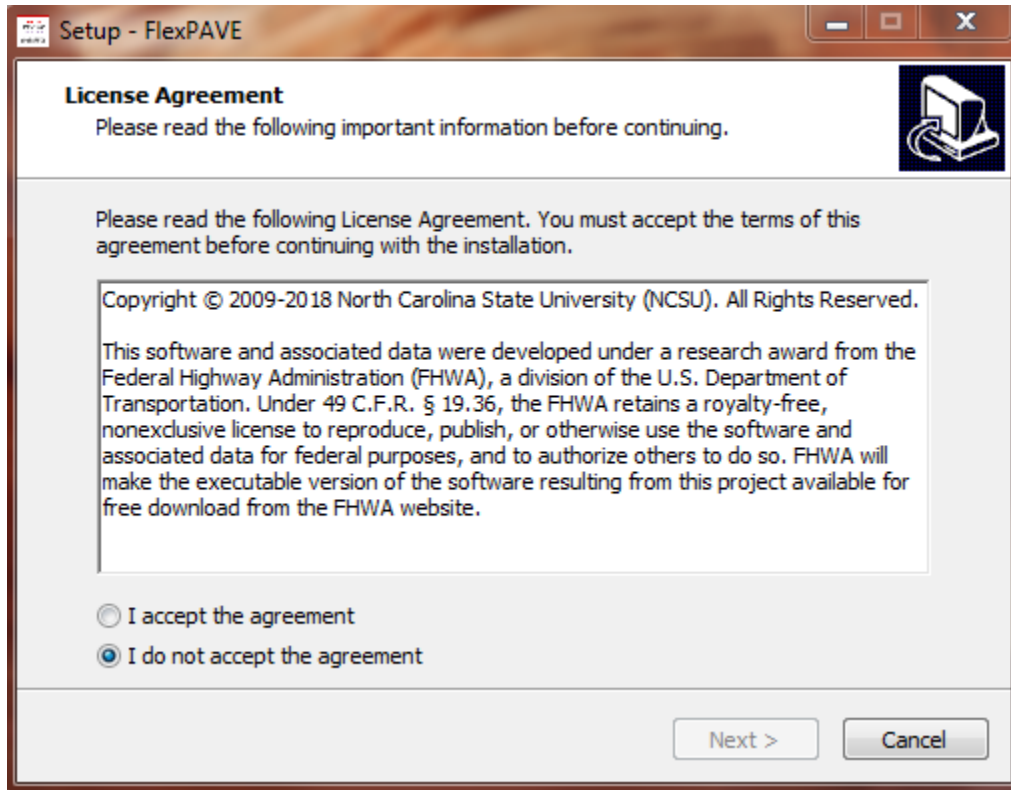


Source: FHWA.

Figure 150. Screenshot. Window to start FlexPAVE setup.

Step 2—Accept License Agreement

Carefully read the license agreement (Figure 151) and choose “I accept the agreement” to continue installation.

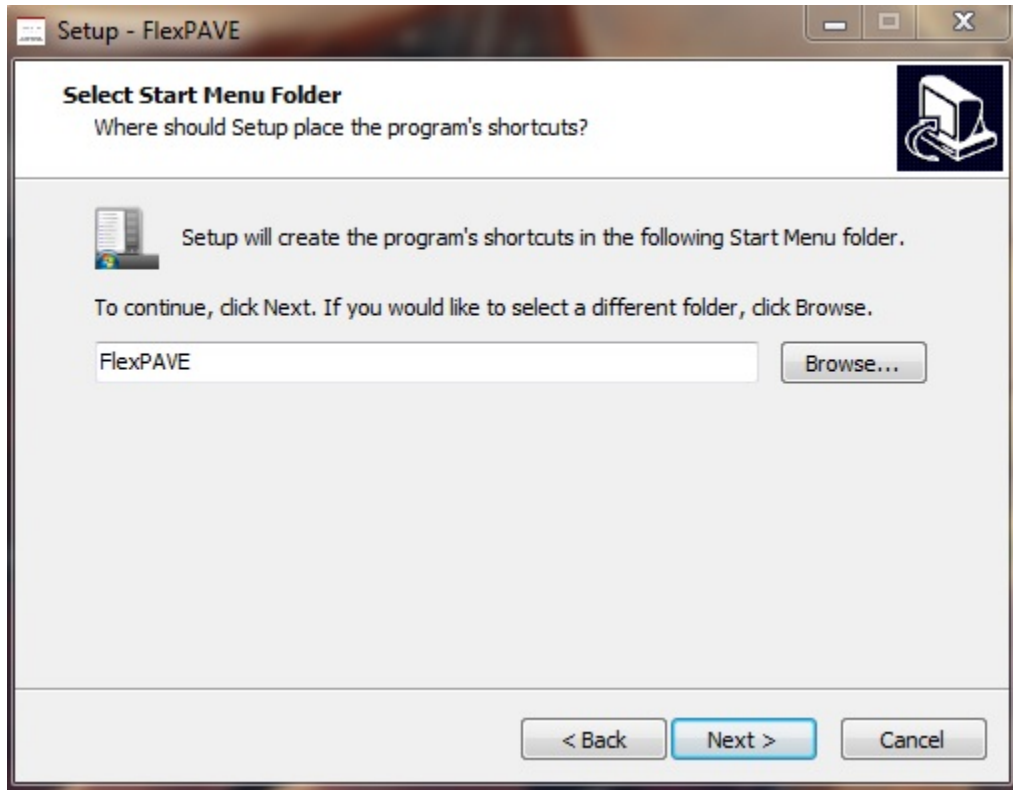


Source: FHWA.

Figure 151. Screenshot. FlexPAVE license agreement.

Step 3—Set Up Destination Folder, Start Menu Folder, and Desktop Shortcut

The Installation folder, Start Menu folder, or Desktop Shortcut cannot be changed using Setup Wizard options. FlexPAVE automatically installs them on C:/FlexPAVE/. See figure 152.

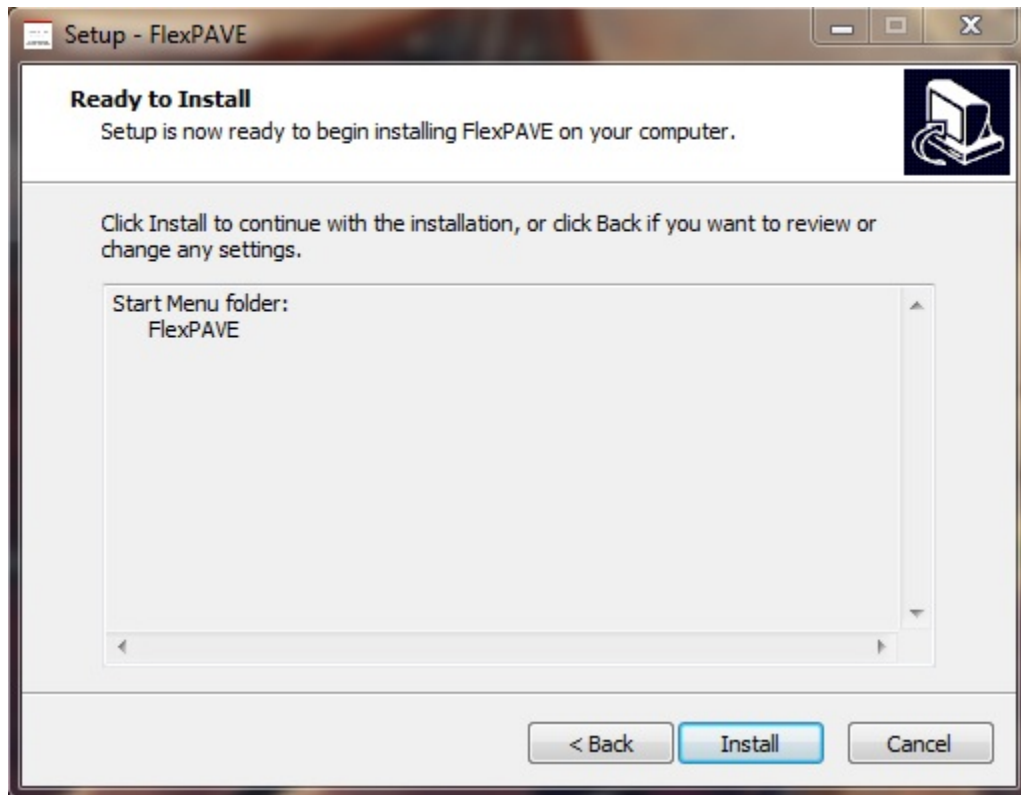


Source: FHWA.

Figure 152. Screenshot. Selecting the destination location.

Step 4—Start Installation

Click Install to initiate the process. See figure 153.

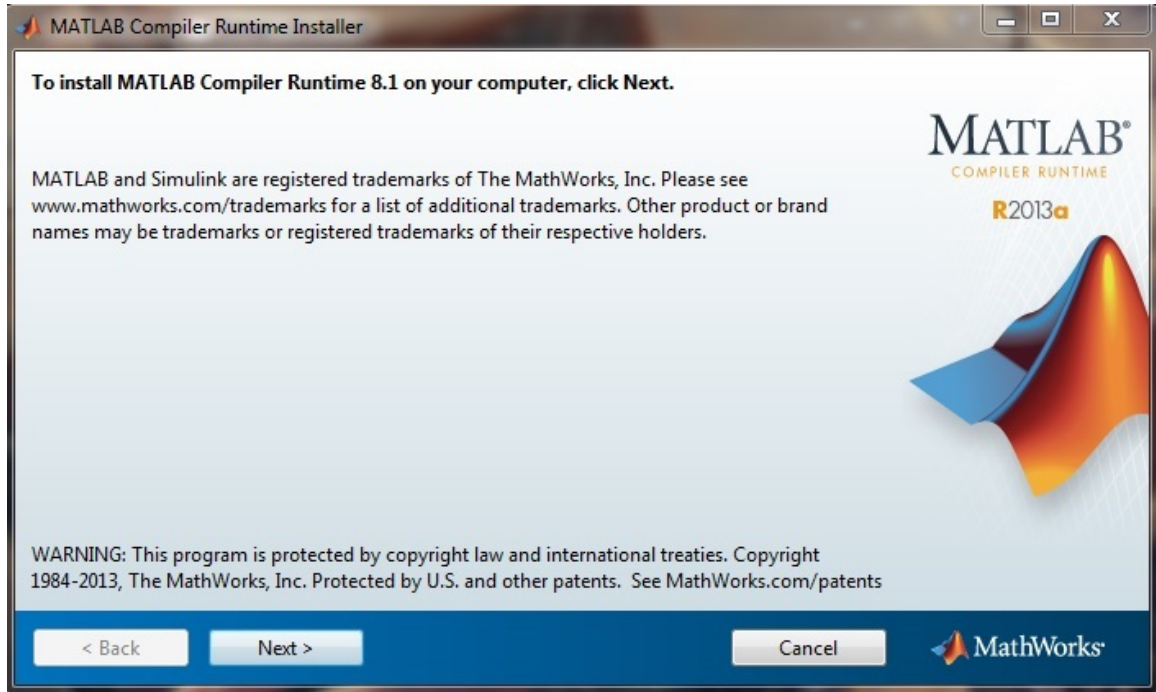


Source: FHWA.

Figure 153. Screenshot. Start installation.

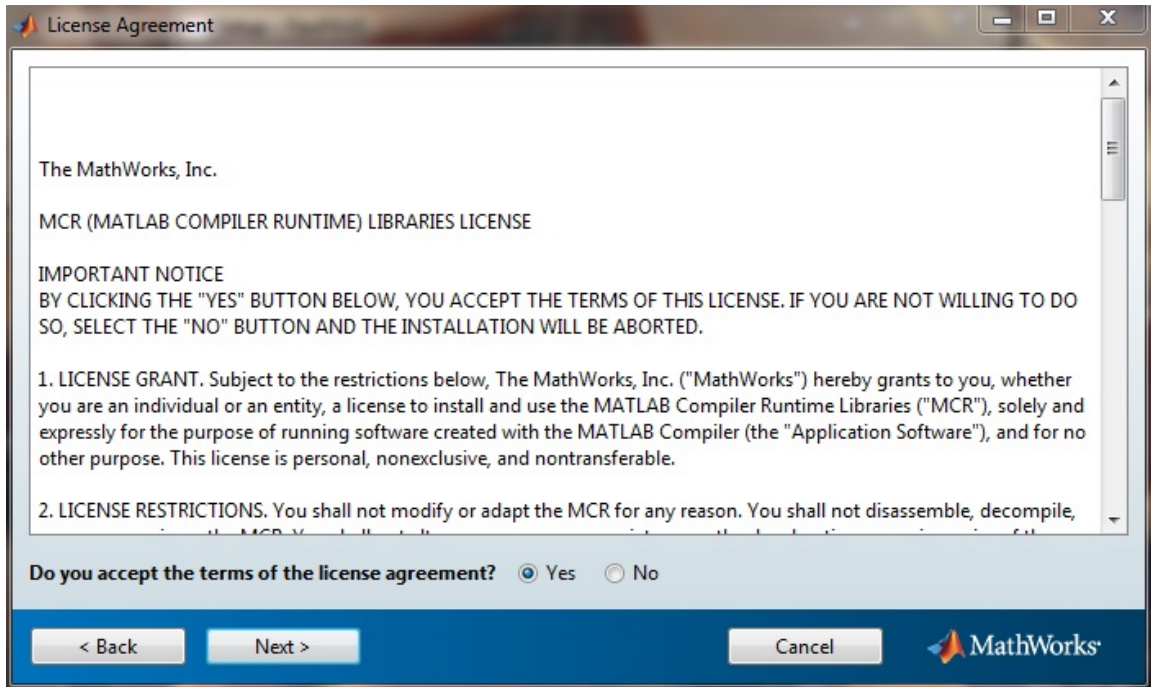
Step 5—Install MCR

FlexPAVE is a MATLAB-based program and requires specific MATLAB components included in MCR-R2013a and MCR-R2016a⁽¹²⁰⁾ to be installed on the computer. The Setup Wizard automatically installs the MCRs. Carefully read the MCR license agreement and follow the MCR Setup Wizard to install the MATLAB components. Figure 154 and figure 155 show the installation process for MCR-R2013a. Follow the same procedure to install MCR-R2016a.



© 2013 MATLAB. (DTFH61-08-H-00005)

Figure 154. Screenshot. MCR installer.

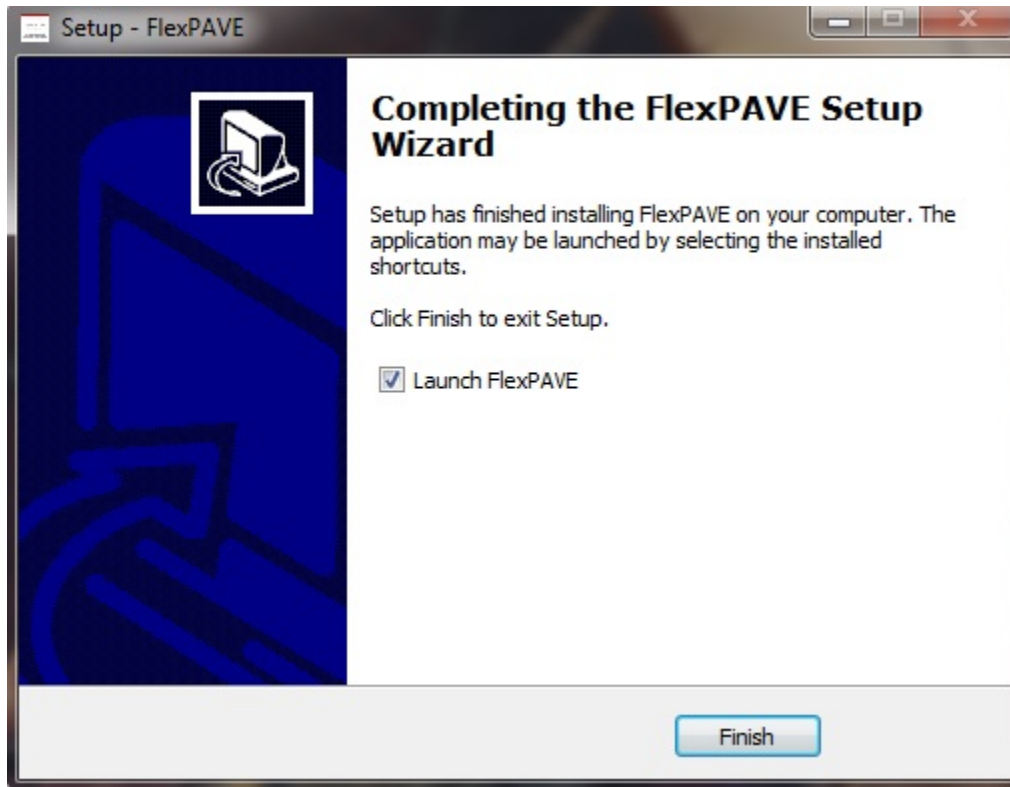


© 2013 MATLAB. (DTFH61-08-H-00005)

Figure 155. Screenshot. MCR license agreement.

Step 6—Finalize the Installation

Once MCR installation is complete as shown in figure 156, finalize the installation by restarting the computer. This action (i.e., restarting the computer to complete the FlexPAVE) setup, is strongly recommended.



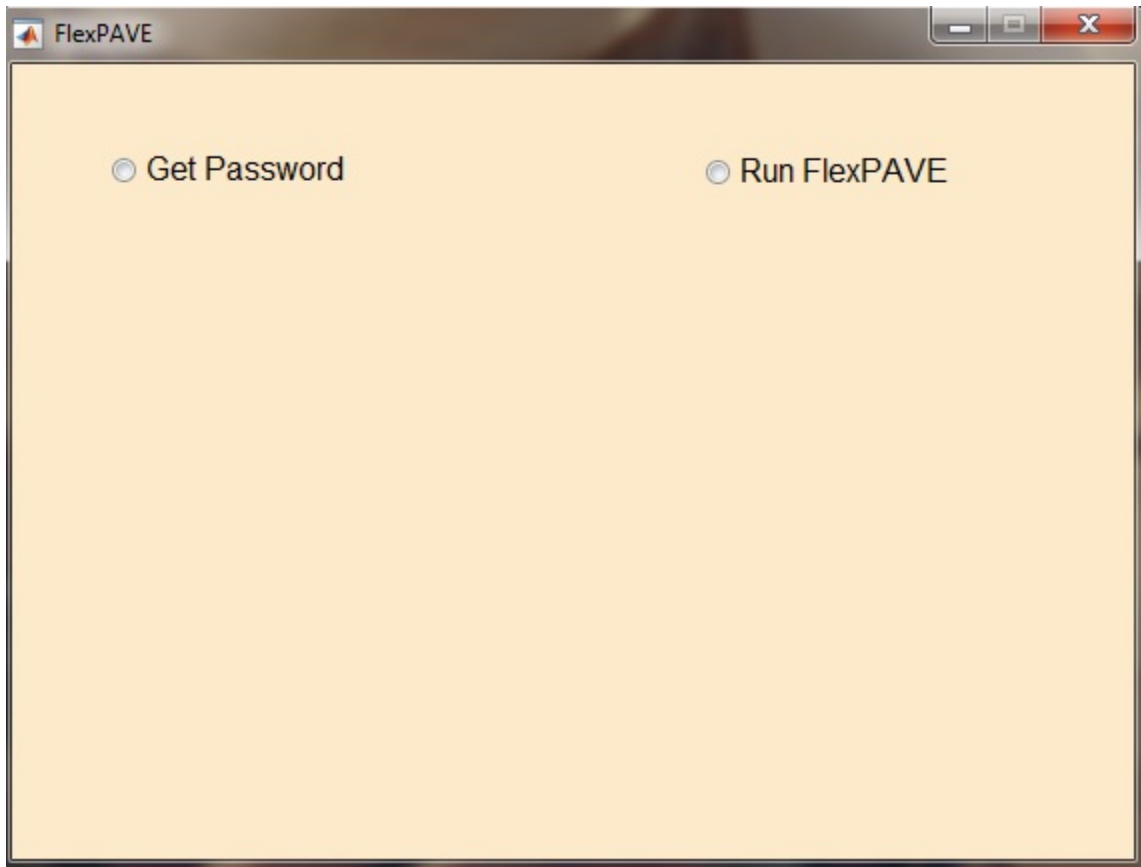
Source: FHWA.

Figure 156. Screenshot. Finalize the FlexPAVE setup.

Wrapper

After initiating FlexPAVE, a start window will appear. Figure 157 shows an overview of the FlexPAVE wrapper. This feature has been added to FlexPAVE for registering users and assigning passwords to them. The wrapper requires an internet connection to check the user information, so ensure internet connection is strong. Wait a few minutes for the MATLAB compiler to load.

If it takes more than 5 min for the wrapper to load, close the banner and reopen the FlexPAVE program.



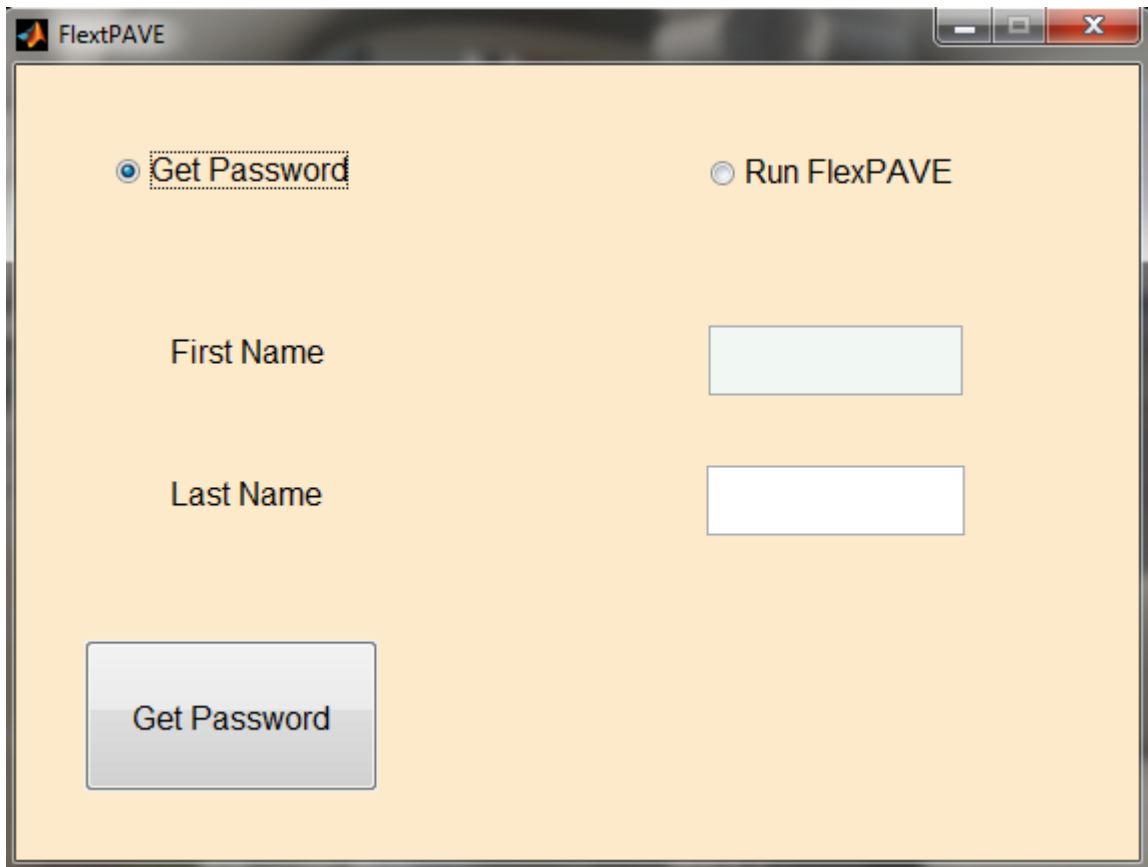
Source: FHWA.

Figure 157. Screenshot. Overview of FlexPAVE wrapper.

Get Password

Once user registration is complete, select Get Password at the top left of the window (figure 158) and enter First Name and Last Name. After completing the two required fields and clicking Get Password at the bottom of the screen (figure 158), an email will be sent to the email address users provided earlier in the process. This email will contain the username and password needed to launch FlexPAVE. Write down the password. This option (i.e., Get Password) can also be used for password retrieval in the case of a forgotten password.

The FlexPAVE license is limited to one computer per user, and cannot be run on any other computer unless that user also obtains a license.

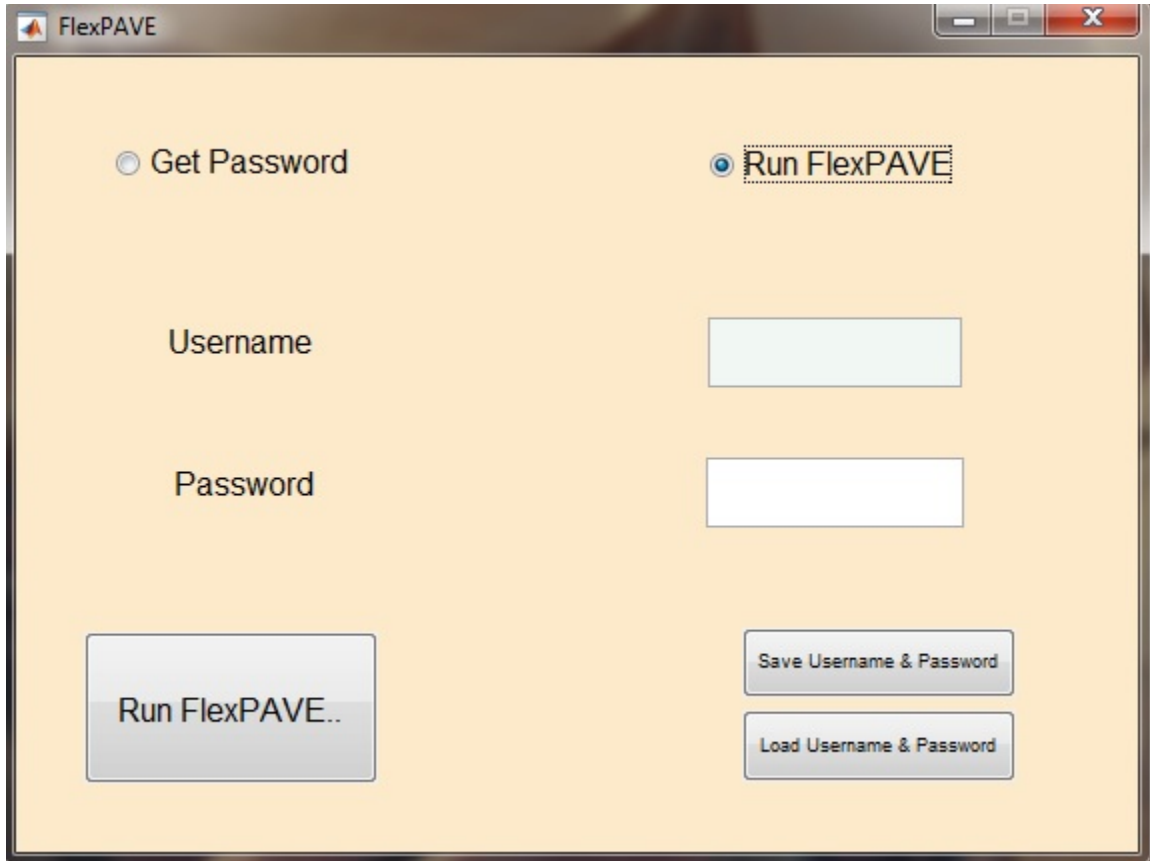


Source: FHWA.

Figure 158. Screenshot. Get Password window.

Run FlexPAVE

After receiving the password, select Run FlexPAVE at the top right of the window (figure 159) and enter the required information (i.e., username and password) to launch FlexPAVE. The window also offers the option in the bottom right to save the username and password on the computer for use in the future (figure 159).



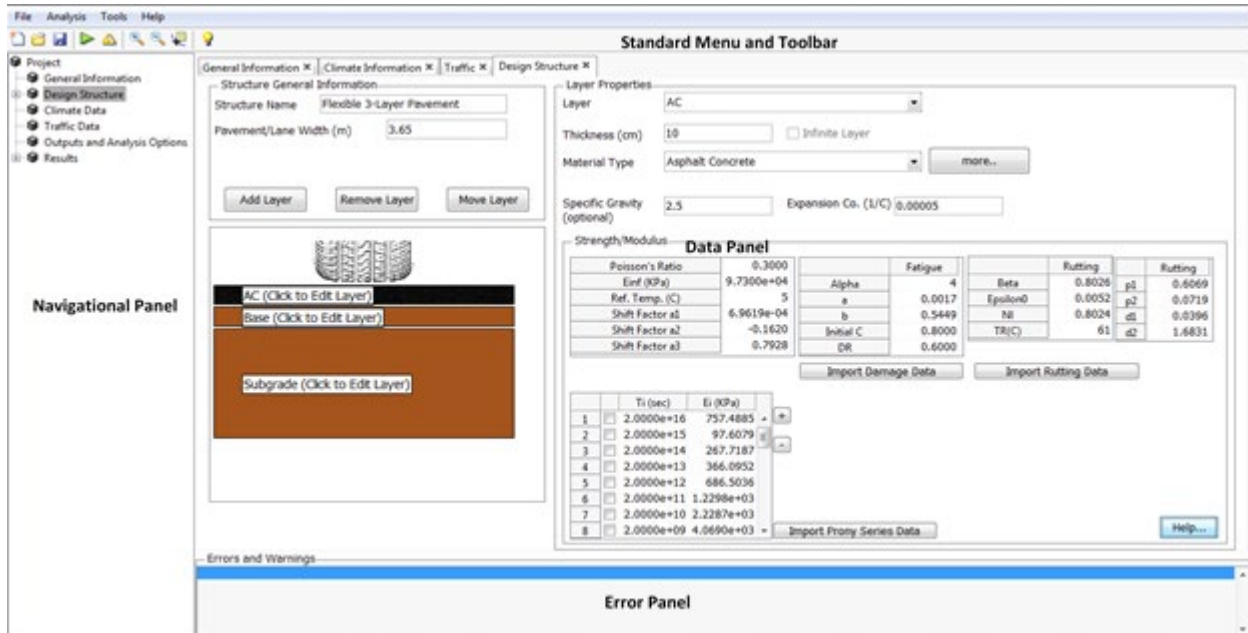
The screenshot shows a window titled "FlexPAVE" with a light orange background. At the top, there are two radio buttons: "Get Password" (unselected) and "Run FlexPAVE" (selected). Below the radio buttons are two input fields: "Username" and "Password". At the bottom, there are four buttons: "Run FlexPAVE.." on the left, and "Save Username & Password" and "Load Username & Password" on the right.

Source: FHWA.

Figure 159. Screenshot. Run FlexPAVE window.

GUI OVERVIEW

Figure 160 presents an overview of the GUI for FlexPAVE. The interface includes four main sections: standard menu and toolbar; navigational panel; data panel; and error panel. When resizing the main window, horizontal and vertical scroll bars will appear. Sometimes the project tree nodes in the navigational panel (on the left side of the screen) will disappear. If this happens, scroll up and down several times to make the project tree nodes reappear.

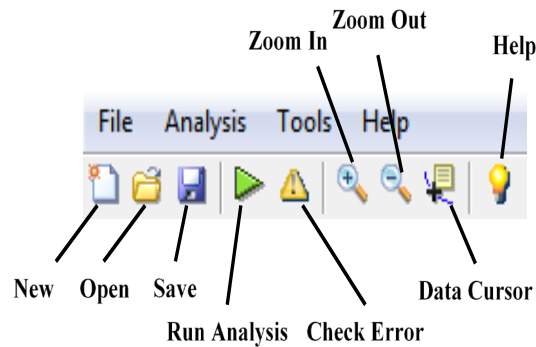


Source: FHWA.

Figure 160. Screenshot. Overview of FlexPAVE GUI.

Standard Menu and Toolbar

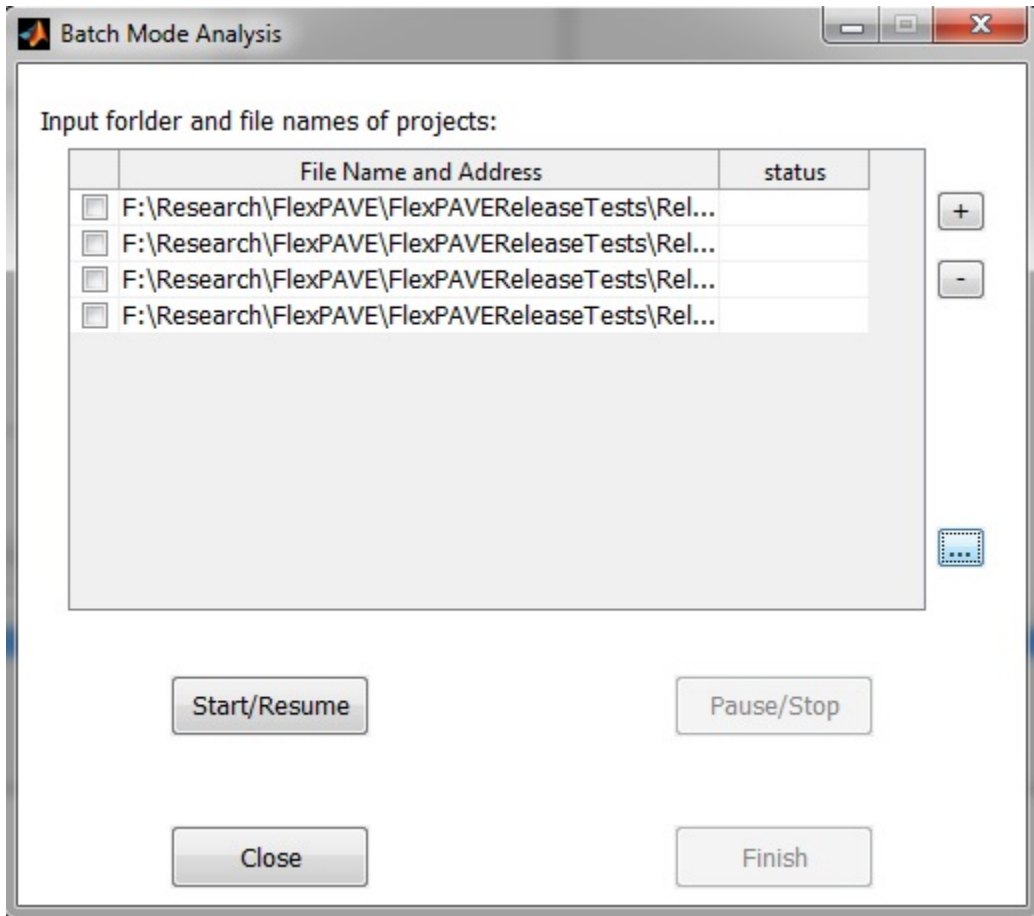
The standard menu and toolbar (figure 161) include a set of tools that can be used to create a new project, open a saved project, or save a current project. The standard menu is a drop-down menu containing all the functionalities in the toolbar. Analyses can also be performed and input data can be checked for any possible errors. Additionally, the toolbar contains a zoom icon and data cursor for extracting data from the analysis results, as well as a Help function.



Source: FHWA.

Figure 161. Screenshot. Standard menu and toolbar.

Under the Analysis tab, Batch Mode Analysis (figure 162) enables several projects to be run continuously. Input values can be checked under the Check Error tab. Databases for vehicle information can be constructed under Add Vehicle to Database under the Tools tab. The saved material properties and vehicle information from the database can be loaded if necessary.



Source: FHWA.

Figure 162. Screenshot. Batch Mode Analysis window.

Navigational Panel

The navigational panel is shown in figure 160 and is composed of input and output tabs. The input tabs are General Information; Design Structure; Climate Data; Traffic Data; and Outputs and Analysis Options. The output tab, Results, has three submenus: Response; Fatigue Cracking; and Rutting.

The properties of a layer can be directly accessed by selecting its name from the navigation tree. The order of the tabs in the navigational panel is the same as for the input procedure; therefore, the inputs can be entered following this order to complete the simulation.

Data Panel

The data panel is shown in figure 160 and is a communication window that can be used to enter all the information about the simulation and to view simulation results. The data panel consists of five tabs for pavement inputs (General Information; Design Structure; Climate Data; Traffic Data; and Output and Analysis Options) and three tabs for analysis outputs (Response; Fatigue Cracking; and Rutting), which are shown in the navigational panel. Each tab can be opened by

selecting its name from the navigation tree. Section 'INPUT' provides details about the input tabs, and section 'OUTPUT' describes the outputs.

Error Panel

The error panel is shown in figure 160. The model can be checked by selecting the Check Error icon on the toolbar or choosing Check Error from the Analysis menu. Any error or warning found in the input data will be displayed in the error panel. The information provided in the error description can be used to locate the error and try to fix it. The analysis cannot be carried out even if a single error occurs, although analysis can still be performed with multiple warning messages. The formats of the error and warning messages are:

- Error (Error Number): Tab Name / Input Data / Error Description.
- Warning (Warning Number): Tab Name / Input Data / Warning Description.

INPUTS

The FlexPAVE inputs are classified into five groups: General Information; Design Structure; Climate Data; Traffic Data; and Outputs and Analysis Options. A separate tab is designated for each group of required data. A tab can be opened by clicking its name in the navigational panel.

General Information

This section provides general information regarding the pavement analysis and project site. Figure 163 shows an overview of the General Information tab.

The screenshot shows the 'General Information' tab with the following details:

- Pavement Type:** Radio buttons for 'New Pavement' (selected) and 'AC-on-AC overlay Rehabilitation'.
- Pavement Location:** Input fields for 'Latitude' and 'Longitude', both containing '0.0'.
- Traffic:** Radio buttons for 'Design Vehicle' (selected) and 'Traffic Spectrum'.
- Analysis Options:** Radio buttons for 'Pavement Response Analysis' (selected) and 'Pavement Performance Analysis'. Below are two columns of checkboxes: 'Fatigue Options' (checked for 'Fatigue Cracking' and 'Thermal Stress', unchecked for 'Healing' and 'Aging') and 'Rutting Options' (checked for 'Rutting').
- Pavement Construction Timeline:** Three dropdown menus: 'Pavement Construction Date' (January, 2014), 'Traffic Opening Date' (January, 2014), and 'Pavement Design Life (years)' (20).
- Optional Description:** A table with columns for Project Name, Author, City/State, Date, and Note.
- Buttons:** 'Units' and 'Advanced' buttons at the bottom.

Source: FHWA.

Figure 163. Screenshot. General Information tab.

Basic Information

The General Information tab provides information like pavement type, pavement location, traffic options, and optional descriptions.

Pavement Type

Two types of pavement are considered for FlexPAVE: New Pavement and AC-on-AC overlay Rehabilitation. The Rehabilitation option is currently unavailable but may be included in future versions.

Pavement Location

The pavement location is defined in terms of latitude and longitude and is used to obtain climate data. For this FlexPAVE version, Pavement Location is unavailable.

Traffic

The type of traffic data can be selected in this section. Currently, FlexPAVE uses only Design Vehicle to carry out the analysis. Traffic Spectrum will be included in future versions.

Optional Description

These fields include additional information, such as Project Name, Author, City/State, Date, and Note, which can be used to distinguish between projects.

Units

The units of the input parameters can be changed in the Units dialog box, found below the Optional Description box (see bottom left of figure 163). The default units are SI units. The ability to change units is unavailable in the current version.

Analysis Options

FlexPAVE can perform two types of analysis: Pavement Response Analysis and Pavement Performance Analysis, as found in the Analysis Options panel (figure 163). Pavement Response Analysis only produces stress–strain and displacement results. Pavement Performance Analysis provides all information, including fatigue cracking, thermal stress, rutting data, etc., depending on the selection of the performance items.

Based on the analysis type selected, the user must provide data for the material properties, climate, and traffic. If Pavement Response Analysis is chosen, the user can move on to the next step. If Pavement Performance Analysis is chosen, additional inputs are required, as listed under Fatigue Options, Rutting Options, and Pavement Construction Timeline (figure 163).

Fatigue Options

Fatigue Cracking can be added to the analysis from the Fatigue Options panel, which also includes Thermal Stress, Healing, and Aging. Currently, healing and aging models are not available. The program implements two material models (i.e., the G^R -based criterion and D^R -based criterion) for predicting fatigue damage growth.

Rutting Options

Rutting analysis can be added to the Pavement Performance Analysis by selecting the Rutting option. The program calculates rut depth and permanent strain as a function of pavement life.

Pavement Construction Timeline

The Pavement Construction Timeline includes Pavement Construction Date, Traffic Opening Date, and Pavement Design Life (years). Analysis starts from the pavement construction date; however, the program applies thermal loading during the period between the pavement construction date and the traffic opening date. After the traffic opening date, the program applies vehicle loading to the analysis.

DESIGN STRUCTURE

The Design Structure tab, shown in figure 164, consists of three sections: Structure General Information, Layer Properties, and the pavement schematic. A name can be provided for the pavement structure (Structure Name) and its width (Pavement/Lane Width) under Structure General Information. FlexPAVE can handle pavements with an unlimited number of material layers. Layers can be added or removed and the layer position can be changed by clicking Add Layer, Remove Layer, and Move Layer. Pavement structure can then be reviewed in the pavement schematic box.

General Information | Design Structure | Climate Information

Structure General Information

Structure Name: Flexible 3-Layer Pavement

Pavement/Lane Width (m): 3.65

Add Layer Remove Layer Move Layer

Layer Properties

Layer: AC

Thickness (cm): 10 Infinite Layer

Material Type: Asphalt Concrete more.. GR Based Criterion DR Based Criterion

Specific Gravity (optional): 2.5 Expansion Co. (1/C): 0.00005

Strength/Modulus

Poisson's Ratio	0.3000	Alpha	Fatigue	Beta	Rutting	p1	Rutting
Einf (KPa)	9.7300e+04	C11	4	Epsilon0	0.8026	p2	0.6069
Ref. Temp. (C)	5	C12	0.0017	NI	0.0052	d1	0.0396
Shift Factor a1	6.9619e-04	Initial C	0.8000	TR(C)	0.8024	d2	1.6831
Shift Factor a2	-0.1620	Gamma	1000000		61		
Shift Factor a3	0.7928	Delta	-1.3500				

	Ti (sec)	Ei (KPa)
1	<input type="checkbox"/> 2.0000e+16	757.4885
2	<input type="checkbox"/> 2.0000e+15	97.6079
3	<input type="checkbox"/> 2.0000e+14	267.7187
4	<input type="checkbox"/> 2.0000e+13	366.0952
5	<input type="checkbox"/> 2.0000e+12	686.5036
6	<input type="checkbox"/> 2.0000e+11	1.2298e+03
7	<input type="checkbox"/> 2.0000e+10	2.2287e+03
8	<input type="checkbox"/> 2.0000e+09	4.0690e+03

Import Damage Data Import Rutting Data

Please note that FlexPAVE 1.0 uses the power function with the C11 and C12 coefficients to define damage characteristic curve instead of an exponential function.

Import Prony Series Data Help...

Source: FHWA.

Figure 164. Screenshot. Design Structure tab.

Layer Properties

The main part of the Design Structure tab is Layer Properties. The Layer Properties panel includes two sections: general information, which includes Layer, Thickness, Material Type, G^R Based Criterion/D^R Based Criterion, Specific Gravity; and the (thermal) Expansion Coefficient, and Strength/Modulus information. The properties of each layer can be accessed by choosing the layer name from the drop-down menu at the top of the Layer Properties section. Each layer can also be edited by selecting the layer on the navigation tree or by clicking the layer's name in the pavement schematic box. In the Strength/Modulus section, different values must be provided based on the material type selected for the current layer. Input details for the different material types are discussed in the following sections.

Asphalt Concrete

The type of asphalt concrete (AC) layer can be selected by clicking the "more.." button beside Material Type. The types are Viscoelastic with Damage, Linear Elastic, and Anisotropic Elastic.

Linear Viscoelastic Properties

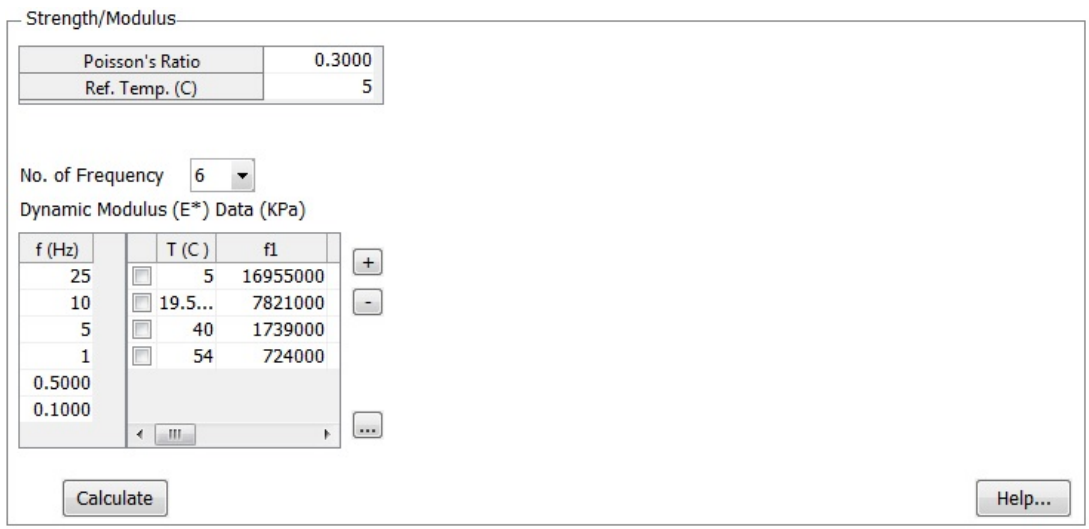
Asphalt concrete is a mainly linear viscoelastic material whose properties can be defined using dynamic modulus test inputs, the master curve of the dynamic modulus, or the Prony series. Options are provided by clicking the “more..” button beside Material Type. FlexPAVE provides three ways to enter the viscoelastic properties: dynamic modulus test inputs, master curve of the dynamic modulus, and Prony series.

Dynamic Modulus Test

The required inputs for the dynamic modulus test are the Poisson’s ratio, reference temperature, number of frequencies, and dynamic modulus ($|E^*|$) experimental data, which can be prepared in Excel as a CSV (comma delimited) file conforming to the format presented in table 37. In table 37, the first line presents the frequencies at which the dynamic modulus tests are carried out. The values in the first column are the temperatures and the remaining values are the dynamic modulus values at different temperatures and frequencies. FlexPAVE determines the master curve, shift factor function, and Prony series using these data. These results can be accessed by clicking the Calculate button below the experimental dynamic modulus table (figure 165). Figure 166 presents the screenshot of the viscoelastic material parameters obtained from the test data.

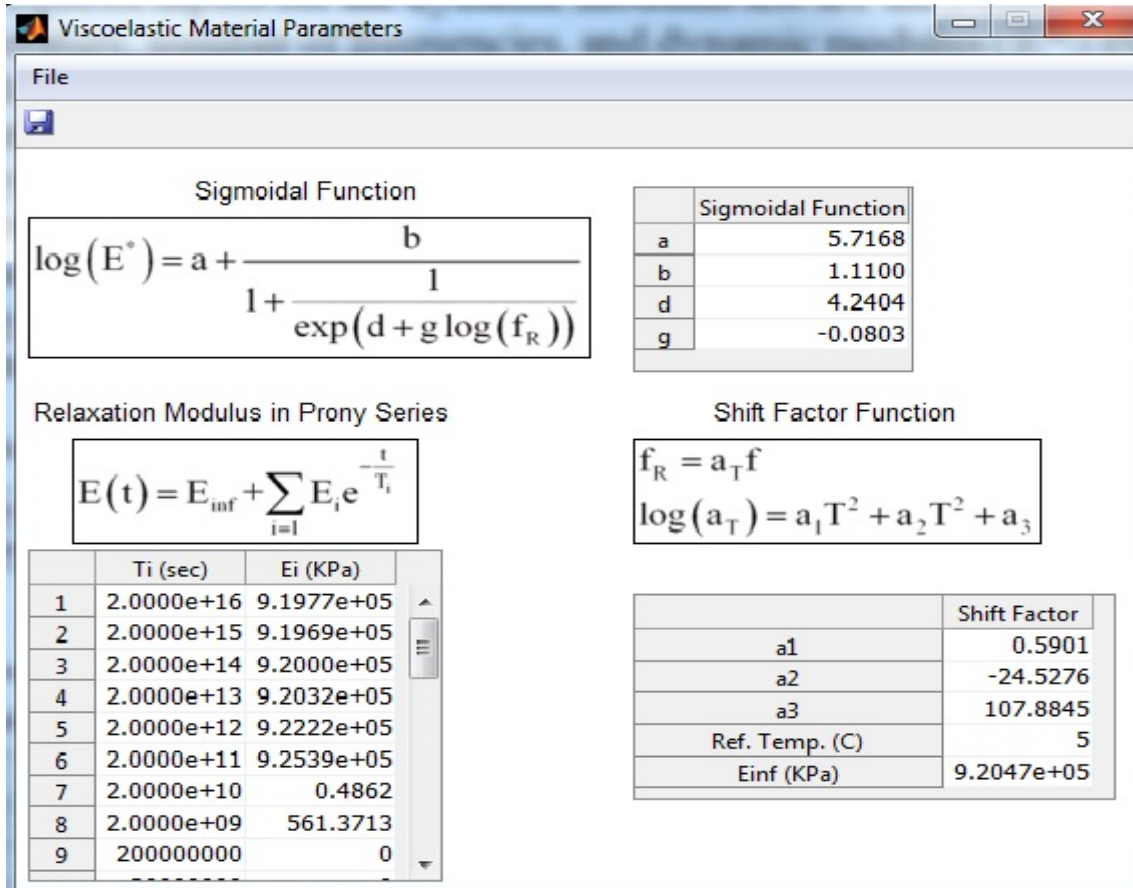
Table 37. Format of text file to input dynamic modulus experimental data.

T(°C)/f(Hz)	25	10	5	1	0.5	0.1
4	2646226	2543195	2468863	2133113	1926399	1539293
20	1363786	1184835	1048823	744960.3	649764.7	431177.6
40	457874	352108.9	284652.5	159915.7	129689.8	80626.48
54	171285.2	128373.6	102611.3	62542.45	54276.02	40667.13



Source: FHWA.

Figure 165. Screenshot. Dynamic modulus input screen.



Source: FHWA.

Figure 166. Screenshot. Viscoelastic material parameters obtained from test data.

Master Curve of Dynamic Modulus

The required inputs for the dynamic modulus master curve are the Poisson's ratio, reference temperature, shift factor coefficients a_1 , a_2 , and a_3 , and coefficients for the sigmoidal function, a , b , d , and g . Equation 132 and equation 133 define the shift factor and sigmoidal functions, respectively.

$$f_R = a_T f \text{ and } \log(a_T) = a_1 T^2 + a_2 T + a_3 \quad (132)$$

$$\log(|E^*|) = a + \frac{b}{1 + e^{-(d+g \log(f_R))}} \quad (133)$$

The Prony series fitted to a given sigmoidal function can be obtained by clicking the Calculate button.

The required inputs for the Prony series are the Poisson's ratio, reference temperature, shift factor coefficients a_1 , a_2 , and a_3 , and Prony coefficients E_∞ , ρ_i and E_i , as shown in equation 134.

$$E(t) = E_{\infty} + \sum_i E_i e^{-\frac{t}{\rho_i}} \quad (134)$$

For the sake of simplicity, Poisson's ratio, E_{∞} , reference temperature (T_{ref}), and t-T shift factor coefficients can be imported from the FlexMAT-Cracking format file using the format shown in table 38. This option is available only for Prony series types.

Table 38. Format of Excel file to input dynamic modulus data.

E_{∞}	193176.8
Poisson's Ratio	0.3
T_{ref}	5
Shift Factor a1	0.000644
Shift Factor a2	-0.15822
Shift Factor a3	0.775
T_i (sec)	Ei (kPa)
200000000	8643.581
20000000	17135.86
2000000	34849.2
200000	73925.88
20000	166573.3
2000	399175.1
200	962605
20	2035875
2	3,243,321
0.2	3,477,141
0.02	3,420,026
0.002	2,493,795
0.0002	1,655,458
0.00002	1,008,823
0.000002	591,621.4
0.0000002	338,034.7
0.00000002	190,693.7

Fatigue Properties

For asphalt concrete, the coefficients of the VECD model are also needed if conducting Pavement Performance Analysis; these coefficients are α , a , b , E_R , *Initial C*, γ , δ , and D^R . VECD model derivation starts from equation 135.

$$\frac{dS}{dt} = \left(-\frac{\partial W^R}{\partial S} \right)^\alpha \quad (135)$$

Finally, the VECD model is given by equation 136 to represent damage growth in the asphalt pavement.

$$C(S) = 1 - C_{11} S^{C_{12}} \quad (136)$$

D^R , expressed by equation 137, is used to calculate fatigue life (i.e., the number of cycles to failure (N_f)).

$$D^R = \frac{\int_0^{N_f} (1 - C) dN}{N_f} \quad (137)$$

G^R , expressed by equation 138, also is used to calculate fatigue life (i.e., the number of cycles to failure (N_f)).

$$G^R = \gamma N_f^\delta \quad (138)$$

Note that α , a , b , G^R parameters (i.e., γ and δ), D^R , and S_{app} can be imported from the FlexMAT-Cracking format file using the format shown in table 39.

Table 39. Format of Excel file to input S-VECD fatigue property data.

α	3.78
C vs. S	Value
C_{11}	4.16E-03
C_{12}	0.392
G^R failure criterion	Value
gamma	9.40E+09
delta	-1.827
D^R failure criterion	Value
D^R	0.64
Damage capacity	Value
S_{app}	2.76E+01

Rutting Properties

The shift model parameters must be provided to conduct asphalt concrete Pavement Performance Analysis. In this model, the viscoplastic strain is defined in equation 139.

$$\varepsilon_{vp} = \frac{\varepsilon_0 N_{red}}{(N_I + N_{red})^\beta} \quad (139)$$

Where:

β , ε_0 , and N_I = model coefficients.

N_{red} = number of load cycles at the reference temperature and reference vertical stress.

N_{red} can be determined by shifting the actual (physical) number of load cycles as shown in equation 140 and equation 141.

$$N_{red} = N^{physical} \times 10^{a_{total}} \quad (140)$$

$$a_{total} = p_1 \log_{10}(\xi_p) + p_2 + (d_1 T + d_2) \left(\log_{10} \left(\frac{\sigma_v}{p_0} \right) - 0.877 \right) \quad (141)$$

Where:

ξ_p = reduced pulse time.

σ_v = vertical stress due to vehicle loading.

ε_0 , N_I , β , reference temperature (T_{ref}), p_1 , p_2 , d_1 and d_2 can be imported from the FlexMAT-Rutting format file using the format shown in figure 167.

	A	B	C	D
1	Reference Model			
2	e0	1.10E-03		
3	N1	3.611631		
4	β	0.71431		
5				
6	Reduced Load Time Shift Factor Model			
7	p1	0.897209		
8	p2	0.357035		
9				
10	Vertical Stress Shift Factor Model			
11	d1	0.19399		
12	d2	-3.60365		
13				
14	Tref (°C)	44.88858		
15				
16				
17				
18				

Source: FHWA.

Figure 167. Screenshot. Format of Excel file to input rutting property data.

In addition to being defined as viscoelastic material, an asphalt concrete layer can be defined as linear elastic or anisotropic elastic. The required inputs for these material types are similar to those of the base and subgrade (detailed in the Base and Subgrade sections).

Base

Three base types are available for the base layer: asphalt-treated base, aggregate base, and cement-treated base. The required input for asphalt-treated base is exactly the same as for asphalt concrete; thus, this type of base is considered linear viscoelastic material. The aggregate base and cement-treated base can be treated as linear elastic or anisotropic elastic materials. The following inputs are required for each material type:

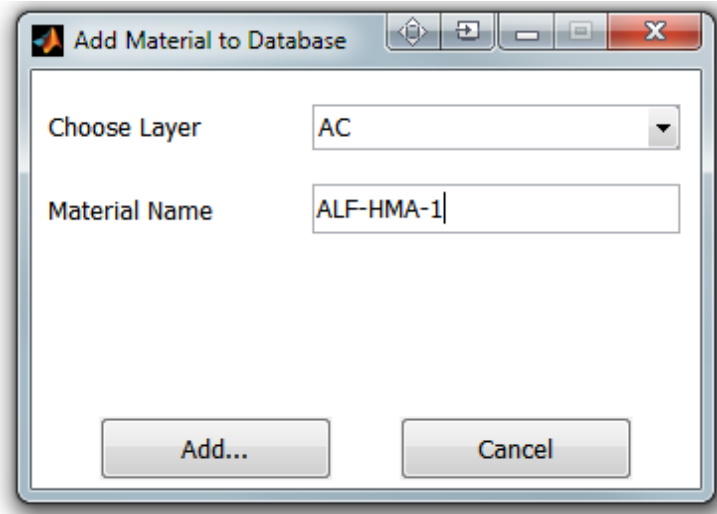
- Linear elastic: only requires the elastic modulus and Poisson's ratio.
- Anisotropic elastic: requires elastic modulus 11, elastic modulus 33, Poisson's ratio 13, Poisson's ratio 23, and shear modulus 13.

Subgrade

Similar to the base, the subgrade can be treated as linear elastic or anisotropic elastic.

Saving a Material

Finally, the defined materials can be saved and added to the program as shown in figure 168.



Source: FHWA.

Figure 168. Screenshot. Adding material properties to program database.

Climate Data

By clicking the Climate Information tab (a button option at the top of the Design Structure tab, shown in figure 164), the temperature profile of the asphalt pavement must be provided for analysis. Depending on the analysis type, different options are available.

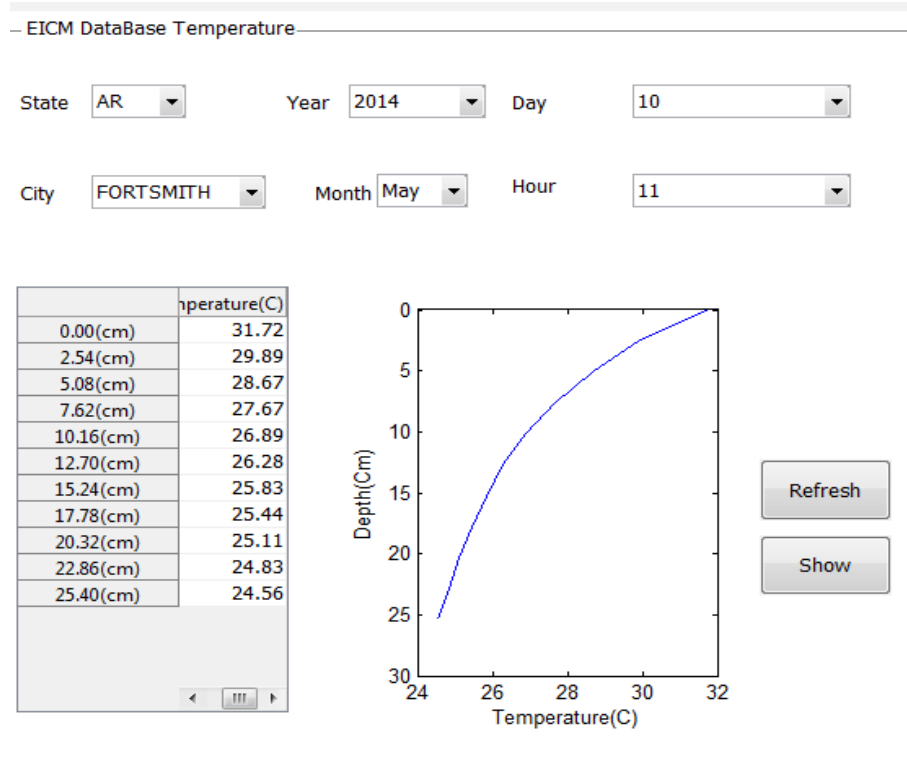
Temperature for Response Analysis

Currently, the temperature data for the response analysis can be input four ways: from the EICM database, as an EICM text file, as an isothermal condition, or manually.

EICM

FlexPAVE includes a complete database of States in the United States. For each State, major cities data are available. The temperature variation for 1 yr is stored for each city. Figure 169 provides an example of State (Arkansas) and City (Fort Smith) EICM data. A specific location and time also need be selected.

Due to an internal MATLAB program glitch, the City drop-down box does not load when the State is changed. In this case, another State must be input first and then the desired State must be selected again.



Source: FHWA.
 0°C = 32°F; 1 cm = 0.4 inch.

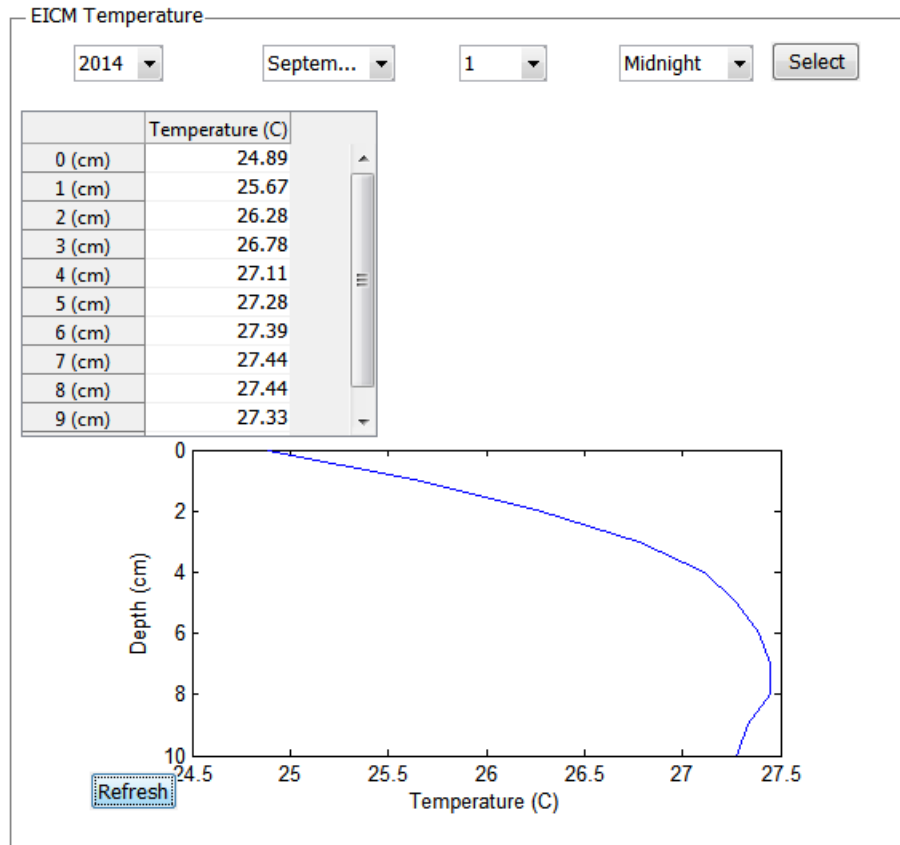
Figure 169. Screenshot. EICM database module.

EICM Text File

Table 40 presents the format of an EICM text file. An hourly temperature text file can be prepared that conforms to the format presented in table 40. The date and time for extracting the temperature profile from the EICM data can be chosen. The vertical temperature variation can be defined by specifying the temperature at different nodes along the pavement depth. Various nodes can be chosen based on the analysis conditions. The example shown in table 40 describes five nodes (Nodes 0–4) along the depth with a specified depth (noted in cm) and hourly temperature. The temperature profile can also be plotted or modified, as shown in figure 170.

Table 40. Format of EICM text file (e.g., WY nodal temp).

Date	Node 0 Depth 0 cm	Node 1 Depth 0.625 cm	Node 2 Depth 1.875 cm	Node 3 Depth 3.125 cm	Node 4 Depth 4.375 cm
1 Sep 2001 0:00	12.5	14.6	16.4	18.0	19.2
1 Sep 2001 1:00	10.6	13.2	15.5	17.2	18.4
1 Sep 2001 2:00	11.1	13.2	15.0	16.6	17.8
1 Sep 2001 3:00	11.1	12.9	14.6	16.0	17.2
1 Sep 2001 4:00	10.6	12.5	14.2	15.6	16.7
1 Sep 2001 5:00	13.7	13.9	14.1	15.3	16.3



Source: FHWA.
 0°C = 32°F; 1 cm = 0.4 inch.

Figure 170. Screenshot. EICM temperature data for pavement response analysis.

Isothermal

The isothermal condition can be used for constant temperature analysis throughout the entire pavement depth. After selecting the Isothermal option, the temperature for analysis can be entered (figure 171).

Temperature Profile Input

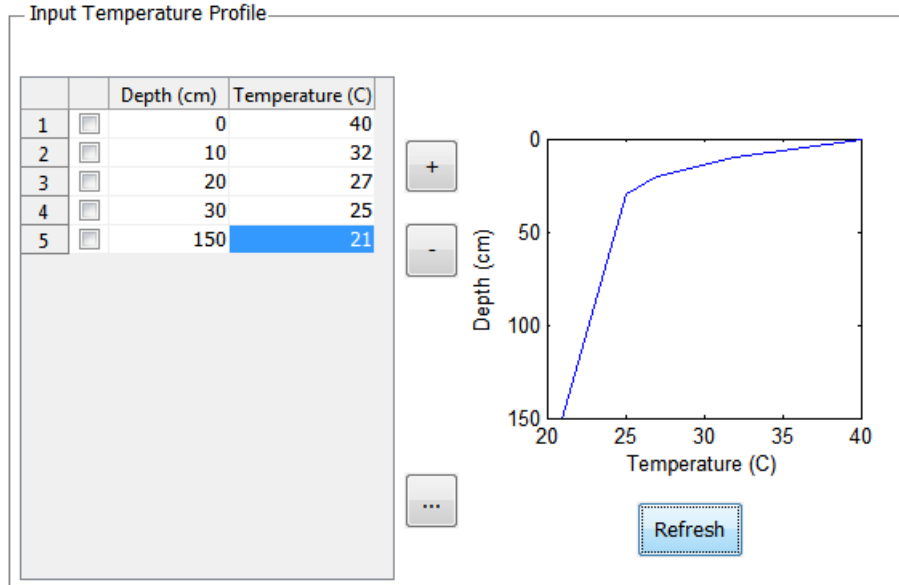
EICM
 EICM Text File
 Isothermal Temperature (C)
 Input Manually

Source: FHWA.

Figure 171. Screenshot. Isothermal temperature input.

Input Manually

The table in figure 172 can be used to input the temperature profile manually. Data points can be added using the + and – buttons. A temperature profile can also be generated by importing a text file containing different depths and corresponding temperatures. Table 41 presents the format of the import file. This file can be prepared using Excel and saved as a CSV file.



Source: FHWA.
 0°C = 32°F; 1 cm = 0.4 inch.

Figure 172. Screenshot. Manually input temperature data for pavement response analysis.

Table 41. Format of text file to input temperature manually.

Depth (cm)	Temperature (°C)
0	40
10	32
20	27
30	25
150	21

0°C = 32°F; 1 cm = 0.4 inch.

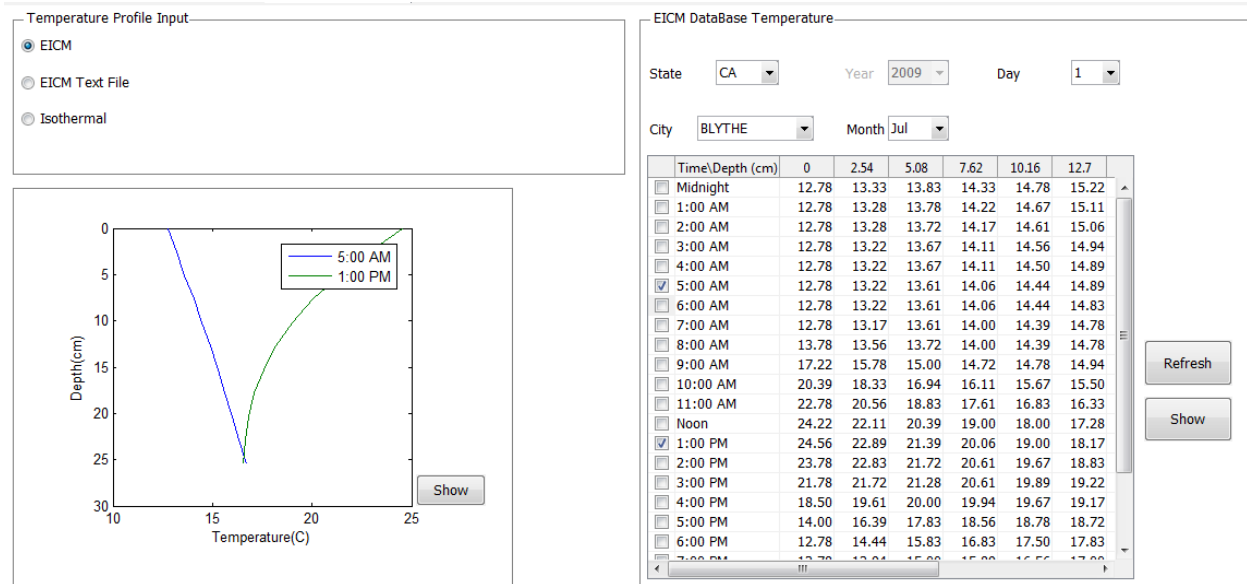
Temperature for Performance Analysis

Currently, the temperature data for performance analysis can be input three ways: using the EICM, EICM Text File, or Isothermal options, as shown in figure 171. There is no manual input option for pavement performance analysis as there is for pavement response analysis. The options are different because a constant temperature profile is an unlikely condition for long-term performance evaluation. Isothermal conditions, while not representative of field conditions, do exist in certain accelerated load facilities.

EICM

In this module, FlexPAVE provides the pavement temperature database for 459 cities in the United States, so a city where a specific project site is located can be selected if included in the primary list. The FlexPAVE program considers 1-yr temperature variation for the selected State and City (figure 173).

As noted previously, due to an internal MATLAB program glitch, the City drop-down box does not load when the State is changed. In this case, another State must be input first and then the desired State must be selected again.



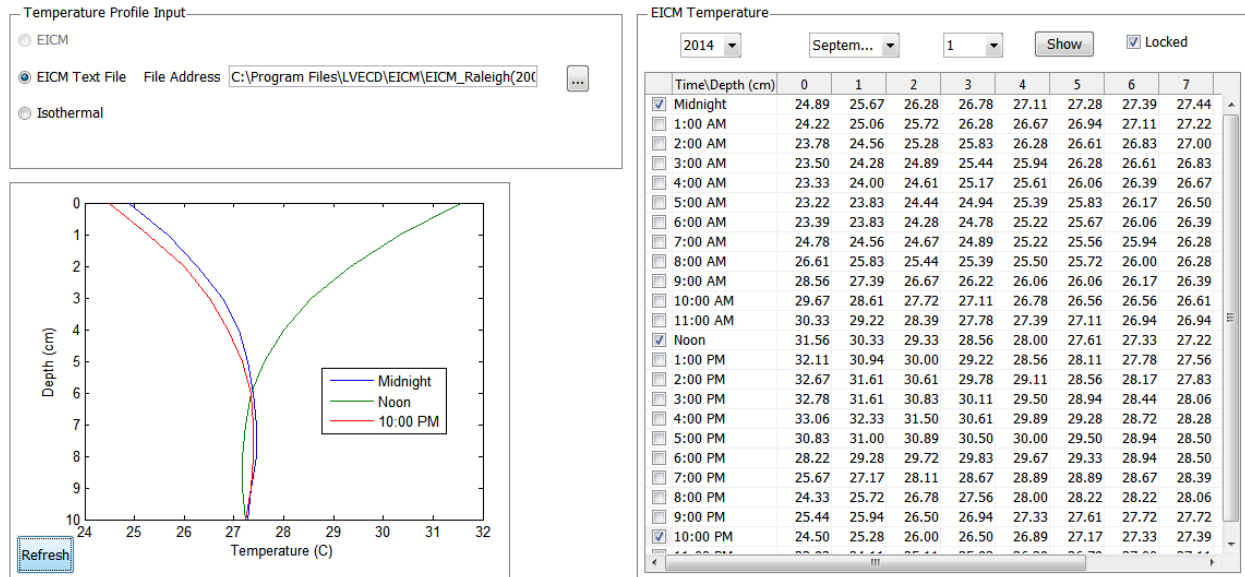
Source: FHWA.
0°C = 32°F; 1 cm = 0.4 inch.

Figure 173. Screenshot. Temperature data from EICM database for pavement performance analysis.

EICM Text File

By clicking EICM Text File (figure 174), temperature profile data can be entered, which may be 1 yr's temperature history. Table 41 illustrates the input file format. If the design life is longer than the period contained in the text file, the program will repeatedly use the temperature data until the length of the design period is filled. If the file specifies a period that is longer than the design life, the program will truncate the data internally. The EICM Text File can also be generated using the EICM program that accompanies the MEPDG software.⁽²⁵⁾

The temperature profile can be reviewed and plotted at different periods in the pavement life using tools provided in the GUI (see EICM Temperature in figure 174). The temperature values can be modified by unchecking the Locked function. The beginning of the EICM data should match the Pavement Construction Date. FlexPAVE utilizes the climate data from the beginning of the EICM text input. Otherwise, FlexPAVE rewrites the EICM dates using Pavement Construction Date and Pavement Life in the General Information tab shown in figure 174.



Source: FHWA.
 0°C = 32°F; 1 cm = 0.4 inch.

Figure 174. Screenshot. Temperature data for pavement performance analysis.

Isothermal

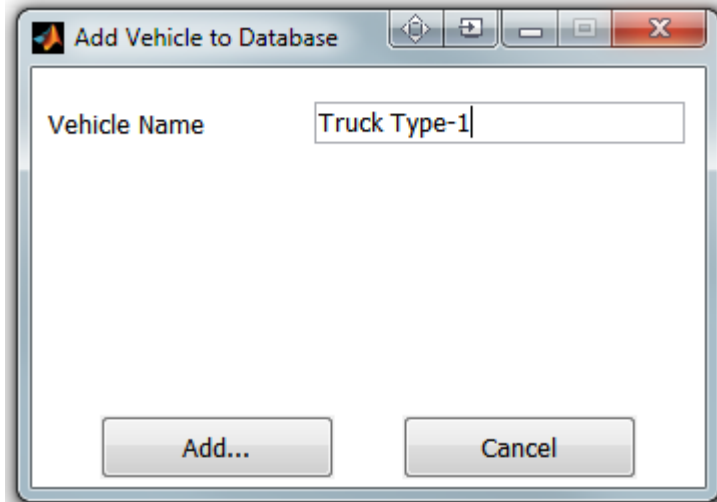
The Isothermal option is the same as for the isothermal analysis in Response Analysis.

Traffic Data

Traffic data can be entered by clicking Traffic Data in the navigational panel (figure 160). When a vehicle is added to the database (figure 175), FlexPAVE can calculate the responses and performance of an asphalt pavement against a standard normal truck or any type of special truck. The geometric configuration information must be specified in Design Vehicle Information (Figure 176). If the Pavement Performance Analysis is chosen in General Information (figure 163), the Traffic Information (Figure 177) must also be given.

Design Vehicle Information

Figure 175 shows the input window for Add Vehicle to Database. For a standard normal truck, a vehicle can be chosen from the program database by selecting it from the drop-down menu. A new vehicle can be generated by providing the following information (see the following General Information section) for all axles. The generated vehicle information can be added to the program database using Tools > Add Vehicle to Database (figure 161).



Source: FHWA.

Figure 175. Screenshot. Adding vehicle data to program database.

Design Vehicle Information

The diagram illustrates a truck with three axle configurations: a single axle at the front, a tandem axle in the middle, and a tridem axle at the rear. Red arrows indicate the distances between the axles, labeled D_2 and D_3 . A note below the diagram states "Note: D_1 is always zero".

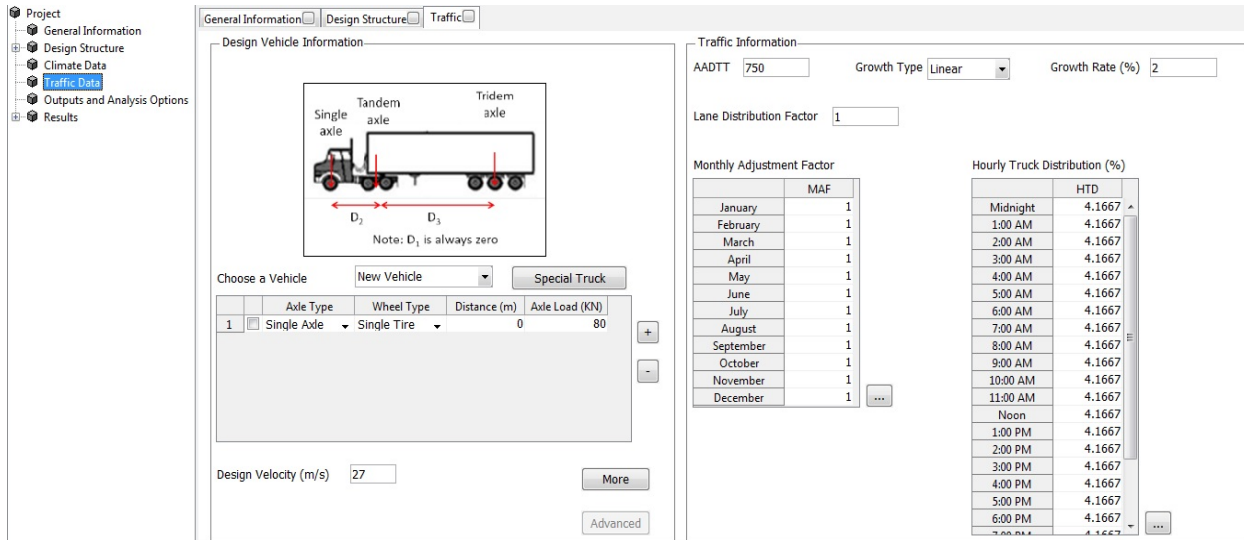
Choose a Vehicle:

	Axle Type	Wheel Type	Distance (m)	Axle Load (KN)
1	<input type="checkbox"/> Single Axle	Single Tire	0	80

Design Velocity (m/s)

Source: FHWA.

Figure 176. Screenshot. Design Vehicle Information tab.



Source: FHWA.

Figure 177. Screenshot. Traffic Data tab.

General Information

This section details the general vehicle load information required in FlexPAVE.

Axle Type

The options are single wheel, single axle, tandem axle, tridem axle, or quadem axle; thus, an input vehicle can be designed according to the truck's configuration.

Wheel Type

Single and dual tire modes can be simulated.

Distance

Distance is defined as the length between consecutive axles. For instance, the distance of the first axle is always zero. In the case of the second axle (D_2 in figure 176), the distance is the length from the first axle to the second axle.

Axle Load

Axle load is the amount of load applied to the axle. For example, 80 kN (18,000 lb) can be entered as the ESAL.

Design Velocity (m/s)

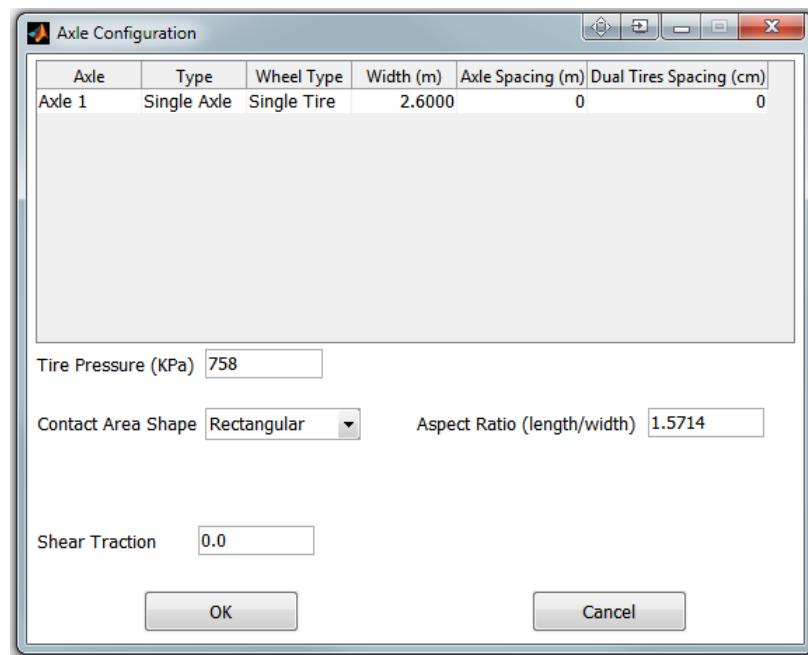
The design velocity is the velocity of the simulated vehicle or design speed at the project site.

Specific Information

The More button (at bottom right of Design Vehicle Information tab shown in figure 176) allows more specific information about traffic and analysis to be input (figure 178).

By clicking the More button (at bottom right of Design Vehicle Information tab shown in figure 176), the width of the axle, the Axle Spacing (for Tandem, Tridem, and Quadem only) and Dual Tires Spacing, can be specified as shown in figure 178.

Tire Pressure can be changed as well. The Contact Area Shape has two options: Rectangular and Circular. In the case of Rectangular, the Aspect Ratio can be defined as the ratio of the length and width of the rectangle. Length is measured along the traffic direction whereas width is perpendicular to the length. The default value is 11/7 (1.5714). The program automatically calculates the contact using the axle load and tire pressure. Shear Traction between the tire and pavement surface can be simulated by entering the value.

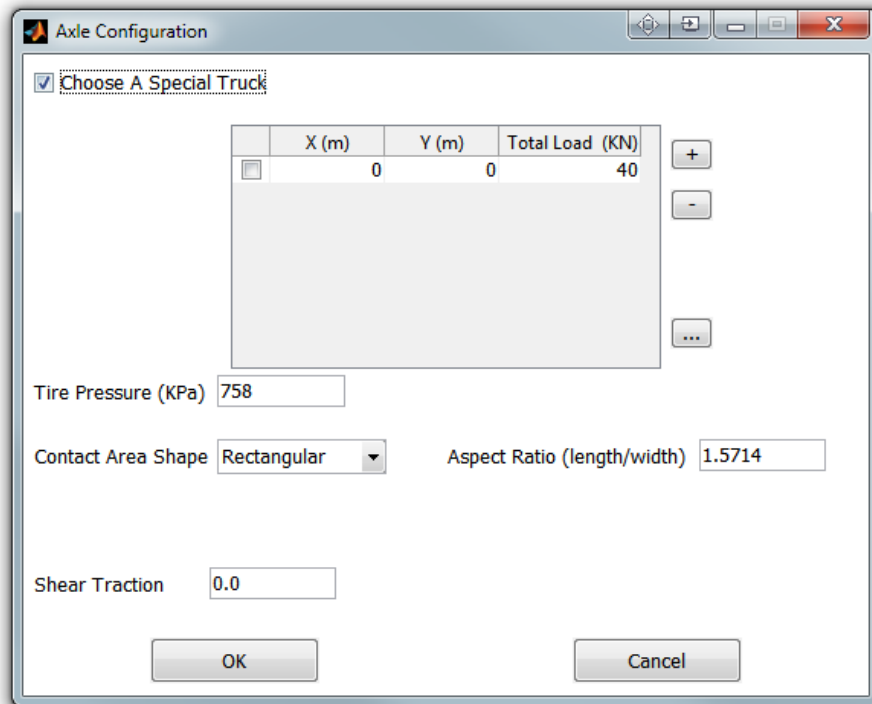


Source: FHWA.

Figure 178. Screenshot. Axle Configuration dialogue box.

Special Truck

By clicking the Special Truck button in the Design Vehicle Information tab (figure 176), a truck with any configuration can be defined in a coordinate system for tires, where the tires and axles are individually considered (figure 179). The origin of the system is located at the center of the last rear axle with the x-axis bound to it. The y-axis is in the direction of the traffic, resulting in an $x-o-y$ plane on the surface of the pavement. The load to be specified at each node is the tire load.



Source: FHWA.

Figure 179. Screenshot. Special truck configuration.

Traffic Information

To predict performance, the traffic information during the design period must be specified. Currently, the program can accept ESAL information; the Traffic Spectrum, as an input, is under development. First, the actual traffic should be converted into an equivalent traffic volume for a design truck, as defined in the previous section, and then the information in the Traffic Data tab must be specified (figure 177). Traffic information can be viewed and changed whenever FlexPAVE Pavement Performance Analysis is activated.

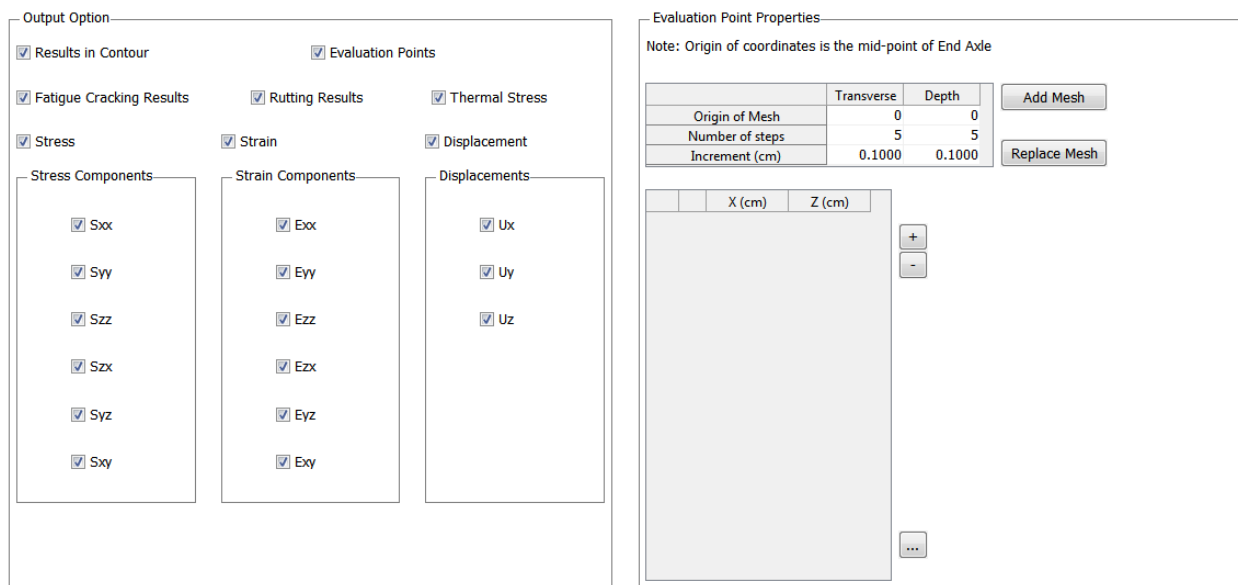
The options in the Traffic Data tab are as follows:

- **AADTT.** The AADTT is the number of passes of the design vehicle specified in General Information. If the design vehicle has an ESAL, the AADTT becomes the ESAL value per day.
- **Growth Type.** Three options are available under Growth Type: no growth, linear, and power.
- **Growth Rate (%).** This option defines the anticipated growth rate of the traffic at the project site.
- **Lane Distribution Factor.** The Lane Distribution Factor accounts for the distribution of the traffic load when two or more lanes are available in one direction.

- **Monthly Adjustment Factor (MAF).** The MAF value represents the distribution of traffic in months. As a result, the MAF represents the seasonal variation of the traffic. The sum of the MAF values must be 12.
- **Hourly Truck Distribution (%).** The Hourly Truck Distribution represents hourly changes in traffic. The sum must be 100 percent.

Output and Analysis Options

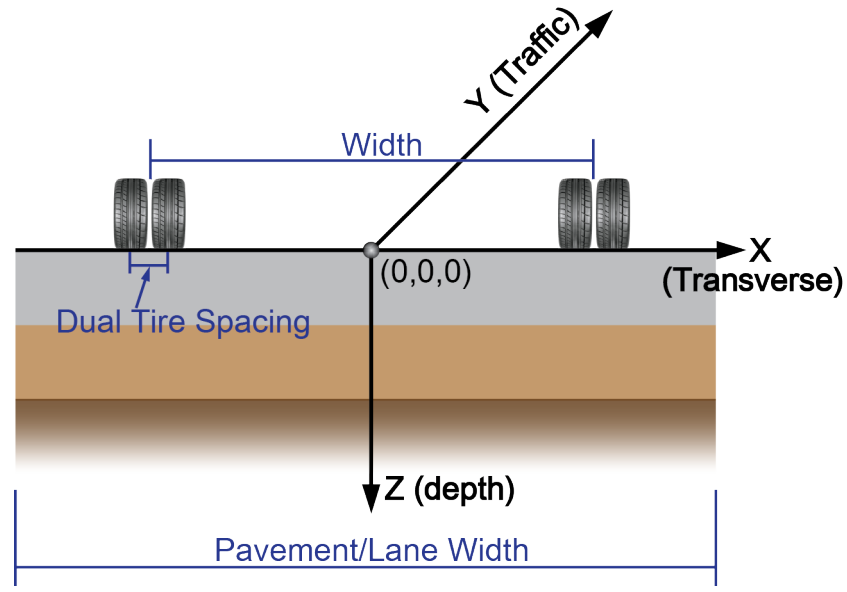
This section illustrates the FlexPAVE’s output. The type of desired outputs can be controlled by clicking Output and Analysis Options in the navigational panel (figure 160). Figure 180 shows the Output and Analysis Options window. The coordinates of the evaluation points can also be specified here, as presented in detail in figure 181 that shows the coordinate system.



Source: FHWA.

Figure 180. Screenshot. Output and analysis options.

The evaluation points are specified in a vertical coordinate system (xz) established in the cross-section of the pavement. The origin and x-axis are the same as those used in the coordinate system to define each tire’s location, and the z-axis vertically moves downward into the pavement.



Source: FHWA.

Figure 181. Illustration. Coordinate system.

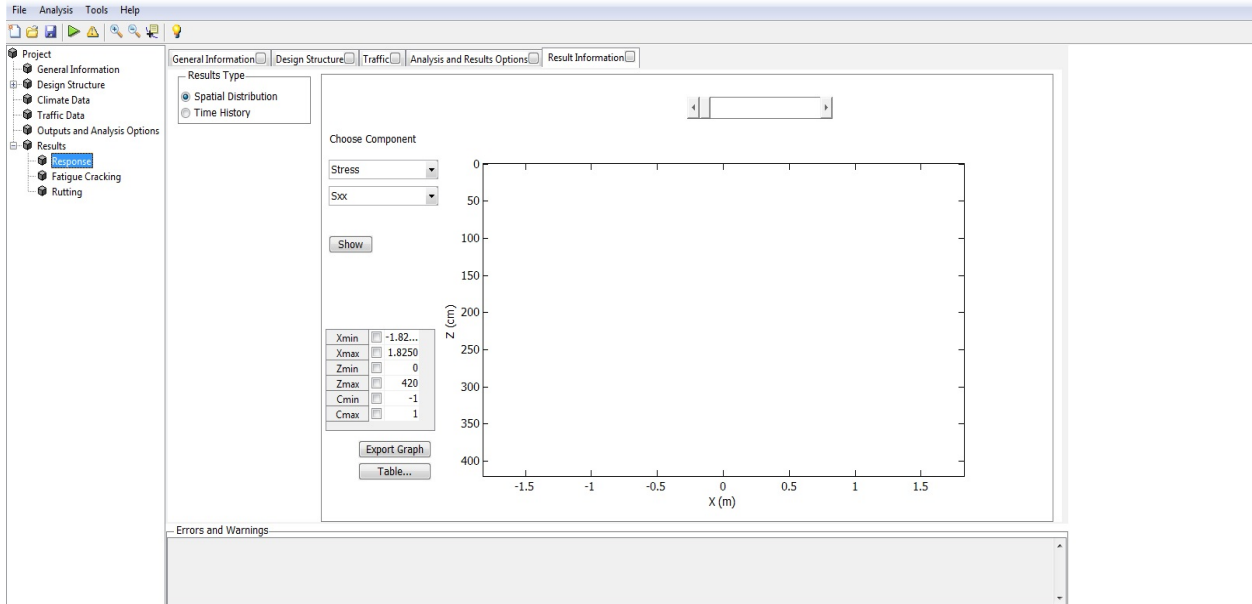
The evaluation points can be manually input and generated as a mesh using tools provided in the GUI or imported from a text file. The text file should be provided in the format specified in table 42.

Table 42. Format of the text file to input coordinates of evaluation points.

X (cm)	Z (cm)
0	0
10	4
20	12
30	20

OUTPUTS

Figure 182 presents a screenshot of the Output tab. The outputs of the pavement analysis are classified into two groups: time history and spatial distribution (i.e., contours). Time history plots show the history (i.e., temporal variation) of a selected response at a given evaluation point. Spatial distribution presents the contours (i.e., spatial variation) of a selected response within the pavement cross-section at any time. When Pavement Response Analysis is chosen, the program automatically loads the results and the user can plot the pavement responses immediately. If Pavement Performance Analysis is carried out, users must first load the desired output by choosing the proper time from the menu shown in figure 183.



Source: FHWA.
 1 cm = 0.4 inch; 1 m = 3.28 ft.

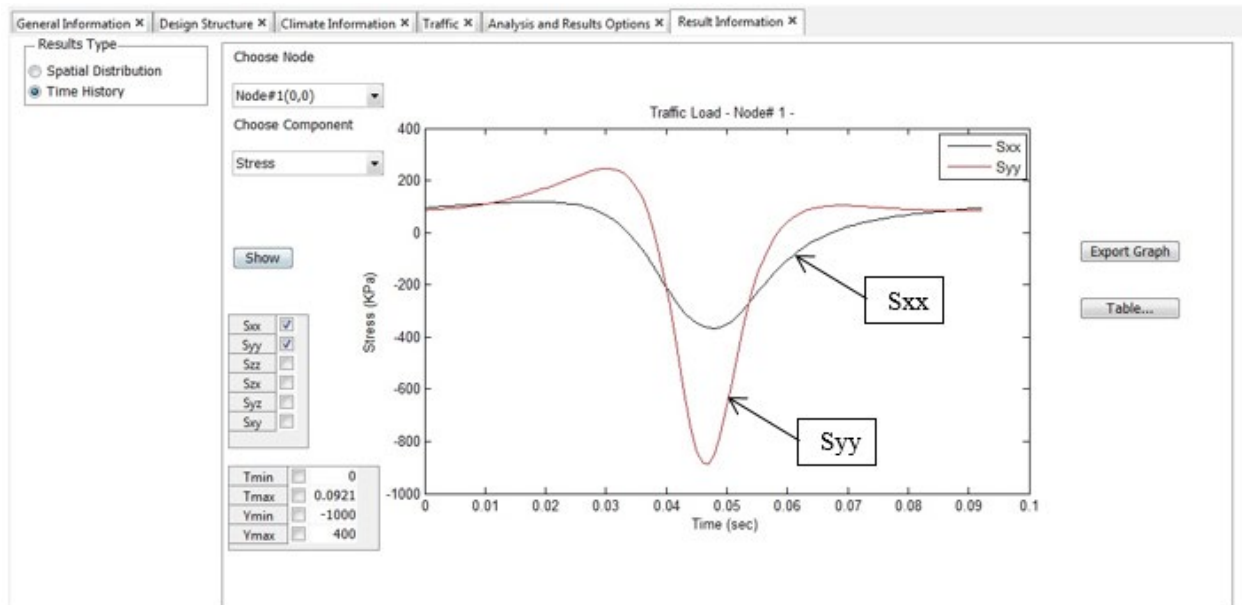
Figure 182. Screenshot. Output tab.

Source: FHWA.

Figure 183. Screenshot. Loading the output for pavement performance analysis.

Time History Plots

Figure 184 shows an example of the stress time history–plot output. First, the evaluation points (already defined in the previous step) must be chosen from the drop-down menu at the top of the Result Information tab. Then, the graph is plotted by clicking the Show button. To view the responses (i.e., displacements, strains, and stresses), the desired component from the table next to the plotting area must be selected. To change the axis limits, the table provided beside the plotting area can be used. The box that corresponds to the limit to be changed and modified must first be checked. The data have to be loaded into the program by clicking Load before the results will be available. The plot will update once Show is clicked.

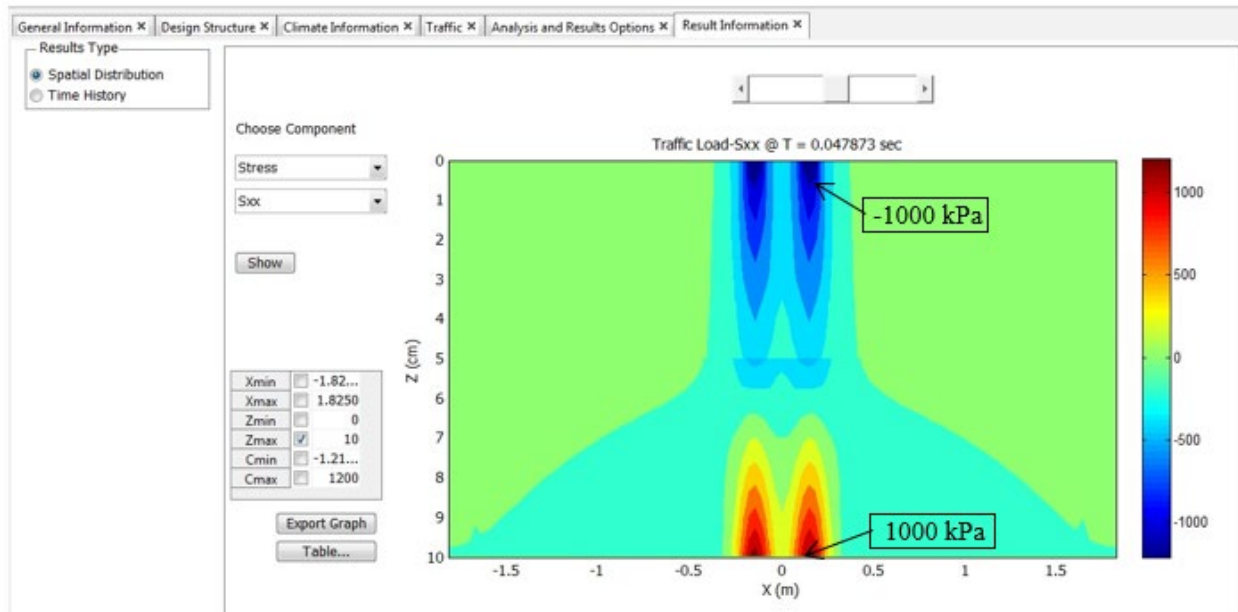


Source: FHWA.
1 kPa = 0.145 psi.

Figure 184. Screenshot. Example of stress time history plot.

Spatial Distribution Contours

Figure 185 shows an example of a contour output. The proper component can be chosen and the results can be viewed by clicking the Show button. Changing the scroll bar located above the plotting area enables the contour plot to be changed to a different time—the contour can be updated by scrolling. Similar to plotting the results, here the axis limits can be modified using the table beside the plotting area. In addition to axis limits, the color bar limits can be changed by editing Cmin and Cmax.



Source: FHWA.

1 cm = 0.4 inch; 1 kPa = 0.145 psi; 1 m = 3.28 ft.

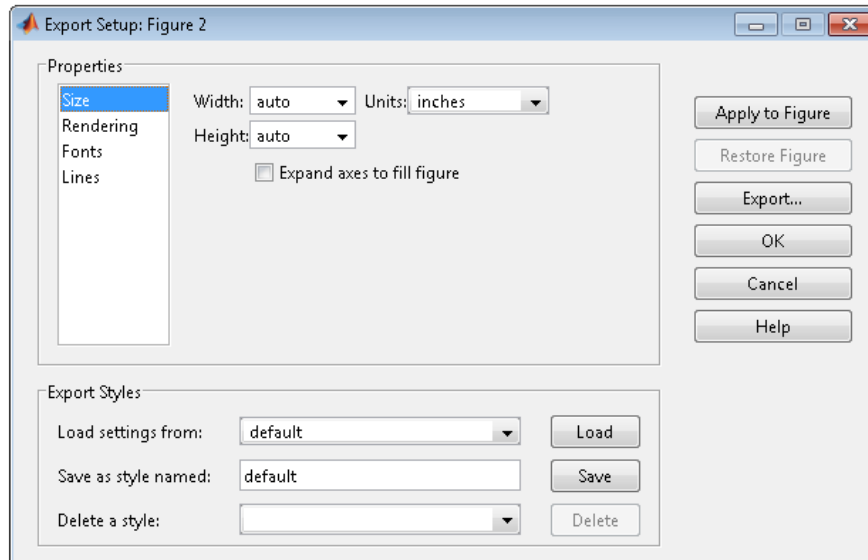
Figure 185. Screenshot. Example of spatial distribution contour plot.

Saving Results

The outputs can be exported in the form of either a graph or a table.

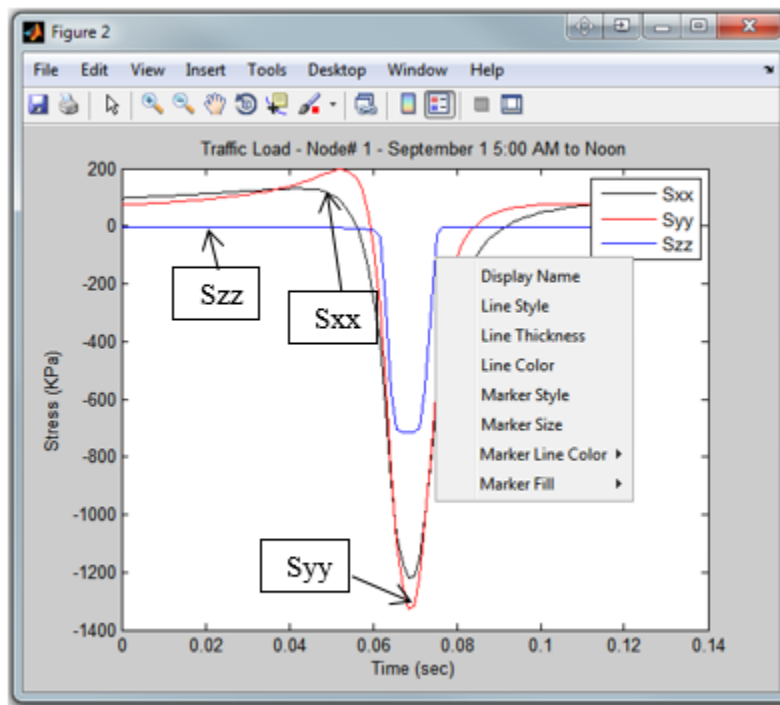
Export Graph

Clicking Export Graph (figure 185) will reopen the plots or contours in a new window. From the reopened window, the graph—including MATLAB figures—can be saved in different formats: JPEG, PDF, TIFF, and so on. The Export Wizard (figure 186) provided in the program helps the user enhance the quality of the image based on desired specifications. The Export Wizard can be accessed by clicking File > Export Setup. The color, style, and thickness of the lines in the plots can be changed by right-clicking them, as shown in figure 187.



Source: FHWA.

Figure 186. Screenshot. Export wizard.

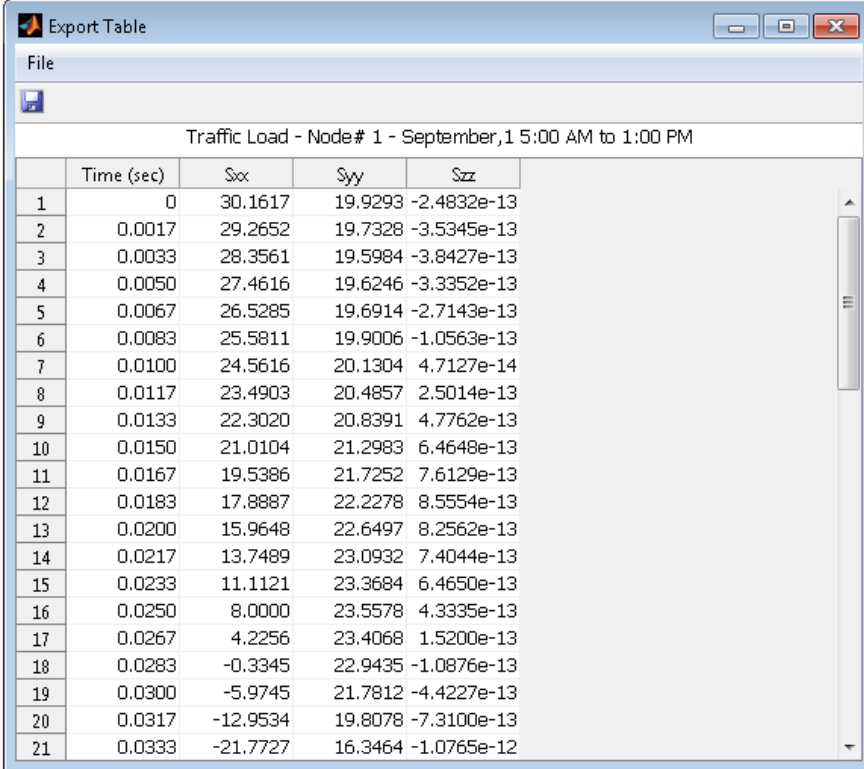


Source: FHWA.
1 kPa = 0.145 psi

Figure 187. Screenshot. Editing plot lines.

Export Table

The results can be saved as a table by clicking the Table button next to the plotting area (figure 184). The results will be presented in a new window, as shown in figure 188. The table can be saved as either a text file or an Excel file (if already installed).



	Time (sec)	Sxx	Syy	Szz
1	0	30.1617	19.9293	-2.4832e-13
2	0.0017	29.2652	19.7328	-3.5345e-13
3	0.0033	28.3561	19.5984	-3.8427e-13
4	0.0050	27.4616	19.6246	-3.3352e-13
5	0.0067	26.5285	19.6914	-2.7143e-13
6	0.0083	25.5811	19.9006	-1.0563e-13
7	0.0100	24.5616	20.1304	4.7127e-14
8	0.0117	23.4903	20.4857	2.5014e-13
9	0.0133	22.3020	20.8391	4.7762e-13
10	0.0150	21.0104	21.2983	6.4648e-13
11	0.0167	19.5386	21.7252	7.6129e-13
12	0.0183	17.8887	22.2278	8.5554e-13
13	0.0200	15.9648	22.6497	8.2562e-13
14	0.0217	13.7489	23.0932	7.4044e-13
15	0.0233	11.1121	23.3684	6.4650e-13
16	0.0250	8.0000	23.5578	4.3335e-13
17	0.0267	4.2256	23.4068	1.5200e-13
18	0.0283	-0.3345	22.9435	-1.0876e-13
19	0.0300	-5.9745	21.7812	-4.4227e-13
20	0.0317	-12.9534	19.8078	-7.3100e-13
21	0.0333	-21.7727	16.3464	-1.0765e-12

Source: FHWA.

Figure 188. Screenshot. Export results as a table.

EXAMPLES

This section presents some examples conducting pavement structural analysis using FlexPAVE.

Response Analysis

A four-layer system is used as an example of the response analysis: 1.92 inch (5 cm) for the first asphalt concrete layer, 1.92 inch (5 cm) for the second asphalt layer, and 11.81 inch (30 cm) and 149.6 inch (380 cm) for the subgrade layers. Table 43 and 1 kPa = 0.145 psi.

Table 44 lists the Prony coefficients and shift factor parameters, respectively. The base and subgrade layers are linearly elastic with modulus values of 250 MPa and 95 MPa, respectively, and Poisson's ratios of 0.35 and 0.4, respectively. The system is subjected to a rectangular load with a total load of 40 kN and tire pressure of 110 psi (758 kPa) on the surface, moving with a constant velocity of 60 mph (27 m/s). The example file for Response Analysis is provided in the installation folder under the name of "Response.lve." Step-by-step procedures are explained in the following sections.

Table 43. Prony coefficients for first asphalt concrete layer (left) and second asphalt concrete layer (right).

Ti	Ei (kPa) Layer (Left)	Ei (kPa) Layer (Right)
2E+8	8.64e3	8.83e3
2E+07	1.71e4	5.7e3
2E+06	3.48e4	1.52e4
2E+05	7.39e4	3.43e4
2E+04	1.67e5	8.91e4
2E+03	3.99e5	2.56e5
2E+02	9.63e5	7.42e5
2E+01	2.04e6	1.85e6
2E+00	3.24e6	3.41e6
2E-01	3.48e6	4.42e6
2E-02	3.42e6	4.21e6
2E-03	2.49e6	3.23e6
2E-04	1.66e6	2.16e6
2E-05	1.01e6	1.34e6
2E-06	5.92e5	7.90e5
2E-07	3.38e5	4.54e5
2E-08	1.91e5	2.65e5
Einf	2.78e4	2.78e4

1 kPa = 0.145 psi.

Table 44. Shift factor parameters for first (top) and second (bottom) asphalt concrete layer.

Shift Factor Parameter	a1	a2	a3	TR (°C)
Top layer	6.436e-04	-0.158	0.775	5
Bottom layer	1.2e-04	-0.1937	3.211	21.1

0°C = 32°F.

General Information

New Pavement and Pavement Response Analysis must be selected for the response analysis under the General Information tab (figure 189). The Fatigue and Rutting options and Pavement Construction Timeline are deactivated for this analysis. More information about a project can be entered in the Optional Description box. The project can be saved by clicking the Save icon or File > Save or Ctrl+S. The project should be saved on a routine basis to avoid possibly losing input data.

The screenshot shows a software interface for pavement analysis. On the left is a navigation tree with the following items: Project, General Information (selected), Design Structure, Climate Data, Traffic Data, Outputs and Analysis Options, Results, Response, Fatigue Cracking, and Rutting. The main window is titled 'General Information' and contains several sections:

- Pavement Type:** Radio buttons for 'New Pavement' (selected) and 'AC-on-AC overlay Rehabilitation'.
- Pavement Location:** Input fields for Latitude (0.0) and Longitude (0.0).
- Traffic:** Radio buttons for 'Design Vehicle' (selected) and 'Traffic Spectrum'.
- Analysis Options:** Radio buttons for 'Pavement Response Analysis' (selected) and 'Pavement Performance Analysis'. Below are checkboxes for 'Fatigue Cracking' (checked), 'Thermal Stress' (checked), 'Healing' (unchecked), and 'Aging' (unchecked). To the right, under 'Rutting Options', 'Rutting' is checked.
- Pavement Construction Timeline:** Drop-down menus for 'Pavement Construction Date' (September, 2001), 'Traffic Opening Date' (September, 2001), and a text input for 'Pavement Design Life (years)' (20).
- Optional Description:** A table with the following data:

Project Name	Example of Response Analysis
Author	NCSU Asphalt Group
City/State	Raleigh, NC
Date	Mar,4,2017
Note	Provide for Example

At the bottom of the main form are 'Units' and 'Advanced' buttons. Below the main form is an 'Errors and Warnings' section.

Source: FHWA.

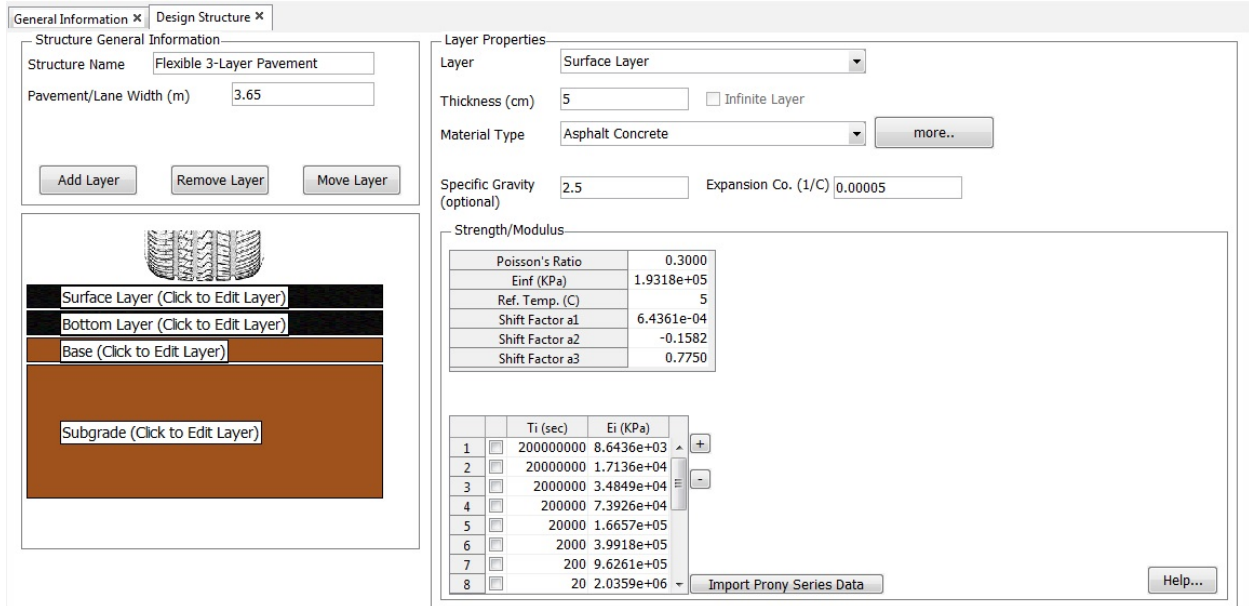
Figure 189. Screenshot. General Information tab for pavement response analysis.

Design Structure

All the material and structural properties must be entered under the Design Structure tab (Figure 190). Under Structure General Information, a name for the pavement structure and the pavement width can be input. For this example, Flexible 3-Layer Pavement is entered for the Structure Name, and 3.65 m is entered as the Pavement/Lane Width (m) in figure 190.

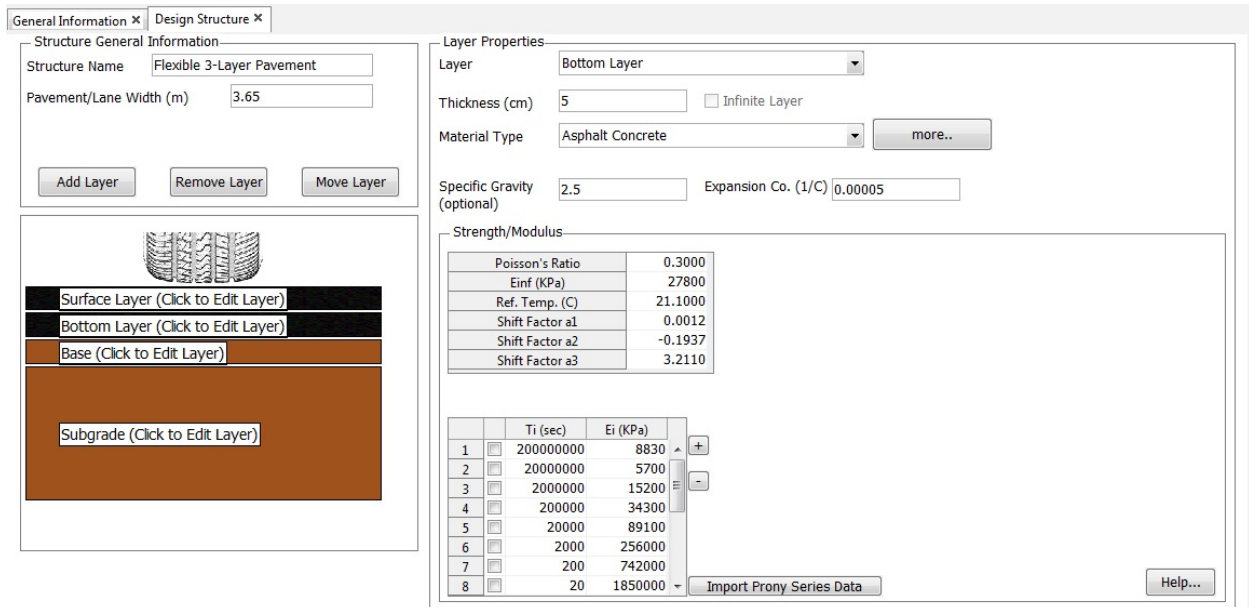
Asphalt Layer

AC must be chosen either in the navigational panel or from the drop-down menu in the data panel, and then Asphalt Concrete must be the selected Material Type under Layer Properties (figure 190 and figure 191). All asphalt layer that are described in the example must be entered. When Asphalt Concrete is the selected material in the Material Type menu, the default values—including the performance parameters (fatigue and rutting parameters)—show automatically. The parameters for performance analysis are not required for response analysis; accordingly, the parameters for performance analysis do not need to change.



Source: FHWA.

Figure 190. Screenshot. Material properties of first asphalt layer.



Source: FHWA.

Figure 191. Screenshot. Material properties of second asphalt layer.

Base Layer

Base must be chosen either in the navigational panel or from the drop-down menu in the data panel, and then Aggregate Base must be selected from among Asphalt-Treated Base, Cement-Treated Base, and Aggregate Base (figure 192). The modulus value and Poisson's ratio must be entered.

The screenshot displays a software interface for defining pavement layer properties. It is divided into several sections:

- General Information:** Structure Name: Flexible 3-Layer Pavement; Pavement/Lane Width (m): 3.65. Buttons: Add Layer, Remove Layer, Move Layer.
- Layer Properties:** Layer: Base; Thickness (cm): 20; Material Type: Aggregate Base. Specific Gravity (optional): 2.5; Expansion Co. (1/C): 1.0e-5.
- Strength/Modulus:** Elastic Modulus (KPa): 250000; Poisson's Ratio: 0.3500.
- Structure General Information:** A diagram showing four layers: Surface Layer, Bottom Layer, Base, and Subgrade.

Source: FHWA.

Figure 192. Screenshot. Material properties of aggregate base layer.

Subgrade

Subgrade must be chosen either in the navigational panel or from the drop-down menu in the data panel, and then Subgrade must be selected (figure 193). The modulus value and Poisson's ratio must be selected.

General Information x Design Structure x

Structure General Information

Structure Name Flexible 3-Layer Pavement

Pavement/Lane Width (m) 3.65

Add Layer Remove Layer Move Layer

Layer Properties

Layer Subgrade

Thickness (cm) 380 Infinite Layer

Material Type Subgrade more..

Specific Gravity (optional) 2.5 Expansion Co. (1/C) 1.0e-5

Strength/Modulus

Elastic Modulus (KPa)	95000
Poisson's Ratio	0.4000

Surface Layer (Click to Edit Layer)

Bottom Layer (Click to Edit Layer)

Base (Click to Edit Layer)

Subgrade (Click to Edit Layer)

Source: FHWA.

Figure 193. Screenshot. Material properties of subgrade layer.

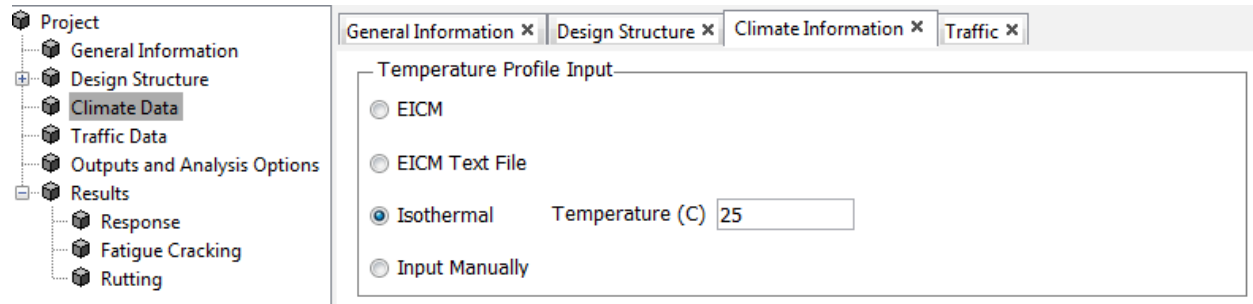
Add, Remove, and Move Layer

Layers can be added or removed, and their the positions can be changed by clicking Add Layer, Remove Layer, or Move Layer, which have the following functions:

- **Add layer.** A new layer name can be entered by clicking on the Add Layer option. The user can choose the layer type (AC, Base, or Subgrade) from the drop-down menu. The layer's location can be specified as to whether it is above or below the reference layer (i.e., the chosen layer type).
- **Remove layer.** Any layer can be selected and deleted using this option. To delete a certain layer, the layer must be selected and then the Delete button must be clicked.
- **Move layer.** Any layer from the list can be selected by scrolling up or down in this dialog box.

Climate Data

To simulate constant temperature conditions, the Isothermal option in the Temperature Profile Input box can be selected and then 25°C must be entered in the dialog box (Figure 194).

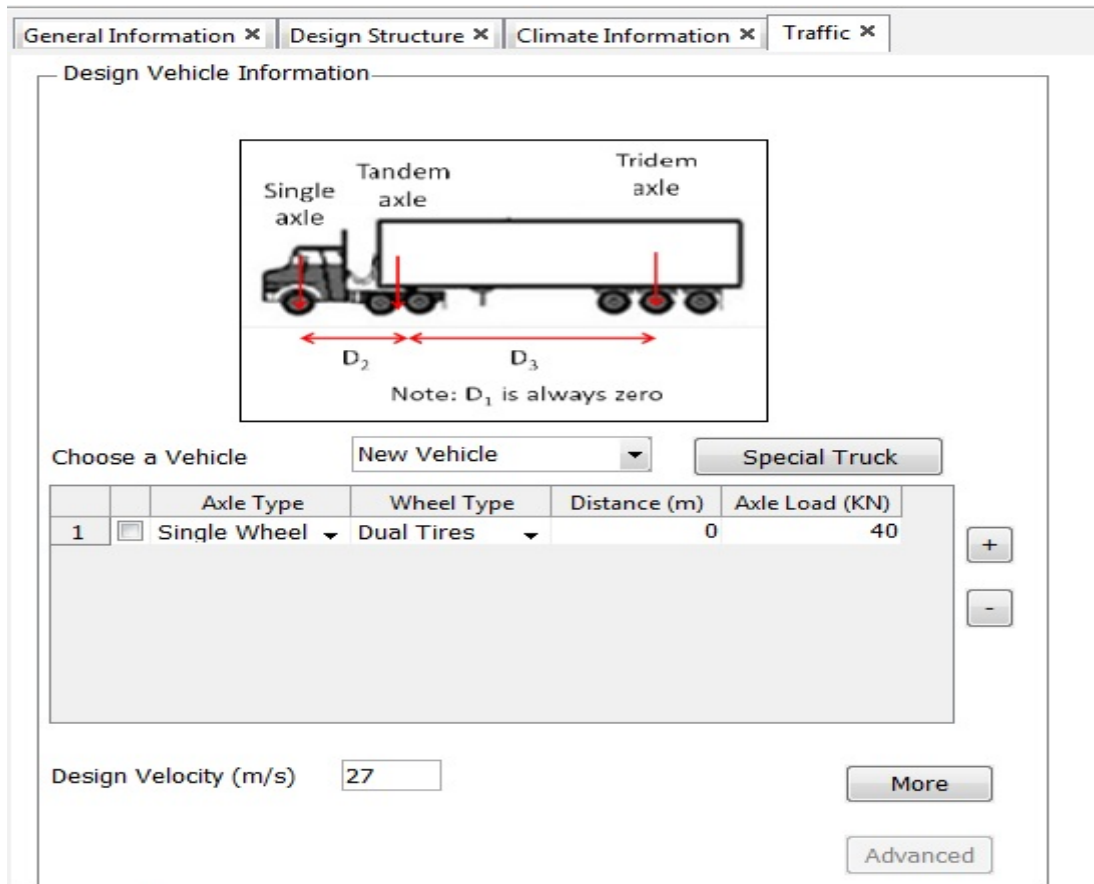


Source: FHWA.

Figure 194. Screenshot. Isothermal input for climate data.

Traffic Data

Selecting Single Wheel with an Axle Load of 40 kN will provide a simple analysis of the project traffic data (figure 195).

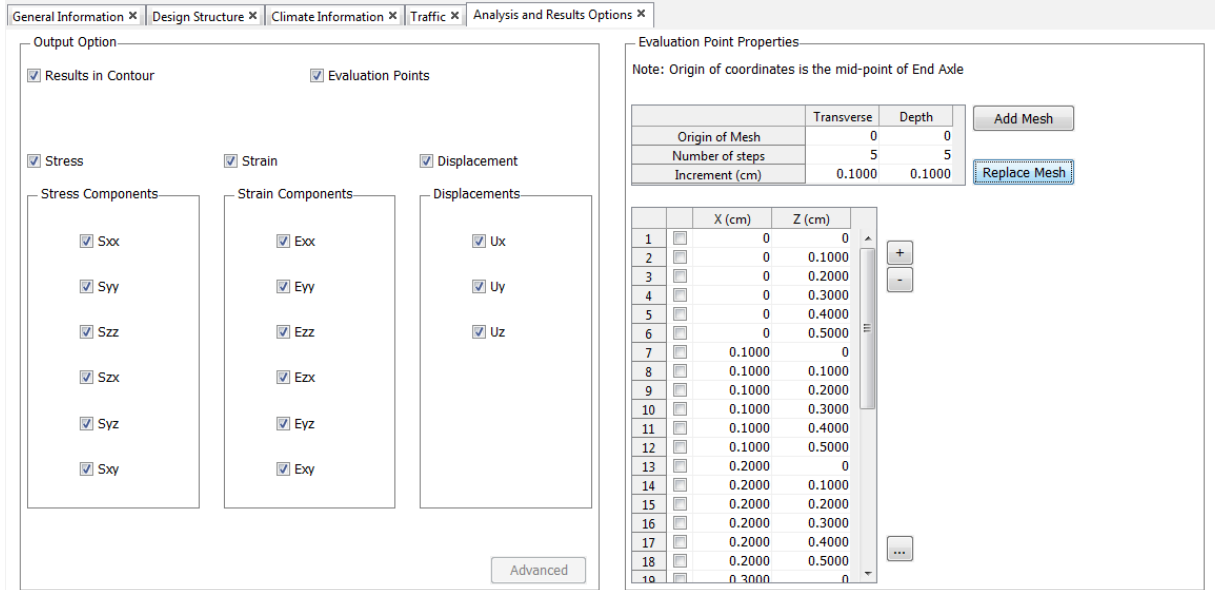


Source: FHWA.

Figure 195. Screenshot. General inputs for traffic load.

Output and Analysis Options

When Single Wheel is the selected option instead of Single Axle, the program applies the moving load to the center of the lane (figure 181). The center of the load is chosen as the evaluation point property along with the asphalt pavement depth, and all the displacement, stress, and strain values can be investigated (figure 196). Therefore, the x coordinate for the center is zero, and z increases from 0 to 10 cm in 2-cm increments.



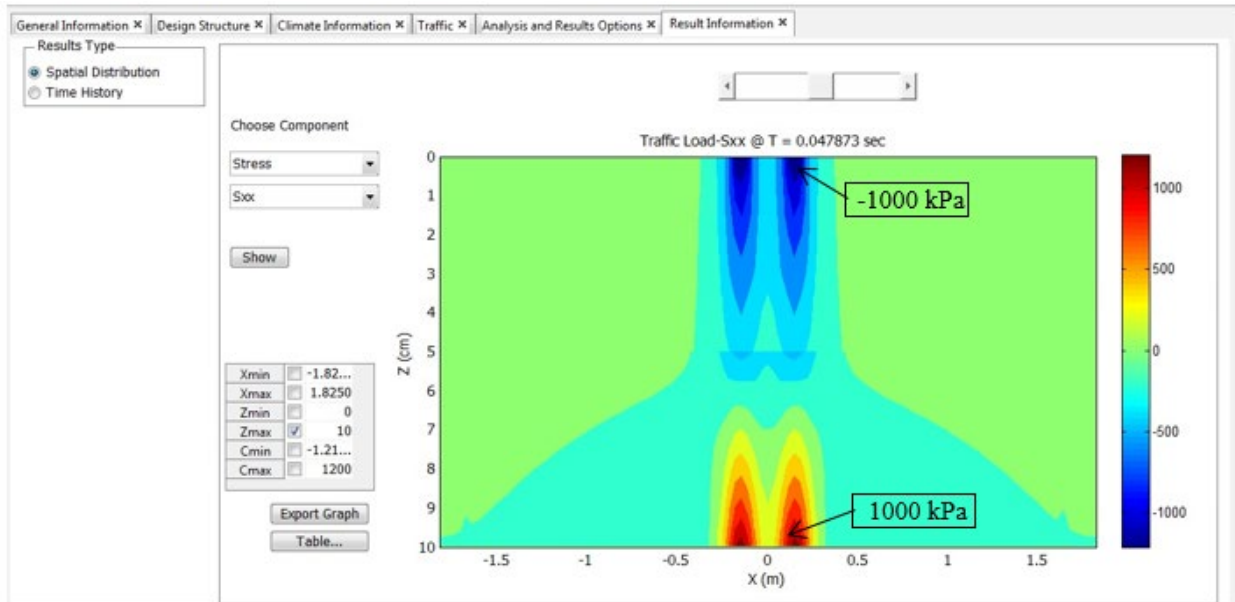
Source: FHWA.

Figure 196. Screenshot. Evaluation points.

Output

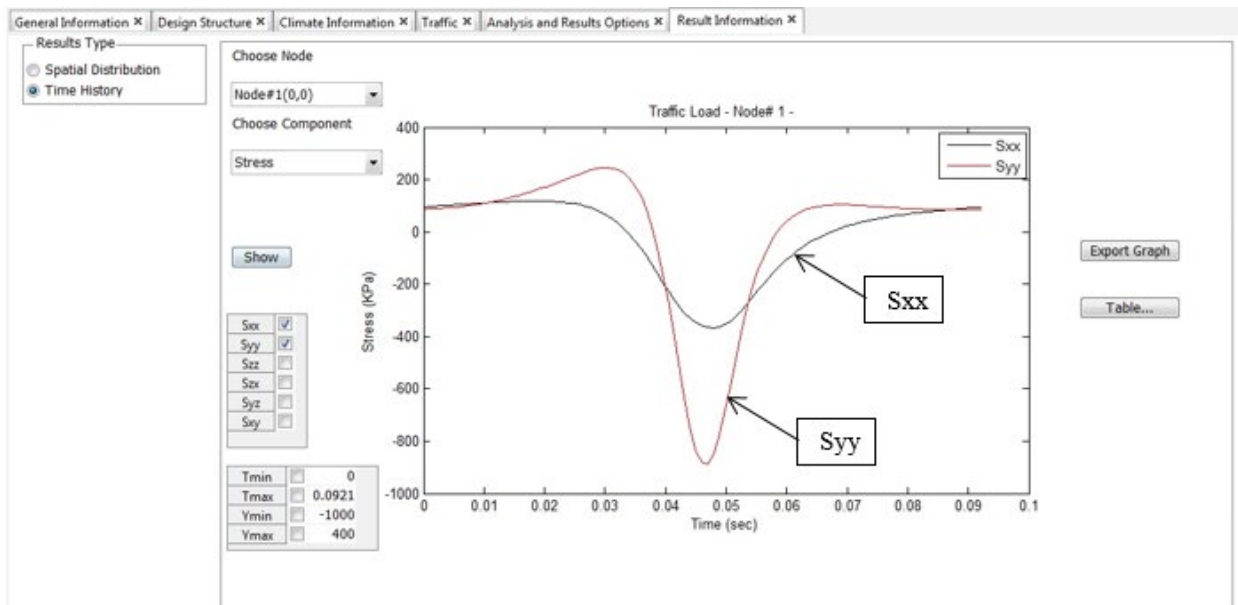
The response output can be viewed via the Results tab after the response analysis has been run.

The transverse normal stress (S_{xx}), is chosen in Spatial Distribution (i.e., the contour plot) (figure 197). The stress distribution can be investigated by scrolling the bar. Figure 197 presents the transverse stress distribution at the peak stress time. The strain, stress, and displacement values at predefined nodes can be plotted by choosing the Time History option (figure 198).



Source: FHWA.
 1 cm = 0.4 inch; 1 kPa = 0.145 psi; 1 m = 3.28 ft.

Figure 197. Screenshot. S_{xx} distribution at peak stress time.



Source: FHWA.
 1 kPa = 0.145 psi.

Figure 198. Screenshot. Stress history plot at center of wheel path.

Performance Analysis

For performance analysis, assume the same pavement structure as in the previous example for response analysis. The pavement is now subjected to a single-axle load with a total load of

9,000 lb (40 kN) (i.e., ESAL analysis). The contact area of the tires is rectangular with tire pressure of 110 psi (827.37 kPa) on the surface, moving with a constant velocity of 60 mph (27 m/s). Table 45 and table 46 presents the fatigue model parameters for the asphalt concrete layer. The temperature profile is for Wyoming. The example file for performance analysis is provided in the installation folder under the name “Performance.lve.”

Table 45. Fatigue performance model parameters for first (top) and second (bottom) asphalt concrete layer.

Coefficients	Top Layer	Bottom Layer
a	6.73E-04	1.21E-04
b	0.757	0.712
α	4.15	3.38
E_R	1	1
C_0	0.8	0.8
D^R	0.712	0.44

Table 46. Rutting performance model parameters for first (top) and second (bottom) asphalt concrete layer.

Coefficients	Top Layer	Bottom Layer
ϵ_0	0.00384	0.00263
N_1	0.0588	3.196
β	0.555	0.748
T_{ref}	61	53.7
p_1	0.748	0.734
p_2	0.2382	0.292
d_1	3.574	2.213
d_2	-2.913	-0.08

General Information

Pavement Performance Analysis must be selected under Analysis Options and all performance distress types (i.e., fatigue cracking, rutting, and thermal stress) must be chosen (figure 199). The program assumes the pavement was constructed in September and opened to traffic within the same month. The pavement design life is 20 yr. Other input parameters are the same as the previous response analysis example.

General Information x

Pavement Type

New Pavement

AC-on-AC overlay Rehabilitation

Pavement Location

Latitude: 0.0

Longitude: 0.0

Traffic

Design Vehicle

Traffic Spectrum

Optional Description

Project Name	Example of performance analysis
Author	NCSU Rersearch Group
City/State	Raleigh, NC
Date	March, 10, 2017
Note	Provided for Example

Units Advanced

Analysis Options

Pavement Response Analysis

Pavement Performance Analysis

Fatigue Options

Fatigue Cracking

Thermal Stress

Healing

Aging

Rutting Options

Rutting

Pavement Construction Timeline

Pavement Construction Date: January 2014

Traffic Opening Date: January 2014

Pavement Design Life (years): 20

Source: FHWA.

Figure 199. Screenshot. General information for performance analysis.

Design Structure

All information for the pavement performance analysis is the same as for the response analysis example, but the parameters for performance prediction must be applied; the parameters shown in previous chapters (FlexPAVE Program Engines section) are entered for the asphalt layer (figure 200 and figure 201).

General Information x Design Structure x

Structure General Information

Structure Name: Flexible 3-Layer Pavement

Pavement/Lane Width (m): 3.65

Add Layer Remove Layer Move Layer

Layer Properties

Layer: Surface Layer

Thickness (cm): 5 Infinite Layer

Material Type: Asphalt Concrete more..

GR Based Criterion DR Based Criterion

Specific Gravity (optional): 2.5 Expansion Co. (1/C): 0.00005

Strength/Modulus

Poisson's Ratio	0.3000	Alpha	3.7800	Beta	0.8026	p1	0.6069
Einf (KPa)	1.9318e+05	C11	0.0042	Epsilon0	0.0052	p2	0.0719
Ref. Temp. (C)	5	C12	0.3920	NI	0.8024	d1	0.0396
Shift Factor a1	6.4361e-04	Initial C	0.8000	TR(C)	61	d2	1.6831
Shift Factor a2	-0.1582	DR	0.6400				
Shift Factor a3	0.7750						

Import Damage Data Import Rutting Data

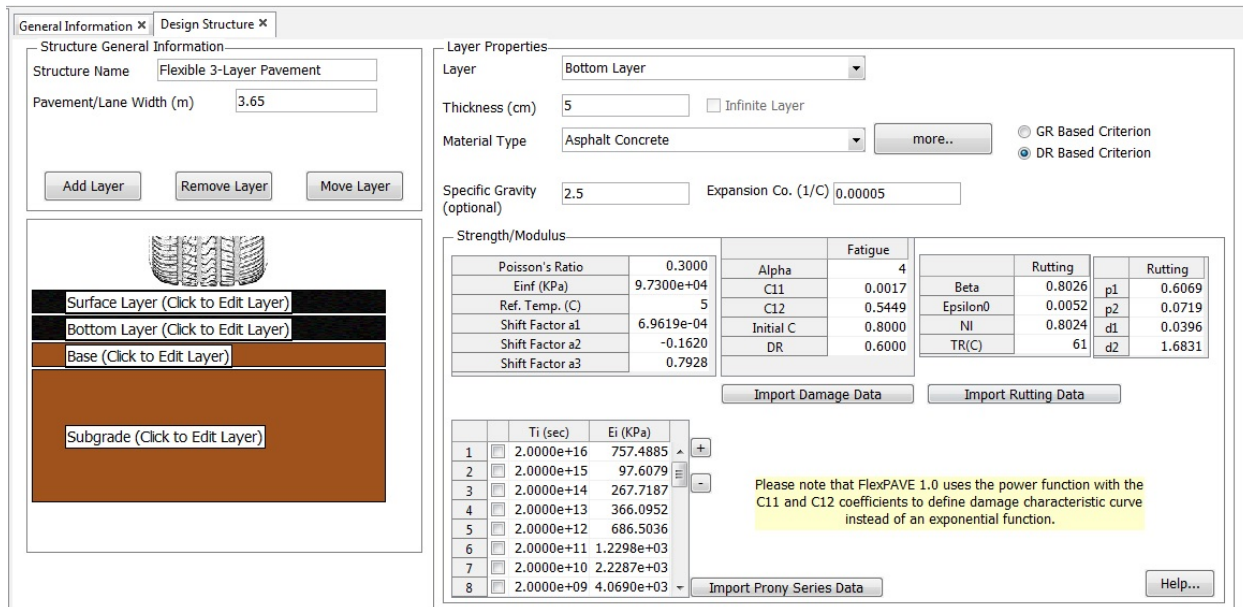
	Ti (sec)	Ei (KPa)	
1	200000000	8.6436e+03	+
2	20000000	1.7136e+04	
3	2000000	3.4849e+04	-
4	200000	7.3926e+04	
5	20000	1.6657e+05	
6	2000	3.9918e+05	
7	200	9.6261e+05	
8	20	2.0359e+06	

Import Prony Series Data Help...

Please note that FlexPAVE 1.0 uses the power function with the C11 and C12 coefficients to define damage characteristic curve instead of an exponential function.

Source: FHWA.

Figure 200. Screenshot. Material properties of first asphalt concrete layer for performance analysis.

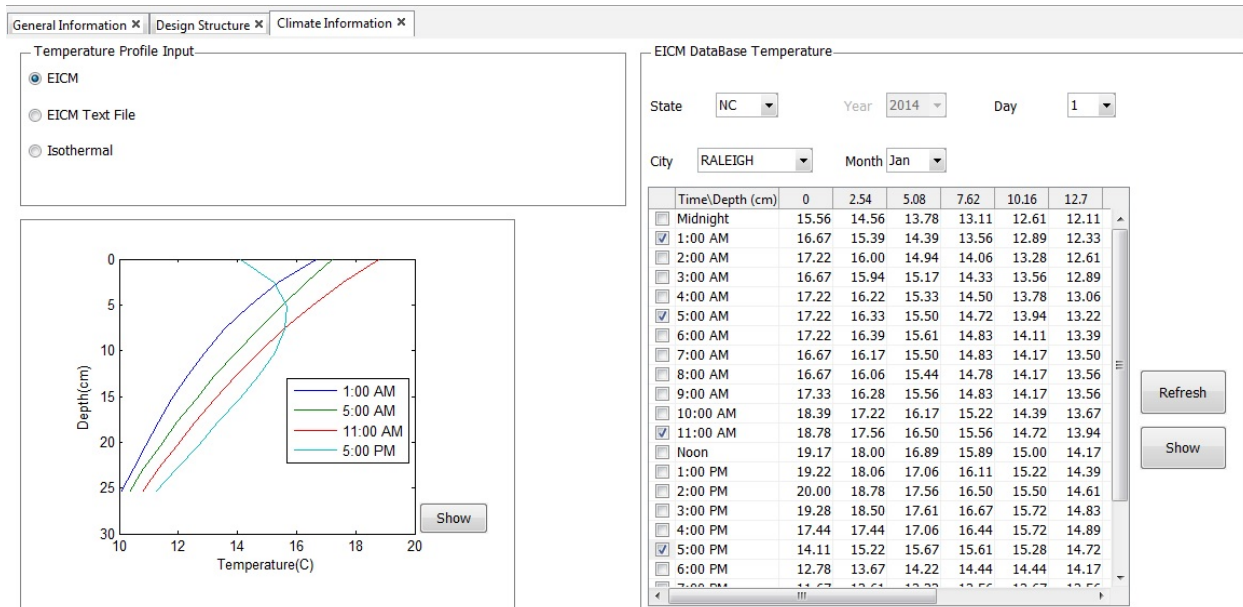


Source: FHWA.

Figure 201. Screenshot. Material properties of second asphalt concrete layer for performance analysis.

Climate Data

At least 1 yr of asphalt pavement temperature data is required for the performance analysis of a simulation of 1 yr or longer. The program converts climate data to pavement temperatures using EICM data (figure 202).



Source: FHWA.

0°C = 32°F; 1 cm = 0.4 inch.

Figure 202. Screenshot. EICM input.

Traffic Data

Instead of single-wheel analysis, FlexPAVE uses single-axle analysis (ESAL analysis) (figure 203). Therefore, Single Wheel and Dual Tires are chosen. The Axle Load is 40 kN (9,000 lb). The AADTT is 700 with a linear growth rate. Figure 203 shows monthly and hourly traffic distributions. Figure 204 presents wheel properties.

Design Vehicle Information

Diagram labels: Single axle, Tandem axle, Tridem axle. Distances: D_2 , D_3 . Note: D_1 is always zero.

Choose a Vehicle:

	Axle Type	Wheel Type	Distance (m)	Axle Load (KN)
1	Single Wheel	Dual Tires	0	40

Design Velocity (m/s):

Traffic Information

Daily ESAL: Growth Type: Growth Rate (%):

Lane Distribution Factor:

Monthly Adjustment Factor

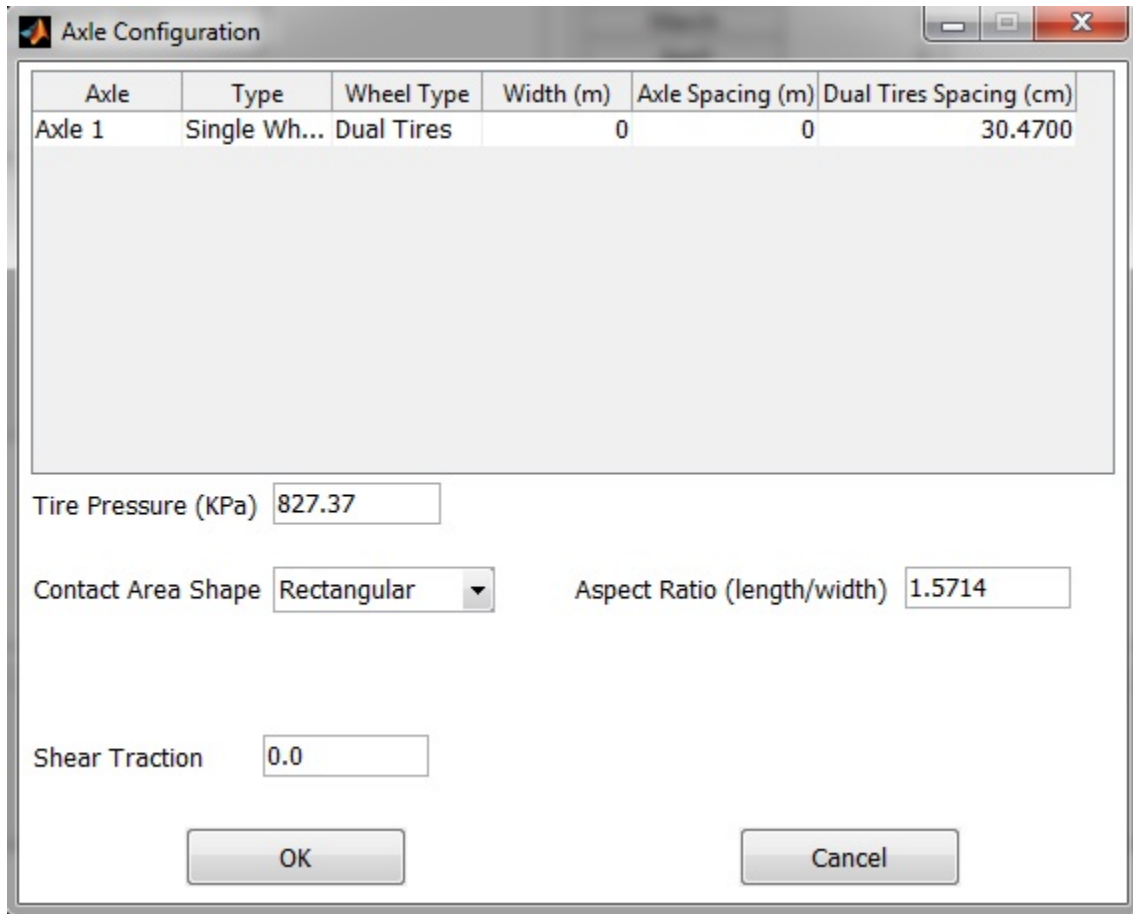
	MAF
January	1
February	1
March	1
April	1
May	1
June	1
July	1
August	1
September	1
October	1
November	1
December	1

Hourly Truck Distribution (%)

	HTD
Midnight	4.1667
1:00 AM	4.1667
2:00 AM	4.1667
3:00 AM	4.1667
4:00 AM	4.1667
5:00 AM	4.1667
6:00 AM	4.1667
7:00 AM	4.1667
8:00 AM	4.1667
9:00 AM	4.1667
10:00 AM	4.1667
11:00 AM	4.1667
Noon	4.1667
1:00 PM	4.1667
2:00 PM	4.1667
3:00 PM	4.1667
4:00 PM	4.1667
5:00 PM	4.1667
6:00 PM	4.1667

Source: FHWA.

Figure 203. Screenshot. Traffic input for performance analysis.

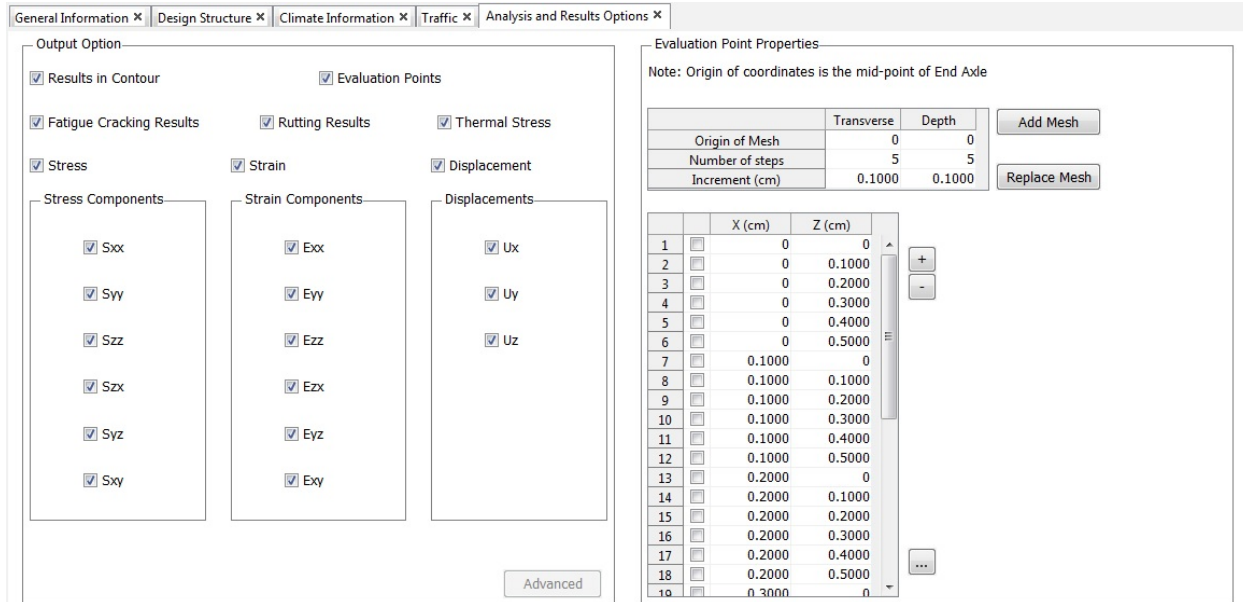


Source: FHWA.

Figure 204. Screenshot. Wheel properties.

Output and Analysis Options

Because the program applies single-wheel dual tire analysis, the x coordinate for the center of the right tire becomes 15.23 cm (30.47 cm/2; thus, 30.47 is dual tire spacing). The left wheel's location is -15.23 cm, and the right wheel's location is +15.23 cm. The evaluation points are generated at both wheels in terms of asphalt pavement depth using the auto-generating Evaluation Points tool (Figure 205).



Source: FHWA.

Figure 205. Screenshot. Output and analysis options.

Outputs

All outputs, response results (stress, strain, and displacement values), fatigue cracking (damage development), and rut depths can be investigated in FlexPAVE.

Response Analysis

By choosing a certain time, stress, strain, and displacement values can be plotted. Spatial contour and history plots can be created at a predetermined node (figure 206). To see the response analyses for different sets of month and time of day, clicking Load will load the results before clicking Show.

Fatigue Cracking

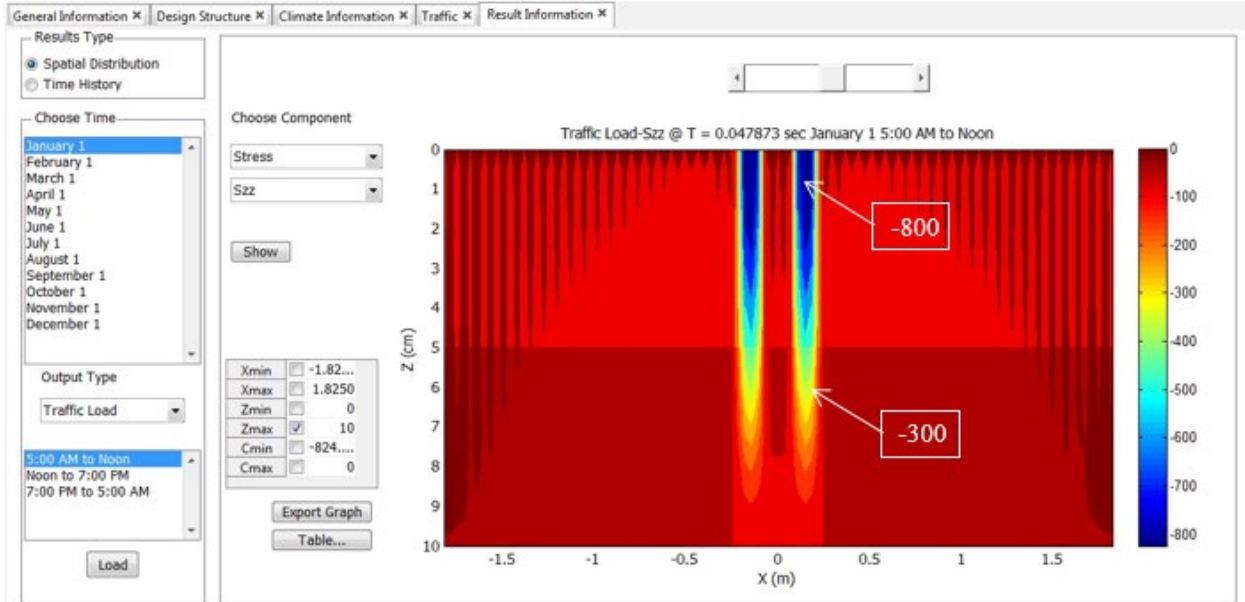
The damage (C , i.e., the modulus after damage) can be plotted as a contour at a given time or history at a predetermined node. Figure 207 presents the damage factor distribution, defined as N/N_f , where N is the current number of cycles and N_f is the number of cycles at failure. When the damage factor becomes 1.0, the asphalt element is considered completely cracked.

Damage Evolution

The damage evolution for the whole pavement life can be plotted. Figure 207 presents the percent damage evolution as a function of time.

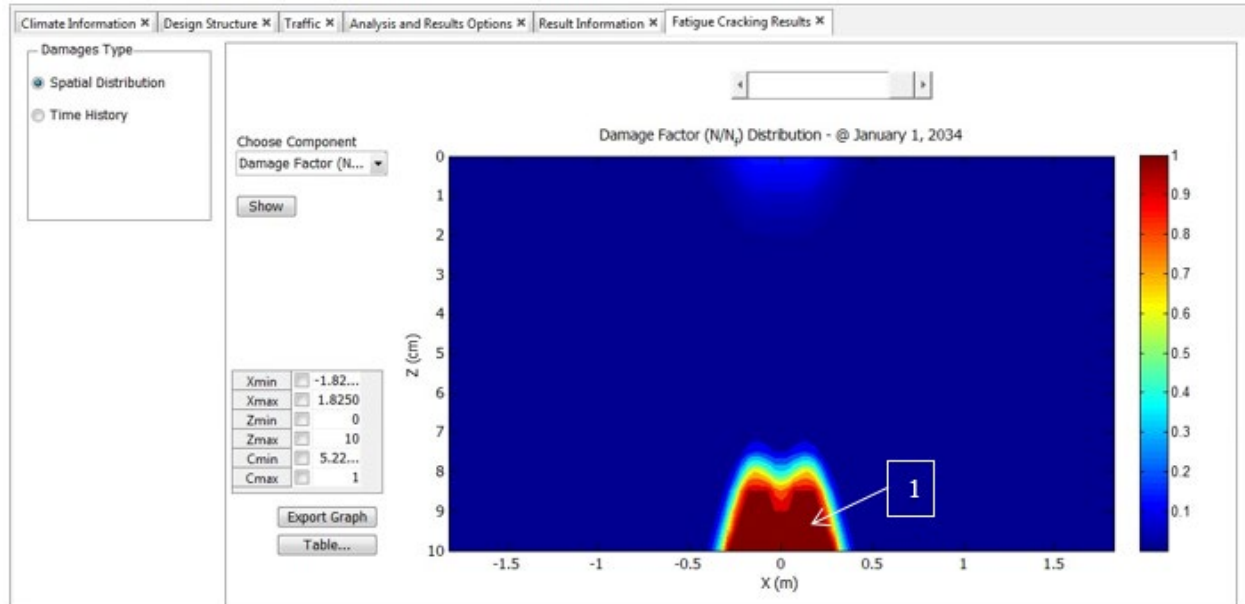
Rutting

Rut depth development over time is provided, as presented in figure 208 and figure 209.



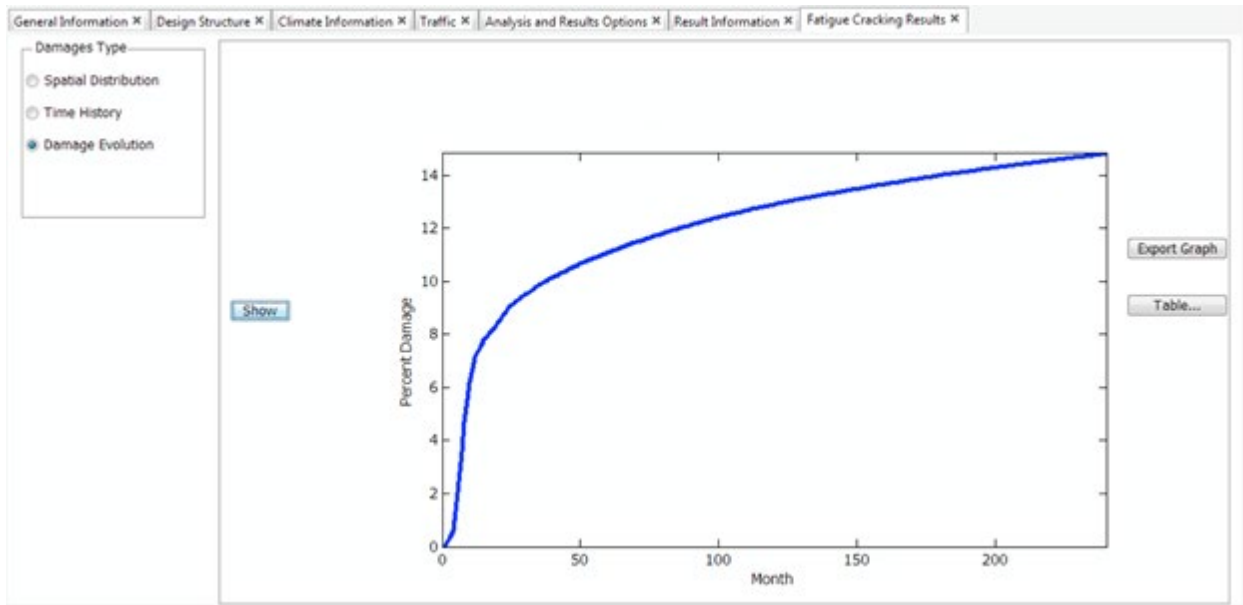
Source: FHWA.
 1 cm = 0.4 inch; 1 m = 3.28 ft.

Figure 206. Screenshot. Transverse stress distribution (response results).



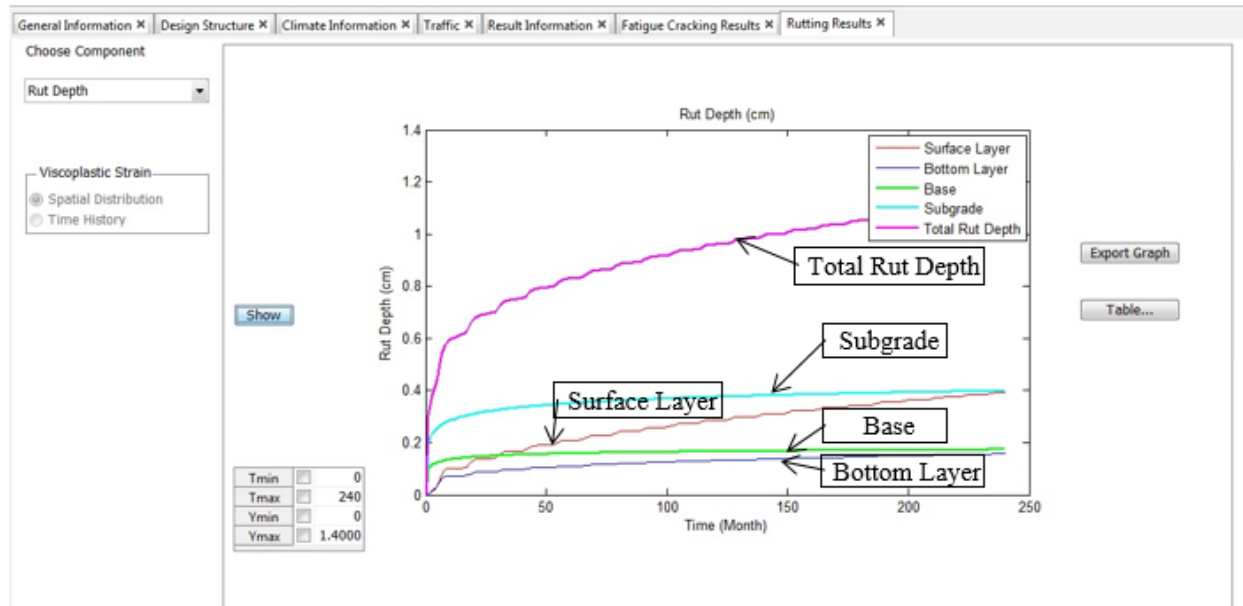
Source: FHWA.
 1 cm = 0.4 inch; 1 m = 3.28 ft.

Figure 207. Screenshot. Damage factor distribution after 20-yr simulation.



Source: FHWA.

Figure 208. Screenshot. Percent damage distribution as a function of time.



Source: FHWA.
1 cm = 0.4 inch.

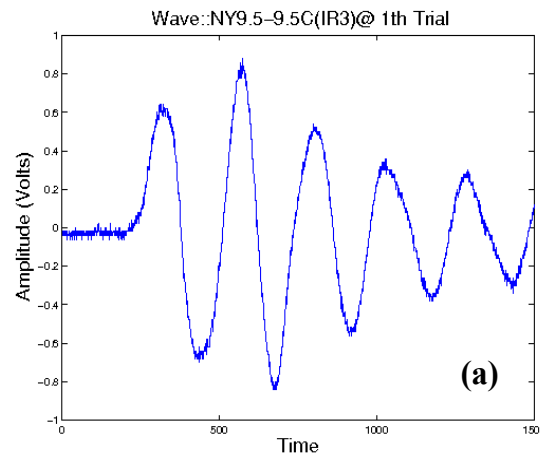
Figure 209. Screenshot. Rut depth development.

APPENDIX B. IR DYNAMIC MODULUS TEST

BACKGROUND

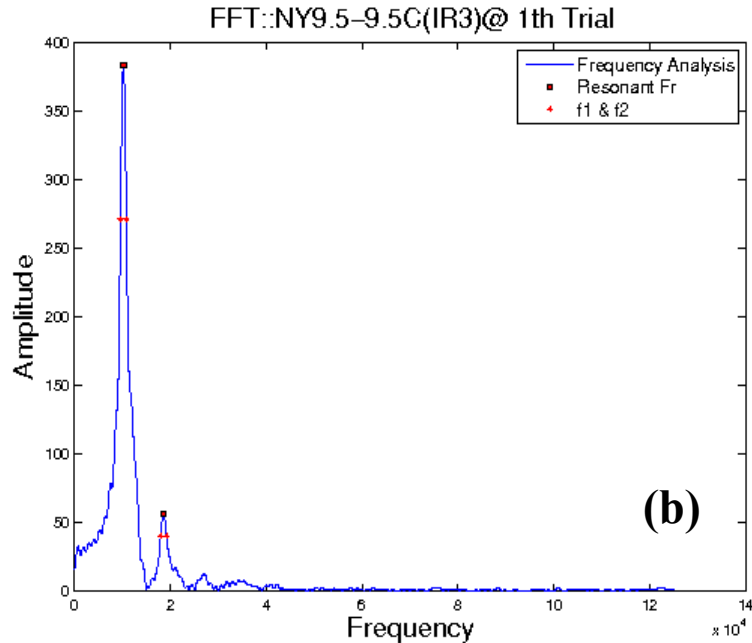
The research team employed the IR test method to induce an excitation using some mass to strike a specimen and measure the tested specimen's resultant natural vibration, which the team then used to determine the specimen's material properties. Inducing an excitation on a specimen does not cause any permanent change to the specimen and allows the elastic properties of the material to be examined in a nondestructive manner. Frequency equations derived on the basis of a suitable theory, which depend on the specimen's geometry, mass, and modulus, provide accurate values of natural frequencies. The primary components of IR testing are the specimen, support, accelerometer, signal conditioner (amplifier), and signal analyzer (oscilloscope).

In IR tests, a specimen rests on a support and a steel ball dropped onto the specimen creates an impact. The specimen has an attached accelerometer for measuring the vibration due to the impact load. The specimen freely vibrates on the support such that it follows the assumptions of free boundary conditions. Performing FFT converts the waveform in the time domain to the frequency domain, as shown in figure 210.



Source: FHWA.

A. Example of signals in time domain (time in micro s).

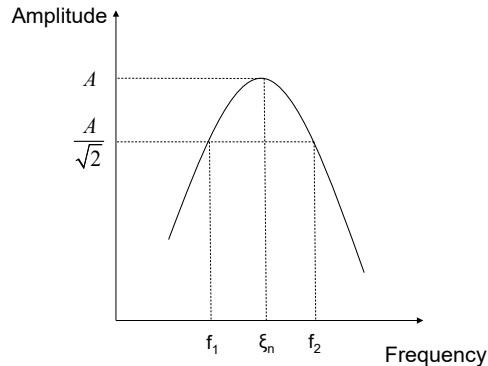


Source: FHWA.

B. FFT plot in frequency domain (frequency in Hz).

Figure 210. Graphs. Example of signals for one of the specimens.

Obtaining a response curve in the frequency domain allows the resonant frequency and damping ratio (ξ) to be determined. The natural frequency is the frequency of a system’s natural vibration in which the system vibrates to dissipate its energy due to an impact. The resonant frequency is the frequency that corresponds to the highest peak in the amplitude of the frequency domain signal, which is often referred to as the first resonant frequency. Asphalt mixtures exhibit high viscous damping, so the damping ratio of the sample affects the response curve from an impact. There are various methods for measuring the damping of a vibration system. One of the most common methods is estimating the damping ratio from the frequency domain, which is known as the half-power bandwidth method, as shown in figure 211. In this method, the amplitude drops to $1/\sqrt{2}$ (3 dB) of its highest peak value at two points, (i.e., the half-power points).



Source: FHWA.

Figure 211. Illustration. Half-power bandwidth method.

The damping ratio (ξ) is defined as the frequency range between the two half-power points and the natural frequency, as shown in equation 142.

$$\xi = \frac{f_2 - f_1}{2f_n} \quad (142)$$

Where:

f_1 = lower frequency.

f_2 = upper frequency.

f_n = resonance frequency.

IR TEST METHOD FOR THIN DISK SPECIMENS

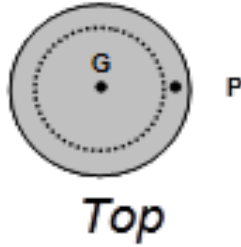
Asphalt mixtures are sensitive to temperature and loading frequency. The temperature and loading frequency dependency is captured in the dynamic modulus ($|E^*|$) master curve using the t-TS principle as described in AASHTO T 378 and R 84.^(9,10) Applying theoretical relationships among $|E^*|$ and these properties provides the relaxation modulus and creep compliance.

Case 1

ASTM E 1876-09 is a standardized procedure for determining the elastic properties of material using thin disk IR testing.⁽⁴⁶⁾ This method considers two modes of vibration: antiflexural vibration and axisymmetric flexural vibration. Antiflexural vibration occurs when the displacements in the cross-sectional plane are normal to the plane and symmetrical around two orthogonal diameters in the plane of the disk, causing the disk to twist. Axisymmetric flexural vibration occurs when the displacements in the cross-sectional plane are normal to the plane and are uniform in displacement for a given radial distance from the center point through the entire 360-degree circle. The main advantage of the ASTM E 1876-09 method is that it allows Poisson's ratio to be measured using the ratio of two resonant frequencies obtained from two natural vibrations of a single specimen.⁽⁴⁶⁾ Therefore, the impact and pick-up points for the two modes of vibration are extremely important in determining the modulus values of the materials used in IR testing for the case 1 method, as shown in table 47. In this method, the pick-up point of the disk is close to the outer circumference, and the ball strikes the center of the specimen. Four hard support points along nodal lines support the specimen. The points where the nodal circle from the first mode and the nodal diameters from the second mode meet are the suggested support points. To ensure accurate support locations, the nodal circle diameter of the test specimen is calculated as 0.681 of the geometrical mean diameter, which is 102 cm in diameter for 150-mm thin disk-shaped specimens. The test device and setup are shown in Figure 212 through figure 214.

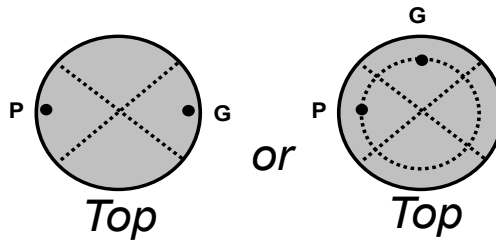
Table 47. IR test set-up summary for thin disk specimens.

Method	Case 1	Case 1	Case 2
Mode of vibration	Axisymmetric flexural	Antiflexural	Axisymmetric flexural
Case	Case 1-1 (Mode 1)	Case 1-2 (Mode 2)	Case 2



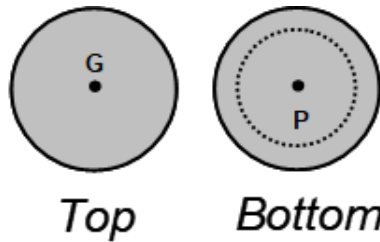
© 2017 Journal of Testing and Evaluation. (DTFH61-08-H-00005)
 G = impact load point; P = single pick-up point.

A. Pickup and impact points in case 1-1.



© 2017 Journal of Testing and Evaluation. (DTFH61-08-H-00005)
 G = impact load point; P = single pick-up point.

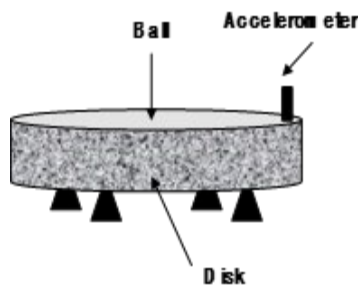
B. Pickup and impact points in case 1-2.



© 2017 Journal of Testing and Evaluation. (DTFH61-08-H-00005)
 G = impact load point; P = single pick-up point.

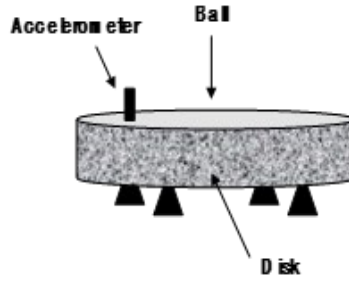
C. Pickup and impact points in case 2.

Figure 212. Illustrations. Pickup and impact points in different cases for IR test setup.⁽¹²¹⁾



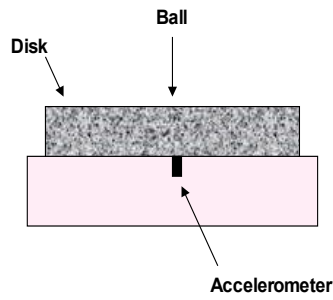
© 2017 Journal of Testing and Evaluation. (DTFH61-08-H-00005)

A. Test setup in case 1-1.



© 2017 Journal of Testing and Evaluation. (DTFH61-08-H-00005)

B. Test setup in case 1-2.



© 2017 Journal of Testing and Evaluation. (DTFH61-08-H-00005)

C. Test setup in case 2.

Figure 213. Illustrations. Test setup in IR tests. ⁽¹²¹⁾



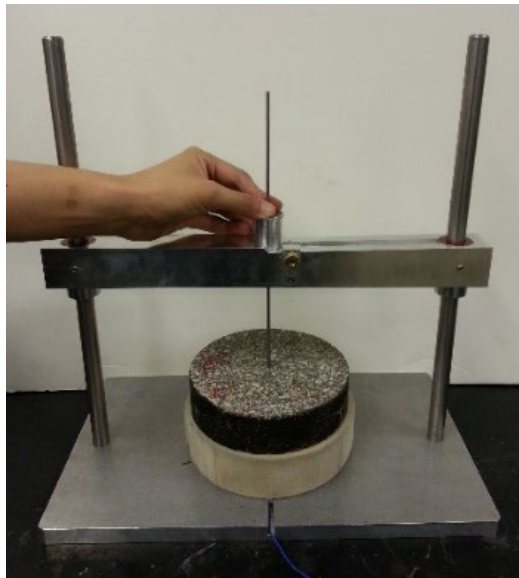
© 2017 Journal of Testing and Evaluation. (DTFH61-08-H-00005)

A. Test device setup for case 1-1.



© 2017 Journal of Testing and Evaluation. (DTFH61-08-H-00005)

B. Test device setup for case 1-2.



©2017 Journal of Testing and Evaluation. (DTFH61-08-H-00005)

C. Test device setup for case 2.

Figure 214. Photos. Test device in different setups in IR tests.⁽¹²¹⁾

The practical application of the IR test method for thin disk specimens depends on whether the natural frequency of the flexural vibration of a plate (disk) with a free edge is known. The natural frequencies of flexural vibration in a circular plate can be obtained from frequency equations, as derived from plate theory. Equation 143 determines natural vibration frequencies.

$$\omega = \frac{K}{R} \sqrt{\frac{P_c}{\rho h}} \quad (143)$$

Where:

ω = natural frequency.

K = geometric factor, computed for various conditions of h/R and Poisson's ratio, ν .

P_c = plate constant.

h = thickness of the disk.

R = radius of the disk.

ρ = mass density of the disk.

Equation 144, which is based on the transverse vibration in circular plate theory, calculates the storage modulus (E'), which is equivalent to the elastic part of $|E^*|$. Two calculations of storage modulus (E'_1 and E'_2) are independently from the two resonant frequency measurements (f_{r1} and f_{r2}). Only the K_1 and K_2 values can be separately from a calculated look-up table for those two frequencies.

$$E'_1 = \frac{48\rho f_{r1}^2 R^2 \pi^2 (1-\nu^2)}{K_1^2 h^2}$$

$$E'_2 = \frac{48\rho f_{r2}^2 R^2 \pi^2 (1-\nu^2)}{K_2^2 h^2} \quad (144)$$

Where f_r is the first natural resonant frequency.

As mentioned previously, the half-power bandwidth method uses the response curve to determine the damping ratio (ξ). To convert the storage modulus to the dynamic modulus, the phase angle is needed.⁽⁴⁰⁾ Equation 145, which is the relationship suggested by Clough et al., calculates the phase angle ϕ .⁽¹²²⁾

$$\phi = \tan^{-1}(2\xi) \quad (145)$$

Once the storage modulus and phase angle are determined, the dynamic modulus value can be calculated using equation 146. The final dynamic modulus value is determined by averaging the two $|E^*|$ values ($|E^*|_1$ and $|E^*|_2$) obtained from the two tests by dividing the storage modulus value by the phase angle value (ϕ_1 and ϕ_2).

$$\begin{aligned}
|E^*|_1 &= \frac{E_{s1}}{\cos(\phi_1)} \\
|E^*|_2 &= \frac{E_{s2}}{\cos(\phi_2)} \\
|E^*| &= \frac{|E^*|_1 + |E^*|_2}{2}.
\end{aligned}
\tag{146}$$

Case 2

The IR test method has historically been used to evaluate PCC disks. Leming et al. conducted one of the studies that focused on determining the elastic modulus of concrete disks.⁽⁴⁷⁾ The authors developed a method for accurately, quickly, and nondestructively determining the elastic modulus of concrete disks using the IR test method. Table 47 shows the components of the test setup for this case 2 method. In this method, the specimen rests on soft foam and the accelerometer is attached to the bottom center by cutting an opening in the soft foam.

The researchers used plate theory, which was developed by Hutchinson to understand the axisymmetric flexural vibration of a thick, free circular plate to determine the storage modulus.⁽⁴⁸⁾ After measuring the first natural frequency f , the diameter of the disk dia , and the mass density of the disk ρ , and estimating Poisson's ratio, the research team used equation 147 to calculate the storage modulus.

$$E' = 2(1+\nu)\rho \left[\frac{\pi \times f_1 \times dia}{\Omega_0} \right]^2
\tag{147}$$

Where:

Ω_0 = frequency parameter associated with the fundamental mode of vibration.

f_1 = first natural frequency.

dia = diameter of the disk.

After determining the storage modulus value, the research team used equation 145 and equation 146 to calculate the $|E^*|$ values.

EXPERIMENTAL INVESTIGATION

This section describes the materials, specimen fabrication methods, and testing plan used in the experimental investigation.

Materials and Specimen Fabrication

The research team used specimens in this study that were comprised of three different mixtures: NY9.5, NY19, and NY25. The numbers in the mixtures' names stand for the NMAAS. The team obtained the loose mixtures used in this study from common New York mixtures. They mixed all specimens with PG 64-22 binder from a leading petroleum company, and prepared the

gyratory-compacted specimens using the Servopac Superpave gyratory compactor in accordance with AASHTO T 342-11.⁽³⁷⁾

Modulus calculations of thin disk specimens are based on plate theory; thus, the diameter-to-depth ratio is an important factor because the specimen should be thin enough to obey plate-theory assumptions. The diameter-to-depth ratio should be at least 4.0, with a value of 10.0 to 20.0 recommended for experimental accuracy.⁽⁴¹⁾ However, a thin disk specimen would not be representative of the whole property of the specimen, especially in the case of a specimen with large aggregate particles.

Given the field conditions, diameter-to-depth ratio, RVE, and gyratory-compacted samples, specimen dimension of 150 × 38 × 25 mm was applied as thin disk geometry candidates for this IR study. However, the research team considered a thickness of 38 mm may not be thin enough to obey plate-theory assumptions because the diameter-to-depth ratio was close to the minimum recommended value. Additionally, a 25-mm thickness may not be thick enough to represent the global properties of a large aggregate size (in terms of NMAS).

The research team cut and cored cylindrical specimens 100 mm in diameter by 150 mm in height from gyratory-compacted specimens 150 mm in diameter by 178 mm in height. The team cut three 38-mm thick-disk specimens from a 150-mm diameter by 150-mm tall gyratory-compacted specimen and prepared three 25-mm thick disk specimens from a 150-mm-diameter by a 130-mm-tall specimen. The research team measured the air void contents using the vacuum sealing method. The target air void contents were 3.3 percent, 6.1 percent, and 6.2 percent for the NY9.5, NY19, and NY25 mixtures, respectively. The air void content of a sample for testing should fall within the target range of ±0.5 percent.

Testing Plan

One of the goals of this IR study was to determine optimized test procedures and test conditions using existing protocols. However, these protocols do not specify test conditions for asphalt concrete specimens like ball size, drop height, and temperature. Therefore, the research team investigated parameters of thickness, drop height, ball size, and temperature by comparing two proposed protocols for developing an IR test procedure for thin disk geometry asphalt specimens. Due to the nondestructive nature of IR testing, the same three specimens could be used as replicates for each set of test conditions.

To develop an IR test procedure for thin disk geometry specimens, the research team designed an experimental plan for determining the optimal test parameters to obtain the dynamic properties of the asphalt mixtures. To determine the optimal test conditions, the team investigated two methods (i.e., case 1 and case 2) and various drop heights and ball sizes. The research team applied specimen dimensions of 150 × 38 × 25 mm as thin disk geometry candidates in this study. The 38-mm thickness may not be thin enough to obey plate-theory assumptions because the diameter-to-depth ratio is close to the minimum recommended value. The 25-mm thickness may not be thick enough to represent the global properties of a large aggregate size (in terms of NMAS). Thus, the research team could not select the final geometry until after testing large aggregate size mixtures. For this purpose, the research team fabricated three types of specimens, as shown in table 48.

First, to determine optimal test conditions, the research team conducted IR tests on the NY9.5 mixture specimens with 25-mm thickness at five temperatures: 10, 20, 30, 40, and 50°C using 9-, 13-, and 16-mm diameter steel balls with 10-, 15-, and 20-cm drop heights. The team conducted 10 trials at each temperature for each specimen. They used a dummy specimen, 150 mm in diameter by 38 mm in height, to monitor the actual test temperature. The research team then performed all IR tests under the optimal test conditions using the NY19 and NY25 mixtures to decide the appropriate thickness for the thin disk specimen geometry.

The research team also conducted IR tests on long cylindrical specimens at 10, 30, and 50°C to compare the results of the thin disk specimens. The team used the existing test procedure for long cylindrical specimens, as shown in table 48.⁽⁴⁰⁾

In addition to the IR testing, the research team also performed the AASHTO T 342-11 dynamic modulus test using 100-mm-diameter, 150-mm-tall cylindrical specimens.⁽³⁷⁾ After the team completed the test in accordance with the T 342 specifications, they performed additional testing at 54°C to obtain a master curve with a better definition of the lower asymptote.

Table 48. Summary of IR test conditions.

Test Method	Thin Disk Specimens	Long Cylindrical Specimens
Mixture	NY9.5, NY19, and NY25	NY9.5, NY19, and NY25
Geometry (d × h) (mm)	150 × 38 ^b and 150 × 25	100 × 150
Temperature (°C)	10 ^b , 25 ^b , and 40 ^b (10, 20, 30, 40, and 50) ^a	10, 30, and 50
Ball size (mm)	16 ^b (9, 13, and 16) ^a	16
Drop height (cm)	20 ^b (10, 15, and 20) ^a	20
Support condition	Four hard supports with one layer of polyurethane foam	Two layers of polyurethane foam

0°C = 32°F; 1 cm = 0.4 inch; 1 mm = 0.04 inch.

^a test conditions for NY9.5 mixture.

^b represents optimal test conditions.

OPTIMAL TEST CONDITIONS

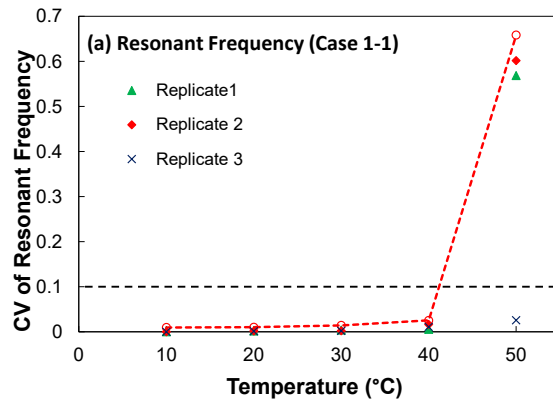
This section discusses the results of all IR tests performed in this study. After performing IR tests for the NY9.5 mixture under different conditions, as shown in table 48, the research team selected the optimal test conditions based on the coefficients of variation (CVs) of the resonant frequency and phase angle, and the closest match to the $|E^*|$ values obtained from standard $|E^*|$ tests. The CV is defined as the ratio of the standard deviation (σ) to the mean (μ), as shown in equation 148, and represents the repeatability among ball drops.

$$CV = \frac{\sigma}{\mu} \quad (148)$$

The IR tests of the thin disk specimens produce reliable results up to 40°C using PG 64-22 binder. Therefore, the research team used 10, 25, and 40°C as the IR test temperatures in this study. Case 1 is advantageous over case 2 in terms of measuring Poisson’s ratio from the IR test itself. The response signals were the most repeatable from the case 1 method that used a 16-mm steel ball with a 20-cm drop height. The research team proposes a recommended 38-mm thickness of the thin disk specimen. The IR test results obtained under each different condition are individually and in detail, as follows.

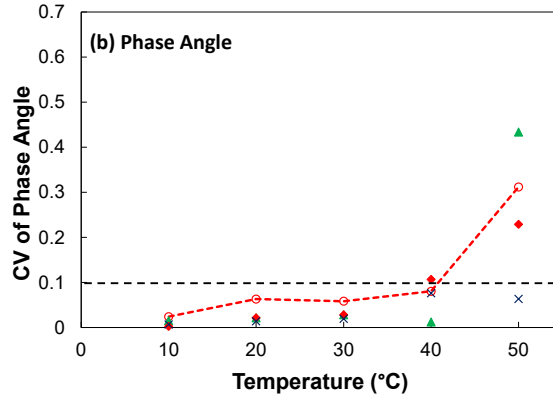
Test Temperature

The research team performed testing from 10° to 50°C on thin disk specimens using both the case 1 and case 2 methods. For case 1, the CV results show that IR tests of thin disk specimens can be performed up to 40°C to produce reliable IR test results using PG 64-22 asphalt binder because the variability dramatically at 50°C for both resonant frequency and phase angle, as shown in figure 215.



© 2017 Journal of Testing and Evaluation. (DTFH61-08-H-00005)
0°C = 32°F.

A. CVs of resonant frequency for case 1-1.



© 2017 Journal of Testing and Evaluation. (DTFH61-08-H-00005)
0°C = 32°F.

B. CVs of phase angle for case 1-1.

Figure 215. Graphs. CVs of resonant frequency and phase angle for case 1-1.⁽¹²¹⁾

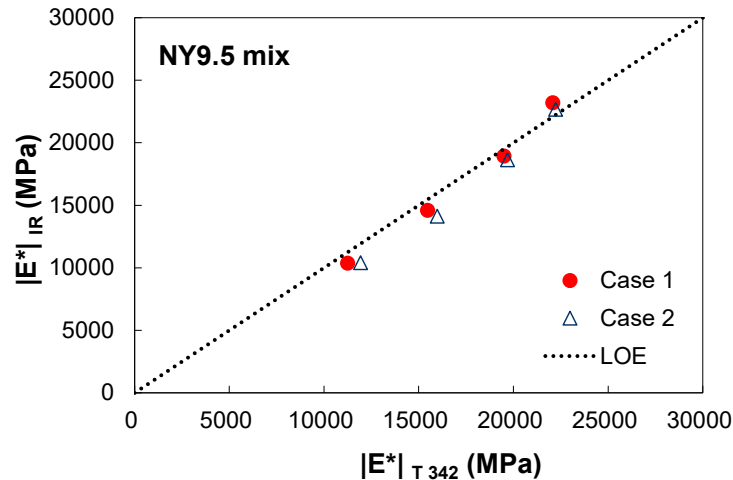
Case 1 Versus Case 2

The case 1 method uses two modes of vibration and thus requires a little longer testing time and effort than case 2. However, case 1 more easily measures Poisson's ratio than case 2. Case 1 uses the measured Poisson's ratio as an input for the dynamic modulus calculations, whereas case 2 assumes the Poisson's ratio. The Poisson's ratios used in the work of Whitmoyer and Kim are presented in table 49.⁽¹²³⁾ The Poisson's ratio changes depending on the mixture, thickness of the specimen, and temperature. However, the assumed Poisson's ratios for case 2 are fixed numbers; as a result, the case 2 method produces less accurate dynamic modulus values compared with case 1, as presented in figure 216.

Table 49. Measured and assumed Poisson's ratios for case 1 and case 2.

Test Conditions	Measured Poisson's Ratio			Assumed Poisson's Ratio ⁽¹²³⁾
	Case 1	Case 1	Case 1	Case 2
Method	Case 1	Case 1	Case 1	Case 2
Thickness (mm)	25	25	25	25
Mixture	NY9.5	NY19	NY25	All mixtures
IR test temperature 10°C	0.26	0.25	0.22	0.28
IR test temperature 25°C	0.30 (at 20°C)	0.28	0.25	0.30 (at 20°C)
IR test temperature 25°C	0.37 (at 30°C)	0.28	0.25	0.33
IR test temperature 40°C	0.41	0.38	0.37	0.39

0°C = 32°F; 1 mm = 0.04 inch.



© 2017 Journal of Testing and Evaluation. (DTFH61-08-H-00005)
 1 MPa = 145.04 psi.

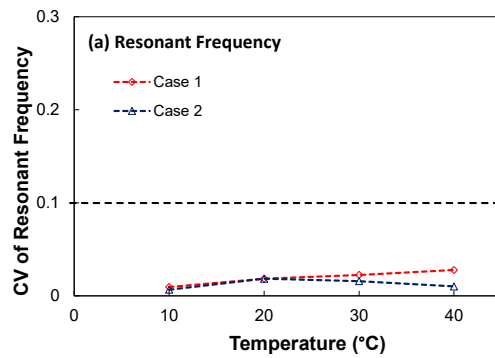
Figure 216. Graph. Comparison of dynamic modulus values between IR test and conventional test.⁽¹²¹⁾

The case 1 method uses two modes of vibration; the main advantage of using two modes of vibration is it allows for measuring the Poisson's ratio. The research team then used the measured Poisson's ratio as an input for the $|E^*|$ calculation of each IR test sample. The Poisson's ratio of asphalt mixtures is a fundamental material property that is an important input parameter for the viscoelastic pavement analysis; however, due to the complexity of accurately measuring Poisson's ratio, the value is currently assumed in most pavement analyses. Recent studies on performance predictions for flexible pavement revealing high sensitivity of asphalt layers to Poisson's ratio have pointed out the importance of a more accurate three-dimensional characterization of bituminous mixtures.⁽¹²⁴⁾ If the IR tests produce reasonable Poisson's ratios, then the measured Poisson's ratios can be inputs for pavement level analysis. This benefit is another advantage of using IR tests for thin disk specimens. The measured Poisson's ratio the case 1 method provides seems reasonable, as summarized in table 49.

The case 2 method uses only the axis-symmetric mode of vibration. Thus, the Poisson's ratio should be assumed for the $|E^*|$ calculation. The Poisson's ratio can be assumed based on the work of Whitmoyer and Kim, as presented in table 49.⁽¹²³⁾ The Poisson's ratio changes depending on the mixture, thickness of the specimen, and temperature. However, the assumed Poisson's ratios for case 2 are fixed numbers; as a result, this method produces less accurate $|E^*|$ values compared with the $|E^*|$ values from case 1, as presented in figure 216.

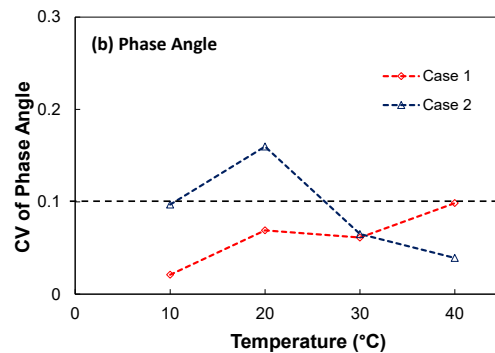
Figure 216 plots the line of equality (LOE) of the $|E^*|$ from the IR test ($|E^*|_{IR}$) and the $|E^*|$ from the T 342-11 test ($|E^*|_{T\ 342}$) at the same reduced frequency to evaluate which IR test condition yields $|E^*|$ values closest to the $|E^*|$ values obtained from the T 342-11 test. In general, the case 1 method resulted in $|E^*|$ values closer to the $|E^*|_{T\ 342}$ values than the case 2 method, as shown in figure 216, which plots the data points using the NY9.5 mixture with 25-mm thickness. How to calculate $|E^*|$ values from IR tests is discussed in the next section.

Figure 217 through figure 219 show the CVs of the resonant frequency and phase angle obtained under various test conditions. The variability of the resonant frequency and phase angle values increases as the test temperature increases because of the damping associated with the increasingly viscous behavior of the asphalt as the temperature rises. The research team considered variability lower than 10 percent to be acceptable, as shown by the dotted line in figure 217 through figure 219, because the recommended CV for the mean of three specimens is 7.5 percent based on the current AASHTO T 342-11 standard.⁽³⁷⁾ The CVs of the phase angle for case 2 at low temperatures are very high, as shown in figure 217. This outcome may be due to the setup of the IR tests in which the accelerometer is attached to the bottom center of the sample through an opening cut into the soft foam. In some cases, this scenario creates double peaks in the first highest peak in the frequency domain and affects the damping ratio calculation. The research team concluded case 1 is more effective than case 2 because case 1 can measure the Poisson's ratio and produce better $|E^*|$ correlations with those from standard testing.



Source: FHWA.
0°C = 32°F.

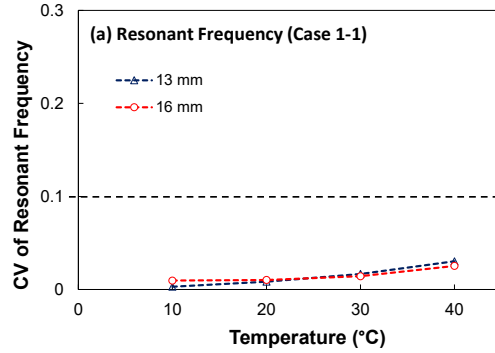
A. CVs of resonant frequency in case 1 and case 2.



Source: FHWA.
0°C = 32°F.

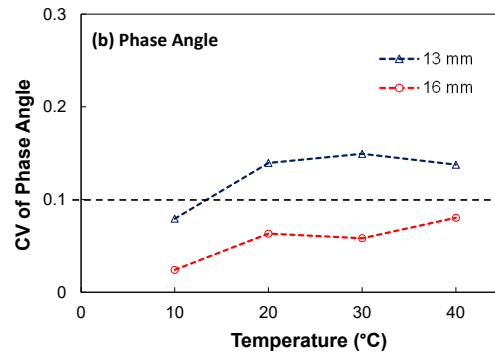
B. CVs of phase angle in case 1 and case 2.

Figure 217. Graphs. CVs in case 1 and case 2.



© 2017 Journal of Testing and Evaluation. (DTFH61-08-H-00005)
 0°C = 32°F; 1 mm = 0.04 inch.

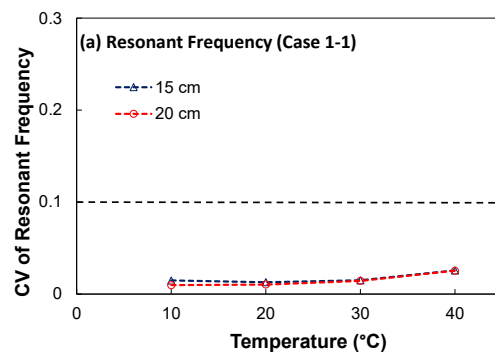
A. CVs of resonant frequency with different ball sizes.



© 2017 Journal of Testing and Evaluation. (DTFH61-08-H-00005)
 0°C = 32°F; 1 mm = 0.04 inch.

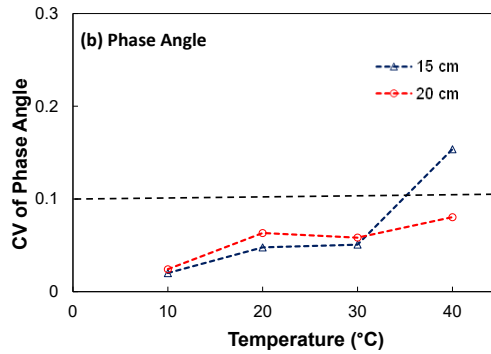
B. CVs of phase angle with different ball sizes.

Figure 218. Graphs. CVs with different ball sizes.⁽¹²¹⁾



© 2017 Journal of Testing and Evaluation. (DTFH61-08-H-00005)
 0°C = 32°F; 1 cm = 0.4 inch.

A. CVs of resonant frequency with balls dropped at different heights.



© 2017 Journal of Testing and Evaluation. (DTFH61-08-H-00005)
 0°C = 32°F.

B. CVs of phase angle with balls dropped at different heights.

Figure 219. Graphs. CVs with balls dropped at different heights. (121)

Ball Size and Drop Height

The research team investigated the effects of steel ball size and drop height to increase the repeatability (ball drop to ball drop) and consistency of the IR tests using the thin disk geometry, minimize variability (sample to sample), and allow for the closest match with the $|E^*|$ data from standardized testing. The 9-mm ball was too small to make a strong signal, or any signal in some cases. The research team did not use steel balls with diameters larger than 16 mm because they could damage the specimens, especially at high temperatures; thus, the research team assumed a smaller ball that could supply enough energy to produce a strong enough signal was the best option. The variability in phase angle was greater when using a ball with a 13-mm diameter. The results indicate that the repeatability and variability were best when the research team used a 16-mm-diameter ball, as shown in figure 218-B.

The research team used drop heights of 10 and 20 cm to investigate the effect of drop height on IR signal quality. Figure 219-B shows the results of the different drop heights. In general, the results show the drop height has an insignificant effect compared with other factors because the CV of the phase angle remains low. The shorter (10 cm) drop height was too low to provide a strong signal at 40°C, as indicated by the large CV value at 40°C. The variabilities of resonant frequency and phase angle remained below 10 percent at the 20-cm drop height. The research team determined it was undesirable to perform IR tests using a drop height of more than 20 cm because the height would require a taller temperature chamber. Therefore, the team selected the 20-cm drop height for further testing.

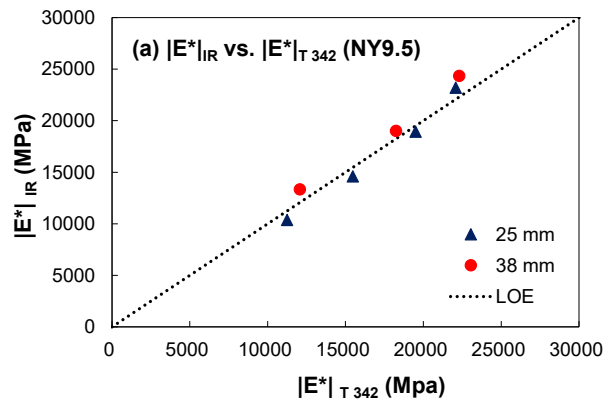
Specimen Thickness

Specimen thickness is an important factor because the IR test specimen should act like a plate to obey plate-theory assumptions, as discussed previously. The research team selected the optimal IR test condition (case 1: 20-cm drop height and 16-mm-diameter ball) based on IR test results with 25-mm thick specimens because thinner specimens moved more like a plate with the same diameter. Then, the research team performed all IR tests with 38-mm thick specimens under the

optimal test conditions using the NY19 and NY25 mixtures to select the appropriate thickness for the thin disk specimen geometry.

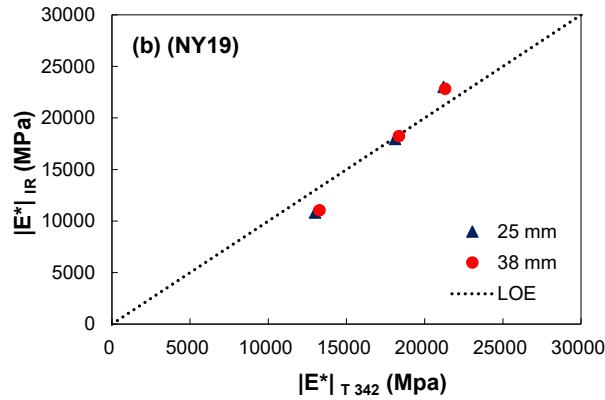
Figure 220-C shows the LOEs for the $|E^*|_{IR}$ and the $|E^*|_{T\ 342}$ from specimens of the two thicknesses at the same reduced frequency to investigate the effect of thickness with different NMAS. The IR test results show that both the 25-mm and 38-mm geometries produce reasonable $|E^*|$ data, as presented in Figure 220-C. The average difference between the $|E^*|_{IR}$ and $|E^*|_{T\ 342}$ values was less than 10 percent for all mixtures and even less than 5 percent for the 38-mm-thick samples. These results indicate that 38 mm is thin enough to obey plate-theory assumptions. The asphalt community uses 38-mm-thick specimens to perform $|E^*|$ testing in indirect tension mode because these specimens are easier to prepare in practice than 25-mm-thick specimens. Thicker specimens are more likely to represent the global properties of the material than thinner specimens, as shown in Figure 220-C with 25-mm (large) NMAS. Therefore, the research team recommends 38 mm thickness for thin disk geometry.

Thus, the optimal test conditions for the IR tests are case 1, 16-mm-diameter steel ball, 20-cm drop height, and 38-mm-thick specimens. The research team applied these test conditions to further IR tests to create reasonable dynamic modulus master curves.



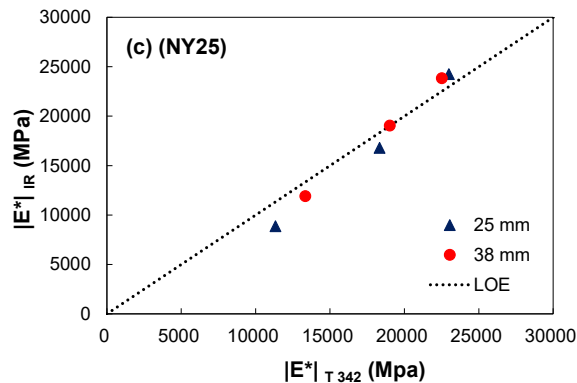
© 2017 Journal of Testing and Evaluation. (DTFH61-08-H-00005)
 1 mm = 0.04 inch; 1 MPa = 145.04 psi.

A. Comparison of $|E^*|_{T\ 342}$ and $|E^*|_{IR}$ test results obtained from specimens at different thicknesses for the NY9.5 mixture.



© 2017 Journal of Testing and Evaluation. (DTFH61-08-H-00005)
 1 mm = 0.04 inch; 1 MPa = 145.04 psi.

B. Comparison of $|E^*|_{T342}$ and $|E^*|_{IR}$ test results obtained from specimens at different thicknesses for the NY19 mixture.



© 2017 Journal of Testing and Evaluation. (DTFH61-08-H-00005)
 1 mm = 0.04 inch; 1 MPa = 145.04 psi.

C. Comparison of $|E^*|_{T342}$ and $|E^*|_{IR}$ test results obtained from specimens at different thicknesses for the NY25 mixture.

Figure 220. Graphs. Comparison of $|E^*|_{T342}$ and $|E^*|_{IR}$ test results obtained from specimens at different thicknesses. ⁽¹²¹⁾

COMPARISON WITH DYNAMIC MODULUS TESTING

A proper comparison of the $|E^*|$ values from the IR tests to those from the T 342-11 tests requires using reduced frequency because the resonant frequencies from the IR test are much higher than the loading frequencies used in the T 342-11 test at the same testing temperature. equation 149 calculates reduced frequency (f_R).

$$f_R = a_T \times f \quad (149)$$

Where:

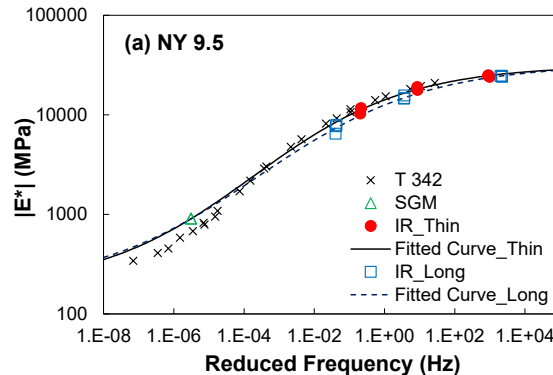
a_T = t-T shift factor.

IR tests cannot provide time-temperature (t-T) shift factors. Therefore, building dynamic modulus master curves requires t-T shift factors. LaCroix and Kim reported that using averaged-or measured-binder shift factors to shift $|E^*|$ data from IR tests produces $|E^*|$ values that are not statistically different from the $|E^*|$ values from the AASHTO T 378 $|E^*|$ protocol.^(42,9) In this study, the research team utilized the averaged-binder shift factor ($(a_T)_{avg,binder}$) function proposed by Sakhaei Far, as shown in equation 150.⁽¹²⁵⁾

$$\log(a_T)_{avg,binder} = 0.0011 \cdot T^2 - 0.1727 \cdot T + 3.018 \quad (\text{Reference temperature} = 20^\circ\text{C}) \quad (150)$$

Where T is the temperature.

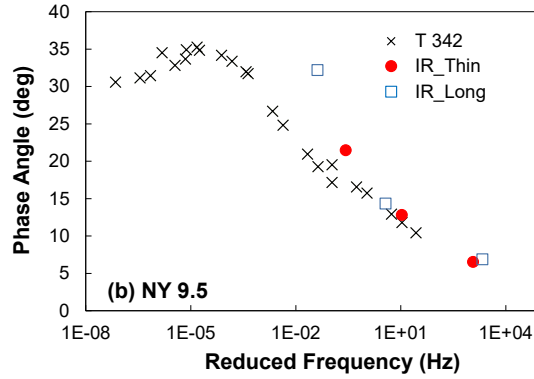
Figure 221 shows the comparison of the IR $|E^*|$ and phase angle values from the optimal test conditions derived from case 1 using a 16-mm-diameter ball with a 20-cm drop height on 38-mm-thick specimens against the $|E^*|$ and phase angle master from T 342 testing. Note that SGM (Simplified Global Model) and fitted curves in the legend of figure 221 will be explained later in this section. As discussed previously, the research team obtained IR $|E^*|$ and phase angle values from the IR response curve. Table 50 and Table 51 present raw data for the resonant frequencies and damping ratios. The tables also present the $|E^*|$ and phase angle values from the IR testing of long cylinders. In general, the IR $|E^*|$ master curves, regardless of specimen geometry and mixture type, are in good agreement with the $|E^*|$ master curves from the T 342 testing. There is some discrepancy in phase angle results between the IR test results and the T 342 method results at 40°C for thin disks and 50°C for long cylinders. However, this discrepancy does not affect the agreement of the $|E^*|$ values from the IR tests with the $|E^*|$ values from the T 342-11 tests.



© 2017 Journal of Testing and Evaluation. (DTFH61-08-H-00005)

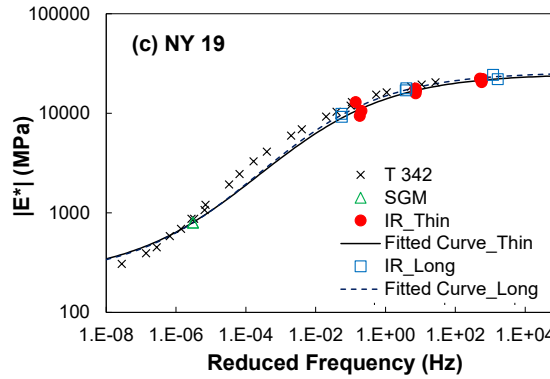
1 MPa = 145.04 psi.

A. Comparison of material properties measured from IR tests and T 342-11 tests for NY9.5 mixture dynamic modulus master curves.



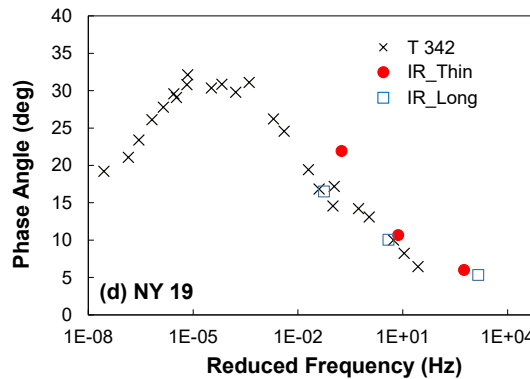
© 2017 Journal of Testing and Evaluation. (DTFH61-08-H-00005)

B. Comparison of material properties measured from IR tests and T 342-11 tests for NY9.5 mixture phase angles.



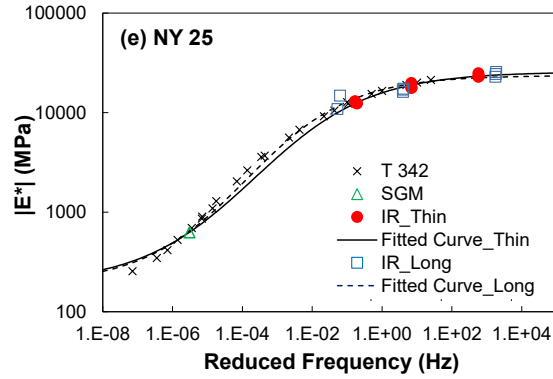
© 2017 Journal of Testing and Evaluation. (DTFH61-08-H-00005)
 1 MPa = 145.04 psi.

C. Comparison of material properties measured from IR tests and T 342-11 tests for NY19 mixture dynamic modulus master curves.



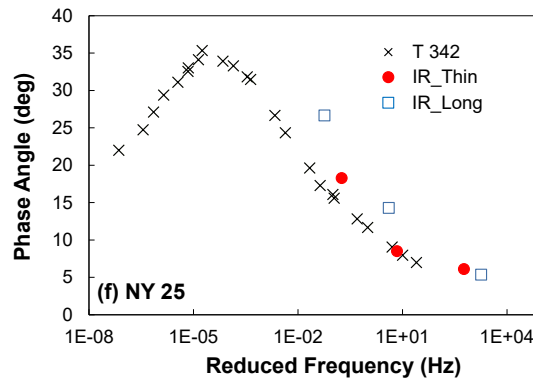
© 2017 Journal of Testing and Evaluation. (DTFH61-08-H-00005)

D. Comparison of material properties measured from IR tests and T 342-11 tests for NY19 mixture phase angles.



© 2017 Journal of Testing and Evaluation. (DTFH61-08-H-00005)
 1 MPa = 145.04 psi.

E. Comparison of material properties measured from IR tests and T 342-11 tests for NY25 mixture dynamic modulus master curves.



© 2017 Journal of Testing and Evaluation. (DTFH61-08-H-00005)

F. Comparison of material properties measured from IR tests and T 342-11 tests for NY25 mixture phase angles.

Figure 221. Graphs. Comparison of material properties measured from IR tests and T 342-11 tests for NY9.5, NY19, and NY25 mixtures.

Table 50. Resonant frequency (Hz) of IR test results for a 16-mm-diameter ball dropped from a 20-cm height.

Temperature (°C)	Case 1 Mode 1 Sample 1	Case 1 Mode 1 Sample 2	Case 1 Mode 1 Sample 3	Case 1 Mode 2 Sample 1	Case 1 Mode 2 Sample 2	Case 1 Mode 2 Sample 3	Case 2 Sample 1	Case 2 Sample 2	Case 2 Sample 3
10	7,144	7,248	7,202	4,622	4,718	4,658	7,104	7,238	7,152
25	6,192	6,414	6,250	3,894	3,950	3,874	6,204	6,306	6,212
40	4,796	5,092	5,224	2,792	2,970	2,798	5,056	5,124	5,018

0°C = 32°F.

Table 51. Damping ratio of IR test results for a 16-mm-diameter ball dropped from a 20-cm height.

Temperature (°C)	Case 1 Mode 1 Sample 1	Case 1 Mode 1 Sample 2	Case 1 Mode 1 Sample 3	Case 1 Mode 2 Sample 1	Case 1 Mode 2 Sample 2	Case 1 Mode 2 Sample 3	Case 2 Sample 1	Case 2 Sample 2	Case 2 Sample 3
10	0.048	0.048	0.056	0.063	0.063	0.065	0.047	0.052	0.050
25	0.084	0.056	0.093	0.120	0.116	0.116	0.093	0.095	0.087
40	0.167	0.197	0.192	0.219	0.197	0.215	0.168	0.166	0.154

0°C = 32°F.

One major weakness of the IR $|E^*|$ test is its inability to measure $|E^*|$ values at low reduced frequencies. This weakness prohibits constructing $|E^*|$ master curves using only. In this study, the research team utilized two predictive methodologies (equations 151 and 152) developed by Sakhaei Far to estimate the low asymptote value in the master curve sigmoidal function and the $|E^*|$ value at low reduced frequency.⁽¹²⁵⁾ Equation 151 was developed using 54.4°C dynamic modulus values in the NCSU database, whereas equation 152 was developed using multiple temperature data. Because equation 151 was developed using high temperature data only, it has better prediction accuracy for the high temperature dynamic modulus values than the global predictive equation 151.

$$a = 5.57975 - 0.00182p_{34} - 0.00579p_{38} - 0.1125p_{200} - 0.07121V_a - 0.05417V_{beff} \quad (151)$$

$$\log |E^*| = 6.39411 - 0.00015p_{34}^2 - 0.00546p_{38} - 0.1175p_{200} - 0.05544V_a - 0.05791V_{beff} + 0.0046V_{beff}^2 + \frac{0.6014 + 0.0004p_{34} + 0.00696p_{38} + 0.16224p_{200} - 0.00535p_{200}^2 + 0.019V_a + 0.15541V_{beff} - 0.00568V_{beff}^2}{1 + e^{(1.8645 - 0.9599 \log |G^*|)}} \quad (152)$$

Where:

- a = low asymptote in the dynamic modulus master curve.
- $|E^*|$ = dynamic modulus of HMA, psi.
- p_{200} = percentage of aggregate passing the #200 sieve.
- p_{38} = percentage of aggregate passing the 3/8-in sieve.
- p_{34} = percentage of aggregate passing the 3/4-in sieve.
- V_a = percentage of air voids (by volume of mix).
- V_{beff} = percentage of effective asphalt content (by volume of mix).
- $|G^*|$ = dynamic shear modulus of binder, psi.

Because the primary strength of IR testing is its simplicity, the research team's goal was to obtain the binder $|G^*|$ value without additional testing. In this study, the team used $|G^*|$ values available from the binder purchase specification. In the standard purchase specification grading system, the research team performed dynamic shear rheometer (DSR) tests at 10 rad/s on unaged and rolling thin film oven (RTFO)-aged asphalt binders at relatively high temperatures (46°C–82°C). The exact test temperatures depend on the material chosen and the environmental region where these materials will be placed.⁽¹²¹⁾ The RTFO-aged $|G^*|$ value is appropriate for this study because the RTFO condition is similar to the aging condition used for $|E^*|$ test specimens.

Predicting the $|E^*|$ value at 54°C requires the $|G^*|$ RTFO value at 54°C. However, the $|G^*|$ RTFO data from specification tests are usually the test results at a high PG temperature at 10 rad/s. The research team used the PG 64-22 binder for all NY mixtures; thus, the $|G^*|$ RTFO data were available at 64°C and at 10 rad/s. The research team used the t–T shift factor to convert the DSR loading frequency of 10 rad/s at 64°C to the reduced frequency at the reference temperature of 5°C, which is 3.09×10^{-6} Hz. The team input the NY binder's $|G^*|$ value in the binder purchase specification to obtain the mixture $|E^*|$ value at the reduced frequency of 3.09×10^{-6} Hz. Figure 221 plots these $|E^*|$ values for the three study mixtures with a legend title of SGM.

The research team used the sigmoidal function to fit the master curve using $|E^*|$ values from the IR tests at different temperatures, the predicted $|E^*|$ value at 3.09×10^{-6} Hz, and the lower asymptote predicted from equation 151. Figure 221-A, C, and E plot the fitted IR $|E^*|$ master curves from the thin disk IR data and long cylinder IR data. In general, the IR master curves from the two specimen geometries match well. The discrepancy between the IR master curve and the T 342 master curve is greater than of those between the two IR specimen geometries; however, considering the benefit of IR testing, this much discrepancy may be acceptable for certain situations, such as quality control and assurance purposes.

APPENDIX C. EXCEL FLEXMAT VERSION 1.1 MANUAL

OVERVIEW

The FlexMAT version 1.1 Excel templates analyze AMPT dynamic modulus, cyclic fatigue, and SSR data. The dynamic modulus and cyclic fatigue analyses are combined into a single Excel FlexMAT template. The dynamic modulus and cyclic fatigue FlexMAT template determines the $t-T$ shift factor model and Prony series model coefficients using dynamic modulus test results. The dynamic modulus analysis results are integrated with the AMPT cyclic fatigue data to determine the S-VECD model coefficients and failure criteria parameters. In addition, the FlexMAT template can be used to predict fatigue life at any strain amplitude, temperature, and loading frequency of interest. The AMPT SSR is a separate FlexMAT Excel template. The AMPT SSR FlexMAT template calculates the shift model parameters. The results of both the dynamic modulus and cyclic fatigue and SSR FlexMAT templates can be used to generate FlexPAVE material inputs files. The material presented in this appendix provides specific instructions for using the two Excel templates.

Both templates use Excel macros, and when using macros in Excel, macros must first be enabled. Newer versions of Excel offer users prompts to allow or disallow macros upon opening a file. If these prompts are not present at startup, then the templates may not perform as expected and, in these cases, Excel may present error prompts when attempting to clear or load data. One potential fix is opening the Excel file and saving it to a local folder through the Excel prompts. Regardless of the security settings, some versions of Excel will not allow access to macros unless the file is locally saved through the program. Ensure all other Excel windows are closed before saving the file. If this approach does not work, consult your agency's Information Technology staff to enable macros.

DYNAMIC MODULUS AND CYCLIC FATIGUE TEMPLATE

The dynamic modulus and cyclic fatigue FlexMAT template contains six tabs: Instructions; Input Data; Dynamic Modulus Data; Fatigue Data Validity; Output Fatigue; and Input to FlexPAVE. The template is designed so that it works from the leftmost tab to the rightmost tab sequentially. The following six sections provide specific instructions for using each tab.

Instructions

The Instructions tab provides general instructions for using the FlexMAT template.

Input Data

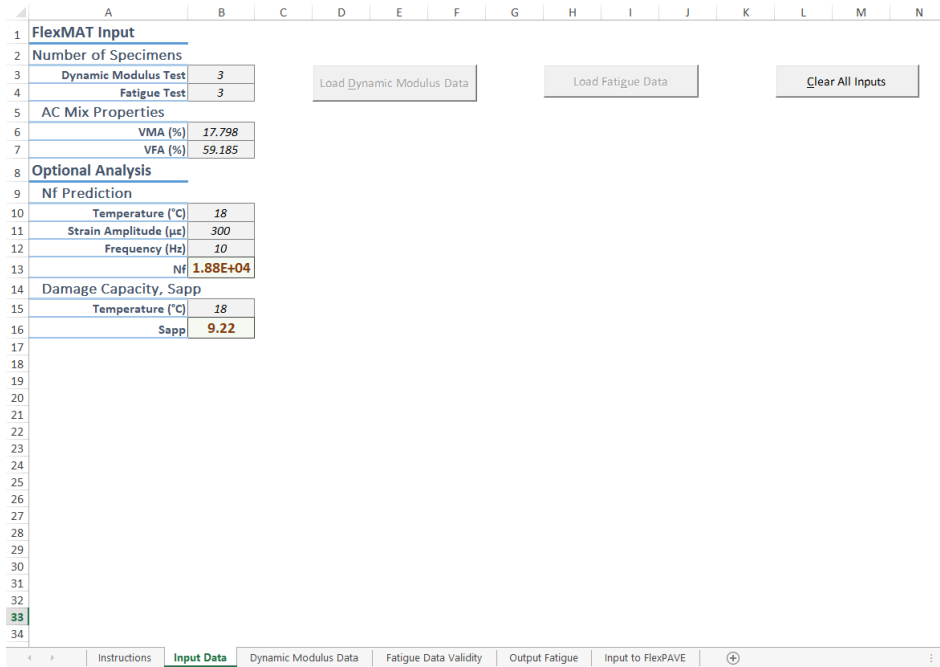
The Input Data tab should be used to automatically import dynamic modulus and cyclic fatigue test data from the data output files of the AMPT. The FlexMAT template requires using the summary dynamic modulus test files and both the Initial 5 S-VECD Fatigue Test Cycles and S-VECD Fatigue Test Analyzed Data cyclic fatigue test files. No data entry is required for the other tabs because all necessary data will be imported through the Input Data tab. Mixture volumetric properties (VMA and VFA) must be entered in this tab as well. Separate folders must

be created for each dynamic modulus test and cyclic fatigue test. Each folder must contain the AMPT data output files for one dynamic modulus test or one cyclic fatigue test.

Figure 222 shows a screen shot of the Input Data tab. If data are already loaded into the spreadsheet, then those data must be cleared from the file by clicking the Clear All Inputs button. If an error appears after clicking this button, it is most likely a result of not properly following the instructions detailed in the Overview section of this Appendix regarding proper enabling of macros in Excel.

The next step is selecting the number of test replicates for both the dynamic modulus and fatigue tests from the dropdown lists in cells B3 and B4, respectively. Clicking on the Load Dynamic Modulus Data button imports dynamic modulus data into the FlexMAT template and a prompt will appear. The appropriate folder for the first specimen will need to be selected, then the folders for the second and third specimens will need to be selected accordingly. The dynamic modulus test data will be imported into the required cells within the FlexMAT template.

Clicking on Load Fatigue Data will import cyclic fatigue test data for the first cyclic fatigue test and a prompt will appear. The appropriate folder for the first specimen will need to be selected, then the folders for the second, third, and fourth replicates will need to be selected accordingly. The cyclic fatigue test data will be imported into the required cells within the FlexMAT template. For cyclic fatigue test analysis, some optional analyses in the Input Data tab may be enabled only after loading the fatigue test data. Temperature, strain amplitude, and frequency can be entered into cells B10, B11, and B12, respectively, to compute the number of cycles to failure, N_f . Temperature can also be entered into cell B12 to compute the fatigue cracking index parameter, S_{app} . S_{app} has been developed under the FHWA's project DTFH61-13-C-00025, Develop and Deploy PRS for Pavement Construction, and represents the amount of fatigue damage a mixture can tolerate under cyclic loading.^(126,127) S_{app} is determined at the average temperature of the high and low PGs as given in LTPP Bind Online at the location for the project of interest, -3°C .

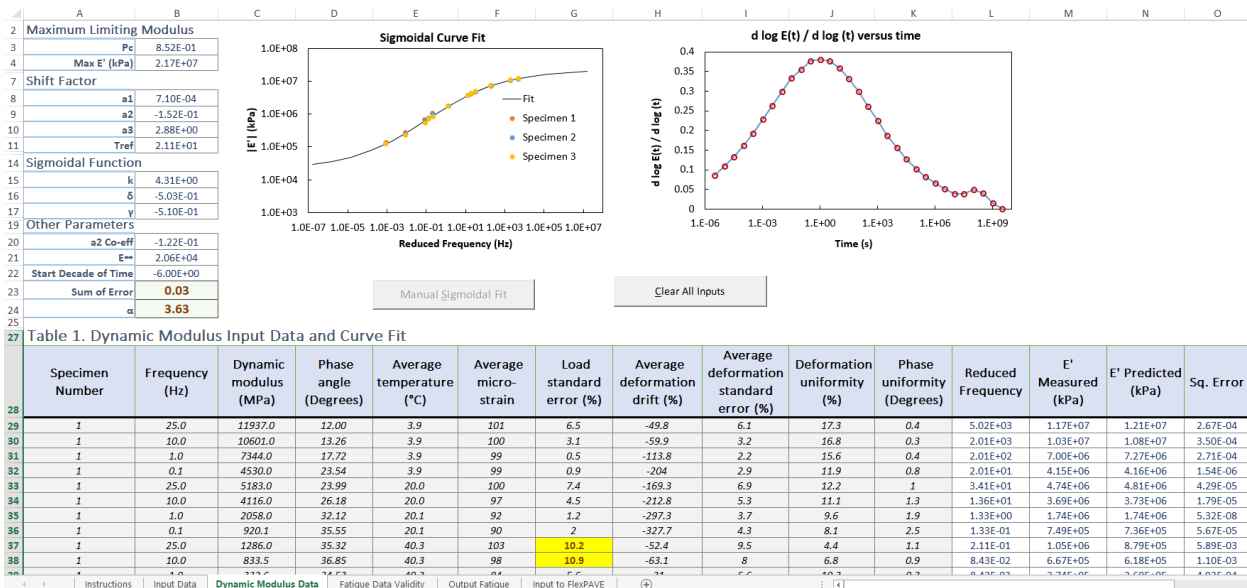


Source: FHWA.

Figure 222. Screenshot. Input Data tab.

Dynamic Modulus Data

The sigmoidal model fit, Prony series coefficients, and alpha value can be obtained in the Dynamic Modulus Data tab. Figure 223 shows a screenshot of the Dynamic Modulus Data tab.



Source: FHWA.
1 kPa = 0.145 psi.

Figure 223. Screenshot. Dynamic Modulus Data tab.

The sigmoidal and $t-T$ shift factor models are optimized to the storage modulus data obtained from the dynamic modulus test results. Sample-to-sample variability and the quality of the $t-T$ shift factor and sigmoidal model predictions can be visually evaluated by viewing the storage modulus (E') versus reduced frequency graphs. Any erroneous dynamic modulus data reported in Table 1 in the Dynamic Modulus Data tab can be modified or deleted. Blank cells may appear in Table 1 in the Dynamic Modulus Data tab once the erroneous data are deleted. With any modification, the Manual Sigmoidal Fit button will be enabled and must be clicked to update the sigmoidal fit.

The load standard error, average deformation drift, average deformation standard error, deformation uniformity, and phase uniformity cells can be reviewed within the Dynamic Modulus Input Data and Curve Fit table. The cells will appear yellow in cases where the AASHTO T 378 and AASHTO R 84 data quality requirements are not met, which may indicate an invalid test.^(9,10)

The Prony series coefficients (E_m and ρ_m) are calculated within the Dynamic Modulus Data tab. The method first uses the sigmoidal model for the storage modulus to calculate an array of storage modulus values (given in Table 2 in the Dynamic Modulus Data tab) and then it uses a matrix method to determine the Prony series coefficients; see Table 3 of the Dynamic Modulus Data tab, as shown in figure 224. No data entry or action is required.

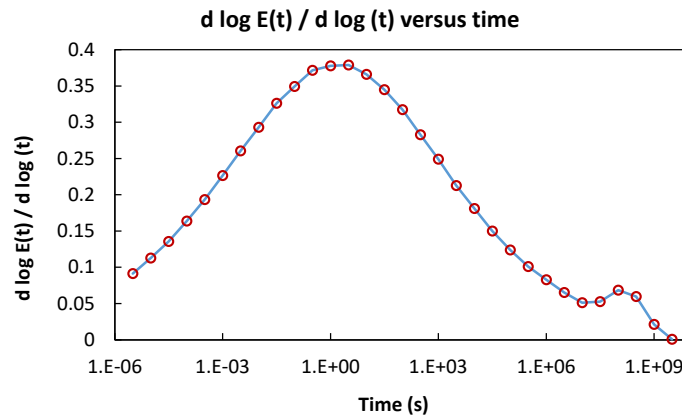
	V	W
27	Table 3. Prony Series	
	$\rho_m(s)$	E_m
28		
29	2.00E+08	3.40E+03
30	2.00E+07	1.54E+03
31	2.00E+06	3.93E+03
32	2.00E+05	7.08E+03
33	2.00E+04	1.42E+04
34	2.00E+03	3.10E+04
35	2.00E+02	7.41E+04
36	2.00E+01	1.91E+05
37	2.00E+00	4.97E+05
38	2.00E-01	1.17E+06
39	2.00E-02	2.21E+06
40	2.00E-03	3.21E+06
41	2.00E-04	3.59E+06
42	2.00E-05	3.25E+06
43	2.00E-06	2.53E+06
44	2.00E-07	1.79E+06
45	2.00E-08	1.22E+06
46		

Source: FHWA.

Figure 224. Screenshot. Prony Series table.

The alpha value is the continuum damage power term related to material time dependence based on the maximum log-log slope of the relaxation modulus master curve. Figure 225 shows a screenshot of the alpha value calculation. The relaxation modulus ($E(t)$) is determined using

Prony series fit. The graph of $d \log E(t)/d \log(t)$ versus time should display a clear peak, similar to that shown in the graph in figure 225-A. No data entry is required.



Source: FHWA.

A. Derivative of the relaxation modulus curve.

Reduced Time (s)	E(t)	dlogE/dlogt
1.00E-06	1.57E+07	-
3.16E-06	1.43E+07	9.15E-02
1.00E-05	1.28E+07	1.13E-01
3.16E-05	1.10E+07	1.36E-01
1.00E-04	9.33E+06	1.64E-01
3.16E-04	7.54E+06	1.93E-01
1.00E-03	5.98E+06	2.26E-01
3.16E-03	4.48E+06	2.60E-01
1.00E-02	3.28E+06	2.93E-01
3.16E-02	2.28E+06	3.26E-01
1.00E-01	1.55E+06	3.49E-01
3.16E-01	1.02E+06	3.71E-01
1.00E+00	6.59E+05	3.78E-01
3.16E+00	4.28E+05	3.79E-01
1.00E+01	2.75E+05	3.66E-01
3.16E+01	1.84E+05	3.45E-01
1.00E+02	1.24E+05	3.17E-01
3.16E+02	8.87E+04	2.83E-01
1.00E+03	6.49E+04	2.49E-01
3.16E+03	5.00E+04	2.13E-01
1.00E+04	3.98E+04	1.81E-01
3.16E+04	3.30E+04	1.50E-01
1.00E+05	2.82E+04	1.24E-01
3.16E+05	2.48E+04	1.01E-01
1.00E+06	2.23E+04	8.28E-02
3.16E+06	2.05E+04	6.54E-02
1.00E+07	1.92E+04	5.11E-02
3.16E+07	1.82E+04	5.25E-02
1.00E+08	1.70E+04	6.85E-02
3.16E+08	1.56E+04	5.96E-02
1.00E+09	1.48E+04	2.13E-02
3.16E+09	1.48E+04	7.15E-04
1.00E+10	1.48E+04	-

Source: FHWA.

B. Numerical solution for finding the slope of the relaxation modulus curve in log-log scale.

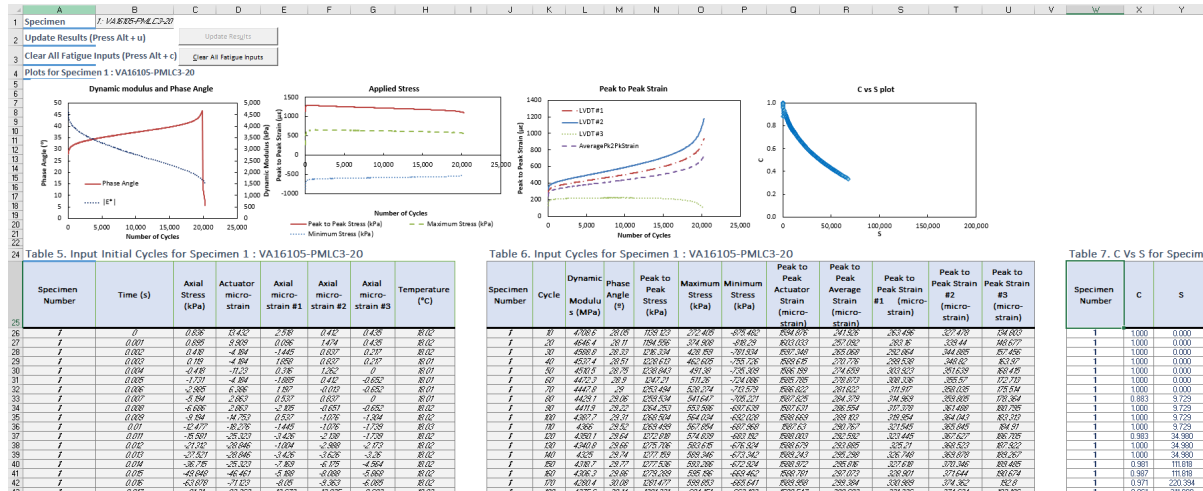
Figure 225. Screenshot. Alpha calculation.

Fatigue Data Validity

FlexMAT processes the cyclic fatigue test results output from the AMPT and then calculates the S-VECD fatigue model coefficients. After the cyclic fatigue test data are input through the Input

Data tab, the Fatigue Data Validity tab presents the intermediate analysis results for the cyclic fatigue tests.

Figure 226 presents a screenshot of the Fatigue Data Validity tab. The results from each individual specimen can be reviewed independently by selecting the specimen ID from the dropdown list in cell B1. The following paragraphs provide detailed information also presented in the rest of the Fatigue Data Validity tab.



Source: FHWA.

Figure 226. Screenshot. Fatigue Data Validity tab.

Table 5 in the Fatigue Data Validity tab screenshot presents the input test data for the first loading path in a cyclic fatigue test. The data in this table along with Prony fit are used to calculate the pseudostrain for the first loading path. Table 6 in the screenshot shows the cyclic data loaded from the Input Data tab. Users can modify (not delete) any erroneous data in Table 5 and Table 6 (using, e.g., the interpolation technique between good adjacent data points). These tables should not contain any blank rows. The charts at the top of Table 6 will show any modifications made in Table 6.

The Update Results command button will be enabled if Table 5 and/or Table 6 have any user modifications. Clicking the Update Results button after making any data modifications will refresh the cyclic fatigue test results in the Output Fatigue worksheet. The Clear All Fatigue Inputs button can be used to clear all user inputs of the cyclic fatigue test data and start fresh with the loading fatigue data.

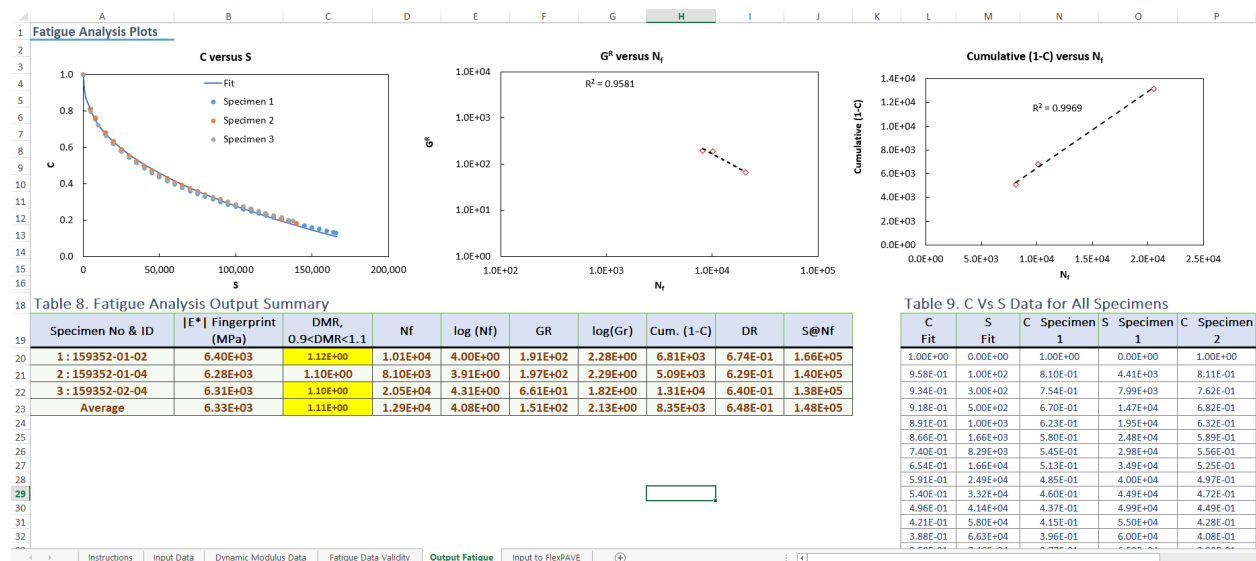
Four graphs are presented in the Fatigue Data Validity tab for evaluating the individual cyclic fatigue test data. The figures with the titles of Dynamic Modulus and Phase Angle and Peak to Peak Strain can be reviewed here. The phase angle versus number of cycles plot should display as a clear peak corresponding to an increase in the rate of the dynamic modulus reduction, similar to the results displayed in the graph shown in figure 226. In the Peak to Peak Strain figure, the peak-to-peak strain of the three linear variable differential transformers should generally show good agreement until the specimen approaches failure. The results shown in the graphs in figure 226 represent an acceptable test.

Pseudostiffness (C) and damage parameter (S) are calculated based on the imported test data shown in Table 5 and Table 6 in the Fatigue Data Validity. The C versus S plot presents the damage evolution curve. The damage evolution curve in the graph should resemble the general shape of the curve shown in figure 226.

Output Fatigue

The Output Fatigue tab presents the failure criteria parameters and optimizes the damage characteristic curve model coefficients.

Figure 227 shows a screenshot of the Output Fatigue tab. The quality of the damage characteristic curve model fit and repeatability of cyclic fatigue test results can be observed in the C versus S graph. The C versus S curves from all the cyclic fatigue tests should be in good agreement, similar to the results presented in figure 227. The failure criteria parameters are calculated automatically. The pseudostrain energy release rate (G^R) versus N_f and $Cumulative (1 - C)$ versus N_f graphs also can be used to assess sample-to-sample variability. The relationship between G^R and N_f should be linear in log space. The relationship between $Cumulative (1 - C)$ and N_f should be linear in arithmetic space. Thus, the repeatability of the cyclic fatigue tests can be assessed by the R^2 values reported in the G^R versus N_f and $Cumulative (1 - C)$ versus N_f graphs, and outliers can be identified by observing deviations from the trend line of the other data points in these plots. The results presented in figure 227 demonstrate good repeatability.



Source: FHWA.

Figure 227. Screenshot. Output Fatigue tab.

The dynamic modulus ratio (DMR) value of each fatigue test is reported in Table 8, Fatigue Analysis Output Summary, shown in the screenshot. The DMR values represent the consistency between the cyclic fatigue test specimens and the dynamic modulus test specimens. The DMR values should be between 0.9 and 1.1. A DMR value outside this range could indicate an invalid

test. If the DMR value exceeds the limit, the corresponding cell will change to yellow as a warning sign, as shown in figure 227.

Input to FlexPAVE

The Input to FlexPAVE tab provides a summary of the dynamic modulus and fatigue analysis results that can be used as inputs to the FlexPAVE pavement analysis software. Clicking the button within the Input to FlexPAVE tab will generate a material input file that can be imported directly into FlexPAVE™. No data entry is required, however, and using this tab is optional.

Figure 228 shows a screenshot of the Input to FlexPAVE tab. Clicking the Export FlexPAVE Dyn. Modulus Inputs button exports a dynamic modulus material input file for use in FlexPAVE. Clicking the Export FlexPAVE Fatigue Inputs button exports a fatigue material input file for use in FlexPAVE. Upon clicking either button, a prompt will appear where a file name must be entered and a file directory must be selected to save the FlexPAVE input file.

Table 10. Linear Viscoelastic Properties	
Property	Value
E _{inf}	2.06E+04
Poisson's Ratio	0.30
T _{ref}	21.10
Shift Factor a ₁	7.10E-04
Shift Factor a ₂	-1.52E-01
Shift Factor a ₃	2.88E+00

Table 11. Prony Series	
Ti(s)	Ei (kPa)
2.00E+08	3.40E+03
2.00E+07	1.54E+03
2.00E+06	3.93E+03
2.00E+05	7.08E+03
2.00E+04	1.42E+04
2.00E+03	3.10E+04
2.00E+02	7.41E+04
2.00E+01	1.91E+05
2.00E+00	4.97E+05
2.00E-01	1.17E+06
2.00E-02	2.21E+06
2.00E-03	3.21E+06
2.00E-04	3.59E+06
2.00E-05	3.25E+06
2.00E-06	2.53E+06
2.00E-07	1.79E+06
2.00E-08	1.22E+06

FlexPAVE S-VECD Fatigue Properties	
alpha	3.63
C vs. S	
C11	6.36E-03
C12	4.11E-01
GR Failure Criterion	
gamma	1.69E+07
delta	-1.25
DR Failure Criterion	
DR	0.65
Damage Capacity	
S _{app}	11.12

Source: FHWA.

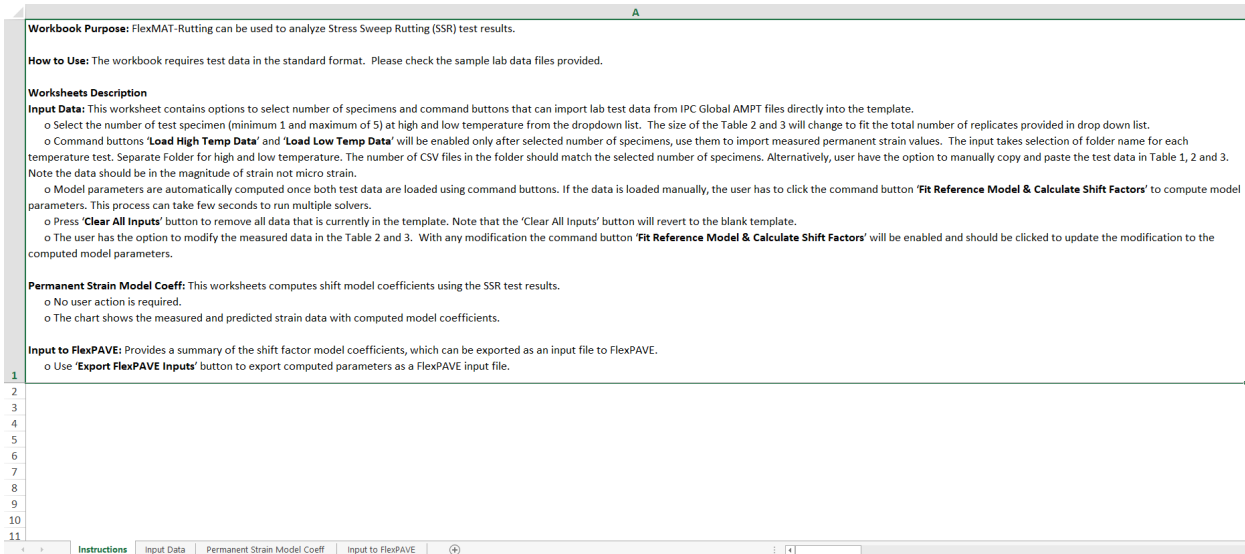
Figure 228. Screenshot. Input to FlexPAVE tab.

SSR TEMPLATE

The SSR FlexMAT template contains four tabs: Instructions, Input Data, Permanent Strain Model Coeff, and Input to FlexPAVE. The template is designed so that it works from the leftmost tab to the rightmost tab sequentially. The following four sections provide specific instructions for using each tab.

Instructions

The Instructions tab provides general instructions for using the FlexMAT template shown in Figure 229. The Input to FlexPAVE tab provides a summary of the shift model coefficients that can be used as inputs to the FlexPAVE pavement analysis software. Clicking the button within the Input to FlexPAVE tab generates a material input file that can be imported directly into FlexPAVE.



Source: FHWA.

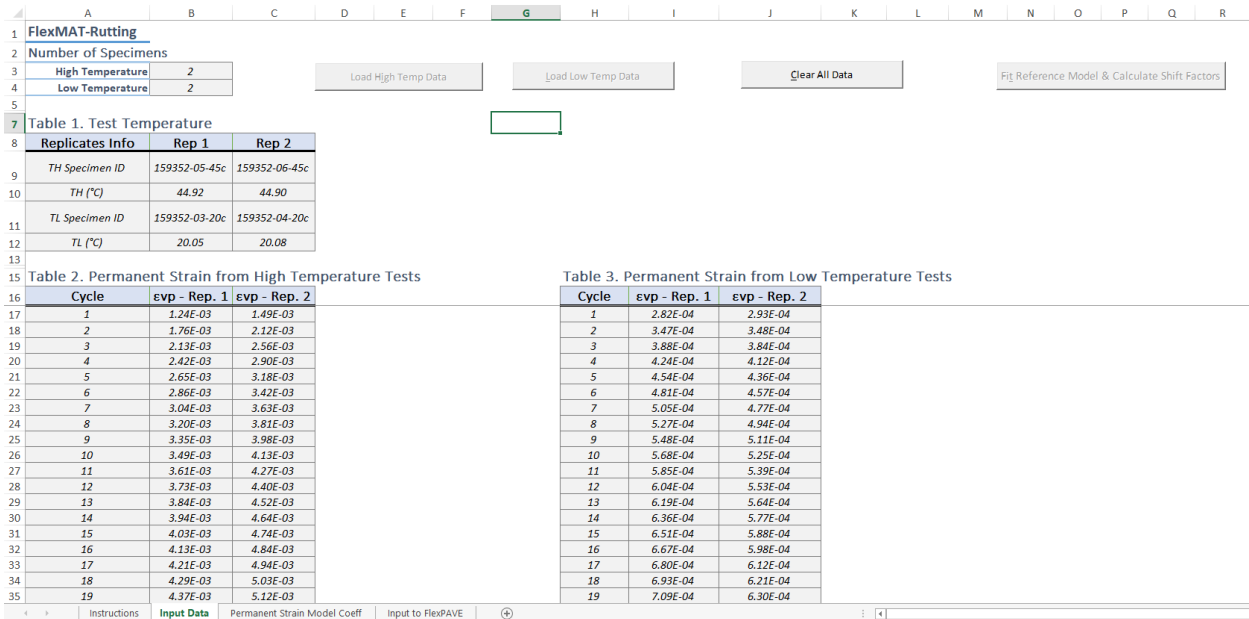
Figure 229. Screenshot. Instructions tab.

Input Data

The Input Data tab should be used to automatically import the SSR test results and optimize the shift model parameters to these test results. The FlexMAT template requires using the exported data files for SSR tests from the AMPT. The input files must be placed in one of two folders. All high-temperature test data must be placed into a single folder and all low-temperature test data must be placed into a single, but different folder from the high-temperature test data. No data entry is required for the other tabs because all necessary data will be imported through the Input Data tab.

Figure 230 shows a screenshot of the Input Data tab. If data are already loaded into the spreadsheet, clicking the Clear All Data button will clear the previously imported data. The number of test replicates for the high- and low-temperature tests can be selected from the dropdown lists in cells B3 and B4, respectively. Clicking on the Load High Temp Data button will import data into the FlexMAT template and a prompt will appear. The appropriate folder for the high-temperature test data must be selected. The data from the rutting tests will be imported into the required cells within the FlexMAT template. This procedure should be repeated to import the low-temperature test data by clicking the Load Low Temp Data button. The reference model coefficients and the shift model coefficients will be automatically optimized and calculated after loading the data.

There is also an option to enter data manually. The data can be entered into the gray cells in the Input Data tab. If the data are entered manually, the Fit Reference Model & Calculate Shift Factors button must be clicked to compute the model parameters.

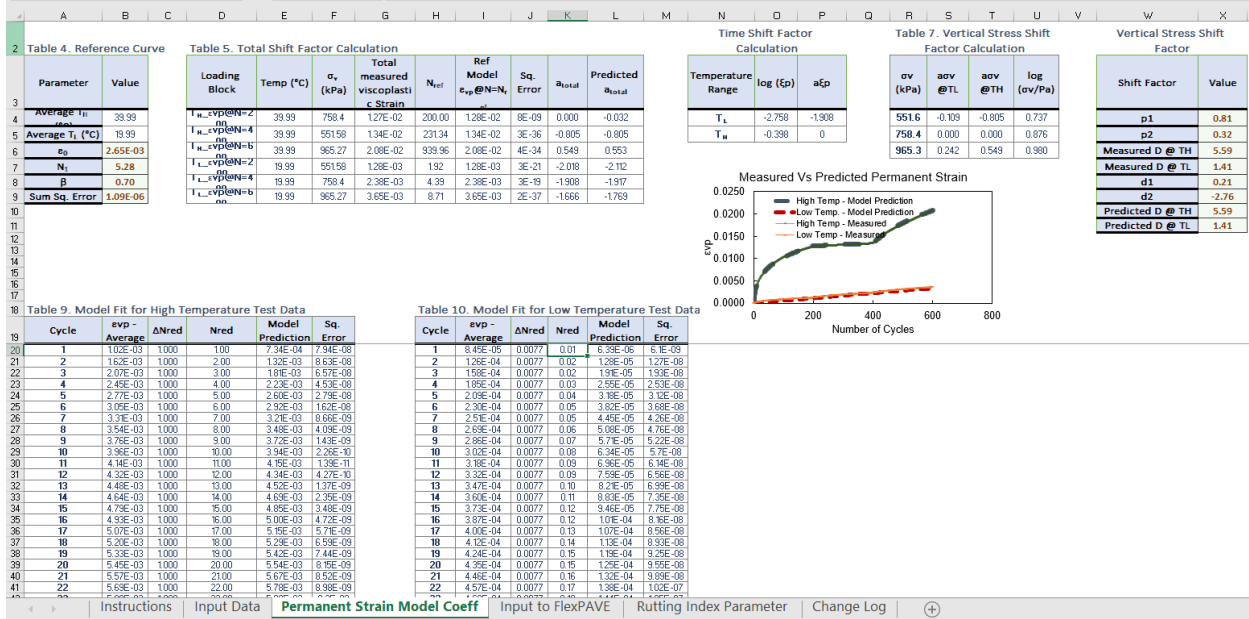


Source: FHWA.

Figure 230. Screenshot. Input Data tab.

Permanent Strain Model Coeff

The Permanent Strain Model Coeff tab shows the model coefficients and total shift factor. No data entry is required for this tab. The agreement between the measured data and shift model predictions can be visually in the graph shown in this tab. The graph presented in Figure 231 demonstrates acceptable shift model predictions of permanent strain.



Source: FHWA.

Figure 231. Screenshot. Permanent Strain Model Coeff tab.

Input to FlexPAVE

The Input to FlexPAVE tab provides a summary of the shift factor model coefficients, which can be exported as a material input file to FlexPAVE. No data entry is required. Using this tab is optional. Figure 232 shows a screenshot of the Input to FlexPAVE tab. Clicking on the Export FlexPAVE Inputs button will export a FlexPAVE input file. A prompt will appear where a file name must be entered and file directory must be selected to save the FlexPAVE input file.

	A	B	C	D	E	F	G
1							
2	Inputs to FlexPAVE						
3	Reference Model						
4	ϵ_0	2.65E-03					
5	N1	5.28					
6	β	0.70					
7							
8	Reduced Load Time Shift Factor Model						
9	p1	0.81					
10	p2	0.32					
11							
12	Vertical Stress Shift Factor Model						
13	d1	0.21					
14	d2	-2.76					
15							
16	Tref (°C)	39.99					
17	Export FlexPAVE Inputs (Press Alt + x)			Export FlexPAVE Inputs			
18							
19	Rutting Strain Index (RSI)						
20	State	FL					
21	City	DAYTONABEACH					
22	Layer Type	Intermediate Layer					
23	Calculate RSI (Press Alt + s)			Rutting Strain Index (RSI)			
24							

Source: FHWA.

Figure 232. Screenshot. Inputs to FlexPAVE tab.

Rutting Strain Index (RSI) shown in figure 233 is the rutting index parameter that has been developed under the FHWA’s project DTFH61-13-C-00025, Develop and Deploy PRS for Pavement Construction. RSI is the average permanent strain in percent and is defined as the ratio of the permanent deformation in an asphalt layer to the thickness of that layer at the end of a 20-yr pavement service life with 30 million 18-kip standard axle load repetitions for a standard pavement structure.⁽¹²⁸⁾

	A	B
1	Rutting Strain Index (RSI)	
2	Layer Type:	Intermediate Layer
3	State:	FL
4	City:	DAYTONABEACH
5	RSI for 20 year Traffic:	3.18%
7		
8	Table 11. Average Permanent Strain Over 20 years	
9	Time (Month)	Average Permanent Strain
10	0	0.00E+00
11	1	5.32E-03
12	2	7.09E-03
13	3	8.14E-03
14	4	8.93E-03
15	5	9.59E-03
16	6	1.01E-02
17	7	1.06E-02
18	8	1.10E-02
19	9	1.13E-02
20	10	1.17E-02
21	11	1.20E-02
22	12	1.25E-02
23	13	1.31E-02

Source: FHWA.

Figure 233. Screenshot. Rutting Strain Index parameter tab.

REFERENCES

1. Choi, Y.T. and Kim, Y.R. (2013). “Development of a Calibration Testing Protocol for the Permanent Deformation Model of Asphalt Concrete.” *Transportation Research Record: Journal of the Transportation Research Board*, 2373, pp. 34–43, Transportation Research Board, Washington, DC.
2. Underwood, B.S., Kim, Y.R., Savadatti, S., Thirunavukkarasu, S., and Guddati, M.N. (2009). “Simplified Fatigue Performance Modeling of ALF Pavements Using VECD+ 3-D Finite Element Modeling.” Presented at the 7th International RILEM Symposium on Advanced Testing and Characteristic of Bituminous Materials, Rhodes, Greece.
3. Lee, H.J and Kim, Y.R. (1998). “Viscoelastic Constitutive Model for Asphalt Concrete Under Cyclic Loading.” *Journal of Engineering Mechanics*, 124(1), pp. 32–40, American Society of Civil Engineers, Reston, VA.
4. Lee, H.J. and Kim, Y.R. (1998). “Viscoelastic Continuum Damage Model of Asphalt Concrete with Healing.” *Journal of Engineering Mechanics*, 124(11), American Society of Civil Engineers, Reston, VA.
5. Daniel, J.S. and Kim, Y.R. (2002). “Development of a Simplified Fatigue Test and Analysis Procedure Using a Viscoelastic Continuum Damage Model.” *Asphalt Paving Technology*, 71, pp. 619–650, Association of Asphalt Paving Technologists, Lino Lakes, MN.
6. Chehab, G. R., Kim, Y.R., Schapery, R.A., Witczack, M., and Bonaquist, R. (2003). “Characterization of Asphalt Concrete in Uniaxial Tension Using a Viscoelastoplastic Model.” *Asphalt Paving Technology*, 72, pp. 315–355, Association of Asphalt Paving Technologists, Lino Lakes, MN.
7. Underwood, B.S., Kim, Y.R., and Guddati, M.N. (2006). “Characteristic and Performance Prediction of ALF Mixtures Using a Viscoelastoplastic Continuum Damage Model.” *Asphalt Paving Technology*, Association of Asphalt Paving Technologists, 75, pp. 577–636, Association of Asphalt Paving Technologists, Lino Lakes, MN.
8. American Association of State Highway and Transportation Officials. (2014). *Standard Method of Test for Determining the Damage Characteristic Curve of Asphalt Concrete from Direct Tension Cyclic Fatigue Tests*, Report No. TP 107, American Association of State Highway and Transportation Officials, Washington, DC.
9. American Association of State Highway and Transportation Officials. (2017). *Standard Method of Test for Determining the Dynamic Modulus and Flow Number for Hot Mix Asphalt (HMA) Using the Asphalt Mixture Performance Tester (AMPT)*, Report No. T 378-17, American Association of State Highway and Transportation Officials, Washington, DC.

10. American Association of State and Highway Transportation Officials. (2017). *Developing Dynamic Modulus Master Curves for Asphalt Mixtures Using the Asphalt Mixture Performance Tester (AMPT)*, Report No. R 84-17, American Association of State Highway and Transportation Officials, Washington, DC.
11. Wang, Y. and Kim, Y.R. (2017). “Development of a Pseudo Strain Energy-Based Fatigue Failure Criterion for Asphalt Mixtures.” *International Journal of Pavement Engineering*, 20(10), pp. 1182–1192, Taylor and Francis, Oxfordshire, UK.
12. Subramanian, V. (2011). “A Viscoplastic Model with Rate-Dependent Hardening for Asphalt Concrete in Compression.” Ph.D. diss., North Carolina State University.
13. Choi, Y. and Kim, Y.R. (2013). “Development of Characterisation Models for Incremental Permanent Deformation Model for Asphalt Concrete in Confined Compression.” *Road Materials and Pavement Design*, 14, pp. 266–288, Taylor and Francis, Oxfordshire, UK.
14. Chamberlain, W.P. (1995). *Performance-Related Specifications for Highway Construction and Rehabilitation*, NCHRP Synthesis Report No. 212, Transportation Research Board, Washington, DC.
15. Hughes, C.S. (2005). *State Construction Quality Assurance Programs*, NCHRP Synthesis Report No. 346, Transportation Research Board, Washington, DC.
16. Fernando, E.G., Anderson, D.A., Luhr, D.R., Antle, C.E., and Siddiqui, Z. (1987). “A Conceptual Framework for Development of Performance-Based Specifications.” *Asphalt Paving Technology*, 56, Association of Asphalt Paving Technologists, Lino Lakes, MN.
17. Epps, J.A., Hand, A., Seeds, S., Schulz, T., Alavi, S., Ashmore, C., Monismith, C.L., et al. (2002). *Recommended Performance-Related Specification for Hot-Mix Asphalt Construction: Results of the WesTrack Project*, NCHRP Report No. 455, Transportation Research Board, Washington, DC.
18. Chen, D.H., Scullion, T., Bilyeu, J., Yuan, D., and Nazarian, S. (2002). “Forensic Study of Warranty Project on US82.” *Journal of Performance of Constructed Facilities*, 16(1), American Society of Civil Engineers, Reston, CA.
19. Kopac, P.A. (2002). “Making Roads Better and Better.” *Public Roads*, 66(1), pp. 25–29, FHWA, Washington, DC.
20. Rao, S., Smith, K.L., and Darter, M.I. (2007). *Development and Implementation of a Performance-Related Specification for a Jointed Plain Concrete Pavement—I-39/90/94 Madison, Wisconsin*, Report No. WI/SPR-01-06, Wisconsin Department of Transportation, Madison, WI.
21. Darter, M.I., Abdelrahman, M., Okamoto, P.A., and Smith, K.D. (1993). *Performance-Related Specifications for Concrete Pavements: Volume I—Development of a Prototype*

- Performance-Related Specification*, Report No. FHWA-RD-93-042, Federal Highway Administration, Washington, DC.
22. Scott S., Konrath, L., Ferragut, T., and Loulakis, M. (2013). *Performance Specifications for Rapid Highway Renewal*, Report No. S2-R07-RR-1, Transportation Research Board, Washington, DC.
 23. Fugro Consultants, Inc. and Arizona State University. (2011). *A Performance-Related Specification for Hot-Mixed Asphalt*, NCHRP Report No. 704. Transportation Research Board, Washington, DC.
 24. Shook, J., Diaz, M., Stroup-Gardiner, M., and Seeds, S. (1993). *Performance-Related Specifications for Asphalt Concrete – Phase II*, Report No. FHWA-RD-91-070, Federal Highway Administration, Washington, DC.
 25. ARA, Inc. (2004). *Guide for Mechanistic-Empirical Design of New and Rehabilitated Pavement Structure*, NCHRP Report No. 1-37A, Transportation Research Board, Washington, DC.
 26. Gibson, N., Qi, X., Shenoy, A., Al-Khateeb, G., Kutay, M.E., Andriescu, A., Stuart, K., et al. (2012). *Performance Testing on Superpave and Structural Validation*, Report No. FHWA-HRT-11-042, Federal Highway Administration, Washington, DC.
 27. West, R., Timm, D., Willis, R., Powell, B., Robbins, M., Taylor, A.J., Smit, A., et al. (2009). *Phase III NCAT Test Track Findings*, Report No. 09-08, National Center for Asphalt Technology, Auburn, AL.
 28. West, R., Timm, D., Willis, R., Powell, B., Tran, N., Watson, D., Sakhaeifar, M., et al. (2012). *Phase IV NCAT Pavement Test Track Findings*, Report No. 10-12, National Center for Asphalt Technology, Auburn, AL.
 29. Seo, Y. (2010). “Distress Evolution in Highway Flexible Pavements: A 5-Year Study at the Korea Highway Corporation Test Road.” *Journal of Testing and Evaluation*, 38(1), pp. 1–10, ASTM International, West Conshohocken, PA.
 30. Cao, W., Norouzi, A., and Kim, Y.R. (2016). “Application of Viscoelastic Continuum Damage Approach to Predict Fatigue Performance of Binzhou Perpetual Pavements.” *Journal of Traffic and Transportation Engineering*, 3(2), pp 104–115, Elsevier, Amsterdam, Netherlands.
 31. Prowell, B.D. and Brown, E.R. (2007). *Superpave Mix Design: Verifying Gyration Levels in the N_{design} Table*, NCHRP Report No. 573, Transportation Research Board, Washington, DC.
 32. Blankenship, P.B. (1993). “Gyratory Compaction Characteristics: Relation to Service Densities of Asphalt Mixtures.” Master’s thesis, University of Kentucky.

33. ASTM International. (2009). *Standard Practice for Sampling Bituminous Paving Materials*, Report No. D-979. ASTM International, West Conshohocken, PA.
34. ASTM International. (2009). *Standard Practice for Random Sampling of Construction Materials*, Report No. D-3665. ASTM International, West Conshohocken, PA.
35. ASTM International. (2011). *Standard Practice for Reducing Samples of Aggregate to Testing Size*, Report No. C-702. ASTM International, West Conshohocken, PA.
36. American Association of State Highway and Transportation Officials. (2008). *Standard Method of Preparing and Determining the Density of Asphalt Mixture Specimens by Means of the Superpave Gyrotory Compactor*, Report No. T 312, American Association of State Highway and Transportation Officials, Washington DC.
37. American Association of State Highway and Transportation Officials. (2015). *Standard Method of Test for Determining Dynamic Modulus of Hot Mix Asphalt (HMA)*, Report No. T 342-11, American Association of State Highway and Transportation Officials, Washington, DC.
38. Park, S.W., Kim, Y.R., and Schapery, R.A. (1996). "A Viscoelastic Continuum Damage Model and Its Application to Uniaxial Behavior of Asphalt Concrete." *Mechanics of Materials*, 24(4), pp. 241–255, Elsevier, Amsterdam, Netherlands.
39. Bari, K. (2005). "Development of a New Revised Version of the Witczak E* Predictive Models for Hot Mix Asphalt Mixtures." Ph.D. diss., Arizona State University.
40. Kweon, G. and Kim, Y.R. (2006). "Determination of the Complex Modulus of Asphalt Concrete Using the Impact Resonance Test." *Transportation Research Record: Journal of the Transportation Research Board*, 1970, pp. 151–160, Transportation Research Board, Washington, DC.
41. ASTM International. (2002). *Standard Test Method for Fundamental Transverse, Longitudinal and Torsional Resonant Frequencies of Concrete Specimens*, Report No. C215-08, ASTM International, West Conshohocken, PA.
42. Lacroix, A. and Kim, Y.R. (2009). "Constructing the Dynamic Modulus Mastercurve Using Impact Resonance Testing." *Asphalt Paving Technology*, 78, pp. 67–95, Association of Asphalt Paving Technologists, Lino Lakes, MN.
43. Gudmarsson, A., Ryden, N., and Birgisson, B. (2012). "Application of Resonant Acoustic Spectroscopy to Asphalt Concrete Beams for Determination of the Dynamic Modulus." *Materials and Structures*, 45, pp. 1903–1913, Springer, Berlin, Germany.
44. Gudmarsson, A., Ryden, N., and Birgisson, B. (2013). "Nondestructive Evaluation of the Complex Modulus Master Curve of Asphalt Concrete Specimens." *AIP Conference Proceedings*, 1511, pp. 1301, AIP Publishing, Melville, NY.

45. Ryden, N. (2009). "Determining the Asphalt Mastercurve From Free-Free Resonant Testing on Cylindrical Samples." Presented at the 7th International Symposium on Nondestructive Testing in Civil Engineering, Nantes, France.
46. ASTM International. (2009). *Standard Test Method for Dynamic Young's Modulus, Shear Modulus and Poisson's Ratio by Impulse Excitation of Vibration*, Report No. E1876-09. ASTM International, West Conshohocken, PA.
47. Leming, M.L., Nau, J.M., and Fukuda, J. (1996). "Nondestructive Determination of the Dynamic Modulus of Concrete Disks." *Materials Journal*, 95(1), pp. 50–57, American Concrete Institute, Farmington Hills, MI.
48. Hutchinson, J.R. (1979). "Axisymmetric Flexural Vibrations of a Thick Free Circular Plate." *Journal of Applied Mechanics*, 46(1), pp. 139–144, American Society of Mechanical Engineers, New York, NY.
49. Schapery, R.A. (1990). "A Theory of Mechanical Behavior of Elastic Media with Growing Damage and Other Changes in Structure." *Journal of Mechanics and Physics of Solids*, 38(2), pp. 215–253, Elsevier, Amsterdam, Netherlands.
50. Underwood, B.S., Kim, Y.R., and Guddati, M.N. (2010). "Improved Calculation Method of Damage Parameter in Viscoelastic Continuum Damage Model." *International Journal of Pavement Engineering*, 11, pp. 459–476, Taylor and Francis, Oxfordshire, UK.
51. Reese, R. (1997). "Properties of Aged Asphalt Binder Related to Asphalt Concrete Fatigue Life." *Asphalt Paving Technology*, 66, pp. 604–632, Association of Asphalt Paving Technologists, Lino Lakes, MN.
52. Bonnaure, F., Gravois, A., and Udron, J. (1980). "A New Method for Predicting the Fatigue Life of Bituminous Mixes." *Asphalt Paving Technology*, 49, pp. 499–529, Association of Asphalt Paving Technologists, Lino Lakes, MN.
53. Allen, D.H. and Searcy, C.R. (2001). "A Micromechanical Model for a Viscoelastic Cohesive Zone." *International Journal of Fracture*, 107, pp. 159–176, Springer, Berlin, Germany.
54. Castelo Branco, V.T.F., Masad, E., Bhasin, A., and Little, D.N. (2008). "Fatigue Analysis of Asphalt Mixtures Independent of Mode of Loading." Presented at the 87th Annual Transportation Research Board Meeting, Transportation Research Board, Washington, DC.
55. Masad, E., Castelo Branco, V.T.F., Little, D.N., and Lytton, R.L. (2008). "A Unified Method for Analysis of Controlled-Strain and Controlled-Stress Fatigue Testing." *International Journal of Pavement Engineering*, 9(4), pp. 233–246, Taylor and Francis, Oxfordshire, UK.

56. Kim, Y. (2011). "Cohesive Zone Model to Predict Fracture in Bituminous Materials and Asphaltic Pavements: State-Of-The-Art Review." *International Journal of Pavement Engineering*, 12(4), pp. 343–356, Taylor and Francis, Oxfordshire, UK.
57. Chiangmai, C.N. and Buttlar, W.G. (2015). "Cyclic Loading Behavior of Asphalt Concrete Mixture Using Disk-Shaped Compact Tension (DC(T)) Test and Released Energy Approach." *Asphalt Paving Technology*, 84, pp. 593–614, Association of Asphalt Paving Technologists, Lino Lakes, MN.
58. Kim, Y.R. and Little, D.N. (1990). "One-Dimensional Constitutive Modeling of Asphalt Concrete." *Journal of Engineering Mechanics*, 116(4), pp. 751–772, American Society of Civil Engineers, Reston, VA.
59. Zhang, J., Sabouri, M., Kim, Y.R., and Guddati, M.N. (2013). "Development of a Failure Criterion for Asphalt Mixtures Under Fatigue Loading." Presented at the 88th Association of Asphalt Paving Technologists' Annual Meeting, Denver, CO.
60. Gudipudi, P., and Underwood, B.S., (2016). "Reliability Analysis of Fatigue Life Prediction from the Viscoelastic Continuum Damage Model." *Transportation Research Record: Journal of the Transportation Research Board*, 2576, pp. 91–99. Transportation Research Board, Washington DC.
61. Shen, S. and Carpenter, S.H. (2005). "Application of Dissipated Energy Concept in Fatigue Endurance Limit Testing." *Transportation Research Record: Journal of the Transportation Research Board*, 1929, pp. 165–173, Transportation Research Board, Washington, DC.
62. Bhasin, A., Castelo Branco, V.T.F., Masad, E., and Little, D.N. (2009). "Quantitative Comparison of Energy Methods to Characterize Fatigue in Asphalt Materials." *Journal of Materials in Civil Engineering*, 21(2), pp. 461–470, American Society of Civil Engineers, Reston, VA.
63. Hou, T., Underwood, B.S., and Kim, Y.R. (2010). "Fatigue Performance Prediction of North Carolina Mixtures Using Simplified Viscoelastic Continuum Damage Model." *Asphalt Paving Technology*, 79, pp. 35–80, Association of Asphalt Paving Technologists, Lino Lakes, MN.
64. Schapery, R.A. (1984). "Correspondence Principles and a Generalized J-integral for Large Deformation and Fracture Analysis of Viscoelastic Media." *International Journal of Fracture*, 25, pp. 195–223, Springer, Berlin, Germany.
65. Sabouri, M. and Kim, Y.R. (2014). "Development of Failure Criterion for Asphalt Mixtures Under Different Modes of Fatigue Loading." *Transportation Research Record: Journal of the Transportation Research Board*, 2447, pp. 117–125, Transportation Research Board, Washington, DC.
66. Wang, Y., Norouzi, A.H., and Kim, Y.R. (2016). "Comparison of Fatigue Cracking Performance of Asphalt Pavements Predicted by Pavement ME and LVECD Programs."

- Transportation Research Record: Journal of the Transportation Research Board*, 2590, pp. 44–55, Transportation Research Board, Washington, DC.
67. Lee, K., Pape, S., Castorena, C., and Kim, Y.R. (2017). “Evaluation of Small Specimen Geometries for Asphalt Mixture Performance Testing and Pavement Performance Prediction.” *Transportation Research Record: Journal of the Transportation Research Board*, 2631, pp. 74–82, Transportation Research Board, Washington, DC.
 68. Wang, Y.D., Keshavarzi, B., and Kim, Y.R. (2018). “Fatigue Performance Prediction of Asphalt Pavements with FlexPAVE™, the S-VECD Model, and DR Failure Criterion.” *Transportation Research Record: Journal of the Transportation Research Board*, 2672, pp. 217–227, Transportation Research Board, Washington, DC.
 69. Desai, C.S., Somasundaram, S., and Frantziskonis, G. (1986). “A Hierarchical Approach for Constitutive Modelling of Geologic Materials.” *International Journal for Numerical and Analytical Methods*, 10(3), pp. 225–257, Wiley, Hoboken, NJ.
 70. Gibson, N.H. (2006). “A Viscoelastoplastic Continuum Damage Model for the Compressive Behavior of Asphalt Concrete.” Ph.D. diss., University of Maryland.
 71. Yun, T. and Kim, Y.R. (2011). “Experimental Investigation of Rate-Dependent Hardening-Softening Behavior of Hot Mix Asphalt in Compression.” *Road Materials and Pavement Design*, 12(1), pp. 99–114, Taylor and Francis, Oxfordshire, UK.
 72. Darabi, M.K., Al-Rub, R.K., Masad, E.A., Huang, C., and Little, D.N. (2012). “A Modified Viscoplastic Model to Predict the Permanent Deformation of Asphaltic Materials Under Cyclic-Compression Loading at High Temperatures.” *International Journal of Plasticity*, 35, pp. 100–134, Elsevier, Amsterdam, Netherlands.
 73. Yun, T. (2008). “Development of a Viscoplastic Constitutive Model Using a Rate-Dependent Yield Criterion for HMA in Compression.” Ph.D. diss., North Carolina State University.
 74. Von Quintus, H.L., Mallela, J., Bonaquist, R., Schwartz, C.W., and Carvalho, R.L. (2012). *Calibration of Rutting Models for Structural and Mix Design*, NCHRP Report No. 719, Transportation Research Board, Washington, DC.
 75. Choi, Y., Subramanian, V., Guddati, M., and Kim, Y.R. (2012). “An Incremental Model for the Prediction of Permanent Deformation of Asphalt Concrete in Compression.” *Transportation Research Record: Journal of the Transportation Research Board*, Transportation Research Board, Washington, DC.
 76. Chehab, G., Kim, Y.R., Schapery, R.A., Witzack, M., and Bonaquist, R. (2002). “Time-Temperature Superposition Principle for Asphalt Concrete Mixtures with Growing Damage in Tension State.” *Asphalt Paving Technology*, 71, pp. 559–593, Association of Asphalt Paving Technologists, Lino Lakes, MN.

77. Zhao, Y. and Kim, Y.R. (2003). "Time-Temperature Superposition for Asphalt Mixtures with Growing Damage and Permanent Deformation in Compression." *Transportation Research Record: Journal of the Transportation Research Board*, 1832, pp. 161–172, Transportation Research Board, Washington, DC.
78. Schwartz, C.W., Gibson, N., and Schapery, R.A. (2002). "Time-Temperature Superposition for Asphalt Concrete at Large Compressive Strains." *Transportation Research Record: Journal of the Transportation Research Board*, 1789, pp. 101–112, Transportation Research Board, Washington, DC.
79. Yun, T., Underwood, B.S., and Kim, Y.R. (2010). "Time-Temperature Superposition for HMA With Growing Damage and Permanent Strain in Confined Tension and Compression." *Journal of Materials in Civil Engineering*, 22(5), pp. 415–422, American Society of Engineers, Reston, VA.
80. Schapery, R.A. (1969). "On the Characteristic of Nonlinear Viscoelastic Materials." *Polymer Engineering and Science*, 9(4), pp. 295–310, Wiley, Hoboken, NJ.
81. Haj-Ali, R.M. and Mulianan, A.H. (2004). "Numerical Finite Element Formulation of the Schapery Non-linear Viscoelastic Material Model." *International Journal for Numerical Methods in Engineering*, 59(1), pp. 25–45, Wiley, Hoboken, NJ.
82. Mahmoud, F.F. et al. (2012). "A Numerical Solution for Contact Problem with Finite Deformation in Nonlinear Schapery Viscoelastic Solids." *Ain Shams Engineering Journal*, 3(2), pp. 141–151, Elsevier, Amsterdam, Netherlands.
83. Saadeh, S., Masad, E.A., and Little, D.N. (2007). "Characterization of Asphalt Mix Response under Repeated Loading Using Anisotropic Nonlinear Viscoelastic-Viscoplastic Model." *Journal of Materials in Civil Engineering*, 19(10), pp. 912–924, American Society of Civil Engineers, Reston, VA.
84. Huang, C., Masad, E.A., Muliana, A.H., and Bahia, H. (2007). "Nonlinearly Viscoelastic Analysis of Asphalt Mixes Subjected to Shear Loading." *Mechanics of Time-Dependent Materials*, 11(2), pp. 91–110, Springer, Berlin, Germany.
85. Akinary, A.E. and Brostow, W. (2001). "Long-Term Service Performance of Polymeric Materials from Short-Term Tests: Prediction of the Stress Shift Factor from a Minimum of Data." *Polymer Engineering and Science*, 42(10), pp. 4527–4532, Wiley, Hoboken, NJ.
86. Akinary, A.E., Brostow, W., and Maksimov, R. (2001). "Prediction of Long-Term Service Performance of Polymeric Materials from Short-Term Tests: Creep and Prediction of the Stress Shift Factor of a Longitudinal Polymer Liquid Crystal." *Polymer Engineering and Science*, 41(6), pp. 977–981, Wiley, Hoboken, NJ.
87. Brostow W. (2000). "Time-Stress Correspondence in Viscoelastic Materials: An Equation for the Stress and Temperature Shift Factor." *Materials Research Innovations*, 3(6), pp. 347–351, Springer, Berlin, Germany.

88. Wenbo, L., Ting-Qing, Y., and Aunli, A. (2001). "Time-Temperature-Stress Equivalence and Its Application to Nonlinear Viscoelastic Materials." *Acta Mechanica Solida Sinica*, 14(3), pp. 95–199, Springer, Berlin, Germany.
89. Jazouli, S., Wenbo, L., Bremand, F., and Vu-Khanh, T. (2005). "Application of Time-Stress Equivalence to Nonlinear Creep of Polycarbonate." *Polymer Testing*, 24(4), pp. 463–467, Elsevier, Amsterdam, Netherlands.
90. Azari, H. and Mohseni, A. (2012). "Incremental Repeated Load Permanent Deformation Testing of Asphalt Mixtures." Presented at the Transportation Research Board 91st Annual Meeting, Washington, DC.
91. Choi, Y.T. and Kim, Y.R. (2013). "A Mechanistic Permanent Deformation Model for Asphalt Concrete in Compression." *Asphalt Paving Technology*, 82, pp. 617–649, Association of Asphalt Paving Technologists, Lino Lakes, MN.
92. Hao, W., Al-Qadi, I.L., and Stanciulescu, I. (2012). "Simulation of Tyre-Pavement Interaction for Predicting Contact Stresses at Static and Various Rolling Conditions." *International Journal of Pavement Engineering*, 13(4), pp. 310–321, Taylor and Francis, Oxfordshire, UK.
93. De Beer, M., Fisher, C., and Jooste, F.J. (1997). "Determination of Pneumatic Tire Pavement Interface Contact Stresses Under Moving Loads and Some Effects on Pavements with Thin Asphalt Surfacing Layers." Presented at the 8th International Conference on Asphalt Pavement, Seattle, WA.
94. LTPPBind: A New Tool for Selecting Cost Effective Superpave Asphalt Binder Performance Grades. (1999). Federal Highway Administration, Research, Development & Technology, Turner-Fairbank Highway Research Center, McLean, VA.
95. Eslaminia, M., Thirunavukkarasu, S., Guddati, M.N., and Kim, Y.R. (2012). "Accelerated Pavement Performance Modeling Using Layered Viscoelastic Analysis." Presented at the 7th International RILEM Conference on Cracking in Pavements, Delft, Netherlands.
96. American Association of State Highway and Transportation Officials. (2017). *Standard Practice for Preparation of Cylindrical Performance Test Specimens Using the Superpave Gyrotory Compactor (SGC)*, Report No. R 83-17, American Association of State Highway and Transportation Officials, Washington, DC.
97. Kim, D. and Kim, Y.R. (2017). "Development of Stress Sweep Rutting (SSR) Test for Permanent Deformation Characterization of Asphalt Mixture." *Construction and Building Materials*, 154, pp. 373–383, Elsevier, Amsterdam, Netherlands.
98. Mohseni, A. and Azari, H. (2014). *Effective Temperature for Permanent Deformation Testing of Asphalt Mixtures*. Taylor and Francis, Oxfordshire, UK.

99. Choi, Y. and Kim, Y.R. (2014). “Implementation and Verification of a Mechanistic Permanent Deformation Model (Shift Model) to Predict Rut Depths of Asphalt Pavement.” *Road Materials and Pavement Design*, 15, pp. 195–218, Taylor and Francis, Oxfordshire, UK.
100. Kim, D. (2015). “Modulus and Permanent Deformation Characterization of Asphalt Mixtures and Pavements.” Ph.D. diss., North Carolina State University.
101. Ashouri, M. (2014). “Modeling Microdamage Healing in Asphalt Pavement Using Continuum Damage Theory.” Ph.D. diss., North Carolina State University.
102. Prowell, B.D., Brown, E.R., Anderson, R.M., Daniel, J.S., Swamy, A.K., Quintus, H.V., Shen, S., et al. (2010). *Validating the Fatigue Endurance Limit for Hot Mix Asphalt*, NCHRP Report No. 646, Transportation Research Board, Washington, DC.
103. Lee, K., Castorena, C., and Kim, Y.R. (2018). “Improving the Reliability of Damage Characteristic Curves in the Simplified Viscoelastic Continuum Damage Model.” *Transportation Research Record: Journal of the Transportation Research Board*, 2672(28), pp. 493–502, Transportation Research Board, Washington, DC.
104. Zaghoul, S.M. and White, T. (1993). “Use of a Three-Dimensional, Dynamic Finite Element Program for Analysis of Flexible Pavement.” *Transportation Research Record: Journal of Transportation Research Board*, 1388, pp. 60–69, Transportation Research Board, Washington, DC.
105. Kim, Y.R., Guddati, M.N., Underwood, B.S., Yun, T.Y., Subramanian, V., and Savadatti, V. (2008). *Development of a Multiaxial VEPCD-FEP++*, Report No. FHWA-HRT-08-073, Federal Highway Administration, Washington, DC.
106. Huang, Y.H. (2003). *Pavement Analysis and Design*. Prentice-Hall, Englewood Cliffs, NJ, second edition.
107. Baek, C. (2010). “Investigation of Top-down Cracking Mechanisms Using the Viscoelastic Continuum Damage Finite Element Program.” Ph.D. diss., North Carolina State University.
108. Kim, Y. R. (2009). *Modeling of Asphalt Concrete*. McGraw Hill, Inc., New York, NY.
109. Wang, Y.D., Keshavarzi, B., and Kim, Y.R. (2018). “Fatigue Performance Analysis of Pavements with RAP Using Viscoelastic Continuum Damage Theory.” *KSCE Journal of Civil Engineering*, 22, pp. 2118–2125, Springer, Berlin, Germany.
110. American Association of State and Highway Transportation Officials. (2013). *Standard Practice for Developing Dynamic Modulus Master Curves for Hot Mix Asphalt*, Report No. R 62, American Association of State and Highway Transportation Officials, Washington, DC.

111. Norouzi, A. and Kim, Y.R. (2017). “Mechanistic Evaluation of the Fatigue Cracking in Asphalt Pavements.” *International Journal of Pavement Engineering*, 18(6), pp. 530–546, Taylor and Francis, Oxfordshire, UK.
112. Kim, D., Norouzi, A., Kass, S., Liske, T., and Kim, Y.R. (2017). “Mechanistic Performance Evaluation of Pavement Sections Containing RAP and WMA Additives in Manitoba.” *Construction and Building Materials*, 133, pp. 39–50, Elsevier, Amsterdam, Netherlands.
113. Porras, J., Hajj, E.Y., Sebaaly, P.E., Kass, S., and Liske, T. (2012). “Performance Evaluation of Field-Produced Warm-Mix Asphalt Mixtures in Manitoba, Canada.” *Transportation Research Record: Journal of the Transportation Research Board*, 2294, pp. 64–73, Transportation Research Board, Washington, DC.
114. Norouzi, A., Kim, D., and Kim, Y.R. (2016). “Numerical Evaluation of Pavement Design Parameters for the Fatigue Cracking and Rutting Performance of Asphalt Pavements.” *Materials and Structures*, 49, pp. 3619–3634, Springer, Berlin, Germany.
115. Shandong Highway Society, Shandong Traffic Science Research Institute, Qilu Transportation Development Group, Shandong Highway Construction Group. (2016). “Development and Application of Perpetual Pavement in Shandong Province.” Presented at the International Conference on Perpetual Pavements 2016, Shandong, China.
116. Tseng, K. and Lytton, R. (1989). “Prediction of Permanent Deformation in Flexible Pavement Materials,” in *Implication of Aggregates in the Design, Construction, and Performance of Flexible Pavements*, ed. H. Schreuders and C. Marek, pp. 154–172, ASTM International, West Conshohocken, PA.
117. Lytton, R.L., Luo, X., Saha, S., Chen, Y., Deng, Y., Gu, F., and Ling, M. (2019). *Proposed Enhancements to Pavement ME Design: Improved Consideration of the Influence of Subgrade and Unbound Layers on Pavement Performance*. NCHRP Report No. 1-53, Transportation Research Board, Washington, DC.
118. Lacroix, A. (2010). “Performance Prediction of the NCAT Test Track Pavements Using Mechanistic Models.” Ph.D. diss., North Carolina State University.
119. Eslaminia, M. and Guddati, M.N. (2012). “Fourier-Finite Element Analysis of Pavements Under Moving Vehicular Loading.” *International Journal of Pavement Engineering*, 17, pp. 1–13, Taylor and Francis, Oxfordshire, UK.
120. MATLAB® (2018). The MathWorks, Inc., Natick, MA.
121. Kim, D. and Kim, Y.R. (2017). “Determination of Dynamic Modulus Values of Asphalt Mixtures Using Impact Resonance Testing of Thin Disk Specimen.” *Journal of Testing and Evaluation*, 45(2). pp 509–520, ASTM International, West Conshohocken, PA.
122. Clough, R.W. and Penzien, J. (1993). *Dynamics of Structures*. McGraw-Hill, Inc., New York, NY, second edition.

123. Whitmoyer, S.L. and Kim, Y.R. (1994). "Determination of Elastic Properties of Asphalt Concrete Using Vibrational Analysis." *Journal of Testing and Evaluation*, 22(2) pp. 139–148, ASTM International, West Conshohocken, PA.
124. Schwartz, C.W., Li, R., Ceylan, H., Kim, S., and Gopalakrishnan, K. (2013). "Global Sensitivity Analysis of Mechanistic-Empirical Performance Predictions for Flexible Pavements." Presented at the 92nd Transportation Research Board Annual Meeting, Washington, DC.
125. Sakhaei Far, M. (2011). "Development of New Dynamic Modulus Predictive Models for Hot Mix Asphalt Mixtures." Ph.D. diss., North Carolina State University.
126. Wang, Y.D., Underwood, B.S., and Kim, Y.R. (2020). "Development of a Fatigue Index Parameter, Sapp, for Asphalt Mixes Using Viscoelastic Continuum Damage Theory." *International Journal of Pavement Engineering*. Available at: <https://www.tandfonline.com/doi/full/10.1080/10298436.2020.1751844>.
127. Federal Highway Administration. (2019). *FHWA Cyclic Fatigue Index Parameter for Asphalt Performance Engineered Mixture Design Tech Brief*, Report No. FHWA-HIF-19-091, Federal Highway Administration, Washington, DC.
128. Ghanbari, A., Underwood, B.S., and Kim, Y.R. (2020). "Development of a Rutting Index Parameter Based on the Stress Sweep Rutting Test and Permanent Deformation Shift Model." *International Journal of Pavement Engineering*. Available at: <https://www.tandfonline.com/doi/full/10.1080/10298436.2020.1748190>.

